Abstract

Title of Dissertation: TRANSIENT DYNAMICS OF HELICOPTER ROTOR WAKES USING A TIME-ACCURATE FREE-VORTEX METHOD

Mahendra J. Bhagwat, Doctor of Philosophy, 2001

Dissertation directed by: Professor J. Gordon Leishman
Department of Aerospace Engineering

A second-order accurate predictor-corrector type algorithm has been developed to obtain a time-accurate solution of the vortical wake generated by a helicopter rotor. The rotor blade flapping solution was fully integrated with the wake geometry solution using the same time-marching algorithm. The analysis was used to predict the locations of wake vortex filaments under transient flight conditions, where the rotor wake may not be periodic at the rotational frequency. Applications of this analysis include prediction of the rotor induced velocity field and blade airloads during transient flight and maneuvers.

The stability of the rotor wake structure is important from the perspective of free-vortex wake models. The wake stability was examined using a linearized stability analysis, and the rotor wake was shown to be physically unstable. Therefore, the stability of the numerical algorithm is an important consideration in developing robust

wake methodologies. Both the stability and accuracy of the numerical wake solutions algorithms was rigorously examined. The straight-line vortex segmentation used in the present analysis was shown to be second-order accurate. The overall numerical solution was also demonstrated to converge with a second-order accuracy. A technique for increasing the order of accuracy for high resolution solutions is also described.

Along with a formal (mathematical) verification of solution accuracy, the numerical solution for the rotor wake problem was compared with experimental results for both steady-state and transient operating conditions. The steady-state wake model was shown to give good predictions of rotor wake geometry, induced inflow distribution as well as performance trends. Under transient conditions, such as those following a pitch input during a maneuver, the time-accurate wake model was shown to correctly model the dynamic response of rotor wake. In axial descent passing through the vortex ring state, the present analysis was shown to properly model the associated power losses as shown by experimental results. The present analysis was also shown to give improved predictions of wake distortions during simulated maneuvering flight with various imposed angular rates of the rotor.

TRANSIENT DYNAMICS OF HELICOPTER ROTOR WAKES USING A TIME-ACCURATE FREE-VORTEX METHOD

by

Mahendra J. Bhagwat

Dissertation submitted to the Faculty of the Graduate School of the
University of Maryland, College Park in partial fulfillment
of the requirements for the degree of
Doctor of Philosophy
2001

Advisory Committee:

Professor J. Gordon Leishman, Chairman/Advisor
Associate Professor James D. Baeder
Associate Professor Roberto Celi
Professor Inderjit Chopra
Associate Professor Jian-Guo Liu, Dean's Representative

Dedication

*T*o those

*W*ho have left so much behind . . .

Acknowledgements

I would like to take this opportunity to express my sincere gratitude towards all the people here at the University of Maryland who have helped in making this possible. Notably, my dissertation committee, Profs. James Baeder, Roberto Celi, Inderjit Chopra, and Jian-Guo Liu. They have been truly a advisory committee, constantly guiding me through many challenging tasks during the course of my work. Special thanks to Prof. Alfred Gessow for many helpful discussions and encouragement.

I cannot put down in words my gratitude towards my advisor and mentor, Prof. Gordon Leishman, who has played a key role in not only this work, but also in my career. If not for him, I would not be here, and I would simply like to say, "thanks for giving me a chance."

This work would not have come to a fruition without the aid of my friends and colleagues at the Rotorcraft Center who have been both helpful and patient with me over the past years. Many thanks to Preston Martin and Greg Puglese for sharing their fascinating experiments, and their fascination with the Blue Ridge mountains. Also, thanks to Dan Griffiths, Manikandan Ramasamy and Shreyas Ananthan, and also Dario Fusato and Rendy Cheng for their help and support. Special thanks to Dr. Ashish Bagai who's always been very encouraging and eager to help solve many of my problems. Thanks also to the 10 Forward management for carrying me through those late night vigils.

The support of the National Rotorcraft Technology Center through various grants is also gratefully acknowledged.

Last, but not the least, I must acknowledge the love and support of my family and friends, who have taught me to be more.

Table of Contents

Appendices

List of Tables

List of Figures

Nomenclature

A	asymptotic radial contraction in Landgrebe's wake model	
A	rotor disk area, $= \pi R^2$	m^2
c	rotor blade chord	m
C_d	sectional drag coefficient, $dD/(1/2\rho V_\infty^2 c)$	
C_l	sectional lift coefficient, $dL/(1/2\rho V_\infty^2 c)$	
C_{l_α}	lift curve slope	rad^{-1}
C_P	rotor power coefficient, $= P/\rho A(\Omega R)^3$	
C_Q	rotor torque coefficient, $= Q/\rho A(\Omega R)^2 R$	
C_T	rotor thrust coefficient, $= T/\rho A(\Omega R)^2$	
$\mathbf{E}$	Legendre's elliptical integral of second kind	
e	spanwise location of flapping hinge	m
h	time marching step, $= \Delta t$	s
I_β	flapping moment of inertia of the blade	$\mathrm{kg\,m}^2$
$\mathbf{K}$	Legendre's elliptical integral of first kind	
K_x	longitudinal inflow coefficient, $= \lambda_{1c}/\lambda_0$	
K_y	lateral inflow coefficient, $= \lambda_{1s}/\lambda_0$	
k_1, k_2	axial settling rates in Landgrebe's wake model	
k_β	flapping spring stiffness	$\mathrm{N\,m\,rad}^{-1}$
M_β	flapping moment at the hinge	N m
$\overline{M}_\beta$	non-dimensional flapping moment, $= M_\beta/(I_\beta \Omega^2)$	
m	blade mass per unit length	$\mathrm{kg\,m}^{-1}$
m_a	apparent mass of the rotor disk	kg
N	number of helical vortex filaments	
N_b	number of blades	

P	rotor shaft power	$\mathrm{N\,m\,s^{-1}}$
P_0	rotor profile power	$\mathrm{N\,m\,s^{-1}}$
P_h	ideal rotor induced power in hover, $= T^{3/2}/\sqrt{2\rho A}$	$\mathrm{N\,m\,s^{-1}}$
P_i	rotor induced power	$\mathrm{N\,m\,s^{-1}}$
p	helical pitch angle	rad
p	rotor roll rate	$\mathrm{rad\ s^{-1}}$
Q	rotor shaft torque	N m
q	rotor pitch rate	$\mathrm{rad\ s^{-1}}$
R	rotor radius	m
r, θ, z	cylindrical polar coordinates	(m, rad, m)
$\vec{r}$	position vector of a wake collocation point	(m, m, m)
r_c	vortex core radius	m
T	rotor thrust	N
T_h	reference rotor thrust in hover	N
S_β	static flapping inertia moment of the blade	kg m
t	time	s
U	resultant air velocity at blade section, $= \sqrt{U_P^2 + U_T^2}$	$\mathrm{m\,s^{-1}}$
U_P	air velocity at blade section, normal to rotor disk	$\mathrm{m\,s^{-1}}$
U_R	air velocity at blade section, radial component	$\mathrm{m\,s^{-1}}$
U_T	air velocity at blade section, chordwise component	$\mathrm{m\,s^{-1}}$
$\vec{V}$	velocity vector at a wake collocation point	$\mathrm{m\,s^{-1}}$
V_c	axial (vertical) climb velocity	$\mathrm{m\,s^{-1}}$
V_h	ideal rotor induced velocity in hover, $= \sqrt{T/2\rho A}$	$\mathrm{m\,s^{-1}}$
V_i	rotor induced velocity	$\mathrm{m\,s^{-1}}$
V_r, V_θ, V_z	radial, swirl and axial velocities	$\mathrm{m\,s^{-1}}$

V_∞	freestream velocity	$\mathrm{m\,s^{-1}}$
x, y, z	Cartesian coordinates	(m, m, m)
α	angle of attack	rad
α	divergence rate	$\mathrm{s^{-1}}$
$\overline{\alpha}$	non-dimensional divergence rate, $= \alpha/(\Gamma_v/4\pi R^2)$	
α_s	rotor shaft tilt angle	rad
β	blade flapping angle	rad
β_0	coning blade flapping angles	rad
β_{1c}	longitudinal blade flapping angles	rad
β_{1s}	lateral blade flapping angles	rad
χ	rotor wake skew angle, $= \tan^{-1}(\mu/\lambda)$	rad
$\Delta\theta$	angular discretization	rad
$\Delta\psi$	azimuthal discretization	rad
$\Delta\zeta$	vortex age discretization	rad
$\delta\vec{r}$	wake geometry perturbation	(m, m, m)
Γ	vortex circulation (strength)	$\mathrm{m^2 s^{-1}}$
Γ_v	tip vortex circulation (strength)	$\mathrm{m^2 s^{-1}}$
Γ_b	blade bound vortex circulation (strength)	$\mathrm{m^2 s^{-1}}$
ϕ	sectional induced angle, $= V_i/\Omega R = \lambda/r$	rad
κ_v	additional induced power loss factor in axial descent	
λ	rotor inflow ratio, $= V_i/\Omega R$	
λ_0	linear mean inflow coefficient	
λ_{1c}	linear longitudinal inflow coefficient	
λ_{1s}	linear lateral inflow coefficient	
λ_h	reference rotor inflow ratio in hover, $= \sqrt{C_T/2}$	

$\overline{\lambda}$	radial contraction exponent in Landgrebe's wake model	
μ	advance ratio, $= V_\infty/\Omega R$	
ν_β	non-dimensional rotating blade flapping frequency, $= \omega_\beta/\Omega$	
Ω	rotor rotational speed	$\mathrm{rad\,s^{-1}}$
ω	wave number for a normal mode	
ω_{ex}	wave number for a normal mode	
ω_0	non-rotating blade flapping frequency, $= k_\beta/I_\beta\Omega^2$	$\mathrm{rad\,s^{-1}}$
ω_β	rotating blade flapping frequency	$\mathrm{rad\,s^{-1}}$
ψ	azimuth angle	rad
ψ_b	blade azimuth, $= \Omega t$	rad
$\psi_b^{(m)}$	azimuthal location of m^{th}-blade, $= \psi_b + 2\pi(m-1)/N_b$	rad
ψ_{ref}	reference blade azimuthal location, $= \psi_b^{(1)}$	rad
ρ	fluid (air) density	$\mathrm{kg\ m^{-3}}$
σ	eigenvalue of time-integration method	$\mathrm{s^{-1}}$
σ	rotor solidity	$N_b c/\pi R$
θ	rotor collective pitch	rad
θ_0	collective blade pitch angle	rad
θ_{1c}	lateral blade pitch angle	rad
θ_{1s}	longitudinal blade pitch angle	rad
ζ	vortex age	rad

Derivatives

$\dot{(\ )}$	differentiation with respect to time (t)
$\overset{\star}{(\ )}$	differentiation with respect to blade azimuth (ψ)

Abbreviations

CFD	Computational Fluid Dynamics
FCT	Fourier Coordinate Transformation
IGE	In Ground Effect
LHS	Left-Hand Side
ODE	Ordinary Differential Equation
OGE	Out of Ground Effect
PDE	Partial Differential Equation
PCC	Predictor-Corrector with Central difference
PC2B	Predictor-Corrector with 2nd-order Backward difference
PIPC	Pseudo-Implicit Predictor-Corrector
RHS	Right-Hand Side
RMS	Root-Mean-Square
TPP	Tip Path Plane

Chapter 1

Introduction

Helicopters are flying machines with rotating wings or rotors. These rotors provide lift, propulsion as well as control forces, unlike a conventional fixed-wing aircraft where these forces are typically generated by different mechanisms. The obvious advantage of rotating wing aircraft is their unique ability to take-off vertically and hover motionless in still air. The typically large diameters of helicopter rotors accelerate a large mass of air at relatively low velocities, thereby giving a capability to hover with a relatively low power requirements. However, this efficiency in hovering flight also compromises the performance of the helicopter in forward flight, especially in terms of maximum flight speed. Early helicopters were complex, vibrating contraptions that could barely lift their own weight. The modern helicopter, although significantly more efficient, still suffers from many problems, including aeromechanical instabilities, high vibrations and obtrusive noise.

A conventional helicopter uses a single main rotor to generate all the lifting, propulsive and control forces. The tail rotor is used essentially as an anti-torque device to prevent the helicopter from rotating in reaction to the main rotor torque. Therefore, a proper understanding of the aerodynamics of the main rotor is key to all improved developments in helicopters. The development of the early helicopters suffered from this lack of proper understanding of aerodynamics. With scarce information available on the subject, the early designs were guided mainly by intuition. Helicopter pioneer, Igor Sikorsky (Ref. 1) also identified the importance of intuition in design of the rotating machine aircraft

> ...extremely less reliable information was available. But the ability, experience and well-trained intuition of a fine engineering group made it possible to attack the novel and difficult problem successfully.

After more than half a century, there has been significant progress in aerodynamic theory of rotating wings. However, the aerodynamics of helicopters is yet to be completely understood, and neither exact theories nor versatile numerical models are available. Advanced design still relies on intuition, albeit to an increasing lesser extent. The motivation for the present dissertation is to further the understanding of this challenging subject, or in Sikorsky's words, to make "more reliable information available."

Lord Kelvin's theory of vortex matter suggests that all matter is composed of vortices. Although this is not true of matter in general, the flow field surrounding any rotating wing is certainly composed of vortices. Therefore, one key to improved understanding this complex aerodynamic environment surrounding a helicopter rotor lies in understanding of the vortical wake structure. For rotating wing aircraft, by virtue of the rotational motion, the trailed wake remains in close proximity of the rotor for a significantly long time. An example is shown in Figure 1.1, where the tip vortices trailing from the blade tips have been rendered visible by natural condensation (Ref. 2). These wake vortices induce strong velocities at the rotor blades, resulting in highly three-dimensional airloads. The vortices may also interact with other blades, the airframe or empennage, etc., giving rise to complex interactional aerodynamics. The principal motivation for this dissertation is the better understanding of the behavior of these vortices and their influence on the rotor aerodynamics.

The strengths and locations of the wake vortices relative to the rotor depend of several parameters, including the rotor operating conditions. The high vortex induced velocities can produce significant spanwise and temporal variations in the induced inflow at each rotor blade. This can potentially make the flow field highly three-dimensional and unsteady. Accurate prediction of induced inflow is essential to predicting the lift on each blade and, in turn, the rotor thrust and power requirements. The local interactions of the wake vortices with the rotor blades can give rise to oscillatory blade loads, vibrations and noise. Moreover, such oscillatory blade lift distribution can result in fluctuating strengths of the trailed wake vortices leading to more complicated wake-induced inflow field.

Modern helicopters can perform some very challenging maneuvers, similar to an aerobatic fixed-wing aircraft. An example of these maneuvers in shown in Fig. 1.2, where the helicopter is pictured at the end of a vertical loop. It is perceivable that the rotor wake structure and the resulting induced velocity field under such maneuvers can be very complex, and may have a significant influence on the rotor airloads and performance. The rotor blade flapping resulting from the maneuver can also alter the wake structure as well as the blade lift. Therefore, the prediction of the rotor thrust and blade loads under maneuvering flight conditions is a highly coupled and non-linear problem.

The presence of other rotors such as the tail rotor, or multi-rotor configurations, further complicates the rotor wake problem. The interference between the wakes from different rotors blades may have significant influence on their performance capabilities. The ultimate objective of rotor analysts is, of course, to model all these behaviors using a mathematical model with the fidelity necessary to represent all the flow

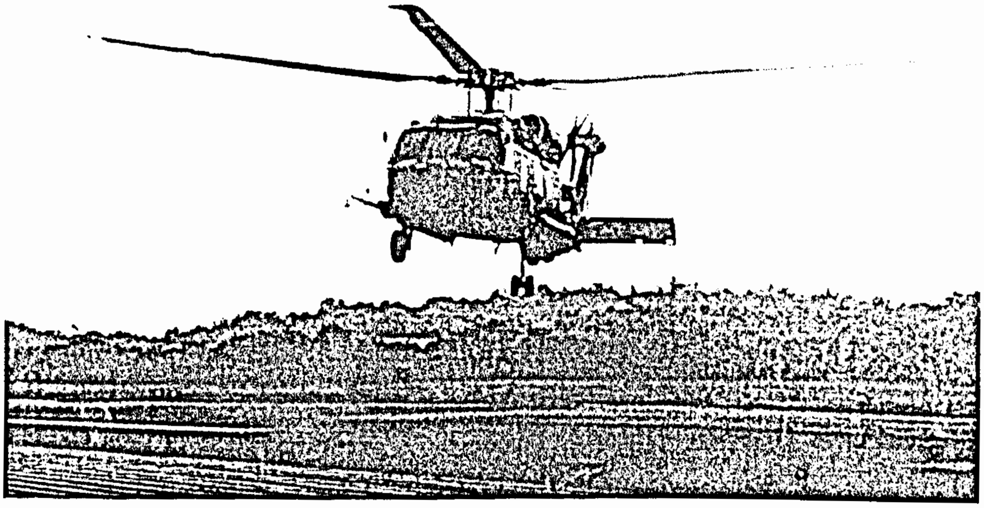

Figure 1.1: Hovering helicopter showing the main rotor vortical wake structure rendered visible by natural condensation of water vapor inside the tip vortex cores (Ref. 2).

physics. However, such a model can become significantly complex and non-trivial. Therefore, the present dissertation focuses on modeling the aerodynamics of the main rotor, although methodology can be readily extended to multiple rotor configurations including a tail rotor. To better understand the methodology, it is necessary to first introduce the fundamental concepts in the rotor aerodynamic problem. These concepts provide a foundation for the analysis developed in this dissertation.

1.1 Description of the Helicopter Rotor Wake Problem

The interdependent nature of the blade aerodynamic forces and the rotor blade motion relative to the hub is necessary to the understanding of a helicopter rotor system. The blade motion and airloads are inherently coupled to each other and, in general, it is

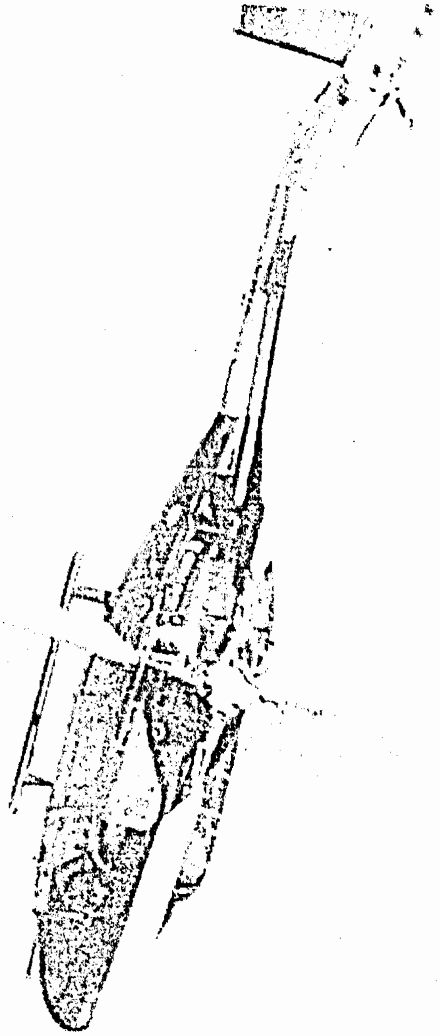

Figure 1.2: A GKN-Westland Lynx helicopter at the end of a vertical loop maneuver. Courtesy of Mr. F. John Perry and GKN-Westland Helicopters.

necessary to solve for both these simultaneously. One of the distinctive features of helicopter rotor blades is that articulation in the form of lead/lag and flapping hinges are incorporated at the blade roots. Modern blade designs may include hingeless flexures that allow motion about a "virtual" hinge. The blade flapping motion is a result of both the aerodynamic force (blade lift), the centrifugal and inertial forces. The blades flap up to provide an equilibrium of moments caused by these forces at the flapping hinge. A similar equilibrium of in-plane forces (aerodynamic drag force and Coriolis forces) gives the lead/lag motion of the blades – see Fig. 1.3. In general, the centrifugal forces are the most dominant and, therefore, the blade flapping angles are typically very small. The drag force is much smaller compared to the blade lift. Therefore, the lead/lag motion is even smaller in magnitude. Therefore in the present level of analysis only the blade flapping motion is considered.

The wake of the rotating blades comprises of a concentrated vortex that forms quickly behind the blade tip. In addition, there is also a vortical shear layer, or a vortex sheet, trailing from the inboard portions of the blade. This vortex sheet contains the trailed vorticity, which is directed normal to the blade trailing edge, and also shed vorticity which is directed chordwise (parallel to the trailing edge). The strengths of these wake vortices depends on the blade bound circulation, which is related to the blade lift through the Kutta-Joukowski theorem. This vortical environment of a rotating blade is schematically shown in Fig. 1.4, which is a schematic based on both flow visualization and velocity field measurements. The aerodynamic environment of a representative blade section is shown in Fig. 1.5. The geometric angle of attack, θ is given by the rotor collective pitch inputs and blade twist. The induced angle of attack, $\phi \approx U_P/U_T$ is a result of the induced velocity in the plane of the rotor. The induced velocities affect not only the magnitude of blade lift, but also its direction. Clearly, the

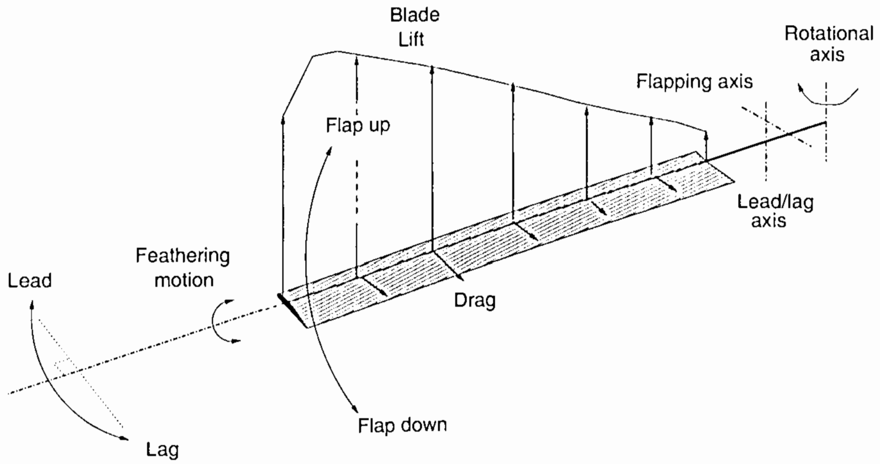

Figure 1.3: Various rigid blade motions and the associated aerodynamic forces.

sectional lift or bound circulation at each blade section is dependent on the structure of the trailed wake through the wake-induced velocities. The strength of the trailed wake vortices is, in turn, dependent on the spanwise distribution of the blade lift.

The three sub-problems pertaining to the rotating wing, that is, the blade lift solution, the vortical wake model and the blade flapping motion, are interrelated and form a highly coupled aerodynamic system. Their interrelation is schematically shown in Fig. 1.6. Because of this strong coupling, it is necessary to solve all three sub-problems simultaneously. While the main objective of the present research is on the wake modeling methodology, the other two sub-problems must also be solved to a comparable fidelity to obtain a consistent solution. In the next section, the various methodologies pertaining to the vortex wake model are reviewed, followed by a detailed description of the present methodology in Chapters 2 and 3. The other two sub-problems pertaining to the blade lift and blade flapping solution are described in Chapter 4.

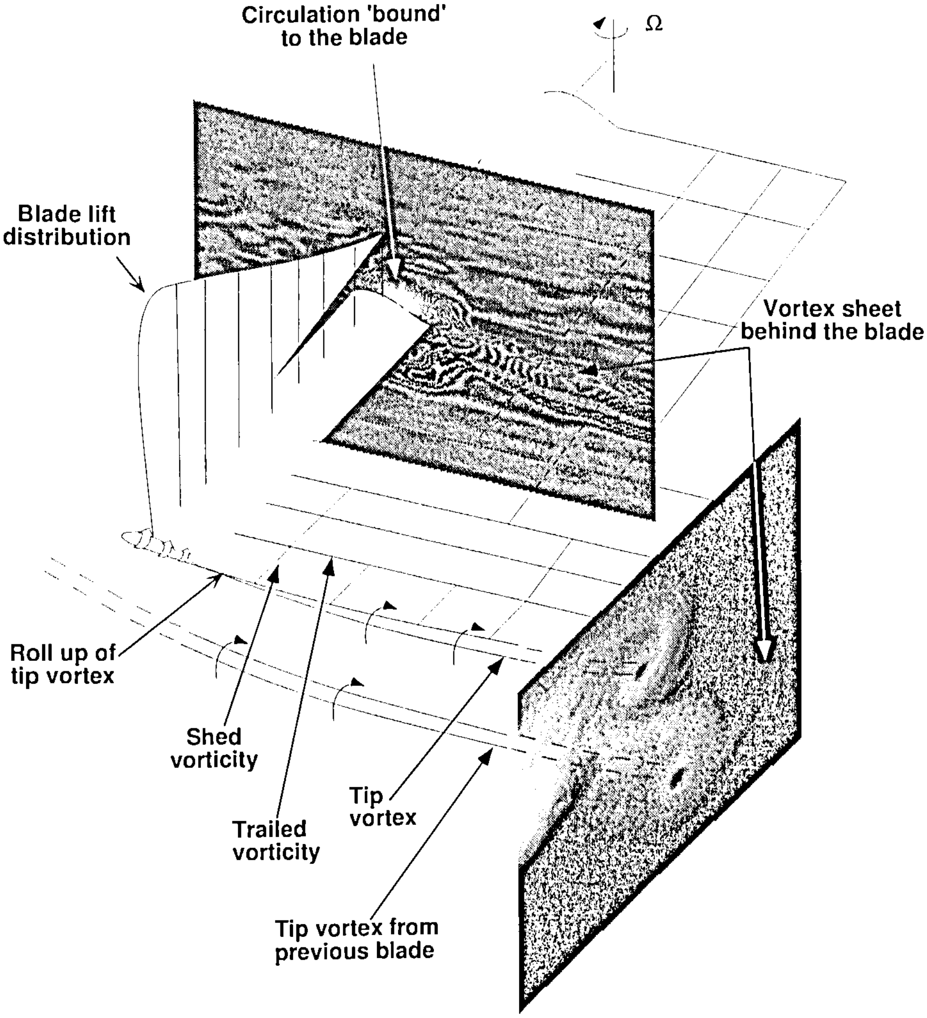

Figure 1.4: Schematic of the wake of a single rotating wing showing the vortical wake sheet and a concentrated tip vortex as well as the bound vorticity on the blade.

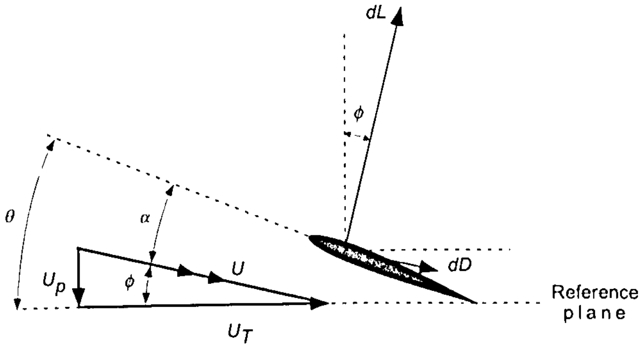

Figure 1.5: The incident velocities at a typical blade element.

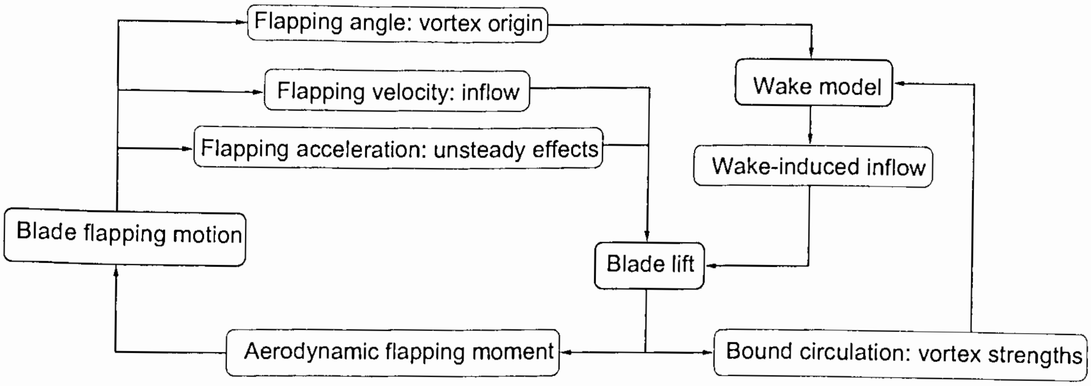

Figure 1.6: Schematic of the interdependence of the rotor blade lift, blade flapping solution and the wake problems.

1.2 Review of Free-Vortex Wake Methodologies

1.2.1 Classical Vortex Theory

The quest for improved predictions of the aerodynamic environment at the rotor is the principal motivation for using vortex methods to model the rotor wake. Classical vortex theory was originally developed for propellers operating in axial flight. This basic vortex theory describes the wake as a series of vorticity cylinders representing the radial variation of circulation (Ref. 3). Prandtl derived an approximation correction to account for the loss of lift near the blade tips resulting from the strong induced effects of the tip vortices generated by a finite number of blades – see, for example, Ref. 2 (Ch. 3, pp. 102–105). Goldstein (Ref. 4) further improved upon the vortex theory with a model for the vortical wake consisting of helicoidal vortex surfaces trailed from each blade. The helix angle was constant, corresponding to a uniform downward convection velocity as suggested by simple momentum theory, and the effects of non-uniform induced inflow, wake contraction, viscous diffusion, etc., were neglected.

Further development of the vortex theory by Lock (Ref. 5) accounted for a non-uniform inflow over the rotor disk and through the wake. In this case, each radial segment was associated with a locally uniform inflow velocity resulting in a radially varying helix angle for each of the helicoidal vortex sheets. For an optimum hovering rotor (i.e., a uniform downwash) the Lock analysis gives the same result as given by Goldstein's analysis.

All the preceding analyses are "exact" or analytic solutions to the wake problem. However, one limitation of these vortex theories is that they are not readily applicable to lightly loaded helicopter rotors or for forward flight when there is a velocity component parallel to the plane of the rotor disk. This is because originally the classical vortex theories were developed for propellers operating in axial flight, where the flow field is axisymmetric. With the advent of digital computers, Piziali & Duvaldt (Ref. 6) improved upon the vortex wake model by representing the wake as a mesh of discrete vortex lines. As in the classical vortex analyses, the spatial locations of the wake elements were based on uniform inflow assumption, and did not account for wake contractions or mutually induced interaction effects that may cause further wake distortion. Although this more computationally expensive model gave similar results as the Goldstein-Lock analysis for hovering rotors, it was also applicable to rotors in forward flight. Piziali & Duvaldt's work in Ref. 6 is perhaps the origin of the classical rigid wake model for helicopter rotors.

Clearly, predicting the vortical wake structures in the wake of a rotor is one key to an improved understanding the complex aerodynamics of the rotating wing aircraft. All the classical vortex theories solve for the wake structure by approximating their convection velocities in some simple form. With improvements in computer architecture and numerical techniques, these "approximations" in the model were successively removed leading to what are now called "free-wake" methods. At the same time, several experimental studies have been conducted to better understand the vortical wake structure. Although the work in this dissertation focuses on the former, that is the numerical methods, experimental studies are essential in helping to recognize and understand various physical aspects of the rotor wake. Even numerical methods depend partly on experimental studies through empirical modeling of physical processes, for example the viscous or, possibly, turbulent diffusion of vorticity.

1.2.2 Fundamentals of Vortex Wake Methods

Vortex methods model the vortical wake structure in the form of continuous vortex lines in a potential (inviscid, incompressible) flow. Based on Helmholtz's vorticity theorems, these vortex lines are transported as material (fluid) lines in a circulation preserving motion (Ref. 7). Therefore, the vortex lines are convected through the flow field in a force-free manner at the local flow velocity. This vorticity transport theorem forms the basis of of all free vortex methodologies.

Mathematically, the vorticity transport theorem can be rewritten as a simple first-order ordinary differential equation (ODE), i.e.,

$$\frac{d\vec{r}}{dt} = \vec{V}_{\text{local}}(\vec{r}) \tag{1.1}$$

which is nothing but the statement that the rate of change of the position vector, $\vec{r}$, of an element on the vortex line equals the local fluid velocity at that point, $\vec{r}$. Although this equation appears trivial, the solution of the helicopter rotor wake problem is far from trivial. This is because the local fluid velocity contains, along with any free-stream and aircraft motion related velocities, the self- and mutually induced velocities from all the vortex structures in the wake. The vortex induced velocities are governed by the Biot-Savart law — see Ref. 8 (Ch. 2, p. 93–94) or Ref. 9 (Ch. 18, pp. 526–530) — and are highly non-linear in nature. As the motion of each vortex element depends on the velocities induced by all vortex elements in the flow field, the vorticity transport theorem forms a highly coupled system of equations. Therefore, solution to this apparently simple equation can be mathematically very challenging. For rotating wing applications, the inherent interdependence of blade-lift and flapping solutions with the development of the vortical wake poses further complications.

It is not, therefore, surprising that early (circa 1970) methods for the solution of the above wake equation suffered from numerical convergence problems – see, for example, Refs. 10–12. These were the first time-marching wake solution methodologies, which integrated the above equations in time starting from an initial guess wake geometry. Simultaneous experimental studies of rotor wakes also identified the presence of vortex instabilities (e.g., Refs. 13 & 14). These instabilities and their relevance to the free-vortex wake methodologies — especially the time-marching methods like those reported in Refs. 10–12 — is described in the following section.

The numerical instabilities found in the wake models manifested as a lack of solution convergence. The addition of numerical damping terms (see, for example, Ref. 15) may partly overcome the convergence issues, yet the solution may then not be physically meaningful. This problem motivated the development of steady-state vortex wake methods — the so-called "relaxation" wake methods — as well as prescribed wake methods. Both these methodologies have seen significant development and application to a wide range of problems over the last three decades. A brief overview of these methods is presented in this section even though the focus of this dissertation is on a time-marching methodology.

To appreciate the mathematical distinction between the time-marching and the relaxation approaches, Eq. 1.1 can be rewritten for the rotor wake problem in a blade-fixed coordinate system as a partial differential equation (PDE), i.e.,

$$\frac{\partial \vec{r}}{\partial \psi} + \frac{\partial \vec{r}}{\partial \zeta} = \vec{V}(\vec{r}) \tag{1.2}$$

where ψ is the blade azimuthal location and ζ is the vortex age – see Fig. 1.7. The vortex "age" is the angle traversed by the vortex relative to its origin at the rotor blade (or, equivalently, the time elapsed since the origin of the vortex). Therefore, the blade azimuth, ψ, is a temporal (time) coordinate while the vortex age, ζ, is a spatial coordinate. The time-marching methods start the solution with an initial condition in ψ and integrate in time (or ψ). The boundary condition for the spatial direction is that the vortex must be trailed from the blade at its origin, i.e., at $\zeta = 0$. These methods are often termed Lagrangian methods because they essentially solve for the motion of a Lagrangian fluid particle in a given flow field. Numerical solution is obtained by discretizing the vortex filaments into elements of length of $\Delta\zeta$, and numerically integrating over a time (azimuthal) step of $\Delta\psi$, as shown in Fig. 1.7.

The relaxation methods assume that the steady-state wake structure is periodic at the rotor frequency. This assumption is imposed on the wake geometry by mapping the temporal (ψ) coordinate as a spatial coordinate with a periodic boundary condition. The governing equations are now modified to include a pseudo-time term, i.e.,

$$\frac{\partial \vec{r}}{\partial \tilde{t}} + \frac{\partial \vec{r}}{\partial \psi} + \frac{\partial \vec{r}}{\partial \zeta} = \vec{V}(\vec{r}) \tag{1.3}$$

This equation is now solved in this pseudo-time domain ($\tilde{t}$) until a steady-state is reached. Note that the iterations, or the pseudo-time steps, do not have a physical significance. However, in the steady-state when the solution does not change with time, the $\tilde{t}$ derivative in Eq. 1.3 vanishes and the original equation (Eq. 1.2) is recovered. Some form of classical relaxation is used in the pseudo-time integration and, there-

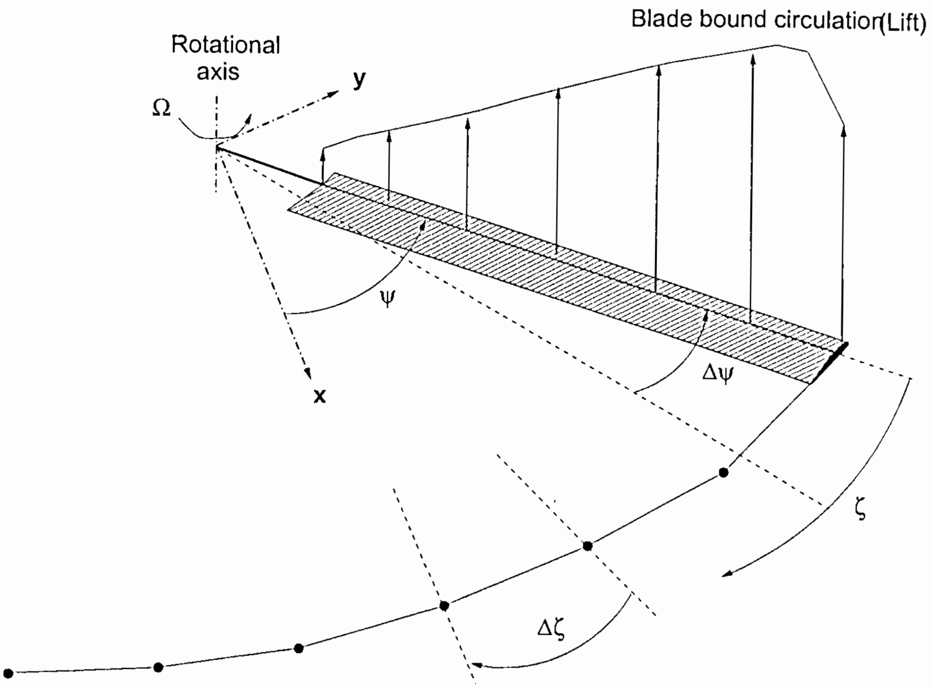

Figure 1.7: Schematic of the discretized tip vortex geometry in blade fixed coordinate.

fore, such steady-state methods are often termed relaxation methods. The relaxation methods show a very rapid convergence characteristic under most flight conditions. Therefore, these methods are best suited for aeromechanical applications that require a steady-state wake solution.

Figure 1.8 is a timeline showing the developments of free vortex methodologies over the past three decades. In the late 1960's, the primary motivation for developing improved wake methodologies was to achieve a better hover performance prediction capability. However, all of the early time-marching approaches were found to be susceptible to numerical instabilities, and fully converged wake geometry could not be obtained. This lead to successful development of another class of wake models – the prescribed wake models. About the same time, came the development of relaxation or iterative wake methods, which explicitly assumed that the rotor wake to be periodic. These methods became popular modeling tools during the 1980's. In the late 1980s, time-marching rotor wake methods were revisited for applications involving high speed flight and rotor wake/airframe interaction problems. More recently, the need for better time-marching wake methods has again received attention because of the increasing need to model the rotor aerodynamics under transient/maneuvering flight conditions. In this section, a chronology of both the time-marching and the relaxation wake methods will be reviewed.

1.2.3 Prescribed Vortex Wake Methods

One relatively simple and popular approach to solve the non-linear wake equations is to use semi-empirical approximations to describe the non-linear induced velocities on the LHS of Eq. 1.2. For example, the classical rigid wake model is obtained by approximating the induced velocity field over the rotor disk by a constant velocity based on momentum considerations. Further improvements in such a model are obtained by assuming a velocity field that varies along the blade span and azimuth depending on operating and flight conditions.

The famous wake visualization experiments by Landgrebe (Ref. 13) laid the foundations of the prescribed wake model for hovering rotor wakes. In this model, the induced velocities are specified based on experimental observations, and the wake geometry is then obtained by solving the governing equation (Eq. 1.2). The wake model was found to be a powerful tool for modeling hovering rotor wakes, where the time-marching approach was unsuccessful because of numerical instabilities. This model was found to give improved predictions of the rotor performance as compared to the classical rigid wake models (Ref. 13).

The rigid wake model consists of undistorted uniform-spacing helical vortex fila-

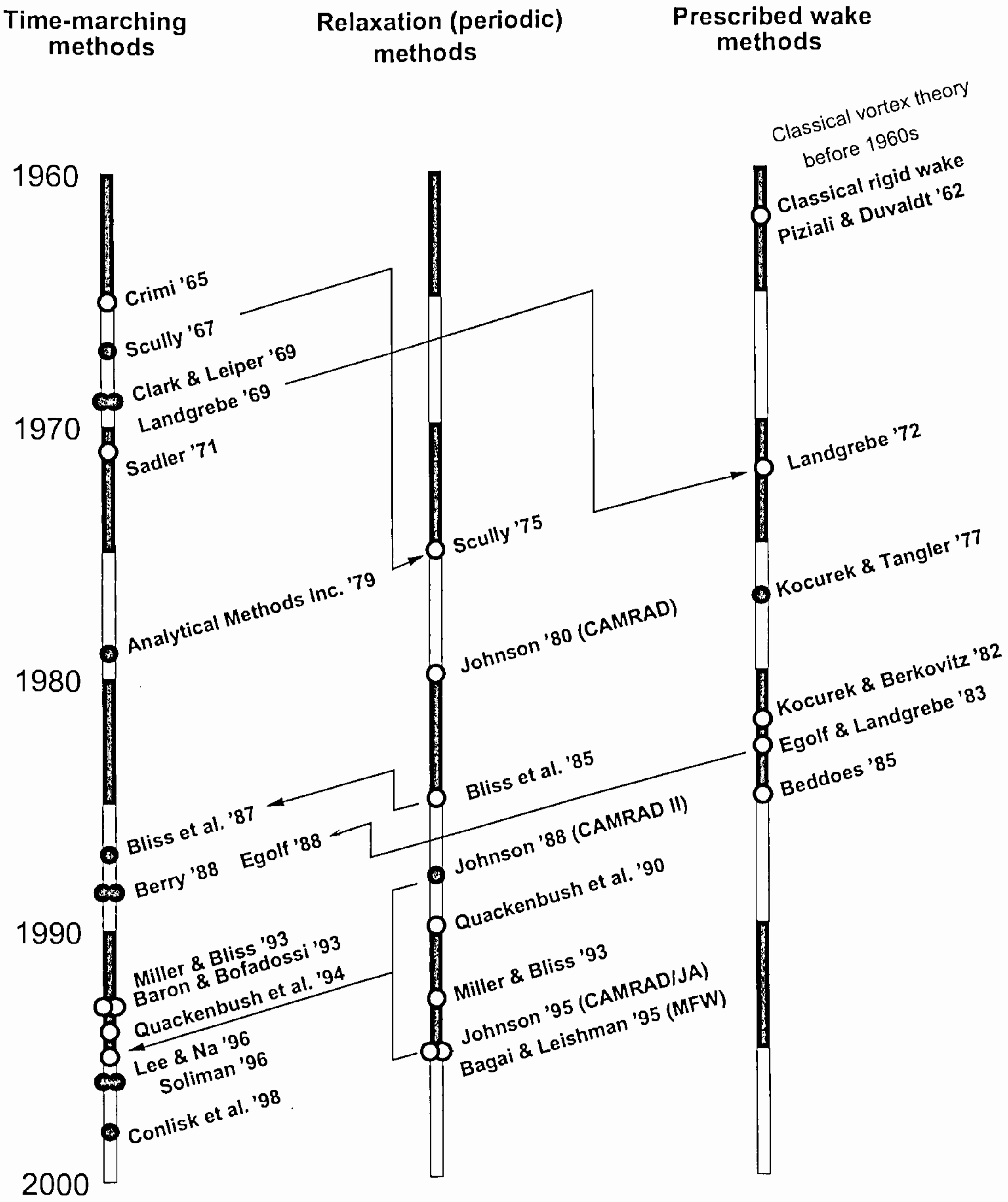

Figure 1.8: Historical development of free-vortex wake methodologies.

ments, as mentioned earlier. Note that such a wake model is also a simplified solution to Eq. 1.2, where the induced velocities are assumed to be constant (equal to the sum of the averaged rotor inflow and freestream velocity). Further improvements to such models are given in Refs. 16 and 17. Several prescribed wake models have also been developed for rotors in forward flight. For example, the UTRC generalized wake model by Egolf & Landgrebe (Ref. 18) and the Beddoes wake model (Ref. 19). These may be extended to multiple rotor configurations by semi-empirically modeling the interference effects on the inflow distribution in the overlap region of the rotors (Refs. 20, 21). All the prescribed wake models are based on the same general principle of empirically modeling the time-averaged induced velocity field, and then computing the wake geometries based on that assumption, with no explicit treatment of the self-induced velocities from the rotor wake.

1.2.4 Time-Marching Free-Vortex Wake Methods

Crimi (Ref. 10) was probably the first to introduce an explicit time-stepping approach for modeling the evolution of rotor wake geometry. Tangler *et al.* (Ref. 14) applied this analysis to understand the vortex instabilities experimentally observed in the wakes of hovering rotors. The time-stepping approach also showed the presence of similar instabilities. However, a properly converged wake solution was not obtained for hovering flight. Scully (Ref. 11) and Clark & Leiper (Ref. 22) also developed explicit time-marching free-vortex wake methodologies. In all these analyses, wake convergence was found to be a formidable problem because of the onset of numerical instabilities.

Scully (Ref. 11) developed an explicit Euler time-marching wake algorithm. However, the numerical solutions showed severe numerical instabilities for hovering flight. The limited success of this and other time-marching algorithms motivated the development of the now famous Scully "relaxation" wake model (Ref. 23). In this case, the wake was constrained to be periodic in time (blade azimuth) and the wake geometry was iteratively solved in a pseudo-time domain. Although the intermediate solutions did not have any physical significance, the final converged wake solution was valid for steady-state flight conditions. This gave rise to a whole new class of wake models called "relaxation" wakes, which are reviewed in the next section.

Clark & Leiper (Ref. 22) were the first to use a predictor-corrector approach to solve the wake equations in an attempt to overcome the numerical instabilities found with time-marching schemes. In their analysis, which was intended primarily for hover performance predictions, the final wake geometry was solved starting from an initial wake geometry using a sequence of corrector steps. Although this algorithm was written in the form of a time-marching algorithm, only one time step was used and the rotor wake was assumed to be axisymmetric. Convergence was not explicitly enforced, but typically two corrector steps were claimed subjectively to be sufficient for convergence. This was probably the first iterative wake methodology with wake periodicity (or axisymmetric flow condition in hovering flight) being explicitly enforced. This method laid the foundations for later developments in relaxation methods, which followed in the 1980's.

The Clark & Leiper hover wake analysis used a near-wake, which was solved as free vortices, along with a far-wake modeled using a stack of vortex rings. The ring spacing was based on the number of blades, as well as the axial settling rate of the last free vortex elements in the near-wake. A peak swirl velocity cut-off method was employed to model the viscous vortex core in view of the uncertainties involved in modeling the viscous core growth and the associated core eddy viscosity. For improved computational speed, the induced velocity field was explicitly calculated only at a few "strategically located" points, and interpolated to the actual wake collocation points. One interesting prediction based on numerical results was the faster axial velocity of the inboard vortex sheet, which has also been observed in experiments (e.g., Refs. 13, 24). The predicted locations of the tip vortices were shown to be in good agreement with the experimentally measured values.

Landgrebe (Ref. 12) also presents a detailed approach to compute wake geometries using an explicit time-stepping approach. The analysis was mainly applied to rotors in forward flight, and the self-induced distortions of the wake were represented using several discrete straight-line vortex segments. At each time-step a new vortex segment was trailed from the rotor blade, while one segment (farthest from the rotor) was deleted from the computational domain to keep the number of vortex elements at a reasonable limit – typically up to five turns below the rotor. A strategy to separate the wake structure as near-wake/far-wake regions was developed, and the velocity contributions from the far-wake was evaluated only once during the entire calculation to facilitate faster computations of the induced velocity field. Computational limitations made it necessary to use a relatively coarse discretization of $\Delta\psi = 15$–30°. Unsteady aerodynamic effects were included, in a two-dimensional sense, using model based on experimental unsteady airfoil data rather than discrete shed vortices. The viscous vortex core size was assumed to be 1% rotor radius, but the wake geometry results were found to be insensitive to the core size.

For the flight conditions examined, the time-stepping approach gave a converged (periodic) solution for the wake geometry. The characteristic distortions of the tip vortex filaments in forward flight, such as wake contraction and roll-up, showed good agreement with experimental observations. The same analysis, however, suffered from numerical instabilities in hovering flight. Similar instabilities were also observed in experiments with hovering rotor wakes – see, for example, Ref. 13. However, the same research group earlier reported the need for improved prediction methods for hovering rotor performance (Ref. 24). In particular, the need to model the wake contraction because of the self-induced velocity of the rotor wake in hover was emphasized. This pressing need for improved wake models combined with the unsuccessful attempts at time-marching wakes, probably paved the way for almost universal use in the 1970's & 1980's of prescribed wake models for rotor performance predictions.

Sadler (Refs. 25, 26) developed an explicit Euler time-marching wake methodology, especially for application to multiple rotors. Both co-rotating and counter-rotating rotors were examined. The vortical wake structure was modeled using both trailed and shed vortices in the near-wake region close to the rotor. The far-wake, however, was modeled using only one tip vortex from each blade. Straight line vortex segments were used except for the calculation of the self-induced velocity, where an arc described by endpoints of two neighboring segments was used. A solid body like vortex core model was used (such as the Rankine vortex model) and the core radius was adjusted to give good correlation with the experimentally measured airloads on the rotor blades. The rotor was impulsively started from rest and an induced velocity cut-off was specified to avoid high induced velocities. Both these latter strategies helped to improve the numerical stability of the wake solution. However, the model was mainly applied to forward flight conditions, where both physical and numerical vortex instabilities are found from experiments to be less severe as compared to those found in hovering flight.

As of 1980 various numerical instabilities found with time-marching wake solutions were still an unresolved issue. An Analytical Methods Inc. report of 1979 addressed the use of an explicit algorithm. Additional numerical damping was found to be necessary to suppress the undesirable numerical instabilities (Ref. 15). However, such an approach raises further questions about to the physical significance of such numerical solutions. Later work with time-marching methods avoided this stability issue by focusing mainly on applications of the analysis to forward flight.

Bliss *et al.* (Ref. 27) developed a time-marching free-vortex wake methodology using curved vortex segments. A predictor-corrector sequence was used to solve the wake equations and to calculate the wake geometry. A far-wake boundary condition based on momentum considerations was used to ensure "physically correct" behavior. However, the crux of this study was primarily to examine the applicability of curved vortex segments and details of the numerical scheme for the wake equations were not given. The curved vortex segments were shown to be relatively more accurate than straight-line segments for modeling the wake with large discretization (azimuthal step). The methodology was found to be susceptible to numerical instabilities for hovering rotor wakes and so was applied mainly to high speed forward flight conditions (Ref. 28). In this case, convergence criterion was based on the requirement of a periodic wake geometry.

More recently, a similar methodology was also successfully applied to the problem of rotor/wake interactions to calculate high resolution airloads (Ref. 29). Several techniques were used to improve the computational efficiency including a fat core vortex model and analytical/numerical matching (ANM). A backward difference time-stepping approach (implicit) was used for improved computational efficiency. This, as will be shown later, may also have been important to help improve the stability of the wake solution.

Berry (Refs. 30, 31) presented an explicit time-marching wake methodology to investigate rotor/body interactions. The rotor wake geometry was allowed to evolve starting impulsively from rest and the resulting unsteady airloads in presence of fuselage were calculated. However, few details of the numerical scheme were given and the stability or accuracy of the time-marching method was not addressed. The use of an explicit scheme, however, suggests that the method was not stable.

Egolf (Refs. 32, 33) developed a time-marching vortex lattice rotor wake model using explicit Euler time integration. Four-sided vortex boxes with a finite core size were used to model the vortical wake. This work focused on extending the numerical methodology for parallel computations (Ref. 32) and on high-speed (μ =0.14 to 0.35) forward flight with BVI like interactions (Ref. 33). Although no wake instabilities were reported under these forward flight conditions, the time-history of the rotor thrust was found to be oscillatory. A convergence criterion based on time-averaged rotor thrust was used rather than convergence of the wake geometry itself. The effect of vortex core size was also examined and it was found that larger core size resulted in "smoother" airloads predictions. This suggests that a larger vortex core, with correspondingly lower induced velocities, may be helpful in suppressing numerical instabilities. This effect will be explained further in Chapter 2.

Miller & Bliss (Ref. 34) showed that a time-marching wake solution is susceptible to instabilities, and does not exhibit convergence at low advance ratios. However, the crux of this work was on periodic solutions, and no details of the time-marching solution methodology were given.

Baron & Boffadossi (Ref. 35) present a second-order time-marching free-vortex wake model using an Adams-Bashforth type method. The rotor was impulsively started to avoid a "guess" for the initial condition. Treatment of the viscous core growth was in a manner consistent with the diffusion of shear layers, with no user-specified ("tuning") parameters. The methodology was successfully applied to main-rotor/tail-rotor interactions, as well as to multiple rotor configurations. However, the presence of numerical instabilities in these cases is again apparent in the solution in the form of non-physical fluctuations in the predicted airloads.

Soliman (Ref. 36) coupled a time-marching wake model with a comprehensive coupled rotor/fuselage model. A prescribed far wake geometry was used along with the free wake. In this case, the far wake geometry was not rigid, but prescribed based on the last two free wake turns. The rotor was impulsively started from rest, but further details of the time integration strategy were not given. The need for proper modeling of the vortex core was highlighted. The methodology was applied to forward flight conditions, but the numerical stability issues were not directly addressed.

Lee & Na (Ref. 37) used a time-marching vortex method for predicting wake geometry and airloads of hovering rotor wakes. Results are presented for an impulsively started and a slowly started rotor. The impulsive start was shown to result in severe vortex instabilities, which are numerical in origin as there is no physical evidence to support such behavior. The slowly started rotor also showed numerical instabilities, but of a much smaller magnitude. The instabilities were clearly observed in the oscillatory nature of predicted airloads.

More recent work on time-marching free wake methods specifically focused on the vortex instabilities observed on hovering rotor wakes. Jain *et al.* (Refs. 38, 39) used a fourth-order Adams-Moulton method with straight-line vortex segments. A far-wake boundary condition was comprised of an semi-infinite cylinder of vorticity, the strength and radius being computed based on momentum considerations. The numerical solution for the wake showed the presence of instabilities. However, similar instabilities were also observed in the rotor experiments of Ref. 40, and the numerical solution (including instabilities) showed qualitative agreement with the experiments.

The authors argued that this vortex pairing instability was not an instability at all, but a steady-state behavior.

Lee *et al.* (Ref. 41) also reported good agreement between numerical solutions and the vortex pairing observed in the experiments of Refs. 40. In this case, a time-stepping vortex blob method similar to that of Ref. 37 was used to predict the wake geometry. Again, the predicted wake structure showed evidence of instabilities that qualitatively agreed with those observed in the experiments.

Both of these more recent studies (Refs. 39, 41) appear to suggest that the instabilities observed in numerical results are of physical significance. However, there is no physical mechanism in the numerical model that may lead to such phenomena. Therefore, the instabilities may be purely numerical in origin. In the next section (Section 1.3) the issue of vortex instabilities in the wake is first introduced, and then is more rigorously examined in Chapter 2.

1.2.5 Relaxation Based (Steady-State) Wake Methods

Although one objective of the present work was to develop time-accurate wake methods, a review of relaxation methods is presented here because both of these solution methods share common building blocks. As described earlier, the first iterative wake model used to predict performance of hovering rotors is due to Clark & Leiper (Ref. 22). However, this was really a time-integration method as opposed to a steady-state, periodic wake solution method.

Perhaps the most famous, and also the most widely used free wake model, is the relaxation wake of Scully (Ref. 23). This was a major revision of the previous work by the same author using a time-marching wake model (Ref. 11). In the case of the relaxation wake, the wake geometry was calculated iteratively with the enforcement of a periodicity condition. A weighted averaging scheme was employed for the induced velocities governing the wake distortions. The velocities from previous iterations were averaged with the velocities calculated from a distorted wake geometry under the effect of blade rotation alone, i.e., wake distortions without any self-induced velocity effects. This is perhaps why this method, and all consequent developments along similar lines, are termed as "relaxation" methods. Convergence was not explicitly enforced but was considered in only a qualitative sense. In hovering flight, a far-wake boundary condition in the form of a semi-infinite cylinder of vorticity was used. A prescribed/rigid inboard vortical wake sheet was also modeled. The wake geometry was typically modeled using 6 to 12 turns in hover, with a semi-infinite vortex cylinder in the far wake. In forward flight, 2 to 4 free wake turns were found to give subjectively "satisfactory" results. The wake methodology was applied to calculate higher harmonic airloads resulting from strong interactions between the vortical wake and the rotor. A desingularized algebraic viscous core model was used, which has become known as the "Scully model" in the rotating wing community. However, an artificially large vortex core size was found necessary to avoid excessively large induced airloads during BVI-type events. The vortex lines were discretized as straight line vortex elements corresponding to an azimuthal step of $\Delta\psi = 15°$,

The same basic methodology was adopted by Johnson (Ref. 42) and implemented in a comprehensive rotor analysis called CAMRAD (Comprehensive Analytical Model of Rotorcraft Aerodynamics & Dynamics) in 1980. The CAMRAD model recognized the importance of modeling the tip vortex roll-up process. The roll-up process was modeled using a near wake region consisting of complete vortex panel along with a tip line-vortex to represent partially rolled up vortex structure. In the far-wake only the completely rolled up tip vortex was considered. A second-order lifting line theory or a lifting-surface correction method could be used to obtain the blade bound circulation. The strengths of the tip vortices were based on the spanwise peak bound circulation. Later in 1988 (Ref. 43) a dual-peak circulation model was introduced to better represent the effects of negative loading on the advancing blades. In hover and axial flight, an approximate but computationally efficient far wake was used where the tip vortex elements were spread into a vortex sheet with axial and spiral components. Shed wake vortices were, in general, included in the analysis, and in the far wake were spread into vertical vortex sheets.

The CAMRAD analysis has been widely used in rotating wing community for various performance, airloads, vibrations, and other aeromechanical applications. Over the years, CAMRAD has undergone significant revisions and improvements. CAMRAD II (1992–97) also includes a time-marching algorithm, where a trapezoidal time-integration algorithm was preferred for stability reasons. However, because of the extra induced velocity calculations associated with the trapezoidal algorithm, an algorithm similar to the Euler explicit algorithm was used, with induced velocities averaged at the same time-step (Ref. 44). Typically a constant viscous core size is used with options to choose several inboard vortex trailers.

Miller (Ref. 45) developed an iterative solution methodology to predict the behavior of hovering rotor wakes. Both two-dimensional as well as three-dimensional wake models were developed. A spatial averaging of the induced velocities was used to iteratively update the positions of the vortex elements. A far-wake boundary condition in the form of vortex sheets for 2-D and vortex cylinder for 3-D was used. The wake convergence was indirectly monitored through the changes in rotor induced velocities, with a tolerance of 5% being specified as the convergence test. Weissinger-L lifting surface model (Ref. 46) was used to solve for the blade bound circulation, and the full spanwise trailed wake was assumed to roll-up into a tip-vortex, a root-vortex and a mid-span vortex. However, the influence of the root vortex on the hover airloads and performance was found to be negligible.

Bliss *et al.* (Ref. 47) developed an influence coefficient based method for rotor wakes in hover and axial flight. A Newton-Raphson type iterative procedure was implemented in a predictor-corrector form. The vortex lines were discretized into curved vortex elements to improve the calculation of the self-induced velocities. It was argued that this approach was more accurate than straight-line segmentation, and allowed for larger discretization levels in the interest of computational efficiency. A large viscous vortex core size (5% of rotor radius) was used with a far-wake boundary condition with a stack of vortex rings. An upwind discretization scheme was used to improve stability characteristics of the numerical method. A "sink" was also included in the flow field to conserve the mass flow through the rotor disk, and to help improve numerical convergence. The methodology was applied to both hovering and axial flight, however, proper wake convergence was demonstrated only in axial climb.

In 1985, Bliss *et al.* (Ref. 48) introduced the concept of a self-preserving wake structure along with the influence coefficient methodology described previously. In this case, the wake was assumed to "self-preserving" in a blade-fixed frame, or in other words, axisymmetric. A free tip vortex and inboard vortex trailers were also included. A far-wake boundary condition was imposed in the form of the vortex filaments extending to infinity as ideal (constant radius, constant pitch) helical filaments. A converged wake solution in hovering flight was demonstrated. The same methodology was later applied to a hover performance analysis and rotor airloads calculation (Ref. 49).

An eigen-analysis of the the wake structure based on the induced velocity influence coefficients was also performed in Ref. 49. It was shown that several unstable modes existed corresponding to positive eigenvalues, which were found to be linearly dependent on the rotational frequency of the rotor. This was one of the first attempts to analyze eigenvalue-based stability of rotor wake solutions. It was also shown that the self-preserving (i.e., axisymmetric) hovering wake solution was unstable, as usually observed in experiments, although the solution did not exhibit instabilities.

Miller & Bliss (Ref. 50) developed an iterative scheme for the direct periodic solution for the rotor wake. The non-linear equations governing the wake, including the Biot-Savart induced velocity terms, were linearized using Taylor expansion about a mean geometry and then solved using second-order accurate predictor-corrector methods. A central difference based Lax-Wendroff method was used, with a backward Beam-Warming at the last collocation point in the far wake. The details of these difference methods can be found in most standard CFD texts, e.g., Ref. 51. Analytical/Numerical Matching (ANM) model (Ref. 52) was used to provide high near-field accuracy as well as good computational efficiency. The ANM uses an efficient approach to calculate far-field velocity components, which comprise the bulk of the induced velocity calculations in the rotor wake solution. The strong near-field velocities are then found with the aid of an analytical correction to the far-field solution. The ANM model was then augmented with a far wake extension to account for the theoretically semi-infinite domain of the wake.

Crouse & Leishman (Ref. 53) developed a relaxation rotor wake method using spatial central differences and a predictor-corrector sequence to solve the wake governing equation. The predictor-corrector methodology was shown to give improved stability than a simple one-step explicit method. Convergence was judged based on relative wake geometry changes between successive iterations and demonstrated in hovering flight. However, the main crux of this work (Ref. 54) was on rotor/fuselage interactions and the wake methodology was essentially developed for that particular application.

Bagai (Ref. 55) developed a comprehensive free-vortex wake methodology based on the relaxation approach. A pseudo-implicit predictor-corrector scheme was used to calculate the wake geometry, with wake periodicity being enforced for the trailing wake generated by all blades. A five-point central difference scheme was introduced for the derivative calculations, and an averaged induced velocity was used. This approach was shown to significantly improve convergence characteristics. The blade loading was determined using the Weissinger-L model. Different discretization steps for the blade azimuth and vortex age were implemented using velocity field interpolation to preserve solution propagation along the correct characteristics. A far-wake boundary condition was comprised of two prescribed wake turns below the free vortex wake. However, such a boundary condition was found to be necessary only in hovering flight, and was not used for other flight conditions. This methodology was successfully applied to both the rotor wake geometry and induced inflow prediction in forward flight (Refs. 56, 57). The methodology was also extended to multi-rotor configurations such as coaxial, tandem and tilt-rotor (Ref. 58). Accelerations technique based on adaptive grid sequencing was developed to improve computational efficiency while preserving the accuracy of the wake solution (Ref. 59). This methodology is also widely used in both academia and industry, and has been coupled with other comprehensive helicopter analysis codes, e.g., Refs. 60 and 61.

1.2.6 Summary

The important issues limiting a time-accurate solution of the rotor wake problem, as found in this literature review, are summarized below.

- Time-marching rotor wake solutions are generally susceptible to vortex instabilities. Predictor-corrector methods are found to be, in general, more numerically stable than explicit one-step methods. Velocity averaging, as in the relaxation methods, is also found to improve the stability of numerical methods.

- Several approaches are available for discretization of vortex filaments like vortex blobs, straight-line/curved segments, etc. However, a discretization approach consistent with the remaining numerical method must be chosen. The accuracy of these discretization models has not been rigorously addressed in the open literature.

- In most cases, a far-wake boundary condition is necessary to account for wake truncation effects. These effects are especially dominant in hovering flight. However, it is necessary to choose a boundary condition that is universally applicable in all flight regimes, including for steady-state as well as unsteady (maneuvering) flight conditions.

- Vortex modeling is an important issue in obtaining physically meaningful wake geometries. Some researchers employ empirical vortex models consistent with experimental observations. However, most methodologies published in the open literature use an arbitrary core size models based on numerical and not physical considerations.

1.3 Instabilities in the Rotor Wake

As mentioned in the preceding section, one problem that strongly influences rotor wake prediction capability is tied into the various types of disturbances and instabilities in the numerical solution for the wake. Although similar instabilities have also been observed in rotor wake experiments, such instabilities in numerical calculations have a degrading effect on the convergence; that is, the solution may often diverge or "blow-off". The vortex instabilities observed on rotor wakes can be both global (i.e., affecting the overall wake structure and induced inflow at the rotor), as well as local (i.e., confined to only a part of tip vortex filaments). In some cases local wake instabilities may lead to vortex bursting, which leads to rapid diffusion of vorticity (e.g., Ref. 62). Local interactions between closely spaced tip vortices can be a source of global wake instabilities in a rotor wake, and can lead to various types of periodic or aperiodic deformations of the wake structure.

Wake instabilities and aperiodic wake formation often find their source in the so-called "vortex pairing" or localized roll-up between two adjacent tip vortex filaments. These effects were first experimentally documented with hovering rotors by Landgrebe (Ref. 13) and by Tangler *et al.* (Ref. 14). The phenomenon was attributed to an inherent characteristic of the unstable vortical wake structure, which was further supported by linearized stability analyses of an infinitely long helical filament (Refs. 63, 64). Gupta & Loewy (Ref. 65) extended this stability analysis to multiple interdigitated helical vortices to examine the stability of multi-bladed rotor wakes. These analytical studies have suggested, although only by analogy to infinite helical vortex filaments, that a hovering rotor wake is intrinsically (physically) unstable with several possible types of instability modes.

Vortex Pairing in Experiments

More recently, periodic interactions between tip vortex filaments in the wake of two-bladed rotors – specifically in the form of tip vortex pairing where adjacent vortices revolve about a common centroid of vorticity – have been experimentally observed and documented by Caradonna *et al.* (Ref. 40) and Martin *et al.* (Ref. 66). Experimental evidence suggests that the susceptibility of the rotor wake to pairing or other instabilities is affected by the number of blades and rotor operating state. In particular, the onset of tip vortex pairing is known to be sensitive to rotor operating conditions, e.g., with increasing thrust (or, alternatively, increasing collective pitch) the vortex pairing occurs at increasing downstream distance below the rotor (Ref. 14). A similar effect was reported with increasing climb velocity in Ref. 40.

This type of vortex pairing instability is present in almost all hovering rotor wakes. In some cases these may be more obvious than others. The phenomenon is illustrated in Fig. 1.9 using a series of shadowgraph images obtained in the wake of a hovering two-bladed propeller. The tip vortex pairing is seen to occur just one rotor revolution below the TPP, where one tip vortex is seen to move radially inward and axially downward, while the other tip vortex appears to move radially outboard and axially upward. This is illustrated using a sequence of close-up images from the region where the vortex pairing is observed. Such relative motion between the two tip vortex filaments gives the impression that the two vortices are rotating around a common centroid like a pair of point vortices, hence the name “vortex pairing.” In the far wake, the pairing phenomenon is even more obvious where the two vortices have rotated almost 180° and have exchanged vertical positions.

While the stability analyses of Refs. 63–65 would suggest that vortex pairing is a form of wake instability, others have suggested otherwise. Jain *et al.* (Ref. 38) suggest

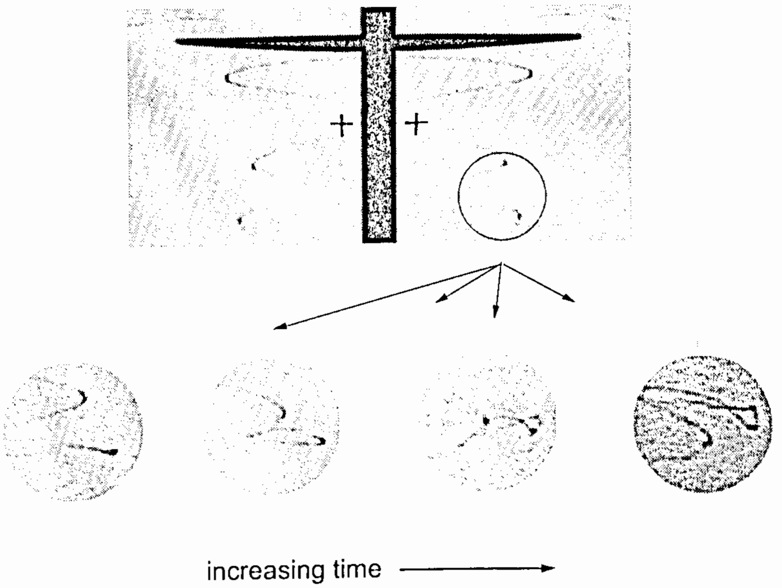

Figure 1.9: Vortex pairing instability as observed in the wake of a two-bladed propeller in hover using shadowgraph flow visualization. Source: University of Maryland.

that vortex pairing in rotor wakes is not an instability at all, but is a result of mutual interactions of two vortex filaments in a form that is analogous to the perpetual leap-frogging motion of two inviscid vortex rings. This implies that the vortex pairing constitutes an equilibrium state of the rotor wake geometry. Note that instability refers to the behavior of a system *disturbed* from its equilibrium state. It could be further argued that the steady, deterministic nature of the wake trajectories observed in some of these recent experiments cannot be an inherent wake instability, mainly because instabilities are more often attributed to stochastic phenomena such as an overall aperiodicity of the rotor wake (Ref. 67).

Clearly, these observations pose considerable challenges to the rotor analyst. From a rotor wake prediction standpoint, the highly periodic and repeatable nature of the wake visualization results observed by Caradonna *et al.* (Ref. 40), and also by Martin *et al.* (Ref. 66) suggests that deterministic first-principle based wake prediction methods should be able to model the tip vortex pairing process. In fact, some vortex wake methods seem to predict a behavior that closely replicates the vortex pairing that has been observed in some experiments — see, for example, Ref. 38 or 41. Furthermore, the fact that the effects are present in some (almost identical) rotor experiments but not in others suggests that the experimental setup, and flow turbulence or other recirculation in the test facility, may be responsible for part, if not all, of the observed behavior of the wake.

Therefore, the fact that some but not all prediction methods show this behavior raises questions as to whether these effects have their source in the numerical methods themselves, rather than being physical in origin. From a prediction standpoint, the most important question this raises is whether or not predictions that provide periodic wake geometries can be considered as equilibrium, steady-state solutions. It is also not immediately obvious as to why, in general, only time-accurate wake solutions are able to properly model this "inherent" physics of interacting tip vortex filaments in the rotor wake. One of the motivations of the present work was to properly understand these vortex instabilities, and their impact on time-accurate predictions. In Chapter 2, the overall behavior of a helicopter rotor wake in axial flight and the onset of instabilities will be described using numerical solutions to the wake problem using free-vortex schemes. These numerical results are also supported using experimental measurements where evidence of tip vortex pairing was found. The problem is then rigorously approached using a linearized eigenvalue stability analysis that is applicable to any general rotor wake structure.

1.4 Objectives of Dissertation

The motivation for the current research stems from various deficiencies in current rotor wake analyses, especially time-accurate free-vortex wake methods. The major drawback with all previous time-accurate wake solution methodologies has been numerical instabilities, as discussed in the previous section. This also restricted the methodologies to only certain flight conditions, such as vertical flight or forward flight. The main objective of this dissertation was to develop a time-accurate wake solution methodology that is general, robust, versatile and numerically stable.

The development of a stable wake methodology involves understanding the stability characteristics of both the solution method and the solution itself. It is known from experience that a hovering rotor wake is physically unstable, and any small disturbances present in the flow field will grow with time. Numerical instabilities tend to mimic the growth of such physical disturbances, thus making it hard to recognize the numerical origin of these instabilities. One objective of the current research was to better understand these physical rotor wake instabilities, and how they are influenced by the rotor geometric and operating conditions.

Properly distinguishing numerical instabilities observed in numerical wake solutions from physical phenomenon is a long-standing issue. The fact that the rotor wake is physically unstable further complicates this issue. In the present work, the stability characteristics of numerical algorithms is examined to properly understand the origin of such numerical instabilities. The objective was to choose a proper time-integration algorithm that will suppress growth of such non-physical instabilities from numerical errors alone. This implies that not only the order of accuracy of the algorithm is important, but also its stability and convergence characteristics.

Besides the method of numerically solving the wake equations, there has been some debate over the type of discretization strategies used to represent the vortex filaments. The straight-line segmentation is, perhaps, the most widely used because of its simplicity. The present work rigorously examines this discretization strategy to understand the associated discretization errors. The objective was to ensure that the mutual and self-induced velocities are correctly represented in the discretized model up to a consistent level of accuracy. This is also important for the overall accuracy of the wake geometry solution.

Another desirable characteristic of any mathematical wake model is that it should be valid under all flight conditions. This means that the analysis should contain the least number of empirical parameters. The present wake model includes empiricism only in the form of a viscous core growth model and induced velocity distribution. One objective of the present work was to examine this empirical model with available experimental results and choose consistent values that would be valid over a broad range of operating conditions.

Finally, the long-term objective of the current work is to formulate a methodology that can be easily integrated into comprehensive aeromechanics, acoustics, and flight mechanics analyses. It is hoped that the present work will prove to be a significant contribution towards a better understanding of the rotating wing aerodynamics and help in the development of more efficient and less expensive rotorcraft.

1.5 Organization of Dissertation

The fundamental problem of determining the rotor blade airloads and induced inflow at the blades was introduced in the beginning of Chapter 1. The current state-of-the-art rotor wake methodologies were then introduced through a literature overview given in Section 1.2. Although there have been significant developments in methodologies to mathematically model the aerodynamic environment at the rotor, most of these schemes have been limited in application. The motivation for the current work stems from a need to rectify some of these deficiencies, as outlined in the previous section.

The remainder of the dissertation is organized in three parts: methodology, results and discussion, and conclusions. Because of its importance to the wake methodology, the analysis of aerodynamic stability of rotor wakes is given separately in Chapter 2. The results and discussion pertaining to rotor wake stability are also included in this chapter because it is somewhat independent of the remaining discussion of the wake methodology. Chapter 3 describes the methodology for solving the wake governing equations, while Chapter 4 describes the rotor blade flapping and blade-lift solution methodologies. The mathematical and numerical aspects of the methodology, such as convergence studies, are also included in these chapters.

Chapters 5 and 6 discuss the numerical results obtained using the present methodology. In Chapter 5, the steady-state wake results are presented along with experimental measurements to validate the analysis. Chapter 6 focuses on results obtained using the time-accurate analysis for rotors in transient flight conditions. These results are also compared with available experimental results. Some results for idealized maneuvering flight conditions and for descending flight are presented in Chapter 7 to help understand the rotor wake behavior. Finally, Chapter 8 summarizes the conclusions drawn from the present work, and provides suggestions for further work.

Additional material which is necessary for the present analysis, but is not directly related to the wake methodology is provided as appendices at the end of the dissertation with appropriate cross-references in the main text. This includes details and explanations of various ideas applied in the present research.

Chapter 2

Aerodynamic Stability of Helicopter Rotor Wakes

Experimental studies suggest that the wake of a helicopter rotor is physically unstable in hovering and axial (vertical) flight. This inference is based on several experimental observations showing presence of vortex instabilities, as well as by analogy to theoretical analyses of helical vortex structures (Refs. 63–65). This chapter describes a new application of a linearized stability analysis to the rotor wake geometry. This analysis helps in understanding the different types of instabilities observed in both experiments and numerical solutions, and also how these are affected by the operating conditions of the rotor.

It should be noted that the term "unstable" inherently implies an unstable *equilibrium*. That is, the hovering rotor wake in a periodic, self-preserving state is in equilibrium, albeit an unstable equilibrium. This unstable equilibrium and the associated divergence (growth) rates are an inherent characteristic of the rotor wake. An instability refers to the behavior after the wake is *disturbed* from this unstable equilibrium. Therefore, the wake instabilities observed in experiments may result from various disturbances present in the flow-field most likely because of artifacts of the experimental set-up. The so-called numerical instabilities, however, are initiated only because of numerical errors. It must be recognized that only the initial equilibrium state and the growth rates associated with growing disturbances, which sustain an instability, are an inherent characteristic of the rotor wake. The following analysis identifies these inherent characteristic growth rates for the rotor wake. The instabilities are only a result of these inherent characteristics and not an inherent characteristic themselves.

In the next section, the vortex instabilities are introduced using numerical as well as experimental results. The problem is then examined using a linearized stability analysis of the equation governing the rotor wake. Both the stability of equilibrium wake geometry and the corresponding deformation modes are examined to better understand the vortex pairing phenomenon. It is shown that the numerical results obtained with free-vortex wake methods are dependent on the numerical algorithm used. It is shown that the round-off and truncation errors in the numerical solution can be responsible for the onset of numerical wake instabilities, which in some cases, can fortuitously replicate the observed (physical) behavior of the rotor wake.

2.1 Motivation: Instabilities in Numerical Solution of the Rotor Wake

The general problem of the rotor wake behavior and the onset of wake instabilities is now introduced using a numerical analysis of the rotor wake using a free-vortex method. Free-vortex wake methods have emerged as popular aerodynamic models for helicopter rotor analyses because they offer high fidelity and versatility at modest computational cost. These methods can be categorized into two main types: time-accurate algorithms where the wake governing equations are integrated in time (Refs. 10–12, 22, 33, 43), and steady-state solution algorithms that solve for a periodic solution either directly (Ref. 68) or by using relaxation methods (Refs. 44, 53, 56, 69).

As described in Chapter 1, the motion of the free vortex elements in the wake is governed by the vorticity transport theorem, i.e.,

$$\frac{d\vec{r}}{dt} = \vec{V}(\vec{r}) \tag{2.1}$$

where $\vec{r}$ is the position vector of the point on the vortex filament and where $\vec{V}(\vec{r})$ is the local fluid velocity at the point $\vec{r}$ resulting from any external velocity as well as the self and mutually induced velocities of the entire vortex wake. Equation 2.1 can also be written in the form of a partial differential equation, as described previously in Chapter 1 (Eqs. 1.1-1.2) as

$$\frac{\partial\vec{r}}{\partial\psi} + \frac{\partial\vec{r}}{\partial\zeta} = \frac{\vec{V}(\vec{r})}{\Omega} \tag{2.2}$$

The free-vortex wake results presented in this chapter for the wake stability analysis, are calculated using a development of the free-vortex wake analysis of Bagai & Leishman (Refs. 56–59). The original analysis used a second-order accurate pseudo-implicit predictor-corrector (PIPC) relaxation formulation to solve for steady-state (periodic) wake geometry solutions. The so-called five-point central difference scheme was used to approximate the LHS of the governing equations (Eq. 2.2), while the induced velocities were evaluated using standard straight-line segmentation of the vortices. This five-point scheme has the special property that for equal discretizations along ψ and ζ, the truncation errors from the LHS of the discretized equations cancel each other resulting in an "exact" representation.

The relaxation approach solves for an equilibrium solution by imposing periodicity conditions. In the present work, these equilibrium solutions were used primarily for wake stability analyses, and as an initial condition for two newly developed time-marching algorithms. These time-marching algorithms are also second-order accurate predictor-corrector formulations, and allow transient wake geometry calculations with no pre-assumed wake periodicity requirements. The first time-marching algorithm, which is referred to as the PCC scheme, uses a five-point central differencing scheme similar to that used in the PIPC relaxation algorithm. The second algorithm, referred to as the PC2B scheme, also uses a central difference scheme for the spatial (ζ) derivatives, but a second-order backward difference scheme for the temporal (ψ) derivatives. Such a difference scheme introduces additional truncation errors which are both dissipative and dispersive. However, these errors are of a higher order, and the overall solution accuracy is still second-order. The details of these algorithms will be described in Chapter 3.

The problem is best introduced by way of an example using numerical solutions of the wake problem. Representative predictions of the wake geometries for a two-bladed hovering rotor as obtained using these three free-vortex wake algorithms is presented in Fig. 2.1, the results being shown for a reference blade azimuth of $\psi_{\text{ref}} = 0°$. The rotor was operated at a thrust coefficient of $C_T = 0.005$, with a tip speed of $\Omega R = 89$ ms^{-1}. The rotor geometry and operating conditions for this two-bladed rotor are described in detail in Ref. 66. For these calculations, four free-wake turns ($\zeta_{\text{max}} = 1440°$) were used with a discretization of $\Delta\psi = \Delta\zeta = 10°$. The solid line shows the vortex filament from blade 1 (the reference blade), while the dashed line shows the vortex filament from blade 2. Note that the relaxation solution shown in Fig. 2.1(a) predicts a smooth wake contraction. The two tip vortices follow the same radial and axial trajectories and are free from any local or global instabilities or from any evidence of vortex pairing. Such axisymmetric, periodic, behavior is typical of the physical wakes generated by many hovering rotors.

This periodic solution for the wake was then used as an initial condition for the two time-accurate algorithms. The calculations were continued in a time-accurate sense for up to fifteen rotor revolutions. The time-accurate solution obtained using PCC algo-

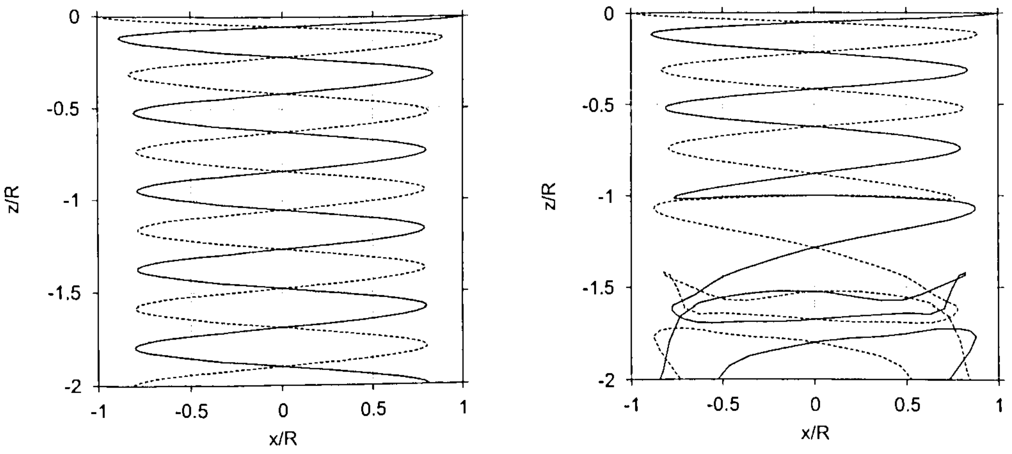

(a) Relaxation (PIPC)

(b) Time-marching (PCC)

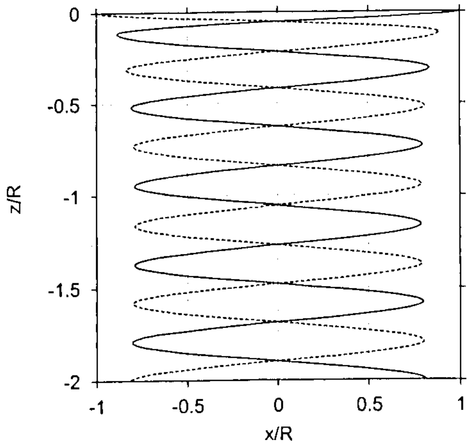

(c) Time-marching (PC2B)

Figure 2.1: Sample free-vortex wake geometries for a two-bladed hovering rotor using (a) Relaxation (PIPC), (b) Time-marching (PCC), and (c) Time-marching (PC2B) algorithms, $C_T = 0.005$, $\psi_{\text{ref}} = 0°$ (Rotor 1).

rithm, as shown in Fig. 2.1(b), produced some apparently erratic distortions after about two rotor revolutions. Prior to this, the wake geometry was found to be almost identical to the relaxation solution. The solution obtained using PC2B algorithm was, however, found to be essentially identical to the relaxation solution, as shown in Fig. 2.1(c).

The wake convergence histories corresponding to these three algorithms are shown in Fig. 2.2 in terms of a root mean squared (RMS) change in wake geometry per rotor revolution or per wake iteration. The PIPC relaxation solution shows a converging trend by virtue of wake periodicity enforcement. Starting from such a converged relaxation solution, the PCC time-marching algorithm shows an increased change in wake geometry. Thereafter, the wake geometry continues to change from one rotor revolution to another, i.e., it is not periodic at the rotational frequency of the rotor. However, notice that the solution is not divergent and the change in wake geometry remains bounded. Therefore, the apparently erratic wake distortions shown in Fig. 2.1(b) are, in reality, deterministic and bounded. The PC2B time-marching solution, however, predicts a continuously converging trend starting from the same initial wake geometry. The change in wake geometry per rotor revolution decreases with time, suggesting that the relaxation solution is, indeed, a steady periodic solution.

Figure 2.3 shows the predicted trajectories of the tip vortices along with the experimental results from Ref. 66, as seen from a fixed radial-axial plane. At early vortex ages near the tip path plane (TPP), the tip vortices from the two blades were seen to follow the same trajectory. At later vortex ages, however, these vortices followed different trajectories with one vortex moving radially inward while the other moving radially outward. The azimuth where the two tip vortices cross in the radial direction is the onset of the so-called "pairing." The PIPC algorithm predicted an axisymmetric wake structure with identical vortex trajectories, and it is the time-accurate PCC

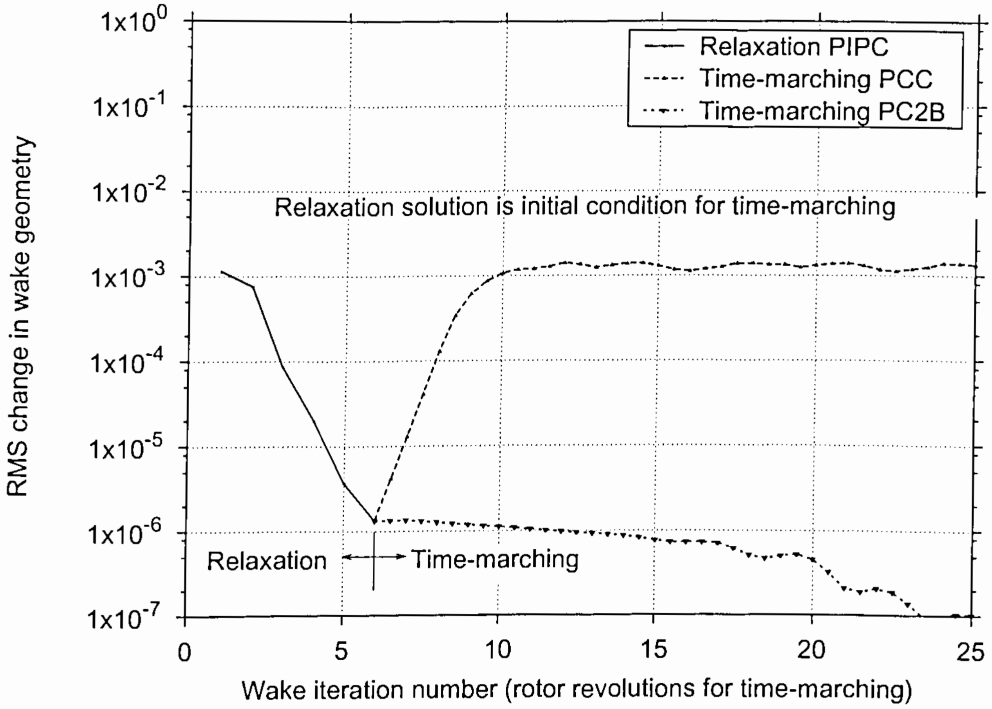

Figure 2.2: Wake convergence histories for free-vortex wake solution using the three solution algorithms, $C_T = 0.005$ (Rotor 1).

algorithm that showed better agreement with experimental results.

This interesting behavior is further elucidated in Fig. 2.4 using an alternate presentation of the predicted results in the form of axial and radial tip vortex displacements as a function of the reference blade (blade 1) azimuthal location, ψ_{ref}. The corresponding locations of other blades are given by the relation

$$\psi_b^{(m)} = \psi_{\text{ref}} + \frac{2\pi(m-1}{N_b} \tag{2.3}$$

Therefore, for the two-bladed rotor in the present case the reference blade azimuth corresponding to the second blade is

$$\psi_{\text{ref}} = \psi_b^{(2)} - \pi \tag{2.4}$$

In this experiment, evidence of vortex pairing was found between tip vortex filaments

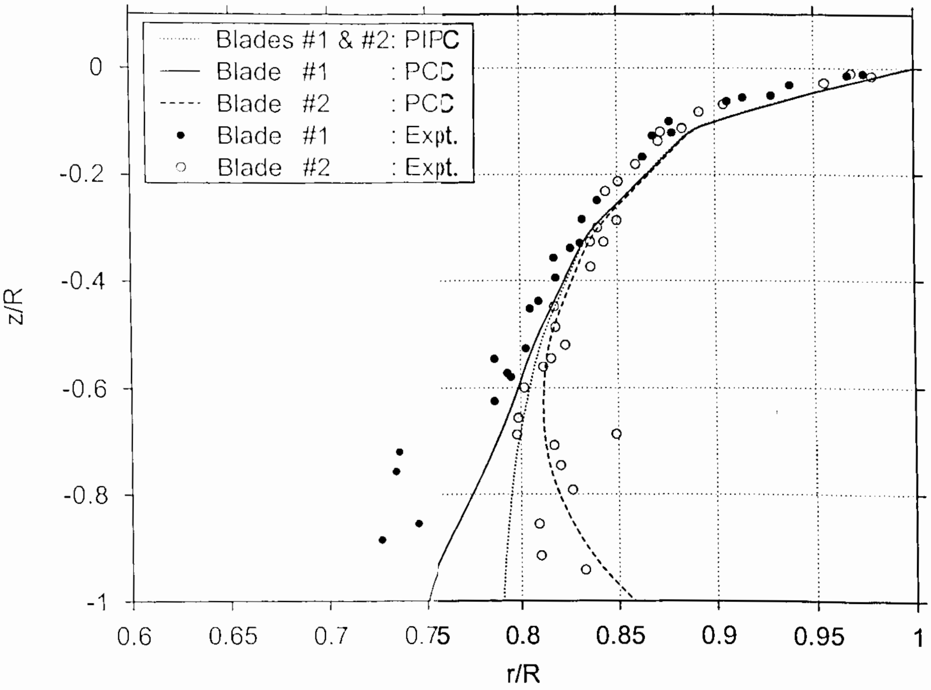

Figure 2.3: Predicted and measured vortex trajectories in hover as observed in a fixed radial-axial plane, $C_T = 0.005$ (Rotor 1). Experimental results from Ref. 66.

that were about two rotor revolutions old downstream of the rotor. This pairing phenomenon is evident from the results shown in Fig. 2.4, which indicate that the trajectories of the two tip vortices cross each other. As noted previously, the relaxation (PIPC) solution is axisymmetric and both tip vortex filaments follow the same trajectory. However, when using the time-accurate solution with the PCC algorithm, the wake was not axisymmetric and the two tip vortex filaments followed different trajectories. In particular, the two vortices formed an interacting vortex pair at an azimuth where the two axial displacement trajectories intersected each other. The computed results show good agreement with measured trajectories at early vortex ages. The time (azimuth) at which the two vortices pair, however, is somewhat over-predicted.

To better understand the onset of vortex pairing, a sequence of predicted wake

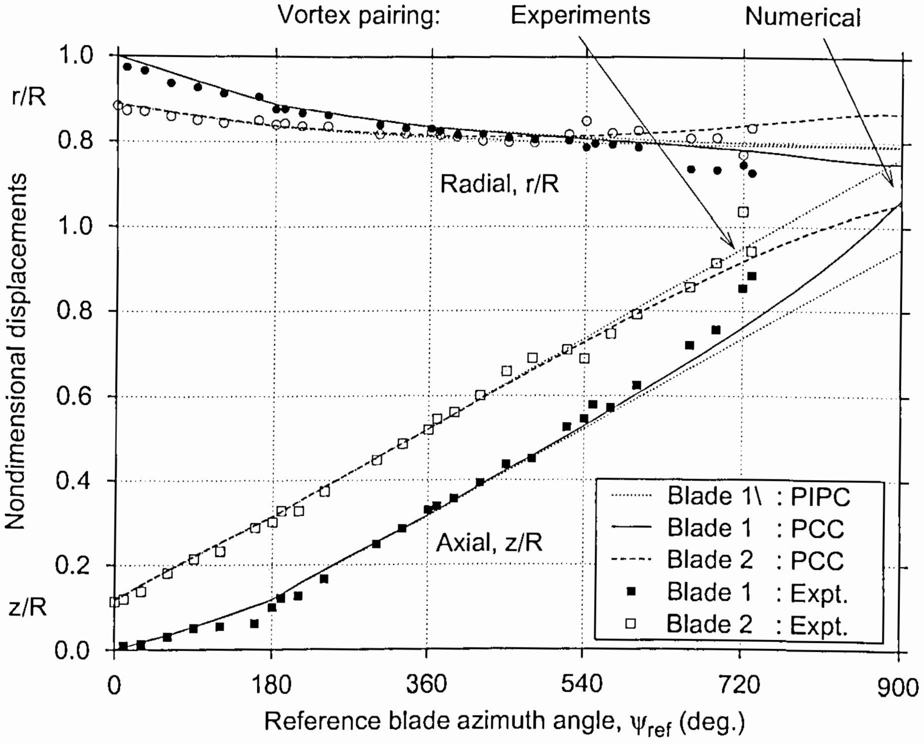

Figure 2.4: Predicted and measured tip vortex displacements as a function of rotor blade azimuthal location: time-accurate wake geometry predictions using the PCC algorithm, $C_T = 0.005$ (Rotor 1). Experimental results from Ref. 66.

structure for different blade positions (reference blade azimuthal locations) is shown in Figs. 2.5(a)–(f). The equilibrium (periodic) wake boundary is shown in dotted line. The symbols in Fig. 2.5(a)–(f) show the vortex trajectories as seen in a fixed radial-axial plane at different times (reference blade azimuth). Note that the vortex filament trailed from blade 1 moves radially inward and axially downward, while that trailed from the blade 2 moves radially outward and axially upward. At $\psi_b \approx 880,^\circ$ one filament loop can be seen to pass through the other. At this azimuth, the two vortices become nearly parallel to the rotor plane forming a vortex pair. This corresponds to the reference blade azimuth shown in Fig. 2.4, where the axial displacements of two vortex filaments are equal.

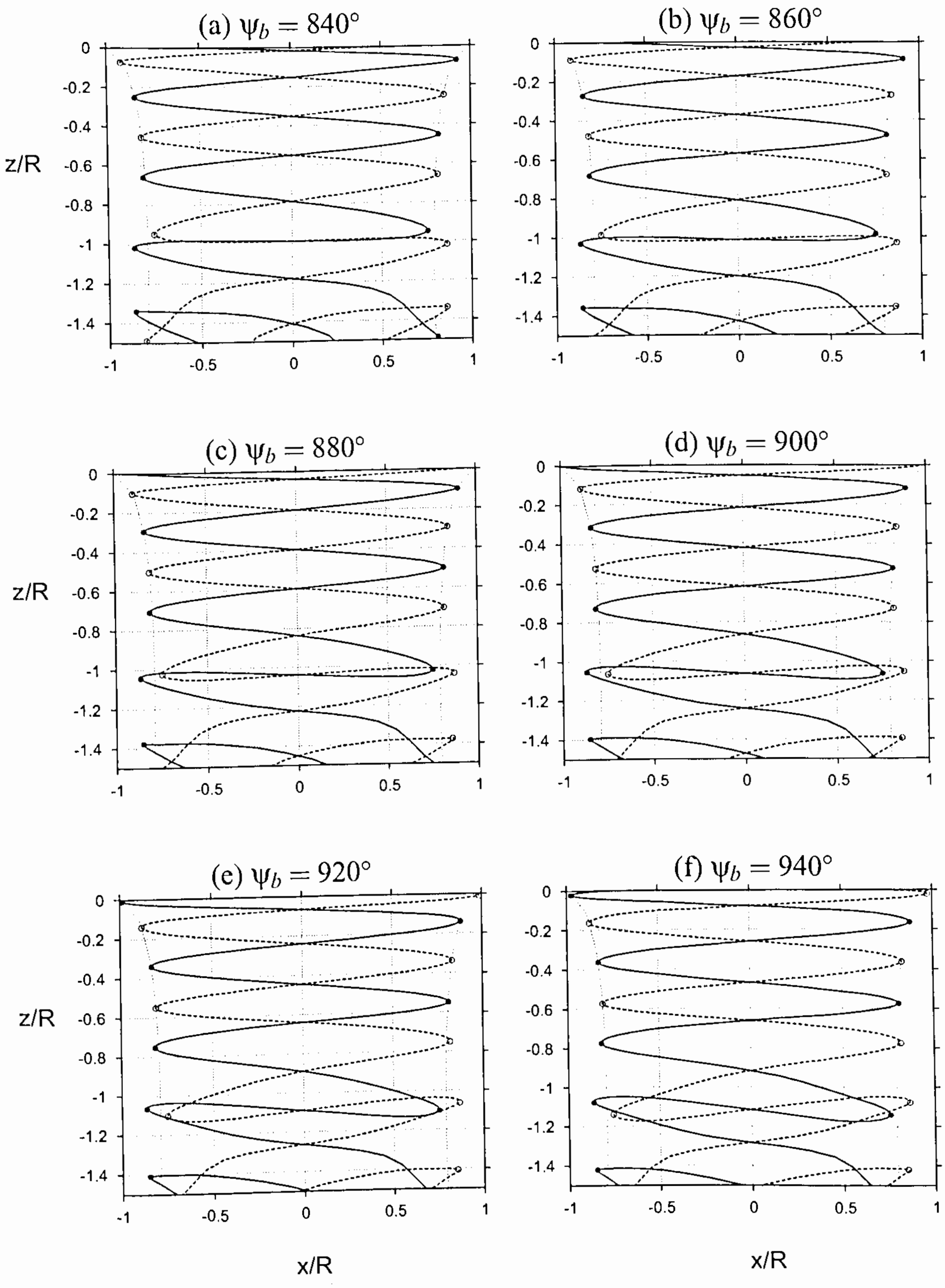

Figure 2.5: Time history of two tip vortex filaments of a two-bladed rotor in hover showing vortex pairing as predicted using the PCC algorithm, $C_T = 0.005$ (Rotor 1). (a) $\psi_b = 840°$, (b) $\psi_b = 860°$, (c) $\psi_b = 880°$, (d) $\psi_b = 900°$, (e) $\psi_b = 920°$, and (f) $\psi_b = 940°$. Symbols indicate the position of the vortices in the *x*-*z* plane.

Although, there is good agreement between predictions and observations of the vortex pairing phenomenon, the underlying physics of why these interactions occur is definitely not clear. For example, it is not immediately obvious as to why the PIPC relaxation algorithm and time-accurate PC2B algorithm fail to predict these vortex interactions despite using identical blade and wake models. The wake vortex trajectories close to the rotor are identical in all three solutions — see Figs. 2.3 & 2.4. Therefore, it is expected that vortex interactions originate away from the rotor and would likely have only a small influence on the inflow and blade loads. The mechanism proposed by Tangler *et al.* (Ref. 14), which is based on experimental observations, also suggests that the wake is relatively stable to disturbances while it is undergoing a radial contraction. The instabilities become apparent only in the region after the initial radial contraction, which is typically after the first rotor revolution. The motivation for the following stability analysis is to better understand the physics of this vortex pairing phenomenon.

2.2 Linearized Rotor Wake Stability Analysis

The rotor wake behavior is now examined for stability following the methodology applied to linearized flow stability analyses. The rotor wake geometry, as given by a solution to Eq. 2.1, is the basic equilibrium solution used as a starting point for the analysis. This equilibrium solution is then perturbed by a small quantity, say $\delta\vec{r}$, with the new geometry being described by $\vec{r}+\delta\vec{r}$. The governing equation applied to this perturbed state of the wake geometry is given by

$$\frac{d(\vec{r}+\delta\vec{r})}{dt}=\vec{V}(\vec{r}+\delta\vec{r}) \tag{2.5}$$

The perturbation equation is the equation governing the behavior of the small wake perturbation (displacement), $\delta\vec{r}$, and can obtained by subtracting the original equilibrium equation (Eq. 2.1) from the perturbed equation (Eq. 2.5), i.e.,

$$\frac{d(\delta\vec{r})}{dt} = \vec{V}(\vec{r}+\delta\vec{r}) - \vec{V}(\vec{r}) \tag{2.6}$$

The induced velocity on the RHS of Eq. 2.5 can be expressed as a series in $\delta\vec{r}$, i.e.,

$$\vec{V}(\vec{r}+\delta\vec{r}) = \vec{V}(\vec{r}) + \delta\vec{V}(\delta\vec{r}) + O\left(\delta\vec{r}^{\,2}\right) \tag{2.7}$$

The above equation gives the exact behavior of the small perturbation, $\delta\vec{r}$, in time. However, this equation is not easily amenable to analysis and requires simplification. At this stage, the perturbation is assumed to be small and, therefore, the higher order perturbation terms can be neglected. The perturbation equation is now linearized by neglecting higher-order terms in $\delta\vec{r}$ to give

$$\frac{d(\delta\vec{r})}{dt} = \delta\vec{V}(\delta\vec{r}) \tag{2.8}$$

The first order velocity perturbation on the RHS of the above equation can be evaluated using the Biot-Savart law.

2.2.1 Perturbation Induced Velocity

The induced velocity, $\vec{V}(\vec{r})$, is obtained by dividing each curvilinear vortex filament comprising the wake into a number of elementary vortex segments, and numerically integrating the induced velocities over the entire filament length. This is most easily accomplished using straight-line segments, which are readily amenable to analytic forms of Biot-Savart law integration (see Section 3.2.1 for a detailed accuracy verification of this straight-line segmentation approach). The total induced velocity at a point is then obtained by summation of the velocity induced by each vortex segment. The

Biot-Savart law, previously formulated in Eq. 3.3, which gives the velocity induced by a vortex element $\vec{l}$ at a point $\vec{r}$ as

$$\vec{V} = \frac{\Gamma}{4\pi}\int_{l} \frac{\vec{dl}\times\vec{r}}{|\vec{r}\,|^{3}} \tag{2.9}$$

Therefore, the velocity at a point P induced by a single, straight-line vortex element extending from point A to B, (see Fig. 2.6) can be expressed in the form

$$\left\{\begin{matrix} V_x \\ V_y \\ V_z \end{matrix}\right\} = \frac{\Gamma_v}{4\pi h}(\cos\theta_1 - \cos\theta_2)\left\{\begin{matrix} e_x \\ e_y \\ e_z \end{matrix}\right\} \tag{2.10}$$

where Γ_V is the circulation strength of the vortex element and

$$\vec{r}_1 = \vec{r}_P - \vec{r}_A, \qquad \vec{r}_2 = \vec{r}_P - \vec{r}_B, \qquad \vec{l}_{12} = \vec{r}_B - \vec{r}_A, \tag{2.11}$$

$\vec{r}_A, \vec{r}_B, \vec{r}_P$ are the position vectors of points A, B, and P respectively. Also, the perpendicular separation distance, h, is

$$h = r_1 \sin\theta_1 = r_2 \sin\theta_2 \tag{2.12}$$

and

$$\cos\theta_1 = \frac{\vec{l}_{12}\cdot\vec{r}_1}{l_{12}r_1}, \qquad \cos\theta_2 = \frac{\vec{l}_{12}\cdot\vec{r}_2}{l_{12}r_2}, \qquad \vec{e} = \frac{\vec{l}_{12}\times\vec{r}_1}{\left|\vec{l}_{12}\times\vec{r}_1\right|} \tag{2.13}$$

Notice that this velocity field corresponds to that of a potential vortex and so must exhibit a singularity as $h \to 0$. A real vortex, like the rotor tip vortex, has a viscous core where the induced velocity resembles solid body rotation. Therefore, the above equation can be modified to include a viscous vortex core with a core radius of r_c. This is accomplished using a general desingularized induced velocity profile with the algebraic form (see Section 3.2.1)

$$V = \left(\frac{\Gamma}{2\pi}\right)\frac{r}{\left(r_c^{2n} + r^{2n}\right)^{1/n}} \tag{2.14}$$

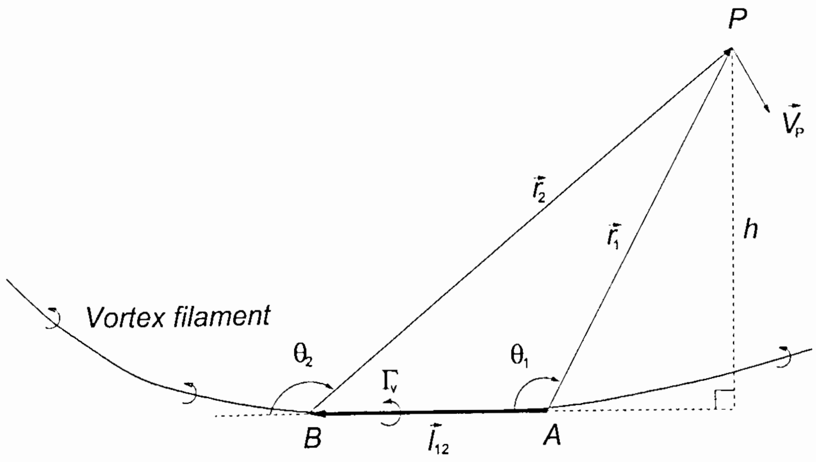

Figure 2.6: Schematic of the velocity induced by a straight-line vortex element.

More details of the algebraic vortex model are given in Appendix A. Note that in the case where $n \to 0$, the Rankine velocity model is obtained; for $n = 1$ this corresponds to the widely used "Scully" model (Ref. 11); for $n = 2$ the induced velocity is almost identical in result to that of the Lamb-Oseen model (Ref. 70). With such a desingularized vortex model the above equation for the induced velocity (Eq. 2.10) is modified into the form

$$\begin{Bmatrix} V_x \\ V_y \\ V_z \end{Bmatrix} = \left(\frac{\Gamma_v}{4\pi}\right) \frac{h}{\left(r_c^{2n} + h^{2n}\right)^{1/n}} (\cos\theta_1 - \cos\theta_2) \begin{Bmatrix} e_x \\ e_y \\ e_z \end{Bmatrix} \tag{2.15}$$

In a similar manner, the induced velocity corresponding to the perturbed state can be calculated. Denoting the perturbed quantities by a prime, the perturbed position vectors of the points A, B and P are given by

$$\vec{r}_P' = \vec{r}_P + \delta\vec{r}_P, \quad \vec{r}_A' = \vec{r}_A + \delta\vec{r}_A, \quad \vec{r}_B' = \vec{r}_B + \delta\vec{r}_B. \tag{2.16}$$

The expression for the induced velocity (Eq. 2.15) is rewritten in terms of the perturbed quantities, e.g., $h' = h + \delta h$, etc. The perturbed induced velocity is evaluated up to first-order by neglecting higher-order terms in the perturbations. Therefore, the linearized perturbed induced velocity is given by

$$\begin{Bmatrix} V'_x \\ V'_y \\ V'_z \end{Bmatrix} = \frac{\Gamma_v}{4\pi}\frac{h}{\left(r_c^{2n}+h^{2n}\right)^{1/n}}\left[h\left(\cos\theta_1-\cos\theta_2\right)\begin{Bmatrix} e_x \\ e_y \\ e_z \end{Bmatrix} \right.$$

$$+h_f\delta h\left(\cos\theta_1-\cos\theta_2\right)\begin{Bmatrix} e_x \\ e_y \\ e_z \end{Bmatrix} \tag{2.17}$$

$$\left. +h\left(\cos\theta_1-\cos\theta_2\right)\begin{Bmatrix} \delta e_x \\ \delta e_y \\ \delta e_z \end{Bmatrix} + h(\delta(\cos\theta_1)-\delta(\cos\theta_2))\begin{Bmatrix} e_x \\ e_y \\ e_z \end{Bmatrix}\right]$$

The factor, h_f, is a multiplicand of the δh term because of the desingularized viscous velocity profile and is given by

$$h_f = 1-\frac{nh^{2n}}{\left(r_c^{2n}+h^{2n}\right)^{1/n}} \tag{2.18}$$

Each of the perturbation quantities on the RHS of Eq. 2.18, like δh, δe_x, δe_y, δe_z, $\delta(\cos\theta_1)$, and $\delta(\cos\theta_2)$, are also evaluated up to the first-order by neglecting the higher-order perturbation terms. For example,

$$\begin{aligned}
&\delta h = \\
&\left(\frac{Cl_{12_x}}{{l_{12}}^3}+\frac{C_y r_{2_z}}{l_{12}C}-\frac{C_z r_{2_y}}{l_{12}C}\right)dr_{A_x}+\quad\left(-\frac{Cl_{12_x}}{{l_{12}}^3}+\frac{C_z r_{1_y}}{l_{12}C}-\frac{C_y r_{1_z}}{l_{12}C}\right)dr_{B_x}+\quad\left(\frac{C_y l_{12_z}}{l_{12}C}-\frac{C_z l_{12_y}}{l_{12}C}\right)dr_{P_x}\\
&\left(\frac{Cl_{12_y}}{{l_{12}}^3}-\frac{C_x r_{2_z}}{l_{12}C}+\frac{C_z r_{2_x}}{l_{12}C}\right)dr_{A_y}+\quad\left(-\frac{Cl_{12_y}}{{l_{12}}^3}+\frac{C_x r_{1_z}}{l_{12}C}-\frac{C_z r_{1_x}}{l_{12}C}\right)dr_{B_y}+\quad\left(\frac{C_z l_{12_x}}{l_{12}C}-\frac{C_x l_{12_z}}{l_{12}C}\right)dr_{P_y}\\
&\left(\frac{Cl_{12_z}}{{l_{12}}^3}-\frac{C_y r_{2_x}}{l_{12}C}+\frac{C_x r_{2_y}}{l_{12}C}\right)dr_{A_z}+\quad\left(-\frac{Cl_{12_z}}{{l_{12}}^3}+\frac{C_y r_{1_x}}{l_{12}C}-\frac{C_x r_{1_y}}{l_{12}C}\right)dr_{B_z}+\quad\left(\frac{C_x l_{12_y}}{l_{12}C}-\frac{C_y l_{12_x}}{l_{12}C}\right)dr_{P_z}
\end{aligned} \tag{2.19}$$

where

$$\vec{C} = \vec{l}_{12}\times\vec{r}_1 = C_x\hat{\mathrm{i}}+C_y\hat{\mathrm{j}}+C_z\hat{\mathrm{k}} \tag{2.20}$$

and $C = |\vec{C}|$ is the magnitude of vector $\vec{C}$. This can be written in a matrix form as

$$\delta h = \{H_A\}^T \begin{Bmatrix} \delta r_{A_x} \\ \delta r_{A_y} \\ \delta r_{A_z} \end{Bmatrix} + \{H_B\}^T \begin{Bmatrix} \delta r_{B_x} \\ \delta r_{B_y} \\ \delta r_{B_z} \end{Bmatrix} + \{H_P\}^T \begin{Bmatrix} \delta r_{P_x} \\ \delta r_{P_y} \\ \delta r_{P_z} \end{Bmatrix} \tag{2.21}$$

Similarly,

$$\delta(\cos\theta_1) - \delta(\cos\theta_2) = \{C_A\}^T \{\delta\vec{r}_A\} + \{C_B\}^T \{\delta\vec{r}_B\} + \{C_P\}^T \{\delta\vec{r}_P\} \tag{2.22}$$

and

$$\begin{Bmatrix} \delta e_x \\ \delta e_y \\ \delta e_z \end{Bmatrix} = [E_A]\{\delta\vec{r}_A\} + [E_B]\{\delta\vec{r}_B\} + [E_P]\{\delta\vec{r}_P\} \tag{2.23}$$

By assembling these individual matrices, the perturbation induced velocity can be expressed in terms of the perturbations of the three points A, B and P, that is

$$\begin{Bmatrix} \delta V_x \\ \delta V_y \\ \delta V_z \end{Bmatrix} = \frac{\Gamma_v}{4\pi} \frac{h}{\left(h^{2n} + r_c^{2n}\right)^{1/n}} \left[[A] \begin{Bmatrix} \delta r_{A_x} \\ \delta r_{A_y} \\ \delta r_{A_z} \end{Bmatrix} + [B] \begin{Bmatrix} \delta r_{B_x} \\ \delta r_{B_y} \\ \delta r_{B_z} \end{Bmatrix} + [P] \begin{Bmatrix} \delta r_{P_x} \\ \delta r_{P_y} \\ \delta r_{P_z} \end{Bmatrix} \right] \tag{2.24}$$

The expressions for these matrices, A, B, and P, are given in Appendix D.

2.2.2 Normal Mode Perturbations

To further simplify the perturbation equations for a stability analysis, the perturbations are assumed to be in the form of a normal mode or a traveling wave. Note that any arbitrary disturbance can be transformed into a series of normal mode perturbations and, therefore, the present analysis remains general even after this simplification. Because of the helical nature of the rotor wake, cylindrical polar coordinates are used. This helps in visualizing various mode shapes, at least for rotor wakes in hovering and axial (vertical) flight. A perturbation vector in cylindrical coordinates is given by

$$\{\delta\vec{p}\} = \begin{Bmatrix} \delta r_0 \\ \delta\theta_0 \\ \delta z_0 \end{Bmatrix} e^{\alpha t + i\omega\zeta} \tag{2.25}$$

where α is the growth rate and ω is the wave number. The wave number ω denotes that the perturbation wave has ω cycles for each rotor revolution. An example is shown in Fig. 2.7 for the radial and axial modes corresponding to $\omega = 1$ and $\omega = 2$. In this case, the equilibrium geometry is a constant pitch, constant radius helix, as shown by the dashed lines, and the perturbed geometry is shown by the solid lines.

The perturbation induced velocities, as derived in the previous section, are evaluated in the Cartesian coordinate system, $\vec{r} = \{x, y, z\}^T$. Therefore, coordinate transformation matrices need to be defined that relate the cylindrical polar coordinates, $\vec{p} = \{r, \theta, z\}^T$, to the Cartesian coordinates. The displacement perturbations are related by the transformation

$$\begin{Bmatrix} \delta x \\ \delta y \\ \delta z \end{Bmatrix} = [T] \begin{Bmatrix} \delta r \\ \delta\theta \\ \delta z \end{Bmatrix} \quad \text{where } [T] = \begin{bmatrix} \cos\theta & -r\sin\theta & 0 \\ \sin\theta & r\cos\theta & 0 \\ 0 & 0 & 1 \end{bmatrix} \tag{2.26}$$

Also, the velocities and perturbation velocities are given by

$$\{\dot{\vec{r}}\} = [T]\{\dot{\vec{p}}\} \tag{2.27}$$

$$\{\delta\dot{\vec{r}}\} = [T]\{\delta\dot{\vec{p}}\} + [T_2]\{\delta\vec{p}\} \tag{2.28}$$

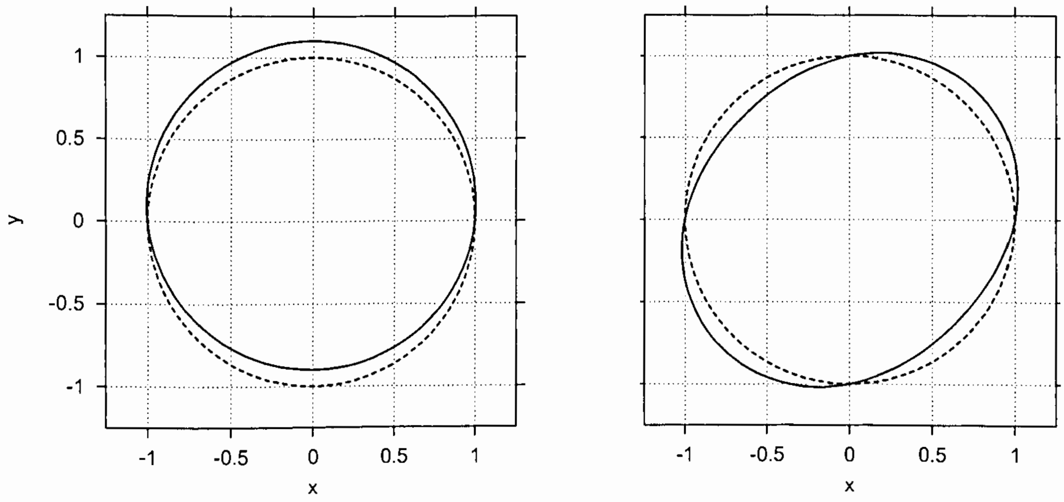

(a) Radial perturbation, $\omega = 1$

(c) Radial perturbation, $\omega = 2$

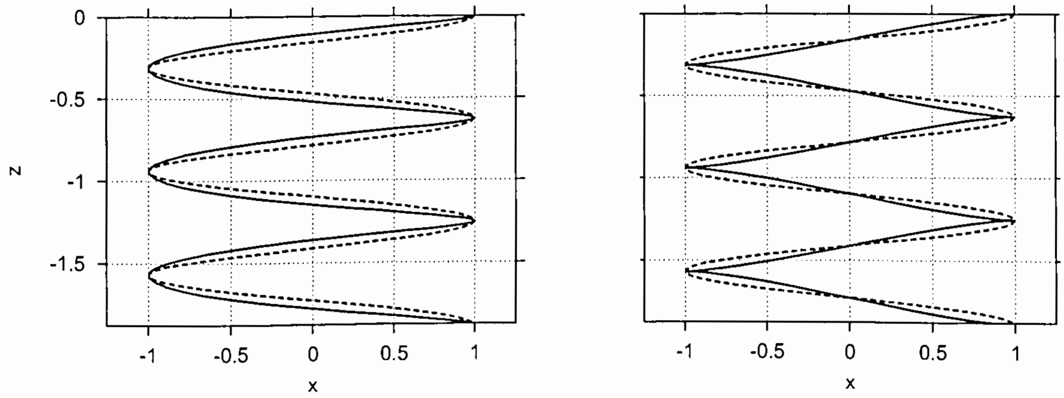

(b) Axial perturbation, $\omega = 1$

(d) Axial perturbation, $\omega = 2$

Figure 2.7: Examples of normal mode perturbations on a helical vortex filament. (a) Radial perturbation, $\omega = 1$, (b) Axial perturbation, $\omega = 1$, (c) Radial perturbation, $\omega = 2$, and (d) Axial perturbation, $\omega = 2$. Dashed lines show the equilibrium geometry while solid lines show the perturbed geometry.

where the second transformation matrix $[T_2]$ is given by

$$[T_2] = \begin{bmatrix} -\dot{\theta}\sin\theta & -\dot{y} & 0 \\ \dot{\theta}\cos\theta & \dot{x} & 0 \\ 0 & 0 & 0 \end{bmatrix} \tag{2.29}$$

2.2.3 Eigenvalue Problem

The governing equations for each perturbation mode can now be solved at a given point P on the vortex filament. Because of the assumption of a normal mode perturbation, this equation can be reduced to a simple eigenvalue problem. The LHS of Eq. 2.8 is given by

$$\begin{aligned} LHS = \{\delta\dot{\vec{r}}\} &= [T]_P\{\delta\dot{\vec{p}}\} + [T_2]_P\{\delta\vec{p}\} \\ &= \Big[\alpha[T]_P + [T_2]_P\Big]\{\delta\vec{p}\} \end{aligned} \tag{2.30}$$

The subscript P in the above equation denotes that the transformation matrices are evaluated at the point P. The perturbation position vector of point P can be transformed to Cartesian coordinates using

$$\{\delta\vec{r}_P\} = [T]\{\delta_0\}e^{\alpha t + i\omega\zeta_P} \tag{2.31}$$

Now, the induced velocity perturbation at point P, resulting from the i^{th} vortex element extending from A to B is written in the form

$$\begin{aligned} RHS = [\delta V_i] &= [A][T]\{\delta_0\}e^{\alpha t + i\omega\zeta_A} + [B][T]\{\delta_0\}e^{\alpha t + i\omega\zeta_B} + [P][T]\{\delta_0\}e^{\alpha t + i\omega\zeta_P} \\ &= \Big[e^{i\omega(\zeta_A - \zeta_P)}[A] + e^{i\omega(\zeta_B - \zeta_P)}[B] + [P]\Big][T]\{\delta_0\}e^{\alpha t + i\omega\zeta_P} \end{aligned} \tag{2.32}$$

Considering only the real part of the above coefficient matrices, this equation becomes

$$\begin{aligned} [\delta V_i] &= \Big[\cos\left(\omega(\zeta_A - \zeta_P)\right)[A] + \cos\left(\omega(\zeta_B - \zeta_P)\right)[B] + [P]\Big]\,[T]\,\{\delta_0\}e^{\alpha t + i\omega\zeta_P} \\ &= [V_i]\,[T]\,\{\delta\vec{p}\} \end{aligned} \tag{2.33}$$

The velocity contributions of all the vortex elements are summed to obtain the total induced velocity perturbation in the matrix form as given above, that is

$$[V] = \sum_i [V_i] \tag{2.34}$$

Therefore,

$$\Big[\alpha[T] + [T_2]\Big]\{\delta\vec{p}\}_P = [[V]\,[T]]\,\{\delta\vec{p}\}_P \tag{2.35}$$

Finally, this equation can be reduced to the standard eigenvalue form

$$\alpha_P\{x\} = [M]_P\,\{x\} \tag{2.36}$$

where,

$$[M]_P = \Big[[V] - [T_2]\,[T]^{-1}\Big]_P \tag{2.37}$$

The eigenvalues α_P give the growth rate of the perturbation at point P on the rotor wake. A positive growth corresponds to an exponentially growing mode, i.e., an unstable mode. A negative eigenvalue corresponds to a damped mode, i.e., a stable mode. A zero eigenvalue corresponds to a neutrally stable mode that does not change with time.

2.3 Eigenvalues of Rotor Wakes

The eigenvalues and the stability results presented in the next sections were obtained using the equilibrium wake geometry and vortex strengths predicted using the free-vortex wake scheme based on the relaxation (PIPC) algorithm. Numerical solutions were chosen mainly because they offer the freedom to study the sensitivity of the results to various rotor geometric and operating parameters, such as number of blades and rotor thrust. However, the eigenvalue analysis developed in the preceding section is completely general, so it can also be applied to any wake geometry including those obtained from experimental measurements.

Two different teetering rotor configurations were studied. In both cases the rotor blades were untwisted with a rectangular planform. The rotor configuration experimentally tested by Martin *et al.* (Ref. 66) is denoted as Rotor 1, while Rotor 2 denotes the rotor used in the experiments of Ref. 40. The geometric parameters for these two configurations are given in Table 2.1.

Figures 2.8 and 2.9 show the maximum predicted divergence rate of the rotor wake as a function of increasing wave number for hovering rotors with one to five blades. Rotor 1 was used to compute these results, and was operated at a rotational frequency of 35 Hz and a blade loading of $C_T/\sigma = 0.075$, i.e., at $C_T = 0.0025, 0.005$, and 0.010 respectively. The divergence rate is plotted in Fig. 2.8 in the non-dimensionalized form $\overline{\alpha} = \alpha / \left(\frac{\Gamma}{4\pi R^2}\right)$ and in dimensional form α in Fig. 2.9. It is significant to note that the hovering rotor wake is unstable in all cases, with the divergence rates showing a sinusoidal type of variation with increasing wave number.

Table 2.1: Rotor configurations used in the present study.

Configuration	Rotor 1 (Ref. 66)	Rotor 2 (Ref. 40)
Rotor radius, (m)	0.4064	1.0414
Blade chord, (m)	0.0425	0.0762
Blade tip speed, (ms^{-1})	89.3	196.3

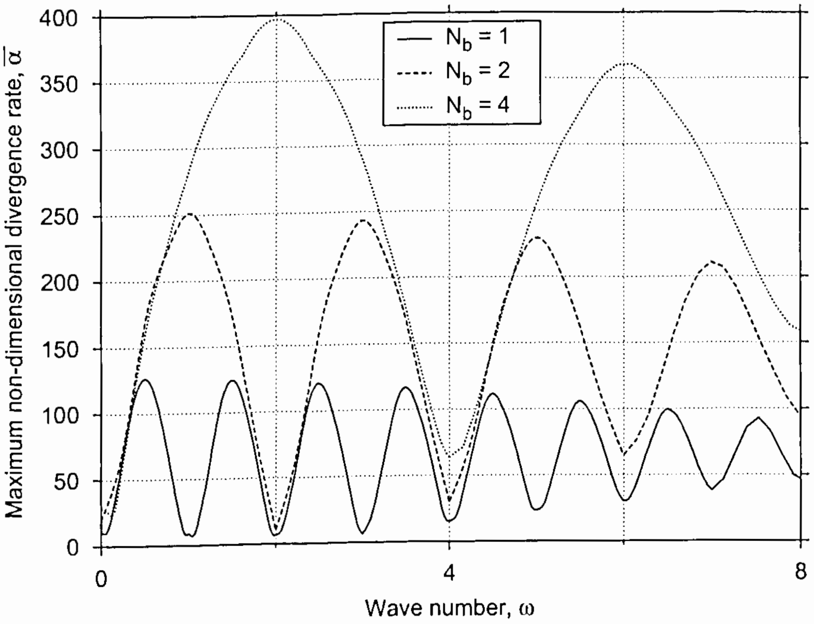
(a) One, two and four-bladed rotors

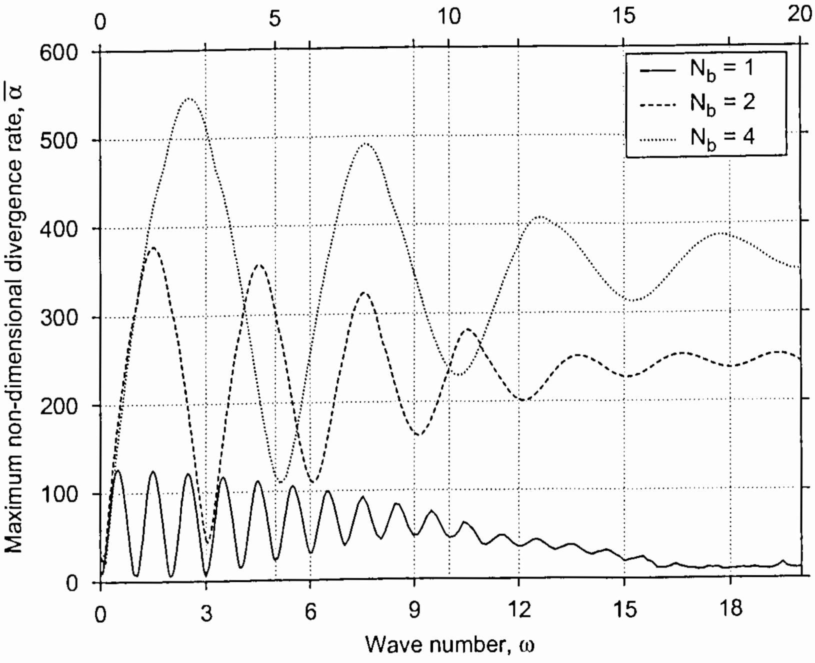
(b) One, three and five-bladed rotors

Figure 2.8: Maximum non-dimensional divergence rates hovering rotors operating at constant blade loading, $C_T/\sigma = 0.075$ (Rotor 1). (a) One, two and four-bladed rotors, (b) One, three and five-bladed rotors.

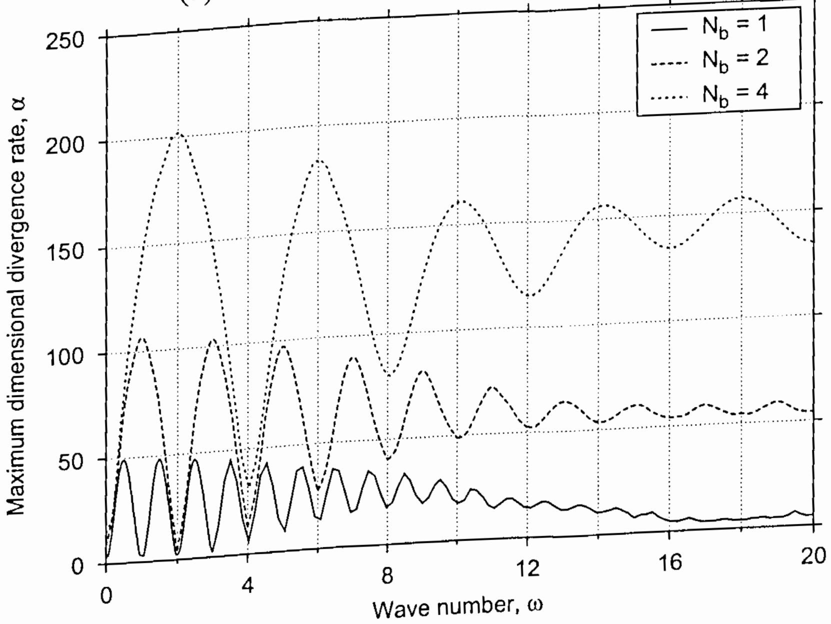

(a) One, two and four-bladed rotors

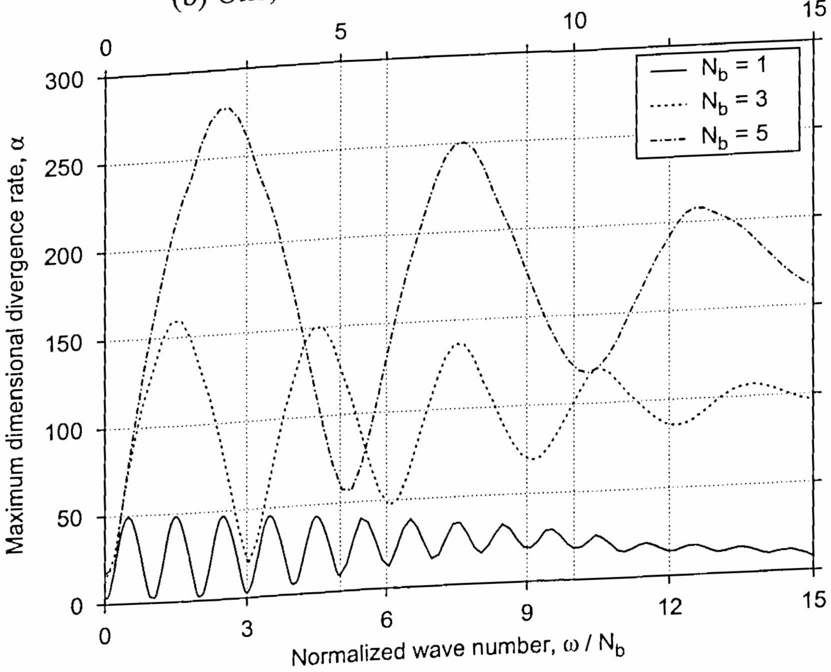

(b) One, three and five-bladed rotors

Figure 2.9: Maximum dimensional divergence rates for hovering rotors operating at constant blade loading, $C_T/\sigma = 0.075$ (Rotor 1). (a) One, two and four-bladed rotors, (b) One, three and five-bladed rotors.

Notice from Figs. 2.8 and 2.9 that the divergence rates increase with increasing number of blades. For rotors operating with the same blade loading (C_T/σ), the one-bladed rotor showed the smallest divergence rates for any given wave number. The dimensional divergence rates (Fig. 2.9) were also found to be corresponding smaller. The behavior at larger wave numbers showed the expected response of the wake to high frequency disturbances. The increasing growth rates for large wave numbers with increasing number of blades suggests increased susceptibility to instabilities from random disturbances, e.g., external turbulence or recirculation in the test facility. This is consistent with the experimental observation that the aperiodicity of a rotor wake has a tendency to increase with increasing number of blades (Ref. 67).

The wave numbers corresponding to the extrema in the divergence rates closely correlate with the number of rotor blades. It can be seen from Figs. 2.10 that a maximum divergence rate occurs at wave numbers equal to half-integer multiples of the number of blades, i.e., at wave numbers $\omega = \left(k + \frac{1}{2}\right) N_b$, for all integer k. A minimum divergence rate occurs at integer multiple of the number of blades, that is $\omega = kN_b$. This behavior is illustrated in Fig. 2.10 where the results from Fig. 2.9 are re-plotted as a function of ω/N_b.

With increasing wave number, the peak-to-peak amplitude decreases (i.e., the difference between maximum and minimum divergence rates decreases), indicating that for very large wave numbers the divergence rate would be independent of the wave number, as can be seen from both Figs. 2.9 and 2.10. A similar trend was reported in Ref. 65 where the stability of interdigitated infinite helical vortices was examined. Thus, even though an infinite helix is not an entirely accurate representation of a rotor tip vortex filament, stability analysis of helical vortices gives a qualitatively accurate estimation of the stability characteristics of an actual helicopter rotor wake.

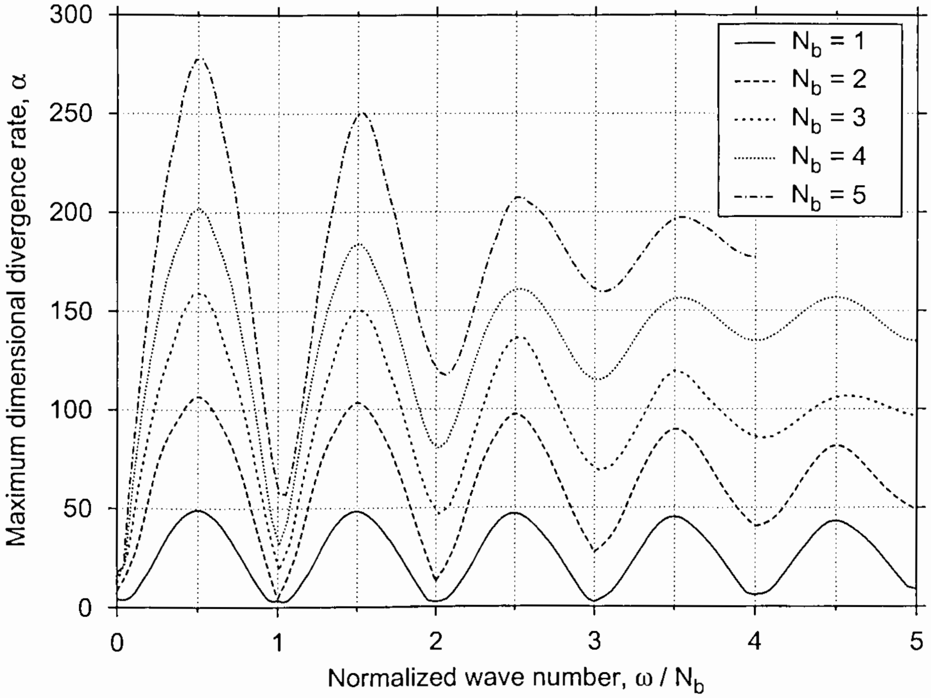

Figure 2.10: Maximum dimensional divergence rates for the one, two, three, four, and five-bladed hovering rotors operating at constant blade loading as a function of normalized wave number, $C_T/\sigma = 0.075$ (Rotor 1).

2.4 Analogy of Rotor Wakes to Helical Vortices

The previous stability analyses of Refs. 63–65 were based on infinite helical vortices and inferred the stability of helicopter rotor wakes only by analogy. To bring out the close resemblance between the stability of helical vortices and a rotor wake, the non-dimensional growth rates for helical filaments with a pitch $p = 0.1$, are shown in Fig. 2.11. Infinite helical vortex filaments were approximated for numerical evaluations by considering ten turns of the filament above and below the part of the vortex filament being examined. However, only two turns of the helix were found sufficient to give acceptable results. The striking similarity between the stability characteristics of these helical vortices and the rotor wake (see Fig. 2.8) is evident from the sinusoidal behavior with respect to wave number. The growth rates also increased with increasing number of intertwining filaments, similar to the effect of increasing number of blades. The growth rates reported by Gupta & Loewy (Ref. 65) showed a quadratically decreasing trend with increasing helical pitch, p.

The present methodology also predicts a similar behavior for different number of intertwining helical filaments. Figure 2.12 shows results for the maximum divergence rate as a function of the helical pitch (distance traversed by one turn of the helix). A logarithmic scale is used on both axes to bring out the quadratic trend as given by the 2:1 slope of the curves. As mentioned previously, the divergence rates also increased with increasing number of vortex filaments.

Similar results are shown in Fig. 2.13 where the results are plotted, not as a function of the pitch, p, but as a function of the separation distance between two adjacent vortex filaments ($= 2\pi p/N$). The quadratically decreasing trend is seen clearly from the 2:1 slope of the logarithmic plot. Increasing the number of intertwining vortex filaments decreases this separation distance thereby increasing the divergence rates, as also reported in Ref. 65. The results for different number of helical filaments were found to coalesce onto a single curve, indicating that the predominant factor affecting the wake divergence rates was the distance between two adjacent tip vortices.

Note that the effects of two interdigitated helical filaments are equivalent to a single helical filament with half the pitch, and so forth. This striking result is expected because the divergence rate of a normal mode depends on the vortex induced velocities, which are proportional to the inverse square of distance from the vortex. This is the reason why the divergence rates may be non-dimensionalized (scaled) using the vortex separation distance, e.g., see Ref. 49.

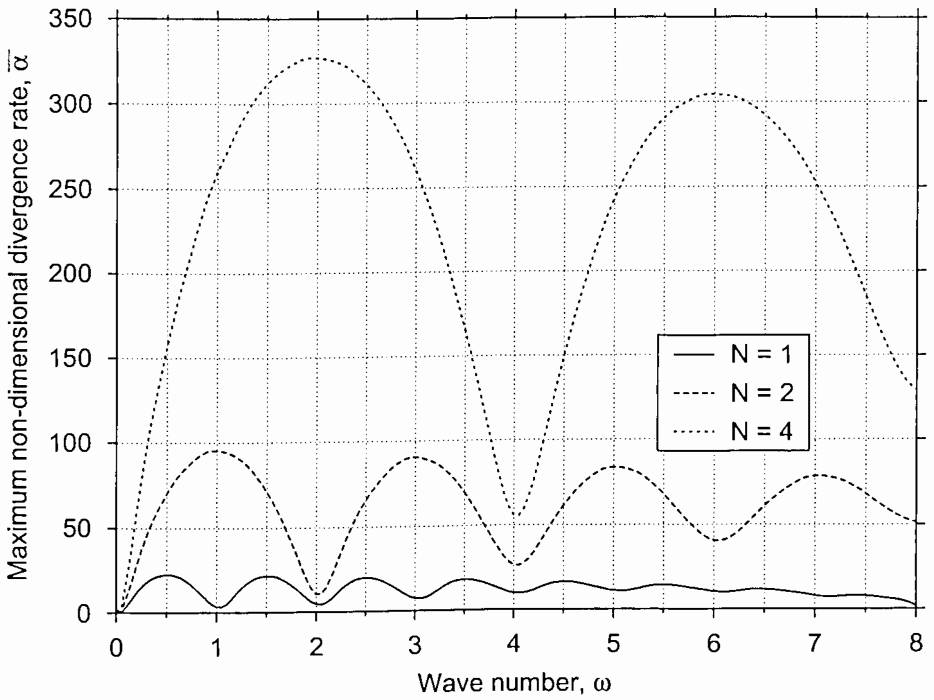

Figure 2.11: Maximum non-dimensional divergence rates for one, two, and four intertwining infinite helical vortex filaments with a pitch $p = 0.1$.

Figure 2.14 shows that the actual hovering rotor wake also gives a similar behavior. Note that the separation distance between two adjacent tip vortex segments is directly proportional to the mean inflow (in the far wake, $V = \Omega R\sqrt{C_T/2}$) and inversely proportional to the number of blades. This is because in hover, the axial displacements of the rotor wake vortices after the first blade passage are given by

$$z = V_z t \qquad \text{or,} \qquad \frac{z}{R} = \lambda\psi \tag{2.38}$$

Two adjacent vortex filaments, i.e., vortices trailing from two adjacent blades, are separated by $\Delta\psi = 2\pi/N_b$. The mean inflow, λ, is proportional to the square root of the rotor thrust in hover, as given by the momentum theory result. Therefore, the vertical separation between two such adjacent vortices can be shown to be

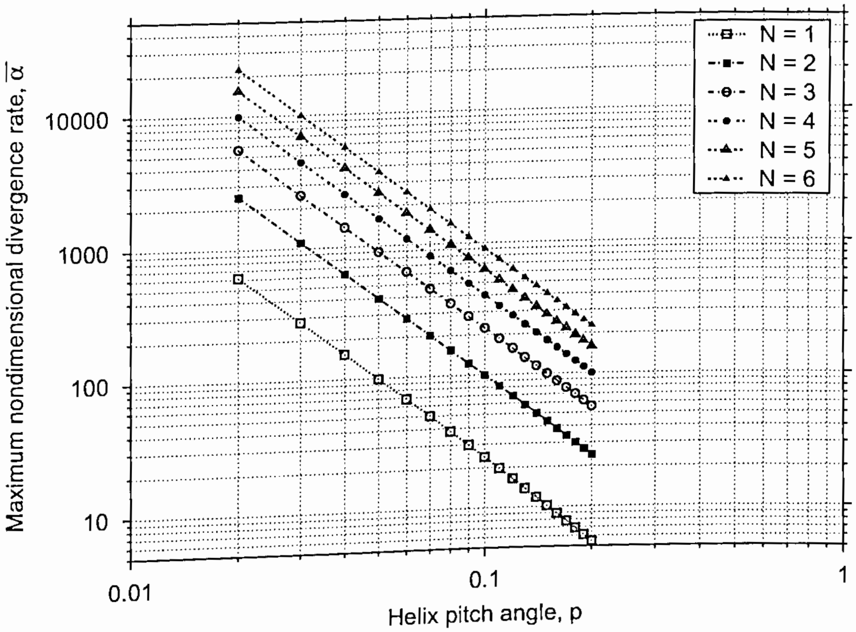

Figure 2.12: Absolute maximum non-dimensional divergence rate for infinite helical vortex filaments as a function of the helical pitch, p.

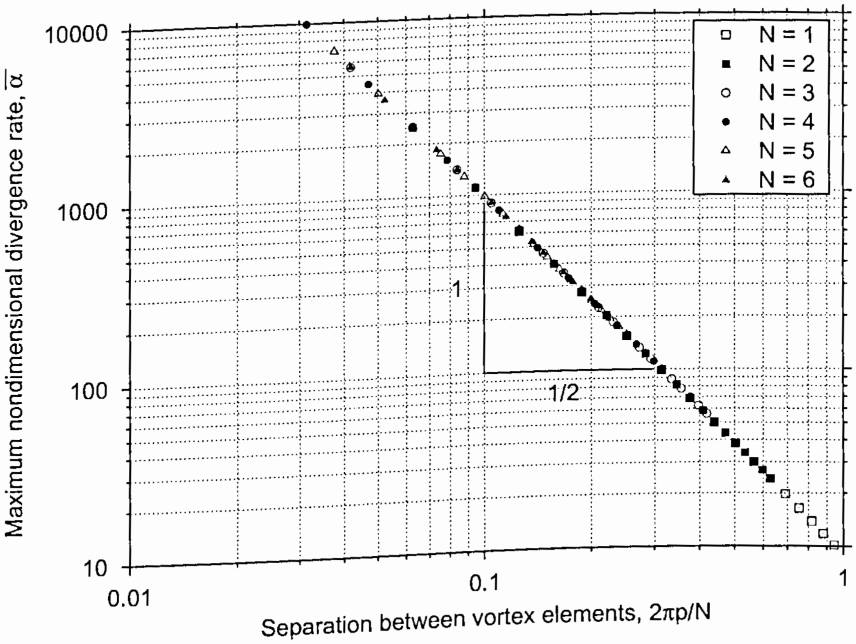

Figure 2.13: Absolute maximum non-dimensional divergence rate for infinite helical vortex filaments as a function of separation between adjacent vortex segments, $2\pi p/N$.

$$\begin{aligned}\text{vertical spacing} = \frac{\Delta z}{R} &\propto \lambda \Delta \psi \\ &\propto \frac{\sqrt{C_T}}{N_b}\end{aligned} \qquad (2.39)$$

Therefore, the absolute maximum divergence rates are plotted as a function of $\sqrt{C_T}/N_b$ in Fig. 2.14. The results showed the same nominal trend as suggested by the helical vortex filament results as shown previously in Fig. 2.13. The deviations from an inverse square trend are because the actual wake geometry does not have a constant pitch and radius like the idealized helical case. However, the qualitative behavior is remarkably similar.

2.5 Vortex Pairing as a Wake Instability

It has been frequently observed in both experimental and numerical results that the trajectories of the two tip vortices were identical up to a vortex age of approximately $\zeta = 180°$. Tangler *et al.* (Ref. 14) postulated that the vortex pairing instabilities are initiated below the rotor in the region, only after the rotor wake has almost completely contracted. To better understand this behavior, the divergence rates of the wake generated by Rotor 1 are plotted in Fig. 2.15 as a function of increasing vortex age for three representative perturbation modes.

Because this is a two-bladed rotor, the $\omega = N_b/2 = 1$ mode showed the largest divergence rate, with a maximum divergence rate occurring just after $\zeta = 180°$. The $\omega = 1/2$ mode showed a similar qualitative trend, but with a smaller magnitude. The $\omega = 2$ mode showed the smallest divergence rate, which was nominally the same for all vortex ages. The small divergence rate at early vortex ages explains the empirical observation that the rotor wake at early vortex ages is mostly free from any instabilities

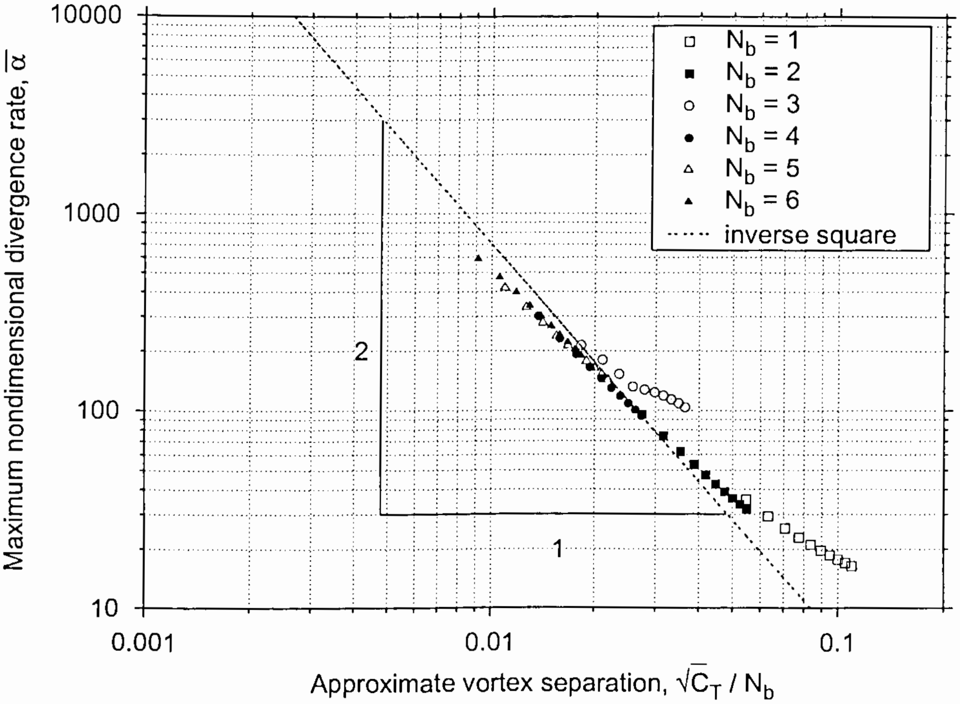

Figure 2.14: Absolute maximum non-dimensional divergence rates for hovering rotor wakes as function of approximate separation distance between adjacent vortex filaments, $\sqrt{C_T}/N_b$, (Rotor 1).

and shows a steady, almost purely periodic behavior. The wake is relatively stable (less unstable) while it is undergoing the initial radial contraction, as postulated by Tangler *et al.* (Ref. 14). The sharp rise in the divergence rates after the wake has undergone maximum radial contraction suggests an increased susceptibility to instabilities.

The most unstable mode for the one-bladed rotor wake is the $\omega = 1/2$ mode, which corresponds to a sub-harmonic disturbance along the length of the tip vortex trajectory. In practice, it is well-known from experimental studies that the wake generated by a one-bladed rotor is the most stable to study experimentally. In experimental tests with rotors, the most common physical disturbances affecting the wake originate from supports, an airframe or other nearby structures, or slight mistracking of the blades.

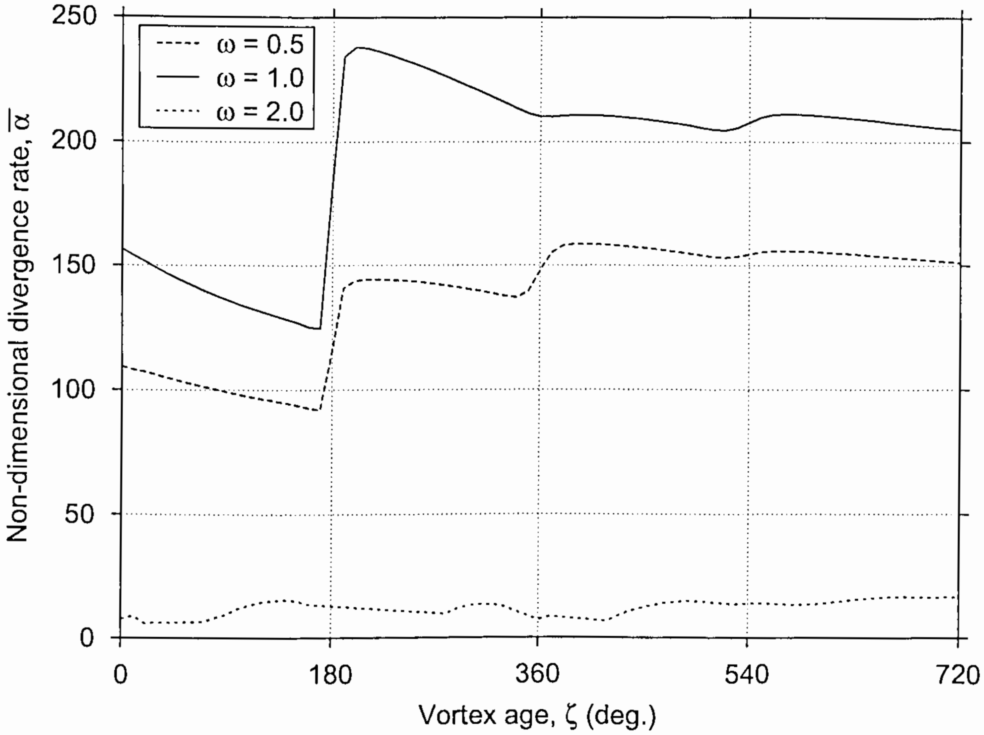

Figure 2.15: Variation in non-dimensional wake divergence rate with increasing vortex age in hover, $C_T = 0.005$ (Rotor 1).

These disturbances would provide a source of a once-per-revolution perturbation to the blade(s) and the rotor wake. It will be seen from Figs. 2.8 and 2.9 that the divergence rate for this ($\omega = 1$) mode is a minimum for the one-bladed rotor. The two-bladed rotor, however, shows a maximum divergence rate corresponding to this wave number, and therefore, this wake deformation mode for two-bladed rotors is most likely to exhibit an instability.

The $\omega = 1$ deformation mode is schematically shown in Fig. 2.16 for a two-bladed rotor wake. Both the radial and axial perturbations are shown with respect to an equilibrium geometry consisting of two helical vortex filaments with constant pitch and radius. For this mode, the perturbations for the two filaments are 180° out-of-phase with respect to each other. The vortex from one blade moves radially inward and axially downward, while the vortex from the other blade moves radially outward and axially upward relative to the respective equilibrium positions. For all perturbation modes with $\omega = \left(k + \frac{1}{2}\right) N_b$, the vortex filament perturbations are out-of-phase, and a local maximum in the divergence rate is obtained for these wave numbers.

Furthermore, with the $\omega = kN_b$ modes the two filament perturbations are in-phase and a minimum divergence rate is observed. Therefore, the stability of the wake geometry is seen to be strongly dependent on the relative phasing of the perturbations of individual vortex filaments. The opposite phasing of the two filaments in Fig. 2.16 appears in the form of a pairing of the two vortices. This confirms that the vortex pairing observed with the wakes of two-bladed rotors is an instability corresponding to the unstable wake deformation mode with a wave number of $\omega = 1$. Therefore, the vortex pairing phenomenon will most likely be observed in the wake of a two-bladed rotor, which seems to be confirmed in light of recent experimental evidence by Martin *et al.* (Ref. 66) and Caradonna *et al.* (Ref. 40).

2.5.1 Mistracked Rotor Experiment

One possible factor initiating a vortex pairing instability is a slight mistracking of the blades. This will result in tip vortices of slightly different circulation strengths, possibly exciting an unstable wake deformation mode. Tangler *et al.* (Ref. 14) postulated such mistracking to be the cause of asymmetry of hovering wake, and also the source of the vortex pairing instability. As an extension of the work of Martin *et al.* (Ref. 66), a laser light sheet flow visualization experiment has been conducted with a deliberately mistracked two-bladed rotor to explore the effects on wake stability. The rotor geometry and operating conditions were same as Rotor 1, with one blade set at 1° lower pitch

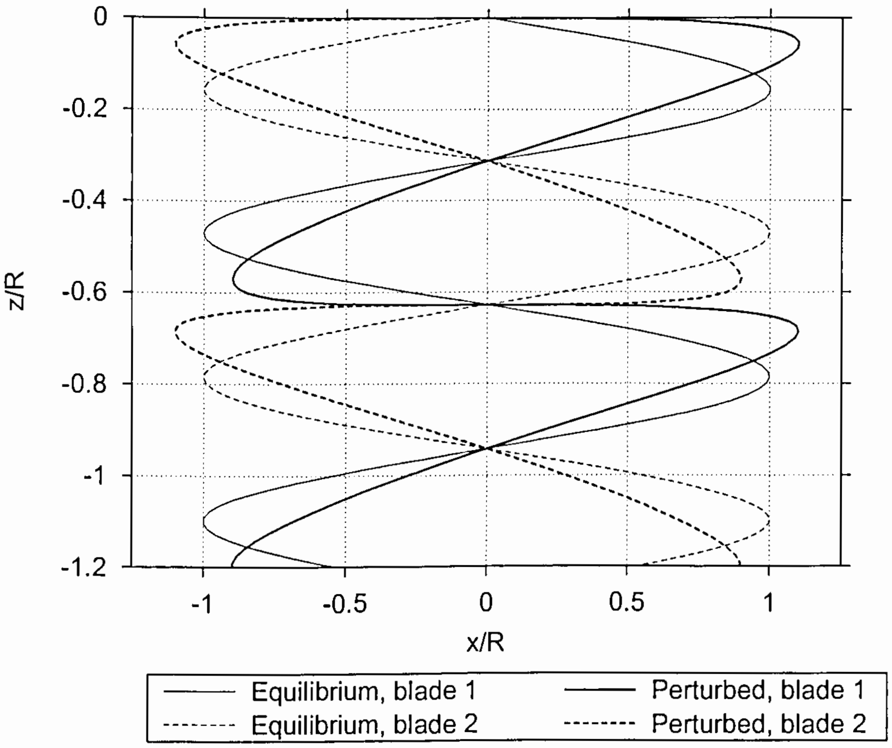

Figure 2.16: Schematic representation of combined radial/axial $\omega = 1$ deformation mode for a two-bladed hovering rotor. The wake geometries are shown for $\psi_{\text{ref}} = 0$

angle. The results are shown in Figs. 2.17 and 2.18.

For the baseline (tracked) rotor, the vortices did not exhibit pairing up $\zeta \approx 900^\circ$, as shown in Fig. 2.17. However, for the mistracked rotor, the vortices formed a pair at $\psi_b \approx 540^\circ$, which is the azimuth where the two vortex trajectories can be seen to intersect in Fig. 2.18. In both cases, the predictions using the free-vortex wake model show good agreement with the experimental results; in particular, the early tip vortex pairing observed with the mistracked rotor is well predicted.

It is interesting to note that the two rotors were operating at nearly the same condition, with the mistracked rotor operating at a slightly lower thrust level because of the lower collective pitch setting on one blade. Therefore, the eigenvalues (divergence rates) of the two rotor wakes are expected to be of approximately the same magnitude.

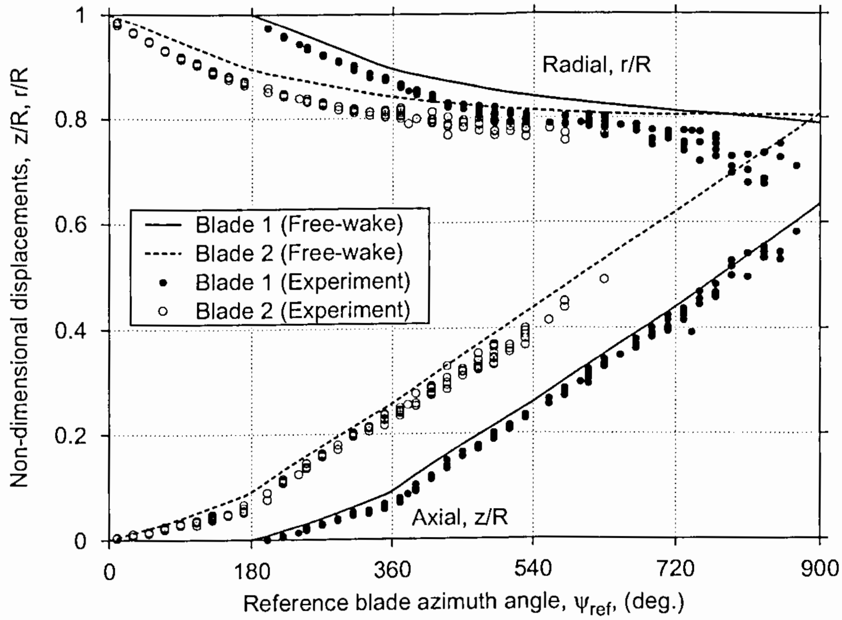

Figure 2.17: Predicted and measured tip vortex locations for the baseline (tracked) rotor, $\theta_0 = 5°$ (Rotor 1).

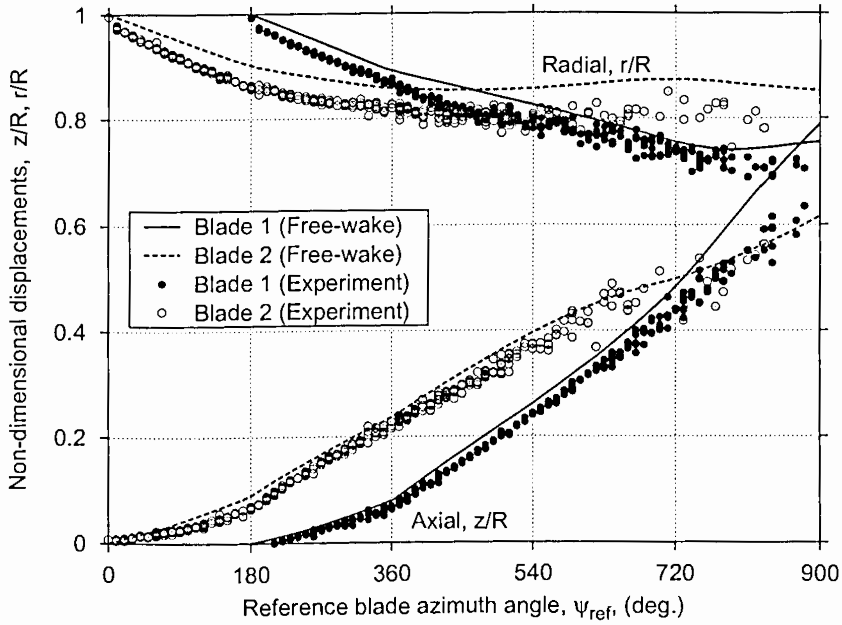

Figure 2.18: Predicted and measured tip vortex locations for the mistracked rotor, blade 1: $\theta_0 = 5°$, blade 2: $\theta_0 = 4°$ (Rotor 1).

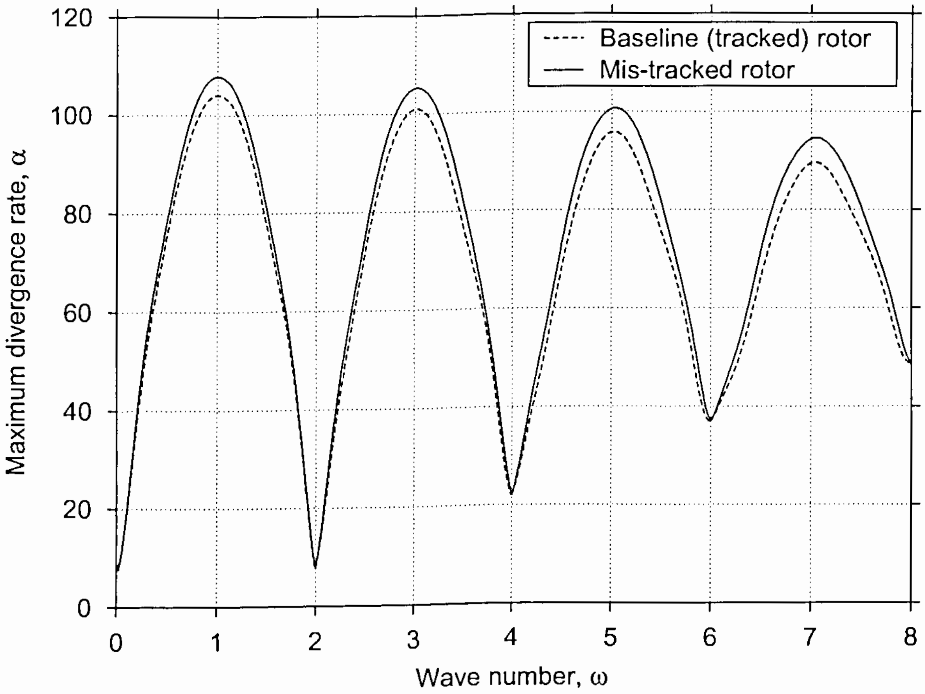

Figure 2.19: Eigenvalues (divergence rates) for the wake of the mistracked rotor, compared with the baseline two-bladed (tracked) hovering rotor.

This is shown in Fig. 2.19 in the form of the growth rates as a function of the spatial wave number. The mistracked rotor wake has only marginally higher growth rates associated with it. Therefore, the earlier onset of the pairing instability is surprising. One reason for the apparently early onset of the vortex pairing lies in the asymmetry of the wake. Because one tip vortex has a larger circulation strength, the other (weaker) tip vortex tends to rotate around it. Therefore, the vortex pairing phenomenon is not axisymmetric and is observed at an early vortex age only on one side of the rotor wake.

This is more evident from the side view of the mistracked rotor wake as shown in Fig. 2.20. The periodic wake boundary is also shown superimposed on the instantaneous wake geometry to bring out the asymmetry of the wake. Clearly, the vortex

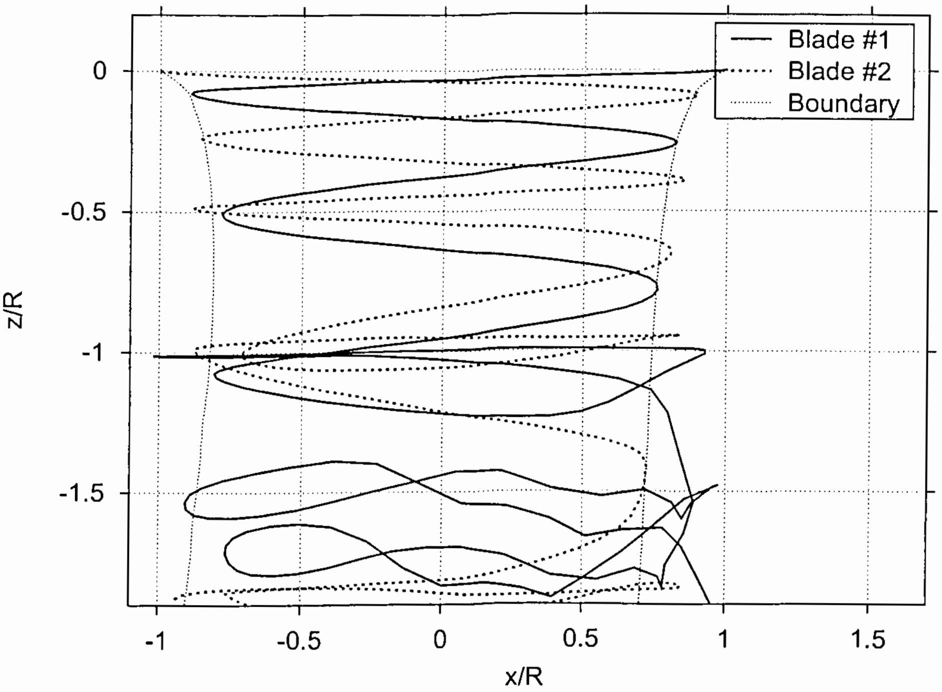

Figure 2.20: Side view of the instantaneous wake geometry for the mistracked rotor showing asymmetric onset of vortex pairing, $\psi_{\text{ref}} = 0$. The periodic wake boundary obtained using the relaxation method is also shown.

pairing onset occurs earlier on one side of the wake, in this case on the left hand side in Fig. 2.20. While on the side opposite, the vortex pairing occurs at a later vortex age.

2.5.2 Effect of Rotor Operating State

Tangler *et al.* (Ref. 14) observed empirically that the vortex pairing occurred farther away from the rotor with increasing rotor thrust. A similar observation is reported by Caradonna *et al.* (Ref. 40) with increasing collective pitch angle, and also with increasing climb rate. Figure 2.21 shows the effect of increasing rotor thrust on the calculated divergence rate of a hovering rotor wake. These results were calculated for

Rotor 2 (Ref. 40).

The divergence rate for a given wave number was found to decrease with increasing thrust, that is the wake becomes less unstable. A less strong instability also indicates that the vortex pairing will be observed at a greater downstream distance from the rotor disk, as has been observed in the experiments of Ref. 40. It must be noted that the wake for Rotor 2 shows as smaller divergence rate in hover compared to that for Rotor 1. This suggests that the wake of Rotor 2 would be relatively less unstable and, therefore, less susceptible to instabilities like the vortex pairing. This appears to contradict the experimental observations because the rotor wake observed in Ref. 40 exhibited a strong, repeatable vortex pairing phenomenon. These differences may be because of different sources of disturbances inherent in the two experimental set-ups, although a definitive explanation requires further study.

It has been shown previously that the wake instability is a consequence of the vortex induced velocities and, therefore, depends on both the vortex strength and separation distance between two vortex filaments. As rotor thrust increases, both the strengths of the vortices and the axial spacing between two vortex filaments increase. Increased vortex strength implies increased divergence rate, while increased axial spacing between the vortices implies a decreased divergence rate. Note that the velocity induced by one vortex element at another is directly proportional to the vortex strength, but inversely proportional to their separation distance. Therefore, the separation distance between adjacent vortices plays a more dominant role than the vortex strength in determining the stability of the rotor wake geometry (Ref. 49).

Figure 2.22 shows the effect of climb rate on the stability of the wake computed at (a) constant rotor thrust of $C_T = 0.004$, and (b) constant collective pitch angle of $\theta_0 = 11°$. The rotor geometry in this case corresponds to Rotor 2. In both cases

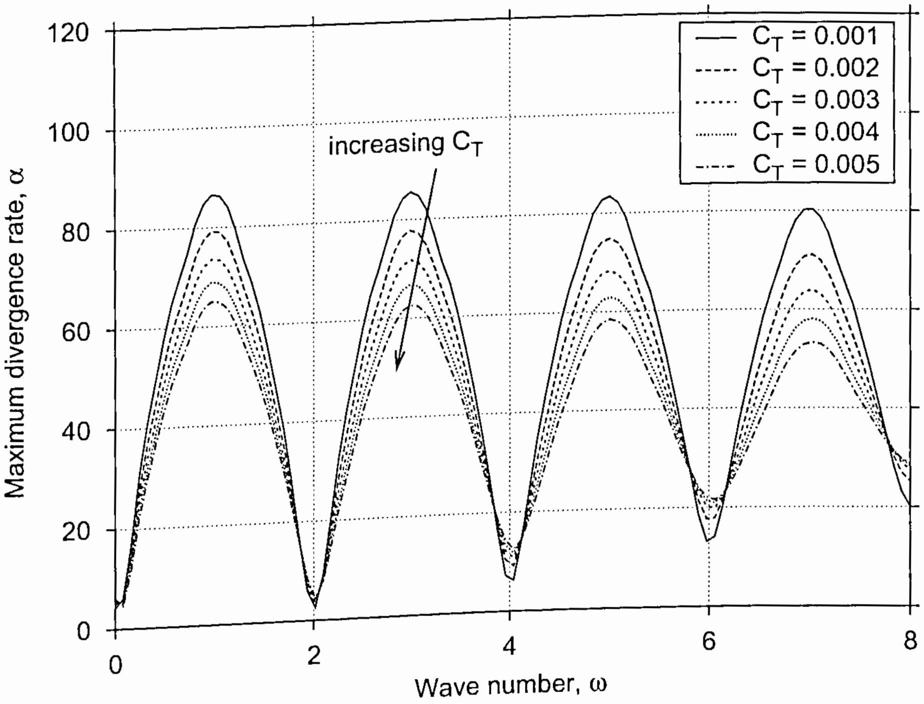

Figure 2.21: Effect of increasing rotor thrust on the maximum divergence rates of the wake in hover (Rotor 2).

the divergence rates decrease with increasing climb rate, so vortex pairing would take place farther downstream in the wake away from the rotor. This is consistent with the trends reported in Ref. 40 for a constant collective pitch input.

In the first case, the tip vortex strengths remain nominally constant, while the axial separation distance between two vortex filaments increases with climb rate. A significant reduction in divergence rate is seen during the transition from hover to a climb, but with successively smaller reductions at higher climb rates. In the second case with constant collective pitch, the rotor thrust and the tip vortex strengths decrease with climb rate, while the axial separation of the vortex filaments increases only relatively slowly. In this case, the wake divergence rates gradually decreased with increasing climb rate. This supports the previous observation that the wake stability is predomi-

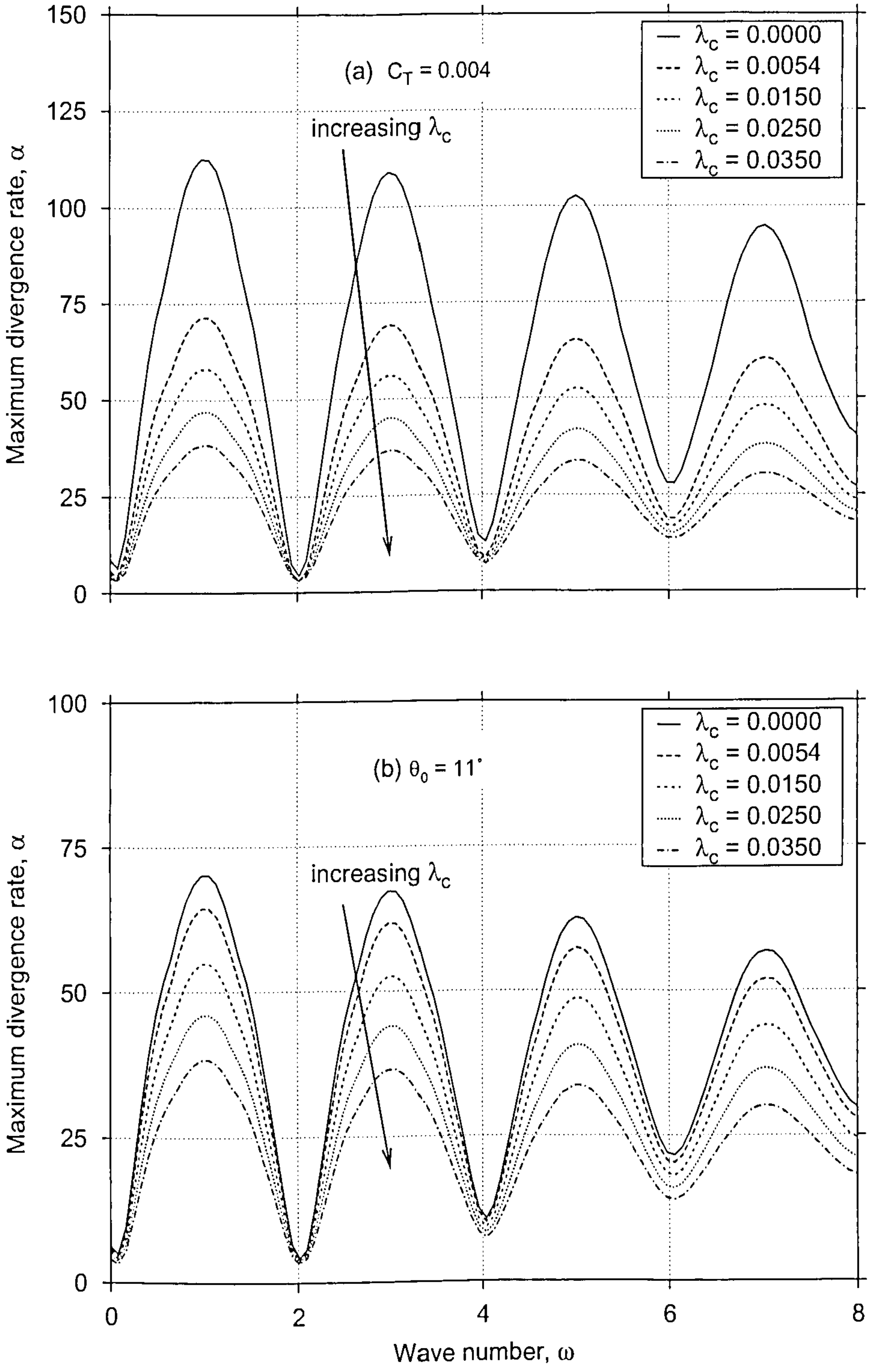

Figure 2.22: Effect of increasing axial climb rate on maximum wake divergence rates with (a) constant thrust, $C_T = 0.004$, (b) constant collective pitch, $\theta_0 = 11°$ (Rotor 2).

nantly dependent on the axial separation distance between adjacent vortex filaments.

The vortex pairing phenomenon is, therefore, an inherent rotor wake characteristic and is a naturally unstable deformation mode of rotor wakes in axial flight. This also implies that in the absence of any perturbations the wake geometry remains in its periodic, equilibrium state. However, in experiments various types of physical disturbances inherent to the experimental set-up may provide the conditions necessary to excite the equilibrium wake geometry and cause it to become unstable. In computational results, it is the numerical truncation and round-off errors that potentially lead to this instability. It is interesting to note that the same unstable mode is excited because of different disturbances. This is analogous to the first natural mode of a vibrating beam, which is the predominant response to arbitrary small disturbances. For a two-bladed rotor, the $\omega = 1$ mode is the first unstable perturbation mode, that is the mode corresponding to the smallest wave number and to a maximum divergence rate. In experiments, this mode will the most predominant in response to small disturbances of different origins.

2.6 Numerical Issues in Rotor Wake Stability

As alluded to previously, numerical truncation errors in free-vortex wake schemes may provide the perturbations to the equilibrium wake geometry, which will manifest as some form of wake instability. These instabilities, in many cases, may closely mimic the physical instabilities observed in experiments. Many free-vortex wake solutions have been found to exhibit a wake instability in hovering flight, i.e., the wake geometry did not converge to an equilibrium solution (e.g., Refs. 10, 44, 69). The instability becomes evident in the form of mutual interaction of vortex filaments, which often results in long-wave disturbances on the vortex filaments, and ultimately in a form of vortex pairing. While similar instabilities have also been observed in sub-scale rotor wake experiments (e.g., Refs. 13 & 14), these instabilities were generally not as severe as those observed in free-vortex wake analyses (e.g., Ref. 71). Subsequent research has demonstrated that many of these numerical instabilities can be overcome through the use of improved numerical methods for solving the wake equations, e.g. semi-implicit (Ref. 34) or pseudo-implicit methods (Refs. 53, 56–59) and influence coefficient based methods (Refs. 44, 69).

In most numerical or computational studies, a physical instability refers to the natural, inherent instability of the solution. A numerical instability, typically, refers to a non-physical instability that is not inherent to the solution, but is caused by the numerical method itself. Because the hovering rotor wake is inherently unstable, any instabilities seen in numerical results are often regarded as physical instabilities. However, this may not always be the case. It is important to remember that by saying that the rotor wake is "unstable" implies that it is in "unstable equilibrium," i.e., the wake structure would remain in this state of unstable equilibrium until it is disturbed because of some external disturbance. An instability is the behavior of the wake caused by such a disturbance to an unstable equilibrium state. Therefore, instabilities observed in experiments imply that the equilibrium wake structure is unstable, and also that external disturbances are present in the flow field.

The wake stability characteristics also give insight into understanding the differences shown between "relaxation" and "time-accurate" free-vortex wake methods, as shown previously in Fig. 2.1. The results shown previously in Fig. 2.8 suggest that the perturbation modes corresponding to $\omega = kN_b$, for integer k, have the smallest wake divergence rates; that is, the wake geometry is least unstable to these perturbation modes. Relaxation based free-wake methods such as the PIPC scheme allow only these $\omega = kN_b$ perturbation modes to arise from numerical errors because periodicity conditions are imposed on the wake geometry. Because these perturbation modes are the least unstable, such numerical errors in the solution do not grow significantly with the number of wake iterations. Therefore, relaxation free-wake solutions usually appear free from any apparent instabilities.

Conversely, transient or time-marching free-wake solutions (which do not enforce periodicity) allow disturbances in the form of all modes. Therefore, the smallest unstable mode is predominantly excited, and these solutions usually show an instability mode closely resembling the $N_b/2$ wave number. However, note from Fig. 2.1 that the PC2B algorithm does not exhibit these instabilities. The reason for this behavior lies in the truncation errors in the PC2B differencing scheme, which provide a higher effective numerical viscosity thereby causing dissipation of the numerical disturbances.

Numerical results, such as those presented in the previous sections, show that the numerical solution is unstable, similar to the real wake geometry. However, the numerical solution may not exhibit an instability. This is because no disturbances are being explicitly modeled in the numerical scheme, and in the absence of any such disturbances the wake must remain in a state of unstable equilibrium. Physical instabilities, such as observed in experiments, may be obtained in numerical simulations by explicitly modeling disturbances in the flow field. In the absence of such disturbances being explicitly modeled, any instability in the numerical solution is always non-physical. Instabilities resulting from disturbances in the form of truncation/round-off errors implicit in the numerical scheme must, therefore, be regarded as a numerical instability. Such numerical errors are almost always present in numerical analyses, and may potentially disturb a solution in unstable equilibrium. Therefore, a proper choice of numerical algorithm is essential to avoid these numerical instabilities.

Because the disturbances leading to the instability observed in the PCC wake solution are of a numerical origin, this numerical instability will be dependent on various numerical parameters such as wake discretization, far-wake truncation, and even the viscous vortex model. For example, Fig. 2.23 shows the influence of wake discretization on the divergence rates of a hovering rotor wake. The wake geometries are obtained for the two-bladed rotor (Rotor 1) using four turns of free-vortex wake. The divergence rates showed a slightly decreasing trend with increased grid resolution (higher fidelity discretization). The rotor operating conditions were identical in all the cases, and therefore, the strength of the tip vortices were nominally constant. The differences in divergence rates must then be a result of different vortex separation distances. This is because of the second-order errors in the induced velocity computations. With improved grid discretization, the induced velocity is computed with smaller errors, and so the tip vortices exhibit slightly different axial displacements. Because the divergence rates (like the induced velocities) are inversely proportional to the separation distance, small variations in vortex separation distance are reflected in the wake divergence rates.

Note that the eigenvalue results shown in Fig. 2.23 suggest that a discretization level of at least $\Delta\theta = 5^\circ$ is required to properly resolve the hovering wake geometry. This is consistent with the observation that a minimum discretization 5° is required for resolving the vortex induced velocities, as will be shown later in Section 3.2.1. A similar resolution limit also applies to the wake geometry solution, as will be shown later in Section 3.4.

The instantaneous tip vortex trajectories after 30 rotor revolutions obtained with different discretization levels are shown in Fig. 2.24. The experimental results from

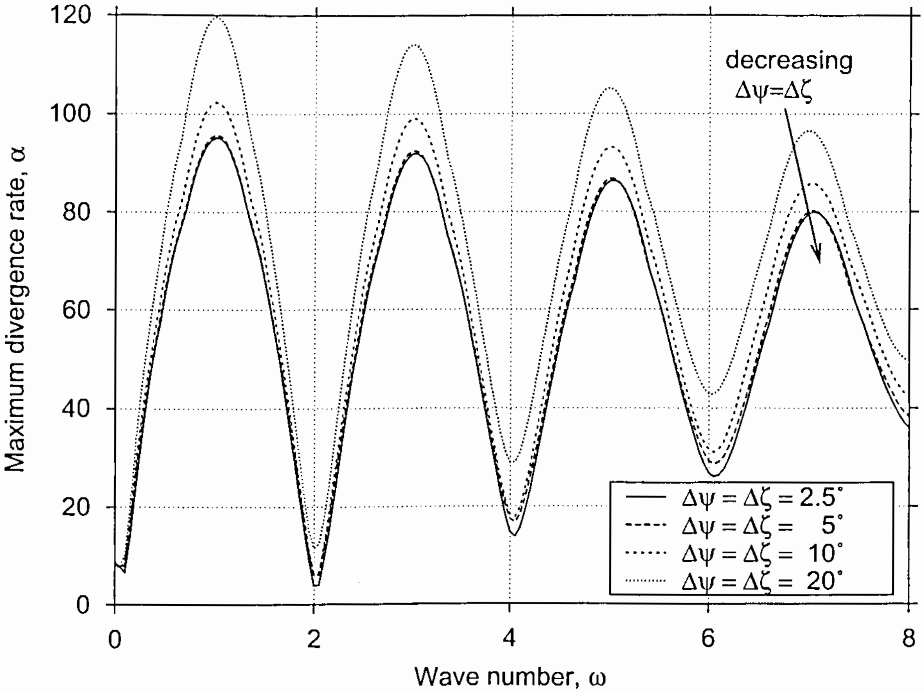

Figure 2.23: Effect of wake discretization on the stability of a numerical wake solution, $C_T = 0.005$ (Rotor 1).

Ref. 66 are also plotted for comparison. It is important to note that the location of vortex pairing, i.e., the location where the two tip vortex trajectories intersect each other, varies significantly with discretization. Therefore, an agreement with the experiments may only be a fortuitous result of a combination of various numerical parameters, such as the discretization level.

Another source of potential errors results from the vortex wake truncation at the far-wake boundary, that is well downstream of the rotor toward infinity. To reduce computational expense free-vortex wake calculations must be performed with a finite number of free wake turns. Because of this finite wake truncation, small errors are introduced in the induced velocity calculation at each collocation point. Although these errors are usually much smaller than the precision required for engineering analysis of

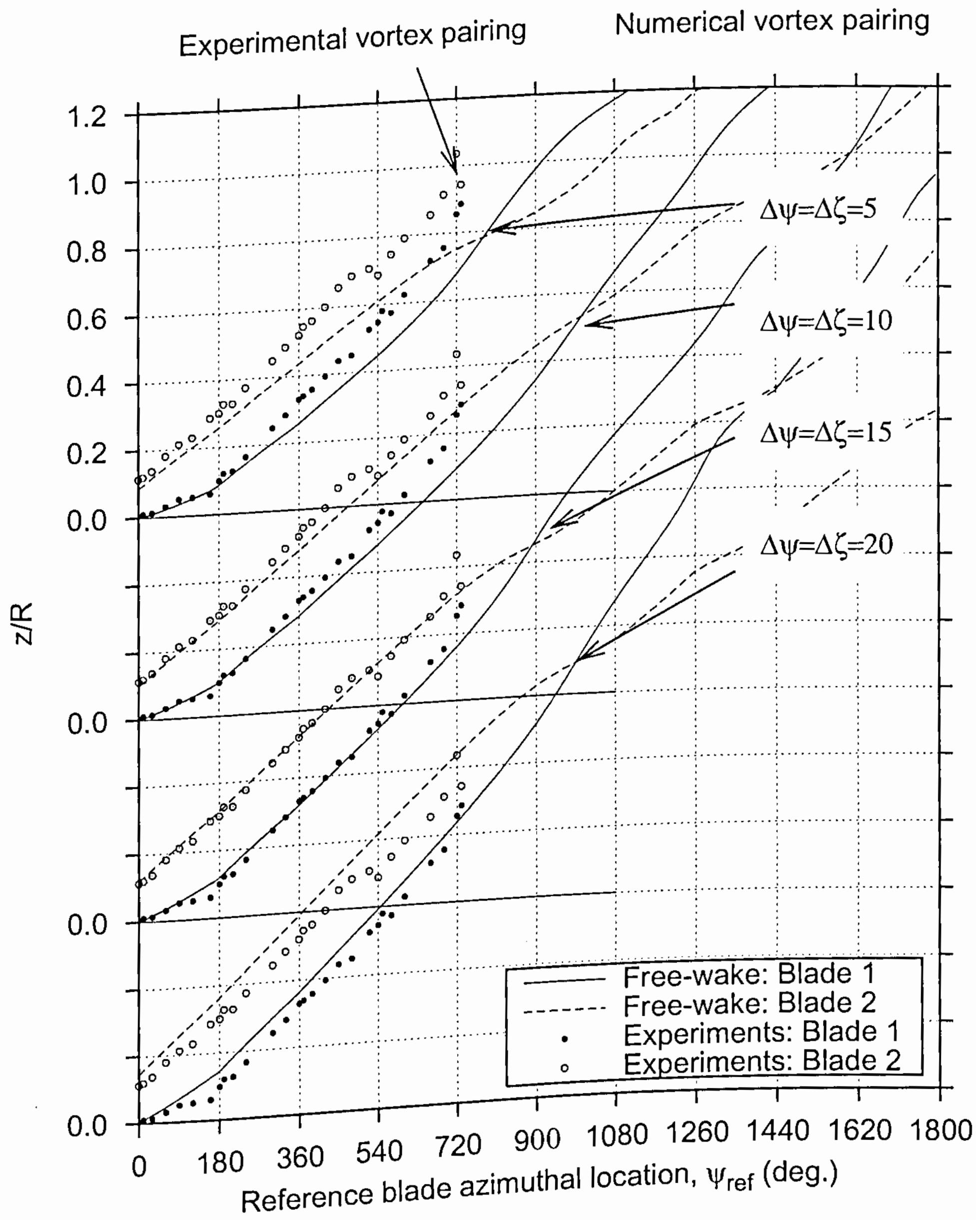

Figure 2.24: Effect of wake discretization on the numerical wake geometry solution, $C_T = 0.005$ (Rotor 1). Experimental results from Ref. 66.

rotor performance and blade loads, they may affect the wake stability and the so the initiation and growth of a vortex pairing instability. In such a case, the wake geometry predictions cannot necessarily be considered representative of the physical behavior of the wake.

To illustrate this effect, the wake geometry was computed using 2, 4, 6 and 8 free-wake turns, and the divergence rates corresponding to these cases is shown in Fig. 2.25. Note that the divergence rates show some sensitivity with fewer number of free-vortex turns of the wake. However, the discrepancy decreases as the number of turns are increased; the divergence rates for 6 and 8 free turns are almost identical. As the divergence rate decreases, the pairing between individual vortex filaments would occur farther downstream in the wake below the rotor.

The time-accurate wake geometry solutions are shown in Fig. 2.26 in the form of axial wake displacements for increasing blade azimuth angle. In all cases, the wake instability manifests in the form of the trajectories of the two tip vortex filaments separating from each other, and from the equilibrium solution. This is analogous to a bifurcation, where a stable solution splits into two unstable modes. The magnitude of the instability grows more slowly with a larger number of free-wake turns, as can be seen from the increasing azimuthal location of vortex pairing, that is, where the two vortex trajectories intersect each other. This confirms the smaller wake divergence rate as predicted using the stability analysis. Also, these results confirm that this vortex pairing is indeed a numerical manifestation of the wake instability and, therefore, can be modified by controlling the numerical parameters of the free-vortex wake scheme. Because the initial deformation leading to the instability (i.e., a perturbation to an equilibrium wake geometry) will be different in experimental tests and numerical results, an agreement between the two may, in many cases, be completely fortuitous.

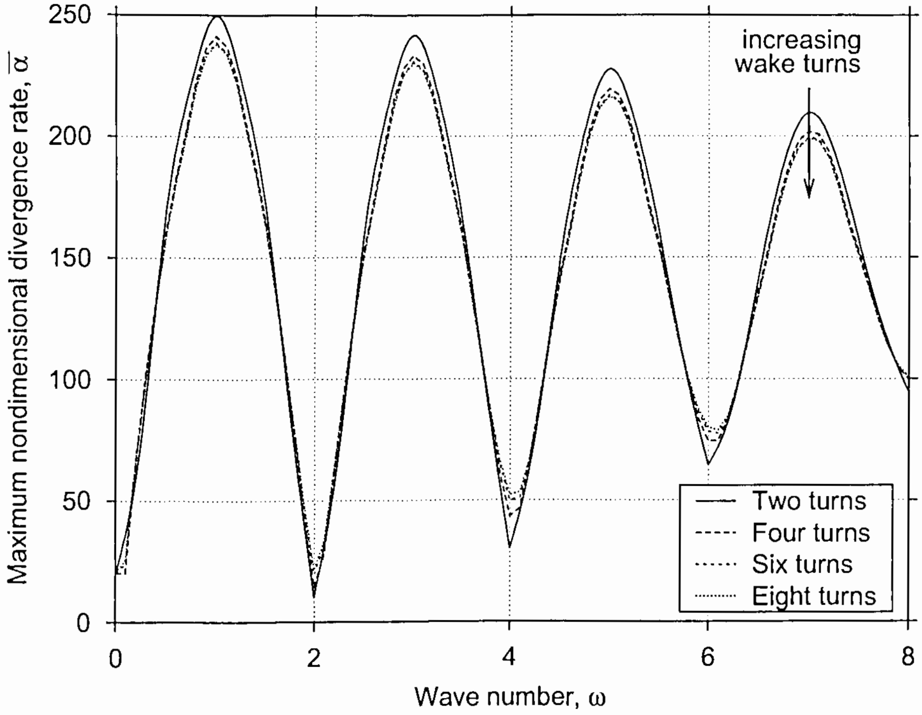

Figure 2.25: Effect of increasing number of free-wake turns on the stability of the numerical wake solution, $C_T = 0.005$, $\Delta\psi = \Delta\zeta = 10°$ (Rotor 1).

As mentioned in the Introduction, the vortex core size also plays a significant role in determining the onset of vortex instabilities in numerical wake solutions. To study this effect, numerical solutions were obtained using increasingly higher viscous diffusion – see Appendix A for details. The variation of core size with vortex age corresponding to these cases is shown in Fig. 2.27(a), along with the experimental results from Ref. 72 are also shown for comparison. Note that the higher values of diffusion result in non-physically large core sizes. The eigenvalues of the corresponding rotor wake solutions are shown in Fig. 2.27(b). Clearly, the divergence rates decrease as the vortex core size increases, and the smaller divergence rates for larger core sizes lead to less severe numerical instabilities. This may be part of the reason why many researchers have used a non-physical (larger) core size in the numerical wake solutions.

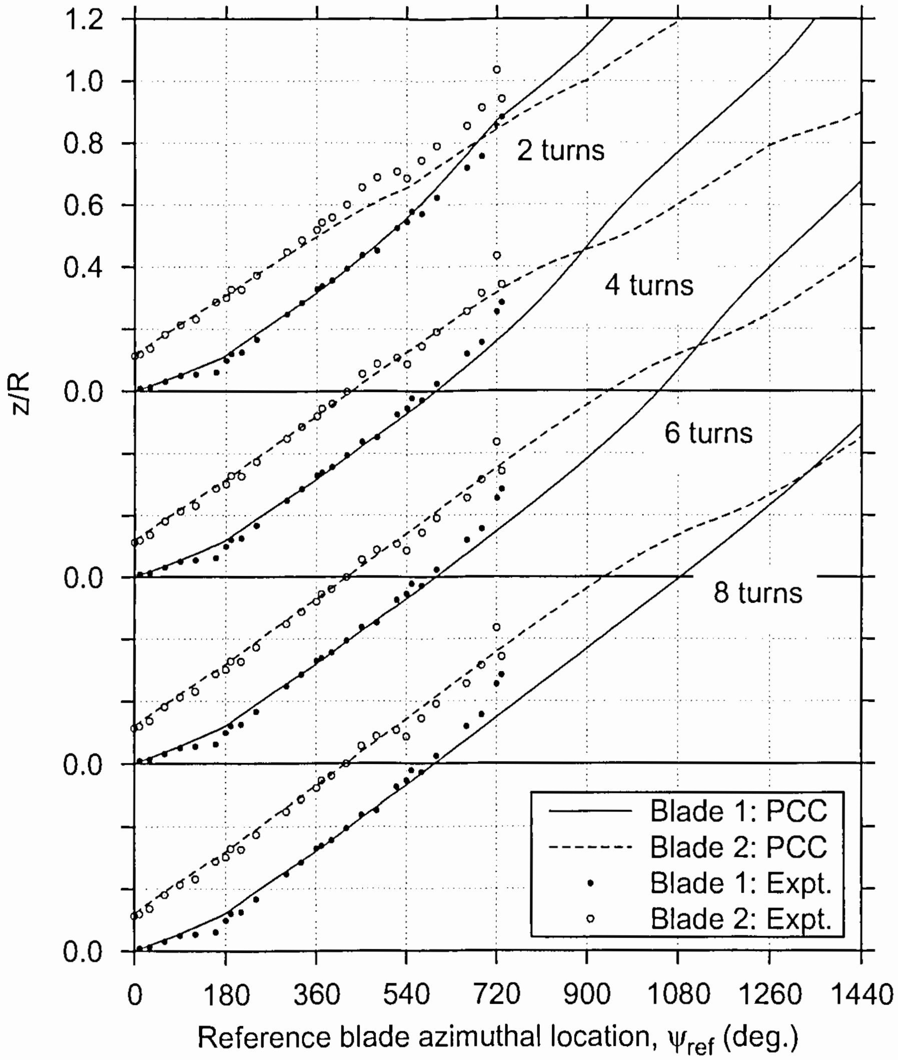

Figure 2.26: Effect of increasing number of free-wake turns on the numerical wake geometry solution, $C_T = 0.005$, $\Delta\psi = \Delta\zeta = 10°$ (Rotor 1), Experimental results from Ref. 66.

(a) Effect of viscous diffusion on vortex core size

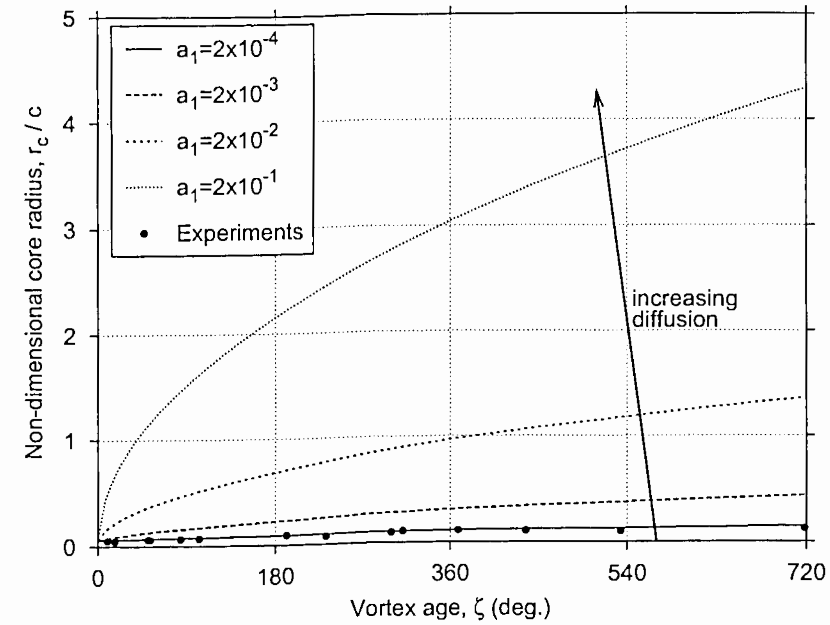

(b) Eigenvalues corresponding to different core sizes

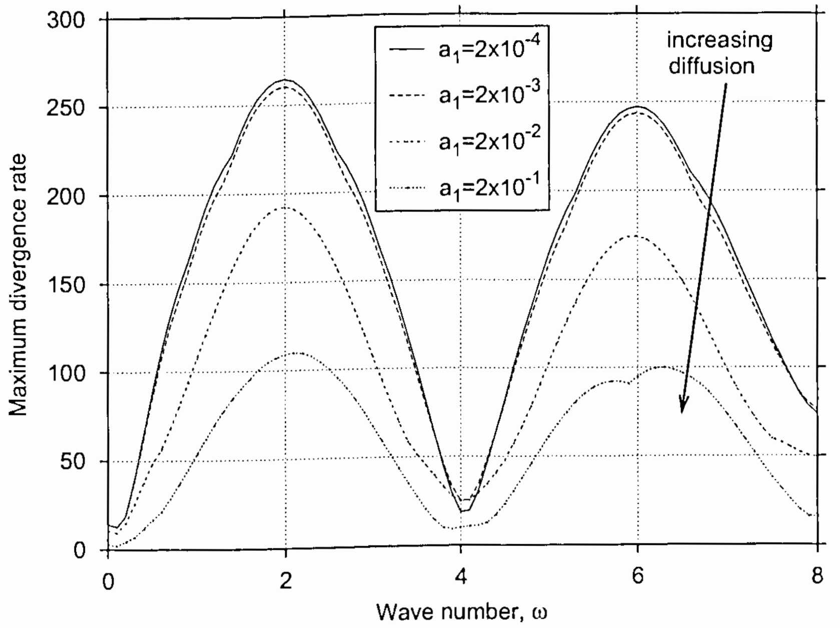

Figure 2.27: Effect of increasing the vortex core size on the stability of the numerical wake solution, Rotor 1, $C_T = 0.005$, $\Delta\psi = \Delta\zeta = 5°$, Six free wake turns. (a) Effect of viscous diffusion on vortex core sizer. Experimental results from Ref. 72. (b) Eigenvalues corresponding to different core sizes.

2.7 Summary

This chapter has focused on outlining the aerodynamic stability characteristics of rotor wakes. The stability of wake solution is important from the standpoint of designing time-accurate wake algorithms, especially so if the wake is physically unstable. An eigenvalue analysis has been developed to study the stability characteristics of helicopter rotor wakes in hover and axial climb. Experimental observations of the rotor wake behavior are used to support the stability results. The wake generated by a hovering helicopter rotor is shown to be intrinsically unstable, with the tip vortices exhibiting several possible unstable deformation modes.

Divergence rates (growth of instabilities) associated with each wake deformation mode depend on the relative phase of the perturbations produced on tip vortex filaments generated by different blades. The wake divergence rates increase sharply after the initial radial contraction of the wake below the rotor. Because divergence rates are governed by the vortex-induced velocities, the divergence rate for any deformation mode decreases with increasing rotor thrust, and also with increasing climb rate. Therefore, the divergence rate for any deformation mode decreases with increasing rotor thrust, and also with increasing climb rate. The so-called tip vortex "pairing" phenomenon, sometimes empirically observed in hovering flight conditions, is shown to be one unstable deformation mode of the rotor wake. It is also shown that in numerical solutions of the wake using free-vortex methods this deformation mode can be artificially excited because of numerical errors. A proper choice of numerical time integration algorithm is necessary to prevent non-physical growth of these numerical errors. This forms the motivation for the accuracy and stability analysis of numerical algorithms described in the next chapter.

Chapter 3

Methodology: Rotor Wake Equations

A detailed description of the time-marching wake solution algorithms is presented in this chapter. The rotor wake governing equations are described, along with the discretization strategies. The accuracy and stability of these numerical algorithms are examined. As shown in Chapter 2, the rotor wake is physically unstable and, therefore, the stability of the time-marching algorithm plays a key role in determining the stability of the numerical solutions. The accuracy of the straight-line vortex segmentation approach is also formally examined. Finally, a numerical convergence study is presented to justify the present choice of the time-integration algorithm.

3.1 Governing Equation for the Rotor Wake

As described previously in Chapter 1, the free-vortex wake analysis is based on the assumption of irrotational incompressible flow (i.e., a potential flow) with the vorticity assumed to be concentrated in a finite number of vortex filaments. By virtue of the vorticity transport theorem (Ref. 73), the motion of a point on a vortex filament is given by the equation of motion of a Lagrangian fluid particle, that is

$$\frac{d\vec{r}}{dt} = \vec{V}(\vec{r}) \tag{3.1}$$

where $\vec{r}$ is the position vector of a collocation point on the vortical wake, and $\vec{V}(\vec{r})$ the local fluid velocity at that point – see Fig. 3.1. In blade fixed coordinates, this equation can be rewritten in the form of a partial differential equation with blade azimuthal location, ψ, as a temporal coordinate, and vortex age, ζ, as a spatial coordinate, i.e.,

$$\frac{\partial \vec{r}}{\partial \psi} + \frac{\partial \vec{r}}{\partial \zeta} = \frac{\vec{V}(\vec{r})}{\Omega} \tag{3.2}$$

The left hand side (LHS) of Eq. 3.2 is, in essence, a one-dimensional wave (advection) equation. The velocity source term, $\vec{V}$, on the right hand side (RHS) is a result of all the wake induced velocities, as well as relative freestream and maneuver velocities of the rotor (helicopter). The wake solution is coupled with the rotor trim/response solution through the blade-attachment boundary condition at the origins of the trailing vortex filaments, with the blade lift solution being coupled through the trailed vortex strengths.

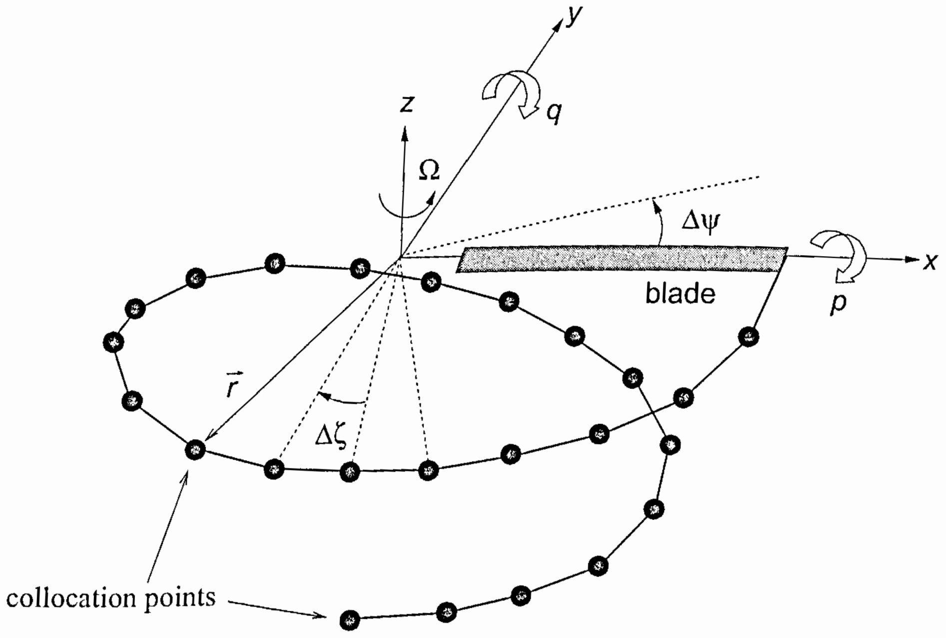

Figure 3.1: Schematic showing the discretized tip vortex geometry.

To solve Eq. 3.2 numerically, the domain of interest (ψ, ζ) is discretized into steps of $\Delta\psi$ and $\Delta\zeta$, and the derivatives on the LHS are approximated using finite difference approximations. The approach used in the free-vortex wake analysis of Bagai & Leishman (Ref. 56) was to solve the discretized equations at the mid-point $(\psi + \Delta\psi/2, \zeta + \Delta\zeta/2)$ of a grid cell $[\psi, \psi + \Delta\psi] \times [\zeta, \zeta + \Delta\zeta]$, with the derivatives being approximated by a second-order accurate five-point central difference. The velocity source term on the RHS includes self and mutual induced velocities, which are given by the Biot-Savart law (Ref. 8, Ch. 2, pp. 93–94) as an integral along the length of each vortex filament. This integral cannot, in general, be evaluated exactly and must be approximated with numerical quadrature. In most analyses, including the present analysis, the induced velocity is evaluated using straight-line vortex segmentation, which is analogous to the trapezoidal rule. In this case, the induced velocity at the mid-point is approximated using a second-order accurate averaging.

The time-marching algorithms were based on a predictor-corrector type sequence, where the predictor step was used to obtain an intermediate solution at the new time-step for the induced velocity calculations. Both the algorithms used a five-point central difference approximation for the spatial (ζ) derivative. A straight-line vortex segmentation was used to numerically evaluate the vortex-induced velocities. The key difference between the two algorithms, which are called the PCC and the PC2B algorithms, was the choice of difference approximation to the temporal (ψ) derivative.

3.2 Accuracy of Solution Algorithm

Any numerical solution is only an approximate solution to the original governing equations. This is because of different types of numerical introduced during the solution procedure. Truncation errors, or discretization errors, are the errors introduced during the discretization of the original governing equations. Clearly these errors depend on the discretization level, or grid size, as well on the discretization schemes that are used. The order of accuracy of a discretization refers to the relation between these errors and the grid size. It is necessary that the truncation errors show at least a first-order behavior. It follows that in the limit of zero grid size all errors will vanish and the original governing equation will be recovered.

The round-off errors are a result of non-exact representation of real numbers in floating-point arithmetic. These errors are somewhat dependent on the computer platform, but mainly depend on the floating-point precision used by the computer program. For the double precision arithmetic used in the present work, these errors have a relative magnitude of approximately 10^{-16}. Therefore, the round-off errors are not a real concern for most practical problems. The discretization errors are much larger in magnitude, and are more important. Therefore, the truncation errors in the discretized problem will be examined in Section 3.2.2.

For the wake governing equations, two types of discretization techniques are required. Firstly, the derivatives are approximated using finite differences and, secondly, the vortex induced velocity is evaluated in a discrete manner. As mentioned previously, it is the non-linear vortex induced velocities that pose a challenge for numerical solution. Therefore, the accuracy of the velocity calculations is examined. The discrete (finite difference) approximations to the derivatives are also examined using a standard numerical analysis approach.

3.2.1 Accuracy of Straight-Line Vortex Segmentation

The numerical solution of the free-vortex problem requires, in part, some form of discretization of the continuous vortex lines into discrete vortex elements or segments. These discrete vortex elements must convect in the velocity field as a result of the induced effects from all the vortical elements in the flow, as well as the influence of externally imposed velocities. Several possible discretization schemes include vortex blobs (Ref. 74), vortex particles (Ref. 52), straight-line segmentation (Refs. 56, 44), curved vortex elements (Ref. 47) or constant vorticity contours (Refs. 28, 75). The constant vorticity contour (CVC) approach differs from the others in the fundamental modeling of the flow field. While other methods model the flow field with continuous vortex lines, the CVC approach represents the wake with contours of constant vorticity. This approach is claimed to be computationally more efficient in modeling the inboard sheet (see, e.g., Ref. 75). However, this particular discretization approach also presents some special difficulties in formulating the governing equations for such contours. Therefore, the focus of this dissertation is on the discretization of the wake using continuous vortex lines.

Straight-line segmentation of the vortex filaments is the most common discretization and has been widely used in both research and production level free-vortex rotor wake analyses. One advantage of straight-line segmentation is that the induced contribution of each vortex segment can be evaluated exactly through the direct application of Biot-Savart law, see, e.g., Ref. 9 (Ch. 18, pp. 526-530), & Ref. 76 (Ch. 10, pp. 540–543). Because of this inherent simplicity, it is also widely employed in several other applications of vortex methods like, e.g., modeling flow turbulence (Ref. 77). Bliss *et al.* (Ref. 47) have shown that the use of curved vortex elements comprising circular/parabolic arcs can significantly reduce the number of segments required to obtain a reasonable level of accuracy for the induced velocity field. Yet, the derivation for the velocity induced by a curved vortex element is non-exact and involves several simplifying approximations and computational overheads that may not be acceptable for some rotor wake problems. This section formally documents the accuracy of straight-line segmentation of general curvilinear vortex filaments, with ultimate application to free-vortex wake analyses. The accuracy of this approach is examined using the vortex ring problem as a basis.

Biot-Savart Law

The Biot-Savart law gives the flow velocity $d\vec{V}$ at a point $\vec{r}$ as induced by an infinitesimally small length $d\vec{l}$ of a vortex with circulation strength Γ, by

$$d\vec{V} = \frac{\Gamma}{4\pi} \frac{d\vec{l} \times \vec{r}}{|\vec{r}|^3} \tag{3.3}$$

This is shown schematically in Fig. 3.2. For a straight-line vortex segment this integral can be readily evaluated, see, e.g., Ref. 9 (Ch. 18, pp. 526–530), & Ref. 76 (Ch. 10, pp. 540–543). The formulation employed in the present analysis and a linearized approximation are described later in Chapter 2.

In the general case of a curvilinear vortex discretized into straight-line segments, the induced velocity can be evaluated by simple numerical integration. To examine the accuracy of this approach, the straight-line discretization has been applied to the problem of calculating the induced velocity field of an inviscid (potential) vortex ring. This problem is of interest to the rotor analyst because a vortex ring can be viewed as an approximation to the vortical wake structure laid down by one revolution of the rotor. The advantage is that an exact solution for the vortex ring problem can be obtained, thereby allowing formal quantification of numerical errors arising because of the discretization.

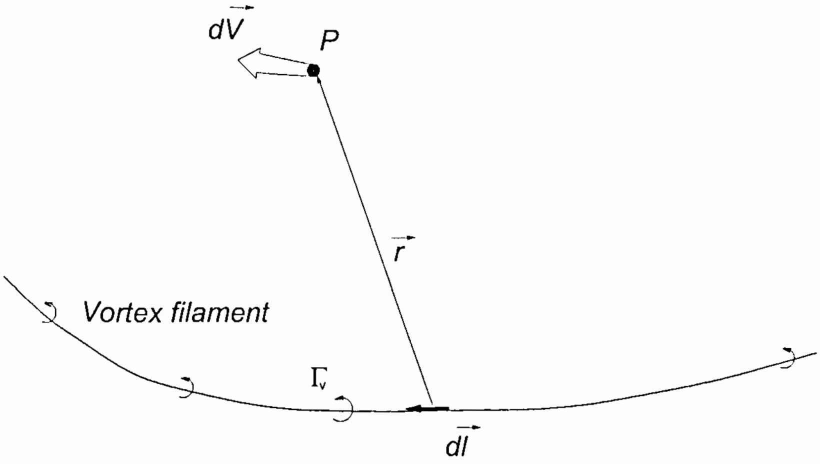

Figure 3.2: Schematic showing the velocity induced by an infinitesimal vortex element $d\vec{l}$ at a point $P(\vec{r})$.

Derivation of the Vortex Ring Solution

Figure 3.3 shows an element, $d\vec{l}$, of a vortex ring with a radius R and circulation strength Γ_v, and the velocity induced at a point $P(r, \theta, z)$. The cylindrical coordinate system has the origin at the center of the ring. Note that the azimuth angle θ is relative to the vortex ring element, i.e., the element $d\vec{l}$ is at $\theta = 0$.

The induced velocity $\vec{V}$, as given by the Biot-Savart law, is directed perpendicular to the plane containing the vectors $d\vec{l}$ and $\vec{r}$, which is the position vector of the point P relative to the vortex element – see Fig. 3.3. Therefore, the individual components of the induced velocity are given by

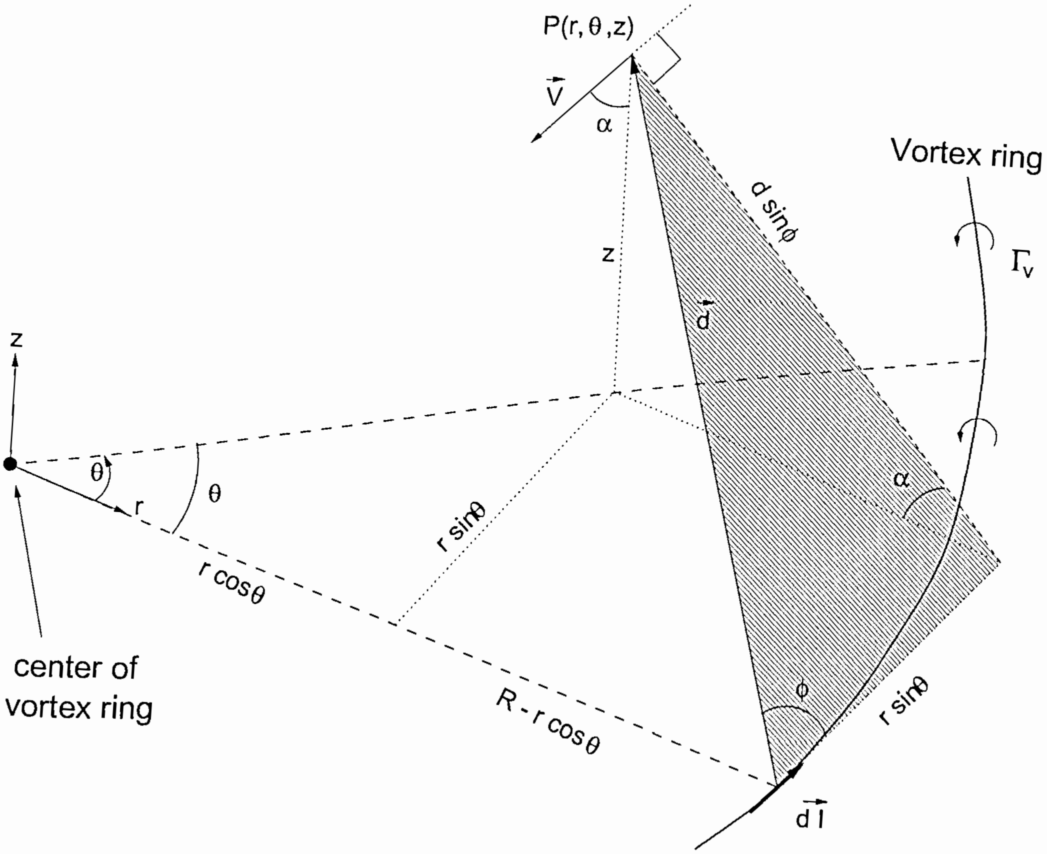

Figure 3.3: Schematic of the velocity induced by an element $d\vec{l}$ of a vortex ring.

$$\begin{aligned} V_r &= -|\vec{V}|\sin\alpha\cos\theta \\ &= -|\vec{V}|\frac{z}{\sqrt{[R-r\cos\theta]^2+z^2}} \end{aligned} \tag{3.4}$$

$$V_\theta = +|\vec{V}|\sin\alpha\sin\theta \tag{3.5}$$

$$\begin{aligned} V_z &= -|\vec{V}|\cos\alpha \\ &= -|\vec{V}|\frac{[R-r\cos\theta]}{\sqrt{[R-r\cos\theta]^2+z^2}} \end{aligned} \tag{3.6}$$

Although there is an azimuthal velocity component $\left(\vec{V}_\theta\right)$ induced by each vortex element, the overall azimuthal velocity induced by the vortex ring must vanish because of symmetry. Therefore, only the radial and axial components are derived in the following analysis.

Similarly, the magnitude of the induced velocity can also be obtained using applying the Biot-Savart law and noting that $|d\vec{l}| = Rd\theta$, i.e.,

$$\begin{aligned} |\vec{V}| &= \left| \frac{\Gamma_v}{4\pi} \frac{d\vec{l} \times \vec{d}}{|\vec{d}|^3} \right| \\ &= \frac{\Gamma_v}{4\pi} \frac{dl\, d \sin\phi}{d^3} \\ &= \frac{\Gamma_v}{4\pi} \frac{R\mathrm{d}\theta \sqrt{[R - r\cos\theta]^2 + z^2}}{(R^2 + r^2 - 2rR\cos\theta + z^2)^{\frac{3}{2}}} \end{aligned} \tag{3.7}$$

The velocity induced by the vortex ring can be now be found by integrating over the perimeter of the ring, i.e.,

$$V_r(r,z) = -\frac{\Gamma_v}{4\pi} \int_{\delta}^{2\pi+\delta} \frac{Rz\cos\theta}{(R^2 + r^2 - 2rR\cos\theta + z^2)^{3/2}} \mathrm{d}\theta \tag{3.8}$$

$$V_z(r,z) = -\frac{\Gamma_v}{4\pi} \int_{\delta}^{2\pi+\delta} \frac{R[R - r\cos\theta]}{(R^2 + r^2 - 2rR\cos\theta + z^2)^{\frac{3}{2}}} \mathrm{d}\theta \tag{3.9}$$

Note that the negative signs indicate that the axial velocity is directed downward inside the ring, while the radial velocity inward above the ring. The above integral can be exactly evaluated in terms of Legendre's elliptical integrals of the first and the second kind. These integrals are defined as

$$\mathbf{K}(x) = \int_0^{\pi/2} \frac{1}{\sqrt{1 - x\sin^2\theta}} d\theta \qquad \text{where } 0 \leq x < 1 \tag{3.10}$$

$$\mathbf{E}(x) = \int_0^{\pi/2} \sqrt{1 - x\sin^2\theta}\, d\theta \qquad \text{where } 0 \leq x < 1 \tag{3.11}$$

Now, the induced velocity components at a point $\vec{r} \equiv (r,z)$ are given by

$$V_z(r,z) = -\frac{\Gamma}{4\pi}\left[\frac{2}{\sqrt{(R-r)^2+z^2}}\left\{\mathbf{K}(x)+\frac{R^2-r^2-z^2}{(R+r)^2+z^2}\ \mathbf{E}(x)\right\}\right] \tag{3.12}$$

$$V_r(r,z) = -\frac{\Gamma}{4\pi}\left[\frac{2z}{r\sqrt{(R-r)^2+z^2}}\left\{\mathbf{K}(x)+\frac{R^2+r^2+z^2}{(R+r)^2+z^2}\ \mathbf{E}(x)\right\}\right] \tag{3.13}$$

where

$$x = \left(\sqrt{\frac{-4rR}{(R-r)^2+z^2}}\right) \tag{3.14}$$

The above solution for the induced velocities is based on a potential vortex ring, and therefore, there is a singularity at the ring itself. This singularity can be overcome by using a viscous vortex model with a core radius r_c, where the tangential velocity induced by a infinite line vortex is given by (see Appendix A)

$$V_\theta = \frac{\Gamma}{2\pi}\frac{r}{\left(r_c^{2n}+r^{2n}\right)^{1/n}} \tag{3.15}$$

where n is an integer. Extending this desingularization to the vortex ring problem, the velocities induced by the vortex ring becomes

$$V_z(r,z) = -\frac{\Gamma_v}{4\pi}\int_{\delta}^{2\pi+\delta}\frac{\left([R-r\cos\theta]^2+z^2\right)}{\left\{r_c^{2n}+\left([R-r\cos\theta]^2+z^2\right)^n\right\}^{1/n}}\frac{R[R-r\cos\theta]}{(R^2+r^2-2rR\cos\theta+z^2)^{\frac{3}{2}}}d\theta \tag{3.16}$$

$$V_r(r,z) = -\frac{\Gamma_v}{4\pi}\int_{\delta}^{2\pi+\delta}\frac{\left([R-r\cos\theta]^2+z^2\right)}{\left\{r_c^{2n}+\left([R-r\cos\theta]^2+z^2\right)^n\right\}^{1/n}}\frac{Rz}{(R^2+r^2-2rR\cos\theta+z^2)^{3/2}}d\theta \tag{3.17}$$

For a desingularized velocity profile as given above, the integrals in Eqs. 3.16 and 3.17 cannot be evaluated to give a closed form solution. In general, these integrals are evaluated numerically by expanding as a series solution.

Verification of Numerical Accuracy

A numerical solution to the velocities induced by a potential vortex ring was obtained by discretizing the ring along its circumference into discrete arcs with a subtended

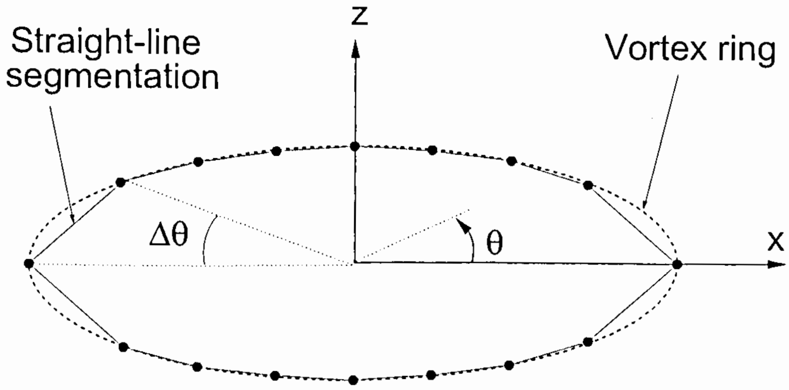

Figure 3.4: Schematic showing the discretization of the vortex ring problem.

angle Δθ. Each arc of the vortex ring is then approximated by a straight-line vortex segment joining the end-points – see Fig. 3.4. The sum of the induced velocities from all of these discrete vortex segments then gives an approximation to the velocity induced by the vortex ring as a whole.

Figure 3.5(a) and (b) show such numerical results for the induced velocity in the plane of the vortex ring as compared to the exact solution given by Eq. 3.12. (In the plane of the ring, only the axial component of velocity, V_z, exists.) Notice that for a potential vortex ring the exact solution to the induced velocity is not defined on the vortex ring itself because of the logarithmic singularity as $\vec{r} \rightarrow 0$. At all other points, the numerical results show a good agreement with the exact solution as shown in Fig. 3.5(a). Figure 3.5(b) shows similar results for a viscous vortex ring, where the core is desingularized using $n = 2$ in Eq. 3.15. In this case, the viscous core radius is $r_c/R = 0.01$ and, the self-induced velocity has a finite value by virtue of the desingularization. Again, the coarsest resolution of 30° shows some differences compared to the exact solution. But with finer resolution even the self-induced velocity is accurately predicted.

(a) Potential vortex ring

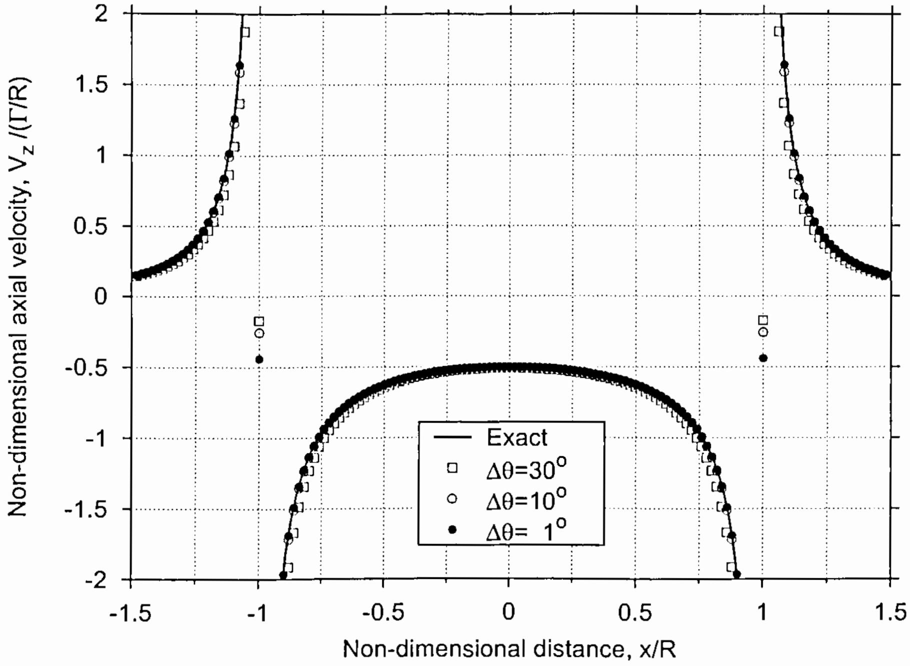

(b) Viscous vortex ring with $r_c/R = 0.01$

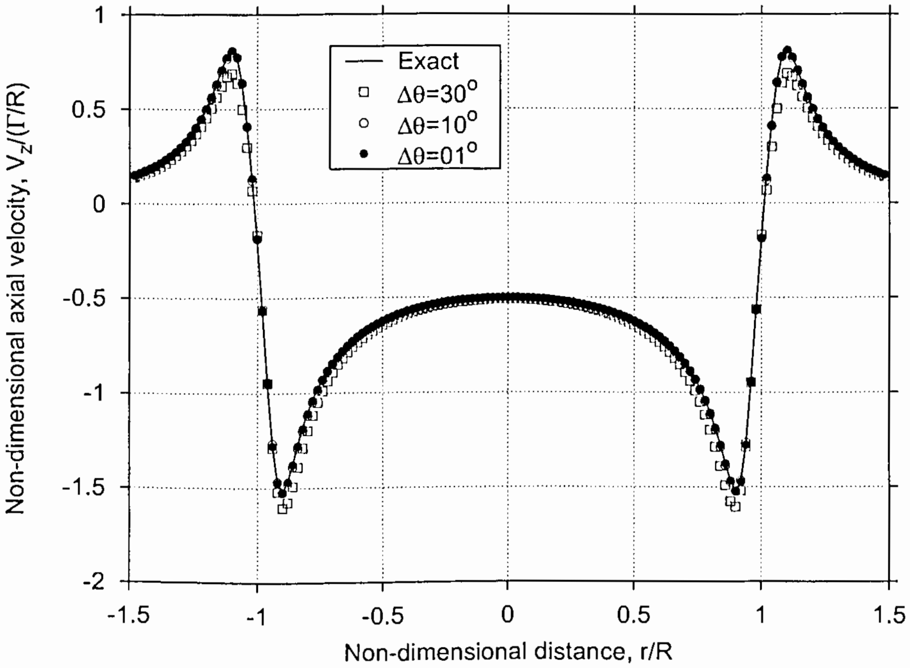

Figure 3.5: Induced velocity in the plane of a vortex ring numerically calculated using straight-line segmentation. Exact solution given by Eqs. 3.12 and 3.13. (a) Potential vortex ring, (b) Viscous vortex ring with $r_c/R = 0.01$.

It is apparent that by refining the discretization, that is, with increasing number of vortex segments, the accuracy of the solution rapidly improves. To better visualize this trend, the numerical errors, which is the difference between the exact and the numerical solution, are shown in Figs. 3.6(a) and (b) for three numerical discretization levels of $\Delta\theta = 30^\circ$, 10° and 1°. Notice that the maximum relative error in the numerical solution occurs close to $r/R = 1$, i.e., at the vortex ring itself. The errors decrease rapidly away from the vortex ring. For $\Delta\theta = 10^\circ$ the numerical errors are almost 10% at the vortex ring. The same trend is observed for a viscous vortex ring with a core radius given by $r_c/R = 0.01$, as shown in Fig. 3.6(b). This is significant for free-vortex calculations because the wake governing equation (Eq. 3.2) requires the velocity induced to be calculated at points on the vortex filament itself. Even this relatively simple test problem suggests that a discretization of $\Delta\theta \leq 10^\circ$ is required to obtain a reasonably accurate solution to the rotor wake problem.

To further appreciate the accuracy obtained with this discrete approximation, the relative errors in the induced velocity in the plane of the ring are shown in Fig. 3.7 as a function of the discretization, $\Delta\theta$. Results for a viscous vortex ring with a finite core size are also shown, where the singularity in the Biot-Savart result as $\vec{r} \rightarrow 0$ has been removed using a desingularized velocity profile as given by Eq. 3.15. An exact (mathematical) solution for a viscous vortex ring is not available and, therefore, the errors were calculated relative to the solution with the finest discretization, i.e., with the largest number of vortex segments. In both these cases, the relative errors were found to decrease quadratically with improved discretization, as is apparent from the 2:1 slope of the results on the logarithmic plot. Therefore, the induced velocity calculated using discrete straight-line segmentation of the vortex ring is formally second-order accurate, for both potential and viscous vortex rings.

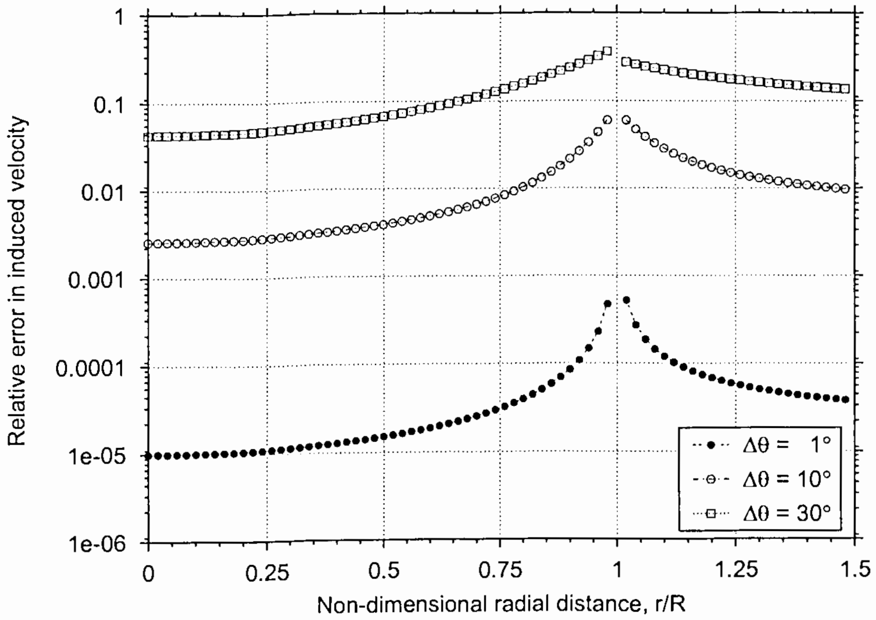

(a) Potential vortex ring

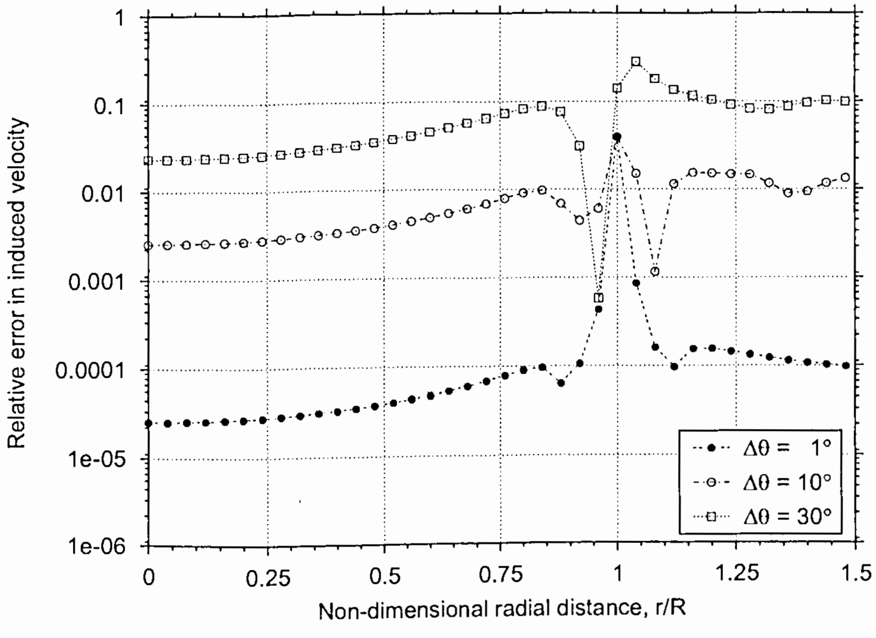

(b) Viscous vortex ring with $r_c/R = 0.01$

Figure 3.6: Numerical errors in the induced velocity in the plane of the vortex ring. (a) Potential vortex ring, (b) Viscous vortex ring with $r_c/R = 0.01$.

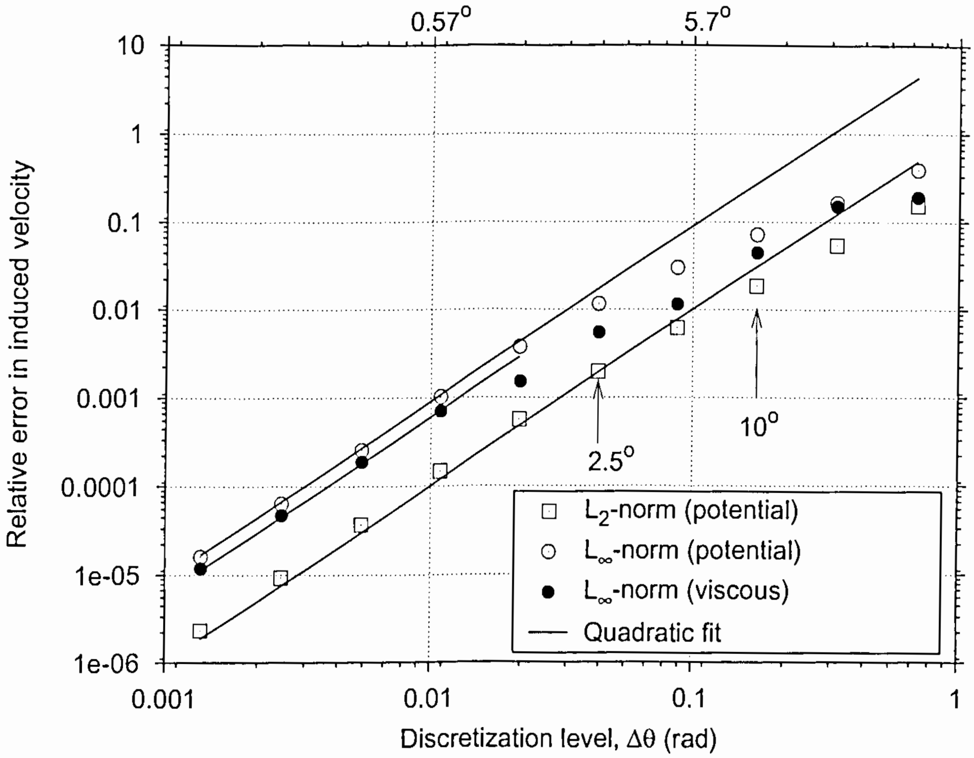

Figure 3.7: Relative error in induced velocity using straight line segmentation for the vortex ring problem. Potential and viscous vortex ring with $r_c/R = 0.01$.

As mentioned previously, the radial component of the induced velocity vanishes in the plane of the vortex ring. At points outside this plane, however, there exists a radial induced velocity. An example is shown in Fig. 3.8, where induced velocities are evaluated along a radial line positioned at $z/R = 0.2$ above the vortex ring. Such a problem is also of interest to the rotor analyst, because it represents situations like blade vortex interactions, where the rotor blades may experience strong induced velocities because of close proximity to the vortical wake structure. Note that in this case the axial velocity is not singular at any point, even for a potential vortex ring. The radial velocity is negative because it is directed towards the center of the vortex ring. Numerical results obtained using a discretization level of $\Delta\theta = 5°$ are also shown along with the exact solution. Clearly, the discretized solution approximates the analytical result very well.

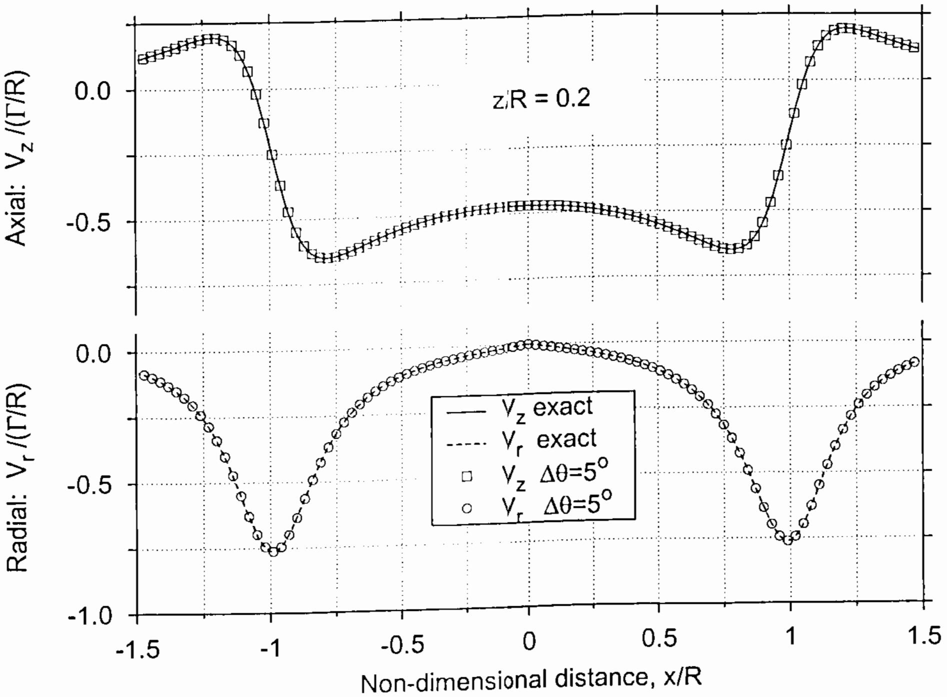

Figure 3.8: Induced velocity components of a potential vortex ring along a radial line at $z/R = 0.2$ calculated using straight-line segmentation. Exact solution given by Eqs. 3.12 and 3.13.

Figure 3.9 shows numerical errors as a function of discretization level for the induced velocity calculations at $z/R = 0.2$ above the vortex ring. The relative errors in the plane of the ring are also re-plotted for comparison. Although the relative errors in induced velocity above the ring are slightly larger than those in-plane, the errors exhibit a quadratically decreasing trend. This confirms that the discretization method gives a second-order accurate result, not only in the plane of the vortex ring, but also for points outside the ring.

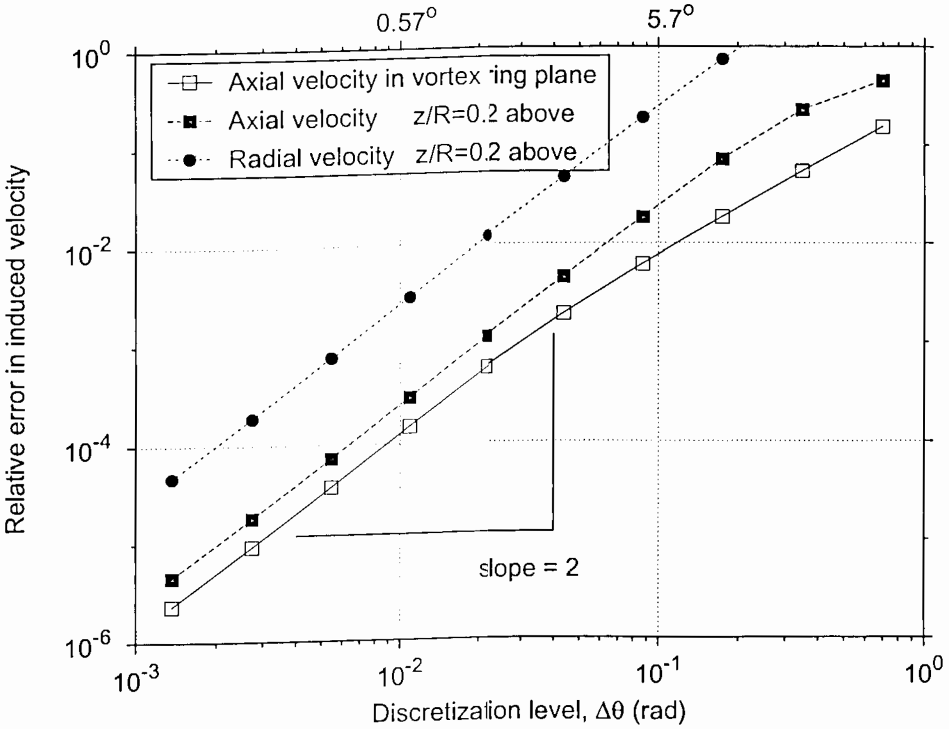

Figure 3.9: Relative error in induced velocity using straight line segmentation for the vortex ring problem for the induced velocities along radial line at $z/R = 0.2$.

Self-Induced Velocity

One of the suggested problems with a straight-line approximation to a curvilinear vortex is the treatment of the self-induced velocity – that is the velocity induced by the curved vortex filament on itself (Ref. 47). Even though the self-induced velocity for an inviscid vortex ring cannot be exactly calculated because of the logarithmic singularity, several acceptable approximations are possible. One approach is to use a cut-off angle to overcome the singularity and allow the induced velocities to be evaluated, i.e., the elliptical integrals in Eqs. 3.12 and 3.13 are evaluated over the azimuthal interval from δ to $2\pi - \delta$.

The results for the self-induced velocity obtained using this approach are shown in Fig. 3.10 as a function of the cut-off angle, δ. The numerical results corresponding to a discretization $\Delta\theta = \delta$ are also shown. A logarithmic scale is used on the ordinate to accentuate the logarithmic singularity in the self-induced velocity. Notice that the numerical results agree well with the "exact" integration with a cut-off. However, notice also that the self-induced velocity is dependent on the cut-off angle or the ring discretization and does not show a convergence in the limit as $\delta \to 0$.

For a viscous vortex ring, analytical approximations to the self-induced velocity have been developed based on asymptotic expansions. The classic result by Kelvin (e.g., Ref. 78) for a thin cored viscous vortex ring (i.e., one where the vorticity is evenly distributed in the core) is given by

$$V_z = \frac{\Gamma}{4\pi R}\left[\log\left(\frac{8R}{r_c}\right) - \frac{1}{4}\right] + O(r_c/R) \tag{3.18}$$

Saffman (Ref. 79) gives results for the case where the velocity around the vortex core is described a Lamb vortex (Ref. 70), that is where

$$V_\theta(r) = \frac{\Gamma}{2\pi r}\left(1 - \exp[-\alpha(r/r_c)^2]\right) \tag{3.19}$$

with $\alpha = 1.25643$. In this case, the self-induced convection velocity of the vortex ring is given by

$$V_z = \frac{\Gamma}{4\pi R}\left[\log\left(\frac{8R}{r_c}\right) - 0.558\right] + O\left(r_c/R \log[r_c/R]^2\right) \tag{3.20}$$

Figure 3.11 shows these analytical solutions as a function of the viscous core radius, along with the numerical results obtained using straight-line segmentation of the viscous vortex. The numerical solution shows a good agreement with the analytical results given by Eqs. 3.18 and 3.20 and proves that the straight-line segmentation approach can be successfully applied to calculate the self-induced velocity of a general curvilinear vortex. Recall that the numerical solution is second-order accurate and, therefore, for $r_c < (\Delta\theta)^2$ the numerical errors will become more significant.

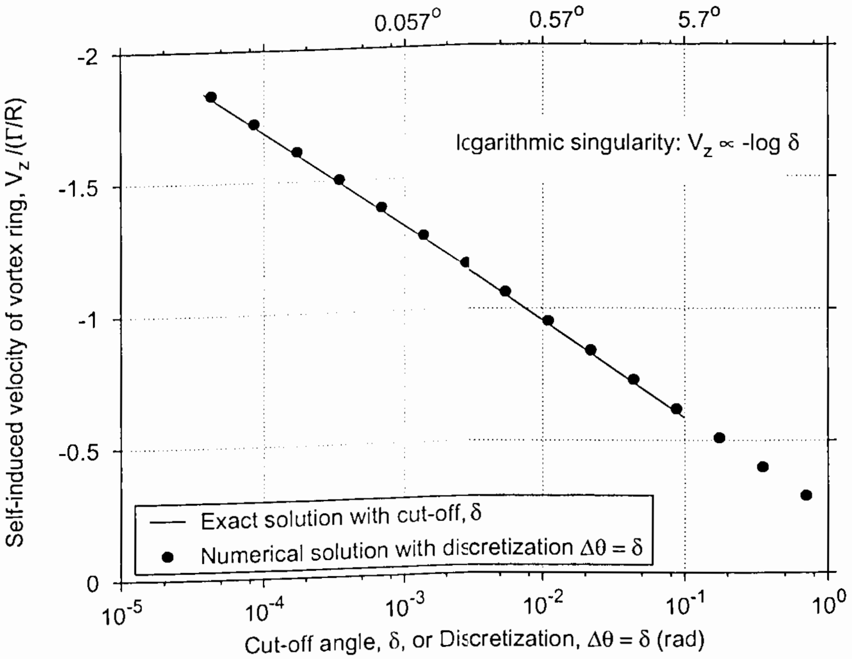

Figure 3.10: Self-induced convection velocity of a potential vortex ring. The exact solution is calculated by evaluating the elliptical integrals with a cut-off, δ, while the numerical solution is obtained using a discretization, $\Delta\theta = \delta$.

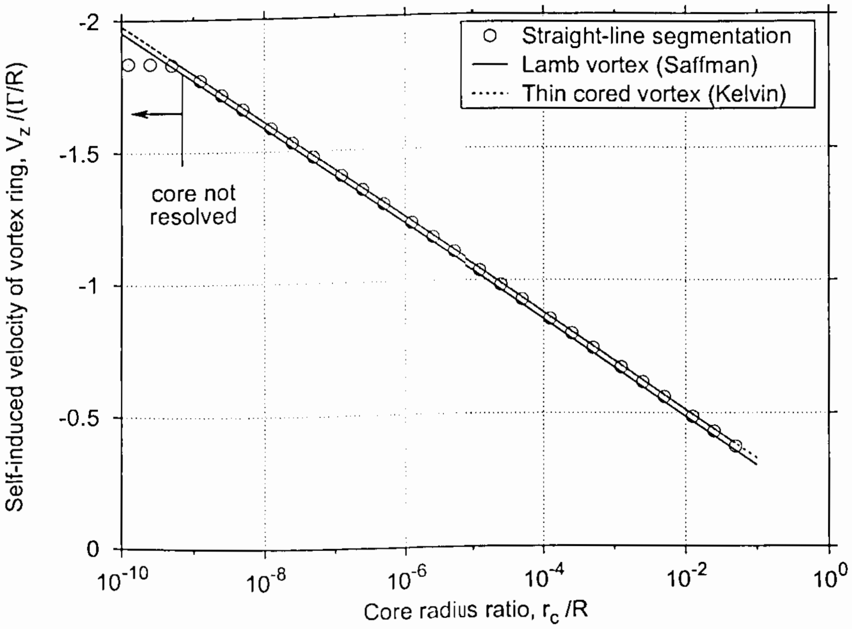

Figure 3.11: Self-induced convection velocity of a finite core vortex ring.

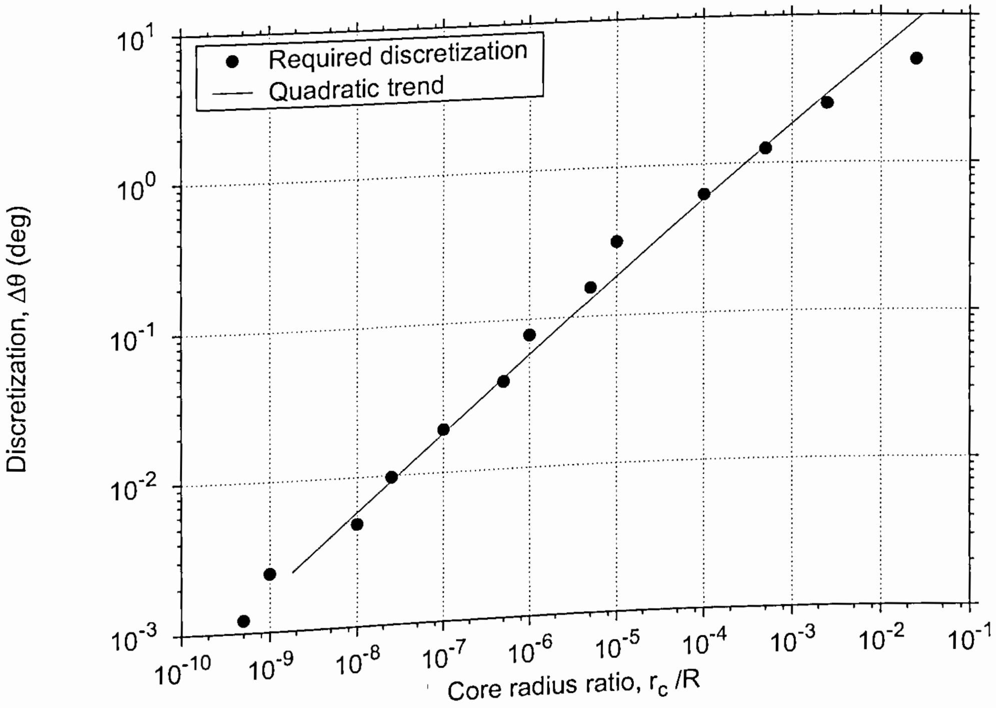

Figure 3.12: Minimum discretization level required for a given core radius.

For very small viscous core radii ($r_c/R < 10^{-8}$ in this case), the numerical solution shows a deviation from the logarithmic trend, which is because of round-off errors in the computations. A summary of the results is shown in Fig. 3.12 where the required discretization, $\Delta\theta$, to obtain a relative error of less than 0.1% is shown as a function of the core radius ratio, r_c/R. Clearly, a discretization of $\Delta\theta \leq (r_c/R)^2$ is required to properly resolve the vortex core. For a typical rotating-wing the physical size of the viscous core radius is about 1% of the rotor radius, which suggests that in a free-vortex scheme, a vortex discretization of $\Delta\theta \leq 5°$ will be required to properly resolve the self-induced velocities.

Improving the Order of Accuracy

One other objective of the accuracy verification undertaken in the present work, was to construct a numerical methodology which is amenable to various numerical analysis techniques for improving the accuracy. Note that the second-order accuracy obtained with the numerical results in the preceding analysis also implies that the discrete approximation may be expressed as an asymptotic expansion of the general form

$$A(\Delta\theta) = A_{\text{exact}} + C_1 \Delta\theta^{n_1} + C_2 \Delta\theta^{n_2} + \cdots \tag{3.21}$$

where $n_1 < n_2 < \cdots$ are integers and $C_1, C_2, \ldots$ are real constants. The second-order accuracy for the ring problem suggested by Fig. 3.13 shows that the solution can be expressed as an asymptotic expansion (Eq. 3.21) with $n_1 = 2$. One technique that can be used to improve the accuracy of the solution is Richardson's extrapolation (Ref. 80). Richardson's extrapolation is, in essence, a linear combination of solutions using two lower discretizations of the problem to obtain a new solution of, potentially, higher order accuracy. This is done by eliminating the leading order term in the asymptotic expansion (Eq. 3.21). For a second-order accurate method this gives

$$\begin{aligned} \tilde{A}(\Delta\theta) &= \frac{4A(\Delta\theta) - A(2\Delta\theta)}{3} \\ &= A_{\text{exact}} + \frac{4 - 2^{n_2}}{3} C_2 \Delta\theta^{n_2} + \cdots \end{aligned} \tag{3.22}$$

This new discrete approximation, $\tilde{A}(\Delta\theta)$, is n_2-order accurate, as shown by the leading term in Eq. 3.22.

This technique can be readily applied to the induced velocity calculations by combining two discrete solutions. For example, a combination of the two solutions corresponding to 10° and 5° gives

$$\tilde{V}^{10^\circ} = \frac{4V^{5^\circ} - V^{10^\circ}}{3} \tag{3.23}$$

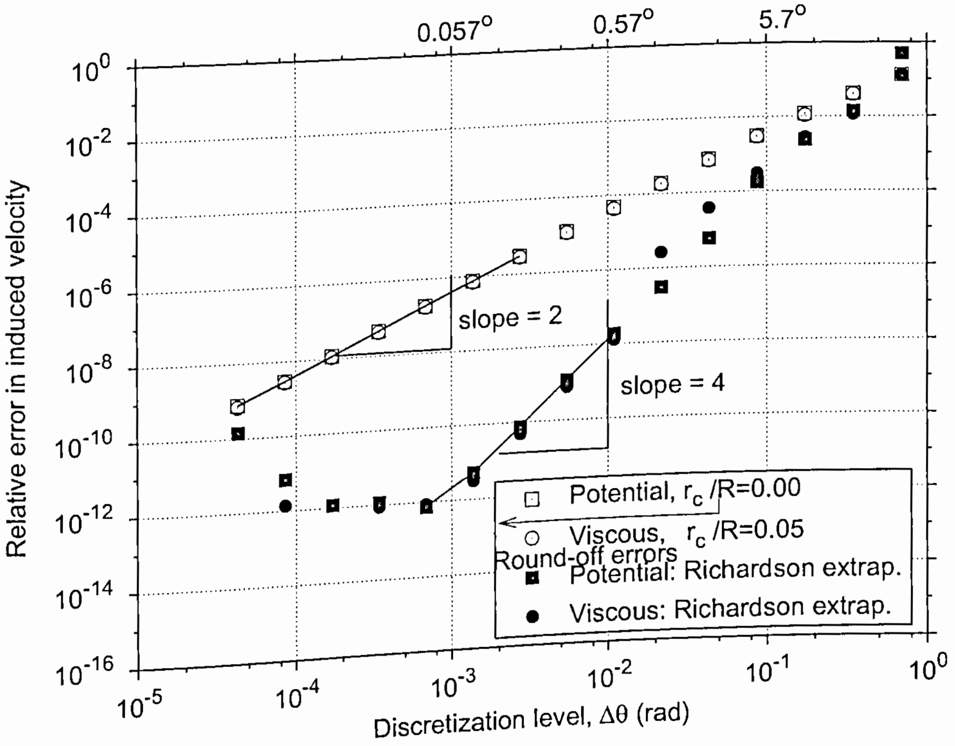

Figure 3.13: Relative error in induced velocity using straight line segments. Richardson's extrapolation provides a higher order of accuracy.

Improved numerical solutions using this approach are shown in Fig. 3.13 along with the baseline second-order accurate solution. Again, the results are plotted in terms of numerical errors as a function of discretization level on a logarithmic plot to bring out the order of accuracy. In this case it is apparent that the numerical results with Richardson's extrapolation are fourth-order accurate, as indicated by the 4:1 slope. This improvement in order of accuracy suggests that the resulting dominant error term is fourth-order, i.e., $n_2 = 4$ in Eq. 3.22.

This process can be repeated indefinitely to annihilate more terms in the asymptotic expansion to obtain an arbitrarily high order of accuracy. This limiting process is also known as Richardson's deferred approach to the limit (Ref. 81) or Romberg integration (Ref. 82). In principle, Richardson's limiting process can be adapted for use in free-vortex wake calculations, where two low resolution wake solutions can be extrapolated to higher order accuracy, and generally at much lower computational cost than for a complete wake solution made at high resolution. These results will be shown later in Section 3.4.

3.2.2 Accuracy of Finite Difference Approximations

Numerical methods employ finite difference formulae to model the derivatives and partial derivatives in the governing differential equations. Ideally, the finite difference approximations are such that in the limiting case of zero discretization they approach the derivatives being approximated. In this section, this idea is extended to verify that finite difference equations approach the original governing differential equations in the zero discretization limit. This procedure is commonly referred to as "consistency" in traditional CFD terminology (Ref. 83). In the preceding section the induced velocity calculations using straight-line vortex segmentation was shown to be second-order accurate. In this section, the accuracy of the finite difference approximations to the derivatives on the LHS of the governing equation (Eq. 3.2) is formally examined. The errors arising because of the discrete evaluation of induced velocity are examined later in Section 3.3.3, where the modified equations are studied.

The analysis of Bagai & Leishman (Ref. 56) is based on the so-called five-point central difference approximations. In this case, the derivatives at the mid-point of a grid cell are approximated using the values at four surrounding grid points. The use of five points, four grid points and an evaluation point – see Fig. 3.14 suggests the name "five-point central difference." This difference approximation is given by

$$
\begin{aligned}
D_\psi &\approx \left.\frac{dr}{d\psi}\right|_{\psi+\Delta\psi/2,\zeta+\Delta\zeta/2} \\
&= \frac{(\vec{r}(\psi+\Delta\psi,\zeta+\Delta\zeta)-\vec{r}(\psi,\zeta+\Delta\zeta))+(\vec{r}(\psi+\Delta\psi,\zeta)-\vec{r}(\psi,\zeta))}{2\Delta\psi}
\end{aligned}
\tag{3.24}
$$

A similar approximation, say, D_ζ, can be readily obtained for the spatial derivative. To analyze the accuracy of these finite difference approximations, each term can be expanded as a Taylor-series around the evaluation point $\vec{r}\,(\Delta\psi/2,\Delta\zeta/2)$. Therefore,

$$
\begin{aligned}
D_\psi+D_\zeta &= \frac{\partial\vec{r}}{\partial\psi}+\frac{\partial\vec{r}}{\partial\zeta} \\
&\quad+\left(\frac{1}{24}\frac{\partial^3\vec{r}}{\partial\psi^3}+\frac{1}{8}\frac{\partial^3\vec{r}}{\partial\psi^2\partial\zeta}\right)\Delta\psi^2+\left(\frac{1}{8}\frac{\partial^3\vec{r}}{\partial\psi\partial\zeta^2}+\frac{1}{24}\frac{\partial^3\vec{r}}{\partial\zeta^3}\right)\Delta\zeta^2+\cdots
\end{aligned}
\tag{3.25}
$$

Note that the partial derivative terms on the RHS are also evaluated at the cell midpoint. The leading terms in the expansion of the difference approximations are of the order of $O\left(\Delta\psi^2\right)$ and $O\left(\Delta\zeta^2\right)$. Therefore the five-point central finite difference approximation is second-order accurate in both ψ and ζ.

The proposed PC2B time-accurate algorithm uses a second-order backward difference approximation for the time (ψ) derivative. In this case, three previous time steps are used in approximating the temporal derivative – see Fig. 3.15. This approximation is given by

$$
\begin{aligned}
D_\psi &\approx \frac{\partial\vec{r}(\psi+\Delta\psi/2,\zeta)}{\partial\psi} \\
&= \frac{3\vec{r}(\psi+\Delta\psi,\zeta)-\vec{r}(\psi,\zeta)-3\vec{r}(\psi-\Delta\psi,\zeta)+\vec{r}(\psi-2\Delta\psi,\zeta)}{4\Delta\psi}
\end{aligned}
\tag{3.26}
$$

Again, using a Taylor-series analysis for about the evaluation point it can be shown that

$$
\tilde{D}_\psi = \left.\frac{\partial\vec{r}}{\partial\psi}\right|_{\psi+\Delta\psi/2,\zeta} - \left.\frac{5}{24}\frac{\partial^3\vec{r}}{\partial\psi^3}\right|_{\psi+\Delta\psi/2,\zeta}\Delta\psi^2+\left.\frac{1}{4}\frac{\partial^4\vec{r}}{\partial\psi^4}\right|_{\psi+\Delta\psi/2,\zeta}\Delta\psi^3+\cdots \tag{3.27}
$$

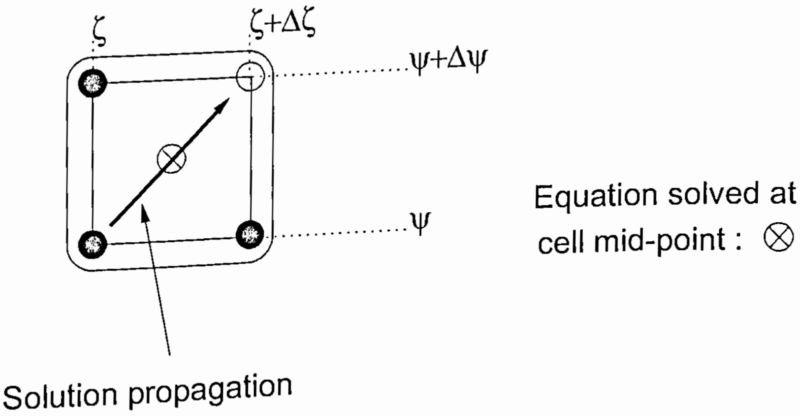

Figure 3.14: Stencil for the five-point central difference approximations used in the relaxation algorithm and the PCC time-marching algorithm.

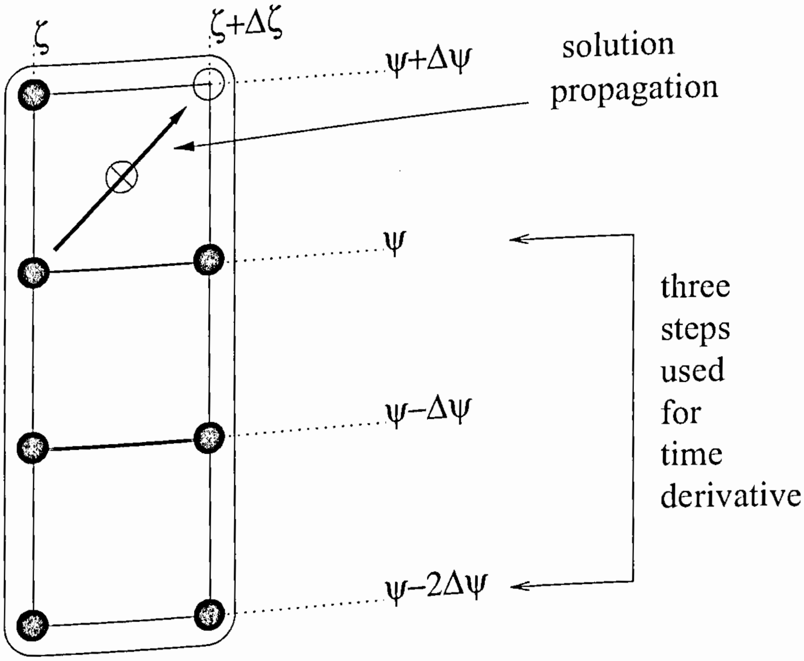

Figure 3.15: Stencil for the second-order backward difference approximation used in the PC2B time-marching algorithm.

Therefore, the backward difference approximation is, indeed, second-order accurate in time (ψ) at the evaluation point.

Using this approximation along with the five-point central difference approximation for the spatial derivative, the LHS of the governing equations can be written as

$$\begin{aligned} \tilde{D}_\psi + D_\zeta &= \frac{\partial \vec{r}}{\partial \psi} + \frac{\partial \vec{r}}{\partial \zeta} + \left(-\frac{5}{24}\frac{\partial^3 \vec{r}}{\partial \psi^3} + \frac{1}{8}\frac{\partial^3 \vec{r}}{\partial \psi^2 \partial \zeta} \right) \Delta\psi^2 + \left(\frac{1}{8}\frac{\partial^3 \vec{r}}{\partial \psi \partial \zeta^2} + \frac{1}{24}\frac{\partial^3 \vec{r}}{\partial \zeta^3} \right) \Delta\zeta^2 \\ &\quad + \frac{1}{4}\frac{\partial^4 \vec{r}}{\partial \psi^4} \Delta\psi^3 + \cdots \end{aligned} \tag{3.28}$$

where all the derivatives are evaluated at the grid mid-point, $\vec{r}(\Delta\psi/2, \Delta\zeta/2)$. The leading error terms are found to be second-order in $\Delta\psi, \Delta\zeta$, indicating a second-order accuracy. Previously, in Section 3.2.1, it was shown that discrete induced velocity calculations were also performed to a second-order accuracy. Therefore, for both the time-marching algorithms, as well as the relaxation algorithm, the governing equations are evaluated up to a second-order accuracy.

3.3 Stability of Wake Solution Algorithm

Because the rotor wake structure is physically unstable, the stability of numerical method is a critical criterion to ensure that the numerical solution converges to a physically correct solution. Traditional CFD methods employ various linear and non-linear stability criteria to ensure proper solution convergence. In the same spirit, numerical methods for the wake solutions will first be examined using a linearized stability analysis, and then using the modified equations.

3.3.1 Linearized Stability of Time-Integration Algorithms

In the present work, the time-marching algorithms were developed following the basic approach as the free-vortex wake analysis of Bagai & Leishman (Refs. 56–58). Therefore, a five-point central difference approximation for the spatial (ζ) derivative was used in both algorithms, while standard straight-line vortex segmentation was used to numerically evaluate the vortex-induced velocities.

The induced velocity from a straight-line segment can be written in a compact form

$$\vec{V}_{BS}(\psi_k, \zeta_l; \zeta_i) \tag{3.29}$$

which represents the velocity induced at a collocation point at $\vec{r}(\psi_k, \zeta_l)$ by the i^{th} straight-line vortex segment extending from $\vec{r}(\psi_k, \zeta_{i-1})$ to $\vec{r}(\psi_k, \zeta_i)$. Therefore, the net induced velocity at $\vec{r}(\psi_k, \zeta_l)$ can be expressed as a sum of induced velocity from all such vortex elements, i.e.,

$$\vec{V}\left(\vec{r}(\psi_k, \zeta_l)\right)\Big|_{\text{discrete}} = \sum_{n=1}^{N_b} \sum_{i=1}^{N_\zeta} \vec{V}_{BS}\left(\psi_k + (n-1)\frac{2\pi}{N_b}, \zeta_l; \zeta_i\right) \tag{3.30}$$

With these discrete approximations, the wake equations can be written in the form of an ordinary differential equation (ODE) in ψ as

$$\begin{aligned} \frac{d\vec{r}(\psi,\zeta)}{d\psi} &= \frac{\vec{r}(\psi,\zeta) - \vec{r}(\psi,\zeta+\Delta\zeta)}{\Delta\zeta} + \vec{V}\left(\vec{r}(\psi,\zeta)\right)\Big|_{\text{discrete}} \\ &= F(\vec{r}(\psi), \psi) \end{aligned} \tag{3.31}$$

The key difference between the PCC and the PC2B algorithms is the treatment of the time (ψ) derivative in the above ODE (Eq. 3.31).

To analyze the linearized stability of a time-integration algorithm, the algorithm is applied to a simpler ordinary differential equation, which can be exactly solved by direct integration. Consider the representative equation

$$\frac{du}{dt} = \lambda u + a e^{\mu t} \tag{3.32}$$

where λ, a and μ are constants. The exact solution to Eq. 3.32 is given by

$$u(t) = u(0)e^{\lambda t} + a\left(\frac{e^{\mu t} - e^{\lambda t}}{\mu - \lambda}\right) \tag{3.33}$$

where $u(0)$ is the initial condition for the time-dependent problem. The solution eigenvalue λ corresponds to the eigenvalues of spatial discretization, obtained using the method of lines to transform a PDE to an ODE. From physical considerations, these eigenvalues must be negative so that the resulting ODE is stable. The forcing term $ae^{\mu t}$ is, however, independent of the spatial discretization. In the context of the wake governing equations, the spatial eigenvalues, λ, are a result of the finite difference approximation to the spatial (ζ) derivative, while the forcing function is the nonlinear velocity source term on the RHS.

The PCC algorithm applied to the representative equation gives

Predictor:

$$\tilde{u}_{n+1} = u_n + \frac{1}{2}\lambda h\left(\tilde{u}_{n+1} + u_n\right) + \frac{1}{2}ahe^{\mu hn} \tag{3.34}$$

Corrector:

$$u_{n+1} = u_n + \frac{1}{2}\lambda h\left(u_{n+1} + u_n\right) + \frac{1}{2}ah\left(e^{\mu hn} + e^{\mu h\widetilde{(n+1)}}\right) \tag{3.35}$$

where h is the time step $\left(t^{n+1} - t^n\right)$. Note that the predictor step is used only for the induced velocity calculation and, therefore, appears only in the exponential forcing term.

By writing $u_n = \sigma^n u_0$, i.e., $u_{n+1} = \sigma u_n$, the determinant of the above system of equations can be written as a polynomial in σ, say $P(\sigma)$, known as the characteristic polynomial. The eigenvalues of the time-marching algorithm, σ, are given by the roots of the characteristic polynomial, i.e., solutions of $P(\sigma) = 0$. For the above time-marching algorithm in Eqs. 3.34 and 3.35 the characteristic polynomial is given by

$$P(\sigma) = (1 - \frac{1}{2}\lambda h)\sigma - (1 + \frac{1}{2}\lambda h) \tag{3.36}$$

and the eigenvalue is given by

$$\sigma = \frac{1 + \frac{1}{2}\lambda h}{1 - \frac{1}{2}\lambda h} = 1 + \lambda h + \frac{1}{2}\lambda^2 h^2 + \cdots \frac{1}{2^{n-1}}\lambda^n h^n + \cdots \tag{3.37}$$

Note that first three terms of the eigenvalue are identical to the first three terms in the Taylor-series expansion of the exact solution, $e^{\lambda h}$, i.e.,

$$e^{\lambda h} = 1 + \lambda h + \frac{1}{2}\lambda^2 h^2 + \cdots + \frac{1}{n!}\lambda^n h^n + \cdots \tag{3.38}$$

Therefore, the PCC algorithm is second-order accurate in time.

Similarly, the PC2B algorithm applied to the representative equation gives

Predictor:

$$\tilde{u}_{n+1} = u_n + \frac{1}{2}\lambda h\,(\tilde{u}_{n+1} + u_n) + \frac{1}{2}ahe^{\mu hn} \tag{3.39}$$

Corrector:

$$3u_{n+1} = u_n + 3u_{n-1} - u_{n-2} + 2\lambda h\,(u_{n+1} + u_n) + 2ah\left(e^{\mu hn} + e^{\mu h(\widetilde{n+1})}\right) \tag{3.40}$$

In this case, the eigenvalues are given by solutions of the characteristic equation

$$(3 - 2\lambda h)\sigma^3 - (1 + 2\lambda h)\sigma^2 - 3\sigma + 1 = 0 \tag{3.41}$$

Because, in this case, the time-integration involves three time-steps, there are three eigenvalues. These are given by

$$\left.\begin{aligned} \sigma_1 &= 1 + \lambda h + \tfrac{1}{2}\lambda^2 h^2 + \tfrac{1}{2}\lambda^3 h^3 + \tfrac{1}{8}\lambda^4 h^4 + \tfrac{1}{8}\lambda^5 h^5 + \cdots \\ \sigma_2 &= \tfrac{1}{3} - \tfrac{1}{9}\lambda h + \tfrac{5}{54}\lambda^2 h^2 + \tfrac{17}{162}\lambda^3 h^3 + \tfrac{269}{1944}\lambda^4 h^4 - \tfrac{1163}{5832}\lambda^5 h^5 + \cdots \\ \sigma_3 &= -1 \end{aligned}\right\} \tag{3.42}$$

The principal eigenvalue, σ_1, is the most important for the accuracy of the solution. Again, the first three terms indicate that the solution is second-order accurate in time. The other two eigenvalues, known as spurious roots, are not important for accuracy but may influence the stability of the solution. The linear stability criterion requires that the amplification factor for each time-step, $|\sigma|$, be less than or equal to unity, i.e.,

$$|\sigma(\lambda = i\omega h)| \leq 1 \tag{3.43}$$

where ω represents the frequency of the spatial solution modes. This implies that the eigenvalues for $\lambda = i\omega h$ must lie within the unit circle in the complex σ-plane.

Figure 3.16 shows the eigenvalues for the two time-marching algorithms. The exact solution of the representative equation (Eq. 3.32) is given by the unit-circle in the complex σ-plane corresponding to $e^{i\omega h}$. Notice that the eigenvalue for the PCC algorithm always has a magnitude of unity, i.e., the algorithm introduces no damping into the solution. However, the principal eigenvalue for PC2B algorithm shows that this solution contains damping that increases with the spatial frequency, ω.

To bring out the relative merits of the proposed algorithms, the principal eigenvalues for the PCC and PC2B algorithms are shown in Fig. 3.17 along with two other time-marching algorithms. The forward Euler algorithm is a one-step explicit method. The Adams-Moulton 4th-order (AM4) algorithm is also a two-step pseudo-implicit predictor-corrector method (see, e.g., Ref. 81), like the PCC and PC2B algorithms. Recall that the stability criterion requires that the eigenvalues lie within the unit circle on the complex σ-plane. The explicit Euler method is clearly unstable because the eigenvalue always lies outside the unit circle. The AM4 algorithm is relatively more stable with the eigenvalue closely following the unit circle for small values of ωh. The PCC algorithm is stable but with no damping, as mentioned previously, whereas the PC2B algorithm is stable with positive damping. It should be noted that the AM4

(a) PCC algorithm using the five-point central difference scheme

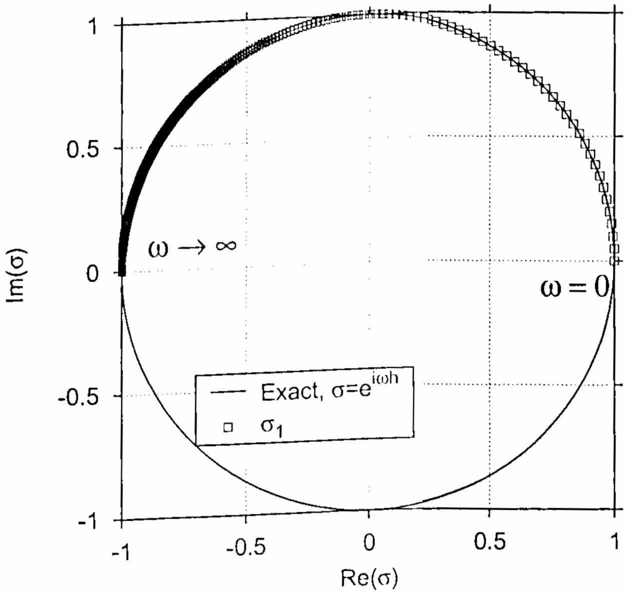

(b) PC2B algorithm using the 2nd-order backward difference scheme

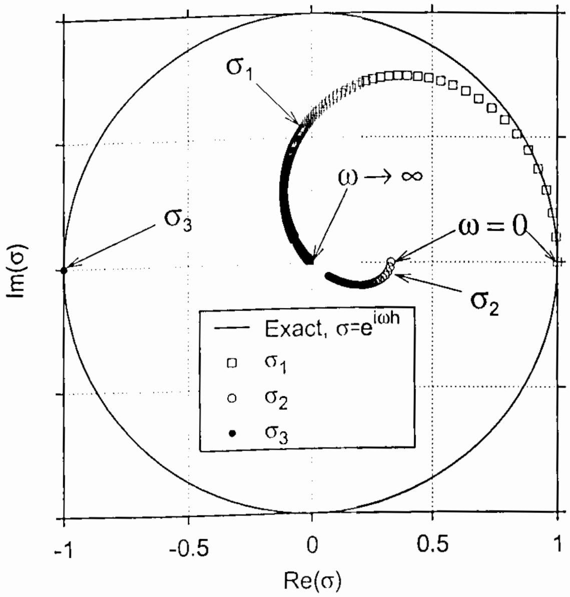

Figure 3.16: Eigenvalues of the time-marching algorithms: (a) PCC algorithm using the five-point central difference scheme, (b) PC2B algorithm using the 2nd-order backward difference scheme.

algorithm is formally 4^{th}-order accurate, and for small ωh it is only mildly unstable. However, for practical rotor applications with typical time-steps of 5° to 15°, this algorithm may not be suitable because it is unstable for larger values of ωh.

3.3.2 Non-Linear Considerations

The stability analysis of the time-marching algorithms as described in the preceding section is strictly applicable only to linear differential equations. The induced velocity source term on the RHS of the wake governing equation (Eq. 3.2) makes the equations highly nonlinear. Linear stability requires that the numerical errors are not unbounded, i.e., the solution does not "blow off" with increasing time. For linear equations, this is synonymous to the method being convergent, given that the discretized equations are consistent with the original governing equations (e.g., Ref. 84). For nonlinear equations the solution may exhibit spurious oscillations, which may be bounded. This implies that the solution is stable in a linear sense, however, it may not be convergent because the oscillations, although bounded for a given discretization, are dependent on the grid discretization. Therefore, to ensure the stability of nonlinear equations, a broader definition of stability must be considered. Following the philosophy of traditional CFD analyses, a given numerical algorithm may be considered to be unstable if the numerical errors, created through interactions of various space and time approximations, start out small and grow with time (e.g., Ref. 83). A stable algorithm ensures that these numerical errors remain small. It follows that a numerical algorithm, which is stable in this sense, will also result in a convergent solution with increasing grid refinement.

To better understand this concept of stability, free-vortex wake solutions using the two algorithms are shown in Fig. 3.18. Results are shown for a two-bladed rectangular

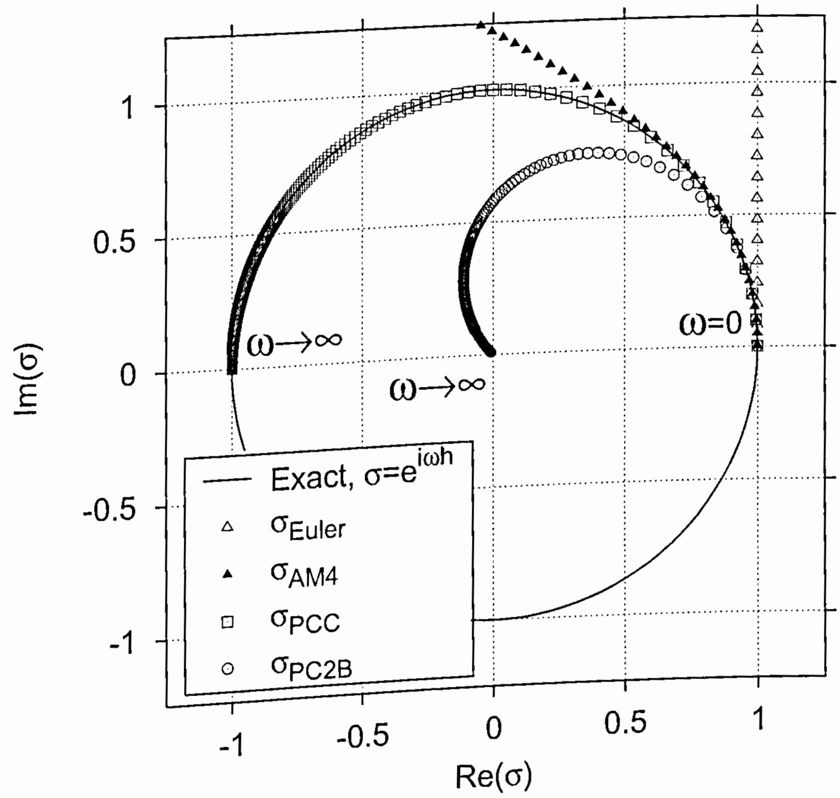

Figure 3.17: Principal eigenvalues for four time-marching algorithms.

untwisted rotor with a radius of 406.4 mm and a chord of 42.5 mm. The collective pitch was set at 5° to obtain a thrust of $C_T = 0.005$ at 35.5 Hz. This rotor geometry and operating conditions correspond to those reported in Ref. 66. The initial condition for both time-integration algorithms was obtained using a steady-state free-vortex wake model based on relaxation (i.e., with the enforcement of periodicity). The solutions are shown in Fig. 3.18 after fifteen rotor revolutions, i.e., at time $t = 15 \times 2\pi/\Omega$, along with the initial wake geometry. The PCC solution, as shown in Fig. 3.18(a), indicates the presence of numerical errors in the form of sinusoidal disturbances. The initial condition did not contain such disturbances and, therefore, these disturbances are numerical in origin and have accumulated over time. The PC2B solution, however, shows no such disturbance growth – see Fig. 3.18(b). This confirms that the spurious oscillations seen in the PCC solution are a result of the accumulation of numerical errors because of the discrete approximations to the temporal and spatial derivatives in the governing equations. Therefore, the PCC algorithm is unstable, while the PC2B algorithm is stable for the nonlinear rotor wake problem.

The two results are shown in a different form in Fig. 3.19 in terms of axial and radial tip vortex displacements as a function of reference blade (blade 1) azimuthal location. The measured vortex trajectories from the experiment, as reported in Ref. 66, are also plotted for comparison. In this experiment, evidence of vortex pairing was found between adjacent tip vortex filaments that were about two rotor revolutions old ($\zeta \approx 720^\circ$) downstream of the rotor. Notice that the early wake displacements are predicted very well by both algorithms. The PC2B solution does not show the experimentally observed pairing between the adjacent vortex filaments. It is significant to note that the PCC algorithm, which is unstable, paradoxically shows a good overall agreement with experimental results. Yet, the numerical "disturbance" observed when using the PCC solution correlates very well with the observed vortex pairing phenomenon.

To further elucidate the grid-dependent nature of these sinusoidal disturbances, Fig. 3.20 shows the wake geometry using the PCC algorithm for different grid discretization levels with $\Delta\psi = \Delta\zeta$. The solution does not show a converging trend with increasing grid refinement, i.e., the PCC solution is grid-dependent. This suggests that these disturbances are some form of numerical instability, even though they are bounded and stable in the linear sense. Also, these numerical errors appear and grow solely because of interactions between the space-time finite difference approximations

(a) PCC algorithm

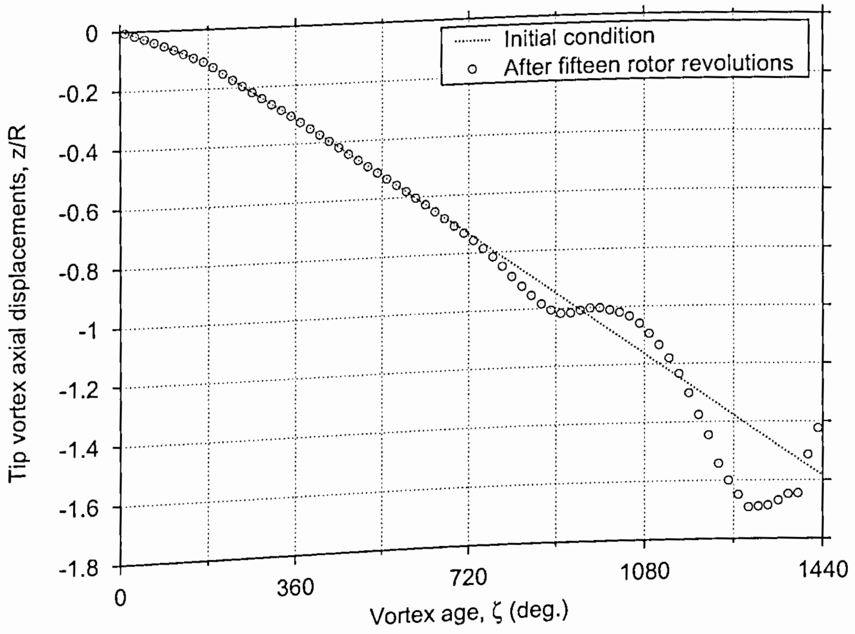

(b) PC2B algorithm

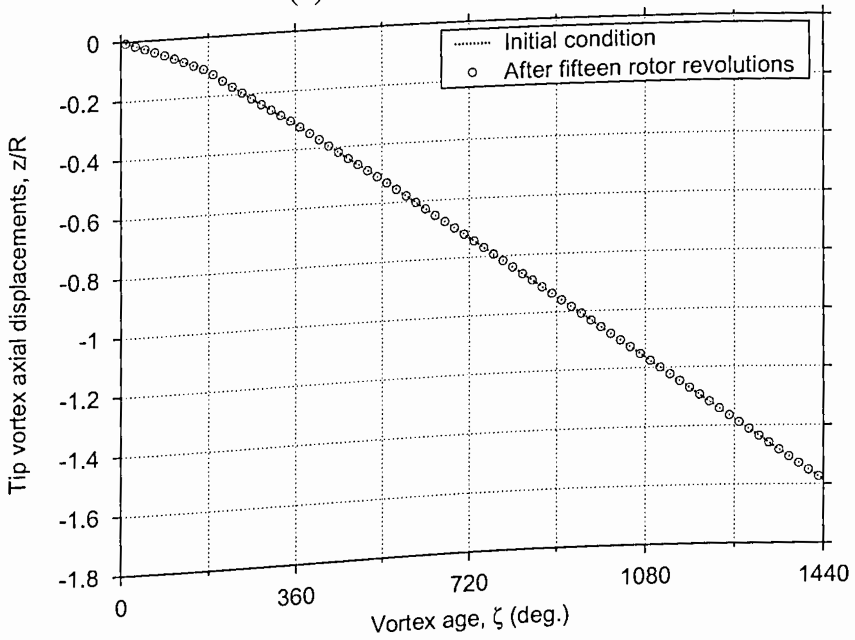

Figure 3.18: Sample results for free-vortex wake calculations using (a) PCC algorithm, and (b) PC2B algorithm, for a two-bladed hovering rotor, showing axial displacements of the tip vortex relative to the reference blade (blade 1), $C_T = 0.005$, $\Delta\psi = \Delta\zeta = 10°$.

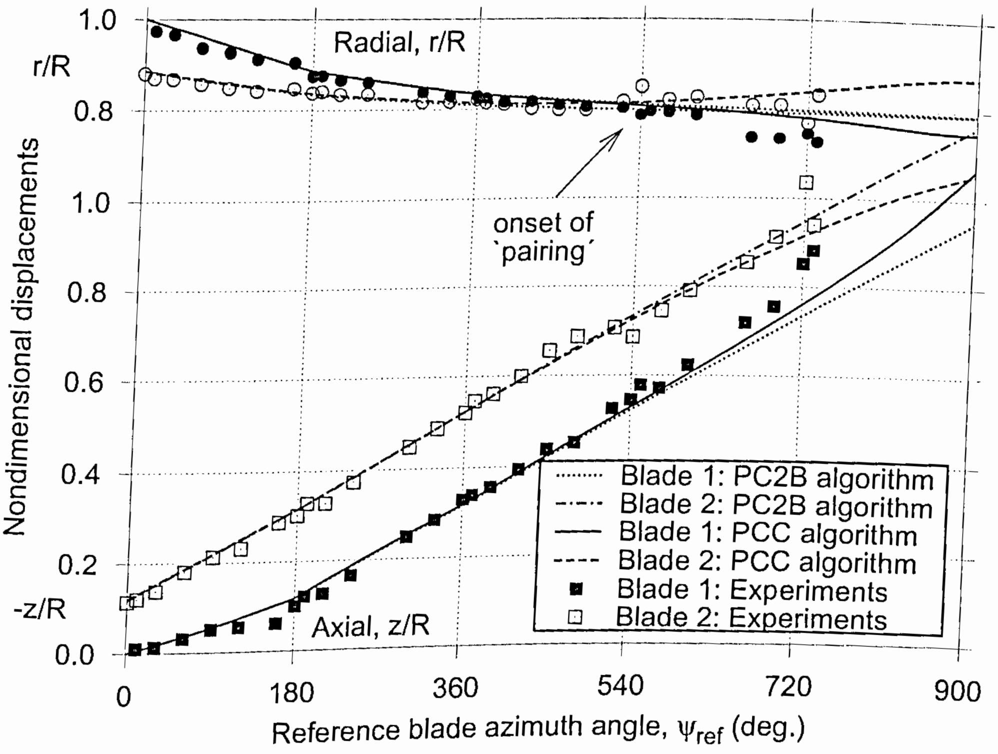

Figure 3.19: Comparison of relaxation and time-marching numerical predictions along with experimental results from Ref. 66, for a two-bladed rotor of operating in hover at $C_T = 0.005$. Free-vortex wake solutions using $\Delta\psi = \Delta\zeta = 10°$.

and are not physical. Therefore, it must be fortuitous that the numerical results, as plotted in Fig. 3.19, show good correlation with experiments for a particular discretization.

The PC2B algorithm gives a converging trend with increasing grid resolution, as shown in Fig. 3.21. Notice that for $\Delta\psi = \Delta\zeta \geq 10°$ the solution shows significant differences. Recall that a discretization of $\Delta\theta = 10°$ showed an almost 10% error in the induced velocity for the vortex ring problem – see Fig. 3.6. Therefore, it is expected that the wake solution will also show some grid sensitivity for discretizations of $\Delta\psi = \Delta\zeta \geq 10°$. Notice that the solutions corresponding to $\Delta\psi = \Delta\zeta = 5°$ and $\Delta\psi =$

$\Delta\zeta = 2.5°$ are almost identical, indicating grid-independence of the wake solution in this case. This convergent nature of the solution obtained using the PC2B algorithm also suggests that the algorithm is stable in a linear as well as a nonlinear sense.

One possible reason for apparent agreement between the PCC solution and the experimental observations is that the rotor wake geometry is physically unstable. It has been shown in Chapter 2 that the hovering rotor wake is inherently unstable and that vortex pairing between adjacent turns of the rotor wake is the most unstable deformation mode of the rotor wake. Therefore, the experimental results may contain growing unstable modes initiated by various disturbances arising from artifacts of the experimental setup. As mentioned previously, these unstable deformation modes may be initiated in numerical results because of numerical errors alone. This can lead to *pseudo*-agreement between experiments and numerical results, even though no disturbances are being explicitly modeled. This is a classical paradox for solution of nonlinear equations because numerical errors often tend to mimic physical behavior. It is well known that numerical dissipation mimics physical dissipation, and numerical instabilities mimic physical instabilities (Ref. 83). Therefore, a reliable and well-documented reference standard is necessary to distinguish between numerical and physical behavior. One may rely on experimental results, however, experimental results sometimes contain artifacts of the specific testing conditions, such as turbulence and disturbances to the flow from test probes, supports, wall effects, and so forth. Such artifacts may be difficult to identify, and correlation studies may indicate errors in numerical methods where none exist.

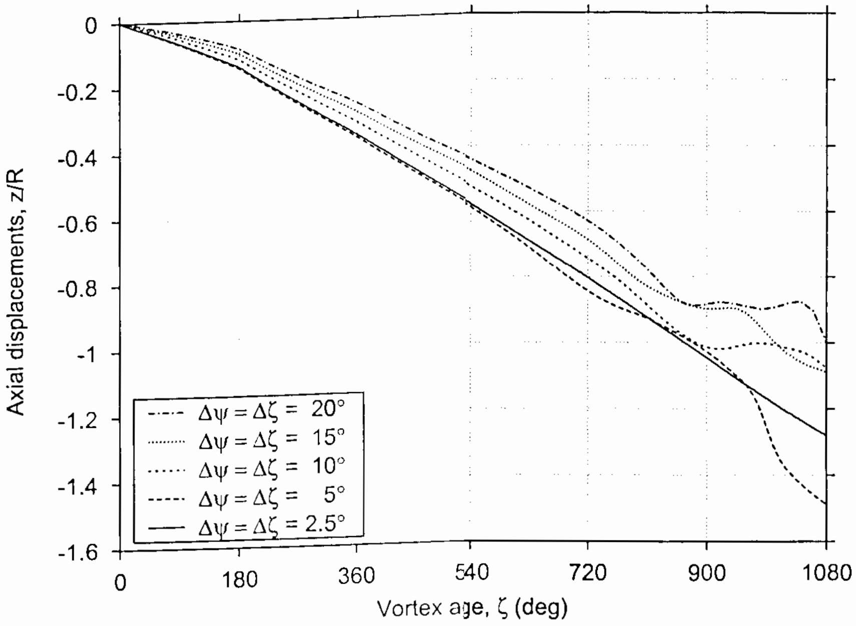

(a) Axial displacements

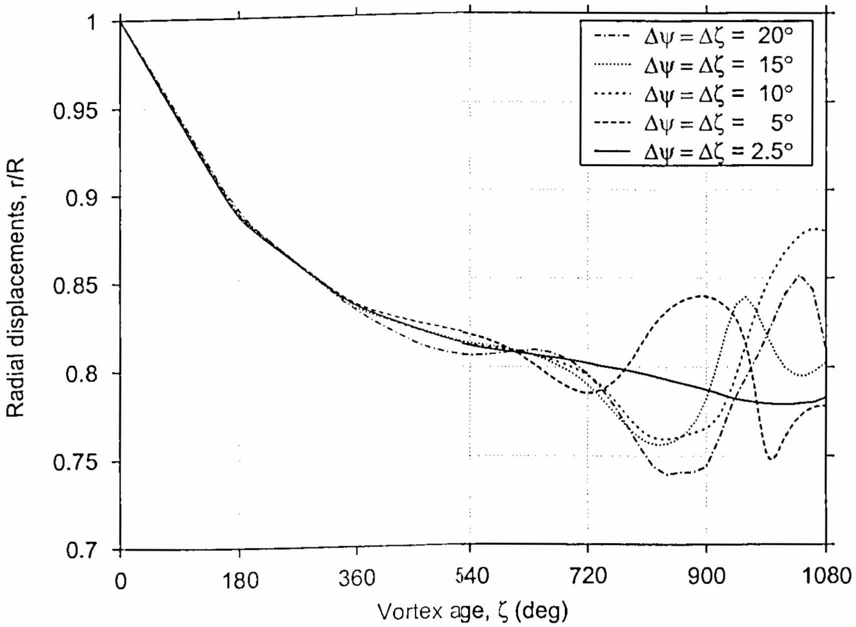

(b) Radial displacements

Figure 3.20: Grid dependent nature of the time-marching numerical solution using PCC algorithm for different discretizations: (a) Axial displacements, and (b) Radial displacements, as a function of vortex age.

(a) Axial displacements

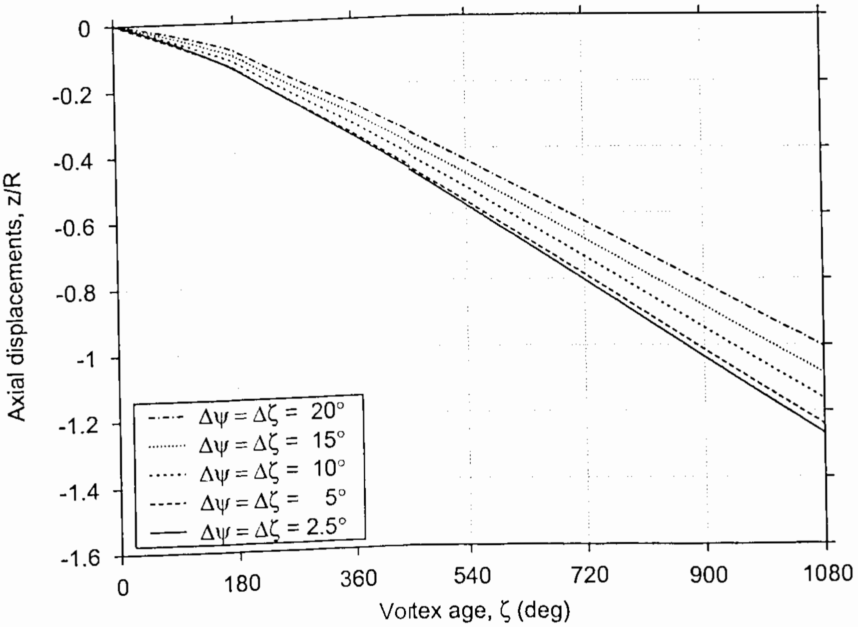

(b) Radial displacements

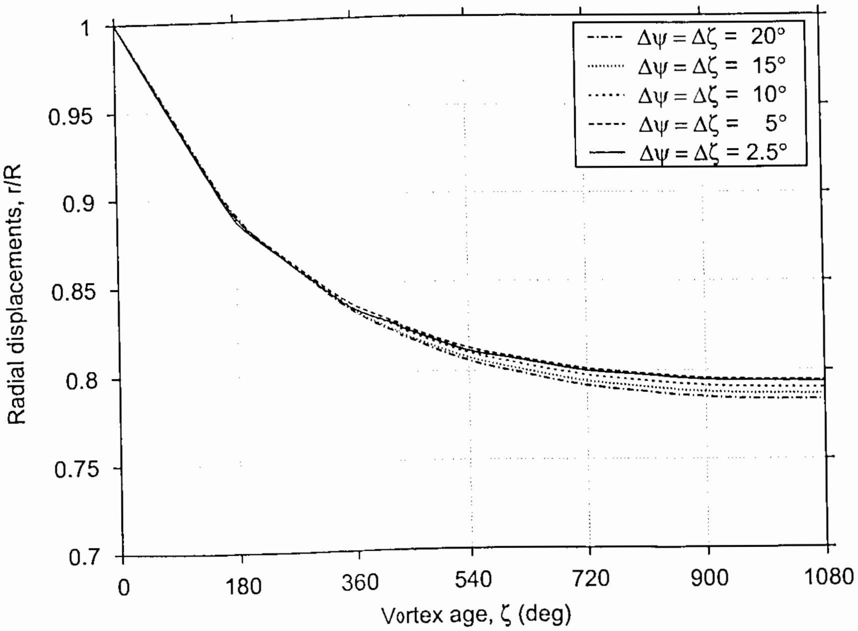

Figure 3.21: Numerical solution using time-marching PC2B algorithm for different discretization levels showing grid independence for finer resolution: (a) Axial displacements, and (b) Radial displacements, as a function of vortex age.

3.3.3 Modified Equations

To ensure that the numerical algorithm is stable, it is necessary to properly understand the various numerical errors associated with discretization. To this end, modified equations for the two algorithms are now examined. The modified equations are the equations resulting from discrete approximations of all terms in the original governing governing equations. It should be noted that any finite-difference method *approximately* solves the governing equations, while it *exactly* solves the complete modified equations. Therefore, the modified equations provide key insights into the behavior of the numerical solution by examining the equations governing this numerical solution rather than the equations governing the wake.

The wake governing equation (Eq. 3.2) can be rewritten using a compact notation for derivatives as

$$r_\psi + r_\zeta = V(r) \tag{3.44}$$

Note that the Ω appearing in the denominator on the RHS of Eq. 3.44 is dropped for simplicity, and the vectors are not explicitly denoted with an arrow. The modified equations are written in a form with all extra terms, i.e., terms other than those in the original governing PDE (Eq. 3.44) are moved to the RHS, and are written in terms of the spatial derivatives of the solution, r. The following analysis of modified equations assumes equal discretization ($\Delta\psi = \Delta\zeta$) for simplicity. Only terms up to $O(\Delta\zeta^2)$ are shown, so that the numerical solution may be considered to be an higher order approximation to the solution of the modified equation.

Truncation Errors in Numerical Integration

The truncation error terms arising because of the finite difference approximations to the derivatives have been reviewed in Section 3.2.2. Also, the discrete induced velocity calculation was shown to be second-order accurate in Section 3.2.1. These second-order errors in the induced velocity calculations can be expressed in the form of a Taylor-series. The numerical integration approach with straight-line vortex segments is equivalent to the trapezoidal integration rule. Therefore, the errors in the induced velocity calculations would have the same fom as that of a trapezoidal quadrature. A Taylor expansion of this integration rule is now examined. Let $F(x)$ denote the exact integral of $f(x)$, i.e.,

$$F(x) = \int f(x)dx \tag{3.45}$$

The exact integral evaluated over the grid cell $[x_i, x_{i+1}]$ is given by

$$\int_{x_i}^{x_{i+1}} f(x)dx = F(x_{i+1}) - F(x_i) \tag{3.46}$$

Using the trapezoidal rule, this integral is approximated as

$$\int_{x_i}^{x_{i+1}} f(x)dx \approx (x_{i+1} - x_i)\left[\frac{f(x_i) + f(x_{i+1})}{2}\right] \tag{3.47}$$

To examine the errors introduced in this approximation, the numerical solution is expanded as a Taylor-series around the mid-point, $x_{i+\frac{1}{2}}$. It can then be shown that

$$\underbrace{(x_{i+1} - x_i)\left[\frac{f(x_i) + f(x_{i+1})}{2}\right]}_{\text{numerical integral}} = \underbrace{F(x_{i+1}) - F(x_i)}_{\text{exact integral}} + \underbrace{(x_{i+1} - x_i)\left[\frac{h^2}{12}f'' + \frac{h^4}{480}f^{(4)} + \cdots\right]}_{\text{truncation errors}} \tag{3.48}$$

where $h = (x_{i+1} - x_i)$ is the grid discretization. The most dominant error term is $E(h) \propto h^2 f''$ and, therefore, for smooth functions the error would decrease quadratically with grid size. The Biot-Savart integral is evaluated by integrating the induced velocity $\vec{V}$ over the length of each vortex filament, i.e., along the vortex age, ζ. Therefore, the most dominant truncation error term is given by

$$\vec{V}_{\text{discrete}} = \vec{V}_{\text{exact}} + \frac{1}{12}\frac{d^2\vec{V}}{d\zeta^2}\Delta\zeta^2 + \cdots \text{ higher order terms} \tag{3.49}$$

Velocity Averaging Errors

The induced velocity at the mid-point is evaluated by averaging the velocities at the four neighboring collocation points. This averaging is also second-order accurate, and results in additional truncation error terms. Note that although such an averaging scheme introduces additional error terms, it was shown to be beneficial for convergence to a steady-state solution (Refs. 53, 56). A Taylor-series analysis shows that

$$\begin{aligned}\vec{V}\left(\psi+\frac{\Delta\psi}{2},\zeta+\frac{\Delta\zeta}{2}\right) = {} & \frac{\vec{V}(\psi+\Delta\psi,\zeta)+\vec{V}(\psi+\Delta\psi,\zeta-\Delta\zeta)+\vec{V}(\psi+\Delta\psi,\zeta)+\vec{V}(\psi,\zeta-\Delta\zeta)}{4} \\ & -\frac{1}{8}\frac{\partial^2\vec{V}}{\partial\psi^2}\Delta\psi^2-\frac{1}{8}\frac{\partial^2\vec{V}}{\partial\zeta^2}\Delta\zeta^2 \qquad (3.50) \\ & -\frac{1}{384}\frac{\partial^4\vec{V}}{\partial\psi^4}\Delta\psi^4-\frac{1}{64}\frac{\partial^4\vec{V}}{\partial\psi^2\partial\zeta^2}\Delta\psi^2\Delta\zeta^2-\frac{1}{384}\frac{\partial^4\vec{V}}{\partial\zeta^4}\Delta\zeta^4-\cdots\end{aligned}$$

Therefore, the discretized RHS velocity source term in Eq. 3.2 can be expressed as

$$\vec{V}_{\text{discrete,averaged}} = \vec{V}_{\text{exact}} + \frac{5}{24}\Delta\zeta^2\frac{\partial^2 V}{\partial\zeta^2} + \frac{1}{8}\Delta\zeta^2\frac{\partial^2 V}{\partial\psi^2} + O\left(\Delta\zeta^4\right) \qquad (3.51)$$

Modified Equation for the PCC Algorithm

The five-point central difference approximations used in the PCC algorithm resulted in additional truncation terms as given by Eq. 3.25. Therefore, the modified equation for the PCC algorithm can be written up to $O\left(\Delta\zeta^4\right)$ as

$$\begin{aligned}\frac{\partial r}{\partial\psi}+\frac{\partial r}{\partial\zeta} &= V+\Delta\zeta^2\left[\left(\frac{5}{24}V_{\zeta\zeta}+\frac{1}{8}V_{\psi\psi}\right)-\left(\frac{1}{24}r_{3\psi}+\frac{1}{8}r_{\psi\psi\zeta}+\frac{1}{8}r_{\psi\zeta\zeta}+\frac{1}{24}r_{3\zeta}\right)\right] \\ &\quad +O\left(\Delta\zeta^4\right) \\ &= V+\Delta\zeta^2\left[\left(\frac{5}{24}V_{\zeta\zeta}+\frac{1}{8}V_{\psi\psi}\right)-\frac{1}{24}\left(V_{\psi\psi}+2V_{\psi\zeta}+V_{\zeta\zeta}\right)\right]+O\left(\Delta\zeta^4\right) \qquad (3.52)\end{aligned}$$

Using the governing equation in Eq. 3.44, the extra terms on the RHS of the above equation can be written in terms of spatial derivatives of the solution. By repeatedly differentiating Eq. 3.44 it can be shown that

$$\left.\begin{aligned}
r_{\psi\psi} &= r_{\zeta\zeta} - 2V_r r_\zeta + V_r V \\
r_{\psi\zeta} &= -r_{\zeta\zeta} + V_r r_\zeta \\
V_\zeta &= V_r r_\zeta \\
V_\psi &= -V_r r_\zeta + V_r V \\
V_{\zeta\zeta} &= V_{rr} r_\zeta^2 + V_r r_{\zeta\zeta} \\
V_{\zeta\psi} &= -V_{rr} r_\zeta^2 + V_{rr} V r_\zeta - V_r r_{\zeta\zeta} + V_r^2 r_\zeta \\
V_{\psi\psi} &= V_{rr} r_\zeta^2 - 2V_{rr} V r_\zeta + V_{rr} V^2 + V_r r_{\zeta\zeta} - 2V_r^2 r_\zeta + V_r^2 V
\end{aligned}\right\} \tag{3.53}$$

Using the above relations, the modified equation for the PCC algorithm can be reduced to a relatively simpler form as

$$\begin{aligned}
\frac{\partial r}{\partial \psi} + \frac{\partial r}{\partial \zeta} &= V + \frac{\Delta\zeta^2}{12}\left[4V_{rr} r_\zeta^2 + 4V_r r_{\zeta\zeta} - 3\left(V_{rr}V + V_r^2\right) r_\zeta - \left(V_{rr}V + V_r^2\right) V\right] + O\left(\Delta\zeta^4\right) \\
&= V + \frac{\Delta\zeta^2}{12}\left[4\left(V_r r_\zeta\right)_\zeta - 3\left(V_{rr}V + V_r^2\right) r_\zeta - \left(V_{rr}V + V_r^2\right) V\right] + O\left(\Delta\zeta^4\right)
\end{aligned} \tag{3.54}$$

The extra terms in the modified equation are all $O(\Delta\zeta^2)$, which confirms that the algorithm is second-order accurate. The modified equation is consistent with the original governing differential equation (Eq. 3.44). As the discretization approaches zero, i.e., $\Delta\zeta \longrightarrow 0$, the original governing PDE is recovered without any additional terms.

Nonlinear Dissipation Term

The first of the extra terms on the RHS of the modified equation for the PCC algorithm given in Eq. 3.54 is a nonlinear implicit numerical dissipation term, which is dependent on the induced velocity field gradient V_r. Physical considerations require that this dissipative term must always be positive. A negative dissipation would imply an unbounded, exponential growth, which is not physical. If this term is negative, the numerical solution will be unstable because the modified equation itself is unstable.

Therefore, this term plays an important role in determining the stability of the numerical solution. The second extra term is a dispersive term, which may lead to phase errors in solution propagation along the characteristics and, therefore, can cause spurious oscillations. This in itself may lead to a form of instability in the sense that numerical errors may accumulate and grow over time. The implicit numerical dissipation may help to contain the accumulation of such phase errors, but only if the induced velocity gradient V_r is positive. The last of the extra terms in Eq. 3.54 is a source term error, which has no direct impact on the stability of the wake solution.

To better understand the stability of the numerical algorithm, it is necessary to investigate the behavior of the implicit artificial dissipation term in the modified equation. The induced velocity gradient, V_r, is, in general, dependent on the rotor configuration, i.e., number of blades, etc., as well as on operating (flight) conditions. To examine representative results for the induced velocity field, the velocity gradients were evaluated using two commonly used prescribed wake models. One advantage of using a prescribed wake model is that it allows calculations of the velocity gradients to be performed analytically rather than numerically and, therefore, this approach was preferred for the present type of analysis.

The tip vortex geometry for a hovering rotor, as given by the Landgrebe's wake model (Ref. 13), can be written in the form

$$\frac{r}{R} = A+(1-A)e^{\bar{\lambda}\zeta} \tag{3.55}$$

$$\frac{z}{R} = \begin{cases} k_1\zeta & 0 \le \zeta \le \frac{2\pi}{N_b} \\ k_1\frac{2\pi}{N_b} + k_2\left(\zeta - \frac{2\pi}{N_b}\right) & \zeta > \frac{2\pi}{N_b} \end{cases} \tag{3.56}$$

where (r,z) are cylindrical polar coordinates with origin at the center of the rotor disk. The axial settling rates, k_1 and k_2, and the radial contraction parameter, $\bar{\lambda}$, are empirically related to the operating conditions and rotor geometry. The asymptotic radial contraction ratio has been experimentally observed to be $A = 0.78$. Landgrebe's wake geometry model consists of contracting non-regular helical tip vortex filaments. The velocity gradients based on this model are shown in Fig. 3.22. Note that the radial contraction results in a negative velocity gradient given by

$$\frac{dV_{\text{radial}}}{dr} = \overline{\lambda} \tag{3.57}$$

This term is destabilizing in nature on the numerical solution because of the anti-dissipative effect of the truncation terms. Notice that the axial settling rate, or the pitch of the helix, changes at the first blade passage, ($\zeta = 2\pi/N_b$), where the discontinuity in axial velocity will result in large gradients and a singularity. This discontinuity was modeled with a exponential distribution with a small non-zero standard deviation as shown in Fig. 3.22(b). Note that the discontinuity in axial velocity has a stabilizing effect because $\partial V_z/\partial z$ is always positive with a peak near the first blade passage.

To describe the wake geometry in forward flight, Beddoes's prescribed wake model (Ref. 19) was used. In this model, the parametric equations defining the wake geometry are given by

$$x = \cos(\psi_b - \zeta) + \mu\zeta \tag{3.58}$$

$$y = \sin(\psi_b - \zeta) \tag{3.59}$$

$$z = \begin{cases} -\lambda\left[1 + \tfrac{1}{2}\chi\left(\cos(\psi_b - \zeta) + \tfrac{\mu\zeta}{2}\right) - \tfrac{\chi}{2}\left(|\sin(\psi_b - \zeta)|\right)^3\right]\zeta, & x < -\cos(\psi_b - \zeta) \\ -2\lambda\left(1 - \tfrac{\chi}{2}\left(|\sin(\psi_b - \zeta)|\right)^3\right)\zeta, & \cos(\psi_b - \zeta) > 0 \\ -\dfrac{2}{\mu}\lambda x\left(1 - \dfrac{\chi}{2}\left(|\sin(\psi_b - \zeta)|\right)^3\right), & x > -\cos(\psi_b - \zeta) > 0 \end{cases} \tag{3.60}$$

(a) Radial velocity gradient

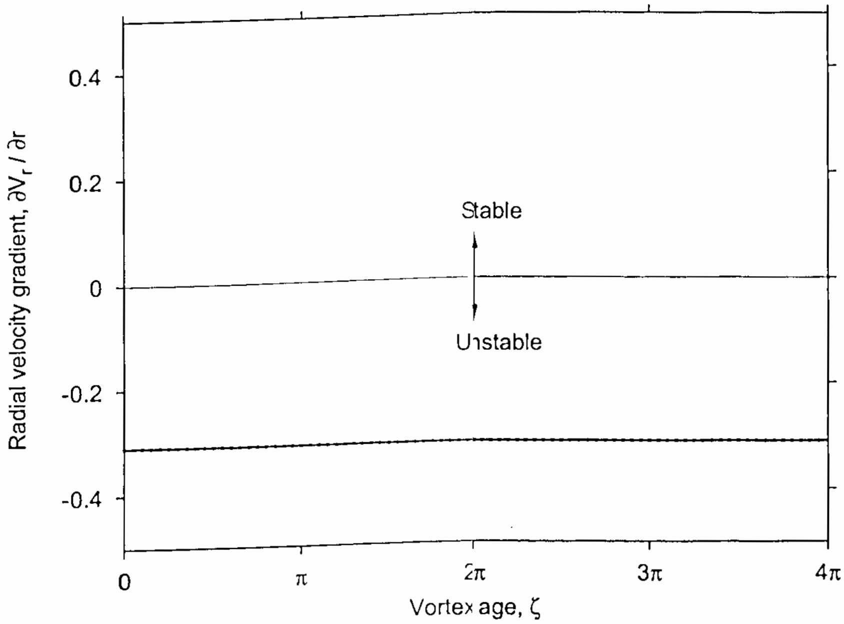

(b) Axial velocity gradient

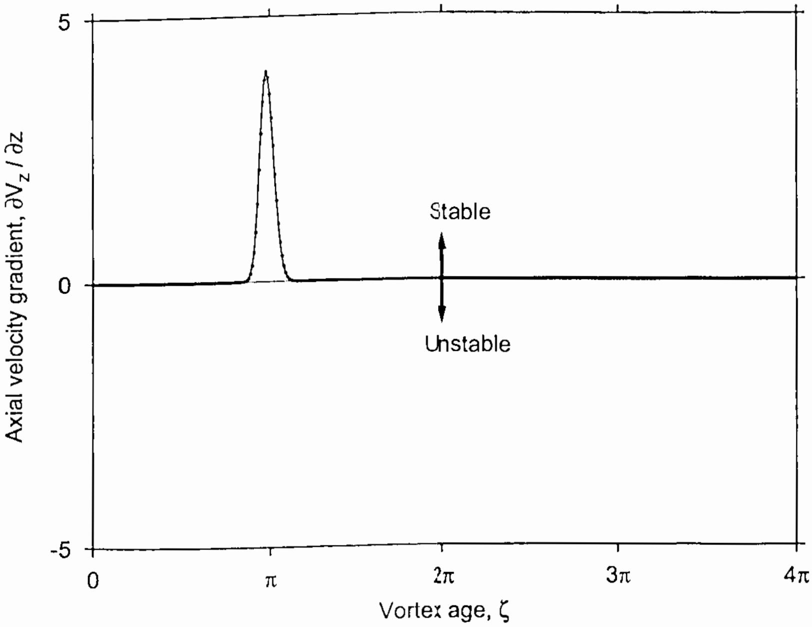

Figure 3.22: Velocity gradients in hover based on Landgrebe's model. (a) Radial velocity gradient, (b) Axial velocity gradient, as a function of vortex age. $C_T = 0.006$, $N_b = 2$.

where ψ_b is the blade azimuthal location and $\chi = \tan^{-1}(\mu/\lambda)$ the wake skew angle. An example of the wake geometry produced by a four-bladed rotor in forward flight at $\mu = 0.1$ is shown in Fig. 3.23. The wake geometry is basically a skewed rigid helix with skew angle χ, with some additional corrections to account for distortions because of the self and mutually induced velocities. The radial displacements are epicycloidal and there is no radial contraction. Therefore, the radial velocity gradient is zero and must have no influence on the stability of the numerical solution. The axial displacements, however, are somewhat more complicated with discontinuities corresponding to strong velocity gradients induced by blades and other vortices.

The axial velocity gradient, $\partial V_z/\partial z$, which is shown in Fig. 3.24, shows large positive and negative gradients because of wake distortions. The non-physical discontinuities in the velocity gradient correspond to the transition between the three regions, as given by Eq. 3.60. Notice that in many regions of the wake the velocity gradient is negative. Therefore, the artificial dissipation term in Eq. 3.54 is negative, i.e., destabilizing. The consequence of this negative dissipation is the presence of numerical instabilities in the solution where the physical wake is in equilibrium. It should be recalled that the physical wake instabilities are an artifact of the hovering flight condition. With increasing forward or axial speeds, the physical wake becomes increasingly stable. However, because of the anti-dissipative effects of the velocity gradients, the numerical wake solution may become unstable. In general, the nature of the induced velocity field is such that the numerical algorithm may be prone to instabilities (in hover as well as forward flight) because of negative implicit numerical dissipation.

The modified equations show that, in general, the PCC algorithm is unstable, and may lead to instabilities in the numerical solutions. It is, therefore, desirable that a

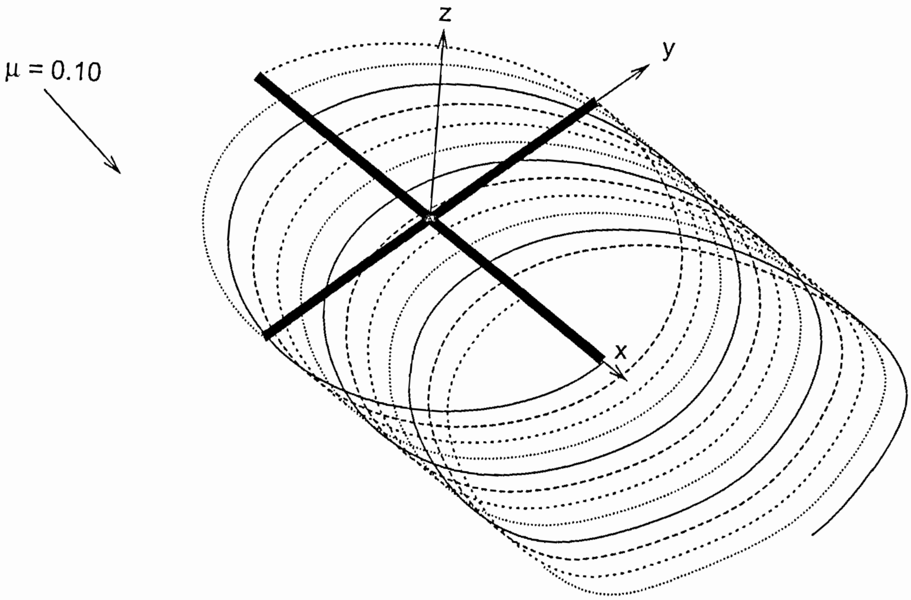

Figure 3.23: Wake geometry for a four-bladed rotor in forward flight based on Beddoes's model, $\mu = 0.1$, $C_T = 0.008$.

time-marching algorithm contain some implicit numerical dissipation that is independent of the velocity field to compensate for the possibly destabilizing effect of the velocity gradients.

Modified Equation for the PC2B Algorithm

The PC2B algorithm has been developed specifically to provide some implicit dissipation, as seen from the linearized stability considerations. The modified equation helps in identifying these dissipative terms and, more importantly, can be used to verify that such dissipative terms are independent of the nonlinear velocity field. The extra terms because of the RHS induced velocity source terms are the same as for the

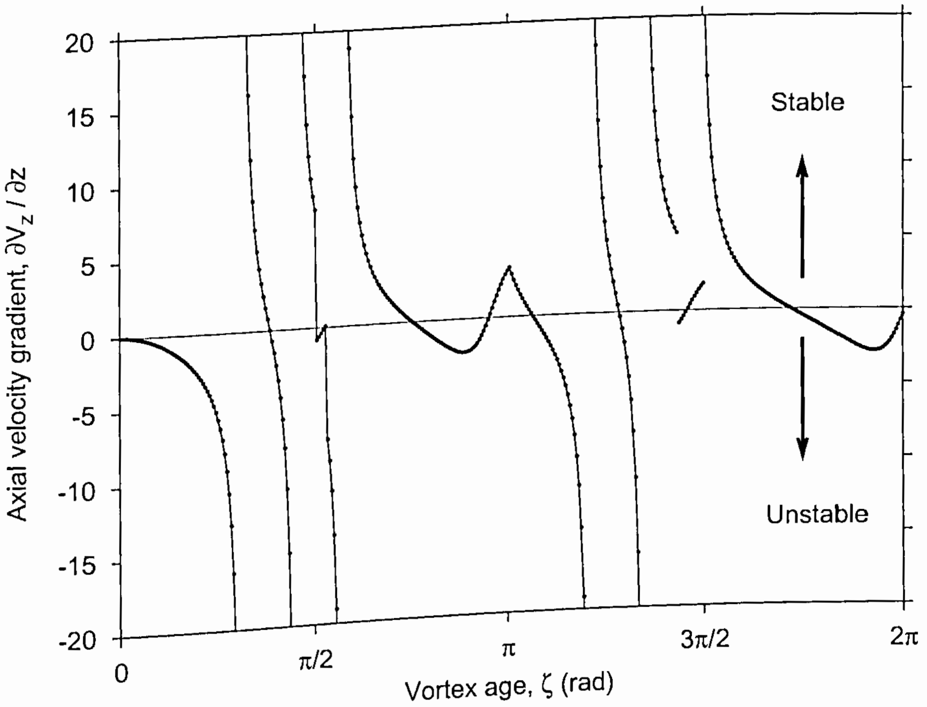

Figure 3.24: Axial velocity gradients in forward flight as a function of vortex age based on Beddoes's wake model, $\mu = 0.1$, $C_T = 0.008$.

PCC scheme. The use of 2^{nd}-order backward difference in time results in additional terms from the LHS. Therefore, the modified equation, up to $O\left(\Delta\zeta^4\right)$ can be written as

$$\frac{\partial r}{\partial \psi} + \frac{\partial r}{\partial \zeta} = V + \Delta\zeta^2 \left[\left(\frac{5}{24} V_{\zeta\zeta} + \frac{1}{8} V_{\psi\psi} \right) - \left(\frac{1}{24} r_{3\psi} + \frac{1}{8} r_{\psi\psi\zeta} + \frac{1}{8} r_{\psi\zeta\zeta} + \frac{1}{24} r_{3\zeta} \right) + \frac{1}{4} r_{3\psi} - \frac{1}{4} r_{4\psi} \Delta\zeta \right] + O\left(\Delta\zeta^4\right) \tag{3.61}$$

That is,

$$\frac{\partial r}{\partial \psi} + \frac{\partial r}{\partial \zeta} = V + \Delta\zeta^2 \left[\begin{array}{l} \text{nonlinear dissipative} \\ \text{and dispersive terms} \end{array} - \frac{\Delta\zeta}{4} r_{4\zeta} \right] + O\left(\Delta\zeta^4\right) \tag{3.62}$$

The $-r_{4\zeta}$ term is a dissipative term, and is independent of the nonlinear velocity field.

This dissipative term is stabilizing and can potentially alleviate the destabilizing effects of other nonlinear anti-dissipative terms. Furthermore, this term is $O(\Delta\zeta^3)$ and so the overall solution is still second-order accurate. This implicit artificial dissipation makes the modified equation for the PC2B algorithm stable and, as a result, the numerical solution is free from spurious oscillations. Note that because the modified equation for the PC2B algorithm is both stable and consistent, the PC2B wake solution is expected to be convergent with grid refinement.

An example of the importance of such an implicit numerical dissipation term for the numerical solution is clear from Fig. 3.25. In this case, numerical solutions for the rotor wake geometry were calculated in forward flight at $\mu = 0.05$ using two numerical algorithms: explicit forward Euler and the pseudo-implicit PC2B algorithm. The calculations were performed using a fairly typical wake discretization of $\Delta\psi = \Delta\zeta = 15°$ and the geometry is shown after forty iterations. The solution obtained using the forward Euler explicit method, as shown by dashed lines, shows the presence of numerical instabilities in the form of sinusoidal disturbances along the length of the vortex filament. Although qualitatively similar disturbances are observed in rotor wake experiments, in this case these disturbances are purely numerical in origin and are non-physical. The solution obtained using the two-step PC2B algorithm, however, shows a relatively smooth wake structure free from such sinusoidal disturbances. The reason for this lies in the fact that the implicit artificial dissipation present in the PC2B algorithm (see Eq. 3.62) damps out the numerical disturbances, which are typically generated by non-exact floating-point calculations in the form of round-off errors. This is also evident from a linearized stability analysis, which showed that the forward Euler algorithm is unstable, as indicated by the principal eigenvalue in Fig. 3.17.

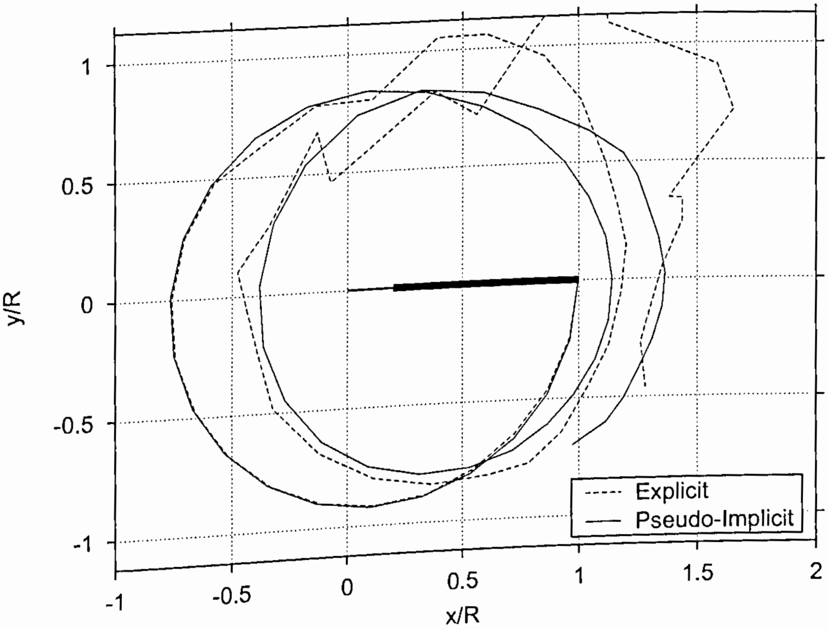
(a) Top view

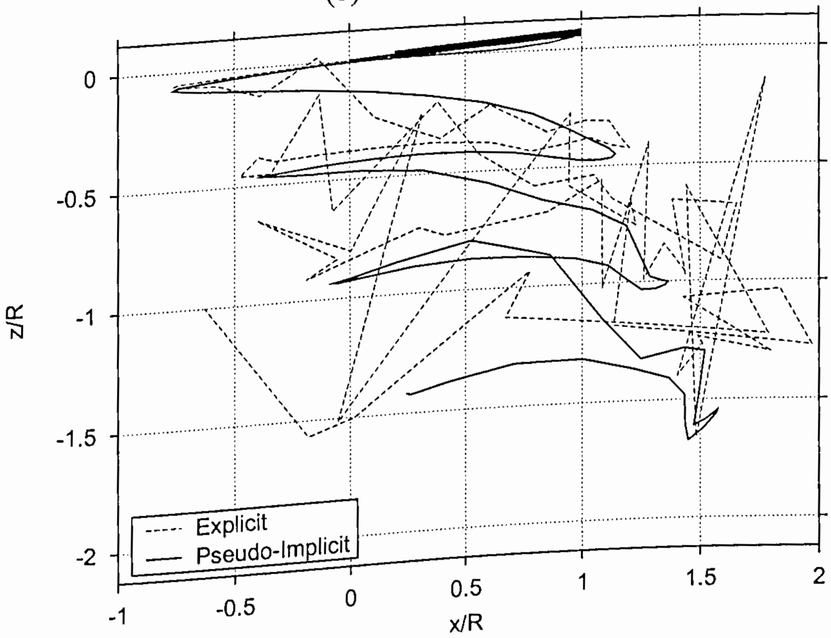
(b) Side view

Figure 3.25: Time-marching free-wake geometry for a four-bladed rotor in forward flight at $\mu = 0.05$ using the Euler explicit and the PC2B pseudo-implicit algorithms with $\Delta\psi = \Delta\zeta = 15°$. Only the tip vortex from reference blade (blade 1) is shown. (a) Top view, (b) Side view.

3.4 Verification of Solution Convergence

A numerical experiment was performed to verify the convergence of the free-vortex wake solution with increasing grid refinement. This experiment verifies that the final wake solution is properly second-order accurate in ψ and ζ, as expected from the preceding analysis. Also, because stability and consistency of the numerical method are necessary for solution convergence, this can also verify the stability of the numerical algorithms. It was shown that both the PCC and the PC2B algorithms are consistent with the original governing equations. Therefore, convergence of the wake solution can be used as a test to establish the stability of the numerical algorithms.

A grid resolution study with the free-vortex wake was performed using both the time-marching algorithms with discretization levels ranging from $\Delta\psi = \Delta\zeta = 2.5^\circ$ to 20°. Although the exact (mathematical) solution for the wake geometry is forever unknown, the numerical solution with the finest grid discretization can be considered as the "exact" solution for the purpose of estimating the order of accuracy. Numerical errors are calculated relative to this wake geometry using the finest grid discretization level, i.e., $(\Delta\psi = \Delta\zeta = 2.5^\circ)$.

Figure 3.26 shows such numerical errors in the wake geometry as a function of grid discretization level. Because the solution is expected to show second-order accuracy, quadratic fits to the numerical results are also shown.

Note that the results using the PCC algorithm do not give the expected second-order accuracy, as shown in Fig. 3.26(a). However, the results for the PC2B algorithm show a behavior closely corresponding to the expected quadratic trend, with the errors being proportional to $\Delta\psi^2$ – see Fig. 3.26(b). These results confirm that the final wake geometry solution obtained using the PC2B algorithm is, indeed, second-order accurate in both space (ζ) and time (ψ). It should be noted that the PCC algorithm is

(a) PCC solution

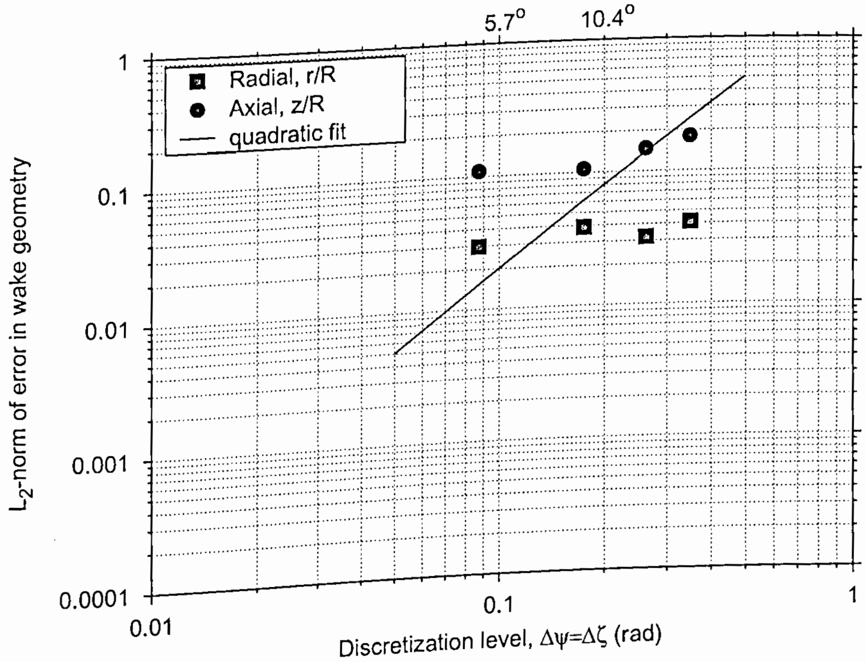

(b) PC2B solution

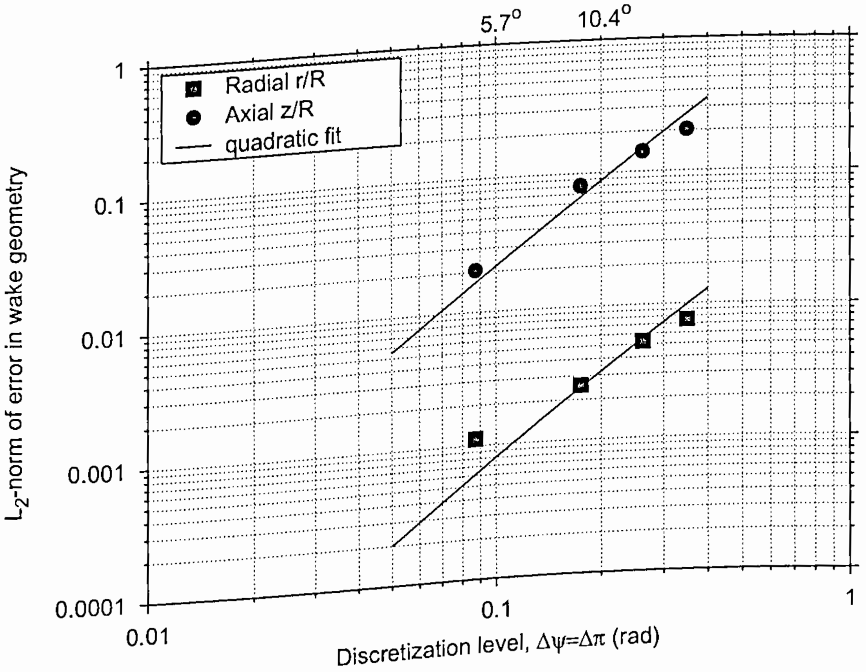

Figure 3.26: Numerical errors in free-vortex wake solution in hover with increasing grid discretization: (a) PCC solution, (b) PC2B solution.

also formally second-order accurate. However, the PCC wake geometry solution does not show the desired accuracy because of numerical instabilities. This accuracy check provides the means to verify that not only the algorithm but also the final numerical solution is stable, consistent and, therefore, convergent.

Finally, the numerical experiment was repeated for a forward flight case at an advance ratio $\mu = 0.1$ to verify wake solution convergence. These calculations were performed for a four-bladed rotor whose geometry and operating conditions correspond to the experiments of Ref. 85. A forward shaft tilt angle of -3° is used with a rotor thrust coefficient of $C_T = 0.008$. The top view of the wake geometry is shown in Fig. 3.27(a) for different levels of discretization. Only the geometry for the tip vortex from a reference blade at $\psi_b = 0^\circ$ is shown, along with experimental results from Ref. 85. Note that only the solution with the coarser discretization of $\Delta\psi = \Delta\zeta = 20^\circ$ shows significant differences from the other solutions. The solutions corresponding to $\Delta\psi \leq 10^\circ$ are almost identical. This is, again, consistent with the previous observation that a resolution of at least 5° would be required to properly resolve the induced velocities. The numerical errors, relative to the $\Delta\psi = 2.5^\circ$ solution, exhibit the expected second-order accuracy, as shown in Fig. 3.27(b). Therefore, the PC2B solution is convergent in both hover and forward flight. It is also interesting to note that the strong distortions in the wake structures are well-preserved, and are not damped-out because of artificial numerical dissipation.

3.4.1 Acceleration Technique: Velocity Field Interpolation

The idea of using interpolated velocity field in the free-vortex wake calculations was first introduced by Bagai & Leishman in Ref. 59 for improving computational efficiency of the free wake algorithms. The underlying principle behind this concept is to

(a) Top view of tip vortex geometry

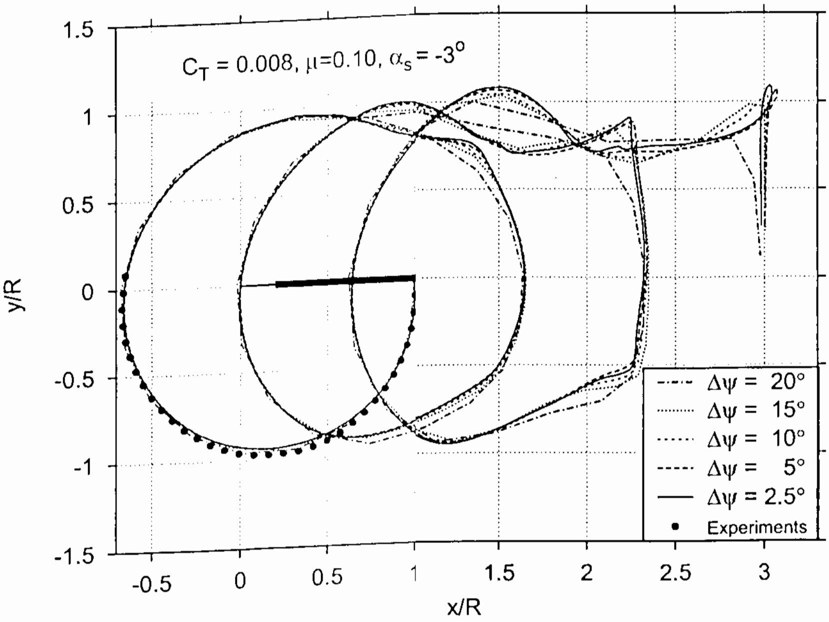

(b) Convergence trend

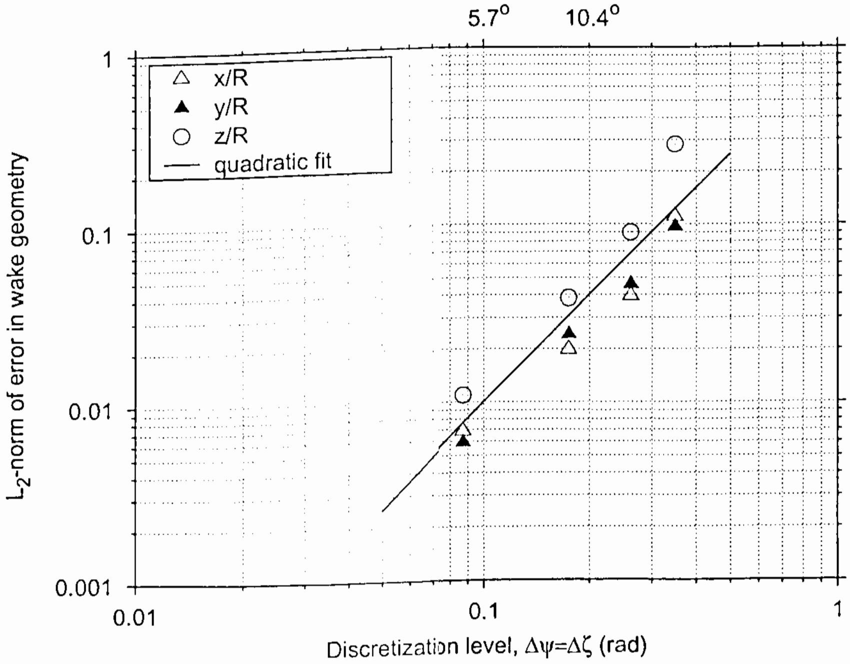

Figure 3.27: Numerical errors with increasing grid discretization are shown as a function of discretization to verify convergence of wake solution in forward flight using the PC2B algorithm. (a) Top view of tip vortex geometry, (b) Convergence trend.

perform fewer explicit induced velocity calculations through the application of Biot-Savart law, whilst retaining the accuracy and fidelity of the wake geometry solutions. This technique is useful for both adaptive grid sequencing with equal discretization sizes in the blade azimuth and vortex age, as well as to preserve the characteristic solution propagation direction in case of unequal discretizations.

The computational efficiency of such an approach results from fewer explicit Biot-Savart induced velocity calculations. The computational cost of a free-vortex wake calculation is directly proportional to the number of Biot-Savart calculations. For equal discretization, $\Delta\psi = \Delta\zeta$ with $N_\psi = 2\pi/\Delta\psi$ azimuthal steps per rotor revolution, the number of vortex segments in each wake turn are $N_\zeta = N_\psi = N$. Therefore, the number of Biot-Savart calculations required per wake turn are given by

$$\begin{aligned} \text{Number of Biot-Savart Calculations} &= N_b N_\psi N_\zeta N_\zeta \\ &= N_b N^3 \end{aligned} \tag{3.63}$$

Using velocity field interpolation, the effective number of Biot-Savart calculations is reduced. The positions of all collocation points in the wake are still determined by applying the vorticity transport theorem, however, the self- and mutual-induced velocities are only calculated at the free collocation points. Linear interpolation of induced velocity field is used at the pseudo-free points or ersatz-free points. Note that a simple interpolation of positions of the wake collocation points would result in a poor wake geometry solution. Interpolating induced velocities is equivalent to interpolation based on the slopes of the vortex filaments, and results in a higher order accuracy.

Vortex Filament Interpolation: $\Delta\zeta > \Delta\psi$

For the case where the vortex age discretization is larger than the azimuthal discretization, i.e., when $\Delta\zeta > \Delta\psi$, a linear velocity interpolation is used along the vortex filament. The induced velocities are calculated only at the free collocation points spaced at $\Delta\zeta$, as shown by filled circles in Fig. 3.28. These sparse, free collocation points are assumed to be end-points of straight-line vortex segments. Therefore, both the number of vortex segments and evaluation points is decreased by a factor corresponding to the ratio of discretizations, $\Delta\zeta/\Delta\psi$. The induced velocity at the ersatz free points, shown by open circles in Fig. 3.28, is approximated using linear interpolation along each vortex filament. For example, with $\Delta\zeta = 2\Delta\psi$ the number of Biot-Savart calculations is reduced to $1/4 N_b N^3$.

This interpolation scheme can be used with both the time-marching and the relaxation algorithms. In the time-stepping approach, the interpolation scheme is applied after each time-step, while for the relaxation algorithm the interpolation is applied over the entire rotor revolution with the assumption of wake periodicity. The numerical errors introduced because of the velocity field interpolation were shown in Ref. 59 to be small, and did not affect the overall solution accuracy.

Interpolation Along Blade Azimuth: $\Delta\psi > \Delta\zeta$

The relaxation algorithm in the present analysis also includes an option to use azimuthal interpolation, where the blade azimuthal discretization was larger than the wake discretization. The basic approach is essentially the same as that described earlier for vortex filament interpolation. The difference being that in this case, the interpolation is performed at constant vortex along the blade azimuth. This results in a computational saving of a factor of $\Delta\psi/\Delta\zeta$ the number of Biot-Savart velocity evalu-

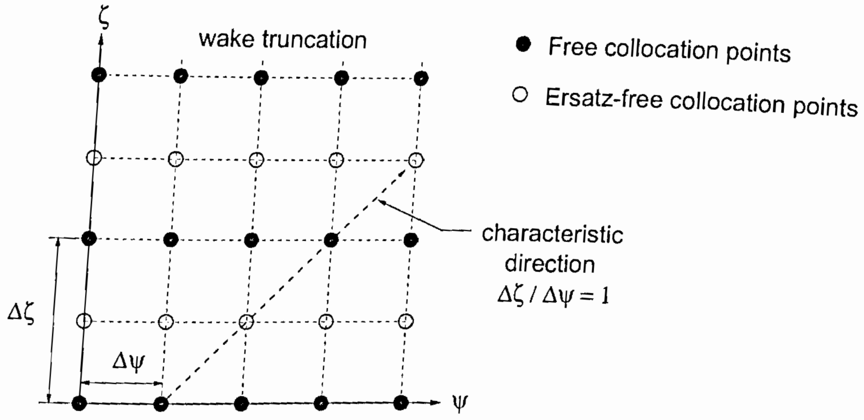

Figure 3.28: Schematic of wake geometry in the computational domain for velocity interpolation along vortex filament, $\Delta\zeta > \Delta\psi$.

ation points. However, the number of vortex segments remains unchanged. For example, with $\Delta\psi = 2\Delta\zeta$ the number of Biot-Savart calculations is reduced to $1/2N_bN^3$. The blade attachment boundary condition (i.e., the first wake collocation point) needs special treatment. These values may be obtained by interpolating the blade flapping angles along the azimuth, or alternatively by exactly solving for periodic blade flapping solution at all azimuthal locations.

The time-marching approach currently does not implement this type of azimuthal interpolation because for accuracy in time it is important to use a small time (azimuthal) step. Another factor is the blade flapping solution, which must be integrated at all azimuthal locations to maintain proper accuracy in time. Any computational savings offered by azimuthal integration may be small, and would also offset the accuracy of the solution.

An example of the wake geometry obtained using this type of linear velocity interpolation is shown in Fig. 3.29. The axial wake displacements are shown in Fig. 3.29(a) as a function of vortex age are shown for two equal discretization levels of $\Delta\psi =$

$\Delta\zeta = 2.5°$ and $5°$ along with a solution obtained using liner velocity interpolation for $\Delta\psi = 2.5°$ and $\Delta\zeta = 5°$. The solution using interpolation closely resembles the solution obtained using finer resolution, i.e. $\Delta\zeta = \Delta\psi = 2.5°$. The convergence trends obtained using the interpolation technique with $\Delta\zeta = 2\Delta\psi$ are shown in Fig. 3.29(b). As mentioned earlier, the velocity interpolation should yield a second-order accuracy in the tip vortex locations. This is confirmed by the quadratically decreasing convergence trend shown by the results. Note that for any given discretization $\Delta\psi$, the errors using interpolation are larger than the corresponding errors for the baseline equal discretization. However, the errors are significantly smaller than the corresponding errors for the baseline solution with $\Delta\psi = \Delta\zeta$, that is the errors in interpolated solution with $\Delta\psi = 5°$ and $\Delta\zeta = 10°$ are smaller than those for the baseline solution with $\Delta\psi = \Delta\zeta = 10°$. Therefore, the velocity field interpolation technique is useful for obtaining reasonably accurate wake solutions without using computationally expensive finer discretization levels.

3.4.2 Extrapolation Technique to Improve Accuracy

Clearly, the vortex induced velocities are the most important factor in the numerical solution for the rotor wake geometry. As mentioned previously in Section 3.2.1, the induced velocity calculation can be readily extended to a higher-order of accuracy using techniques such as Richardson's extrapolation. This technique would not increase the order of accuracy of the solution because the finite difference approximations to the derivatives on the LHS of Eq. 3.2 are only second-order accurate. However, an improved velocity calculation can potentially decrease the absolute magnitude of the numerical errors for a relatively modest increase in computational cost.

In the case of a solution with discretization $\Delta\zeta$, a total of N_ζ^2 induced velocity

(a) Axial wake displacements

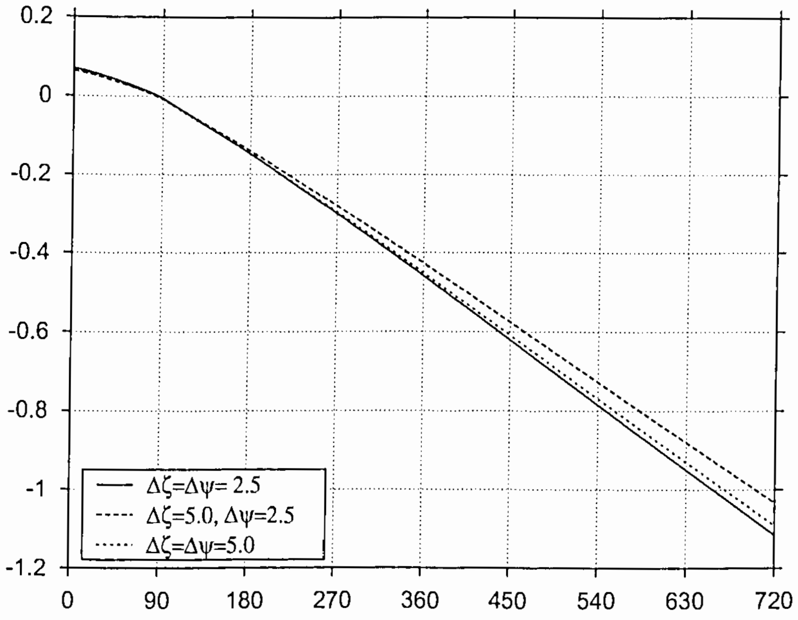

(b) Convergence trend

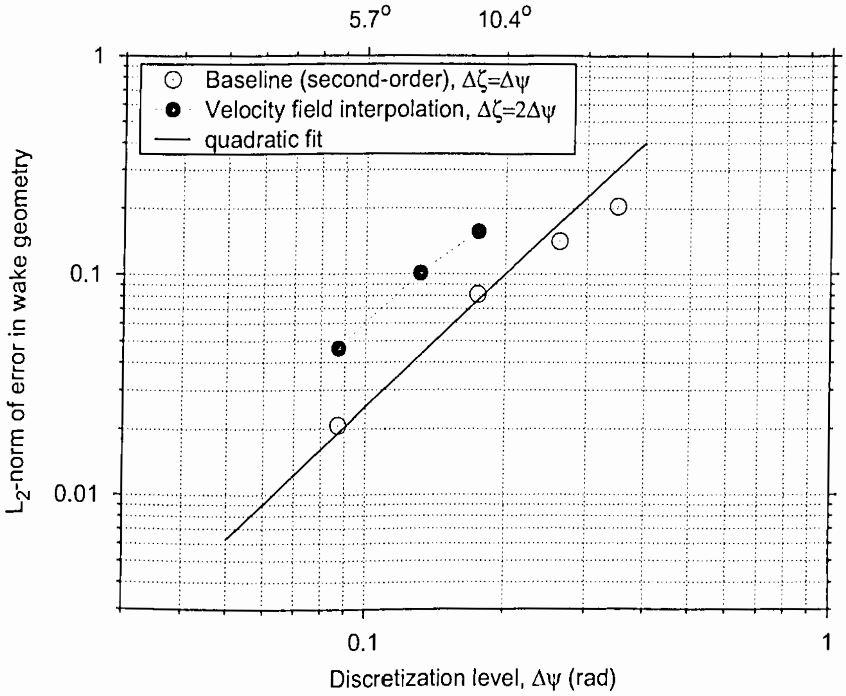

Figure 3.29: Velocity field interpolation used in the free-vortex wake solution with $\Delta\zeta = 2\Delta\psi$ to reduce computational expense. (a) Axial wake displacements, (b) Convergence trend

calculations need to be performed per time-step. In addition, another approximation to the induced velocities is calculated using only every other collocation point on each wake filament, that is, this latter approximation has an effective discretization of $2\Delta\zeta$. Note that the additional induced velocity calculations required per time step are $1/2 N_{\zeta}^{2}$. Using Richardson's extrapolation, a better approximation to the induced velocity can be obtained using

$$V^{(1)}(\Delta\zeta) = \frac{4V(\Delta\zeta) - V(2\Delta\zeta)}{3} + \text{higher order terms} \cdots \tag{3.64}$$

This new induced velocity approximation is expected to be fourth-order accurate, as shown previously in Section 3.2.1.

Examples of the rotor wake geometry obtained using this extrapolation technique are shown in Fig. 3.30(a). In the baseline (second-order) case, the $\Delta\psi = \Delta\zeta = 10°$ wake geometry solution showed significant differences as compared to the $\Delta\psi = \Delta\zeta = 5°$ and the $\Delta\psi = \Delta\zeta = 2.5°$ solutions. However, using the extrapolation technique for improved velocity calculations the differences between these solutions decrease. Therefore, a coarser solution with a 10° resolution also gives satisfactory, almost grid independent predictions. This decrease in the numerical errors is clearly evident from Fig. 3.30(b) where the errors are shown as a function of the discretization. Note that although there is significant improvement in the solution, the order of accuracy of the solution is still second-order. This is because the wake governing equations are solved using only a second-order accurate algorithm. However, there is noticeable reduction in the absolute errors for a given discretization level. Therefore, the Richardson's extrapolation provides a relatively simple means for improving the accuracy of the numerical wake predictions.

The benefits of using such an extrapolation technique are more apparent when these results are plotted in the form of numerical errors as a function of computational cost

(a) Axial wake displacements

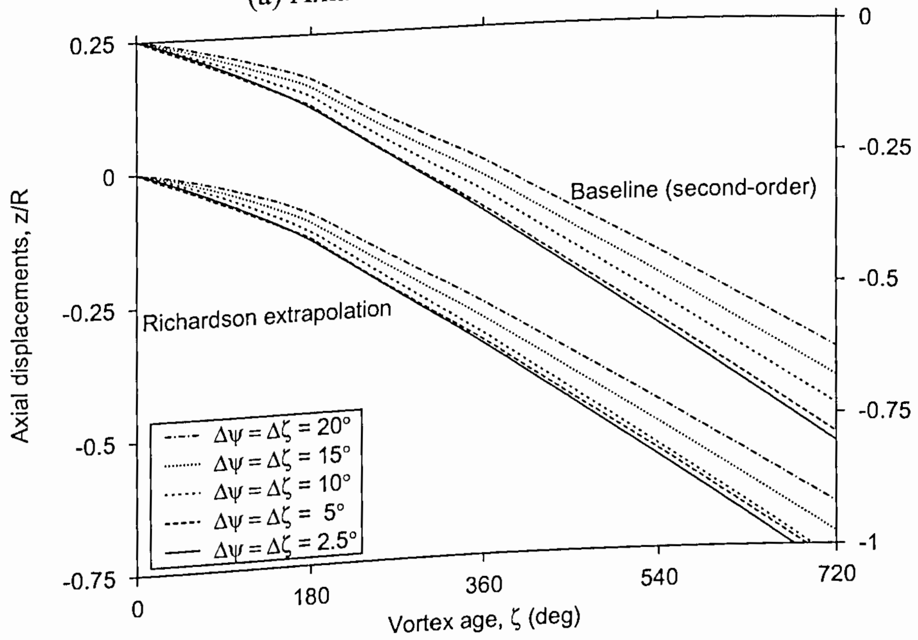

(b) Convergence trend

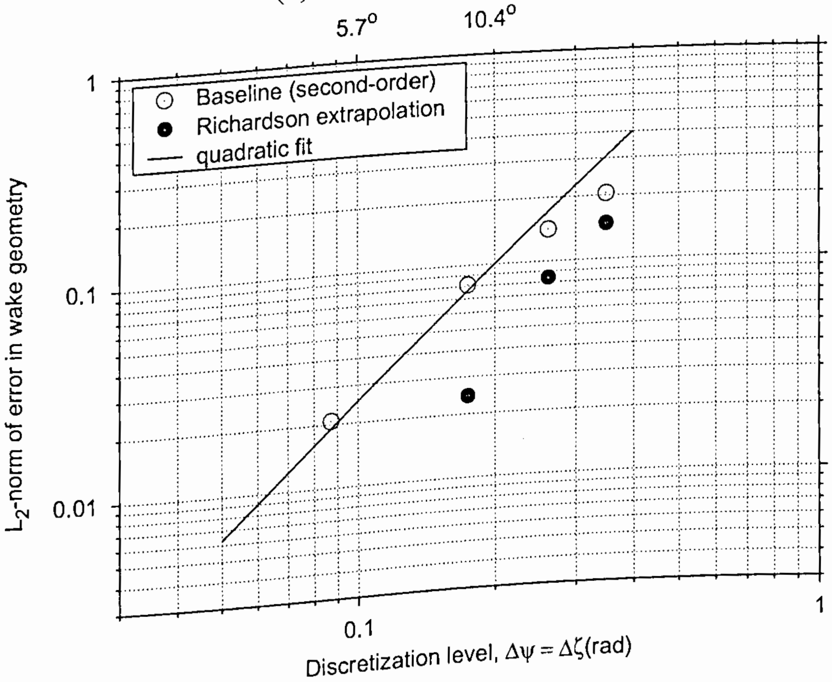

Figure 3.30: Richardson's extrapolation for induced velocity calculations. (a) Axial wake displacements, (b) Convergence trend. Two-bladed hovering rotor of Ref. 66, $C_T = 0.005$.

– see Fig. 3.31. For the rotor free-wake problem, clearly the computationally intensive part is the Biot-Savart law calculations. Therefore, the number of Biot-Savart calculations per rotor revolution (per turn of the wake) is used as the ordinate in this plot. Note that in the baseline second-order case, the number of such calculations is N_ψ^3, while in the case of extrapolation using a coarser grid it is $3/2N_\psi^3$. The results obtained using the linear velocity field interpolation technique, described in the previous section, are also shown for comparison. The interpolation technique follows essentially the same trend as the baseline solution. This is because, the interpolation technique does not really improve the accuracy of the wake solution, but only provides intermediate solutions between two discretization levels. As shown in Fig. 3.31, this technique provides significant improvement in overall solution accuracy for only a modest increase in computational cost.

3.5 Summary

The emphasis of this chapter was on the formulation of the time-accurate wake solution methodology, which is the main focus of this dissertation. The stability, accuracy and convergence of time-marching algorithms for free-vortex rotor wake calculations was examined. A linearized analysis was used to determine the basic stability characteristics. The vortex-induced velocities were calculated through application of the Biot-Savart law using standard straight-line vortex segmentation. This approach was shown to be second-order accurate. However, the discretization resulted in nonlinear dispersion and dissipation terms in the discretized wake equations. These errors were found to be dependent on the induced velocity field, and may be anti-dissipative under many flight conditions. In such cases, the wake geometry solution may not be conver-

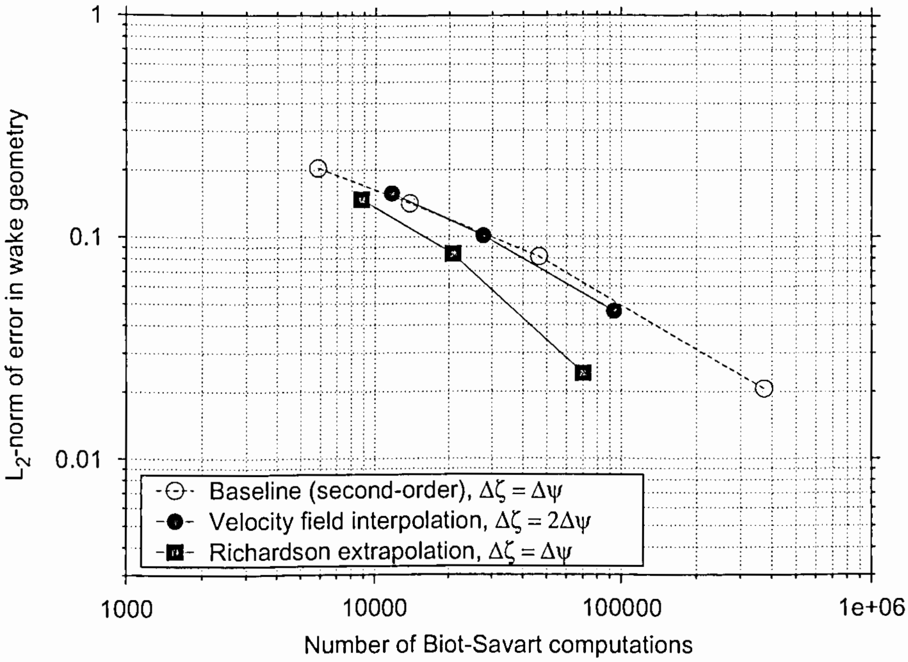

Figure 3.31: Computational costs associated with Richardson's extrapolation for induced velocity calculations. The results obtained using the baseline free-vortex wake solution, and also those with velocity field interpolation are shown for comparison.

gent, even though the numerical algorithm is linearly stable. As shown in the previous chapter, the wake geometry is physically unstable and a more careful assessment of the stability of numerical algorithms is required.

Modified equations were examined to provide further insight into stability of the nonlinear discretized equations. A new time-marching algorithm was proposed using a second-order backward difference approximation for the time derivative to ensure stability and solution convergence. A numerical experiment was performed to verify convergence of the wake geometry solutions obtained using this algorithm. The expected second-order accuracy and grid independent nature of the wake geometry solution was demonstrated, for both hover and forward flight.

Chapter 4

Methodology: Rotor Blade Equations

Besides the vortical wake, the helicopter rotor problem consists of two other coupled parts: the blade-lift solution and a solution for the blade flapping motion. It is necessary to solve for both of these problems in a form that is compatible with the rotor wake solution. In the present chapter, the methodology for these two solutions is described. The blade lift solution is obtained using a Weissinger-L type of lifting surface model, the blade lift being related to the bound circulation through the Kutta-Joukowski theorem. The strength of the trailed wake vortices depends on the spanwise bound circulation distribution, while the bound circulation itself depends on the wake-induced velocity field at each spanwise section of the rotor blades.

The blade flapping motion, typically about a flapping hinge near the root of the blade, is governed by the equilibrium of aerodynamic, centrifugal and inertial moments. The equations are formulated in the same form as the wake governing equations, so they can be solved in a properly coupled manner. The blade flapping motion also depends on the blade lift distribution through the aerodynamic flapping moment about the hinge. The lift solution, in turn, depends on the wake geometry through the wake-induced inflow velocity. The blade flapping motion essentially forms an equation for the first collocation point in the wake, i.e., the origin of the wake vortices is at the blades. This constitutes a boundary condition for the wake geometry solution. This chapter includes both the derivation of the blade flapping equation and the solution strategies developed for both the periodic and time-accurate solutions.

4.1 Blade-Lift Solution

The rotor blade is, typically, modeled as a series of two-dimensional elements using the principles of the standard blade element analysis. If the wake-induced rotor inflow can be determined, then the local angle of attack at each blade element can be determined, and the blade lift calculated by integrating along blade span. Each blade element is assumed to operate as an airfoil section independent of other spanwise blade elements and the local lift is related to the local effective angle of attack as shown in Fig. 4.1. Typically, the velocity component perpendicular to the reference plane (TPP) includes the wake-induced velocities. As mentioned previously, the wake solution itself is coupled to the blade lift through the circulation trailed (and shed) into the wake. Therefore, lifting-line or lifting-surface models can be used, which solve for the blade lift in terms of the bound circulation. The trailed wake circulation can then be easily related to the bound circulation through a roll-up model such as the Betz model (Ref. 86).

The blade model used in the present analysis is based on two basic building blocks: 1. The Weissinger-L (W-L) lifting surface model (Ref. 46) and 2. The Kutta-Joukowski theorem (K-J). In the W-L model, which is essentially a lifting-surface model with only one chord-wise panel, the blade lift is represented using a series of spanwise horseshoe vortex elements, with the flow tangency condition being satisfied. The bound circulation is located at the quarter-chord, while the flow tangency condition is imposed at the 3/4-chord point. This is consistent with the unsteady thin airfoil model (see,

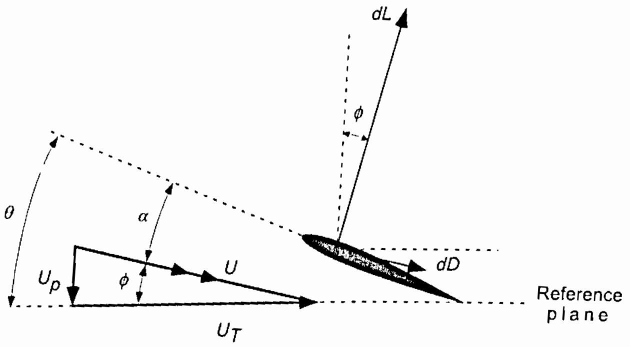

Figure 4.1: Schematic showing the forces and velocities at a representive blade element.

e.g., Ref. 2). The K-J theorem then relates the actual lift (force) to the blade bound circulation.

The Weissinger-L model is shown to give improved prediction of loading for arbitrary planform fixed wings with a range of aspect ratios, sweep and taper (Ref. 87). This is equivalent to Johnson's so-called non-linear lifting line theory (Ref. 88), where the induced velocities are again calculated at the 3/4-chord point. In rotating wing applications also the Weissinger-L model has shown to give good prediction of the spanwise blade loading. Kocurek *et al.* (Ref. 17) showed that the Weissinger-L model gave as good predictions as a panel model with several chordwise panels. Even for blade-vortex interactions, the W-L model is found to give satisfactory results (Ref. 88).

A schematic of the W-L model is shown in Fig. 4.2, where the blade is divided into N_s spanwise panels with the bound circulation located along the quarter-chord line. A control point on each panel is placed at the 3/4-chord location. The trailed wake vortices extend downstream from the blade bound vortex segment end points, located along the quarter-chord. On the basis of Helmholtz's vorticity theorems, the vortex lines are indestructible and, therefore, the trailed circulation can be related to the bound circulation distribution using

$$\Gamma_{\text{trailed}}(r) = \frac{d\Gamma_{bound}}{dr} \tag{4.1}$$

For a discretized bound circulation distribution with spanwise vortex segments of constant strengths Γ_j (see Fig. 4.2), the trailed vortex circulation at each segment end point is given by

$$\Gamma_{\text{trailed}_j} = \Gamma_{\text{bound}_{j-1}} - \Gamma_{\text{bound}_j} \tag{4.2}$$

The blade surface is assumed to be in the same plane as the chord line, and is divided into N_s spanwise segments. For the i^{th} blade segment, the flow tangency condition can be written as

$$V_{b_i} = V_{\infty_i}\alpha_{e_i} \tag{4.3}$$

where V_{b_i} is the velocity induced by the bound vortex at the i^{th} control point, V_{∞_i} the stream velocity at that control point and α_{e_i} the effective angle of attack. The effective angle of attack is a combination of the geometric angle of attack, θ, and the induced angle of attack, ϕ, because of the trailed wake system – see Fig. 4.1. This is simply a mathematically statement ensuring that there is no flow through the airfoil surface, i.e., the flow is tangential to the airfoil surface, at least at the control point.

The trailed system is divided into two parts: a near-wake and a far-wake. The near-wake system is assumed to be rigid and fixed to the blade, while the far-wake evolves in a force free manner as given by the free-vortex model. Equation 4.3 can be now written as:

$$\begin{aligned} V_{b_i} &= V_{\infty_i}(\theta_i - \phi_{FW_i} - \phi_{NW_i}) \\ &= V_{\infty_i}(\theta_i - \phi_{FW_i}) - V_{NW_i} \end{aligned} \tag{4.4}$$

where θ_i is the geometric angle of attack, and ϕ_{FW_i} and ϕ_{NW_i} are the induced angles of attack because of the far-wake and the near-wake, and V_{NW_i} the velocity induced by

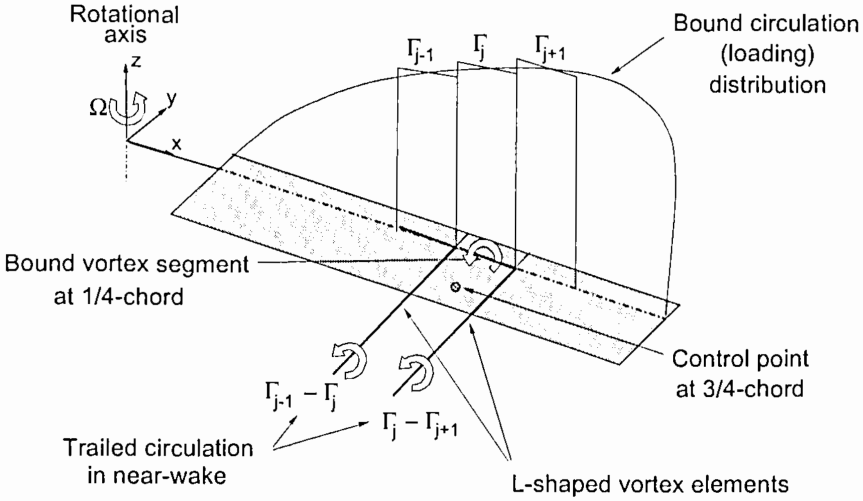

Figure 4.2: The Weissinger-L model for representing the blade bound circulation and the near wake trailed circulation from a rotor blade.

the near-wake at the i^{th} control point. The far-wake induced inflow is calculated using the Biot-Savart law and the free-vortex wake geometry. The bound circulation and the near-wake, however, are geometrically constrained relative to the blade control points. Therefore, the velocities induced by the bound vortex and the fixed near-wake are related to the strength of the bound vortex at the blade segments, Γ_j, through influence coefficient matrices. This can be written using index notation as follows.

$$V_{b_i} = \sum_j I_{b_{i,j}} \Gamma_j \tag{4.5}$$

$$V_{NW_i} = \sum_j I_{NW_{i,j}} \Gamma_j \tag{4.6}$$

It should be noted that all the bound vortex elements, and all the near-wake trailers contribute to the induced velocity at the i^{th} control point. The influence coefficient matrices can be calculated using the blade geometry through the application of Biot-Savart law. Using these relations, the governing equation for the blade lift can be written as

$$\sum_{j=1}^{N_s} \left[I_{b_{i,j}} + I_{NW_{i,j}}\right] \Gamma_j = V_{\infty_i} (\theta_i - \phi_{FW_i}) \tag{4.7}$$

For the blade segments corresponding to $i = 1, \ldots, N_s$, N_s equations in N_s unknowns are obtained, corresponding to the strengths of the bound vortex segments, Γ_j. This linear system of equations can then be solved using standard algorithms to obtain the vortex strengths.

4.1.1 Relation Between Lift and Bound Circulation

The flow-tangency condition can now be written in terms of the strengths of the bound vortex segments as

$$\sum_j I_{b_{i,j}} \Gamma_j = V_{\infty_i} \alpha_{e_i} \tag{4.8}$$

With the assumption of a thin airfoil, i.e., with a lift curve slope of 2π, the local lift-coefficient can be written as

$$C_l = C_{l_\alpha} \alpha_{e_i} = \frac{2\pi}{V_{\infty_i}} \sum_j I_{b_{i,j}} \Gamma_j \tag{4.9}$$

The lift distribution along the blade span can be obtained from the bound circulation distribution through application of the Kutta-Joukowski (K-J) theorem. If the K-J theorem is applied on a segment basis in a 2-D sense, for the i^{th} blade segment then

$$\begin{aligned} L_i ds &= \rho V_{\infty_i} \Gamma_i ds && (4.10) \\ &= \frac{1}{2} \rho V_{\infty_i}^2 c_i C_{l_\alpha} \alpha_{e_i} ds && (4.11) \end{aligned}$$

Therefore, the lift coefficient is given by

$$C_l = C_{l_\alpha} \alpha_{e_i} = \frac{2\Gamma_i}{V_{\infty_i} c_i} \tag{4.12}$$

It must be noted that these two expressions for the lift coefficient, Eqs. 4.9 and 4.12, are inconsistent. This inconsistency stems from the fact that the W-L model includes three-dimensional effects through the contributions from all bound vortex segments, while the inherently two-dimensional K-J theorem includes only the i^{th} bound vortex segment. To remove this discrepancy and to properly include three-dimensional effects the K-J theorem can be rewritten in a more consistent form. The K-J theorem relates the lift to the bound circulation as

$$L_i ds = \rho V_\infty \Gamma_{KJ_i} ds \tag{4.13}$$

where the circulation around the i^{th} blade segment, Γ_{KJ_i} is defined as the closed loop integral of the velocity field around the blade, i.e.,

$$\Gamma_{KJ_i} = \oint_i \vec{V} \cdot \vec{dt} \tag{4.14}$$

This integral is independent, at least in principle, of the choice of integration contour. A circular contour can be chosen with center at 1/4-chord and a radius of $c_i/2$. Figure 4.3 shows such a contour passing through the blade control point. By virtue of axisymmetry it follows that

$$\begin{aligned} \Gamma_{KJ_i} &= 2\pi \frac{c_i}{2} V_{b_i} \\ &= 2\pi \frac{c_i}{2} \sum_j I_{b_{i,j}} \Gamma_j \end{aligned} \tag{4.15}$$

where V_{b_i} is the velocity at the i^{th} control point. Therefore, the lift can be expressed as

$$L_i ds = \rho V_\infty 2\pi \frac{c_i}{2} \sum_j I_{b_{i,j}} \Gamma_j ds \tag{4.16}$$

Now, the expression for the lift coefficient is exactly the same as that obtained from the W-L model (Eq. 4.9), i.e.,

$$C_{l_\alpha} \alpha_{e_i} = \frac{2\pi}{V_{\infty_i}} \sum_j I_{b_{i,j}} \Gamma_j \tag{4.17}$$

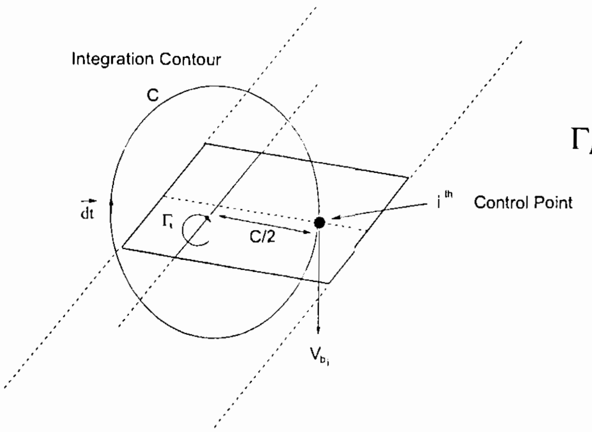

$$\begin{aligned}\Gamma_{KJ} &= \oint_C \vec{V}\cdot\vec{ds} \\ &= 2\pi\left(\frac{c}{2}\right)V_{b_i}\end{aligned}$$

Figure 4.3: Contour for performing velocity field integration.

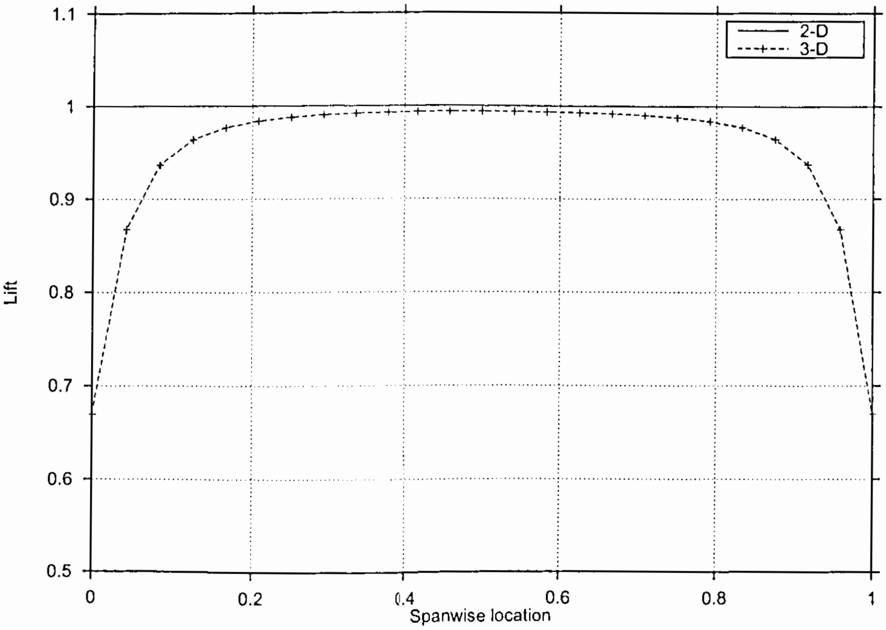

2-D: $$\frac{L_i}{\rho V_\infty \Gamma_0} = 1.0$$

3-D: $$\frac{L_i}{\rho V_\infty \Gamma_0} = 2\pi\frac{c_i}{2}\sum_j I_{b_{i,j}}$$

Figure 4.4: Lift distribution using Kutta-Joukowski theorem for uniform bound vortex.

This interpretation of Kutta-Joukowski theorem is shown in Fig. 4.4 for the case of constant circulation, Γ_0 over the span. The segment lift is calculated using Eqs. 4.12 and 4.16. Clearly, the 3-D approach incorporates the tip loss effects as in the case of the W-L model.

Finally, blade lift model can be summarized as follows. The distribution of bound circulation is obtained from the solution of the linear system of equations,

$$\sum_{j=1}^{N_s} \left[I_{b_{i,j}} + I_{NW_{i,j}}\right] \Gamma_j = V_{\infty_i} \left(\theta_i - \phi_{FW_i}\right) \tag{4.18}$$

and the lift coefficient is related to this bound circulation distribution through the K-J theorem as

$$C_{l_\alpha} \alpha_{e_i} = \frac{2\pi}{V_{\infty_i}} \sum_j I_{b_{i,j}} \Gamma_j \tag{4.19}$$

4.1.2 Effect of Blade Twist on Near-Wake

Because the near-wake trailers are fixed to the blade, when the blade is twisted, the two trailers at the segment endpoints are not in the same plane as the chord line passing through the control point. This effect is shown schematically in Fig. 4.5. It can be seen that the angles made the two trailers are equal and opposite, and therefore, the net velocity induced by the two trailers at the blade control point is normal to the chord line passing through that control point.

4.1.3 Compressibility Correction

In the above analysis, the flow is assumed to be incompressible and inviscid, i.e. potential, and the lift curve slope is that given by thin airfoil theory, i.e., $C_{l_\alpha} = 2\pi$ per radian. To include compressibility effects, the Prandtl-Glauert factor, $\beta = 1/\left(1 - M^2\right)$ is applied on a segment basis to the effective angle of attack. Therefore, the flow-tangency

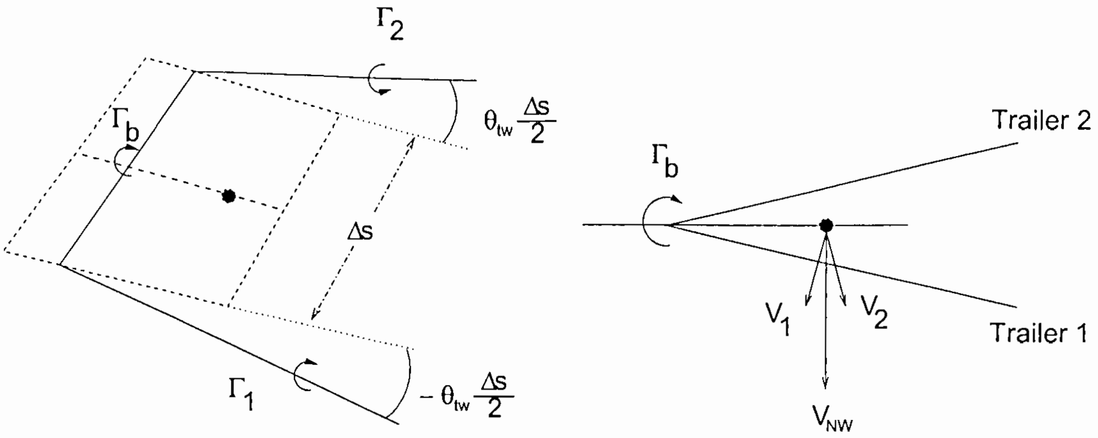

Figure 4.5: Near wake trailers for a twisted blade.

condition is now rewritten as

$$\sum_j I_{b_{i,j}} \Gamma_j = V_{\infty_i} \frac{\alpha_{e_i}}{\beta_i} \tag{4.20}$$

and therefore, the linear system of equations for the bound vortex strengths is given by

$$\sum_{j=1}^{N_s} \left[\beta_i I_{b_{i,j}} + I_{NW_{i,j}}\right] \Gamma_j = V_{\infty_i} \left(\theta_i - \phi_{FW_i}\right) \tag{4.21}$$

The local lift coefficient is the same as before, i.e.,

$$\begin{aligned} C_l &= C_{l_\alpha} \frac{\alpha_{e_i}}{\beta_i} \\ &= \frac{2\pi}{V_{\infty_i}} \sum_j I_{b_{i,j}} \Gamma_j \end{aligned} \tag{4.22}$$

Recall that the lift curve slope is still the same as that given by thin airfoil theory, i.e., $C_{l_\alpha} = 2\pi$. The compressibility correction is applied only to the angle of attack at each blade segment. Therefore, this correction must be applied to both the geometric and the induced angle of attack, i.e.,

$$\theta_i^c = \frac{\theta_i}{\beta_i} \tag{4.23}$$

$$\phi_i^c = \frac{\phi_{FW_i} + \phi_{NW_i}}{\beta_i} \tag{4.24}$$

This shows that the induced angle of attack also increases because of compressibility effects. Also, there is an "aerodynamic twist" introduced by the spanwise variation of compressibility effects.

4.1.4 Airfoil Model

An inviscid lift-curve slope of $C_{l_\alpha} \neq 2\pi$ per radian can be incorporated into the blade model formulation to represent the effects of airfoil shape. A zero-lift angle of attack can also be readily included to account for effects of camber. From K-J theorem, the effective angle of attack is found to be

$$\alpha_{e_i} = \frac{C_{l_\alpha}}{2\pi}\left(\frac{\alpha_{e_i}}{\beta_i}\right) \tag{4.25}$$

The W-L system of equations can be modified to give

$$\sum_{j=1}^{N_s}\left[\frac{2\pi}{C_{l_\alpha}}\beta_i I_{b_{i,j}} + I_{NW_{i,j}}\right]\Gamma_j = V_{\infty_i}(\theta_i - \phi_{FW_i}) \tag{4.26}$$

It is interesting to note that the lift-curve slope does not affect the induced angle of attack, i.e.,

$$\phi_i^c = \frac{\phi_{FW_i} + \phi_{NW_i}}{\beta_i} \tag{4.27}$$

This is because, if the lift curve slope changes, it should only change the magnitude of the lift and not its direction. The sectional drag can also be obtained from the effective angle of attack, α_{e_i} using a simple model of the form

$$C_d = C_{d_0} + D_1\alpha_{e_i} + D_2\alpha_{e_i}^2 \tag{4.28}$$

where C_{d_0} represents the zero lift drag coefficient, and D_1 and D_2 are used to model non-linear effects. The values of these constant parameters are empirically determined.

4.1.5 Momentum Conservation: Newton's Law

The free-wake methodology is based on the vorticity transport theorem, which states that the vorticity is convected along with the fluid at the local velocity, i.e., the vortex elements in the wake are identical to Lagrangian fluid markers. This is same as Helmholtz theorem, which states that in an incompressible flow the vortex lines move as material lines. Therefore, the displacements of the force-free vortex elements can be found by tracing the time-dependent motion of Lagrangian fluid markers. Note that the flow is assumed to be incompressible and inviscid, and therefore, there is no force acting on any vortex element in the wake. However, at the time when a fluid element (or, equivalently, vortex element) is in contact with the lifting body (blade), there must be a force acting on the element that is equal and opposite to the lift. This is a direct consequence of Newton's third law. This impulsive force on the fluid element at the lifting body results in an increase in the momentum of that fluid element.

Figure 4.6 shows an airfoil section in inviscid flow. The Weissinger-L lifting-surface model sets the bound vortex strengths such that the flow is "turned" to satisfy the flow tangency condition. A fluid element leaving the trailing edge has a downwash velocity v as well as the freestream velocity U as shown in the figure. As there is no force acting on this element *after* it leaves the trailing edge, it continues to move with the velocity given by the vector sum of these two components. Therefore, the velocity induced by the bound vortex models the instantaneous momentum change of the fluid at the blade. This also corresponds to total pressure rise over the rotor disk.

To include this momentum addition in the free-wake calculations, the local velocity is rewritten as

$$\vec{V}_{\text{local}} = \vec{V}_{\text{free-stream}} + \vec{V}_{\text{maneuver}} + \vec{V}_{\text{trailed vortices}} + \vec{V}_{\Delta\text{momentum}} \tag{4.29}$$

where, $\vec{V}_{\Delta\text{momentum}}$ is the velocity induced on the fluid element by the bound vortex

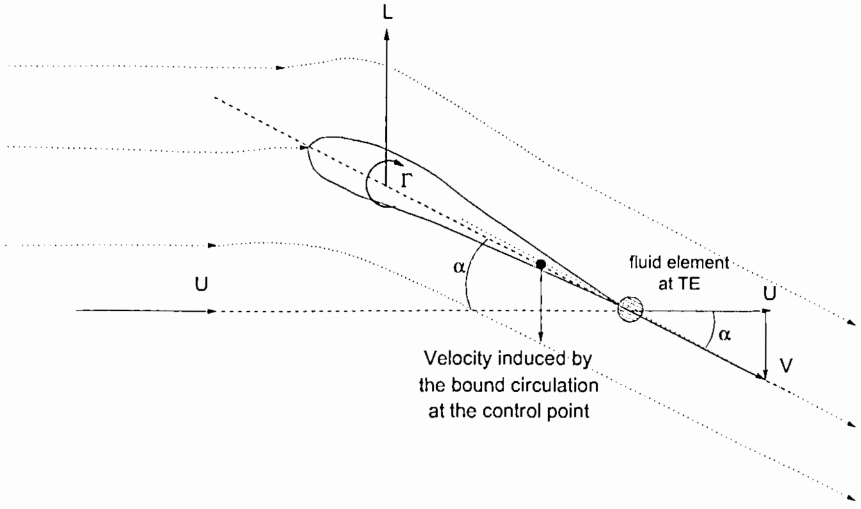

Figure 4.6: Schematic explaining the momentum addition by the blade.

system at the time when the fluid element was attached to the blade, i.e., at a wake age $\zeta = 0°$.

The momentum addition term can be readily identified from the Weissinger-L blade model. The velocity induced by the bound circulation at the blade control points corresponds to the work done by the rotor blade(s) on the air. The surrounding air is turned through an angle to satisfy the flow tangency condition. This increase in momentum of the air generates an equal and opposite reaction on the blade(s) in the form of lift. Therefore, the velocity induced by the bound vorticity on the trailed vortices at their origin at the blades results in a permanent increase in the momentum of the corresponding fluid particles at the wake collocation points. This momentum addition forms a connection between the circulation theory of lift and a momentum-based theory, where the lift on a blade section corresponds to the rate of change of momentum of the fluid passing through a control volume.

4.2 Rotor Blade Flapping Response

There is an interplay of the aerodynamic forces on the rotor blades and the rotor blade motion. The rotor wake geometry is inherently coupled with the blade motion through the origin of the vortical wake at the blade tip (which, as mentioned in the previous section, is a boundary condition for the free wake problem). Most helicopter rotor blades incorporate articulation in the form of flap and lead/lag hinges near the blade root. Modern composite blade/hub designs use hingeless fixtures which mimic blade motion about a virtual hinge location. Under most flight conditions, the dominant blade motion is the flapping motion, which is directly proportional to the aerodynamic lift on the blade. The lead/lag motion is of a much smaller magnitude as it is dependent on the aerodynamic drag force rather than lift. Therefore, in the present study only the flapping motion of the rotor blades is considered. Furthermore, the blades are assumed to be rigid with a flapping hinge. Structural stiffness of hingeless rotors can be modeled with an equivalent flapping spring located at the hinge.

4.2.1 Equation of Motion for a Flapping Blade

Figure 4.7 shows a rigid rotor blade undergoing flapping motion about a flap hinge located at a distance e from the rotational axis. The equilibrium position of the rotor blade, or the blade flapping angle, β, is determined through equilibrium of moments about the flapping hinge because of the various forces acting on the blade. Because the centrifugal force (CF) is much larger the aerodynamic force (blade lift), the flapping angle, β, is typically quite small.

The blade is assumed to have a uniform linear mass density, m. Consider a small element of the blade of length dr. The centrifugal force on of this blade element, acting

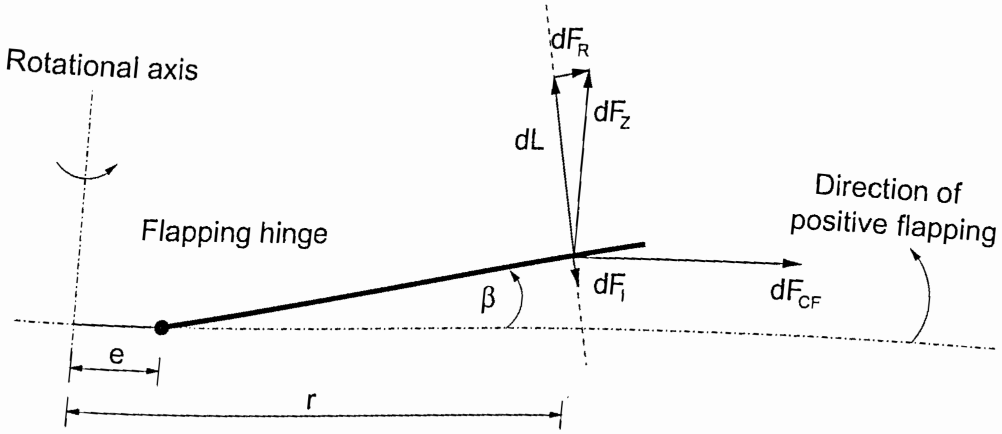

Figure 4.7: Equilibrium of moments about the flapping hinge.

in the plane of rotation, is given by

$$d\left(F_{CF}\right) = (m\,dr)\,r\Omega^2 = m\Omega^2 r\,dr \tag{4.30}$$

where Ω is the rotor rotational frequency. The component of the centrifugal force perpendicular to the blade is

$$d\left(F_{CF}\right)\sin\beta = m\Omega^2 r\sin\beta\,dr \approx m\Omega^2 r\beta\,dr \tag{4.31}$$

the small angle assumption employed in this approximation is justified because in most practical flight conditions, β, is indeed small. Typical values for a helicopter range between 3–6 degrees. Therefore, the CF moment about the flapping hinge is given by

$$\begin{aligned} M_{CF} &= \int_e^R m\Omega^2 r(r-e)\beta\,dr \\ &= \Omega^2\beta\left[\int_e^R m(r-e)^2\,dr + e\int_e^R m(r-e)\,dr\right] \\ &= \left(I_\beta + eS_\beta\right)\Omega^2\beta \end{aligned} \tag{4.32}$$

where the flapping moment of inertia I_β, and the static inertia moment (static droop), S_β, are given by

$$I_\beta = \int_e^R m(r-e)^2 dr \tag{4.33}$$

$$S_\beta = \int_e^R m(r-e) dr \tag{4.34}$$

The flapping motion itself results in an inertia force acting on the blade in the direction opposite to the flapping – see Fig. 4.7. This inertia force on a blade element is given by

$$d(F_I) = (m\,dr)(r-e)\ddot{\beta} = m\ddot{\beta}(r-e)\,dr \tag{4.35}$$

Therefore, the inertia moment about the flapping hinge is

$$M_I = \int_e^R m(r-e)^2 \ddot{\beta}\, dr = I_\beta \ddot{\beta} \tag{4.36}$$

Similarly, the moment because of the aerodynamic forces about the flap hinge can be calculated as

$$M_\beta = \int_e^R (r-e) dL \tag{4.37}$$

It must be noted that the elemental lift, dL, in the above equation depends on the non-linear wake-induced inflow and provides a coupling between the blade flapping dynamics and the wake dynamics. Structural stiffness for hingeless rotors can be modeled as a flapping spring with stiffness k_β. Such a spring would produce a restoring moment, $k_\beta(\beta - \beta_p)$, relative to a precone angle, β_p. Moment equilibrium about the flap hinge now gives the equation for the blade flapping angle, β, i.e.,

$$M_{CF} + M_I + k_\beta(\beta - \beta_p) = M_\beta \tag{4.38}$$

Note that the aerodynamic moment is written on the RHS of the equation because it is a counter-clockwise moment – see Fig. 4.7. Therefore, the flapping equation of motion is given by

$$I_\beta \ddot{\beta} + \left(I_\beta \Omega^2 + e S_\beta \Omega^2 + k_\beta\right)\beta = M_\beta + k_\beta \beta_p \tag{4.39}$$

The above equation is written in a more conventional form by replacing the time derivative with azimuthal (ψ) derivative using the chain rule and the relation, $\psi = \Omega t$. The azimuthal derivatives are conventionally denoted with a $(\star)$. The non-dimensional natural flapping frequency, ν_β, is given by

$$\nu_\beta^2 = 1 + e\frac{S_\beta}{I_\beta} + \frac{k_\beta/I_\beta}{\Omega^2} \tag{4.40}$$

Also, the non-rotating flapping frequency is given by $\omega_0^2 = k_\beta/I_\beta$. Therefore, the flapping equation of motion can be written as

$$\overset{\star\star}{\beta} + \nu_\beta^2\beta = \frac{M_\beta}{I_\beta\Omega^2} + \frac{\omega_0^2}{\Omega^2}\beta_p \tag{4.41}$$

This is a second-order ordinary differential equation. The right hand side term includes the moment caused by aerodynamic loads. This aerodynamic moment provides sufficient damping ($\overset{\star}{\beta}$ term) to stabilize the flap mode.

A common approach to integrate the flapping equation is to write it as a set of first order ordinary differential equations as described in Chapter 4.2. The system of first order ODEs can then be readily integrated as an initial value problem. For steady-state solutions, the flapping response is assumed to be periodic and the individual components are determined through harmonic balance.

4.2.2 Steady-State (Periodic) Response

Even though the main focus of this dissertation is on time-accurate rotor wake solution methodologies, a steady-state solution for the blade flapping response is also required. The relaxation approach, which is used to obtain an initial condition for the wake geometry, requires a steady-state flapping solution not only as a boundary condition for the wake, but also for calculating the trim Jacobian matrix.

The flapping moment can be calculated by assuming the vertical force is equal to the lift, i.e., $F_z \approx L$. Therefore,

$$
\begin{aligned}
M_\beta &= \int_e^R (r-e)dL && (4.42)\\
&= \int_e^R \frac{1}{2}\rho c C_{l_\alpha}\left[U_T^2\theta - U_P U_T\right](r-e)dr && (4.43)\\
&= \int_e^R \frac{1}{2}\rho c C_{l_\alpha}\Omega^2 R^2\left[\overline{U}_T^2\theta - \overline{U}_P\overline{U}_T\right](r-e)dr && (4.44)
\end{aligned}
$$

where the non-dimensional velocities at the blade element at (r,ψ) are given by

$$
\begin{aligned}
\overline{U_T} &= \frac{r}{R} + \mu\sin\psi && (4.45)\\
\overline{U_P} &= \lambda + \overset{\star}{\beta}\,\frac{r-e}{R} + \mu\beta\cos\psi && (4.46)
\end{aligned}
$$

The second term in the flapping moment contains the product $\overline{U}_P\overline{U}_T$, which is given by

$$
\overline{U}_P\overline{U}_T = \lambda\frac{r}{R} + \lambda\mu\sin\psi + \overset{\star}{\beta}\left(\frac{r(r-e)}{R^2}\right) + \beta\mu\cos\psi\left(\frac{r}{R}\right) + \overset{\star}{\beta}\,\mu\sin\psi\left(\frac{r-e}{R}\right) + \beta\mu^2\sin\psi\cos\psi \tag{4.47}
$$

To simplify this expression, each term is associated with an order of magnitude relative to an arbitrary small magnitude $O(\varepsilon)$. The flapping angle, β, the control angle, θ, and the advance ratio, μ, are assumed to be of order $O(\varepsilon)$. Therefore, the above terms are

$$
\begin{array}{l}
\overline{U}_P\overline{U}_T = \\
\begin{array}{ccccccccccc}
\lambda\frac{r}{R} & + & \lambda\mu\sin\psi & + & \overset{\star}{\beta}\,\frac{r(r-e)}{R^2} & + & \beta\mu\cos\psi\frac{r}{R} & + & \overset{\star}{\beta}\,\mu\sin\psi\frac{r-e}{R} & + & \beta\mu^2\sin\psi\cos\psi \\
 & & & & & & & & & & \\
O(\varepsilon) & & O(\varepsilon^2) & & O(\varepsilon) & & O(\varepsilon^2) & & O(\varepsilon^2) & & O(\varepsilon^3)
\end{array}
\end{array}
\tag{4.48}
$$

Based on this ordering scheme, the last three terms in the above equation can be seen to be small compared to the first two terms, which are purely aerodynamic in nature (i.e., not directly dependent on flapping angle). These terms can be neglected for simplifying the present analysis. Thus the flapping moment is given by

$$M_\beta = \int_e^R \frac{1}{2}\rho c C_{l_\alpha}\Omega^2 R^2 \left[\overline{U}_T^2\theta - \lambda\frac{r}{R} - \lambda\mu\sin\psi - \overset{\star}{\beta}\,\frac{r(r-e)}{R^2}\right](r-e)dr \quad (4.49)$$

$$= M_{\beta_A} - \int_e^R \frac{1}{2}\rho c C_{l_\alpha}\Omega^2 R^2\,\overset{\star}{\beta}\,\frac{r(r-e)^2}{R^2}dr \quad (4.50)$$

Therefore,

$$\begin{aligned}\overline{M}_\beta &= \frac{M_\beta}{I_b\Omega^2}\\ &= \frac{M_{\beta_A}}{I_b\Omega^2} - \frac{1}{2}\frac{\rho c C_{l_\alpha}R^4}{I_b}\,\overset{\star}{\beta}\int_{e/R}^1 \bar{r}(\bar{r}-e)^2 d\bar{r}\\ &= \frac{M_{\beta_A}}{I_b\Omega^2} - \frac{\gamma}{2}\,\overset{\star}{\beta}\left[\frac{1}{4} - \frac{2}{3}\left(\frac{e}{R}\right) + \frac{1}{2}\left(\frac{e}{R}\right)^2 - \frac{1}{12}\left(\frac{e}{R}\right)^4\right] \quad (4.51)\end{aligned}$$

where $\gamma = \frac{\rho c C_{l_\alpha}R^4}{I_b}$ is the Lock number. Therefore, the flapping equation can now be written as

$$\overset{\star\star}{\beta} + \frac{\gamma_2}{8}\,\overset{\star}{\beta} + \nu_\beta^2\beta = \overline{M}_{\beta_A} + \frac{\omega_0^2}{\Omega^2}\beta_p \quad (4.52)$$

where the effective Lock number is given by

$$\gamma_2 = \gamma\left[1 - \frac{8}{3}\left(\frac{e}{R}\right) + 2\left(\frac{e}{R}\right)^2 - \frac{1}{3}\left(\frac{e}{R}\right)^4\right] \quad (4.53)$$

and the non-dimensional aerodynamic flapping moment by $\overline{M}_{\beta_A} = M_{\beta_A}/\left(I_b\Omega^2\right)$. Note that $\overline{M}_{\beta_A} = \overline{M}_{\beta_A}(\psi)$. For a simplified analysis, the higher terms in e/R may be neglected.

Now, the blade flapping response can be determined using a harmonic analysis. Considering only the first harmonic, the blade flapping solution is given by

$$\beta(\psi) = \beta_0 + \beta_{1c}\cos\psi + \beta_{1s}\sin\psi \quad (4.54)$$

The flapping moment can also described by the harmonic expansion

$$\overline{M}_{\beta_A}(\psi) = \left(\overline{M}_{\beta_A}\right)_0 + \left(\overline{M}_{\beta_A}\right)_{1c} + \left(\overline{M}_{\beta_A}\right)_{1s} + \cdots \quad (4.55)$$

where the harmonic components are found by integrating the flapping moment over one rotor revolution, i.e.,

$$\left(\overline{M}_{\beta_A}\right)_0 = \frac{1}{2\pi}\int_0^{2\pi}\overline{M}_{\beta_A}\Delta\psi \tag{4.56}$$

$$\left(\overline{M}_{\beta_A}\right)_{1c} = \frac{1}{\pi}\int_0^{2\pi}\overline{M}_{\beta_A}\cos\psi\Delta\psi \tag{4.57}$$

$$\left(\overline{M}_{\beta_A}\right)_{1s} = \frac{1}{\pi}\int_0^{2\pi}\overline{M}_{\beta_A}\sin\psi\Delta\psi \tag{4.58}$$

Substituting the harmonic expansion in Eq. 4.52 and equating similar harmonic terms, the flapping solution can be written as the solution of the system of equations

$$\begin{bmatrix} \nu_\beta^2 & 0 & 0 \\ 0 & \nu_\beta^2 - 1 & \frac{\gamma_2}{8} \\ 0 & -\frac{\gamma_2}{8} & \nu_\beta^2 - 1 \end{bmatrix} \begin{Bmatrix} \beta_0 \\ \beta_{1c} \\ \beta_{1s} \end{Bmatrix} = \begin{Bmatrix} \left(\overline{M}_{\beta_A}\right)_0 + \frac{\omega_0^2}{\Omega^2}\beta_p \\ \left(\overline{M}_{\beta_A}\right)_{1c} \\ \left(\overline{M}_{\beta_A}\right)_{1s} \end{Bmatrix} \tag{4.59}$$

Therefore,

$$\beta_0 = \frac{\left(\overline{M}_{\beta_A}\right)_0 + \frac{\omega_0^2}{\Omega^2}\beta_p}{\nu_\beta^2} \tag{4.60}$$

$$\begin{Bmatrix} \beta_{1c} \\ \beta_{1s} \end{Bmatrix} = \frac{1}{\Delta}\begin{bmatrix} \nu_\beta^2 - 1 & -\frac{\gamma_2}{8} \\ \frac{\gamma_2}{8} & \nu_\beta^2 - 1 \end{bmatrix} \begin{Bmatrix} \left(\overline{M}_{\beta_A}\right)_{1c} \\ \left(\overline{M}_{\beta_A}\right)_{1s} \end{Bmatrix} \tag{4.61}$$

$$\text{where} \qquad \Delta = \left(\nu_\beta^2 - 1\right)^2 + \left(\frac{\gamma_2}{8}\right)^2 \tag{4.62}$$

In general, to include higher harmonic flapping, the solution is given by

$$\beta_0 = \frac{\left(\overline{M}_{\beta_A}\right)_0 + \frac{\omega_0^2}{\Omega^2}\beta_p}{\nu_\beta^2} \tag{4.63}$$

$$\begin{Bmatrix} \beta_{nc} \\ \beta_{ns} \end{Bmatrix} = \frac{1}{\Delta}\begin{bmatrix} \nu_\beta^2 - n^2 & -\frac{n\gamma_2}{8} \\ \frac{n\gamma_2}{8} & \nu_\beta^2 - n^2 \end{bmatrix} \begin{Bmatrix} \left(\overline{M}_{\beta_A}\right)_{nc} \\ \left(\overline{M}_{\beta_A}\right)_{ns} \end{Bmatrix} \tag{4.64}$$

where

$$\Delta = \left(\nu_\beta^2 - n^2\right)^2 + \left(\frac{n\gamma_2}{8}\right)^2 \tag{4.65}$$

Note that in the above analysis the terms containing the advance ratio, μ, are neglected and, therefore, this response is most appropriate for hovering flight, and at small advance ratios in forward flight. The original response calculation in the work of Bagai (Ref. 55) used

$$\begin{aligned}
\beta_0 &= \frac{\left(\overline{M}_{\beta_A}\right)_0 + \frac{\omega_0^2}{\Omega^2}\beta_p}{\nu_\beta^2} \\
\beta_{1c} &= -\left(\overline{M}_{\beta_A}\right)_{1s} \\
\beta_{1s} &= +\left(\overline{M}_{\beta_A}\right)_{1c}
\end{aligned} \tag{4.66}$$

which is a reasonable approximation with $e/R \approx 0$ and $\gamma_2 = \gamma \approx 8$.

Effects of Advance Ratio and Hinge Offset on Blade Flapping Response

In the preceding analysis, the advance ratio was assumed to be small enough such that terms involving product of μ and other similar small quantities were neglected. In general, all the terms in the expression for $\overline{U}_P\overline{U}_T$ in Eq. 4.47 must be included in the solution for the blade flapping motion. In this case, the flapping moment is given by

$$\begin{aligned}
M_\beta &= \int_e^R \frac{1}{2}\rho c C_{l_\alpha}\Omega^2 R^2 \left[\overline{U}^2\theta - \lambda\frac{r}{R} - \lambda\mu\sin\psi - \overset{\star}{\beta}\,\frac{r(r-e)}{R^2} - \beta\mu\cos\psi\frac{r}{R}\right. \\
&\qquad \left. - \overset{\star}{\beta}\,\mu\sin\psi\frac{r-e}{R} - \beta\mu^2\sin\psi\cos\psi\right](r-e)dr \\
&= M_{\beta_A} - \int_e^R \frac{1}{2}\rho c C_{l_\alpha}\Omega^2 R^2 \left[\overset{\star}{\beta}\,\frac{r(r-e)^2}{R^2} + \beta\mu\cos\psi\frac{r(r-e)}{R}\right. \\
&\qquad \left. + \overset{\star}{\beta}\,\mu\sin\psi\frac{(r-e)^2}{R} + \beta\mu^2\sin\psi\cos\psi(r-e)\right]dr
\end{aligned} \tag{4.67}$$

Therefore,

$$\begin{aligned}
\overline{M}_\beta &= \frac{M_\beta}{I_b\Omega^2} \\
&= \frac{M_{\beta_A}}{I_b\Omega^2} - \frac{1}{2}\frac{\rho c C_{l_\alpha} R^4}{I_b}\int_{e/R}^{1}\Big[\overset{\star}{\beta}\,\bar{r}(\bar{r}-\bar{e})^2 + \beta\mu\cos\psi\,\bar{r}(\bar{r}-\bar{e}) \\
&\qquad + \overset{\star}{\beta}\,\mu\sin\psi(\bar{r}-\bar{e})^2 + \beta\mu^2\sin\psi\cos\psi(\bar{r}-\bar{e})\Big]\,d\bar{r} \\
&= \frac{M_{\beta_A}}{I_b\Omega^2} - \frac{\gamma_1}{6}\beta\mu\cos\psi - \frac{\gamma_2}{8}\overset{\star}{\beta} - \frac{\gamma_3}{6}\overset{\star}{\beta}\,\mu\sin\psi - \frac{\gamma_4}{8}\beta\mu^2\sin 2\psi
\end{aligned} \tag{4.68}$$

where

$$\frac{\gamma_1}{\gamma} = \left[1 - \frac{3}{2}\left(\frac{e}{R}\right) + \frac{1}{2}\left(\frac{e}{R}\right)^3\right] \tag{4.69}$$

$$\frac{\gamma_2}{\gamma} = \left[1 - \frac{8}{3}\left(\frac{e}{R}\right) + 2\left(\frac{e}{R}\right)^2 - \frac{1}{3}\left(\frac{e}{R}\right)^4\right] \tag{4.70}$$

$$\frac{\gamma_3}{\gamma} = \left[1 - 3\left(\frac{e}{R}\right) + 3\left(\frac{e}{R}\right)^2 - \left(\frac{e}{R}\right)^4\right] \tag{4.71}$$

$$\frac{\gamma_4}{\gamma} = \left[1 - 2\left(\frac{e}{R}\right) + \left(\frac{e}{R}\right)^2\right] \tag{4.72}$$

Now the flapping equation reduces to

$$\overset{\star\star}{\beta} + \nu_\beta^2\beta + \frac{\gamma_1}{6}\beta\mu\cos\psi + \frac{\gamma_2}{8}\overset{\star}{\beta} + \frac{\gamma_3}{6}\overset{\star}{\beta}\,\mu\sin\psi + \frac{\gamma_4}{8}\beta\mu^2\sin 2\psi = \overline{M}_{\beta_A} + \frac{\omega_0^2}{\Omega^2}\beta_p \tag{4.73}$$

Assuming only first harmonic flapping, the last term on the LHS of the above equation can be expanded using

$$\begin{aligned}
\beta\sin 2\psi &= \beta_0\sin 2\psi + \beta_{1c}\cos\psi\sin 2\psi + \beta_{1s}\sin\psi\sin 2\psi \\
&= \beta_0\sin 2\psi + \frac{1}{2}\beta_{1c}(\sin\psi + \sin 3\psi) + \frac{1}{2}\beta_{1s}(\cos\psi - \cos 3\psi)
\end{aligned} \tag{4.74}$$

Therefore, the flapping equation can now be written in the form of a set of three equations by equating the first harmonics, i.e.,

$$\begin{bmatrix} \nu_\beta^2 & \frac{\mu}{12}(\gamma_1-\gamma_3) & 0 \\ \frac{\gamma_1}{6}\mu & \nu_\beta^2-1 & \frac{\gamma_2}{8}+\mu^2\frac{\gamma_4}{16} \\ 0 & -\frac{\gamma_2}{8}+\mu^2\frac{\gamma_4}{16} & \nu_\beta^2-1 \end{bmatrix} \begin{Bmatrix} \beta_0 \\ \beta_{1c} \\ \beta_{1s} \end{Bmatrix} = \begin{Bmatrix} \left(\overline{M}_{\beta_A}\right)_0+\frac{\omega_0^2}{\Omega^2}\beta_p \\ \left(\overline{M}_{\beta_A}\right)_{1c} \\ \left(\overline{M}_{\beta_A}\right)_{1s} \end{Bmatrix} \tag{4.75}$$

Substituting for the value of β_0 from the first equation into the second equation,

$$\begin{bmatrix} \nu_\beta^2 & \frac{\mu}{12}(\gamma_1-\gamma_3) & 0 \\ 0 & \nu_\beta^2-1-\frac{\mu^2}{\nu_\beta^2}\frac{\gamma_1}{72}(\gamma_1-\gamma_3) & \frac{\gamma_2}{8}+\mu^2\frac{\gamma_4}{16} \\ 0 & -\frac{\gamma_2}{8}+\mu^2\frac{\gamma_4}{16} & \nu_\beta^2-1 \end{bmatrix} \begin{Bmatrix} \beta_0 \\ \beta_{1c} \\ \beta_{1s} \end{Bmatrix} = \begin{Bmatrix} \left(\overline{M}_{\beta_A}\right)_0+\frac{\omega_0^2}{\Omega^2}\beta_p \\ \left(\overline{M}_{\beta_A}\right)_{1c}-\frac{\gamma_1}{6}\frac{\mu}{\nu_\beta^2}\left(\overline{M}_{\beta_A}\right)_0 \\ \left(\overline{M}_{\beta_A}\right)_{1s} \end{Bmatrix} \tag{4.76}$$

Now the β_{1c} and $\beta 1s$ equations are decoupled from the β_0 equation, and can be readily solved. The solution is given by

$$\beta_{1c} = \frac{1}{\Delta}\left[(\nu_\beta^2-1)\left(\left(\overline{M}_{\beta_A}\right)_{1c}-\frac{\gamma_1}{6}\frac{\mu}{\nu_\beta^2}\left(\overline{M}_{\beta_A}\right)_0\right)-\left(\frac{\gamma_2}{8}+\mu^2\frac{\gamma_4}{16}\right)\left(\overline{M}_{\beta_A}\right)_{1s}\right] \tag{4.77}$$

$$\begin{aligned} \beta_{1s} = \frac{1}{\Delta}\Bigg[&\left(\frac{\gamma_2}{8}-\mu^2\frac{\gamma_4}{16}\right)\left(\left(\overline{M}_{\beta_A}\right)_{1c}-\frac{\gamma_1}{6}\frac{\mu}{\nu_\beta^2}\left(\overline{M}_{\beta_A}\right)_0\right) \\ &+\left(\nu_\beta^2-1-\frac{\mu^2}{\nu_\beta^2}\frac{\gamma_1}{72}(\gamma_1-\gamma_3)\right)\left(\overline{M}_{\beta_A}\right)_{1s}\Bigg] \end{aligned} \tag{4.78}$$

where

$$\Delta = \left(\nu_\beta^2-1^2\right)^2+\left(\frac{\gamma_2}{8}\right)^2-\left(\mu^2\frac{\gamma_4}{16}\right)^2+\frac{\mu^2}{\nu_\beta^2}\frac{\gamma_1}{72}(\gamma_1-\gamma_3)\left(\nu_\beta^2-1\right) \tag{4.79}$$

and

$$\beta_0 = \frac{\left(\overline{M}_{\beta_A}\right)_0+\frac{\omega_0^2}{\Omega^2}\beta_p}{\nu_\beta^2}-\frac{\mu(\gamma_1-\gamma_3)}{12\nu_\beta^2}\beta_{1c} \tag{4.80}$$

For the case of zero hinge-offset, the above equations reduce to a relatively simpler form as given by

$$\beta_0 = \frac{(\overline{M}_{\beta_A})_0 + \frac{\omega_0^2}{\Omega^2}\beta_p}{\nu_\beta^2} \tag{4.81}$$

$$\beta_{1c} = -\frac{1}{1-\mu^2/2}\left[\frac{8}{\gamma}(\overline{M}_{\beta_A})_{1s}\right] \tag{4.82}$$

$$\beta_{1s} = \frac{1}{1+\mu^2/2}\left[\frac{8}{\gamma}(\overline{M}_{\beta_A})_{1c} - \frac{4}{3}\mu(\overline{M}_{\beta_A})_0\right] \tag{4.83}$$

4.2.3 Time-Integration of Blade Flapping Equations

The transient rotor response couples blade flapping and the wake evolution. Therefore, it is necessary to integrate the blade flapping equation of motion coupled with the wake equations. The equation of motion of a flapping blade is given by the equilibrium of moments about the flapping hinge, as derived in Section 4.2.1. For a rigid rotor blade this is given by

$$\overset{\star\star}{\beta} + \nu_\beta^2\beta = \frac{M_\beta}{I_\beta\Omega^2} + \frac{\omega_0^2}{\Omega^2}\beta_p \tag{4.84}$$

where the $\overset{\star}{(\;)}$ denotes a derivative with the blade azimuth, ψ, and ν_β is the non-dimensional flap frequency. The moment on the RHS of Eq. 4.84 includes the aerodynamic flapping moment as given by

$$M_\beta = \int_e^R dL\,(r-e) \tag{4.85}$$

where dL is the elemental lift on a spanwise blade element. As mentioned previously, the blade flapping motion constitutes a boundary condition for the rotor wake equations. Therefore, Eq. 4.84 must solved with the wake equations in a properly coupled manner.

The second-order flapping equation of motion (Eq. 4.84) is reduced to a set of first-order equations. This set of equations can then be solved using various standard integration methods. The proposed second-order backward time-integration algorithm for the wake equations is also used for solving these equations. The results are then compared with other algorithms to demonstrate solution convergence obtained using the present algorithm. It must be noted that the flapping equations do not contain an explicit damping term ($\overset{\star}{\beta}$), however, the aerodynamic damping present in the flapping moment, M_β, provides sufficient stability to the solution.

To reduce the flapping equation to a first order system, Eq. 4.84 is rewritten in a matrix form with two variables β and $\overset{\star}{\beta}$,

$$\frac{d}{d\psi}\left\{\begin{matrix} \overset{\star}{\beta} \\ \beta \end{matrix}\right\} + \begin{bmatrix} \nu_\beta^2 & 0 \\ 0 & 1 \end{bmatrix} \left\{\begin{matrix} \overset{\star}{\beta} \\ \beta \end{matrix}\right\} = \left\{\begin{matrix} \dfrac{M_\beta}{I_\beta \Omega^2} + \dfrac{\omega_0^2}{\Omega^2}\beta_p \\ 0 \end{matrix}\right\} \tag{4.86}$$

which can be written in the general form

$$\overset{\star}{Y} + [M]Y = f(Y(\psi), \psi) \tag{4.87}$$

or

$$\overset{\star}{Y} = F(Y(\psi), \psi) \tag{4.88}$$

A number of methods were then examined to integrate the above equations. The stability and accuracy considerations applied to the wake governing equations in the preceding section were also applied to the blade flapping equations. Note that Eq. 4.88 is mathematically the same as Eq. 3.31. Therefore, the same algorithm (PC2B) used for the wake equations was used for blade flapping and a separate analysis is omitted. For the sake of completion, a simple test problem is presented here to verify the accuracy of the numerical algorithms used.

The aerodynamic flapping moment is specified as a periodic function of the form

$$M_\beta(\psi) = M_0 + M_{1c} \cos\psi + M_{1s} \sin\psi \tag{4.89}$$

A harmonic balance on the flapping equation, as performed in the previous section, shows that the resulting blade flapping angles would also follow a similar cyclic variation with a constant coning angle (β_0) and cyclic flapping angles (β_{1c} and β_{1s}), i.e.,

$$\beta(\psi) = \beta_0 + \beta_{1c} \cos\psi + \beta_{1s} \sin\psi \tag{4.90}$$

where the coefficients β_0, β_{1c}, and β_{1s} can be related to the aerodynamic moment as

$$\begin{aligned} \beta_0 &= \frac{M_0}{\nu_\beta^2} && (4.91) \\ \beta_{1c} &= \frac{M_{1c}}{\nu_\beta^2 - 1} && (4.92) \\ \beta_{1s} &= \frac{M_{1s}}{\nu_\beta^2 - 1} && (4.93) \end{aligned}$$

Note that in reality the aerodynamic flapping moment provides a significant damping to the blade flapping motion. However, the flapping moment considered in this test problem contains no damping terms. Such a problem is interesting for examining the stability of numerical integration methods. The rotor flapping frequency is assumed to be constant at $\nu_\beta = 1.1$, which corresponds to a rectangular blade with the flap hinge located at 14% radius. The flapping moment is assumed to have the form given by Eq. 4.89 with

$$\begin{aligned} M_0 &= 5^\circ \nu_\beta^2 \\ M_{1c} &= 0 \\ M_{1s} &= 1.5^\circ \left(\nu_\beta^2 - 1\right) \end{aligned} \tag{4.94}$$

Using Eqs. 4.91-4.93 this should result in a cyclic flapping motion with $\beta_0 = 5.0°$ and $\beta_{1s} = 1.5°$.

The results obtained using numerical integration methods are shown in Figure 4.8(a). The representive methods used for these solutions are explicit Euler, implicit Euler, RK2, RKN, AM4 and the proposed 2nd-order backward method. The flapping integration was continued for 100 time-periods ($\psi = 200\pi$) to verify the solution remains free from accumulation of numerical errors leading to instabilities. Except for the Euler explicit method, all the other solutions show the expected cyclic behavior.

The convergence trends are shown in Figure 4.8(b) in the form of the numerical error versus discretization. The Euler explicit method does not exhibit the expected first-order accuracy because the solution becomes unstable, albeit mildly. The Euler implicit solution exhibits convergence with a first-order, while the PC2B (2nd-order backward) method exhibits a second-order convergence. For this simple test case the AM4 method showed the expected fourth-order accuracy. However, as shown earlier, this method may be unsuitable for wake solutions involving high frequency modes where the numerical method becomes mildly unstable.

Teetering/Gimbaled Rotors

For an articulated or hingeless rotor hub, the flapping motion of each individual blade is governed by the flapping equation as derived in the previous section. A teetering two-bladed hub design or a gimbaled hub design requires some special considerations. This is because, by the nature of the gimbal joint, the flapping motions of different blades are coupled together. Therefore, the equilibrium of flapping moment for each blade is depends on all other blades, and the blade flapping solution must be rederived.

(a) Blade flapping solution

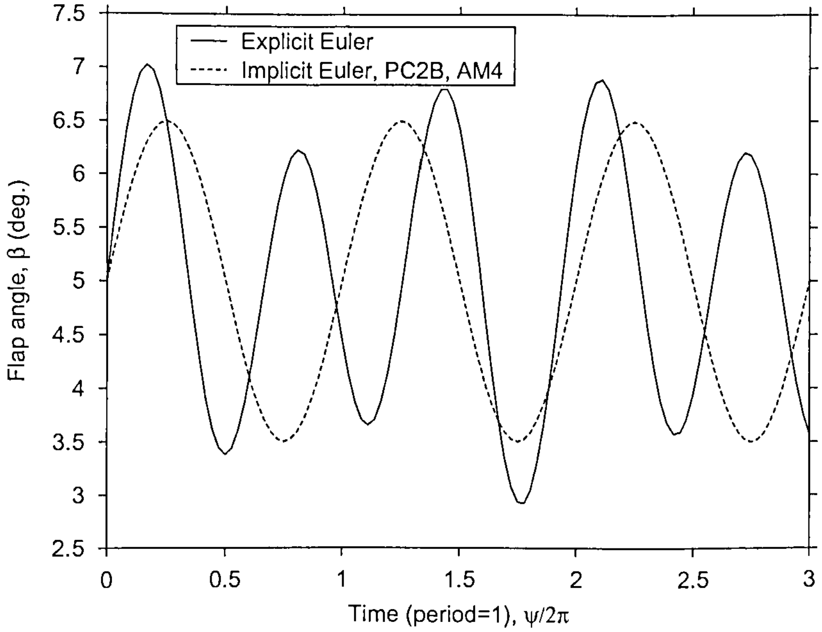

(b) RMS error showing convergence

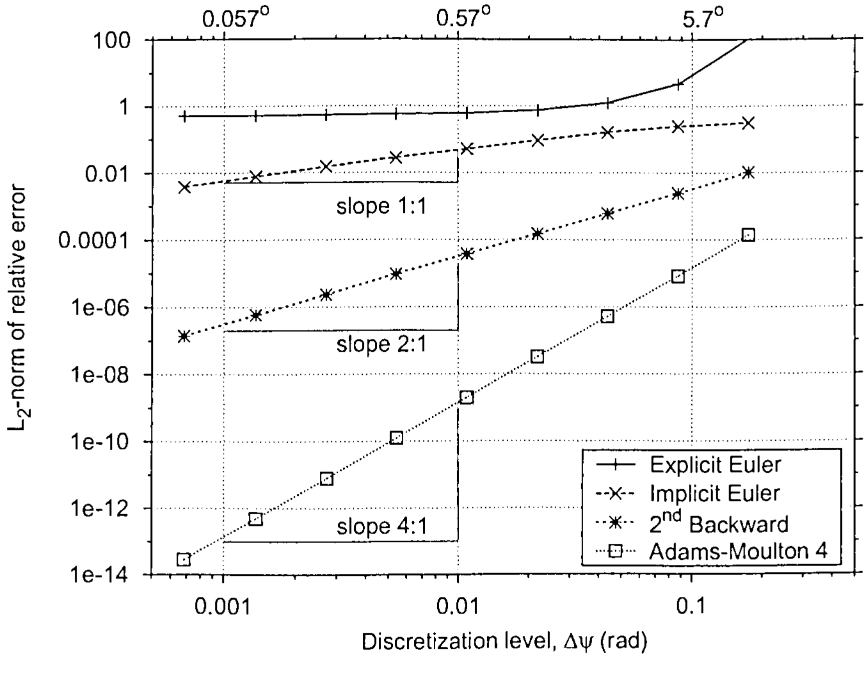

Figure 4.8: Time-integration of blade flapping response with constant (periodic) moment. (a) Blade flapping solution, (b) RMS error showing convergence.

4.2.4 Periodic Solution for a Teetering/Gimbaled Rotor

In this case, the rotor blades flapping motion is similar to a rigid disk flapping about a gimbaled joint. The equivalent flapping moments are calculated for a reference blade, say blade 1, and the flapping equation is solved using harmonic balance for this reference blade. Note that in this case, the flapping moments from all blades have a component in the direction of flapping for the reference. This is schematically shown in Fig. 4.9

Let $M_\beta^{(m)}$ denote the net flapping moment on the m^{th} blade because of that blade itself. Unlike articulated rotors, the flapping moments because of this blade also has a component $M_\beta^{(m)} \cos\psi_m$ in the direction of the flapping moment of the reference blade – see Fig. 4.9 for the notation. The net flapping moment, for each blade is a combination of inertia, centrifugal and the aerodynamic flapping moments, i.e.,

$$\begin{aligned} M_\beta &= \overset{\star\star}{\beta} + \nu_\beta^2\beta + \frac{\gamma_1}{6}\beta\mu\cos\psi + \frac{\gamma_2}{8}\overset{\star}{\beta} + \frac{\gamma_3}{6}\overset{\star}{\beta}\mu\sin\psi - \overline{M}_{\beta_A} - \frac{\omega_0^2}{\Omega^2}\beta_p \\ &= 0 \qquad \text{for equilibrium} \end{aligned} \tag{4.95}$$

Note that the above equation is same as Eq. 4.73 with the higher harmonic μ^2 term being neglected for simplicity. Now, consider the equilibrium of flapping moments for the reference blade. Because of our periodicity assumption, the flapping solution for all other blades is the same as the flapping solution for the reference blade. Therefore, the equivalent blade flapping moment can be written as

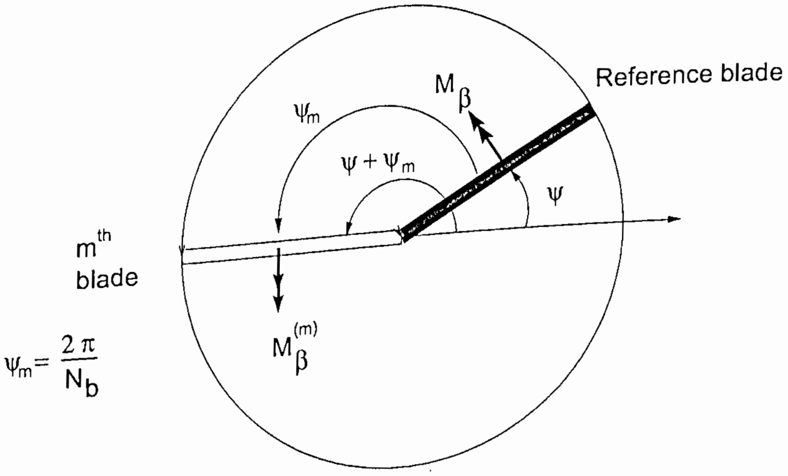

Figure 4.9: Schematic showing equivalent flapping moments experienced by a reference blade.

$$
\begin{aligned}
M_\beta^{eq} &= \sum_{m=1}^{N_b} M_\beta^{(m)} \cos\psi_m \\
&= \sum_{m=1}^{N_b} \Big[\overset{\star\star}{\beta}(\psi+\psi_m) + \nu_\beta^2 \beta(\psi+\psi_m) + \frac{\gamma_1}{6}\beta(\psi+\psi_m)\mu\cos(\psi+\psi_m) \\
&\quad + \frac{\gamma_2}{8}\overset{\star}{\beta}(\psi+\psi_m) + \frac{\gamma_3}{6}\overset{\star}{\beta}(\psi+\psi_m)\mu\sin(\psi+\psi_m) - \overline{M}_{\beta_A}^{(m)} \Big] \cos\psi_m \qquad (4.96) \\
&\quad - \frac{\omega_0^2}{\Omega^2}\beta_p
\end{aligned}
$$

Note that if a flapping spring is used with a teetering/gimbaled rotor, it is not summed over the number of blades. The flapping solution for the reference blade is assumed to be of the form,

$$
\beta^{ref}(\psi) = \beta_{1c}\cos\psi + \beta_{1s}\sin\psi \qquad (4.97)
$$

The flapping motion of other blades has the same form with the corresponding azimuth

$$
\beta^{(m)}(\psi) = \beta^{ref}(\psi + \psi_m) \qquad (4.98)
$$

Now, consider the $\nu^2\beta$ term in the summation in Eq. 4.96, i.e.,

$$\begin{aligned}
\sum_{m=1}^{N_b} \nu_\beta^2 \beta^{(m)}(\psi)\cos\psi_m &= \nu_\beta^2 \sum_{m=1}^{N_b} \beta^{ref}(\psi+\psi_m)\cos\psi_m \\
&= \nu_\beta^2 \sum_{m=1}^{N_b} \left[\beta_{1c}\cos(\psi+\psi_m)+\beta_{1s}\sin(\psi+\psi_m)\right]\cos\psi_m \\
&= \nu_\beta^2 \sum_{m=1}^{N_b} [\beta_{1c}(\cos\psi\cos\psi_m - \sin\psi\sin\psi_m) \\
&\qquad +\beta_{1s}(\sin\psi\cos\psi_m + \cos\psi\sin\psi_m)]\cos\psi_m \\
&= \nu_\beta^2 \sum_{m=1}^{N_b} \left[\beta_{ref}(\psi)\cos^2\psi_m + (\cdots)\sin\psi_m\cos\psi_m\right] \\
&= \frac{N_b}{2}\nu_\beta^2\beta_{ref}(\psi) \qquad (4.99)
\end{aligned}$$

Similarly, other terms in Eq. 4.96 can be simplified to give

$$M_\beta^{eq} = \frac{N_b}{2}\left[\overset{\star\star}{\beta} + \frac{\gamma_2}{8}\overset{\star}{\beta} + \nu_\beta^2\beta\right] - \frac{\omega_0^2}{\Omega^2}\beta_p - \sum_{m=1}^{N_b} M_\beta^{(m)}\cos\psi_m \overline{M}_{\beta_A} \qquad (4.100)$$

Therefore, the equilibrium equation has the same form as that of the flapping equation for the individual blades (Eq. 4.52), i.e.,

$$\overset{\star\star}{\beta} + \frac{\gamma_2}{8}\overset{\star}{\beta} + \nu_\beta^2\beta = \overline{M}_{\beta_A}^{eq} + \frac{\omega_0^{eq\,2}}{\Omega^2}\beta_p \qquad (4.101)$$

where an equivalent aerodynamic flapping moment for a reference blade defined as

$$M_{\beta_A}^{eq} = \frac{2}{N_b}\sum_{m=1}^{N_b} M_{\beta_A}^{(m)}\cos\psi_m \qquad (4.102)$$

with

$$\psi_m = \frac{2\pi}{N_b}(m-1) \qquad (4.103)$$

and the equivalent non-rotating flapping frequency

$$\omega_0^{eq\,2} = \frac{2}{N_b}\omega_0^2 \qquad (4.104)$$

With these definitions, the flapping equation can be readily integrated as described in the previous section. Note that for a two-bladed rotor, the expression for the equivalent aerodynamic flapping moment changes to

$$M_{\beta_A}^{eq} = \frac{1}{2} \sum_{m=1}^{N_b} M_{\beta_A}^{(m)} \cos\psi_m \tag{4.105}$$

and similarly for the equivalent non-rotating flapping frequency.

4.2.5 Time-Integration of Blade Flapping Equation for a Gimbaled/Teetering Rotor

The flapping equation of motion for each blade is given by

$$\overset{**}{\beta} + \nu_\beta^2 \beta = \overline{M}_\beta \tag{4.106}$$

where ν_β is the non-dimensional flapping frequency. For a articulated or a hingeless rotor (with an equivalent hinge offset and stiffness) this equation is integrated for each individual blade. For teetering or gimbaled rotors, the motion of different blades is inherently coupled to each other. For a teetering two-bladed rotor, the flapping angles of the two blades are always equal and opposite. A gimbaled rotor behaves as if it were a rigid circular disk with a three dimensional hinge at its center. The Fourier coordinate transformation (FCT), also known as multi-blade coordinate transformation, is used to solve for these special rotor configurations.

Two-Bladed Teetering Rotor

For time integration of the flapping equation of motion at ψ, first the flapping moment on each blade is calculated at the azimuthal step $(\psi - \Delta\psi)$. In this case, blade 1 is at $(\psi - \Delta\psi)$ while blade 2 is at $(\psi - \Delta\psi + \pi)$. Now, a FCT of the flapping angles, rates and flapping moments is performed to give those quantities in the non-rotating frame. For a two-bladed rotor this gives

$$\beta_0 = \frac{1}{2}\left[\beta^{(1)} + \beta^{(2)}\right] \tag{4.107}$$

$$\beta_1 = \frac{1}{2}\left[-\beta^{(1)} + \beta^{(2)}\right] \tag{4.108}$$

The FCT of $\overset{\star}{\beta}$ and $\overline{M}_\beta$ is also calculated in the similar manner. Note that in this case the flapping moment on the right hand side also contains motion dependent $(\beta, \overset{\star}{\beta})$ terms.

The FCT of the governing equation for each flapping blade has the same form as Eq. 4.106, i.e.,

$$\overset{\star\star}{\beta}_1 + \nu_\beta^2 \beta_1 = \overline{M}_{\beta_1} \tag{4.109}$$

The coning or collective flapping angle, β_0, is identically equal to zero. Therefore, only one equation in β_1 is integrated in time. After integrating the transformed quantities, the flapping angles for individual blades are reconstructed using the inverse FCT relations, i.e.,

$$\beta^{(1)} = -\beta_1 \qquad \beta^{(2)} = \beta_1 \tag{4.110}$$

$$\overset{\star}{\beta}^{(1)} = -\overset{\star}{\beta}_1 \qquad \overset{\star}{\beta}^{(2)} = \overset{\star}{\beta}_1 \tag{4.111}$$

Gimbaled Rotor

For a gimbaled rotor, there are two degrees of freedom, β_{1c} and β_{1s}. Therefore, in the FCT transformed set of equations are solved for the first harmonic components β_{1c} and β_{1s}. Again, the coning as sell as other harmonics are identically zero. The FCT relations in this case are given by

$$\beta_{1c} = \frac{2}{N_b}\sum_{m=1}^{N_b} \beta^{(m)} \cos\psi_m \tag{4.112}$$

$$\beta_{1s} = \frac{2}{N_b}\sum_{m=1}^{N_b} \beta^{(m)} \sin\psi_m \tag{4.113}$$

$$\overset{\star}{\beta}_{1c} = \frac{2}{N_b}\sum_{m=1}^{N_b} \left[\overset{\star}{\beta}^{(m)} \cos\psi_m - \beta^{(m)} \sin\psi_m\right] \tag{4.114}$$

$$\overset{\star}{\beta}_{1s} = \frac{2}{N_b}\sum_{m=1}^{N_b} \left[\overset{\star}{\beta}^{(m)} \sin\psi_m + \beta^{(m)} \cos\psi_m\right] \tag{4.115}$$

The FCT of the flapping moment, $\overline{M}_\beta$ is calculated in the same manner as β.

Note that in this case, the transformed governing equations are different from the original flapping equations (Eq. 4.106). The transformed equations are given by

$$\frac{2}{N_b}\sum_{m=1}^{N_b} (\text{Eq. 4.106}) \cos\psi_m \Rightarrow \overset{\star\star}{\beta}_{1c} + 2\overset{\star}{\beta}_{1s} + \left(\nu_\beta^2 - 1\right)\beta_{1c} = \overline{M}_{1c} \tag{4.116}$$

$$\frac{2}{N_b}\sum_{m=1}^{N_b} (\text{Eq. 4.106}) \sin\psi_m \Rightarrow \overset{\star\star}{\beta}_{1s} - 2\overset{\star}{\beta}_{1c} + \left(\nu_\beta^2 - 1\right)\beta_{1s} = \overline{M}_{1s} \tag{4.117}$$

Although the original equations are decoupled, the two equations in the non-rotating frame are coupled through the flapping damping term. To integrate these coupled equations the same approach as the the rotating-frame equations is followed. The equations are written in the form of a system of ODEs,

$$\frac{d}{d\psi}\begin{Bmatrix} \overset{\star}{\beta}_{1c} \\ \overset{\star}{\beta}_{1s} \\ \beta_{1c} \\ \beta_{1s} \end{Bmatrix} + \begin{bmatrix} 0 & 2 & \nu_\beta^2 - 1 & 0 \\ -2 & 0 & 0 & -\nu_\beta^2 - 1 \\ 1 & 0 & 0 & 0 \\ 0 & 1 & 0 & 0 \end{bmatrix} \begin{Bmatrix} \overset{\star}{\beta}_{1c} \\ \overset{\star}{\beta}_{1s} \\ \beta_{1c} \\ \beta_{1s} \end{Bmatrix} = \begin{Bmatrix} \overline{M}_{1c} \\ \overline{M}_{1s} \\ 0 \\ 0 \end{Bmatrix} \tag{4.118}$$

This can be written in the form of a generic ODE, i.e.,

$$\overset{\star}{Y} + [M]Y = f \tag{4.119}$$

or

$$\overset{\star}{Y} = F\,(Y,\psi) \tag{4.120}$$

This can be readily integrated in time (blade azimuth) using the same algorithm used for the rotor wake or the individual blade flapping equations (see Sections 3.2.2 & 4.2.3).

Finally, the rotating frame flapping angles and rates are reconstructed using inverse FCT relations

$$\begin{aligned} \beta^{(m)} &= \beta_{1c}\cos\psi_m + \beta_{1s}\sin\psi_m && (4.121) \\ \overset{\star}{\beta}_{(m)} &= \left(\overset{\star}{\beta}_{1c} + \beta_{1s}\right)\cos\psi_m + \left(\overset{\star}{\beta}_{1s} - \beta_{1c}\right)\sin\psi_m && (4.122) \end{aligned}$$

4.3 Summary

This chapter has focused on two sub-systems of the rotor problem, which are solved together with the wake equations. As mentioned in the Introduction (Section 1.1), the three sets of equations describing the free-vortex wake, the blade flapping motion, and the blade lift, are highly inter-dependent, and must be solved in a properly coupled manner.

The Weissinger-L method used for the lift solution is a reduced-order lifting surface method with only one chord-wise panel. The Weissinger-L solution for blade bound circulation is related to the blade lift through an application of the Kutta-Joukowski theorem. Although the theoretical basis for the model is inviscid incompressible flow, compressibility and viscous effects can be included using an empirical airfoil lift and drag model.

The equation for blade flapping motion was derived assuming a rigid blade with a flapping hinge. For consistency, a periodic solution was used with the steady-state (relaxation) wake methodology, whereas a time-integration strategy was used with the time-accurate wake. The flapping equation is written in the same form as the wake governing equations, and solved using the same algorithm. A verification of solution accuracy was performed, but a detailed analysis of stability was omitted because it is similar, in principle, to the stability analysis in Chapter 3. The special considerations necessary to model teetering/gimbaled rotor hubs have also been described in detail.

Chapter 5

Results & Discussion: Steady-State Wake Model

In the previous chapters, the numerical methodology for the rotor wake problem was examined using mathematical concepts of accuracy and convergence. In this chapter, the results obtained using the methodology are validated against experimental measurements. This serves to validate the physical aspects of the modeling involved in the present work. First, the steady-state wake geometry results are presented because steady-state experimental results are easier to obtain than unsteady (time-dependent) measurements. Also, as it was shown previously, the time-accurate solution approaches the same steady-state solution after sufficiently long time (rotor revolutions). Therefore, the validation studies presented in this chapter are equally applicable to the time-accurate solution methodology.

5.1 Small Scale Rotors in Hover

In this section, the predictions obtained using the free-vortex wake analysis are validated using measurements performed at University of Maryland (Ref. 72). In these experiments, the wakes generated by one- and two-bladed teetering rotors were examined. These rotors were small-scale with a nominal tip Mach number of 0.3. The wake geometry was documented using flow visualization, while the velocity field measurements were performed using laser Doppler velocimetry (Refs. 89, 90). The rotor geometry and operating conditions for the two rotor configurations are summarized in Table 5.1

Table 5.1: Operating conditions for the two rotor configurations.

Rotor	One-bladed	Two-bladed
Number of blades, N_b	1	2
Rotational speed, Ω	2100 rpm, 35 Hz	2010 rpm, 33.5 Hz
Blade radius, R	406.4 mm	406.4 mm
Blade chord, c	42.5 mm	42.5 mm
Collective pitch, θ_0	4°	5°
Thrust coefficient, C_T	0.003	0.006
Blade loading, C_T/σ	0.09	0.09

Predictions of the rotor wake geometry obtained using the present analysis are shown in Fig. 5.1, along with the experimental measurements obtained using light sheet flow visualization. The free-vortex wake results in this section were calculated using a discretization level of $\Delta\psi = \Delta\zeta = 5°$. Figure 5.1(a) shows results for the one-bladed rotor, where a good agreement is found between the predictions and the measurements. Figure 5.1(b) shows similar results for the two-bladed rotor. In the flow visualization results only the tip vortex geometry from one reference rotor blade is shown. The tip vortex locations for the second blade are identical (symmetric) by virtue of wake periodicity. Again, the free-vortex wake predictions show a good agreement with the experimental observations.

(a) One-bladed rotor, $C_T = 0.0025$

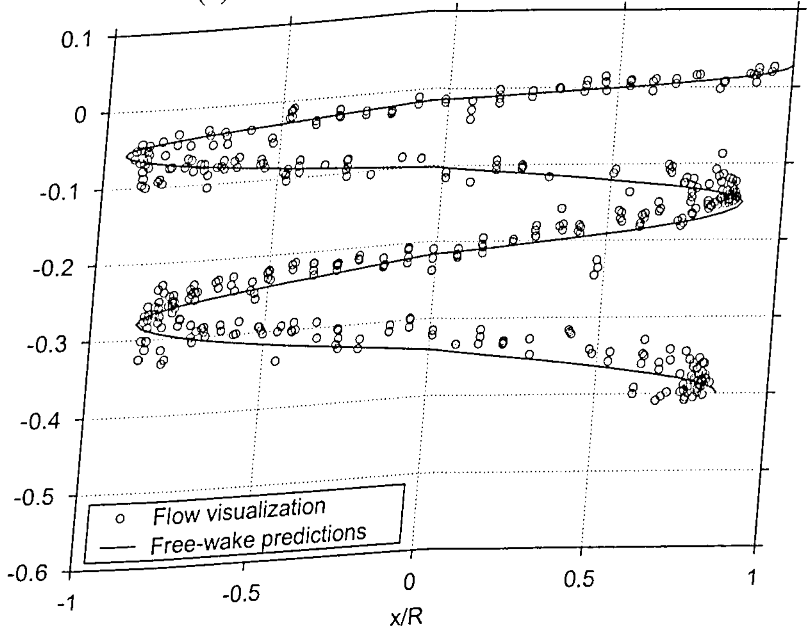

(b) Two-bladed rotor, $C_T = 0.005$

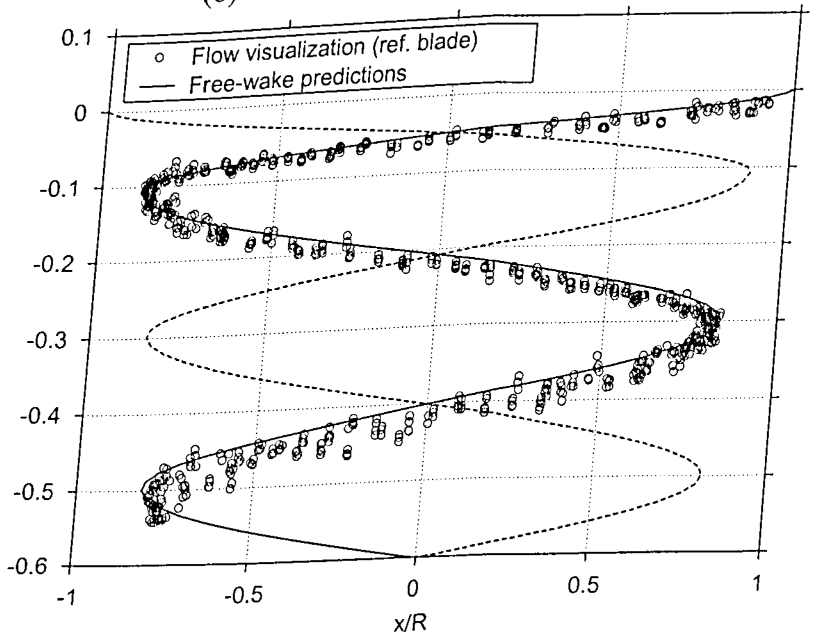

Figure 5.1: Tip vortex geometry predicted using the free-vortex wake analysis along with experimental measurements. (a) One-bladed rotor, $C_T = 0.0025$, (b) Two-bladed rotor, $C_T = 0.005$. Experimental results from Ref. 89.

The time-averaged rotor induced inflow, i.e., the averaged velocity in the TPP, was also measured. These results are shown in Fig. 5.2 for the two rotors. The inflow was found to have an almost linear distribution over most of the blade span. This is expected because the rotor blades are rectangular and untwisted. The free-vortex wake predictions predict this basic trend very well. Near the blade tips, a small upwash induced velocity was measured in the experiments. This is because of the contracting vortical wake below the rotor. Because the wake geometry was accurately predicted by the free-vortex wake analysis, this effect is also predicted well.

The blade bound circulation was also derived in these experiments using a contour integration technique using the velocity field measurements (Ref. 89). It was found that for the one-bladed rotor, the bound circulation was independent of the choice of contour, and was representive of the blade lift through application of the Kutta-Joukowski theorem. The blade lift derived in this manner from the experimental measurements is shown in Fig. 5.3 in the form of $C_l M^2$. The free-vortex wake predictions show a good agreement with the measurements, especially in terms of location and magnitude of the maximum lift. The approximately linear lift distribution along the span is also expected based on simple blade-element considerations for untwisted, rectangular blades.

Figure 5.4 shows similar spanwise lift distribution for the two-bladed rotor. In this case, the free-vortex wake predictions were found to be significantly different from the experimental measurements. It was suggested in Ref. 89 that because of the interference effects of closely spaced tip vortex filaments, these bound circulation measurements may not be representive of blade-lift for the two-bladed rotor. The measured values for the one-bladed rotor are also shown as a reference. The one- and two-bladed were operated at almost the same blade loading. Therefore, each blade

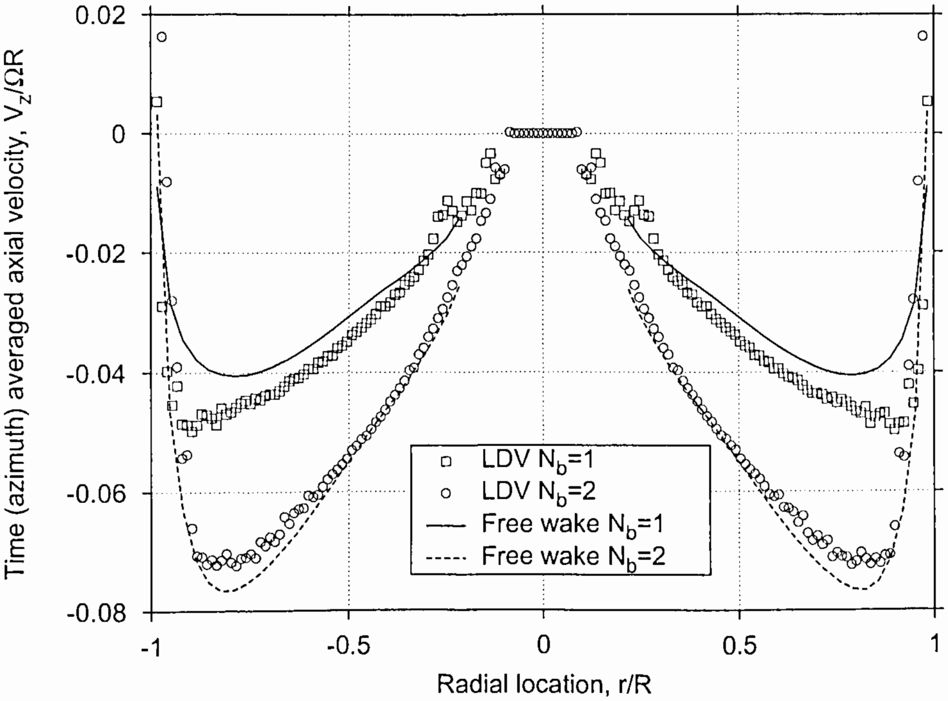

Figure 5.2: Time-averaged rotor induced inflow distribution: LDV measurements and free-vortex wake predictions. Experimental results from Ref. 72.

of the two-bladed rotor would generate a loading distribution essentially the same as that for the one-bladed rotor. It is interesting to note that the lift prediction using the free-vortex wake analysis shows the same trend as that for both one- and two-bladed rotors. This confirms that the measurements of bound circulation for the two-bladed rotor are not representive of the blade lift, as suggested in Ref. 89.

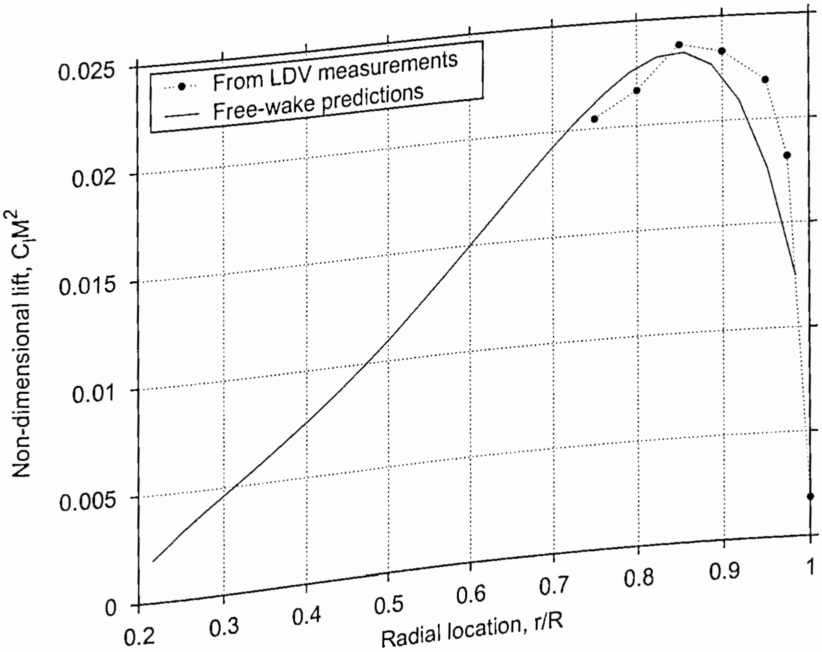

Figure 5.3: Non-dimensional spanwise lift distribution for the one-bladed rotor. Experimental values are derived from bound circulation measurements from Ref. 89.

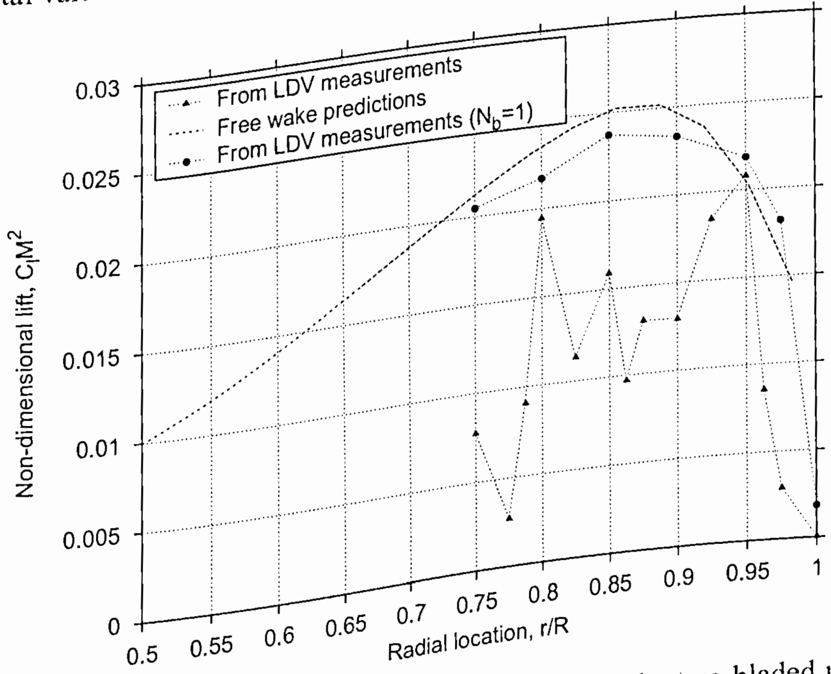

Figure 5.4: Non-dimensional spanwise lift distribution for the two-bladed rotor. Experimental values are derived from bound circulation measurements from Ref. 89.

5.2 Mach-Scaled Rotors: Hover & Forward Flight

5.2.1 Wake Geometry

In this section, the steady-state predictions obtained using the free-vortex wake analysis are compared with experimental results for Mach-scaled rotors. Comparisons are shown for the tip vortex geometries, induced inflow, as well as for performance trends. Clearly, the accurate prediction of the wake geometry is essential for predicting the rotor induced velocity field and the blade airloads. Therefore, the accuracy of wake geometry predictions is first examined through comparison with experimental measurements. The experimental results presented in this section, although from different sources, correspond to essentially the same configuration – the Langley 2MRTS rotor (Refs. 91–93).

Figure 5.5 shows a comparison of predicted and experimental wake boundaries in a plane passing through the longitudinal centerline of the rotor. The free-vortex wake results were calculated using a discretization level of $\Delta\psi = \Delta\zeta = 5^\circ$. The experimental results, for the wake boundary are documented in Ref. 85, where a four-bladed rotor with radius $R = 0.8255$ m and chord $c = 0.0635$ m was used. The blades had a rectangular planform with a linear twist of -13°, and the rotor was operated at 1980 rpm. The wake geometry changes significantly during the transition from hovering to forward flight, and so these cases provide a good general test for evaluating the capabilities of the wake model. Note that in hover, at least in principle, the rotor wake wake is fully axisymmetric. In practice, however, this may not be the case. The results in Fig. 5.5 show some small asymmetry in the hovering wake boundary. Such observed asymmetry in hovering rotor wake may be caused by the asymmetry of the rotor hub fixtures and other support structures.

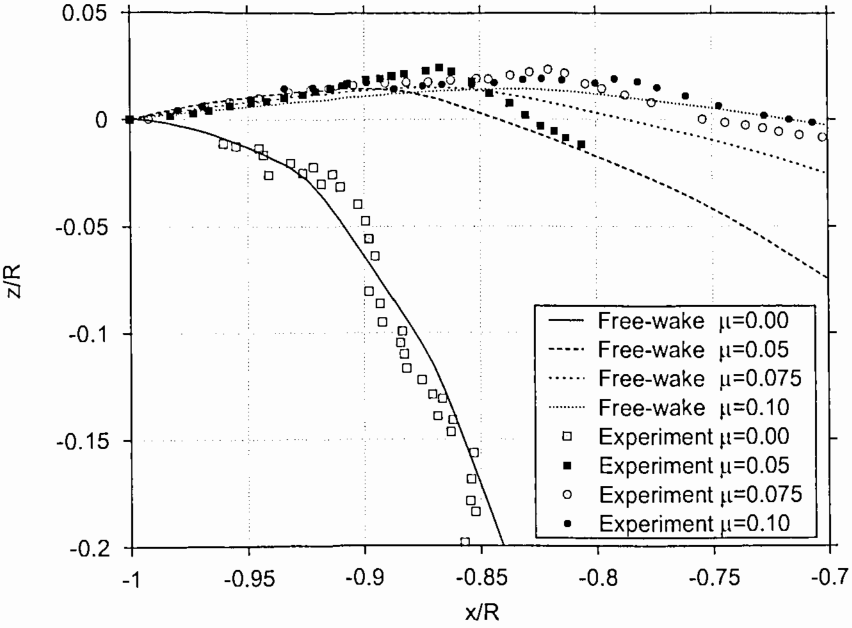

(a) Front of the rotor

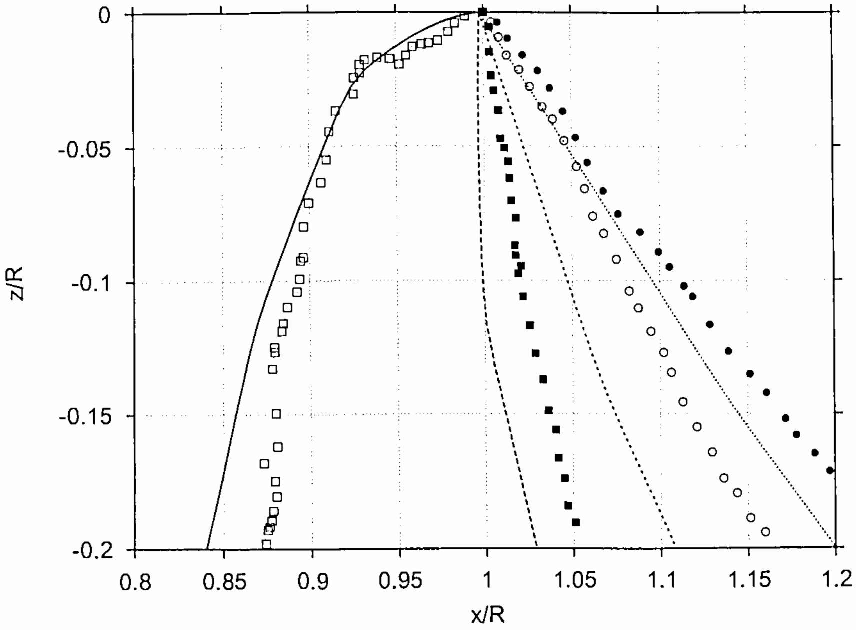

(b) Rear of the rotor

Figure 5.5: Comparison of predicted and measured wake boundaries for a four-bladed rotor in hover and forward flight: (a) Front of the rotor, (b) Rear of the rotor. Experimental results from Ref. 85.

The results in Fig. 5.5 show that as the advance ratio increases the wake is quickly skewed backward by the on-coming freestream flow velocity. The interesting feature on the front of the rotor disk is that the vortices are initially convected above the TPP – see Fig. 5.5(a). As the vortices convect further downstream, they begin to descend toward the TPP and ultimately closely interact with the blade(s). This leads to a perpendicular BVI event. Therefore, the prediction of the wake geometry in such cases is especially important. The present free-vortex wake analysis predicts this initial upward convection of the tip vortices very well.

At the rear of the rotor disk, the overall downwash velocity is higher and the vortices remain well below the TPP. Again, as shown in Fig. 5.5(b), the free-vortex wake predictions show a high sensitivity to small changes in advance ratio. The free wake results appear to somewhat underpredict the streamwise (along the x-axis) displacements. Part of the reason for this discrepancy may be because of the asymmetry of the experimental set-up, which is evident from the wake boundary in hovering flight as mentioned previously. However, the overall agreement between the predictions and the experiments was good.

Figures 5.6 and 5.7 show the top (plan) and side views of the rotor wake in forward flight at an advance ratio of $\mu = 0.15$ and a thrust coefficient of $C_T = 0.008$. The rotor shaft is tilted forward at an angle of three degrees, i.e., $\alpha_s = -3°$. The blade geometry is the same as that discussed earlier. The trajectories of tip vortices from each blade are plotted separately to improve clarity. The predicted trajectories are compared with the measured tip vortex displacements from Ref. 94. When viewed from top, the tip vortex trajectories show very small relative distortions from their epicycloidal form. Only at the lateral edges of the wake some distortion is seen because of the roll-up between individual vortices, and the formation of "super vortices" or vortex bundles. The small radius of curvature of the wake filaments in this region requires a small discretization level in the wake modeling.

Although the streamwise displacements closely resemble an epicycloidal form, the vertical displacements of the tip vortices are significantly different than those given by a rigid wake (undistorted helix). This is shown in Fig. 5.7 in the form of a side view of the tip vortex geometry. The tip vortices remain axially very close to the TPP at the front of the rotor disk. This is especially important from the point of view of predicting any possible perpendicular BVI events. The free-wake predictions show a good overall agreement with the experimental results.

Figures 5.8 and 5.9 show similar results at a higher advance ratio of $\mu = 0.23$. In this case, because of the higher streamwise convection velocity, the top view of the wake geometry very closely resembles the epicycloidal form. The vertical displacements, however, are still significantly different than those for an undistorted helical wake. Again, the free-vortex wake results were found to accurately predict the wake geometry.

5.2.2 Rotor Induced Inflow

One of the salient features of the free-vortex wake methodology is its ability to predict the highly non-linear rotor induced velocity field without any significant assumptions regarding the geometry of the vortical wake. The ability to predict the inflow distribution accurately also implies a better overall rotor performance and blade loads prediction capability. In this section, the inflow predictions using the free-vortex wake analysis are compared with experimental measurements from Refs. 91–93. The induced velocities were measured one chord above the TPP using a laser Doppler velocimetry system. Again, the rotor blade geometry was the same as the two rotors

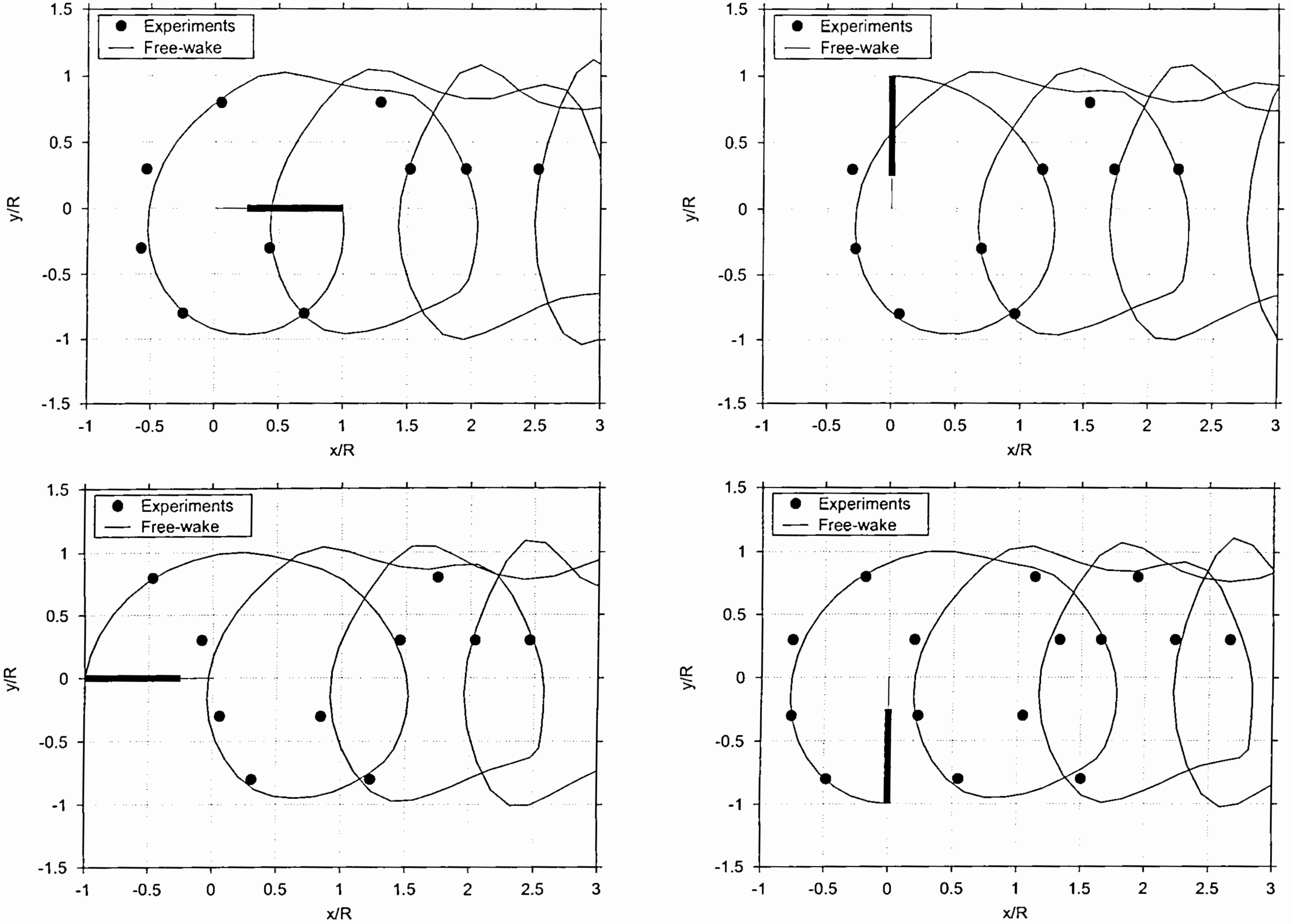

Figure 5.6: Predicted top views of rotor tip vortex trajectories at an advance ratio of $\mu = 0.15$ compared with flow visualization measurements. Results for each blade are shown separately: (a) Blade 1 at $\psi_b = 0°$, (b) Blade 2 at $\psi_b = 90°$, (c) Blade 3 at $\psi_b = 180°$, (d) Blade 4 at $\psi_b = 270°$. Experimental results from Ref. 94.

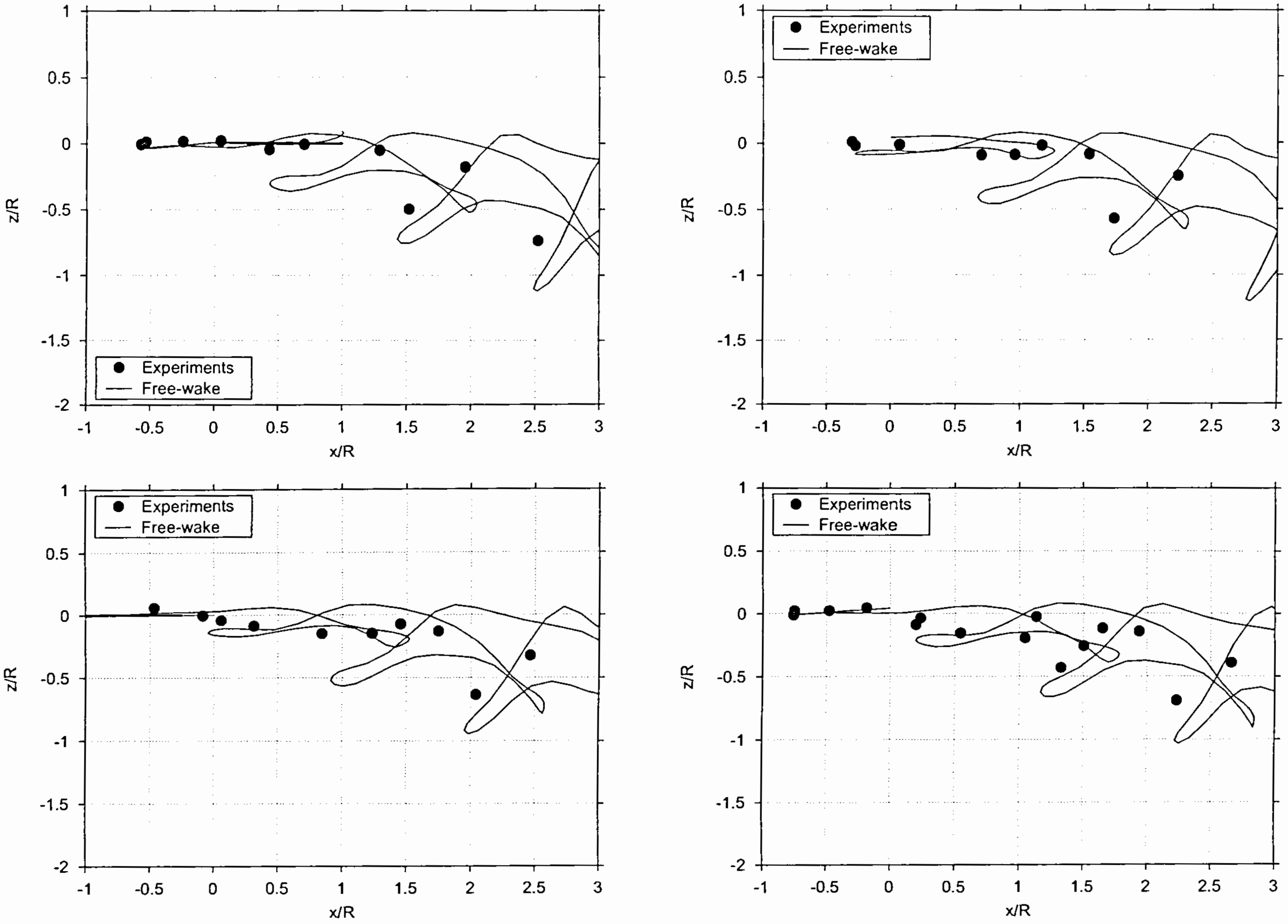

Figure 5.7: Predicted side views of rotor tip vortex trajectories at an advance ratio of $\mu = 0.15$ compared with flow visualization measurements. Results for each blade are shown separately: (a) Blade 1 at $\psi_b = 0°$, (b) Blade 2 at $\psi_b = 90°$, (c) Blade 3 at $\psi_b = 180°$, (d) Blade 4 at $\psi_b = 270°$. Experimental results from Ref. 94.

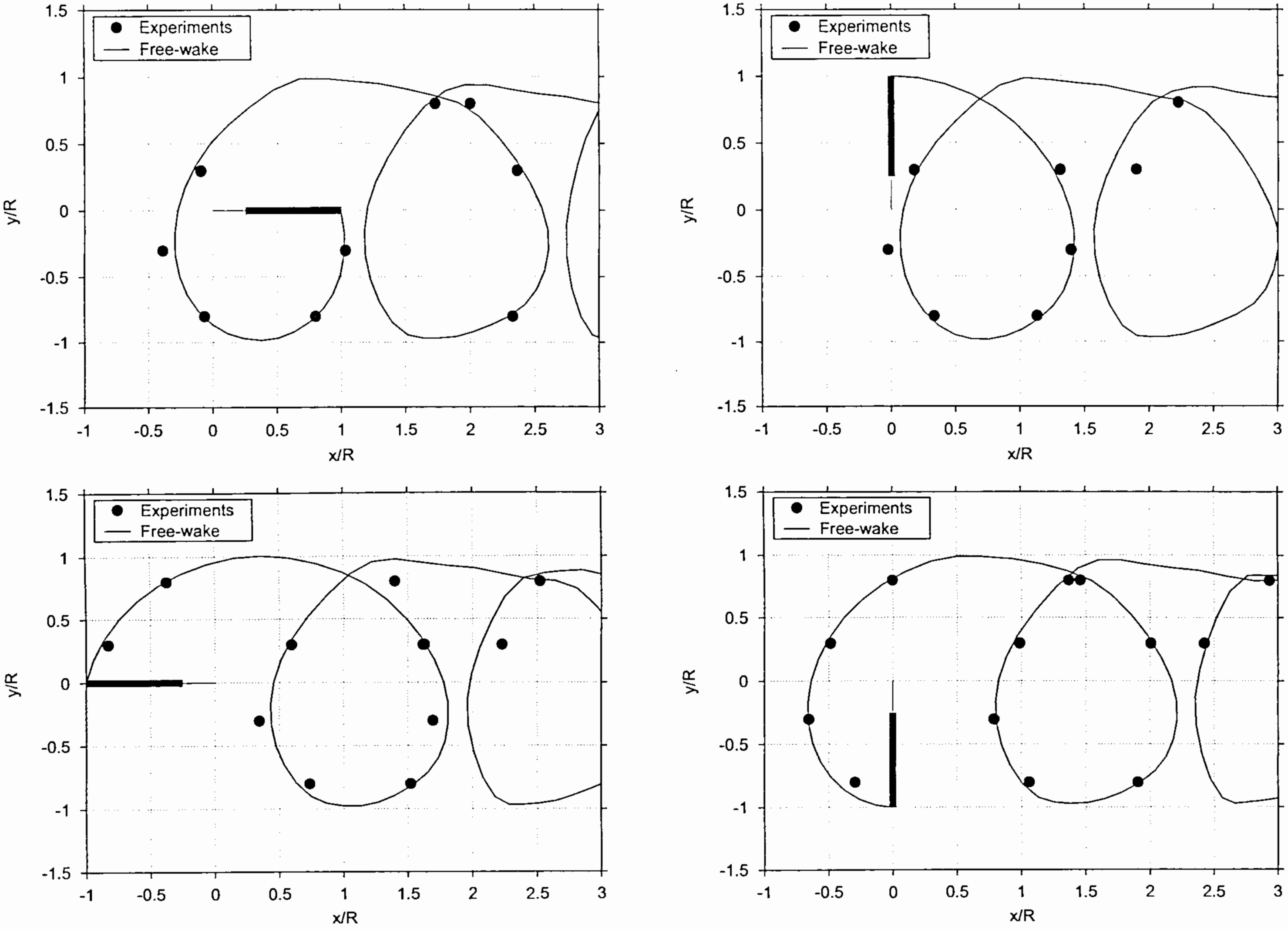

Figure 5.8: Predicted top views of rotor tip vortex trajectories at an advance ratio of $\mu = 0.23$ compared with flow visualization measurements. Results for each blade are shown separately: (a) Blade 1 at $\psi_b = 0°$, (b) Blade 2 at $\psi_b = 90°$, (c) Blade 3 at $\psi_b = 180°$, (d) Blade 4 at $\psi_b = 270°$. Experimental results from Ref. 94.

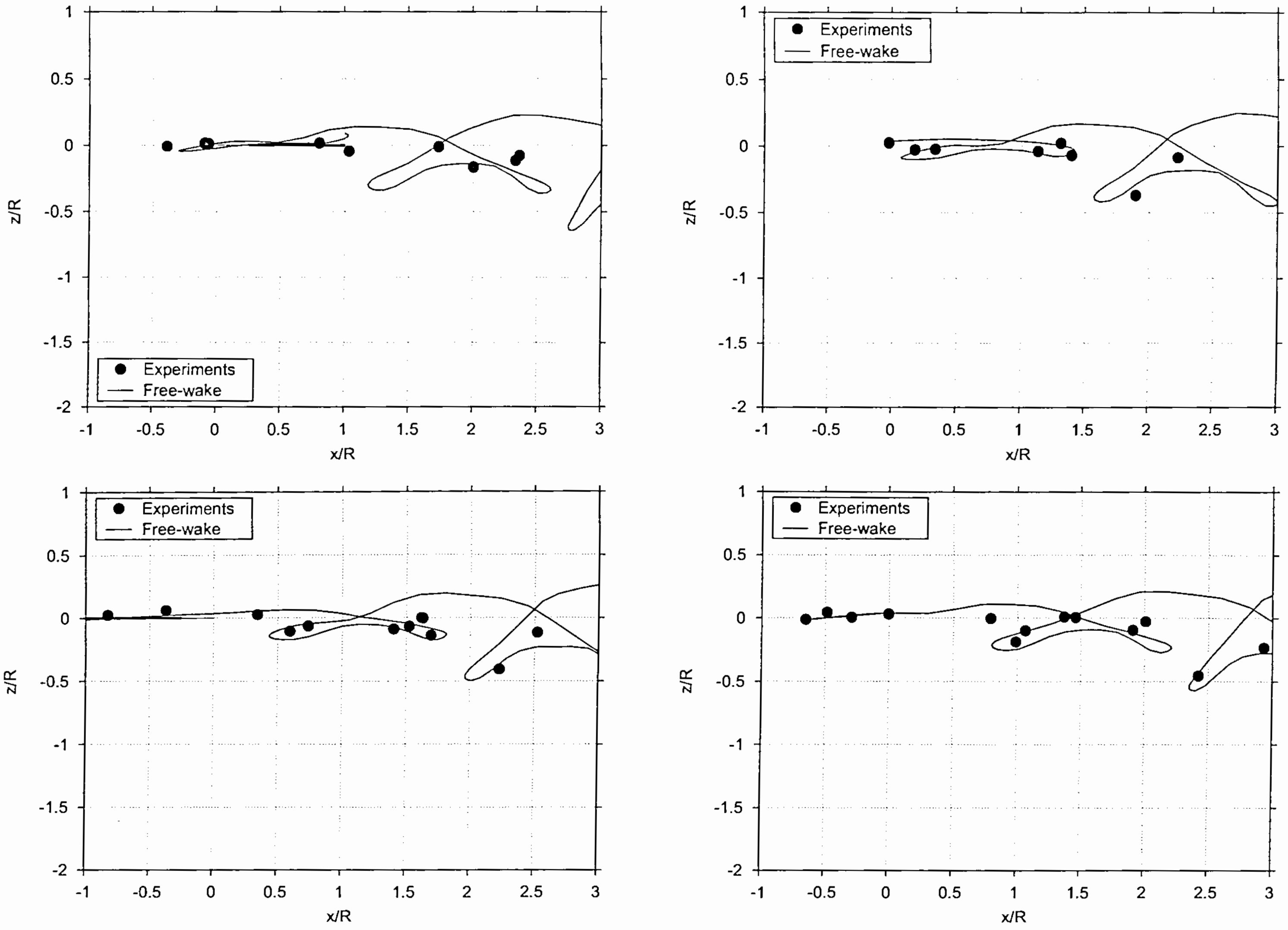

Figure 5.9: Predicted side views of rotor tip vortex trajectories at an advance ratio of $\mu = 0.23$ compared with flow visualization measurements. $C_T = 0.008$, $\alpha_s = -3°$. Results for each blade are shown separately: (a) Blade 1 at $\psi_b = 0°$, (b) Blade 2 at $\psi_b = 90°$, (c) Blade 3 at $\psi_b = 180°$, (d) Blade 4 at $\psi_b = 270°$. Experimental results from Ref. 94.

discussed earlier in this section.

The longitudinal inflow distribution, as given in Fig. 5.10, showed a somewhat linear trend with an upwash on the front of the rotor disk. The free-vortex wake predictions also show the same basic trend. Note that these experiments were performed with a rotor and a fuselage and, therefore, the results may not be considered to be truly representive of an isolated rotor. The lateral inflow distribution, as shown in Fig. 5.11, shows a relatively more uniform distribution. The lateral inflow gradient is seen to increase only slowly with increasing advance ratio. There is also a rapid reduction in inflow near the tips, with small regions of upwash. A linear inflow model would fail to predict this high upwash region. However, the free-vortex wake analysis predicts such a distribution of inflow very well.

Although the lateral inflow distribution showed significant differences from a simple linear inflow model, the longitudinal inflow could be reasonably represented by such models. The inflow predictions obtained using the free-vortex wake predictions are plotted in Figs. 5.12 and 5.13 as the inflow coefficients of a linear inflow model. In this case the inflow distribution over the rotor disk can be represented with a mean inflow, λ_0, and lateral and longitudinal (lienar) inflow gradients, k_x and k_y, i.e.,

$$\begin{aligned} \lambda_i &= \lambda_0 \left(1 + k_x r \cos\psi + k_y r \sin\psi\right) \\ &= \lambda_0 \left(1 + k_x \frac{x}{R} + k_y \frac{y}{R}\right) \end{aligned} \tag{5.1}$$

The linear inflow gradients, k_x and k_y, give weighting functions representing deviations of the inflow from the basic uniform inflow predicted using simple momentum theory. Figure 5.12 shows the uniform inflow component, λ_0, normalized with the hovering mean inflow value, λ_h. Corresponding results obtained using a simple momentum theory are also shown for comparison. The momentum theory results are

(a)

$\mu = 0.15$

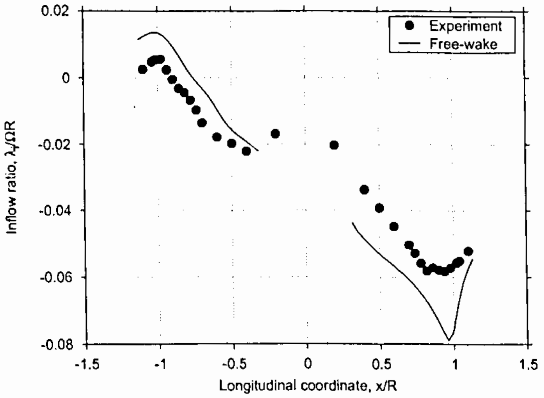

(b)

$\mu = 0.23$

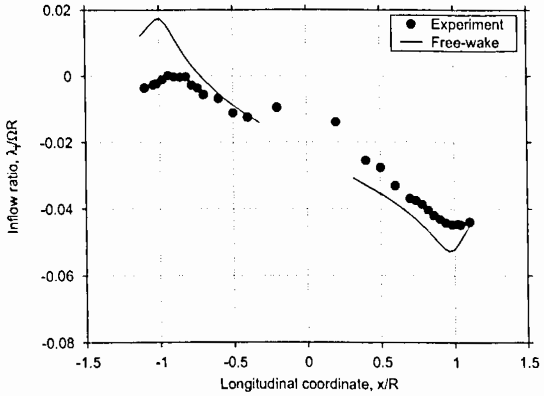

(c)

$\mu = 0.30$

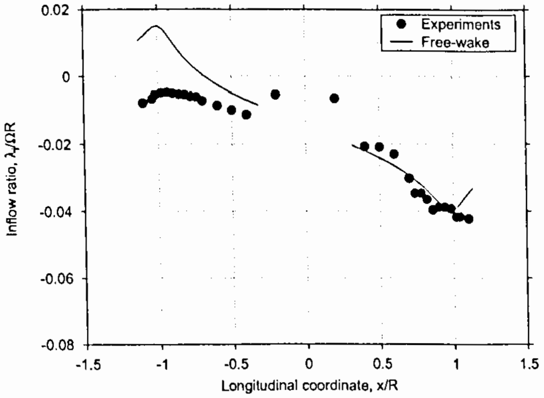

Figure 5.10: Time-averaged longitudinal inflow predictions using the free-vortex wake analysis compared with experimental measurements. $C_T = 0.008$, $\alpha_s = -3°$. Inflow measurements performed one chord above the TPP. Experimental results Refs. 91–93.

(a)

$\mu = 0.15$

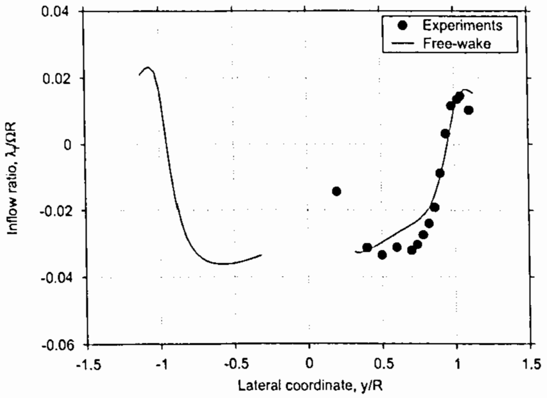

(b)

$\mu = 0.23$

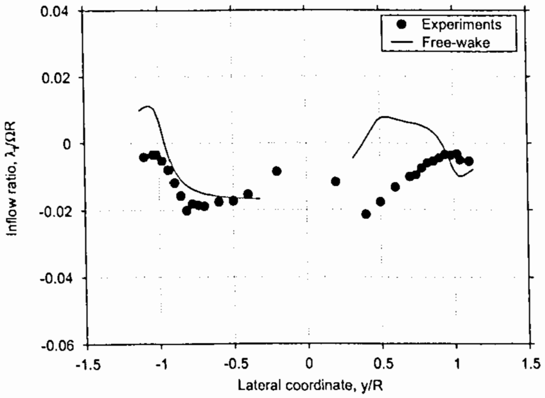

(c)

$\mu = 0.30$

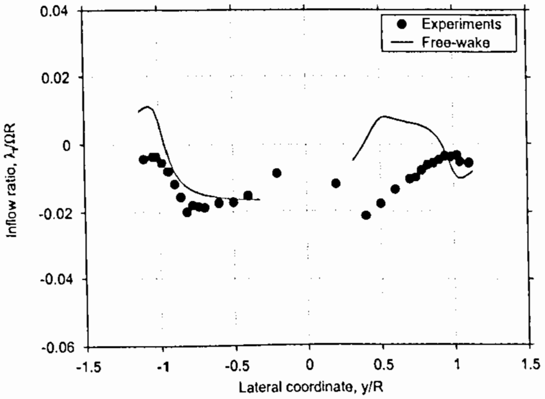

Figure 5.11: Time-averaged lateral inflow predictions using the free-vortex wake analysis compared with experimental measurements. $C_T = 0.008$, $\alpha_s = -3°$. Inflow measurements performed one chord above the TPP. Experimental results Refs. 91–93.

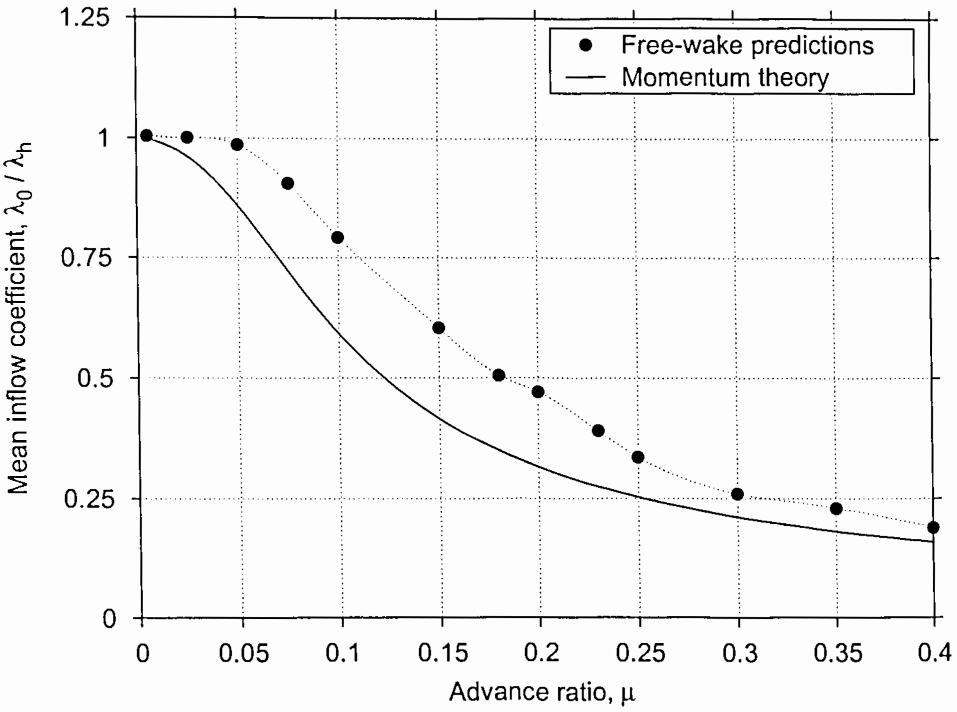

Figure 5.12: Mean inflow coefficient in forward flight predicted using the free-vortex wake analysis.

given by the equation – see, e.g., Ref. 2

$$\frac{\lambda_i}{\lambda_h} = \sqrt{\sqrt{\frac{1}{4}\left(\frac{\mu}{\lambda_h}\right)^4 + 1} - \frac{1}{2}\left(\frac{\mu}{\lambda_h}\right)^2} \tag{5.2}$$

THe results shown Fig. 5.12 represent only the mean inflow portion of the inflow given by the above equation (Eq. 5.2). It is apparent that at least for the mean induced inflow, both momentum theory and vortex theory, i.e., the present free-vortex wake analysis, give qualitatively the same results. Note that the momentum theory inflow coefficients are, in general, slightly smaller than those given by the free-vortex method.

Figure 5.13 shows the linear inflow coefficients extracted from the free-vortex wake predictions of inflow. These results are compared with one commonly used linear inflow model – the Drees model. In Drees's model, the inflow gradients are obtained using a variation of the vortex theory, and are expressed as a function of the wake skew angle (Ref. 76, Ch. 4, pp. 139–141). At low advance ratios, both results agree with each other. However, at higher advance ratios, the free-wake results show significant differences. Part of the explaination for this difference lies in the fact that at higher advance ratios with a low shaft tilt of 3°, there are strong BVI like interactions. These effects are illustrated in Fig. 5.14 with increasing advance ratio. Clearly, as the inflow distribution increases in complexity, a simple linear inflow model is insufficient to properly describe the induced velocity field at the rotor. However, the present free-vortex wake analysis can accurately predict these localized effects.

As shown in Fig. 5.14 for an advance ratio of $\mu = 0.2$, the results show significant interaction between the vortical wake and the rotor, which is apparent from the strong perturbations in the inflow on the front of the rotor disk. For advance ratios lower than this, the inflow distribution was found to be approximately linear over the rotor disk. Small deviations from the linear inflow trend occur only near the blade tips because of the rapid loss lift near the blade tips. At higher advance ratios, however, the induced velocity distribution at the rotor is very complex because of close vortex interactions. Therefore, a simple linear inflow model, such as the Drees model cannot adequately describe the rotor induced velocity field under these flight conditions.

5.2.3 Performance Calculations

Historically, one motivation for the continued development of free-vortex wake methods has been an improved hover performance prediction capability. In this section, the present free-vortex wake analysis is applied to performance predictions for the Mach-scaled rotor configurations described in the previous section. The experiments

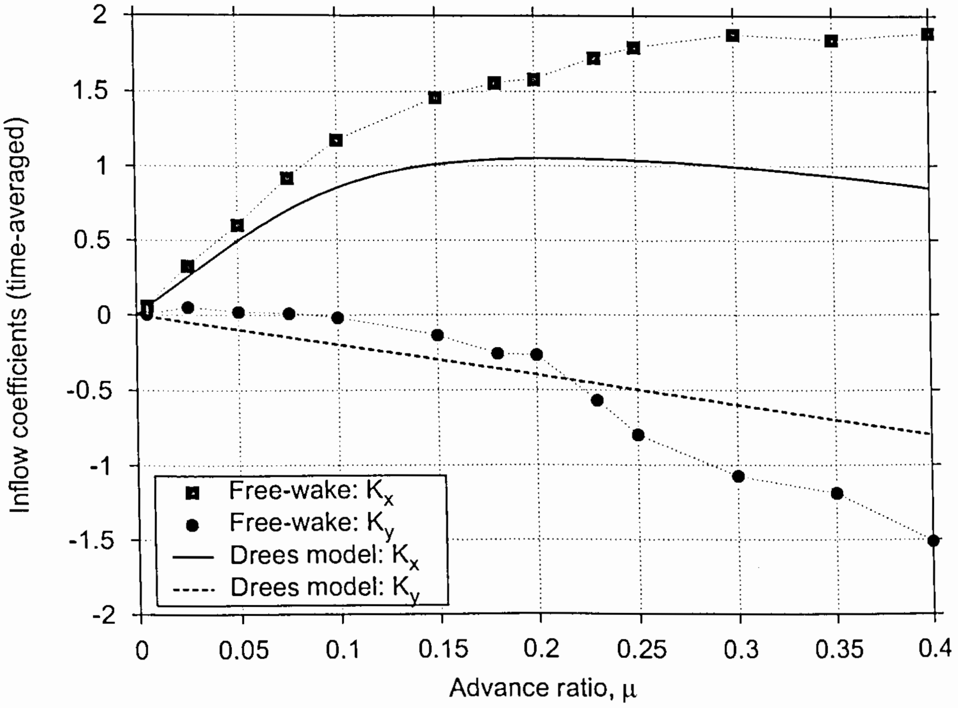

Figure 5.13: Linear inflow coefficient in forward flight predicted using the free-vortex wake analysis. The coefficient given by the Drees inflow model are also shown for comparison.

of Ref. 95 examined the effects of blade planform variation on the hovering rotor performance. Some of these experimental results are now used to validate the free-vortex wake predictions using the present analysis. The performance predictions presented in this section used free-vortex wake calculations with a discretization level of $\Delta\psi = \Delta\zeta = 10°$. This discretization level was found to be sufficient for predictions of rotor airloads and performance.

Figure 5.15 shows the power required and the figure of merit (FM) for a four-bladed rectangular planform hovering rotor at different thrust coefficients. The figure of merit for a hovering rotor is defined as the ratio of the ideal rotor power to the ideal

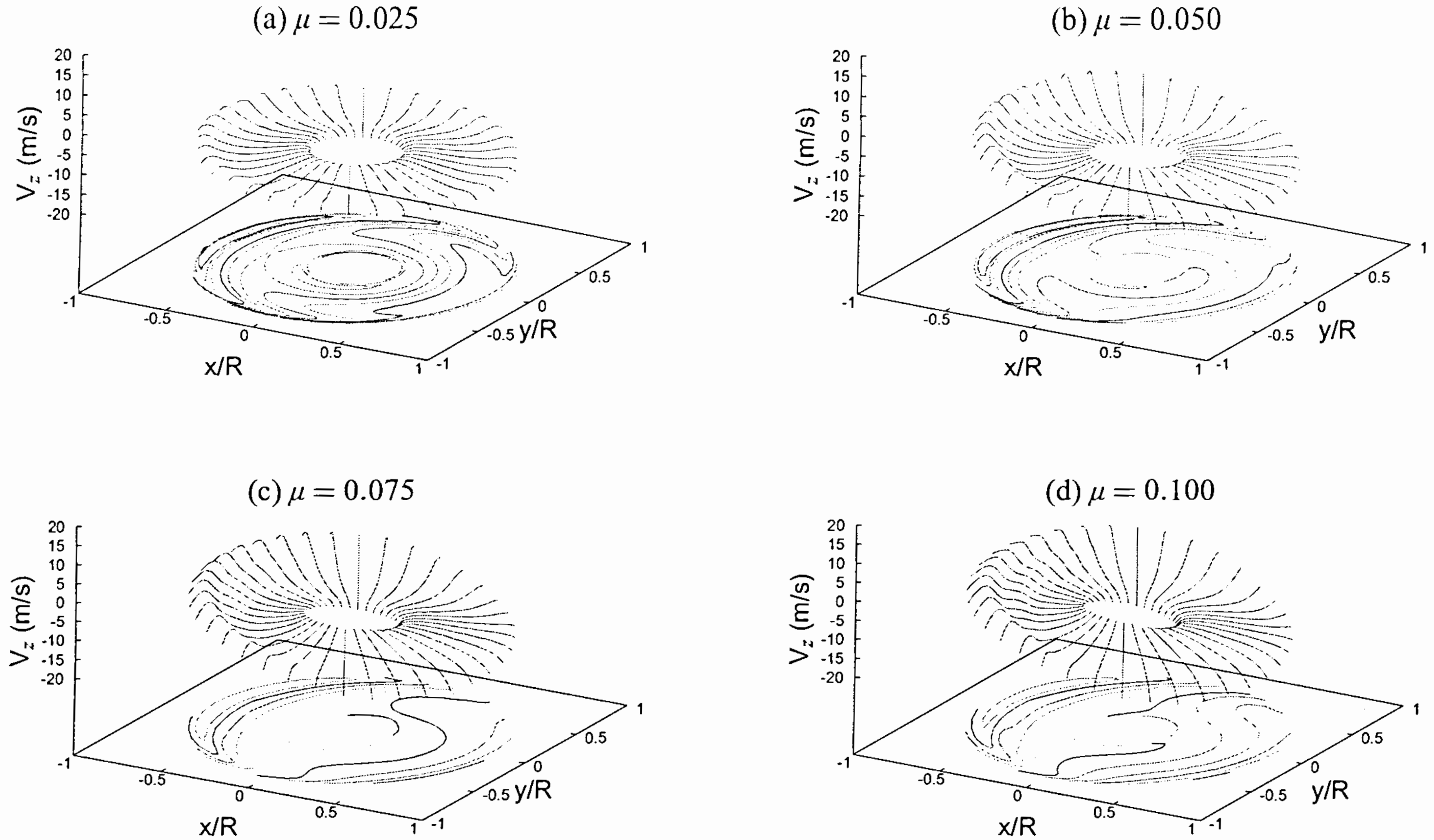
(a) $\mu = 0.025$

(b) $\mu = 0.050$

(c) $\mu = 0.075$

(d) $\mu = 0.100$

Figure 5.14: Predicted inflow distribution using the free-vortex wake method for increasing advance ratio. The inflow is shown as a surface plot along with projected contours to bring out the linear nature of the inflow at lower advance ratios. (a) $\mu = 0.025$, (b) $\mu = 0.05$, (c) $\mu = 0.075$ and (d) $\mu = 0.1$ (contunued).

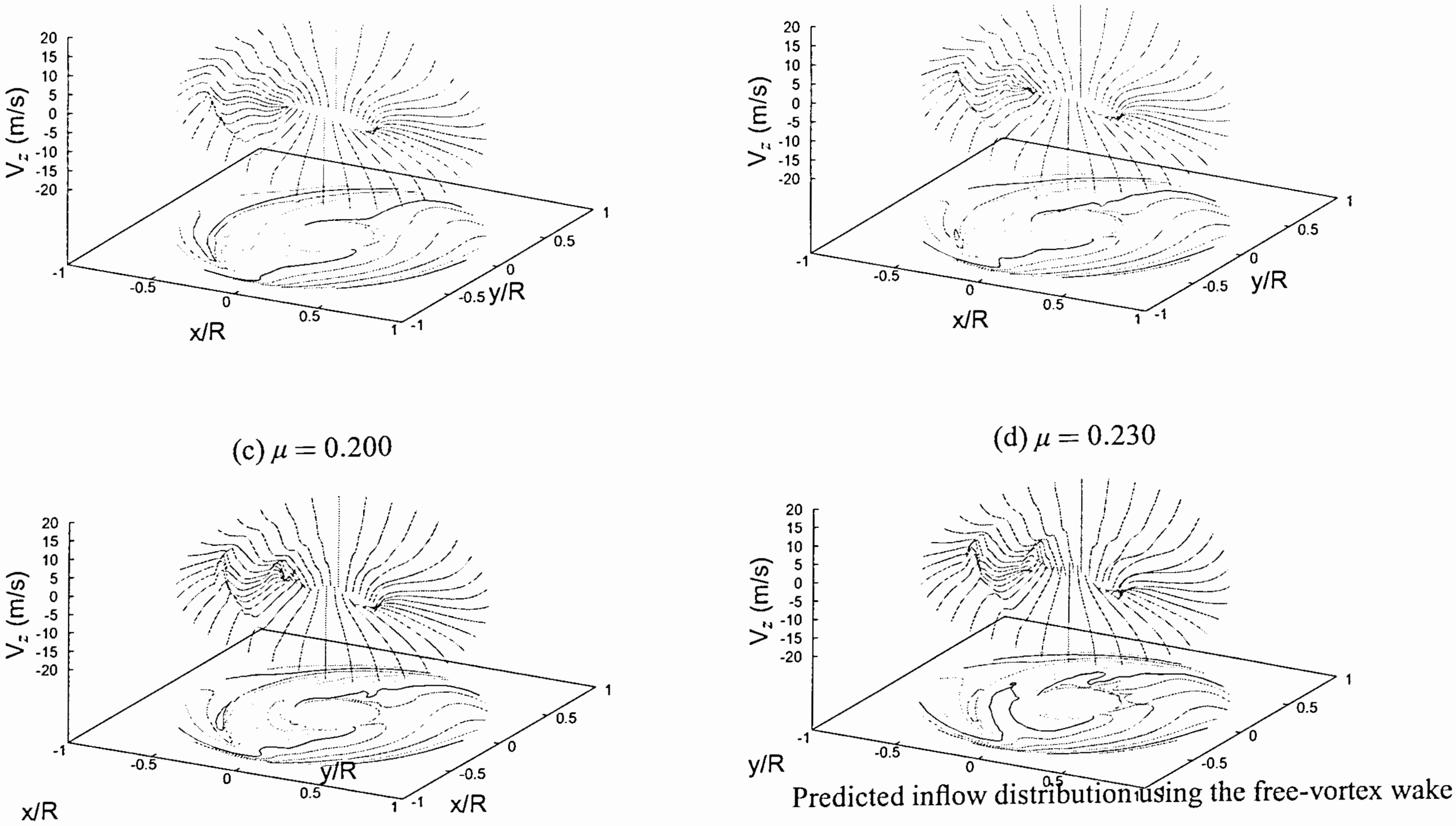

(a) $\mu = 0.150$

(b) $\mu = 0.180$

(c) $\mu = 0.200$

(d) $\mu = 0.230$

Predicted inflow distribution using the free-vortex wake method for increasing advance ratio.

(a) $\mu = 0.15$, (b) $\mu = 0.18$, (c) $\mu = 0.15$ and (d) $\mu = 0.23$ (Fig. 5.14 continued)

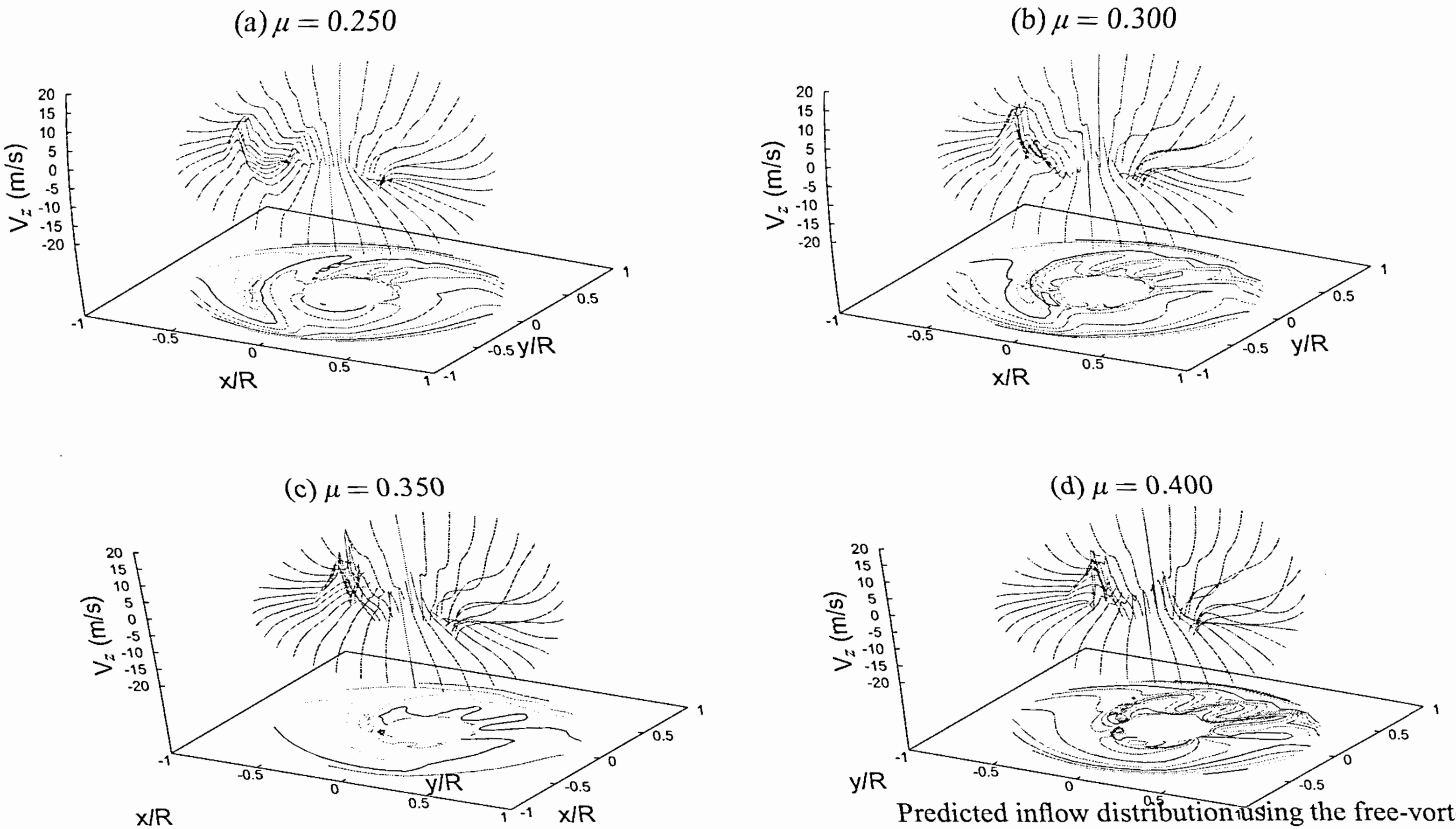
(a) $\mu = 0.250$

(b) $\mu = 0.300$

(c) $\mu = 0.350$

(d) $\mu = 0.400$

Predicted inflow distribution using the free-vortex wake method for increasing advance ratio.

(a) $\mu = 0.25$, (b) $\mu = 0.3$, (c) $\mu = 0.35$ and (d) $\mu = 0.4$ (Fig. 5.14 end) required induced power, i.e.,

$$FM = \frac{P_{ideal}}{P_{actual}} = \frac{C_T^{3/2}/\sqrt{2}}{C_{P_{actual}}} \tag{5.3}$$

The power required was found to increase with rotor thrust with an approximate $C_T^{3/2}$ trend, which is consistent with simple momentum theory (Refs. 2, 76). Because the rotor blades are rectangular and twisted, the basic performance trend is the same as that predicted using simple blade element/momentum theory. The figure of merit also increased with the rotor thrust, and in this case reaches a maximum value at approximately a thrust coefficient of $C_T = 0.009$. At higher thrust levels, the figure of merit showed a gradual decrease because of increasing profile power as a result of boundary layer thickening and the onset of stall.

It should be noted that although the induced power is a major component in the total power required, the profile power is an important factor in predicting the rotor figure of merit. Therefore, an accurate airfoil drag model plays an important role in determining the rotor figure of merit. Figure 5.16 shows the effects of airfoil drag modeling on the free-vortex wake performance predictions. A simple drag model was used to calculate sectional drag using Eq. 4.28, i.e.,

$$C_d = C_{d_0} + D_1 \alpha_{e_i} + D_2 \alpha_{e_i}^2 \tag{5.4}$$

This model model with a only a constant drag coefficient C_{d_0} and $D_1 = D_2 = 0$ underpredicts the power required and, therefore, overpredicts the figure of merit at higher thrust. A slightly improved drag model with a quadratic term in angle of attack ($D_2 = 0.4$) showed significant improvements in performance predictions. Such a drag model is required even when using a simple blade element/momentum theory for performance predictions – see, e.g., Ref. 2.

(a) Power required (torque)

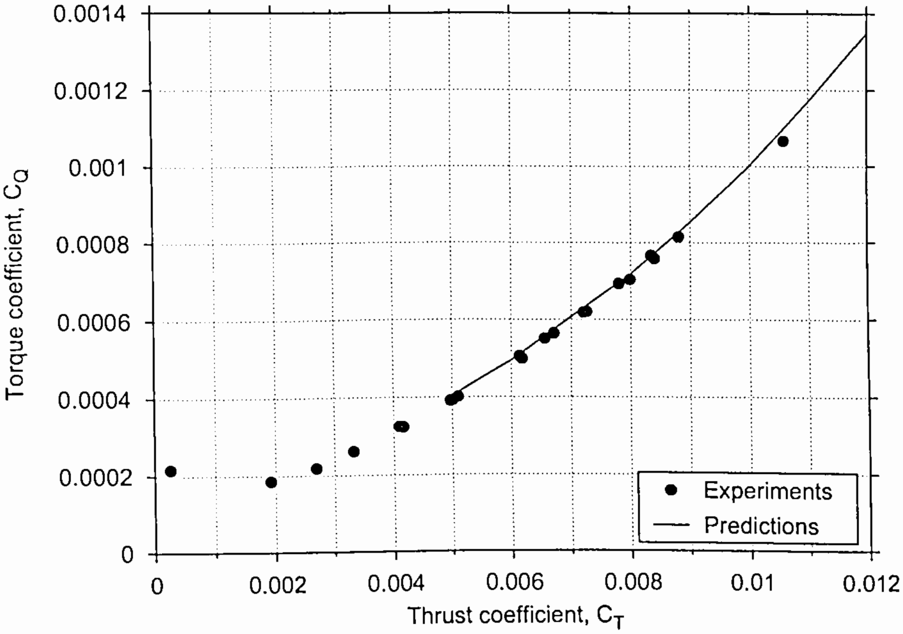

(b) Figure of Merit

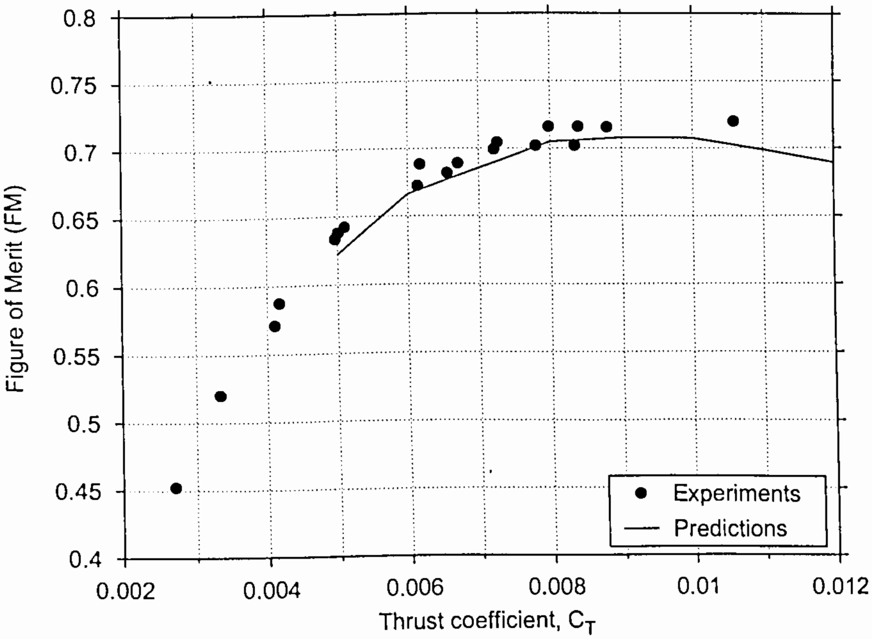

Figure 5.15: Performance of four-blade hovering rotor with rectangular blade planform for increasing rotor thrust. (a) Power required (torque), (b) Figure of Merit. Experimental measurements from Ref. 95.

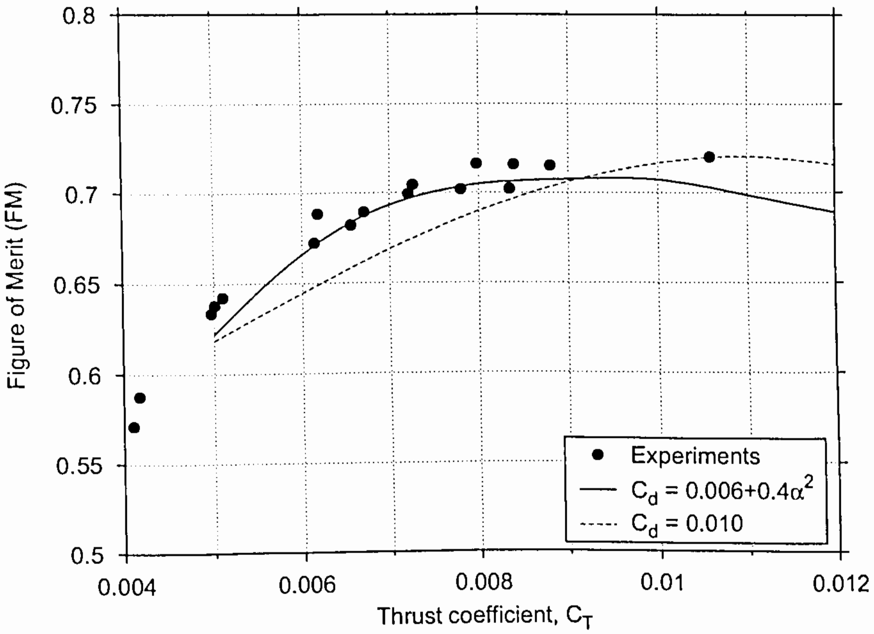

Figure 5.16: Effects of airfoil drag model on the rotor figure of merit prediction. Experimental measurements from Ref. 95.

The present analysis uses a rotor trim procedure, which is explained in Appendix B. In this case, an isolated rotor is trimmed by ensuring that the rotor thrust equals the desired value, and that the rotor TPP remains perpendicular to the shaft. Such a simple trim analysis is especially useful for examining isolated rotors. In hovering flight the trim analysis essentially calculated the collective pitch required to obtain a given thrust. This collective pitch input required to obtain different rotor thrust levels is shown in Fig. 5.17. The experimental values from Ref. 95 are also shown for comparison. Note that the rotor thrust shows an almost linear variation with the collective pitch, except at very low thrust levels. The free-vortex wake predictions also give this basic linear trend. However, the rotor thrust at a given collective pitch is slightly overpredicted. It is interesting to note that the difference between the experimental values and the

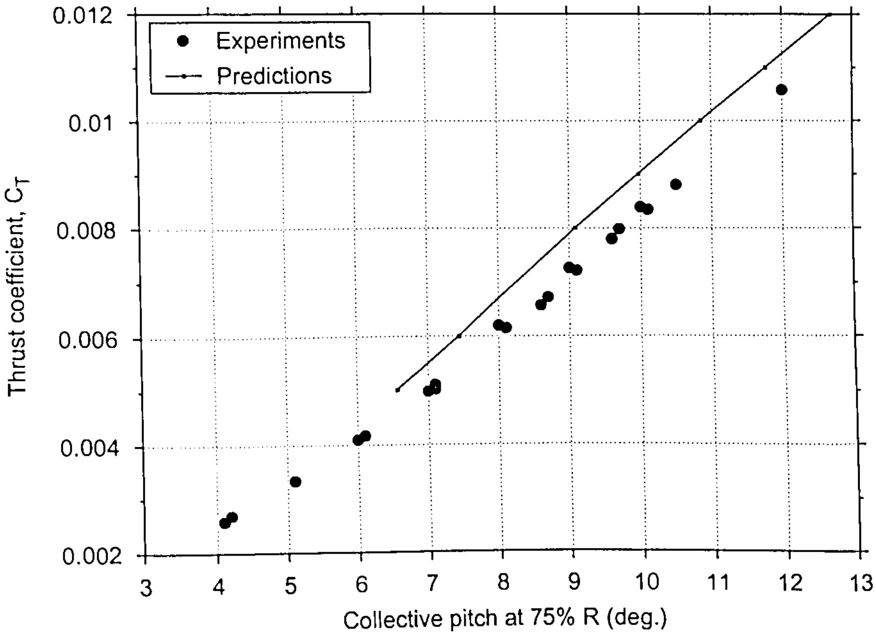

Figure 5.17: Collective pitch as a function of rotor thrust. Experimental measurements from Ref. 95.

numerical predictions is almost constant for thrust values. Note that the present results used a symmetric airfoil model whereas the blades used in the experiments had a cambered section. Therefore, a simple correction for the zero-lift angle of attack of the airfoil is necessary to give better predictions of the collective pitch inputs.

Ref. 95 presents results from different blade planform to evaluate the effects on hover performance. A baseline rectangular blade planform was compared to tapered planform shapes. It was found that a tapered tip was found to give some improvements in hover performance. Free-vortex wake predictions for such a tapered tip are shown in Fig. 5.18. Experimental results as well as the results corresponding to rectangular blades are shown for comparison. The spanwise lift distribution is modified because of the tip taper resulting in some reduction in the induced power.

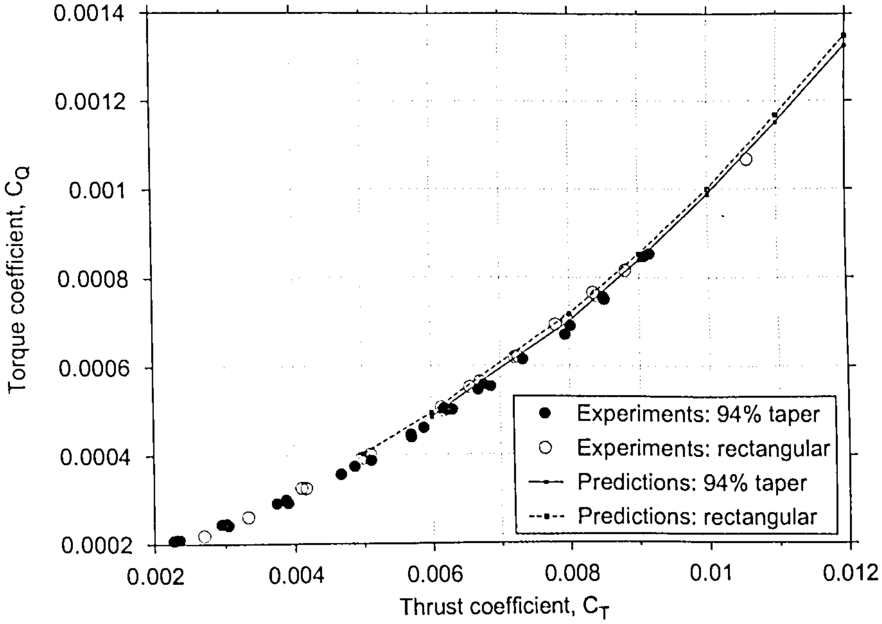

(a) Power required (torque)

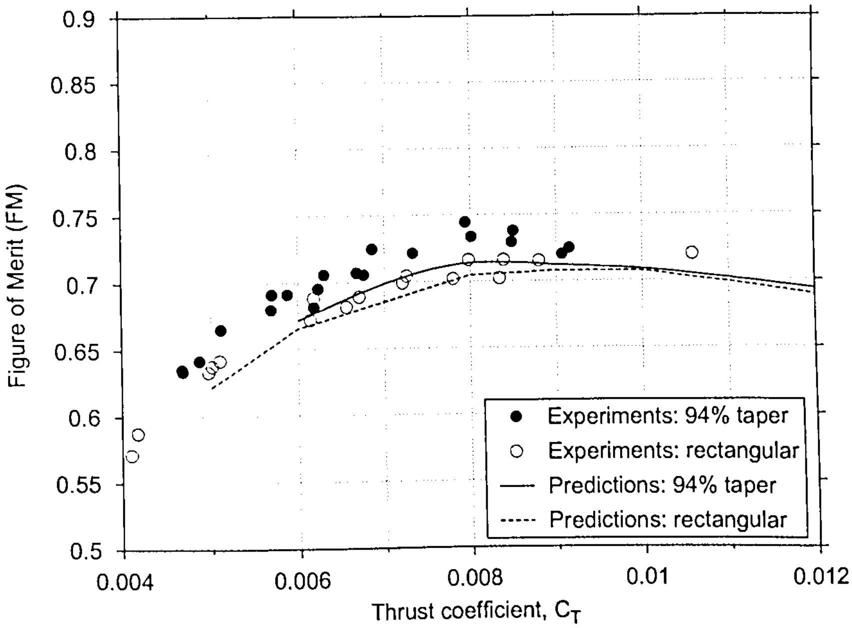

(b) Figure of Merit

Figure 5.18: Performance predictions for a four-bladed hovering rotor with a blade planform tapered at a ratio of 1:3 from 94% radius. (a) Power required (torque), (b) Figure of Merit. Experimental measurements from Ref. 95.

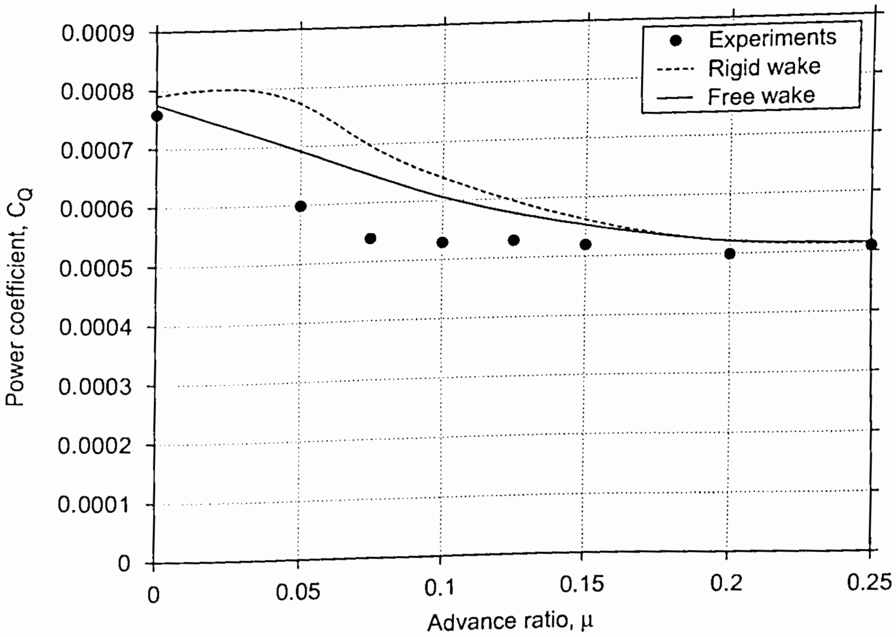

Figure 5.19: Forward flight rotor performance predictions using rigid wake and free-vortex models. Four-bladed rotor with rectangular blade planform. Experimental results from Ref. 85.

In Fig. 5.18(a), it can be seen the measured power is lower for the tapered tip as compared to the baseline rotor with rectangular blades. The free wake predictions accurately predict this beneficial effect of tip taper. Note that although there are some quantitative differences between the measurements and predictions, the relative benefits of tip taper are predicted correctly. Figure 5.18(b) shows the figure of merit values derived from the measured data and the free wake predictions. Again the relative improvement in figure of merit because of a tapered tip is correctly predicted.

Finally, the present analysis is applied to predict rotor performance in forward flight. Figure 5.19 shows the power required as a function of advance ratio. Results obtained using the classical rigid wake model are also shown, along with experimental measurements from Ref. 85. At high advance ratios ($\mu > 0.2$) both the free-wake and rigid wake predictions are almost identical. This is because at such high advance ratios, the rotor inflow is dominated by the freestream convection velocity and the wake-induced inflow is relatively small. However, at low advance ratios the rigid wake substantially overpredicts the power required. The present free-vortex wake analysis shows a better agreement with experimentally measured values.

5.3 Multiple Rotors

The free-vortex wake results presented in this dissertation have concentrated mostly on single rotor configurations. However, the analysis developed in the present work is readily extended to multiple rotor configurations. The performance prediction capabilities described in the previous section can be extended to examine twin-rotor configurations such co-axial, tandem or side-by-side rotors. The time-accurate wake solution can then be applied to study tilt-rotor transitions between helicopter and propeller modes. In this section, preliminary results for multi-rotor configurations are presented to demonstrate the capabilities of the present analysis.

5.3.1 Tandem Rotors

Many heavy-lift helicopters use a tandem rotor configuration because all the available power can be used for generating lift, with no anti-torque devices. The two rotors rotate in opposite directions resulting in no net torque on the helicopter. However, the induced power of the partly overlapping rotors is higher than that for two isolated rotors because of rotor interference effects. The present analysis incorporates opposite rotations through the transformations between fixed and rotating frames as described in Appendix C. The rotor interference effects are then included in the solution process by means of interactions between the two rotor wakes.

A momentum theory analysis of tandem rotors is based on the idea of overlapping areas of the rotor disks – see Ref. 2, Ch. 2, pp. 71–73. With no vertical spacing between the rotors, the overlap area of two rotors separated by a distance d (see Fig. 5.20) is given by $A_{ov} = mA$, and can be shown to be

$$m = \frac{2}{\pi}\left(\theta - \frac{d}{D}\sin\theta\right) \qquad \text{where} \;\; \theta = \cos^{-1}\frac{d}{D} \tag{5.5}$$

and D is the rotor diameter. Application of momentum theory then gives the induced power overlap factor as

$$\kappa_{\text{ov}} = \frac{P_{i_{\text{tandem}}}}{2P_{i_{\text{single}}}} = 1 + m\left(\sqrt{2} - 1\right) \tag{5.6}$$

This result is shown in Fig. 5.20 for increasing separation distance. Note that the momentum theory is based on overlap areas and, therefore, predicts no interference effects for $d/R \geq 1$. Experimental results, however, suggest that some interference effects are present even though the rotors have no overlapping area.

A similar result is predicted by the present analysis, which shows that for $d/D = 1.0$ the interference between the two rotors gives a slightly higher induced power with $\kappa_{ov} = 1.02$. This is because the vortical rotor wakes interact with each other resulting in wake distortion effects which tend to slightly increase the induced power. An example of such wake distortions is shown in Fig. 5.21 where the two rotor are just touching each other with $d/D = 1.0$. The wake geometries presented in this section were calculated using a discretization level of $\Delta\psi = \Delta\zeta = 10°$. The interactions between the two rotor wakes are clearly evident along the edge between the two rotors.

Another interesting observation made in the experiments with tandem rotors in hover was that the overlap factor may be less than unity over some range of separation

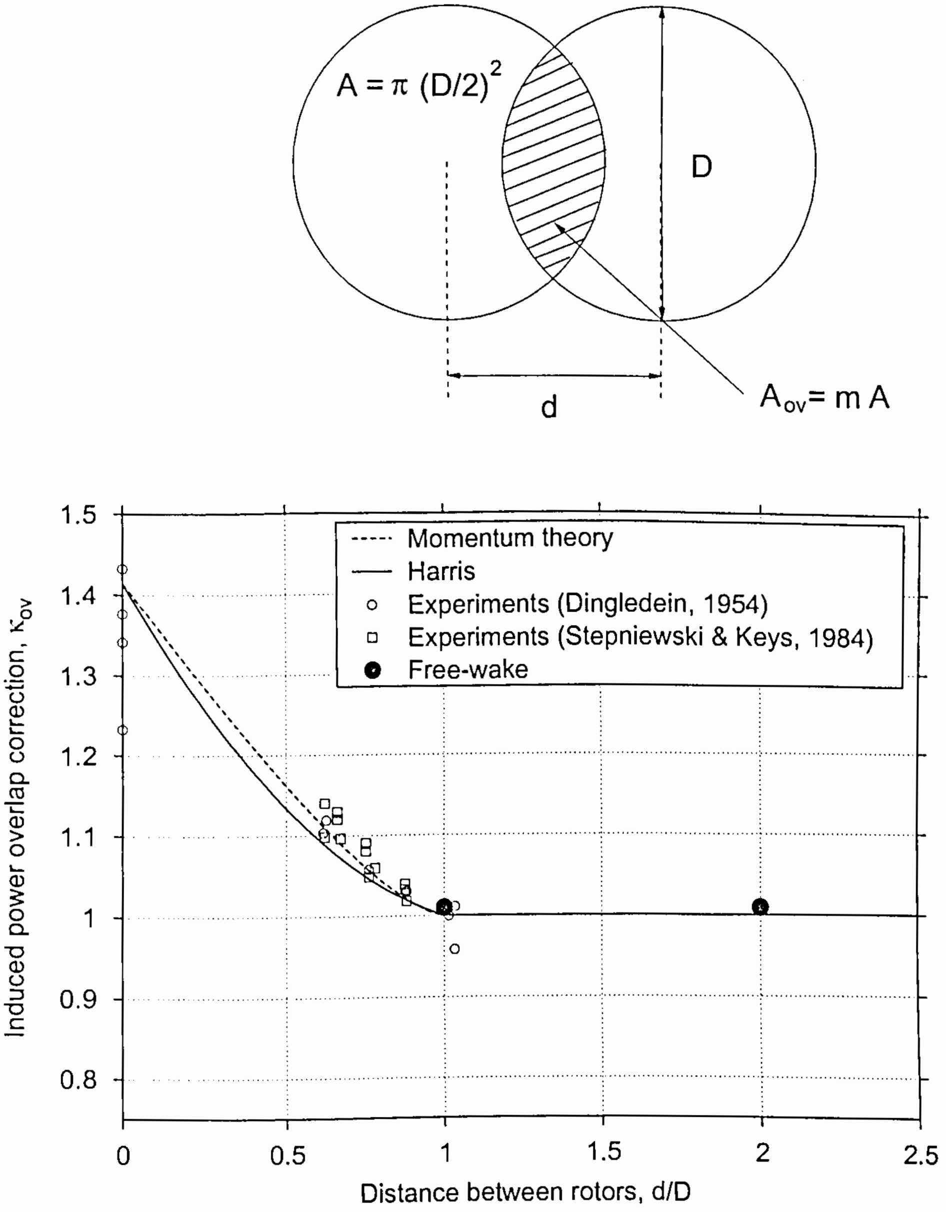

Figure 5.20: Induced power overlap factor for tandem rotors in hover as a function of separation distance between rotors. Preliminary predictions using the present methodology are shown along with experimental results from Ref. 96 & Ref. 97, Vol. II, Ch. 5

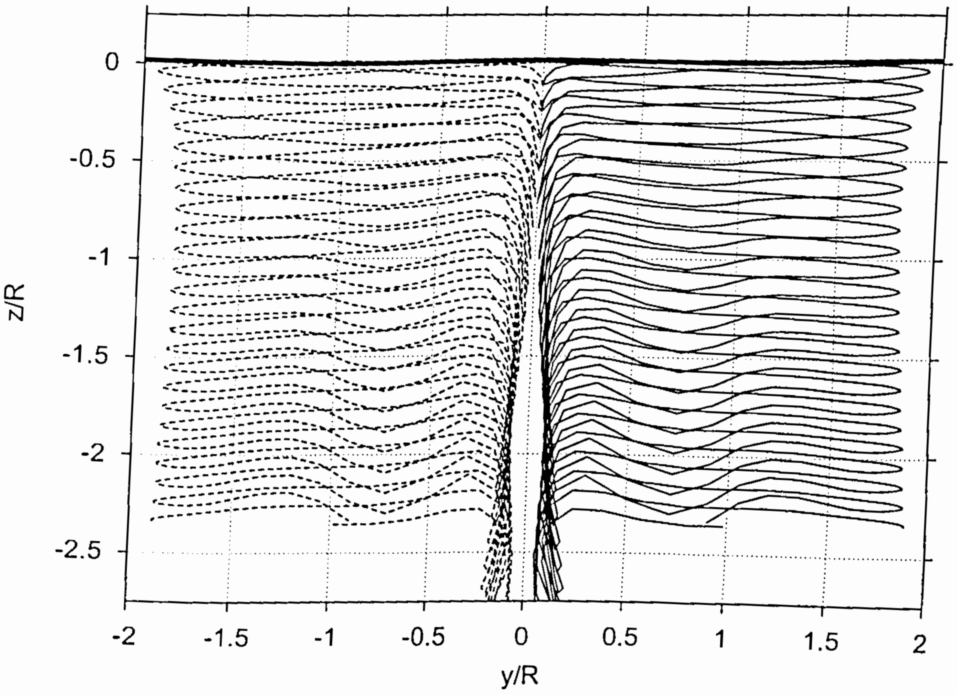

Figure 5.21: Predicted wake geometries for a tandem configuration in hover with a separation distance, $d/D = 1.0$.

distances. This implies that the corresponding tandem rotor configuration would be more efficient than two isolated single rotors. Therefore, the rotor interference effects can potentially be beneficial to the overall performance of the helicopter. The present analysis can be potentially applied to study these effects and to help designing more efficient tandem or side-by-side configurations.

5.3.2 Ground Effect

Rotor performance is significantly affected by the presence of ground, which may constrain the development of the rotor wake. This "ground effect" is a concern for both actual flight operations and wind-tunnel tests. For a hovering rotor close to the ground, the rotor wake expands quickly as it approaches the surface. The slipstream boundary rapidly expands near the ground plane, thereby decreasing the slipstream velocity. Correspondingly, the rotor induced velocity field is also altered resulting in a larger rotor thrust in ground effect (IGE) to that out of ground effect (OGE). The present methodology can be applied to study the ground effect phenomenon by using a twin-rotor configuration to simulate "mirror-image" rotors with respect to the ground plane. Two rotors are oriented such that the thrusts are in opposite directions. The rotors are also counter-rotating to obtain mirror symmetry about the ground plane. An example of the predicted wake geometry in hover IGE is shown in Fig. 5.22. The wake expansion near the ground plane is clearly evident from these results. Corresponding predictions of thrust and power may then be used for quantifying the IGE hovering rotor performance.

An example of ground effect in forward flight is shown in Fig. 5.23 for a four-bladed rotor at an advance ratio of 0.1. The rotor is located at one and a half rotor radii above the ground plane. Another "mirror-image" rotor is located one and a half rotor radii below the ground plane. This second rotor rotates in a sense opposite to that of the first rotor and the thrust direction is vertically downward. The rotors operate at a thrust coefficient of $C_T = 0.008$, advance ratio of $\mu = 0.1$ with a forward shaft tilt of $\alpha_s = 10°$. The side view of the resulting rotor wake structure, as shown in Fig. 5.23(a) suggests significant wake distortions in the region when the wake approaches the ground plane. These distortions also influence the development of the wake upstream and closer to the rotor, and can potentially affect the rotor performance. The top view of the rotor wake shown in Fig. 5.23(b) clearly illustrates the wake expansion resulting from ground effect. Ground effect also appears to alter the roll-up of rotor wake into vortex bundles or "super-vortices," leading to further wake distortions.

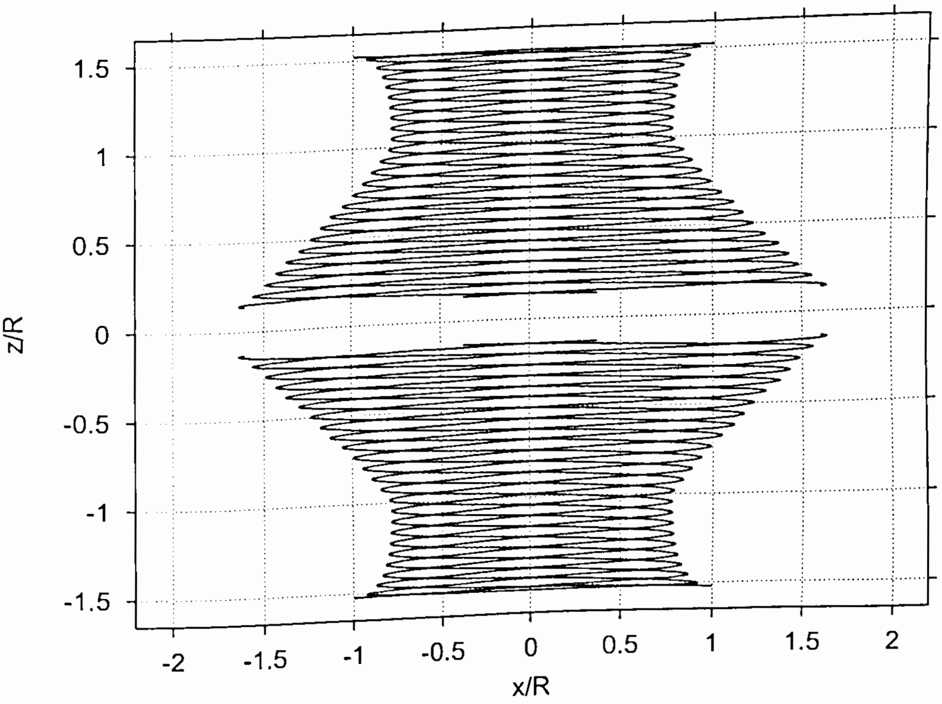

Figure 5.22: Predicted wake geometries using two rotors to simulated ground effect in hover, $C_T = 0.008, N_b = 4$.

The free-vortex wake results shown here for multi-rotor configuration demonstrate the ability of the present methodology to analyze such rotor systems. There are countless number of combinations of twin-rotor systems of practical interest, and a detailed numerical study of these is beyond the scope of the present dissertation. These preliminary results are presented mainly to bring out possible future applications of this work.

(a) Side view

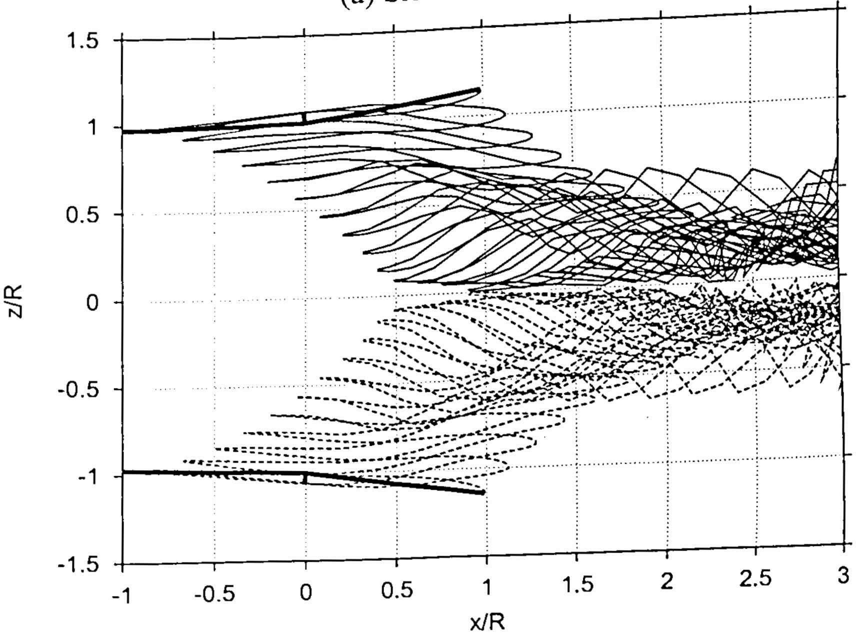

(b) Front view

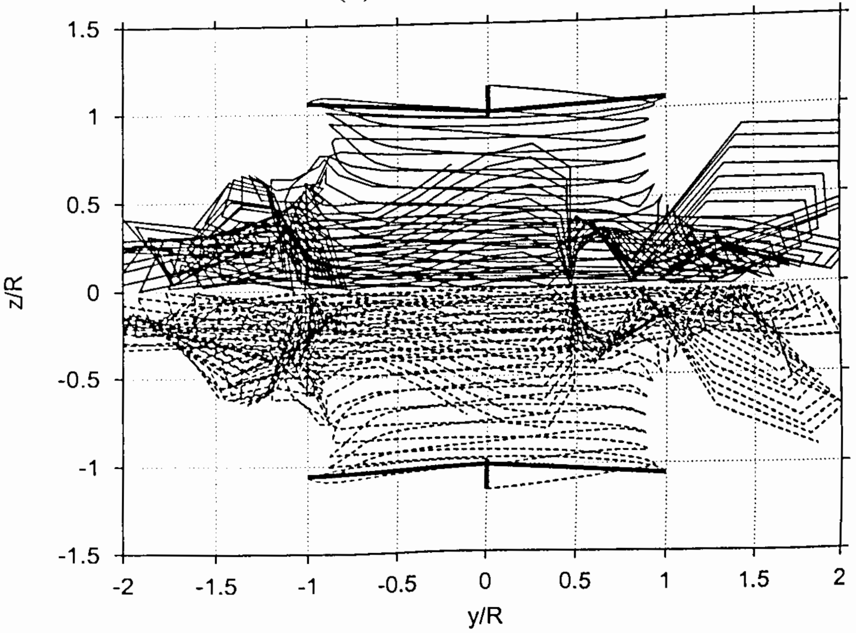

Figure 5.23: Predicted wake geometries using two rotors to simulated ground effect, $C_T = 0.008$, $N_b = 4$, forward shaft tilt $\alpha_s = 10°$. (a) Side view, (b) Front view

Abstract

Title of Dissertation: TRANSIENT DYNAMICS OF HELICOPTER ROTOR WAKES USING A TIME-ACCURATE FREE-VORTEX METHOD

Mahendra J. Bhagwat, Doctor of Philosophy, 2001

Dissertation directed by: Professor J. Gordon Leishman
Department of Aerospace Engineering

A second-order accurate predictor-corrector type algorithm has been developed to obtain a time-accurate solution of the vortical wake generated by a helicopter rotor. The rotor blade flapping solution was fully integrated with the wake geometry solution using the same time-marching algorithm. The analysis was used to predict the locations of wake vortex filaments under transient flight conditions, where the rotor wake may not be periodic at the rotational frequency. Applications of this analysis include prediction of the rotor induced velocity field and blade airloads during transient flight and maneuvers.

The stability of the rotor wake structure is important from the perspective of free-vortex wake models. The wake stability was examined using a linearized stability analysis, and the rotor wake was shown to be physically unstable. Therefore, the stability of the numerical algorithm is an important consideration in developing robust

wake methodologies. Both the stability and accuracy of the numerical wake solutions algorithms was rigorously examined. The straight-line vortex segmentation used in the present analysis was shown to be second-order accurate. The overall numerical solution was also demonstrated to converge with a second-order accuracy. A technique for increasing the order of accuracy for high resolution solutions is also described.

Along with a formal (mathematical) verification of solution accuracy, the numerical solution for the rotor wake problem was compared with experimental results for both steady-state and transient operating conditions. The steady-state wake model was shown to give good predictions of rotor wake geometry, induced inflow distribution as well as performance trends. Under transient conditions, such as those following a pitch input during a maneuver, the time-accurate wake model was shown to correctly model the dynamic response of rotor wake. In axial descent passing through the vortex ring state, the present analysis was shown to properly model the associated power losses as shown by experimental results. The present analysis was also shown to give improved predictions of wake distortions during simulated maneuvering flight with various imposed angular rates of the rotor.

TRANSIENT DYNAMICS OF HELICOPTER ROTOR WAKES USING A TIME-ACCURATE FREE-VORTEX METHOD

by

Mahendra J. Bhagwat

Dissertation submitted to the Faculty of the Graduate School of the
University of Maryland, College Park in partial fulfillment
of the requirements for the degree of
Doctor of Philosophy
2001

Advisory Committee:

Professor J. Gordon Leishman, Chairman/Advisor
Associate Professor James D. Baeder
Associate Professor Roberto Celi
Professor Inderjit Chopra
Associate Professor Jian-Guo Liu, Dean's Representative

Dedication

To those

Who have left so much behind . . .

Acknowledgements

I would like to take this opportunity to express my sincere gratitude towards all the people here at the University of Maryland who have helped in making this possible. Notably, my dissertation committee, Profs. James Baeder, Roberto Celi, Inderjit Chopra, and Jian-Guo Liu. They have been truly a advisory committee, constantly guiding me through many challenging tasks during the course of my work. Special thanks to Prof. Alfred Gessow for many helpful discussions and encouragement.

I cannot put down in words my gratitude towards my advisor and mentor, Prof. Gordon Leishman, who has played a key role in not only this work, but also in my career. If not for him, I would not be here, and I would simply like to say, "thanks for giving me a chance."

This work would not have come to a fruition without the aid of my friends and colleagues at the Rotorcraft Center who have been both helpful and patient with me over the past years. Many thanks to Preston Martin and Greg Puglese for sharing their fascinating experiments, and their fascination with the Blue Ridge mountains. Also, thanks to Dan Griffiths, Manikandan Ramasamy and Shreyas Ananthan, and also Dario Fusato and Rendy Cheng for their help and support. Special thanks to Dr. Ashish Bagai who's always been very encouraging and eager to help solve many of my problems. Thanks also to the 10 Forward management for carrying me through those late night vigils.

The support of the National Rotorcraft Technology Center through various grants is also gratefully acknowledged.

Last, but not the least, I must acknowledge the love and support of my family and friends, who have taught me to be more.

Table of Contents

Appendices

List of Tables

List of Figures

Nomenclature

A	asymptotic radial contraction in Landgrebe's wake model	
A	rotor disk area, $= \pi R^2$	m^2
c	rotor blade chord	m
C_d	sectional drag coefficient, $dD/(1/2\rho V_\infty^2 c)$	
C_l	sectional lift coefficient, $dL/(1/2\rho V_\infty^2 c)$	
C_{l_α}	lift curve slope	rad^{-1}
C_P	rotor power coefficient, $= P/\rho A(\Omega R)^3$	
C_Q	rotor torque coefficient, $= Q/\rho A(\Omega R)^2 R$	
C_T	rotor thrust coefficient, $= T/\rho A(\Omega R)^2$	
$\mathbf{E}$	Legendre's elliptical integral of second kind	
e	spanwise location of flapping hinge	m
h	time marching step, $= \Delta t$	s
I_β	flapping moment of inertia of the blade	$\mathrm{kg\,m}^2$
$\mathbf{K}$	Legendre's elliptical integral of first kind	
K_x	longitudinal inflow coefficient, $= \lambda_{1c}/\lambda_0$	
K_y	lateral inflow coefficient, $= \lambda_{1s}/\lambda_0$	
k_1, k_2	axial settling rates in Landgrebe's wake model	
k_β	flapping spring stiffness	$\mathrm{N\,m\,rad}^{-1}$
M_β	flapping moment at the hinge	N m
$\overline{M}_\beta$	non-dimensional flapping moment, $= M_\beta/(I_\beta \Omega^2)$	
m	blade mass per unit length	$\mathrm{kg\,m}^{-1}$
m_a	apparent mass of the rotor disk	kg
N	number of helical vortex filaments	
N_b	number of blades	

P	rotor shaft power	$\mathrm{N\,m\,s^{-1}}$
P_0	rotor profile power	$\mathrm{N\,m\,s^{-1}}$
P_h	ideal rotor induced power in hover, $= T^{3/2}/\sqrt{2\rho A}$	$\mathrm{N\,m\,s^{-1}}$
P_i	rotor induced power	$\mathrm{N\,m\,s^{-1}}$
p	helical pitch angle	rad
p	rotor roll rate	$\mathrm{rad\ s^{-1}}$
Q	rotor shaft torque	N m
q	rotor pitch rate	$\mathrm{rad\ s^{-1}}$
R	rotor radius	m
r, θ, z	cylindrical polar coordinates	(m, rad, m)
$\vec{r}$	position vector of a wake collocation point	(m, m, m)
r_c	vortex core radius	m
T	rotor thrust	N
T_h	reference rotor thrust in hover	N
S_β	static flapping inertia moment of the blade	kg m
t	time	s
U	resultant air velocity at blade section, $= \sqrt{U_P^2 + U_T^2}$	$\mathrm{m\,s^{-1}}$
U_P	air velocity at blade section, normal to rotor disk	$\mathrm{m\,s^{-1}}$
U_R	air velocity at blade section, radial component	$\mathrm{m\,s^{-1}}$
U_T	air velocity at blade section, chordwise component	$\mathrm{m\,s^{-1}}$
$\vec{V}$	velocity vector at a wake collocation point	$\mathrm{m\,s^{-1}}$
V_c	axial (vertical) climb velocity	$\mathrm{m\,s^{-1}}$
V_h	ideal rotor induced velocity in hover, $= \sqrt{T/2\rho A}$	$\mathrm{m\,s^{-1}}$
V_i	rotor induced velocity	$\mathrm{m\,s^{-1}}$
V_r, V_θ, V_z	radial, swirl and axial velocities	$\mathrm{m\,s^{-1}}$

V_∞	freestream velocity	m s^{-1}
x, y, z	Cartesian coordinates	(m, m, m)
α	angle of attack	rad
α	divergence rate	s^{-1}
$\overline{\alpha}$	non-dimensional divergence rate, $= \alpha/(\Gamma_v/4\pi R^2)$	
α_s	rotor shaft tilt angle	rad
β	blade flapping angle	rad
β_0	coning blade flapping angles	rad
β_{1c}	longitudinal blade flapping angles	rad
β_{1s}	lateral blade flapping angles	rad
χ	rotor wake skew angle, $= \tan^{-1}(\mu/\lambda)$	rad
$\Delta\theta$	angular discretization	rad
$\Delta\psi$	azimuthal discretization	rad
$\Delta\zeta$	vortex age discretization	rad
$\delta\vec{r}$	wake geometry perturbation	(m, m, m)
Γ	vortex circulation (strength)	m^{2}s^{-1}
Γ_v	tip vortex circulation (strength)	m^{2}s^{-1}
Γ_b	blade bound vortex circulation (strength)	m^{2}s^{-1}
ϕ	sectional induced angle, $= V_i/\Omega R = \lambda/r$	rad
κ_v	additional induced power loss factor in axial descent	
λ	rotor inflow ratio, $= V_i/\Omega R$	
λ_0	linear mean inflow coefficient	
λ_{1c}	linear longitudinal inflow coefficient	
λ_{1s}	linear lateral inflow coefficient	
λ_h	reference rotor inflow ratio in hover, $= \sqrt{C_T/2}$	

$\overline{\lambda}$	radial contraction exponent in Landgrebe's wake model	
μ	advance ratio, $= V_\infty/\Omega R$	
ν_β	non-dimensional rotating blade flapping frequency, $= \omega_\beta/\Omega$	
Ω	rotor rotational speed	$\mathrm{rad\,s^{-1}}$
ω	wave number for a normal mode	
ω_{ex}	wave number for a normal mode	
ω_0	non-rotating blade flapping frequency, $= k_\beta/I_\beta\Omega^2$	$\mathrm{rad\,s^{-1}}$
ω_β	rotating blade flapping frequency	$\mathrm{rad\,s^{-1}}$
ψ	azimuth angle	rad
ψ_b	blade azimuth, $= \Omega t$	rad
$\psi_b^{(m)}$	azimuthal location of m^{th}-blade, $= \psi_b + 2\pi(m-1)/N_b$	rad
ψ_{ref}	reference blade azimuthal location, $= \psi_b^{(1)}$	rad
ρ	fluid (air) density	$\mathrm{kg\ m^{-3}}$
σ	eigenvalue of time-integration method	$\mathrm{s^{-1}}$
σ	rotor solidity	$N_b c/\pi R$
θ	rotor collective pitch	rad
θ_0	collective blade pitch angle	rad
θ_{1c}	lateral blade pitch angle	rad
θ_{1s}	longitudinal blade pitch angle	rad
ζ	vortex age	rad

Derivatives

$\dot{(\ )}$	differentiation with respect to time (t)
$\overset{\star}{(\ )}$	differentiation with respect to blade azimuth (ψ)

Abbreviations

CFD	Computational Fluid Dynamics
FCT	Fourier Coordinate Transformation
IGE	In Ground Effect
LHS	Left-Hand Side
ODE	Ordinary Differential Equation
OGE	Out of Ground Effect
PDE	Partial Differential Equation
PCC	Predictor-Corrector with Central difference
PC2B	Predictor-Corrector with 2nd-order Backward difference
PIPC	Pseudo-Implicit Predictor-Corrector
RHS	Right-Hand Side
RMS	Root-Mean-Square
TPP	Tip Path Plane

5.4 Summary

The emphasis of the present chapter was on validating the steady-state predictions obtained using the rotor wake analysis developed in this dissertation by comparison with experimental data. Experimental measurements from several different sources were used to demonstrate the ability of the free-vortex wake analysis to model rotor flow fields of practical interest. The correlation study included comparisons of tip vortex trajectories obtained using flow visualization techniques, rotor induced velocity field measurements, and also isolated rotor performance measurements. Applications of the present methodology to multiple rotor configurations was also demonstrated. In general, it was found that the steady-state free-wake model gave good qualitative agreement with the experimental measurements. Quantitative agreement was also found to be good with only a small discrepancies. Such discrepancies may be associated with not only the uncertainties in experimental measurements, but also the lack of modeling of some viscous and compressible phenomenon in the rotor wake. However, in spite of such discrepancies, the present free-vortex wake analysis is able to properly represents all physical trends of the wake structure and the induced velocity field.

Chapter 6

Results & Discussion: Time-Accurate Wake Model

As shown in Chapter 5, the steady-state (periodic) predictions of the wake gave good agreement with experimental measurements of wake geometries, induced velocity fields as well as rotor performance, for helicopter rotors operating in steady-state flight. In the present chapter, transient (maneuvering) results obtained using the time-accurate solution methodology are presented. The results are compared with experimental measurements obtained under time-varying (non-steady, maneuvering) flight conditions. First, the dynamics of the rotor wake response following a step increase in collective pitch is examined, and compared with experimental measurements for the time histories of the rotor thrust, blade flapping angles and induced inflow. Then, the same idea is extended to steady oscillatory (constant excitation frequency) blade pitch inputs, and the resulting dynamic rotor induced inflow predictions are again validated against experimental measurements of the inflow frequency response.

6.1 Aperiodicity of the Hovering Rotor Wake

Under ideal conditions, the rotor wake is axisymmetric in hovering flight. This implies that the trajectories of all the tip vortices do not vary with azimuth in a blade fixed coordinate system. The numerical solutions calculated free-vortex wake methods (both the relaxation and the stable PC2B time-marching algorithms) also show this behavior, as shown previously in Section 2.1. However, experimental observations using various flow visualization techniques always show evidence of some aperiodicity in the rotor wake – see, e.g., Ref. 72. Aperiodicity means spatial deviations of the phase-resolved locations of the tip vortices relative to the blades. This aperiodic motion of the tip vortices, which is often erroneously termed as wandering or meandering, may lead to errors and uncertainties when performing experimental measurements based on phase-resolved ensemble averaging techniques. It is also observed that the magnitude of aperiodicity increases with the vortex age (Ref. 67). The cause of the aperiodicity in the rotor wake is, however, not yet completely understood.

It was shown in Chapter 2 that the hovering rotor wake is in unstable equilibrium. Therefore, based on the linearized stability analysis in Section 2.2, any small disturbances in the rotor flow field would grow exponentially with time. As the rotor wake vortices convect below the rotor in its induced velocity field, the growing disturbances would be continuously translated away from the rotor. At least part of the aperiodicity in the phase-resolved locations of the rotor tip vortices can be explained based on such growing unstable deformation modes. The initial disturbances present in the flow field that initiate these growing unstable modes may be a result of several artifacts of individual experimental setup, e.g., wall interference, flow turbulence, etc. However, the *growth rate* of these initial disturbances can be predicted using the eigenvalue analysis of the rotor wake (see Section 2.3).

Figure 6.1 shows the measured variation of the aperiodicity of the tip vortex location (that is, the deviations from a purely periodic behavior) as a function of increasing vortex age for two rotor configurations. The measurements are in the blade-fixed coordinate system. Figure 6.1(a) is for the baseline two-bladed rotor (Ref. 66), while Fig. 6.1(b) is for a deliberately mistracked rotor. Note that mistracking of the two blades produces a source of 1/rev aerodynamic excitations to the rotor wake. The operating conditions for these rotors have already been described in Section 2.5.1. The eigenvalue analysis of Section 2.3 gives a maximum growth rate of 53.7 $\sec^{-1}$ for the baseline rotor and 55.5 $\sec^{-1}$ for the mistracked rotor corresponding to the most unstable wake deformation mode, i.e., the deformation mode with the highest growth (divergence) rate. It was shown in Chapter 2 that the most unstable deformation mode for a two-bladed rotor corresponds to the vortex pairing phenomenon – see Section 2.5. It is clear from Fig. 6.1 that the aperiodicity increases with vortex age, as predicted by the eigenvalue-based stability analysis. Notice that a logarithmic ordinate is used in these plots to bring out the exponential growth rate associated with the phenomenon.

As mentioned earlier, the initial disturbances that initiate these growing unstable modes may be affected by several different factors, including random disturbances associated with flow turbulence. These disturbances may not, in general, be repeatable from test to test. Figure 6.2 shows results for the aperiodicity of the wake of the baseline two-bladed rotor as derived from two flow visualization experiments performed on the same rotor setup. The results are presented in the form of variance in the tip vortex locations, i.e., average deviation from a mean (periodic) wake structure. Figure 6.2(a) shows results corresponding to the experiments reported in Ref. 66, while Fig. 6.2(b) shows similar results corresponding to a second set of experiments performed using the same experimental set-up that was used to verify repeatability (Ref. 66). It is interesting to note that the magnitude of the disturbances are different in the two cases. However, it is equally interesting to note that the growth rate for both cases remains unchanged and is repeatable. The growth rate predicted using the eigenvalue analysis

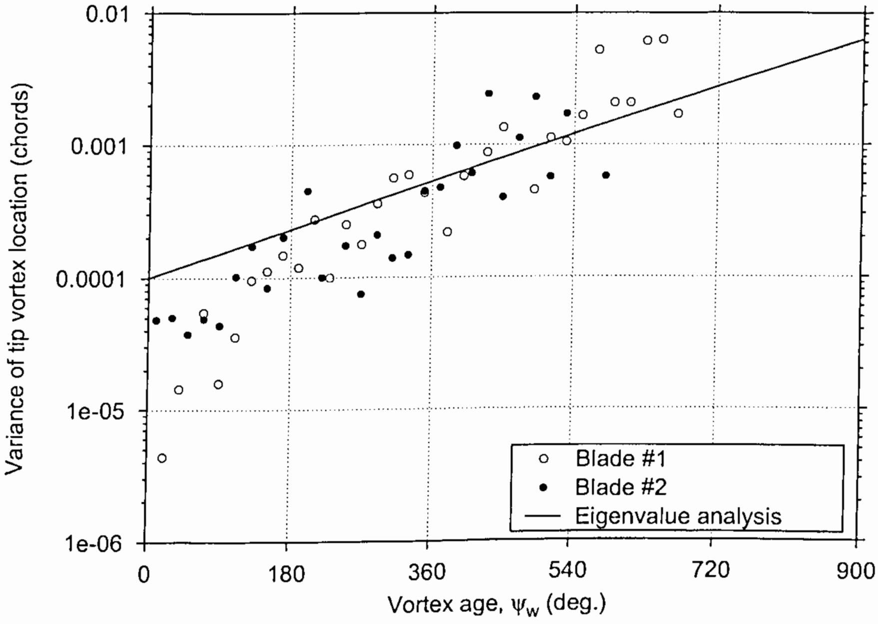
(a) Baseline (tracked) rotor

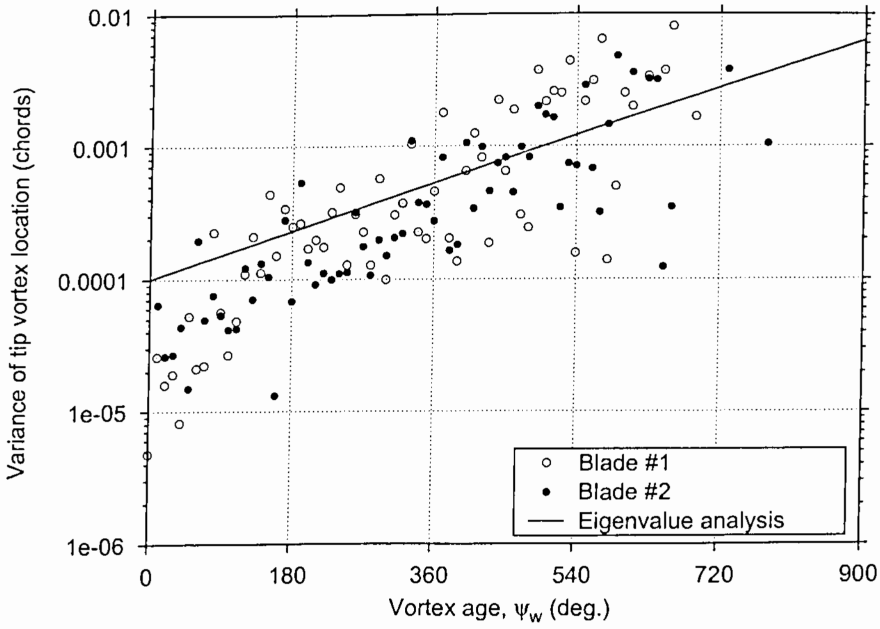
(b) Deliberately mistracked rotor

Figure 6.1: The aperiodicity in the rotor wake as a function of vortex age. (a) Baseline (tracked) rotor. (b) Deliberately mistracked rotor, with one blade set at 1° lower collective pitch.

(a) Experiments reported in Ref. 66 (1998)

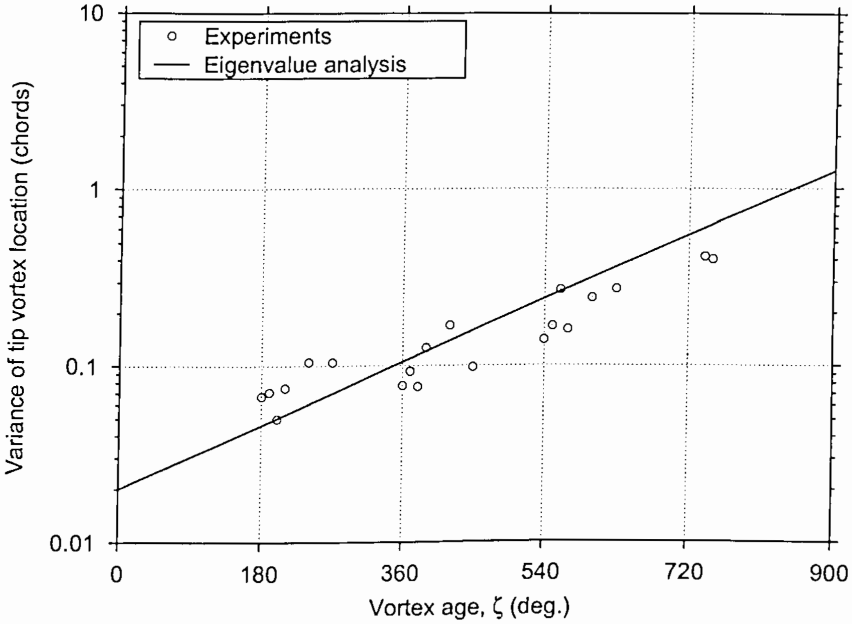

(b) Experiments to verify repeatability

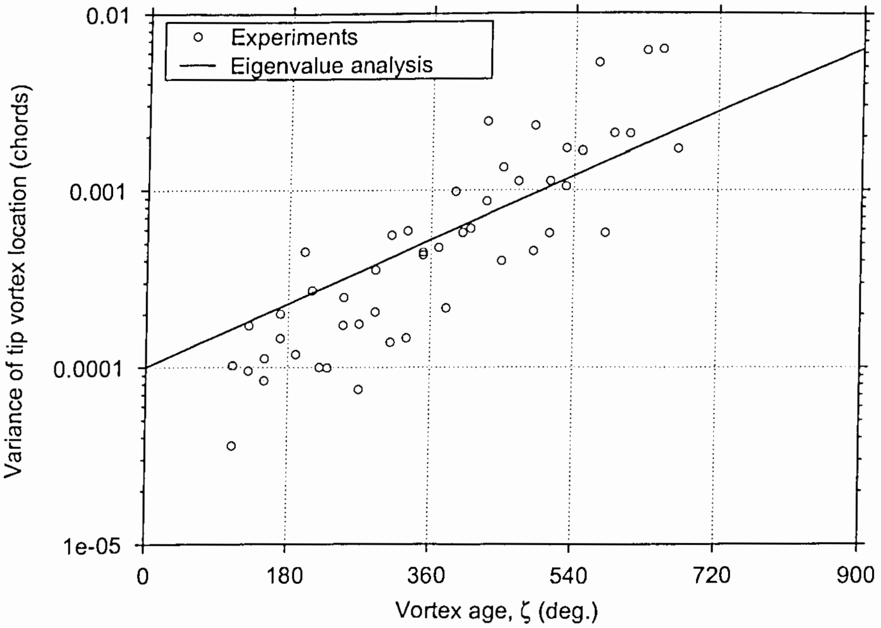

Figure 6.2: The aperiodicity in the rotor wake as a function of vortex age. Experimental results obtained using the same experimental set-up at different times, $N_b = 2$. (a) Experiments reported in Ref. 66 (1998), (b) Experiments to verify repeatability

showed good agreement with both sets of experimental results. These results confirm that the unstable disturbance modes and the associated growth rates are a physical characteristic of rotor wakes. This also verifies that the linearized stability analysis correctly predicts the initial growth rates associated with any disturbances made to the rotor wake.

It was shown in Section 2.6 that the numerical solution to the rotor wake problem obtained using the PCC scheme showed vortex instabilities originating from numerical truncation errors. Therefore, it is only fortuitous that these numerical instabilities mimic the physically observed instabilities, particularly the vortex pairing instability mode. It is possible, however, to use the stable PC2B scheme to attempt to predict such instabilities. This can be done by explicitly modeling disturbances in the rotor flow field. It is, in general, impossible to accurately represent all of the actual disturbances present in any experimental set-up, but several numerical strategies can be adopted to replicate such disturbances. A qualitatively reasonable approximation is to include some random perturbation velocities to represent flow turbulence and other disturbances present in the flow field. For example, three types of disturbances can be considered:

Disturbance 1: A random disturbance of magnitude 1×10^{-8} is applied to the entire wake geometry after every time (azimuthal) step. Because all calculations are performed using double precision arithmetic, this can be easily accomplished by truncating the results to single precision after each time step. The truncation introduces pseudo-randomness into the solution and so represents a simple model of flow turbulence.

Disturbance 2: A relatively larger magnitude (1×10^{-4}) disturbance is added below the first wake turn after each time step. The disturbance field is assumed to be sinusoidal with vortex age. This once-per-revolution variation is representive of blade mistracking or flow disturbances originating from rotor support structures, an airframe, etc.

Disturbance 3: A sinusoidal disturbance with a large magnitude (1×10^{-2}) applied to the far wake (below sixth wake turn) after each time step. This is representive of various turbulent phenomena occurring in the rotor far wake, which may possibly lead to vortex breakdown and transition to a turbulent jet-like flow field.

The numerical solutions found after 15 rotor revolutions as obtained with these representive disturbances, is shown in Fig. 6.3. The experimentally measured tip vortex locations are also plotted for comparison. It is significant to note that although the three disturbance sets were substantially different, only the most unstable deformation mode of the wake (i.e., the vortex pairing mode described in Section 2.5) is predominantly excited in all three cases. This instability is qualitatively similar to the vortex pairing that has been observed in experiments (Refs. 14, 40, 66). However, note that the onset of pairing in the numerical solutions occurs at a later vortex age as compared to the experiments. In fact, any level of agreement with the experiments could be obtained by a different choice of the disturbance velocity field. The purpose here is to emphasize that by modeling some random disturbance field, physically realistic instabilities of the wake can be predicted using the time-accurate wake solution.

For clarity, the numerical results are shown in Fig. 6.4 in the form of deviations from the mean (time-averaged) tip vortex trajectories. This plot essentially shows the aperiodicity of the rotor wake resulting from the disturbances. Again, the growth of the aperiodicity with vortex age shows a trend fully consistent with the eigenvalue analysis, confirming that the aperiodicity does indeed stem from the growth of disturbances present in the rotor flow field.

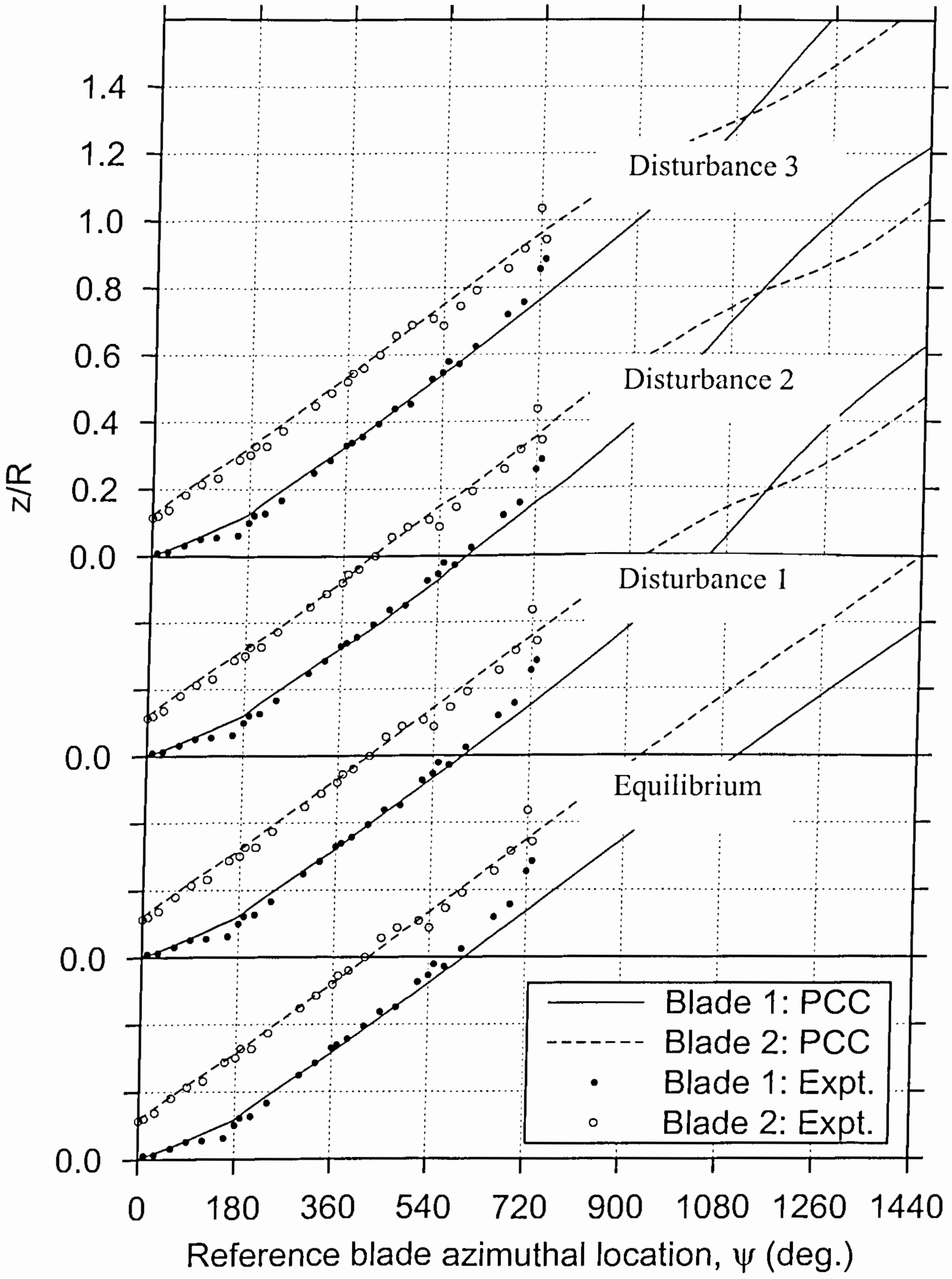

Figure 6.3: Numerical solutions for the tip vortex trajectories from a two-bladed rotor in response to different random disturbances in the flow field. Experimental results from Ref. 66.

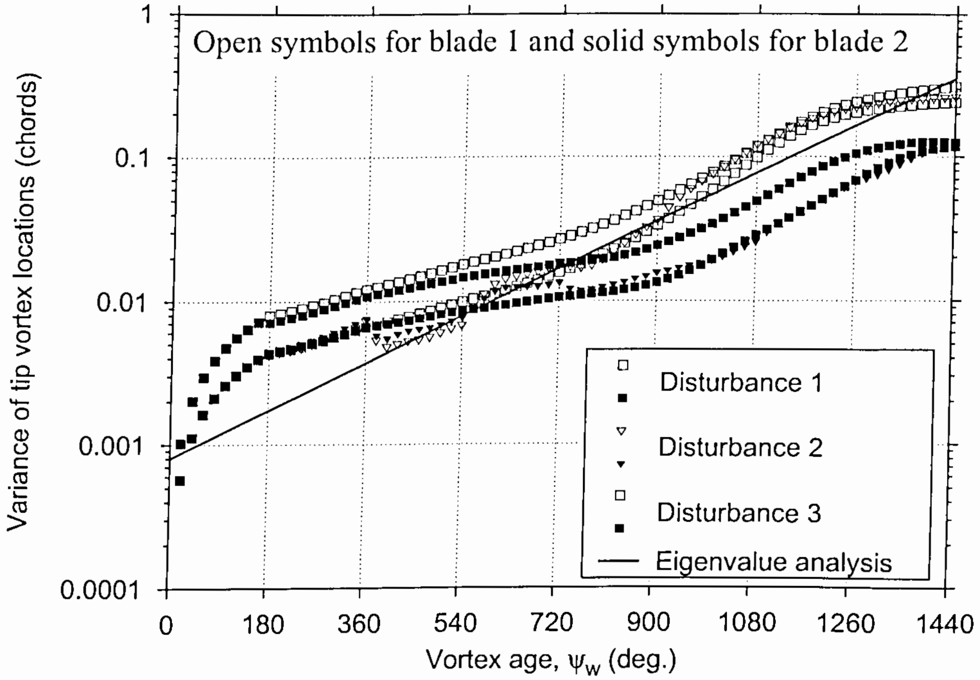

Figure 6.4: Predicted aperiodicity in the rotor wake geometry predictions resulting from different sources of random disturbances.

6.2 Response to Collective & Cyclic Pitch Inputs

6.2.1 Step Increase in Collective Pitch

The time-accurate free-wake model was applied to solve for the transient rotor wake dynamics following an elementary maneuver in the form of a sudden increase in the rotor collective pitch. This is a classic transient problem used to study jump take-offs of autogyros and also, in some cases, helicopters (Ref. 98). In this case, the rotor is rotated at an rpm higher than the normal rotor operating rpm but with zero collective pitch, then the collective pitch is quickly increased to a desired value. The transient overshoot in thrust following such a rapid collective pitch input helps to lift the aircraft off the ground, after which the rotor rpm decays to the normal operating value.

For preliminary numerical calculations of this problem, a teetering rotor in hover is considered to decouple the effects of transient blade flapping response from the induced inflow response resulting from the dynamics of the rotor wake. The geometry and operating conditions of the rotor correspond to the two-bladed rotor studied in the experiments reported in Refs. 89 and 90 and the initial hovering wake geometry corresponds to that at a thrust of $C_T = 0.005$. The steady-state wake geometry and rotor induced inflow for these operating conditions was previously validated with experimental measurements in Section 5.1. This steady-state solution was used as an initial condition for the transient calculations.

A time-accurate calculation was first performed where the collective pitch was increased by 1 degree after 5 rotor revolutions (at time $t = 10\pi/\Omega$)

$$\theta_0 = \begin{cases} 5^\circ & t < 10\pi/\Omega \\ 6^\circ & t \geq 10\pi/\Omega \end{cases} \tag{6.1}$$

The predicted rotor thrust response and mean inflow build-up is shown in Fig. 6.5. Although both the relaxation (periodic) and the time-marching (transient) solutions show a similar initial overshoot in thrust, the subsequent response was noted to be significantly different. The relaxation solution rapidly approached the steady-state solution while suppressing the transient oscillatory behavior. Notice that the intermediate relaxation solutions are not physically meaningful. The transient solution, however, correctly captures the unsteady build-up of inflow resulting from the wake dynamics.

The collective pitch input causes a perturbation in the wake and excites the most unstable deformation mode corresponding to vortex pairing (see Section 2.5). This is evident from the wake geometry after about five rotor revolutions (at $\psi_b = 1890^\circ$) after the collective input, as shown in Fig. 6.6. The two tip vortex filaments showed a tendency to roll around each other at approximately three wake turns (revolutions)

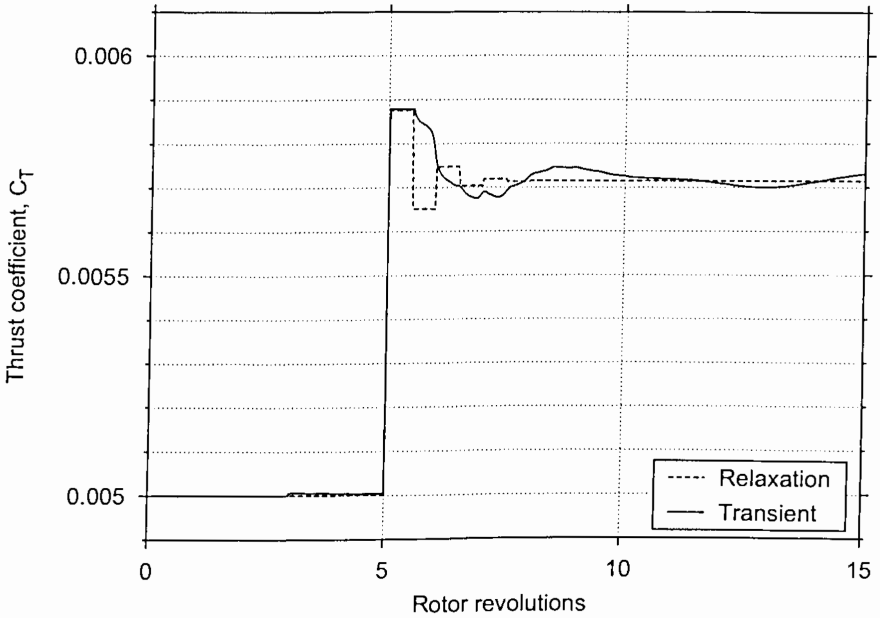
(a) Rotor thrust coefficient

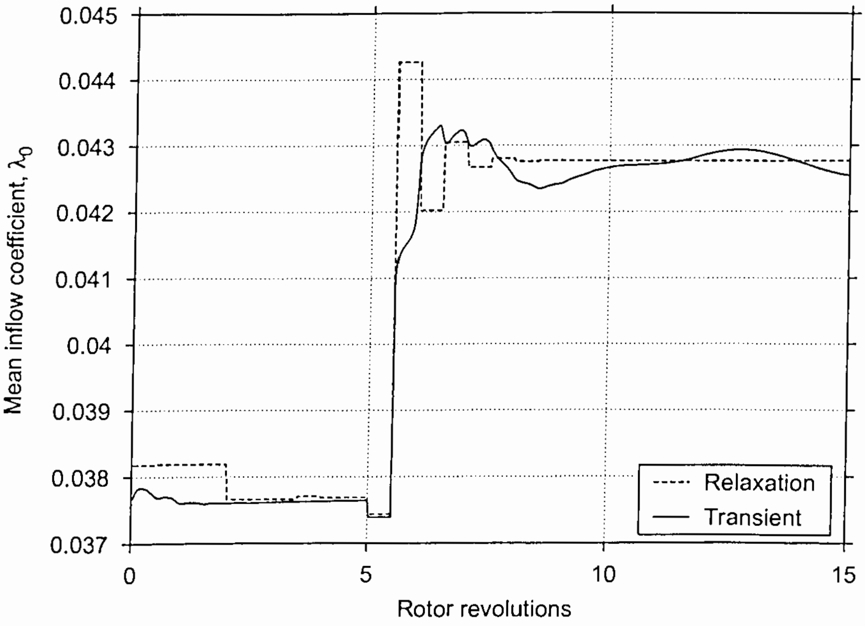
(b) Mean rotor inflow coefficient

Figure 6.5: Thrust and mean inflow following a step increase in collective pitch for a teetering two-bladed rotor in hover using relaxation and transient wake models. (a) Rotor thrust coefficient, (b) Mean rotor inflow coefficient.

below the TPP. After a time corresponding to two more rotor revolutions, as shown in Fig. 6.6(b), the pairing vortices have convected further away from the TPP. Eventually, the pairing vortices are convected sufficiently away from the rotor and outside of the computational domain. The pairing instability develops and grows as the wake is convected below the rotor. However, because of the increased axial flow (inflow) corresponding to the increase in thrust, the pairing vortices are quickly convected away from the rotor. Although the instability is initiated, it is not self-sustained because of the axial convection velocities (induced inflow) and is not present in the steady-state solution. More details of the dynamic evolution of the rotor wake will be shown later in Section 6.2.2. Therefore, a transient wake solution algorithm is clearly necessary to predict the rotor response for even such simple time-varying inputs.

Effects of Unsteady Aerodynamics

The results shown in Fig. 6.5 were calculated using quasi-steady aerodynamics for the blade lift solution. It is often argued that unsteady aerodynamic effects may be important for this problem, at least during the initial transient. Therefore, two approaches to model unsteady aerodynamic effects were examined. In the first case, the rotor wake solution was calculated using only the tip vortex along with a standard blade-element level unsteady aerodynamics model to correct the local blade lift for the shed wake time-history effects, and also for the apparent mass forces (see, e.g., Ref. 2). Note that this approach affects the subsequent wake geometry through the tip vortex strength as well as blade flapping solution. The second approach used to represent unsteady aerodynamic effects was to incorporate the complete set of trailed as well as shed wake vortices into the free-vortex wake solution, as shown in Figure 6.7(a). Note that only the vortex elements up to the first blade passage are shown in this figure for clarity, but

(a) $\psi_b = 1890^\circ$

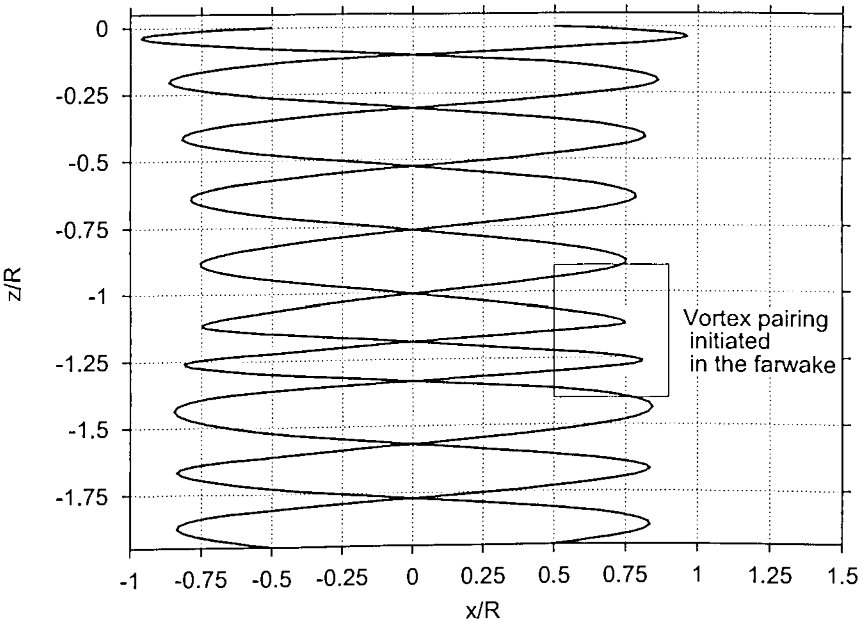

(b) $\psi_b = 2160^\circ$

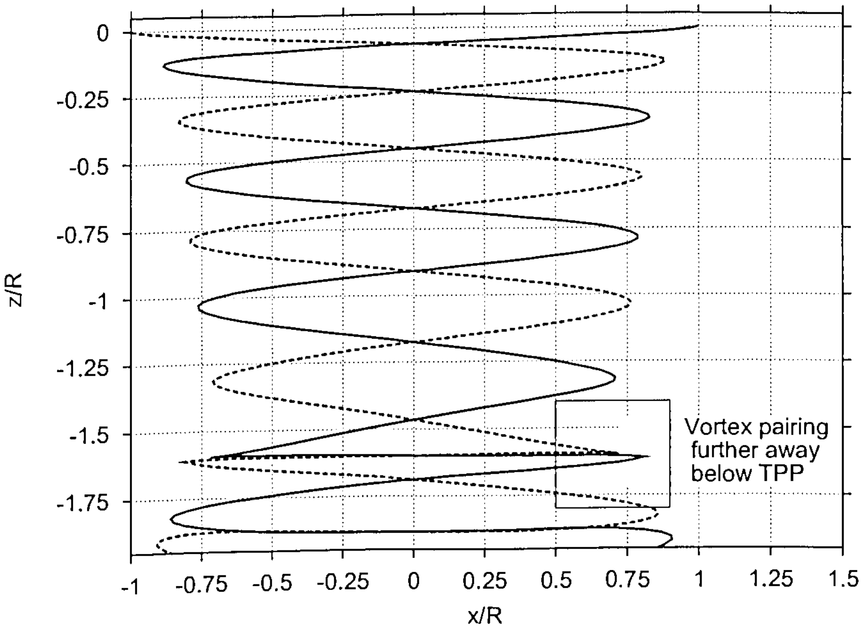

Figure 6.6: The transient behavior of the wake geometry following a step increase in collective pitch for a teetering two-bladed rotor in hover. Side views of the wake geometry are shown at times (a) $\psi_b = 1890^\circ$, and (b) $\psi_b = 2160^\circ$.

all vortex elements were included in the free-vortex wake solution up to four revolutions below the rotor disk. In this case, the force-free positions of both the trailed and shed vortex elements in the wake were solved simultaneously using the free-vortex algorithm, albeit at a significant increase in computational cost. To understand the relative influence of the unsteady effects associated with the shed wake vortices alone, a solution was also obtained using just the trailed wake vortices, i.e., the tip vortex as well as all the vortex trailers representing the trailed vortex sheet from the inboard part of the blade.

The rotor thrust response obtained using these two different approaches is shown in Fig. 6.7(b). The effects of blade-element level unsteady aerodynamic corrections were found to be negligibly small. This is expected because the effective reduced frequencies associated with this type of rotor pitch input are small. The high frequency components in a step change have a relatively small magnitudes, and their effects are restricted to a very small time period. Notice, however, that the inclusion of inboard trailed wake sheet causes a small decrease in the rotor thrust. This is because of the slightly higher inflow induced by these additional inner trailed wake vortices. However, the overall qualitative response of the rotor to a step change in collective pitch remains unaffected. Furthermore, the inclusion of shed wake vortices does not affect this transient rotor response. Clearly, in this case, the unsteady aerodynamic effects associated with the shed wake are negligible, and the transient rotor response is dominated primarily by the dynamics of the trailed wake system.

The above results show the influence of the wake dynamics and the induced inflow resulting from the trailed vortex wake alone. For a teetering rotor in hovering or axial flight, there is no blade flapping by virtue of axisymmetry of blade loads. Even during the transient response, because the wake and collective inputs from both blades are

(a) Wake geometry showing all trailed and shed wake

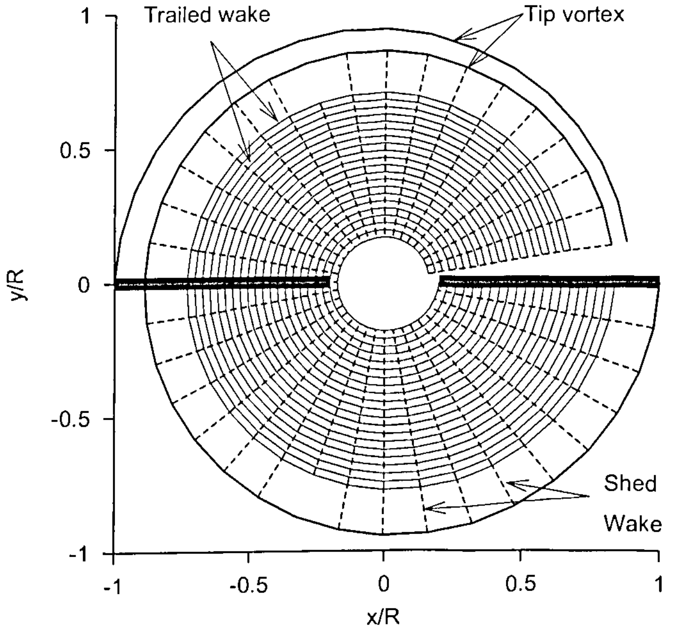

(b) Time-history of rotor thrust coefficient

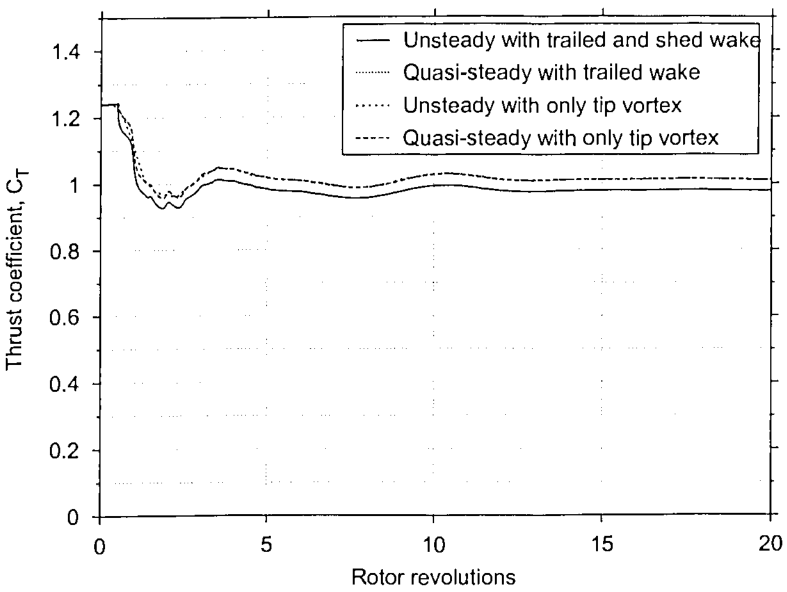

Figure 6.7: Role of unsteady aerodynamic effects in the rotor response following a step increase in collective pitch for a teetering two-bladed rotor in hover. (a) Wake geometry showing all trailed and shed wake, (b) Time-history of rotor thrust coefficient.

the same, the blade flapping is identically zero. Typically, blade flapping dynamics will also augment such a transient overshoot in rotor thrust. This is because following an increase in collective there will be a transient overshoot in blade flapping, which will move the rotor blades upward and further away above the trailed wake. This may result in a further delay in build-up of rotor inflow and a corresponding higher thrust overshoot.

An example of this latter effect is shown in Fig. 6.8, where the numerical calculations were repeated using an articulated rotor with a flapping hinge at the rotational axis. The remaining rotor geometry and operating parameters were the same as the above rotor. Results for the time-history of rotor thrust following a step collective input for the teetering and articulated rotor configurations are shown in Fig. 6.8. Notice that the articulated rotor shows a substantially higher transient rotor overshoot compared to the teetering rotor. Therefore, the overall response of the rotor to such inputs becomes strongly dependent on both the rotor wake dynamics as well as the blade flapping dynamics.

Dynamic Inflow Using Blade Element/Momentum Theory

A transient overshoot in rotor thrust and blade flapping was experimentally measured by Carpenter & Friedovich (Ref. 98). The slow build-up of the mean rotor inflow that was observed in these experiments was attributed to "inertia" effects in the flow. To model this behavior, a dynamic inflow equation was formulated by Carpenter & Friedovich by equating the rotor thrust obtained using local momentum theory to that using a blade-element theory (the combined unsteady blade element/momentum theory or BEMT – see Ref. 98 for details). A derivation of a simple dynamic model along these lines is now presented. In the next section, this dynamic inflow model is com-

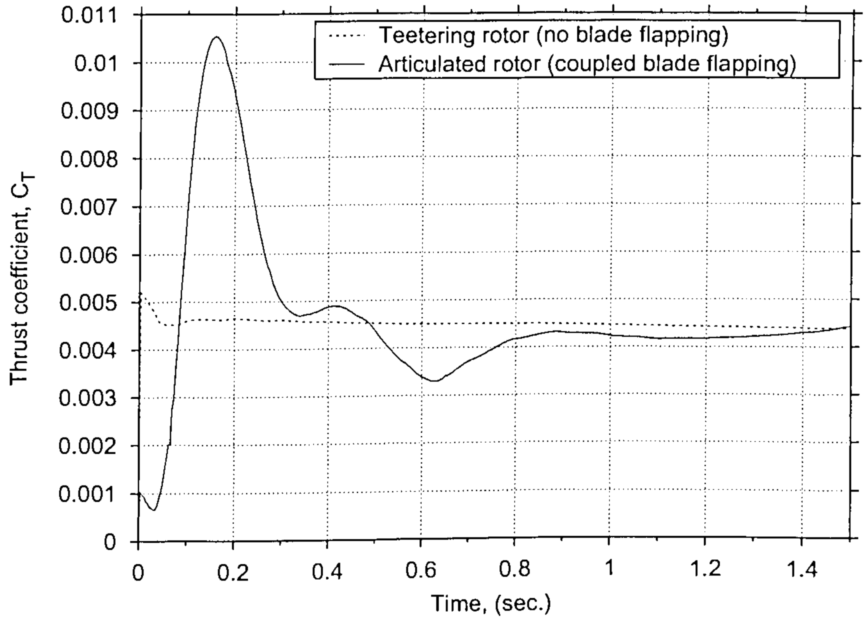

Figure 6.8: Time-history of rotor thrust following a step increase in collective for an articulated and a teetering rotor.

pared with both the experimental measurements and the predictions obtained using the present free-vortex wake analysis.

To model the rotor dynamics during a collective pitch increase, a combination of extended momentum theory and local blade element theory can be employed. Unsteady inflow effects are modeled using the concept of an apparent mass (inertia), where the thrust equation (as given by the simple momentum theory) is modified by addition of an unsteady term to give

$$T = m\dot{v}_i + 2\pi R^2 \rho v_i \left(v_i + \frac{2}{3}\dot{\beta} R \right) \tag{6.2}$$

The term m_a was associated by Carpenter & Friedovich (Ref. 98) with the apparent mass of an impermeable (solid) circular disk accelerating in a stagnant fluid, i.e., a non-circulatory effect. It was further suggested that this apparent mass to be 63.7%

the mass of a sphere of fluid with a radius equal to the rotor radius (see also Ref. 99), i.e.,

$$m_a = 0.637\rho \left(\frac{4}{3}\pi R^3 \right) \tag{6.3}$$

The $m_a \dot{v}_i$ term, therefore, is meant to represent the additional force on the rotor disk because of the accelerating inflow. Note, however, that this concept assumes an equivalence between the force on a solid disk accelerating in a stagnant fluid, and the force on a fluid accelerating through a permeable actuator disk. Such an equivalence is certainly not rigorous, however, a derivation will proceed on the basis of this assumption. Using the blade element theory, the elemental thrust is given by

$$dT = \frac{1}{2} N_b \rho c C_{l_\alpha} \left(\theta - \frac{v_i(r)}{\Omega r} - \frac{\dot{\beta}}{\Omega} \right) \Omega^2 r^2 dr \tag{6.4}$$

Assuming a rectangular planform, i.e., $c(r) = c$, and uniform inflow, i.e., $v_i(r) = v_i$, the total rotor thrust can be found by integrating the above equation to get

$$T = \int_0^R dT \quad = \quad \frac{1}{6} N_b \rho c C_{l_\alpha} \Omega^2 R^3 \left(\theta - \frac{3}{2} \frac{v_i}{\Omega R} - \frac{\dot{\beta}}{\Omega} \right) \tag{6.5}$$

Equating the two thrust expressions (Eq. 6.2 and 6.5), an equation governing the dynamic rotor inflow can be derived. Note that the inflow dynamics is coupled with the blade flapping dynamics, and a second equation governing the blade flapping angle can be found by moment equilibrium around the flapping hinge, as explained previously in Section 4.2. Note that the BEMT assumes a spanwise uniform inflow distribution, which would be the case only for rotors with an ideal blade twist. Therefore, before deriving these equations for the time-dependent inflow and blade flapping, a correction factor must be introduced to account for the non-uniform spanwise inflow distribution.

Correction Factors for Non-Uniform Inflow

The above formulation is based on the combined blade element and momentum theory, where the inflow is assumed to be uniform over the blade span. In general, this may not be the case, and some form of correction may be necessary to include the physical effects of non-uniform inflow. These corrections can be found using the BEMT. Note that the correction factors are calculated only for the steady-state conditions and are assumed to remain constant during intermediate (transient) conditions.

The elemental thrust over an annulus of the rotor disk is given by the local momentum theory applied to an annulus of the rotor disk, i.e.,

$$dT = 2\pi r\,dr\,\rho v_i(r)\cdot 2v_i(r) = 4\pi\rho r[v_i(r)]^2\,dr \tag{6.6}$$

Equating this thrust to the steady part of the elemental thrust given by Eq. 6.5 gives a quadratic equation for $v_i(r)$, i.e.,

$$4\pi\rho r[v_i(r)]^2 + \frac{1}{2}N_b\rho c C_{l_\alpha}\Omega r[v_i(r)] - \frac{1}{2}N_b\rho c C_{l_\alpha}\Omega^2 r^2\theta = 0 \tag{6.7}$$

Therefore, the radial inflow distribution can be determined from this quadratic using

$$v_i(r) = \frac{N_b c C_{l_\alpha}\Omega}{16\pi}\left[-1 \pm \sqrt{1 + \frac{32\pi r\theta(r)}{N_b c C_{l_\alpha}}}\right] \tag{6.8}$$

where only the positive root is physically meaningful. The rotor thrust can now be found by integration along the blade span using this radial inflow distribution, i.e.,

$$\bar{T} = \int_0^R \frac{1}{2}N_b\rho c C_{l_\alpha}\left(\theta(r) - \frac{v_i(r)}{\Omega r}\right)\Omega^2 r^2\,dr \tag{6.9}$$

The uniform inflow, based on simple momentum theory, is given by

$$\bar{v}_i = \sqrt{\frac{\bar{T}}{2\rho\pi R^2}} \tag{6.10}$$

and the correction factor η is found by requiring that this uniform inflow also satisfies the modified blade element thrust relation, i.e.,

$$T = \frac{1}{6} N_b \rho c C_{l_\alpha} \Omega^2 R^3 \left(\theta - \frac{3}{2} \frac{\bar{v}_i}{\Omega R} \eta \right) \tag{6.11}$$

Therefore, the correction factor is given by

$$\eta = \frac{2}{3} \left(\frac{\Omega R}{\bar{v}_i} \right) \frac{\left(\frac{1}{6} N_b \rho c C_{l_\alpha} \Omega^2 R^3 \theta - \bar{T} \right)}{\frac{1}{6} N_b \rho c C_{l_\alpha} \Omega^2 R^3} \tag{6.12}$$

The correction factor for the blade flapping moment is found in a similar manner. The aerodynamic flapping moment is calculated by integration over the blade planform using

$$\bar{M} = \int_0^R r dT \quad = \quad \int_0^R \frac{1}{2} N_b \rho c C_{l_\alpha} \left(\theta(r) - \frac{v_i(r)}{\Omega r} \right) \Omega^2 r^3 dr \tag{6.13}$$

Now, a factor τ may be employed to correct for non-uniform inflow effects in the form given by

$$M = \frac{\gamma}{8} I_b \left(\theta - \frac{4}{3} \frac{\bar{v}_i}{\Omega R} \tau \right) \tag{6.14}$$

This correction factor, τ, can be readily calculated as

$$\tau = \frac{6}{\gamma I_b} \frac{\Omega R}{\bar{v}_i} \left(\frac{\gamma}{8} I_b \theta - \bar{M} \right) \tag{6.15}$$

With these correction factors, the two equations to be solved are the inflow equation

$$m\dot{v}_i + 2\pi R^2 \rho v_i^2 + \frac{4}{3} \pi R^3 \rho v_i \dot{\beta} + \frac{N_b}{6} \frac{\gamma}{R} \Omega I_b \dot{\beta} + \frac{N_b}{4} \frac{\gamma}{R} \frac{\Omega}{R} I_b \eta v_i = \frac{N_b}{6} \frac{\gamma}{R} \Omega^2 I_b \theta \tag{6.16}$$

and the blade flapping dynamics equation

$$\ddot{\beta} + \frac{\gamma}{8} \Omega \dot{\beta} + \Omega^2 \beta + \frac{\gamma}{6} \frac{\Omega}{R} \tau v_i = \frac{\gamma}{8} \Omega^2 \theta \tag{6.17}$$

These two equations are solved simultaneously for $v_i(t)$ and $\beta(t)$ using a predictor-corrector type trapezoidal or a 2nd-order backward integration algorithm. Finally, the instantaneous thrust is calculated using the modified thrust equation

$$T = m\dot{v}_i + 2\pi R^2 \rho \eta v_i \left(\eta v_i + \frac{2}{3}\dot{\beta} R \right) - N_b m_b \ddot{\beta} \frac{R^2}{2} \tag{6.18}$$

where the last term represents the inertia force because of blade acceleration. Note that although this inertial acceleration is negligible under most flight conditions, it is a substantial factor in the transient response immediately following a collective pitch input. This term is not directly included in the dynamic inflow equations obtained using the blade element theory, but included separately in rotor thrust calculation. It should also be noted that the $\ddot{\beta}$ term corresponds to the acceleration of the blade coning or collective flapping angle, and cyclic flapping does not contribute to this additional inertia term.

Non-dimensional Form of the Inflow Equation

The instantaneous rotor thrust as given by the blade element and momentum theory results is

$$\begin{aligned} T &= m_a \dot{v}_i + \rho \left(2\pi R^2\right) v_i \left(v_i + \frac{2}{3}\dot{\beta} R \right) \\ &= \frac{1}{2} N_b \rho c C_{l_\alpha} \Omega^2 R^3 \left(\frac{\theta}{3} - \frac{1}{2}\frac{v_i}{\Omega R} - \frac{1}{3}\frac{\dot{\beta}}{\Omega} \right) \end{aligned} \tag{6.19}$$

or in non-dimensional form the former equation becomes

$$\begin{aligned} C_T &= \frac{m_a}{\rho \pi R^3} \overset{\star}{\lambda} + 2\lambda_i \left(\lambda_i + \frac{2}{3} \overset{\star}{\beta} \right) \\ &= \frac{1}{2} \sigma C_{l_\alpha} \left[\frac{\theta}{3} - \frac{\lambda_i}{2} - \frac{\overset{\star}{\beta}}{3} \right] \end{aligned} \tag{6.20}$$

The corresponding equation for the inflow dynamics is given by

$$m_a \dot{v}_i = \frac{1}{2} N_b \rho c C_{l_\alpha} \Omega^2 R^3 \left[\frac{\theta}{3} - \frac{1}{2}\frac{v_i}{\Omega R} - \frac{1}{3}\frac{\dot{\beta}}{\Omega} \right] - \rho \left(2\pi R^2\right) v_i \left(v_i + \frac{2}{3}\dot{\beta} R \right) \tag{6.21}$$

or, non-dimensionally, the former equation can be written as

$$\frac{m_a}{\rho \pi R^3}\,\overset{\star}{\lambda}_i = \frac{1}{2}\sigma C_{l_\alpha}\left[\frac{\theta}{3} - \frac{\lambda_i}{2} - \frac{\overset{\star}{\beta}}{3}\right] - 2\lambda_i\left(\lambda_i + \frac{2}{3}\overset{\star}{\beta}\right) \tag{6.22}$$

This latter equation must be solved together with the blade flapping equation of motion (Eq. 6.17).

6.2.2 Comparison with Experiments

To validate the time-accurate free-wake calculation methodology for transient problem with time-varying blade pitch inputs, a three-bladed articulated rotor was examined. In this case, the blade flapping dynamics (Eq. 4.88) were also coupled with the wake solution during every time-step. This problem was experimentally examined by Carpenter & Friedovich (Ref. 98) using a full-scale helicopter rotor. The rotor blades had a radius of 5.8 m (19 ft.) and the solidity was 0.042. A nominal operating rotational frequency was approximately 220 rpm. In the transient experiments, the blade collective pitch was increased linearly at various constant rates to a maximum angle of 12 degrees. The blade flapping angles, the rotor thrust, and the mean rotor inflow were measured in the experiment.

The results using the dynamic inflow model, as described in the previous section, are shown in Figs. 6.9-6.11 along with the corresponding results using the present free-vortex wake analysis. The RHS of Eq. 6.22 contains the non-dimensional apparent mass component, which is found using Eq. 6.3 to be equal to ≈ 0.85. An approximate time constant of the dynamic inflow equation can be estimated using only the linear portion of Eq. 6.22, i.e.,

$$0.85\,\overset{\star}{\lambda}_i = -\frac{1}{4}\sigma C_{l_\alpha}\lambda_i \tag{6.23}$$

or

$$\frac{0.85 \times 4}{\sigma C_{l_\alpha}} \overset{\star}{\lambda_i} = -\lambda_i \tag{6.24}$$

Now, assuming $C_{l_\alpha} = 2\pi/\text{rad}$, the inflow time constant can be identified as

$$\tau = \frac{0.541}{\sigma} \text{ radians } = \frac{0.541}{2\pi\sigma} \text{ rotor revolutions} \tag{6.25}$$

Therefore, using $\sigma = 0.042$ for Carpenter & Friedovich's rotor experiment the time constant for the unsteady flow development is found to be approximately two rotor revolutions, which is a relatively large time-lag.

The transient free-vortex wake results for this problem were obtained using an initial wake geometry corresponding to a very small thrust coefficient. The initial mean inflow and coning angle were also negligibly small. The wake geometry and the blade flapping response were then calculated (in a coupled manner) by integrating in time the respective equations (Eqs. 3.31 & 4.88). Figure 6.9 shows the results for a ramp rate of 200 degrees per second along with the experimental measurements of Carpenter & Friedovich (Ref. 98). Note that the collective input in the experiments shows some oscillatory behavior, which is because of blade torsion. As a result, the transient overshoot in flapping (coning) is slightly under-predicted. However, the predicted rotor thrust response and build-up in the inflow showed good agreement with the experimental measurements. The slow build-up of inflow (which is modeled as a time-lag because of apparent mass effects in the dynamic inflow theory) is found to be, in actuality, a result of the transient evolution of the trailed rotor wake, i.e., a circulatory effect. The dynamic inflow response approximately resembles the first-order linear system given by Eq. 6.24; the inflow reaches the steady-state value in about three time periods, i.e., after six rotor revolutions or 0.81 seconds. This effect is predicted very well by the time-accurate wake algorithm, as shown in Fig. 6.9. A good correlation

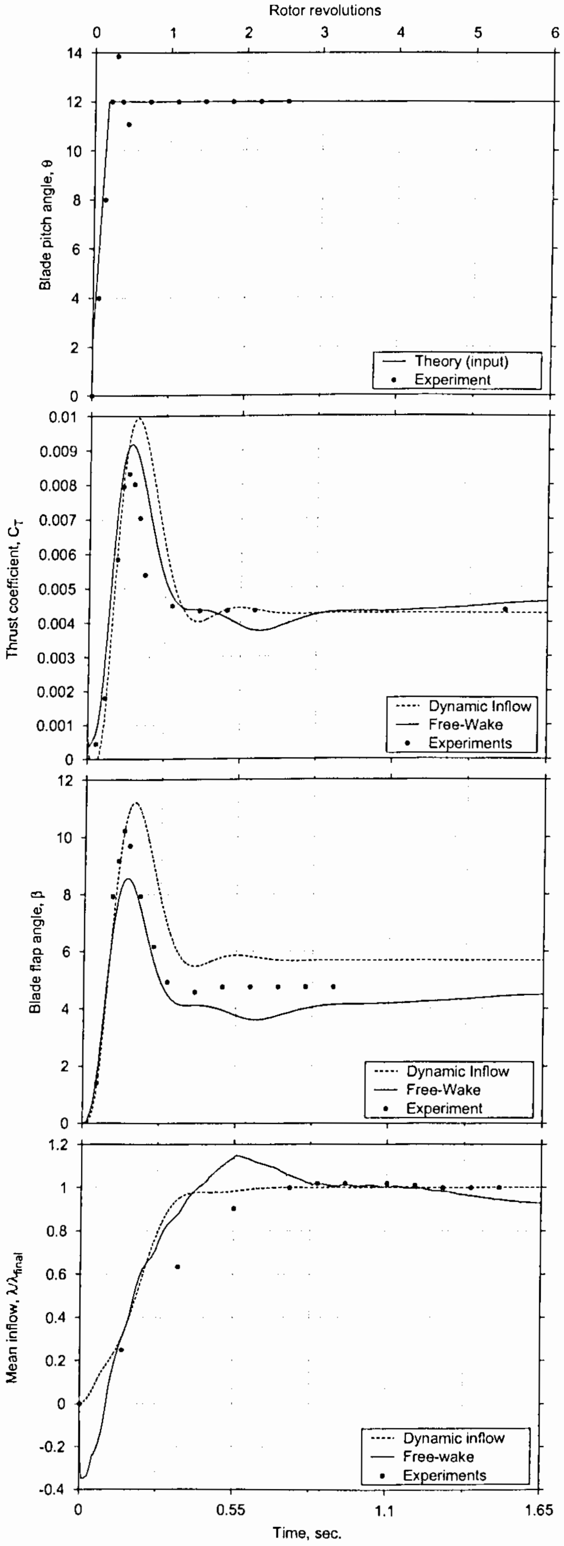

Figure 6.9: Ramp increase in rotor collective pitch angle at rate of 200 deg/sec. Experimental measurements from Ref. 98.

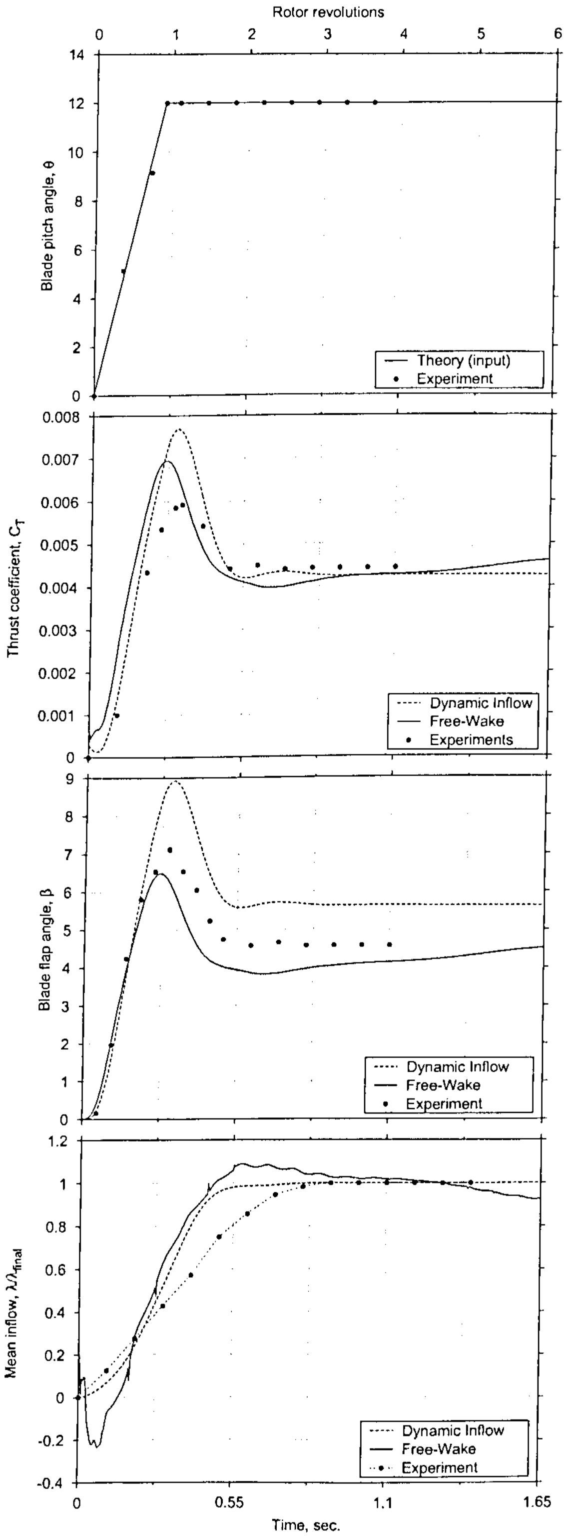

Figure 6.10: Ramp increase in rotor collective pitch angle at rate of 48 deg/sec. Experimental measurements from Ref. 98.

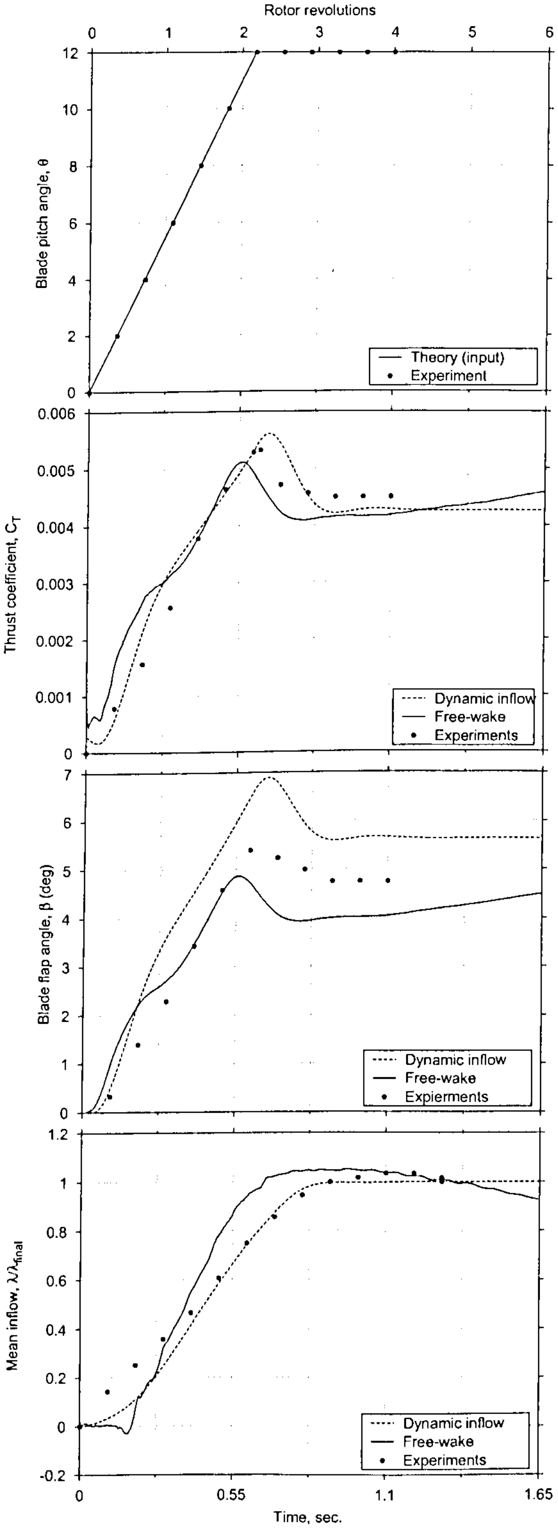

Figure 6.11: Ramp increase in rotor collective pitch angle at rate of 20 deg/sec. Experimental measurements from Ref. 98.

with experimental measurements of Ref. 98 was also obtained for lower ramp rates of 48 degrees per second (Fig. 6.10), and 20 degrees per second (Fig. 6.11).

To explain this point further, the dynamic evolution of the vortical wake structure following a ramp increase in collective pitch at 200 degrees per second is shown in the sequence in Fig. 6.12. The geometry of the tip vortices trailed from the three blades is shown at approximately 2, 4, 6, 8, 10 & 16 rotor revolutions after the collective pitch was applied. Note that the trailed wake before the collective input is not shown because for a non-lifting rotor with zero collective pitch, the strength of the trailed wake is always zero, i.e., there is no trailed circulation. As shown in Fig. 6.12(a), the tip vortices bundle up resembling a vortex ring below the rotor. This is because the vortices trailed from the blade tips immediately after the collective pitch input convect only relatively slowly. As shown previously in Fig. 6.9, the inflow builds up slowly with a time-lag of approximately two rotor revolutions. Therefore, the newer trailed vortices convect at a relatively high induced velocity, as can be seen from Fig. 6.12(b). The closely bundled vortex structure formed by the initial trailed wake is highly unstable; recall from Chapter 2 that the instability or divergence rates of the rotor wake are inversely proportional to the vortex separation distance. This vortex structure shows the presence of sinusoidal deformation modes, which grow with time as seen in Figs. 6.12(c)–(e). As the rotor induced inflow reaches the steady-state value, the growing sinusoidal wake deformations are also convected further downstream from the rotor blades. After about 16 rotor revolutions, as shown in Fig. 6.12(f), these disturbances were convected more than one and a half rotor radii below the rotor. After even longer time (a larger number of rotor revolutions), these instabilities are convected sufficiently far below the rotor, and their influence on the rotor diminishes. The wake then reaches a steady-state (periodic) structure, typical of rotors operating in hovering flight.

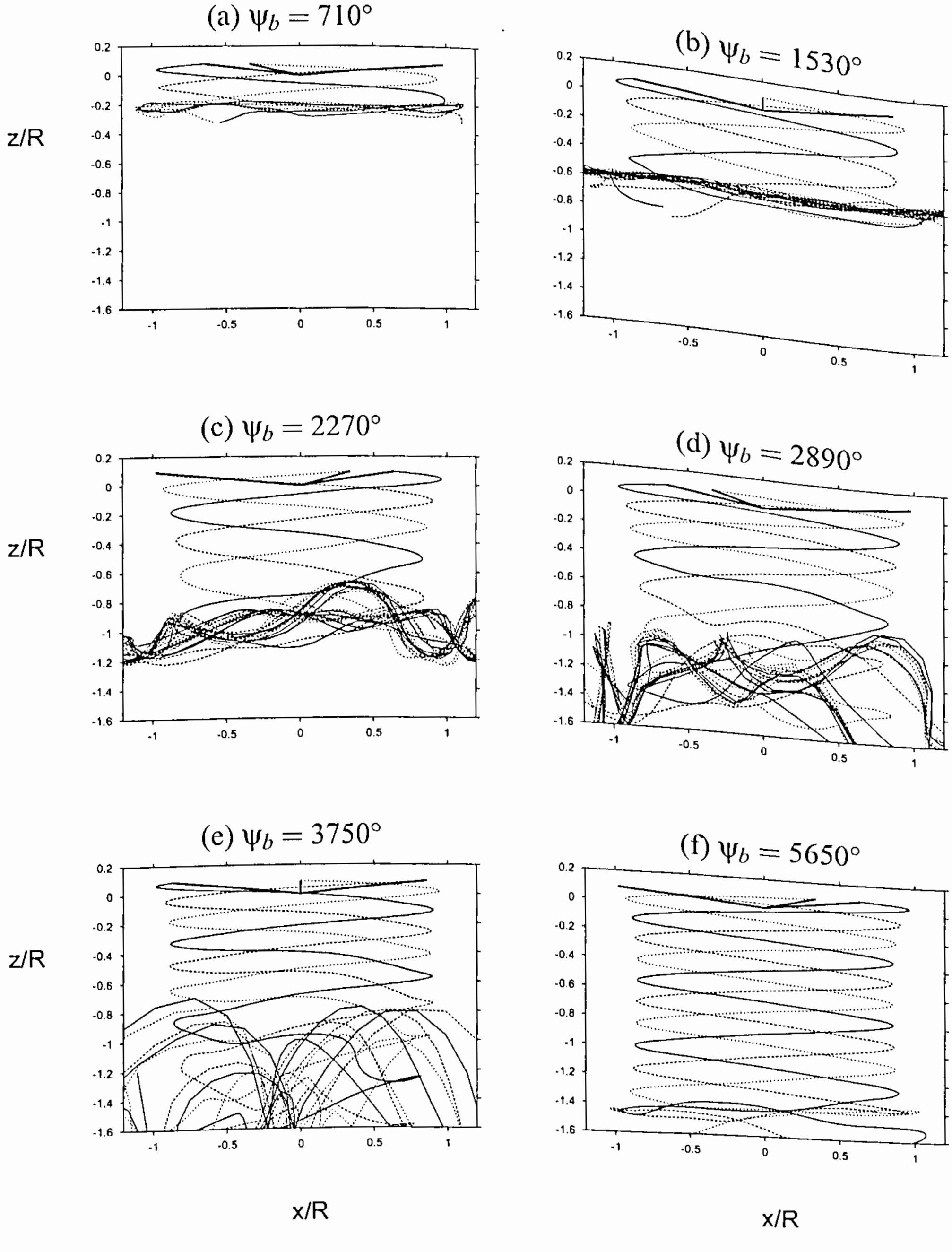

(a) $\psi_b = 710°$

(b) $\psi_b = 1530°$

(c) $\psi_b = 2270°$

(d) $\psi_b = 2890°$

(e) $\psi_b = 3750°$

(f) $\psi_b = 5650°$

Figure 6.12: Dynamic evolution of the tip vortices trailed from a three-bladed rotor (Ref. 98) following a 200 deg/sec ramp increasing in collective pitch. (a) $\psi_b = 710°$, (b) $\psi_b = 1530°$, (c) $\psi_b = 2270°$, (d) $\psi_b = 2890°$, (e) $\psi_b = 3750°$, and (f) $\psi_b = 5650°$.

Unsteady Aerodynamics (Apparent Mass) Effects

Finally, the proper role of the blade apparent mass (flow inertia or acceleration) terms in the transient rotor response was examined. For these calculation, the appropriate blade-element unsteady aerodynamic terms corresponding to the apparent mass effects (e.g., Ref. 2) were included in the blade lift solution (see Section 4.1.1) as given by the circulatory and non-circulatory terms, i.e., now the lift coefficient is given by

$$C_l \quad = \quad C_l^c + C_l^{nc} \tag{6.26}$$

where the non-circulatory part of the lift is given by

$$C_l^{nc} = \frac{1}{2} c C_{l\alpha} \left[\frac{1}{2} \frac{\dot{\alpha}}{U_T} + \frac{1}{2} \frac{\ddot{h}}{U_T^2} + \frac{c}{8} \frac{\ddot{\alpha}}{U_T^2} \right] = \frac{1}{2} c C_{l_\alpha} \left[\frac{1}{2} \frac{\dot{\alpha}}{U_T} + \frac{1}{2} \frac{r\ddot{\beta}}{U_T^2} + \frac{c}{8} \frac{\ddot{\alpha}}{U_T^2} \right] \tag{6.27}$$

The results including these extra terms in the solution are shown in Fig. 6.13 for the 200 degrees per second ramp rate change in rotor collective pitch. Again, these unsteady aerodynamic effects were found to be relatively negligible, as also shown earlier for the teetering rotor case (see Fig. 6.7). It can be concluded, therefore, that the overshoots in rotor thrust and blade flapping observed in this type of maneuver are a result mostly of the transient trailed wake evolution, i.e., a circulatory effect. The evolution of the vortex wake following the collective pitch change results in a relatively slow build-up of the rotor induced inflow, thereby leading to transient overshoot in rotor thrust. The time-constant in the dynamic inflow equation (Eq. 6.21) given by Carpenter & Friedovich (Ref. 98) represents this effect as an inertial effect. Yet it must be remembered that this effect is, in fact, associated with the dynamics of the trailed wake and the convection of vorticity below the rotor, and is not primarily associated with any apparent mass (non-circulatory) effects.

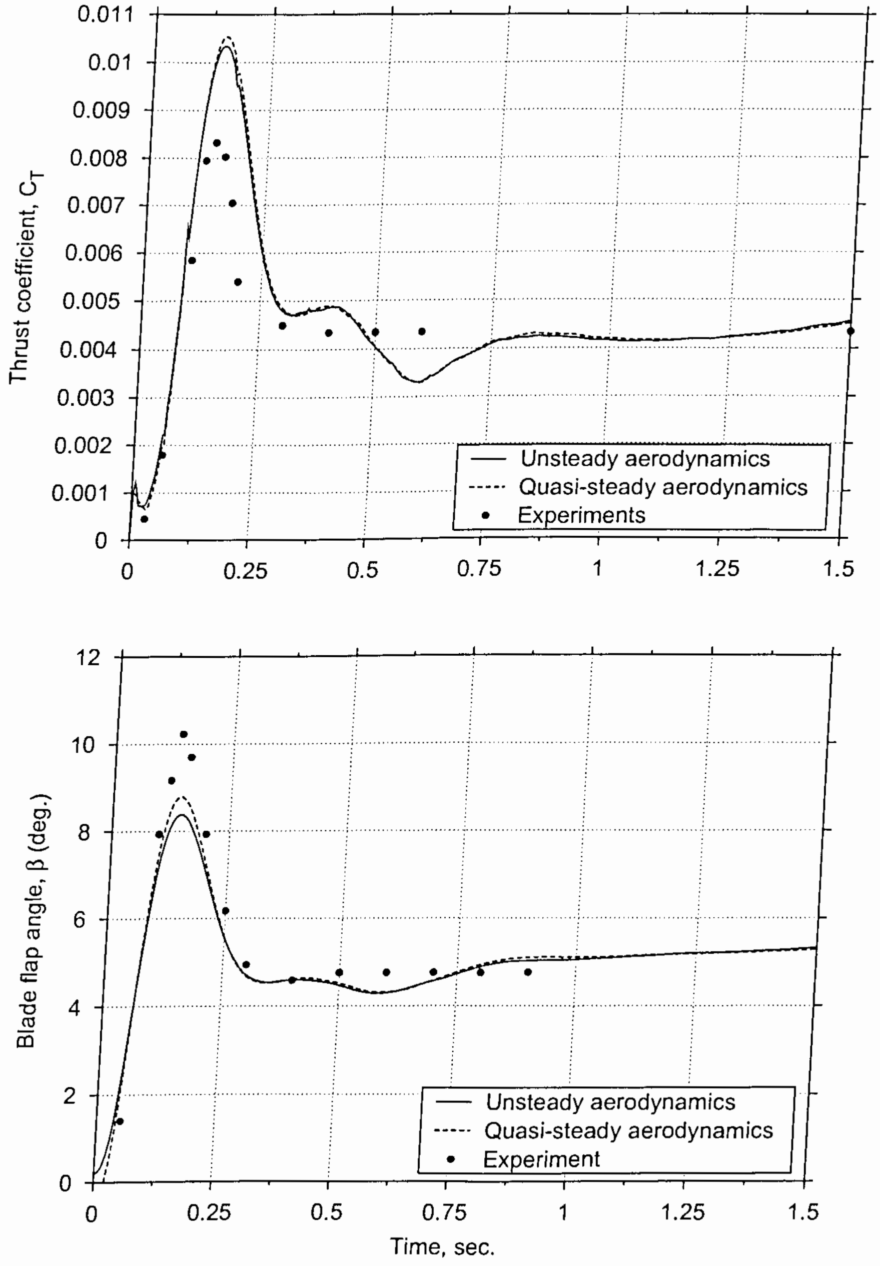

Figure 6.13: Effect of unsteady aerodynamic effects on the rotor response following a ramp increase in collective pitch at 200 degrees/sec. Experimental results from Ref. 98.

6.2.3 Cyclic Pitch Inputs

In a manner similar to the step/ramp increase in collective pitch, the basic rotor and wake response to a step change in collective pitch was also examined. The rotor configuration used in this case is the same as that used in the experiments of Carpenter & Friedovich (Ref. 98), described in the previous section, although no experimental results were available for this problem. The initial condition used in this case was the steady-state solution found after the collective pitch increase. The collective pitch was held constant thereafter, and only a change in cyclic pitch was applied.

Figure 6.14 shows the rotor flapping response following a one degree step input in lateral cyclic, θ_{1c}, i.e.,

$$\theta = \begin{cases} 12^\circ & t < 10\pi/\Omega \\ 12^\circ + 1^\circ \cos\psi & t \geq 10\pi/\Omega \end{cases} \tag{6.28}$$

Notice that during a small transient after the step input, the blade flapping is not periodic and the three blades show different flapping angles. However, within two rotor revolutions, the blade flapping reaches a steady-state, and all three blades follow the same periodic flapping motion.

Fourier coordinate transforms (FCT) were used to bring out this transient behavior. In the steady-state, the FCT gives the same results as the periodic solution expanded as harmonics. However, the FCT coefficients are time dependent and give the correct representation during the initial non-periodic transient. Figure 6.15 shows the FCT of the rotor response in terms of (a) blade flapping angles, and (b) rotor induced inflow as a function of time or rotor revolutions. It is interesting to note that the coning angle, β_0, is not affected by the cyclic input. This is because the overall rotor thrust is not affected significantly by cyclic pitch inputs in hovering flight. This behavior is also seen in the inflow time-history, where the mean inflow is found to remain almost invariant.

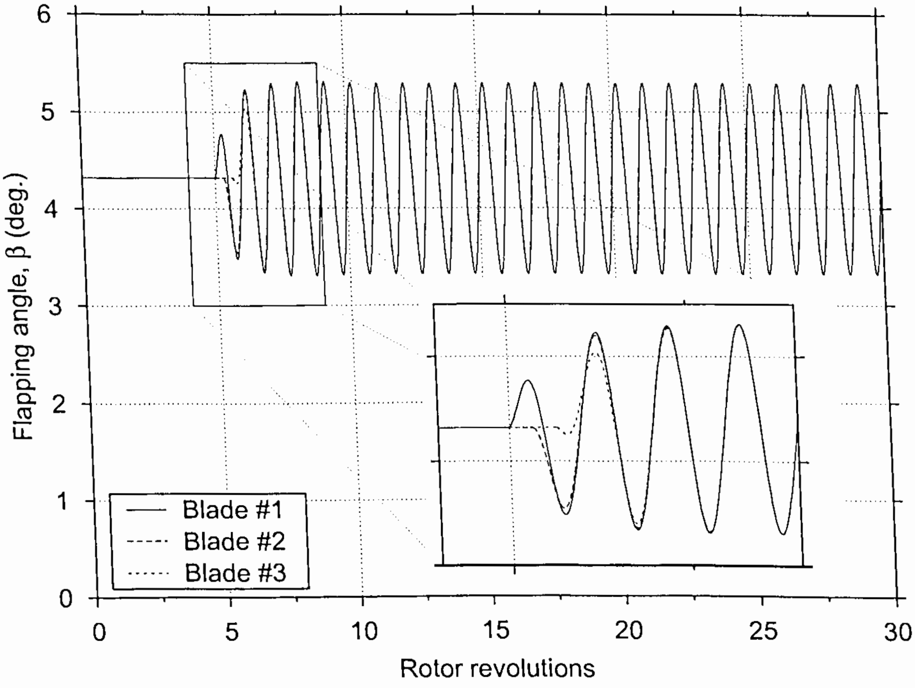

Figure 6.14: Time-history of individual blade flapping angles following a step lateral cyclic input. Initial transient (non-periodic) response is enlarged.

The transient behavior in the blade flapping response is a direct result of the high transient rotor induced inflow, as shown in Fig. 6.15. During the initial transient, a lateral inflow variation is dominant, therefore longitudinal flapping is found to be more pronounced initially. This is expected because immediately following a lateral cyclic input the rotor wake had not deformed enough to produce a longitudinal inflow gradient. Within half a rotor revolution, however, the longitudinal inflow gradient builds up to a maximum value. Then both cyclic inflow components gradually reduce as the wake reaches another equilibrium (steady-state) structure. In the steady-state, the blade exhibits a lateral flapping (β_{1s}) response to a lateral cyclic pitch input (θ_{1c}) as expected based on the 90° phase-lag between the flapping response and the pitch

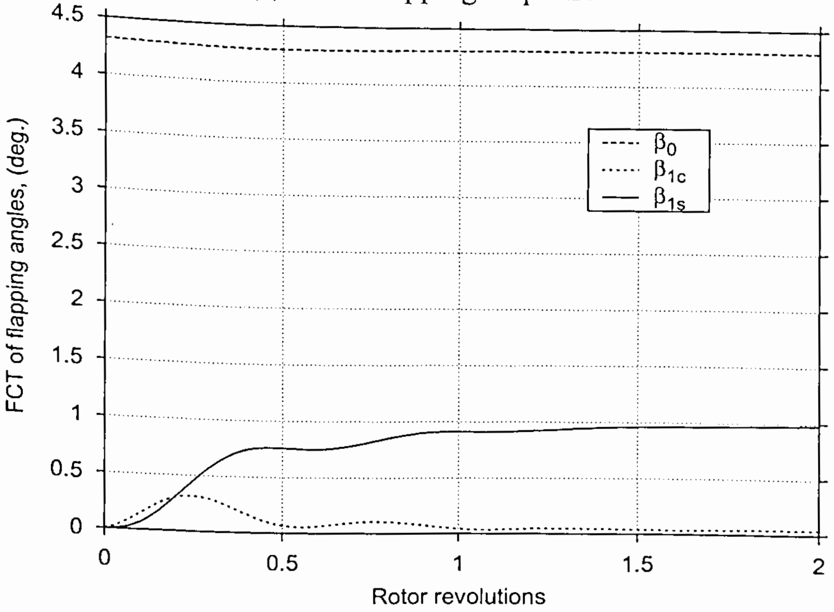

(a) Blade flapping response

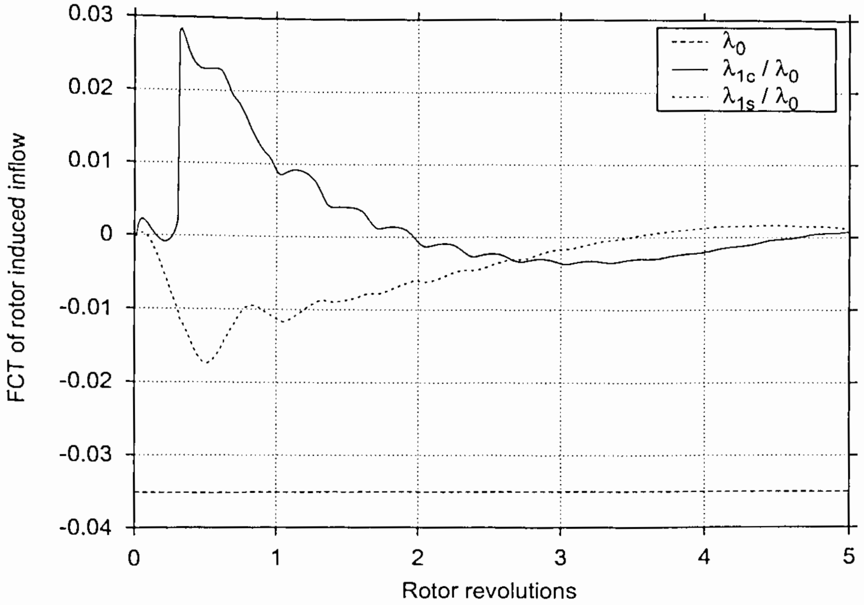

(b) Rotor induced inflow coefficients

Figure 6.15: Time-history of blade flapping angles and rotor induced inflow following a step lateral cyclic input, shown as the Fourier transforms. (a) Blade flapping response, (b) Rotor induced inflow coefficients.

input for a rotor with blade flapping hinge located on the rotational axis.

The rotor wake is axisymmetric in hover and, therefore, the response to a longitudinal cyclic would be essentially the same as the previous (lateral cyclic input) case, but with a 90° phase-lag. The blade flapping and inflow time-histories following a longitudinal cyclic are shown in Fig. 6.16. The longitudinal cyclic pitch was applied as a step change, i.e.,

$$\theta = \begin{cases} 12^\circ & t < 0 \\ 12^\circ + 1^\circ \sin\psi & t \geq 0 \end{cases} \tag{6.29}$$

The response to lateral cyclic input is also shown to bring out the axisymmetric nature of the rotor wake in hover. The rotor response to both longitudinal and lateral cyclic pitch inputs are exactly the same, with a 90° phase-lag. This also verifies that the present wake model correctly represents the rotor axisymmetry in hover, even though axisymmetry or periodicity is not explicitly enforced in the time-accurate free-vortex wake model.

Clearly, the transient blade flapping depends on both the blade flapping dynamics as well as the transient induced inflow associated with the dynamics of the rotor wake. To examine the relative importance of these two factors, results were obtained by assuming a constant rotor induced inflow and integrating only the blade flapping dynamic equation (Eq. 6.17) in time. The results obtained using this approach are shown in Fig. 6.17, along with the previous results obtained using the inflow distribution calculated with the free-vortex wake algorithm. In this case, only the flapping response to a one degree step longitudinal cyclic input is shown. The response to a lateral cyclic pitch input is essentially the same.

The interesting observation that can be made from Fig. 6.17, is that the predominant rotor response comes from the blade flapping dynamics, and the dynamic effects

(a) Blade flapping response

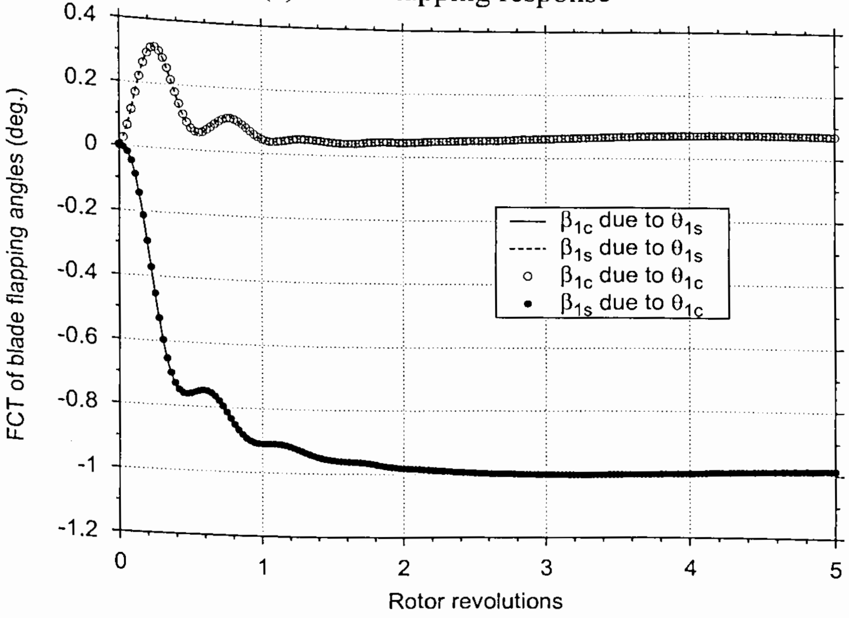

(b) Rotor induced inflow coefficients.

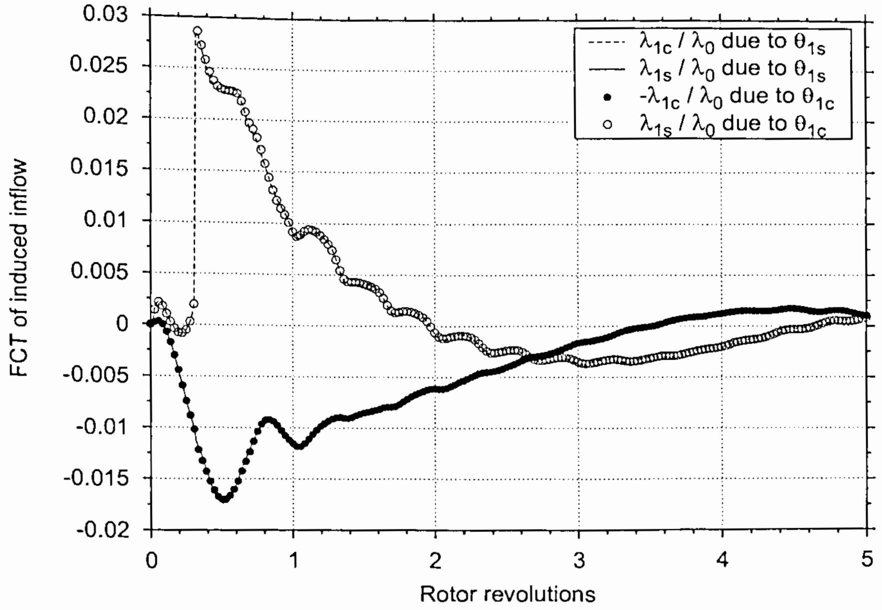

Figure 6.16: Time-history of blade flapping angles and rotor induced inflow following step cyclic inputs, shown as the Fourier transforms (a) Blade flapping response. (b) Rotor induced inflow coefficients.

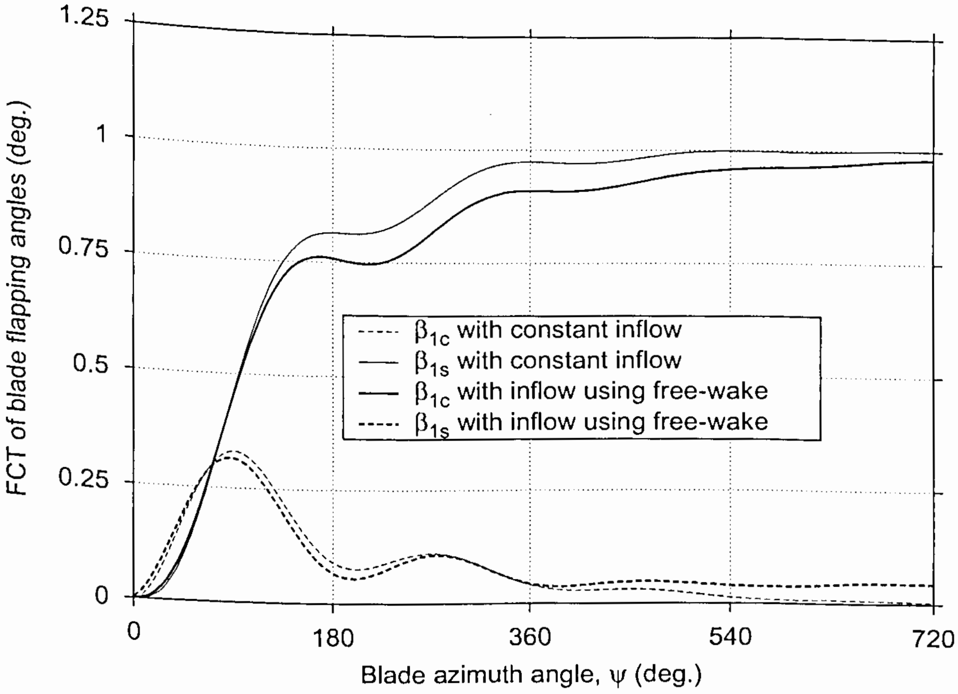

Figure 6.17: Time-history of individual blade flapping angles following a step lateral cyclic input with and without the inflow dynamics associated with the free vortex wake

of the wake induced inflow are very small. Note that this is not true in general, but is only in this case of cyclic inputs to an isolated rotor. On a real helicopter, a cyclic blade pitch input would also generate angular motion of the helicopter or the rotor hub, which may subsequently influence the dynamic behavior of the rotor wake. Such dynamic effects of hub motion on the wake are examined later in Section 7.1.

A similar numerical experiment was performed for a collective pitch input to examine the relative effects of the inflow dynamics and blade flapping dynamics. Recall that the dynamic inflow model showed essentially the same inflow response as the free-vortex wake model. Therefore, only the relative effects of dynamic inflow and blade flapping were examined. Figure 6.18 shows the build-up of rotor inflow and the thrust coefficient as a function of time following a step increase in collective pitch. The rotor geometry was identical to the experiments of Carpenter & Friedovich (Ref. 98). However, in this case the rotor was assumed to be gimbaled and so there was no blade flapping in hovering flight. Note that the inflow build-up is nearly the same for both the dynamic inflow and the free-wake models. The rotor thrust, however, is substantially overpredicted with the dynamic inflow model. This suggests that the dynamic inflow theory is limited in application to specific rotor configurations, unless empirical corrections to the dynamic inflow coefficient (the time-lag in Eq. 6.22) are used.

Figure 6.19 shows the results for the Carpenter & Friedovich rotor obtained using dynamic inflow along with results obtained by eliminating the inflow dynamics. In this case, the inflow is assumed to be proportional to the collective pitch input, as predicted using the simple momentum/blade element theory. The blade flapping results, as shown in Fig. 6.19(b), bring out the importance of inflow dynamics on the blade flapping response. Notice that the results obtained using a constant inflow significantly underpredict the blade flapping. However, it is interesting to note that the overshoot in thrust obtained with a constant inflow is the same as that obtained using dynamic inflow. Therefore, the blade flapping dynamics certainly plays a dominant role in determining the transient rotor response. It must be noted that although a constant inflow model predicts the magnitude of the thrust overshoot correctly, the phase is substantially different from that observed in experiments. Also notice from Fig. 6.9, that the maximum value of thrust was measured at time $t \approx 0.2$ after the application of the pitch input. With a constant inflow assumption, the maximum thrust was predicted at a much earlier time of $t \approx 0.1$ – see Fig. 6.19(a). The dynamic inflow theory, however, correctly predicts the phase of the thrust overshoot by representing the time-lag in the build-up of inflow.

(a) Mean rotor inflow coefficient

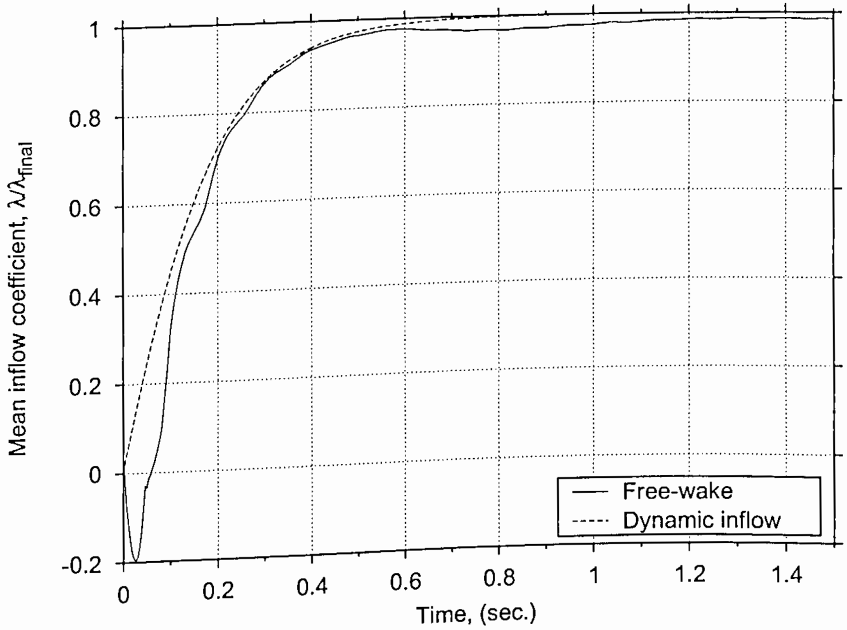

(b) Rotor thrust coefficient

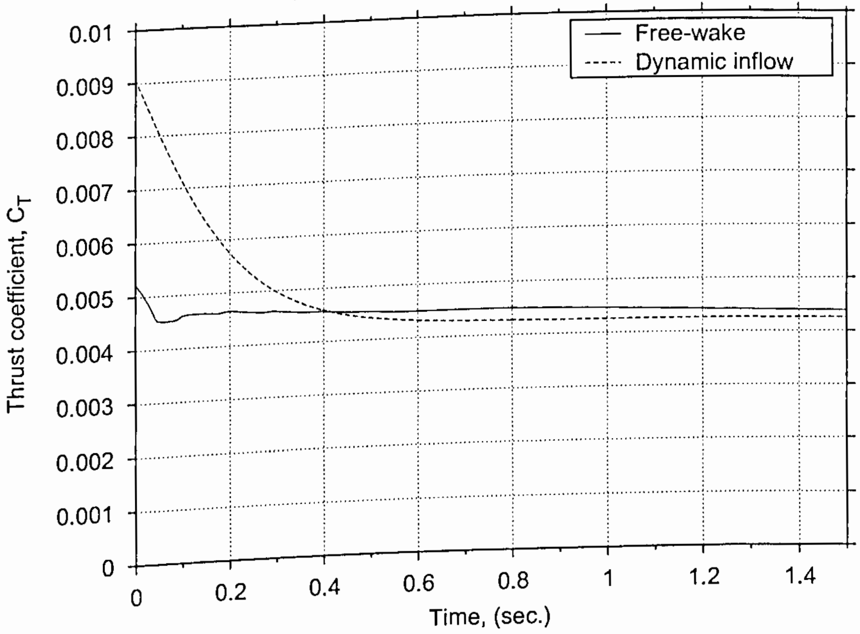

Figure 6.18: Time-history of rotor thrust and inflow response of a teetering rotor following a ramp increase in collective pitch obtained using the free wake analysis and dynamic inflow theory. (a) Mean rotor inflow coefficient, (b) Rotor thrust coefficient.

(a) Rotor thrust coefficient

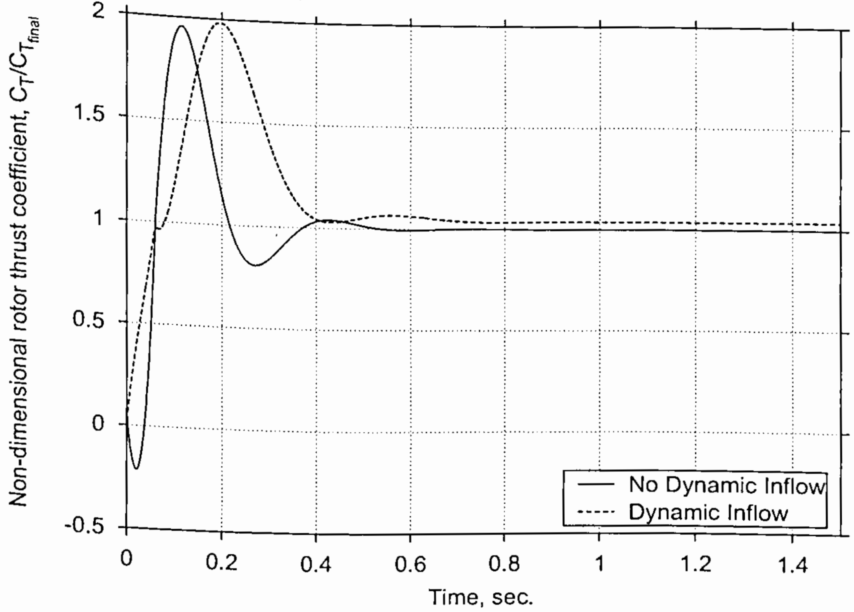

(b) Blade flapping response

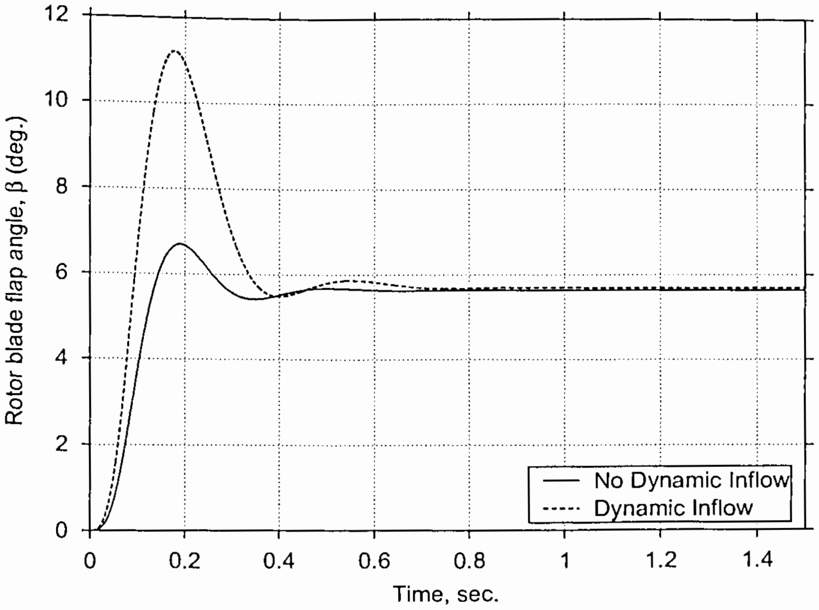

Figure 6.19: Time-history of rotor blade flapping and thrust for an articulated rotor following a ramp increase in collective pitch obtained with and without inflow dynamics effects. (a) Rotor thrust coefficient, (b) Blade flapping response.

6.3 Frequency Response to Pitch Inputs

The dynamic response of the rotor wake to a step or ramp change in the collective pitch can be idealized a combination of responses to a series of inputs at several different frequencies. In this section, the behavior of the inflow induced by the rotor wake over a range of blade pitch excitation frequencies is examined. This behavior has been experimentally examined in the past to provide some empirical insights into dynamic inflow models (Refs. 100, 101). The rotor wake dynamic response at low and intermediate range of frequencies below the rotational frequency is also of particular interest from the perspective of helicopter flight dynamics and handling qualities.

The experimental results presented in this section that are used to validate the numerical simulations are from Ellenrieder & Brinson (Ref. 102). In these experiments, a four-bladed rotor was used with rectangular planform, untwisted blades. The rotor radius was 0.77 m, the chord was 0.06 m, and the rotor was operated at a nominal rotational speed of 1200 rpm (125.66 $\mathrm{rad\,s^{-1}}$). The rotor blades were mounted on a hub without any flap or lag hinges, resulting in a very stiff rotor with an equivalent flapping hinge offset of 25%R. The measured non-dimensional flapping frequency of the rotor was found to be 1.22, with a control phase-lag angle of 55° in hover. The rotor was operated at a nominal thrust of 280N or at a thrust coefficient of 0.013. However, the rotor thrust was not directly measured, but only estimated using a simple performance analysis. The blade pitch inputs for both collective and cyclic excitations consisted of root pitch changes of 1.5° in magnitude.

6.3.1 Collective Pitch Excitation

The collective pitch excitation was accomplished by changing the pitch settings of all four blades exactly in phase. Figure 6.20 shows an example of the collective pitch excitation at 27.0 Hz and the corresponding rotor induced inflow at two radial locations. The inflow time-history showed a small initial transient, after which the predominant response was at the excitation frequency. As seen in Figs. 6.20(b) and (c), the inflow response at the excitation showed some modulations of lower frequencies indicating presence of other frequency components. However, it is clear that the most dominant inflow response was at the blade pitch excitation frequency, as shown in Fig. 6.20(a).

Note that the vortical wake also experiences oscillatory perturbations because of the oscillatory blade pitch excitation. An example of the wake geometry is shown in Fig. 6.21 for collective pitch excitation at $\omega_{ex} = 12.5$ Hz. The perturbations can be clearly seen as alternating regions of axial expansion and contraction in the wake. The axial contraction of the wake is qualitatively similar to that observed for the impulsively started rotor in the previous section – see Fig. 6.12. However, because of the continuous oscillations in the rotor collective pitch this region of contraction is followed by a region of expansion where the wake vortices have a large vertical separation. This sequence recurs over the wake as the perturbations travel in the wake system at the pitch excitation frequency. The induced inflow at the rotor disk also shows an oscillatory behavior, as shown in Fig. 6.20, because the wake experiences periodic waves of contraction and expansion.

A frequency analysis was performed to find the amplitude and phase of the inflow response. These inflow frequency responses are shown in Fig. 6.22 as a function of the blade pitch excitation frequency at three representive radial locations at (a) $r/R = 0.41$, (b) $r/R = 0.57$, and (c) $r/R = 0.73$, respectively. The free-vortex wake results are

(a) Collective
pitch excitation
at 27.0 Hz

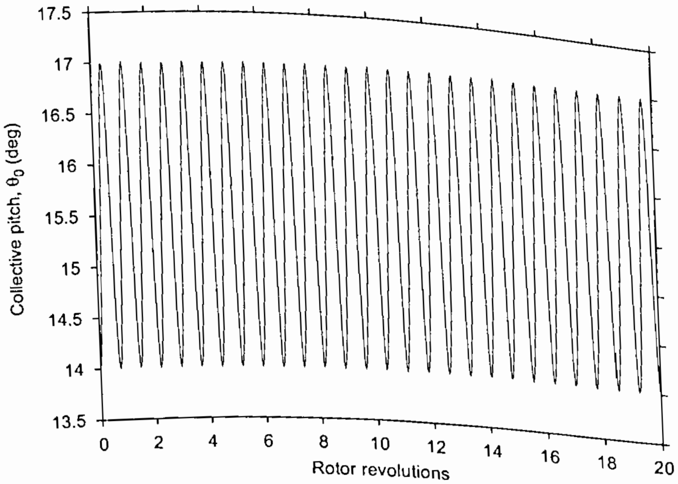

(b) Inflow at
$r/R = 0.217$

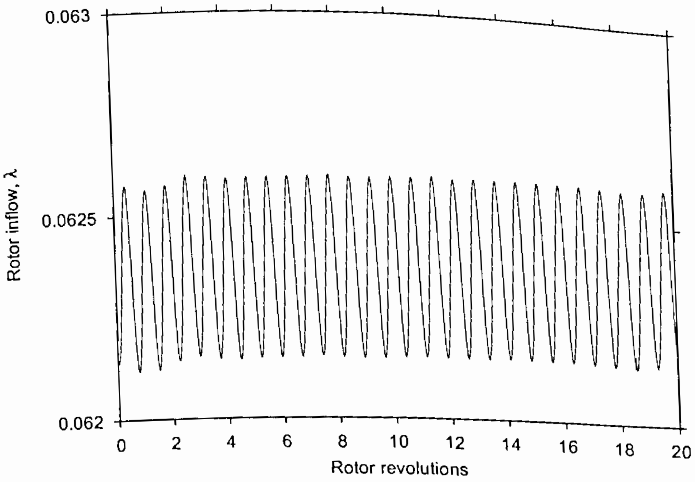

(c) Inflow at
$r/R = 0.979$

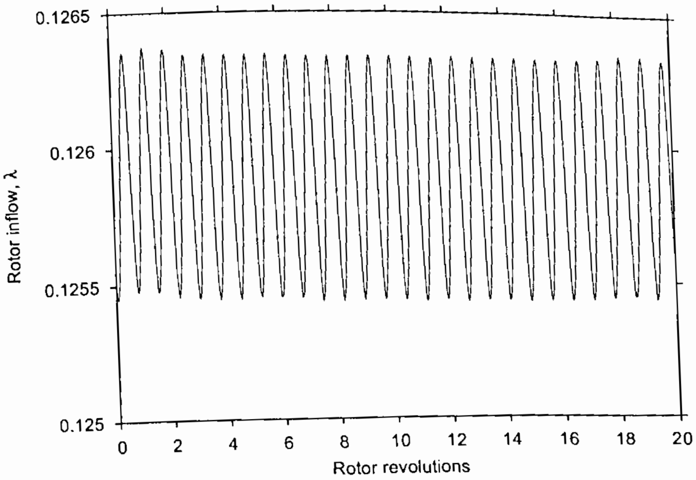

Figure 6.20: Sample oscillatory collective pitch excitation and resulting inflow response. (a) Collective pitch input at 27.0 Hz, (b) Inflow at $r/R = 0.217$, (c) Inflow at $r/R = 0.979$.

(a) Side view

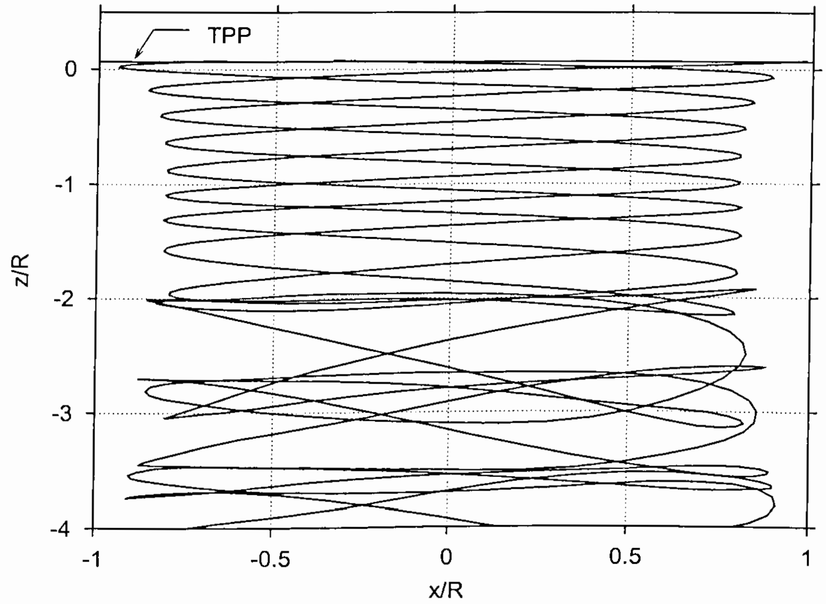

(b) Rear view

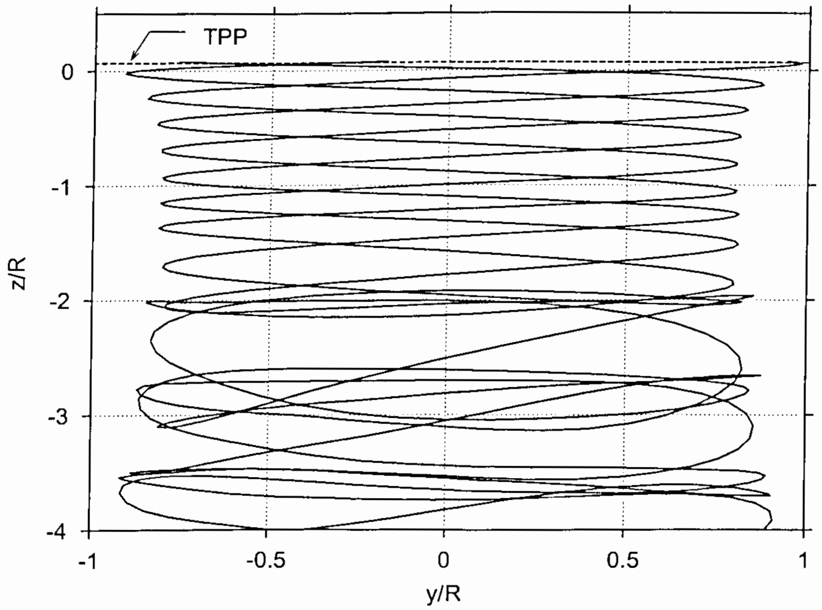

Figure 6.21: Side view of wake geometry for oscillatory collective pitch excitation at $\omega_{ex} = 12.5$ Hz. (a) Side view, (b) Rear view.

shown as solid lines, while the corresponding experimental measurements are shown with symbols connected by dotted lines. The interesting feature of these results is the relatively flat gain slope observed at low excitation frequencies, followed by a decrease in gain at half the rotational frequency, and a subsequent gain recovery near the natural frequency of blade flapping (1.22Ω). The free-vortex wake methodology predicts these features correctly, but the magnitude of the gains is somewhat underpredicted at low frequencies and overpredicted at higher frequencies. These discrepancies may be because of several reasons, including the fact that experimental measurements were not made at the TPP but at a small distance below to avoid risk of sensor contact with the rotor. However, the overall qualitative agreement between predictions and experiments is considered good, and better than those predicted by other analyses (e.g., see Ref. 101). The phase angles were predicted very well by the free-vortex wake analysis. The small phase-lag at frequencies lower than the blade flapping natural frequency is an interesting result. Most commonly used dynamic inflow models resort to empirical values for the time-lag in the inflow equations to model this behavior, whereas the present analysis predicts the inflow dynamics starting from first principles.

Figure 6.23 shows the gain of the dynamic inflow response to collective excitation along the rotor radius. Clearly, the frequency response shows significant variations with both frequency and the radial location. For low excitation frequencies, the inflow response is nominally constant over the blade span. As the excitation frequency increases, the inflow response appears to be concentrated near the tip region at about $0.8R$. This trend is also observed in the experiments of Ref. 102. This is an interesting observation because the maximum in the inflow response approximately corresponds to the spanwise location of the maximum in blade lift. This is consistent with the BEMT, where the induced inflow is proportional to the local (sectional) rotor thrust.

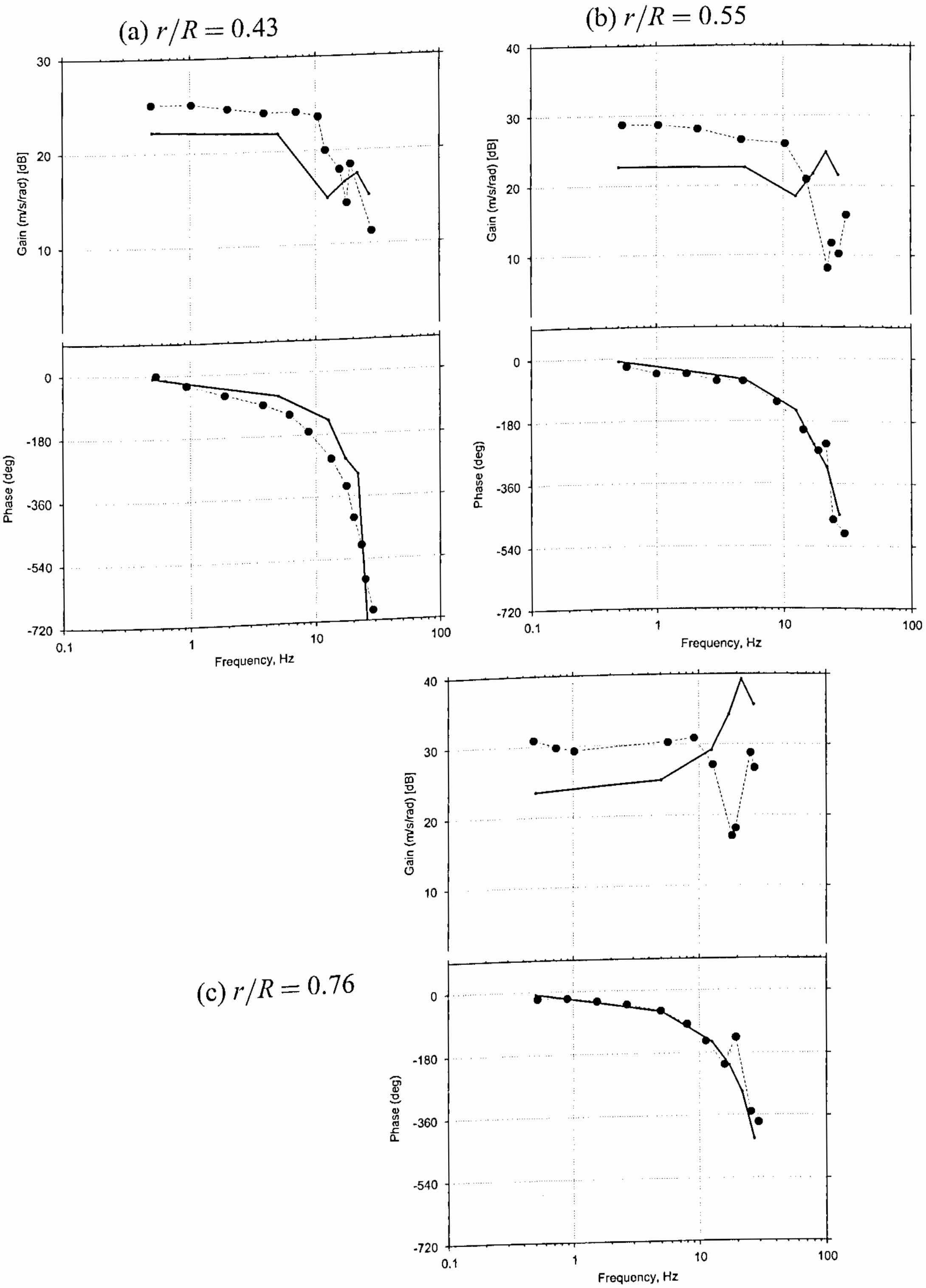

(a) $r/R = 0.43$

(b) $r/R = 0.55$

(c) $r/R = 0.76$

Figure 6.22: Inflow frequency response to oscillatory collective pitch excitation. Symbols are experiments of Ref. 102 while solid lines are predictions obtained using the present free-vortex wake analysis. (a) $r/R = 0.43$, (b) $r/R = 0.55$, and (c) $r/R = 0.76$.

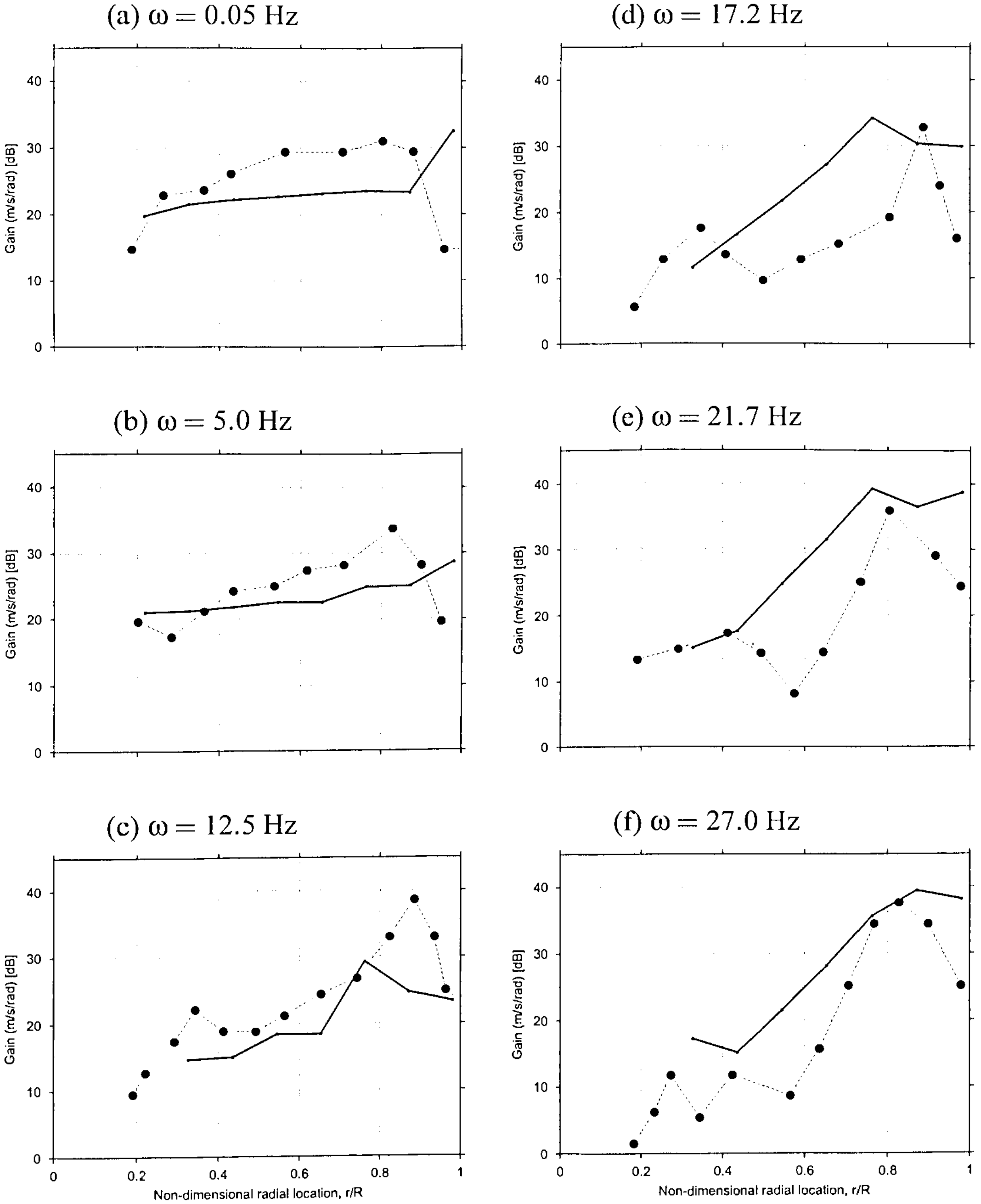

Figure 6.23: Radial variation in the gain of dynamic inflow response at different excitation frequencies of oscillatory collective blade pitch input. Symbols are experiments of Ref. 102 while solid lines are predictions obtained using the present free-vortex wake analysis. (a) ω = 0.05 Hz, (b) ω = 0.5 Hz, (c) ω = 12.5 Hz, (d) ω = 17.2 Hz, (e) ω = 21.7 Hz, and (f) ω = 27.0 Hz.

The phase of the inflow response along the blade span is shown in Fig. 6.24. At low frequencies, the inflow is essentially in phase with the collective pitch excitation. As the excitation frequency is increased, however, the phase-lag increases over the inboard portion of the blades. This trend, as observed in the experiments of Ellenrieder & Brinson (Ref. 102), is well modeled by the free vortex wake analysis. The authors state that the increasing phase-lag over the inboard sections of the blade is suggestive of the fact that the trailing vorticity from the blade tips is the most dominant flow structure. This is confirmed by the present analysis because the numerical results presented in this section are obtained without including any unsteady aerodynamic modeling associated with the shed wake. Therefore, the numerical inflow response must be because of the dynamic evolution of the trailing tip vortices alone. The good overall agreement with experimental measurements confirms the assumption that the blade tip vortices are the most dominant flow structure in a rotor wake.

Further evidence of the phase-lag in the inflow response is shown in the measurements of Liou *et al.* (Ref. 103), where a hysteresis effect was found when the measured time-dependent induced inflow results were plotted against the excitation root pitch angle. Measurements were performed only at one excitation frequency. The hysteresis effect was observed to be diminishing along the blade span from the root to the tip. It was postulated that this diminishing hysteresis trend was a result of the effects of shed vorticity on the inboard portions of the blade. The free-vortex wake predictions also show a similar hysteresis effect. Figure 6.25 shows the hysteresis plots for pitch excitation at 27.0 Hz at six different radial locations. The hysteresis effect is seen to increase near the blade tip. This can be better understood from the wake geometry, as shown in Fig. 6.21. The periodic disturbances in the wake structure occur mainly over a region close to the blade tips. Therefore, the hysteresis effect in the inflow response

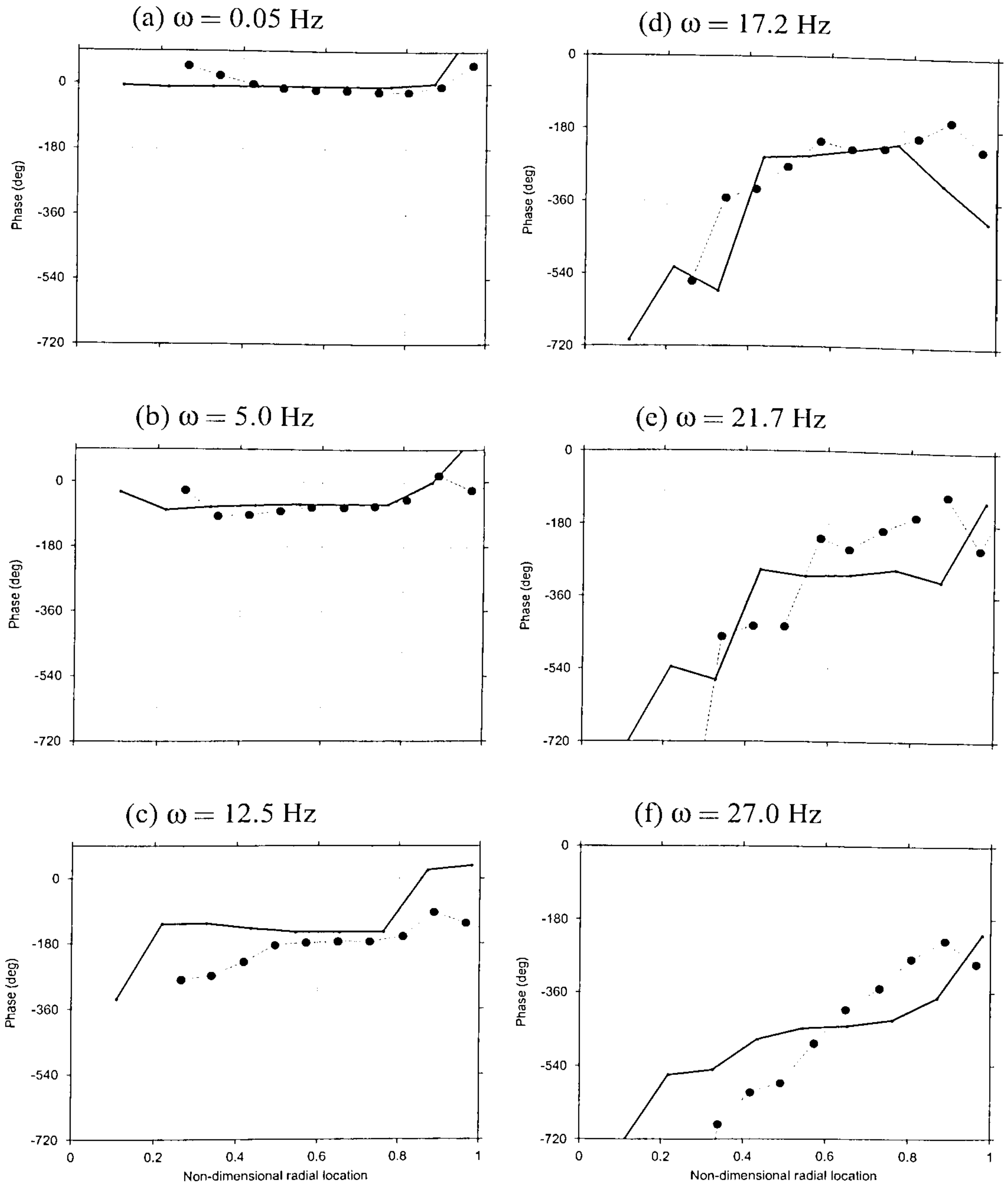

Figure 6.24: Radial variation in the phase of dynamic inflow response at different excitation frequencies of collective pitch. Symbols are experiments of Ref. 102 while solid lines are predictions obtained using the present free-vortex wake analysis. (a) ω = 0.05 Hz, (b) ω = 0.5 Hz, (c) ω = 12.5 Hz, (d) ω = 17.2 Hz, (e) ω = 21.7 Hz, and (f) ω = 27.0 Hz.

would also be larger near the blade tips. This again suggests that the trailing wake vorticity is the most dominant flow feature, as opposed to the inboard shed vorticity. This is consistent with the previous observation made from both the numerical free vortex wake results, as well as the experiments of Ellenrieder & Brinson (Ref. 102).

The effect of excitation frequency on this hysteresis behavior is shown in Fig. 6.26, where the inflow near the blade tip ($r/R = 0.97$) is plotted against the root pitch for six different excitation frequencies. At the lowest excitation frequency (0.5 Hz), the results show only a very small amount of hysteresis. This is because, for very low excitation frequencies the inflow response is essentially in phase with the oscillatory pitch inputs. Recall that in the idealized maneuvers examined earlier, the wake behavior was found to be essentially periodic at very small angular rates. Similarly, for very low pitch excitation frequencies the wake behavior is nearly periodic (steady-state). Therefore, the hysteresis effect is negligible at these low frequencies. The hysteresis effect is seen to increase with the excitation frequency, as shown by the increased area contained within the hysteresis loop. This increasing hysteresis effect indicates an increased phase-lag in the inflow build-up, which mainly a result of the dynamic evolution of the trailed wake, as shown earlier for the case of a ramp increase in collective — see Figs. 6.9–6.11. Remember that a ramp collective pitch input can be represented by a combination of several frequency modes, including some very high frequencies. Also, recall that the phase-lag in inflow build-up was found be significantly long (as long as two rotor revolutions), which is consistent with the observation that the hysteresis effect increases with excitation frequency.

(a) $r/R = 0.10$

(b) $r/R = 0.21$

(c) $r/R = 0.43$

(d) $r/R = 0.54$

(e) $r/R = 0.87$

(f) $r/R = 0.97$

Figure 6.25: Hysteresis effect in the predicted dynamic inflow response to oscillatory collective pitch excitation at 27.0 Hz at different spanwise (radial) locations. (a) $r/R = 0.10$, (b) $r/R = 0.21$, (c) $r/R = 0.43$, (d) $r/R = 0.54$, (e) $r/R = 0.87$, and (f) $r/R = 0.97$.

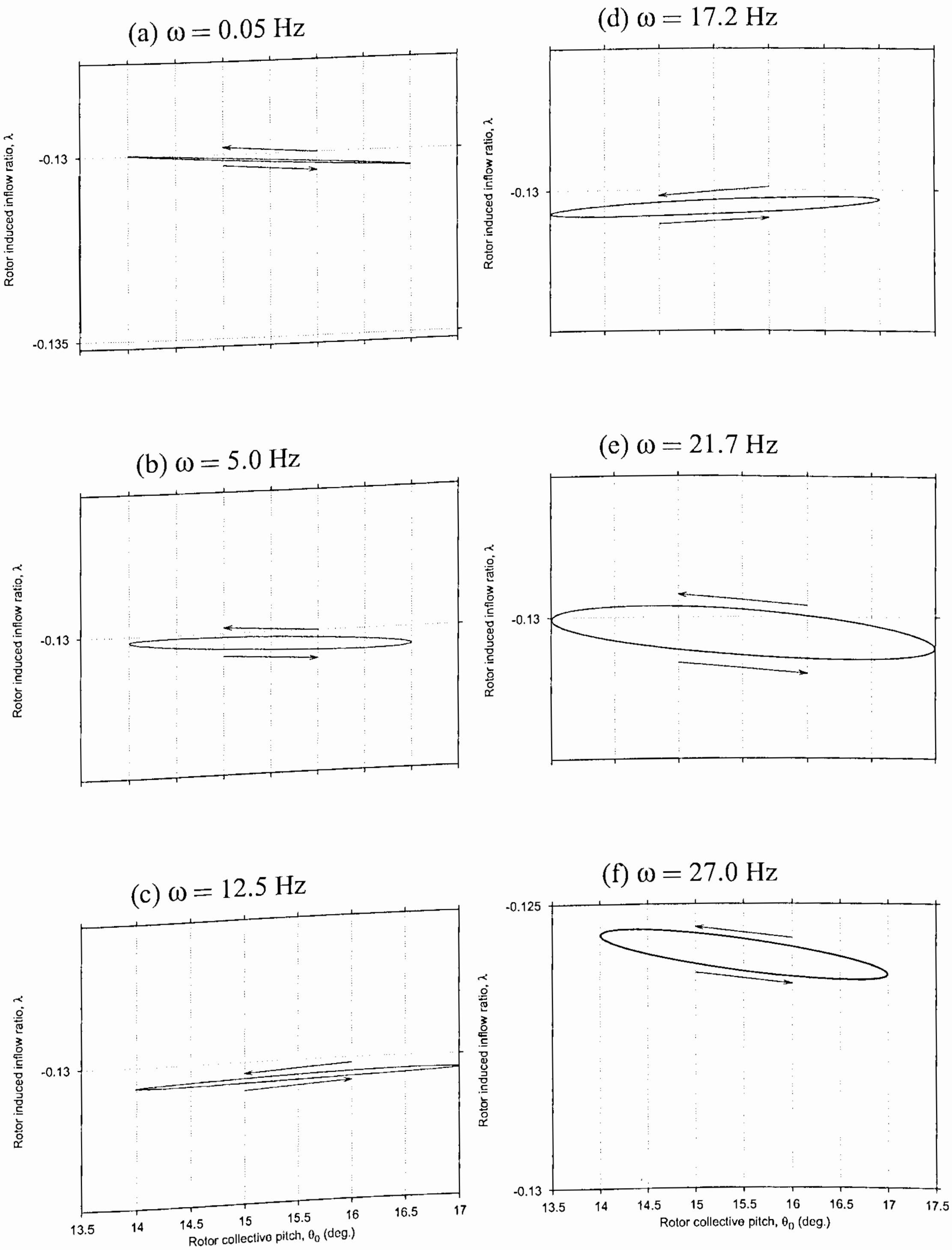

Figure 6.26: Hysteresis effect in the predicted dynamic inflow response to oscillatory collective pitch excitation. Effect of increasing excitation frequency is shown at an example radial location near the blade tip at $r/R = 0.97$. (a) $\omega = 0.05$ Hz, (b) $\omega = 0.5$ Hz, (c) $\omega = 12.5$ Hz, (d) $\omega = 17.2$ Hz, (e) $\omega = 21.7$ Hz, and (f) $\omega = 27.0$ Hz.

6.3.2 Cyclic Pitch Excitation

The experiments of Ellenrieder & Brinson (Ref. 102) also included results for cyclic pitch excitations, although these results were more limited in scope. In this case, the root blade pitch for the four blades were excited with a successive phase-lag angles of 90°, thereby constituting a "cyclic" excitation.

Examples of the cyclic pitch excitation and corresponding inflow response are shown in Fig. 6.27. The phase-lag between the pitch inputs applied to different blades is evident from Fig. 6.27(c). The inflow response was noted to be far more complicated than that resulting from collective pitch excitations. At the lowest frequency of 0.5 Hz, the dominant response appeared to be at the excitation frequency itself. However, as the frequency increased, other harmonics in the induced inflow response became increasingly more dominant.

A frequency domain analysis was again performed to help identify the various modes of the inflow response. These results are shown in Fig. 6.28 in the form of the inflow gain at different frequencies. As mentioned earlier, at an excitation frequency of 0.5 Hz the dominant response is at the excitation frequency of 0.5 Hz. The small disturbances seen in the time-history in Fig. 6.27(a) are because of the inflow response at 4/rev (80 Hz). At the excitation frequency ω_{ex}=5.0 Hz, the predominant response is again at that frequency. However, the responses at $2\omega_{ex}$ and $3\omega_{ex}$ were also found to be significant. At higher frequencies, these multiples of the excitation frequency were also found to be increasingly more dominant in the inflow response. Such effects are especially important from rotor wake modeling standpoint — most simple wake or inflow models would only predict the response at the excitation frequency.

The presence of higher inflow harmonics is related to the periodic perturbations to the rotor wake because of the blade pitch excitation. An example of the wake distor-

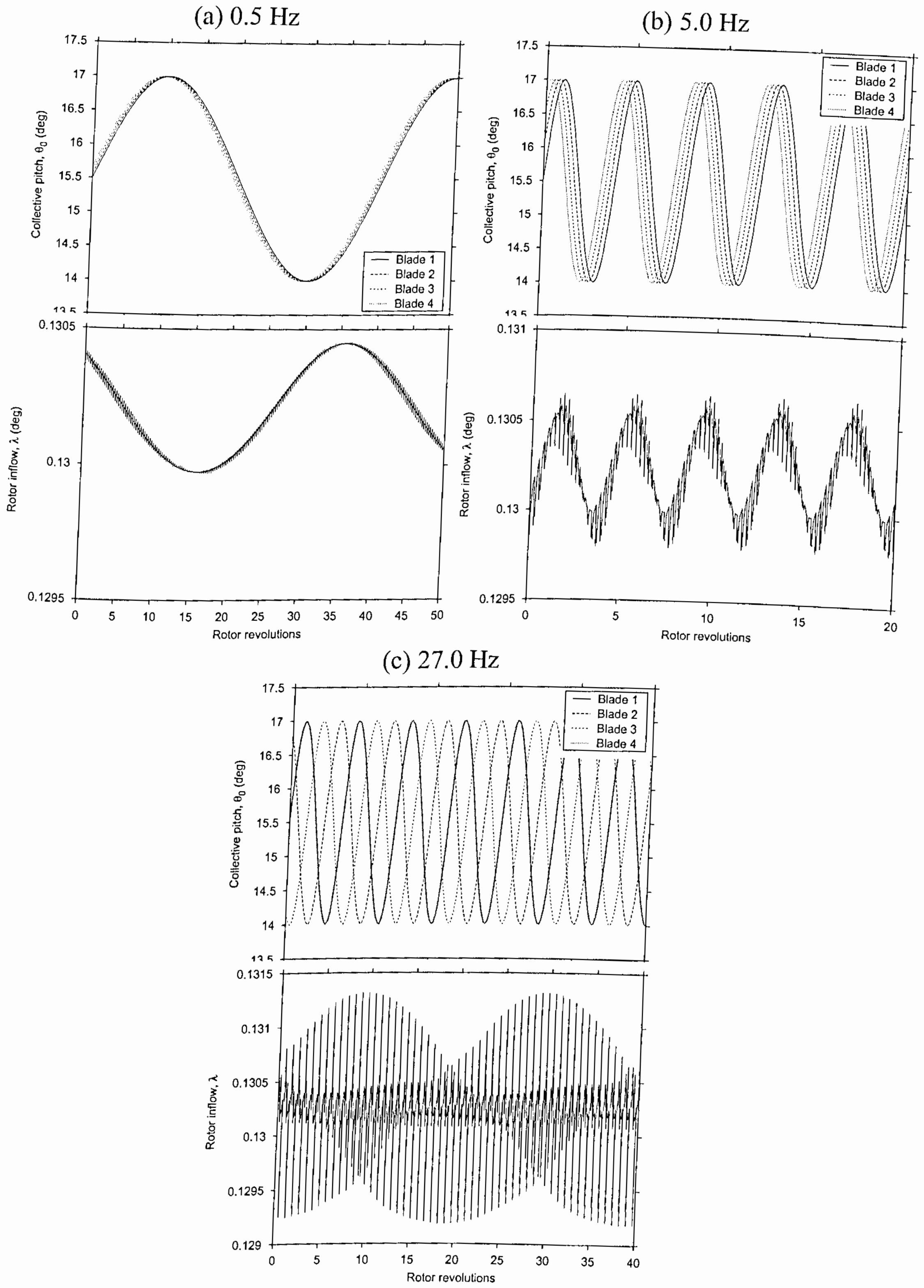

Figure 6.27: Sample oscillatory cyclic pitch excitation and the resulting inflow response predictions. Cyclic pitch excitation at (a) 0.5 Hz, (b) 5.0 Hz, (c) 27.0 Hz.

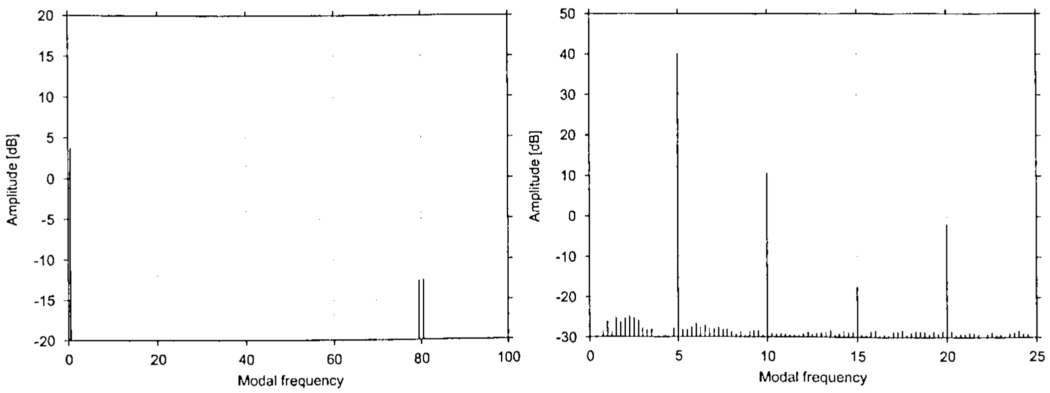

(a) 0.5 Hz

(b) 5.0 Hz

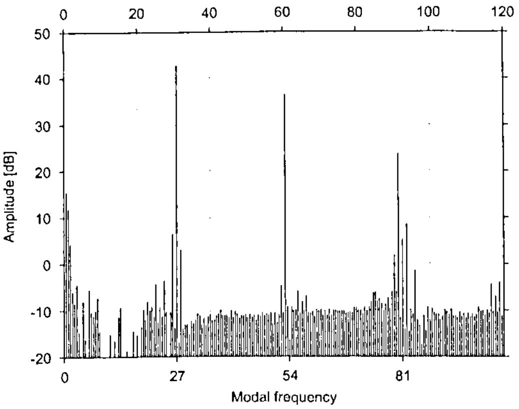

(c) 27.0 Hz

Figure 6.28: Sample frequency domain inflow response for oscillatory cyclic pitch excitation. The inflow time history at $r/R = 0.979$ is plotted in the frequency domain for three excitation frequencies, (a) 0.5 Hz, (b) 5.0 Hz, and (c) 27.0 Hz.

tions for a cyclic pitch excitation at $\omega_{1x} = 12.7$ is shown in Fig. 6.29. In this case, the wake structure also showed wave-like behavior with alternate regions of axial contraction and expansion. However, because the blade pitch was excited in a cyclic manner, these wave structures propagate in the wake at different azimuthal locations in the form of a helical disturbance.

The response of the rotor induced inflow field to such a cyclic excitation is shown in Fig. 6.30 as a function of the excitation frequency. Three representative spanwise blade locations at $r/R = 0.41,\ 0.57$ and 0.73 are shown. The experimental results are identified with solid symbols. The inflow response to cyclic excitation was found to be different from that in response to a collective excitation. The diminishing gain in the intermediate frequencies below half the rotational frequency is interesting. This frequency range is especially important for determining the basic characteristics of helicopter handling qualities and control. The phase response was also found to be different from the phase response to collective pitch excitation. Overall, the free-vortex wake predictions show good agreement with the basic trends observed in experiment.

Figure 6.31 shows the cyclic inflow gain along the blade span for six different excitation frequencies. As for the collective pitch excitation, the inflow response with increasing frequency was found to be more concentrated near the blade tips. The high inflow gain in the region of maximum blade lift is even more pronounced than the corresponding results for the inflow response to collective pitch excitations (Fig. 6.23). The predicted results also show this high gain in the tip region. The overall agreement between the numerical results and experiments was found to be good.

Results for the radial variation in the corresponding phase of the predicted inflow response are shown in Fig. 6.32. The phase-lag in inflow build-up increased on the inboard spanwise locations. Note that this is similar to the behavior observed for the

(a) Side view

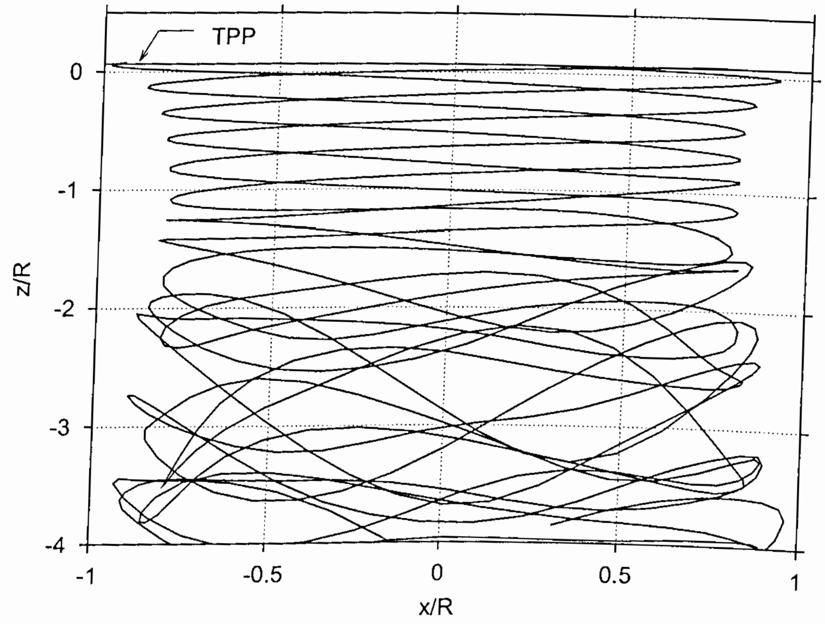

(b) Rear view

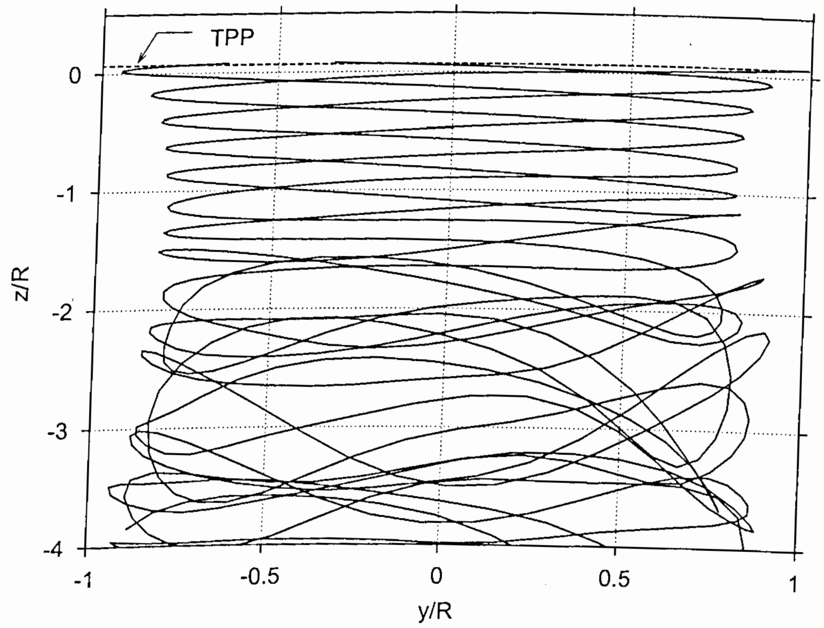

Figure 6.29: Example side view of the rotor wake for oscillatory collective pitch excitation at $\omega_{ex} = 12.5$ Hz showing periodic axial compression and expansion of the wake structure. (a) Side view, (b) Rear view.

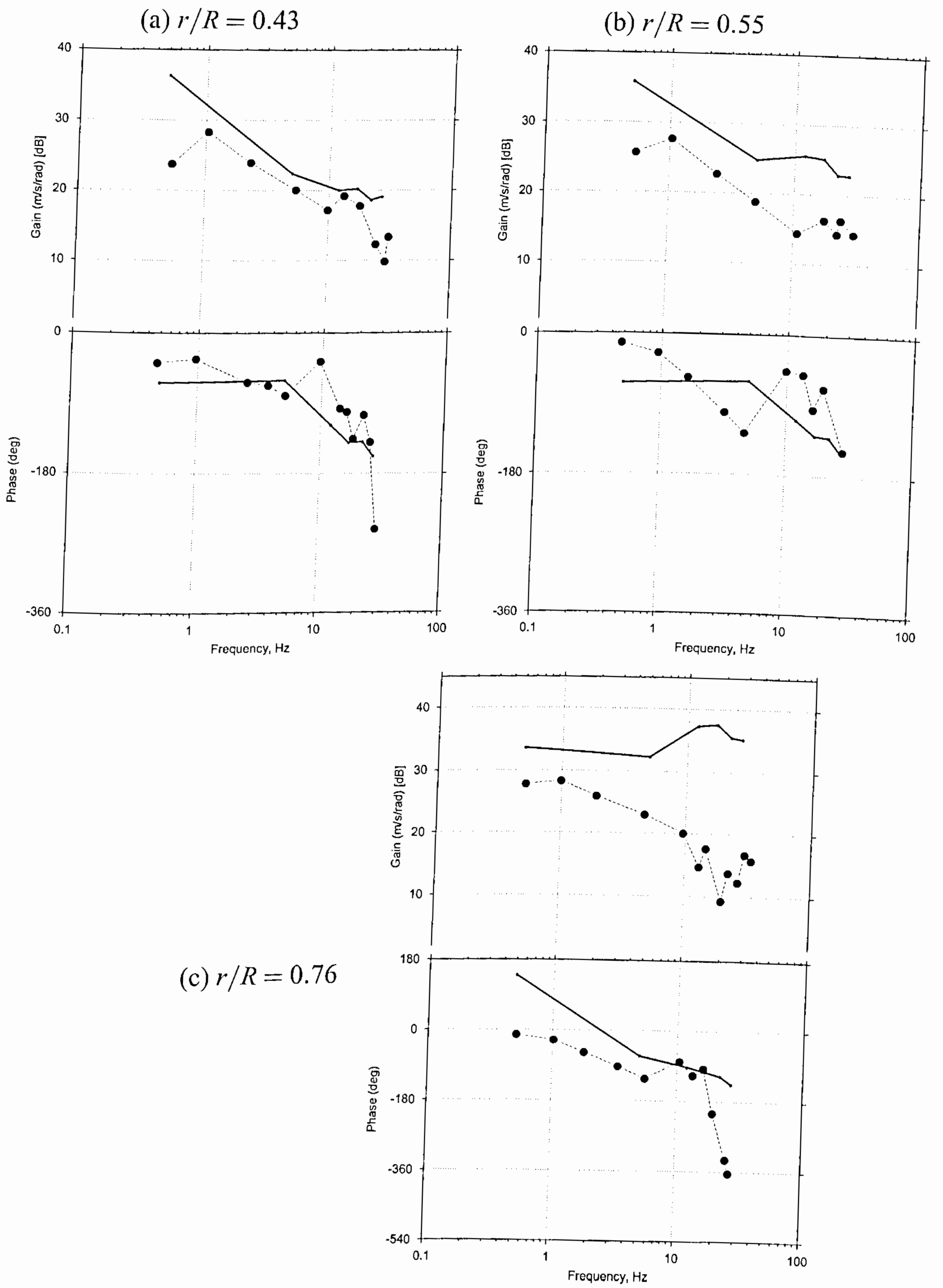

Figure 6.30: Inflow frequency response to oscillatory cyclic pitch excitation. Symbols are experiments of Ref. 102 while solid lines are predictions obtained using the present free-vortex wake analysis. (a) $r/R = 0.43$, (b) $r/R = 0.55$, and (c) $r/R = 0.76$.

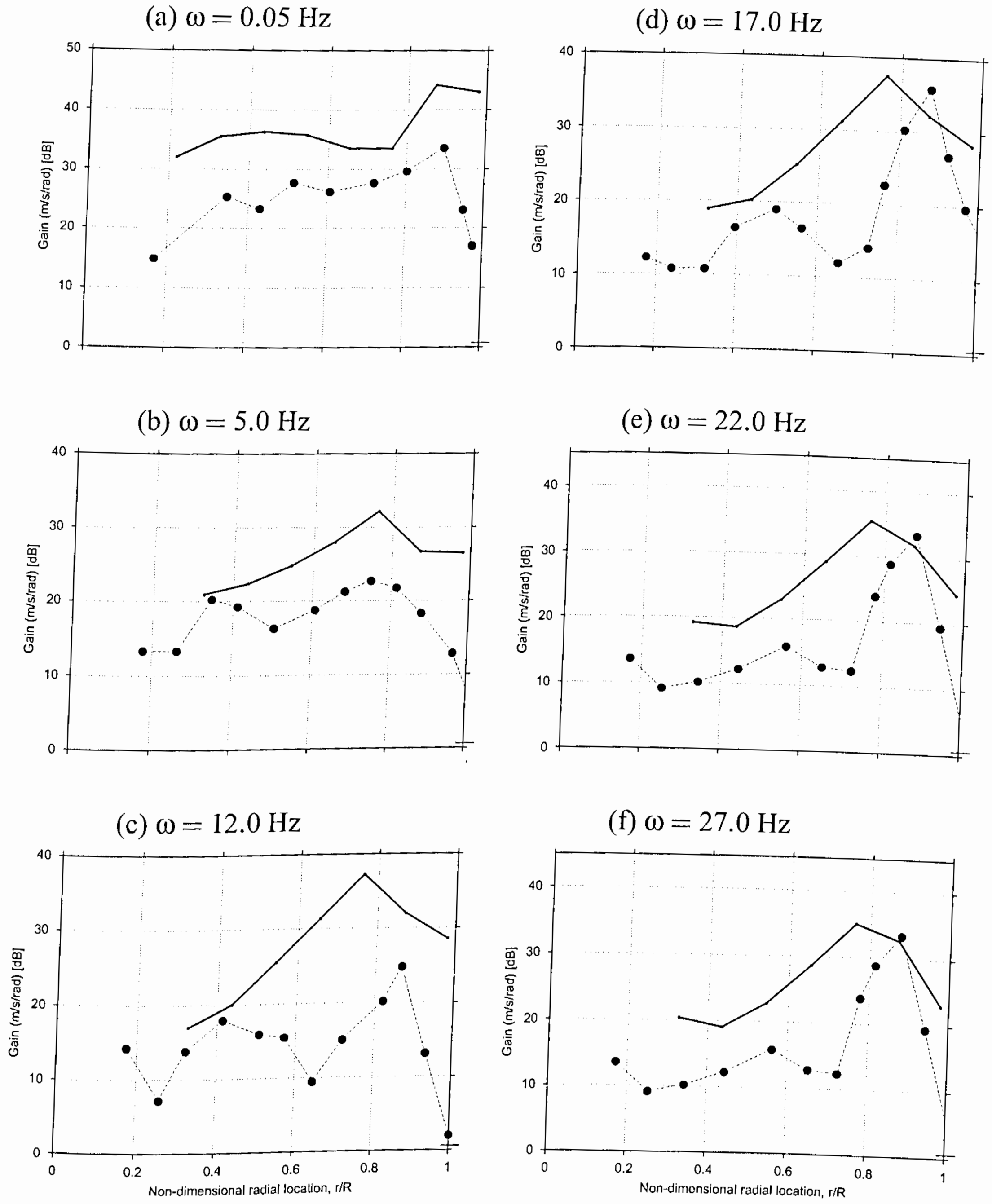

Figure 6.31: Radial variation in the gain of dynamic inflow response at different excitation frequencies of cyclic pitch. Symbols are experiments of Ref. 102 while solid lines are predictions obtained using the present free-vortex wake analysis. (a) ω = 0.05 Hz, (b) ω = 0.5 Hz, (c) ω = 12.0 Hz, (d) ω = 17.0 Hz, (e) ω = 22.0 Hz, and (f) ω = 27.0 Hz.

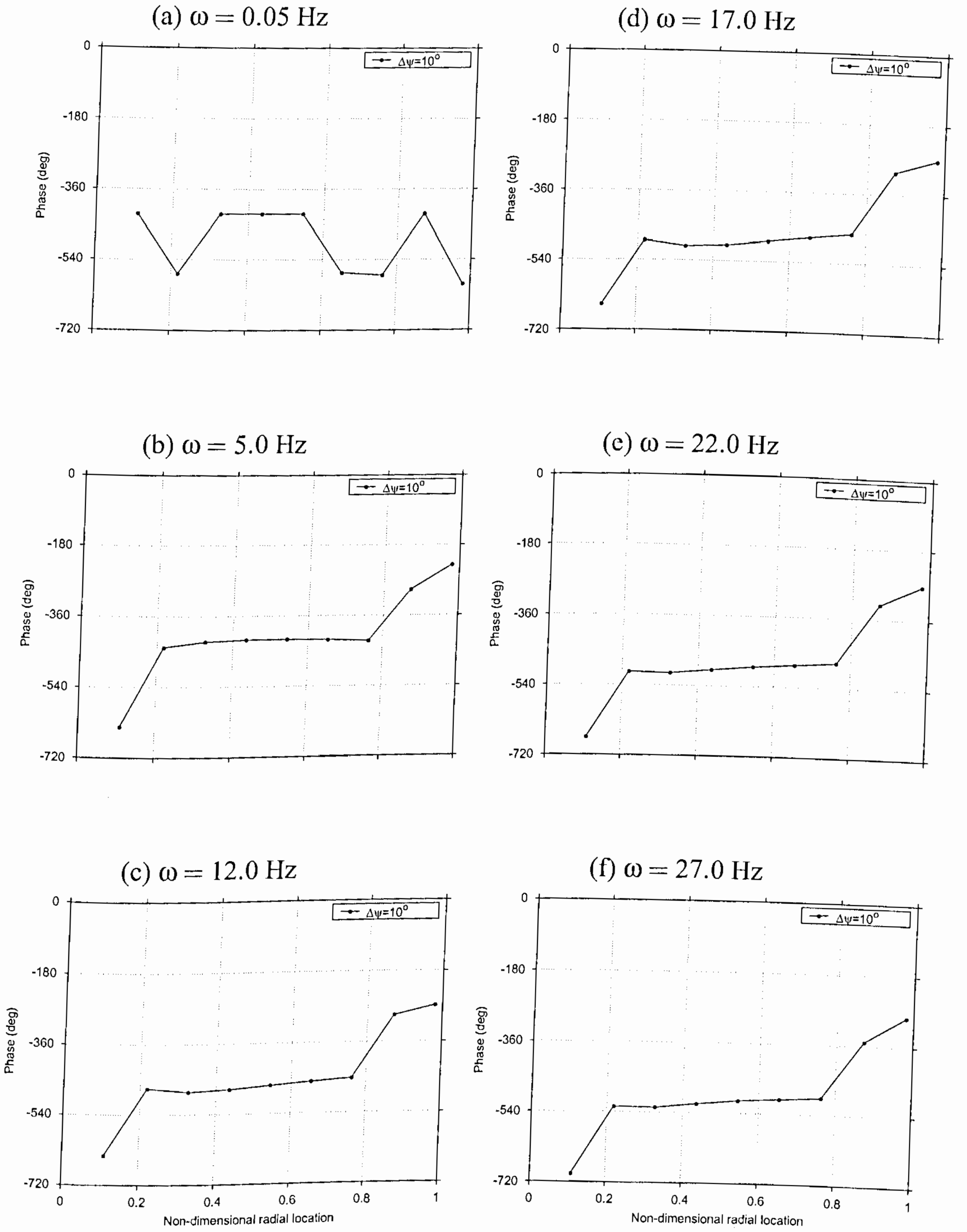

(a) ω = 0.05 Hz

(d) ω = 17.0 Hz

(b) ω = 5.0 Hz

(e) ω = 22.0 Hz

(c) ω = 12.0 Hz

(f) ω = 27.0 Hz

Figure 6.32: Predicted radial variation in the phase of dynamic inflow response at different excitation frequencies of cyclic pitch. Experimental data unavailable. (a) ω = 0.05 Hz, (b) ω = 0.5 Hz, (c) ω = 12.0 Hz, (d) ω = 17.0 Hz, (e) ω = 22.0 Hz, and (f) ω = 27.0 Hz.

collective pitch excitation, and suggests that the tip vortices are the most dominant structure influencing the rotor induced velocity field.

6.3.3 Blade Flapping Response

For the collective pitch excitations, the blade flapping response is essentially of the same form as the pitch input, except for a small initial transient. This is because the rotor induced inflow response is also predominantly at the blade pitch excitation frequency. For cyclic pitch excitations, however, several higher harmonics of the excitation frequency were also found in the rotor induced inflow response. The successive phase-lag in the pitch inputs applied different blades also constitutes an excitation at the rotational frequency. Therefore, the flapping response is also expected to reveal the presence of some higher harmonics. One motivation for the experiments of Ellenrieder & Brinson (Ref. 102) had been the inability of most wake models to predict the response at the intermediate frequency range. The present free-vortex wake results show that the inflow response is predicted well at these pitch excitation frequencies. Therefore, it would appear that the flapping response may also be important for determining the overall rotor response.

One example of the rotor response is shown in Fig. 6.33, where the blade flapping resulting from both collective and cyclic blade pitch applied at an excitation frequency of 27.0 Hz is shown. The collective pitch excitation was found to result in blade flapping predominantly at the excitation frequency, as expected. For the cyclic excitation, however, there are higher harmonics present in not only the initial transient response but also in the steady-state flapping.

A frequency domain analysis was used to analyze the higher harmonic flapping response. Figure 6.34 shows the magnitude of flapping as a function of excitation

(a) Collective pitch excitation at 27.0 Hz

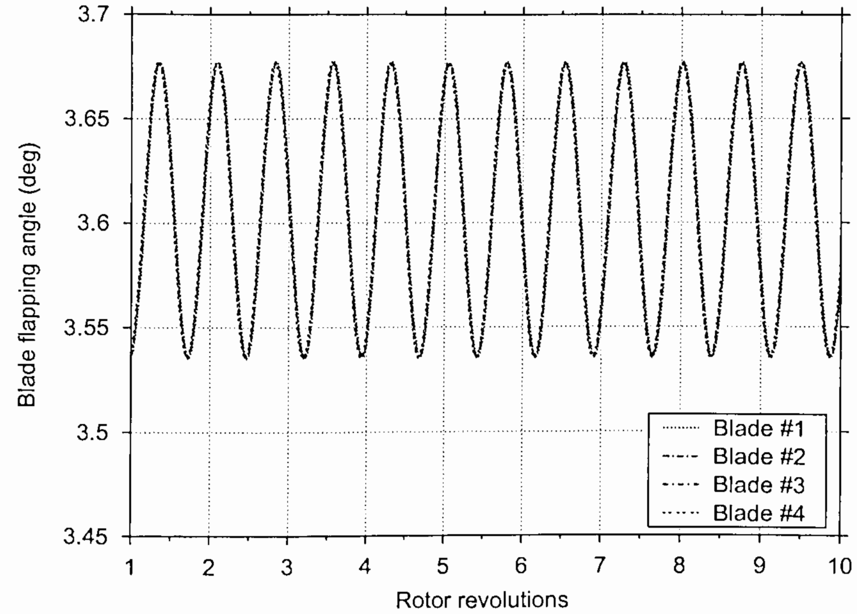

(b) Cyclic pitch excitation at 27.0 Hz

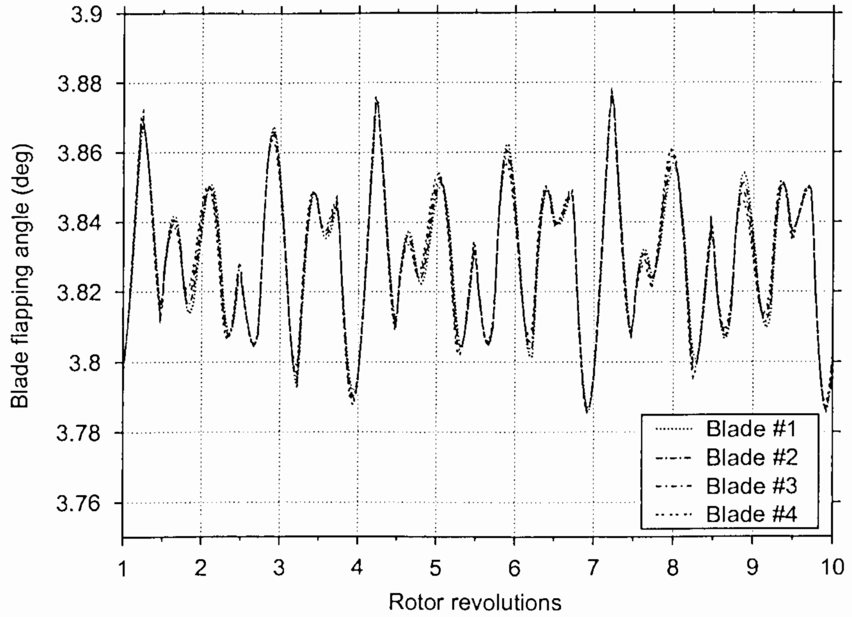

Figure 6.33: Examples of predicted blade flapping time history for oscillatory collective and cyclic pitch inputs. (a) Collective pitch excitation at 27.0 Hz. (b) Cyclic pitch excitation at 27.0 Hz.

frequency. For all the excitation frequencies (ω_{ex}), the response shows significant flapping at 1/rev$\pm\omega_{ex}$. At the lowest frequency of $\omega_{ex} = 0.5$ Hz, the predominant flapping response is at the excitation frequency itself. However, at higher frequencies the 1/rev$+\omega_{ex}$ harmonic dominates the blade flapping response. At the intermediate frequency range around 10.0 Hz (half the rotational frequency), the 2/rev$-\omega_{ex}$ harmonic flapping is more dominant than the primary (expected) blade flapping response at the excitation frequency. Most wake or inflow models, such as the dynamic inflow models, do not account for the presence of higher harmonics of inflow and may also fail to capture these harmonics in the subsequent blade flapping response.

Figure 6.35 shows the magnitude of blade flapping as a function of excitation frequency. Figure 6.35(a) shows the basic flapping response at the excitation frequency. The nature of this response is essentially that of a damped spring-mass system. The highest amplitude is found near the resonance or natural frequency, which is 1.22Ω in this case. Measured values of flapping magnitude from the experiments of Ref. 104 are also shown for comparison. Both the experimental measurements and the predictions using the present free-vortex wake analysis show the same qualitative trend in the blade flapping response, which is similar to a damped spring-mass system.

Figure 6.35(b) shows similar results including the magnitudes corresponding to other flapping harmonics, along with the basic response at the blade pitch excitation frequency. It is interesting to note that at the intermediate frequencies the flapping response at 1/rev$+\omega_{ex}$ is much more dominant than the primary response at the excitation frequency. At half the rotational frequency, even the 2/rev$-\omega_{ex}$ harmonic flapping is more significant. All these harmonics appear to decay at frequencies higher than the natural flapping frequency of the rotor.

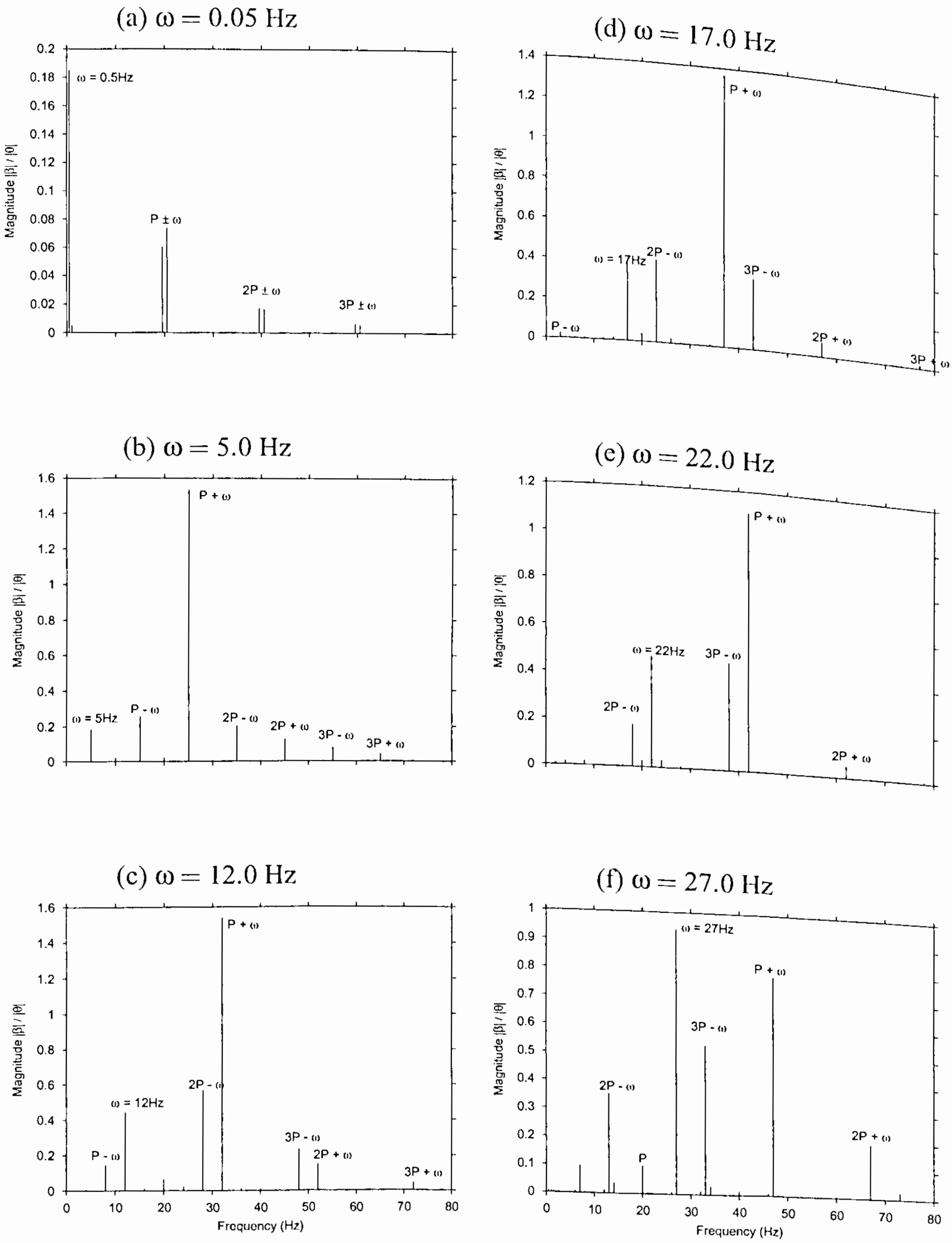

(a) $\omega = 0.05$ Hz

(b) $\omega = 5.0$ Hz

(c) $\omega = 12.0$ Hz

(d) $\omega = 17.0$ Hz

(e) $\omega = 22.0$ Hz

(f) $\omega = 27.0$ Hz

Figure 6.34: Frequency response of blade flapping magnitude for six excitation frequencies for oscillatory cyclic pitch inputs. (a) $\omega = 0.05$ Hz, (b) $\omega = 0.5$ Hz, (c) $\omega = 12.0$ Hz, (d) $\omega = 17.0$ Hz, (e) $\omega = 22.0$ Hz, and (f) $\omega = 27.0$ Hz.

(a) Flapping response at the excitation frequency

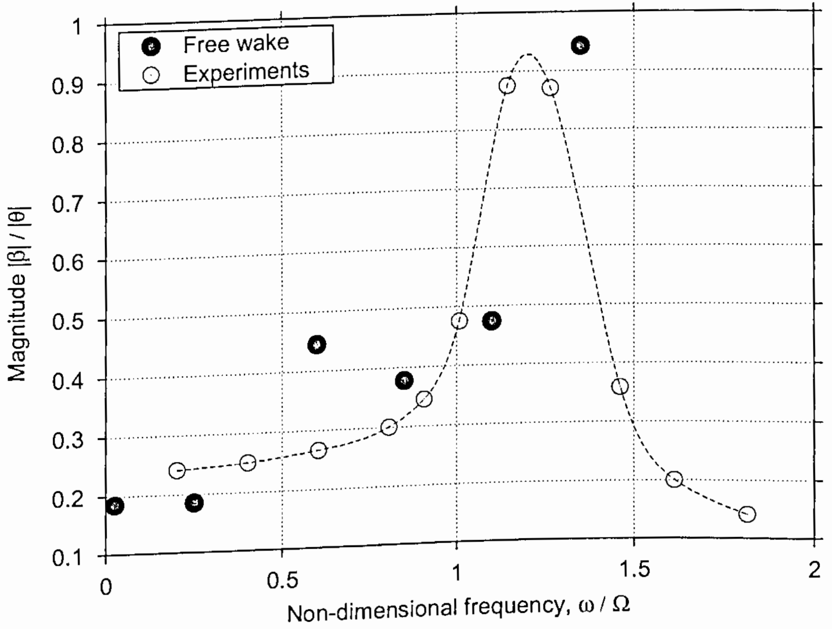

(b) Flapping response at other harmonics

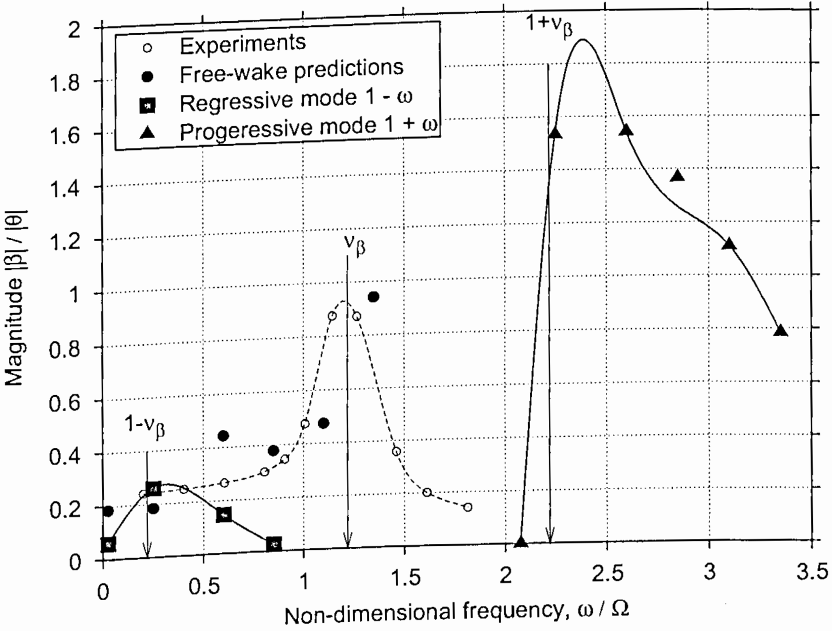

Figure 6.35: Blade flapping magnitude as a function of excitation frequency for oscillatory cyclic pitch inputs. (a) Flapping response at the excitation frequency, (b) Flapping response at other harmonics.

6.4 Summary

The present chapter has focused on time-accurate predictions of the dynamic evolution of the vortical wake generated by a rotor. The predictions obtained using the present analysis were validated using available experimental measurements during transient flight conditions. The dynamic build-up of rotor induced inflow resulting from an increase the collective pitch at several different ramp rates was found to agree well with experimental measurements. The slow build-up of rotor inflow following a change in the rotor collective pitch was shown to be a circulatory effect resulting from the dynamic evolution of the trailed vortical wake structure below the rotor. The inflow frequency response to oscillatory collective and cyclic pitch excitations was also predicted well with the present free-vortex wake analysis. These encouraging results confirm that the present analysis faithfully models the dynamics of the vortical rotor wake under non-steady conditions, where the rotor response as well as the wake may be non-periodic.

Chapter 7

Results & Discussion: Applications of the Time-Accurate Wake Model

In Chapters 5 and 6 the present wake solution methodology was validated for steady-state and transient flow conditions. One motivation for developing the time-accurate wake model was to examine the transient behavior of the rotor wake and its effect of the rotor response. In the current chapter, the methodology is applied to a parametric study of rotor response for some idealized maneuvering flight situations, including idealized pitch and roll rate inputs under hovering and forward flight. The methodology is also applied the problem of a rotor in descending flight, where the rotor flow field may become unsteady (non-periodic) because of the close proximity of the rotor to its own wake. The analysis was sucesfully applied to predict the rotor performance and response during transition through a complex, recirculating flow state known as the vortex ring state.

7.1 Idealized Maneuvers

The ability to determine the response of a helicopter rotor under maneuvering flight conditions has been one motivation for the development of the time-accurate wake solution methodology previously described. A steady-state vortex wake model, such as a relaxation wake model, can also be used to model the aerodynamic effects during some types of maneuvering flight problems. The assumption of a "steady-state" solution is valid, provided that the transient effects introduced into the wake resulting from the maneuver are of a relatively short time-period. Many helicopter maneuvers involve small angular rates compared to the rotor rotational frequency (typical rates are $p/\Omega, q/\Omega \leq 0.025$). The rotor wake itself is periodic at the rotational frequency, and various transients are propagated into the wake at N_b-per-revolution. Therefore, it would appear that the maneuver related effects on the rotor wake should have a relatively short time-period compared to the overall wake behavior. In many cases with short maneuver time-periods, a steady-state wake solution may be valid, except for the small initial transient immediately after the beginning of the maneuver. However, in general, a time-accurate wake model will be necessary to properly represent the transient behavior. Steady-state wake geometry results are, nevertheless, useful in understanding the overall features associated with maneuver induced wake distortion effects. The results presented in this section are obtained using the time-accurate free-vortex wake methodology. The steady-state results are simply time-accurate solutions obtained after a sufficiently large period of time (that is, sufficiently large number of rotor revolutions) when the rotor wake attains a nearly periodic flow structure.

When a helicopter rotor undergoes an angular motion about the hub, the structure of the rotor wake is significantly affected. The effects of simple maneuvers in the form of angular motions can be modeled using an additional contribution to the local velocity field. This effect is schematically illustrated in Fig. 7.1(a), where the rotor is shown undergoing a nose-up pitching motion. The vortical wake structure generated by the rotor also experiences a similar angular motion about the hub. Equivalently, an additional external (rotational) free-stream velocity component may be applied to the rotor and its trailing wake structure. Such an additional velocity because of the maneuver rates is analogous to the addition of a constant freestream velocity to the rotor and its wake to represent the forward flight velocity of the helicopter. Note that the inflow perturbation at the rotor disk is a longitudinal inflow gradient, as shown in Fig. 7.1(a), with an increased inflow on the front of the rotor disk resulting from the nose-up pitching motion.

For pitch and roll motions about the rotor hub, the additional velocity contributions will be a function the pitch/roll rates as well as the position vector of any point in the flow field relative to the maneuver axis or rotor hub. The equivalent velocity because of angular rotations can be determined by a cross product of the maneuver rate vector and the position vector, $\vec{r} \equiv (x,y,z)$. Therefore, the maneuver-related velocities at a point $\vec{r}$ are given by

$$\begin{aligned} \vec{V}_{\text{man}} &= -\{p\hat{\imath}+q\hat{\jmath}\} \times \vec{r} \\ &= -\{p\hat{\imath}+q\hat{\jmath}\} \times \{x\hat{\imath}+y\hat{\jmath}+z\hat{k}\} \\ &= -(qz)\hat{\imath}+(pz)\hat{\jmath}+(qx-py)\hat{k} \end{aligned} \qquad (7.1)$$

where p and q are the roll and pitch rates, respectively. Note that the negative sign means that the relative flow velocities seen by the rotor and the wake are in a direction opposite to the angular (maneuver) rates.

The first term, which is the x-component of the velocity resulting from a pitch rate, q, produces an skewing distortion of the wake, as shown in Fig. 7.1(b). The second

(a) Initial wake structure

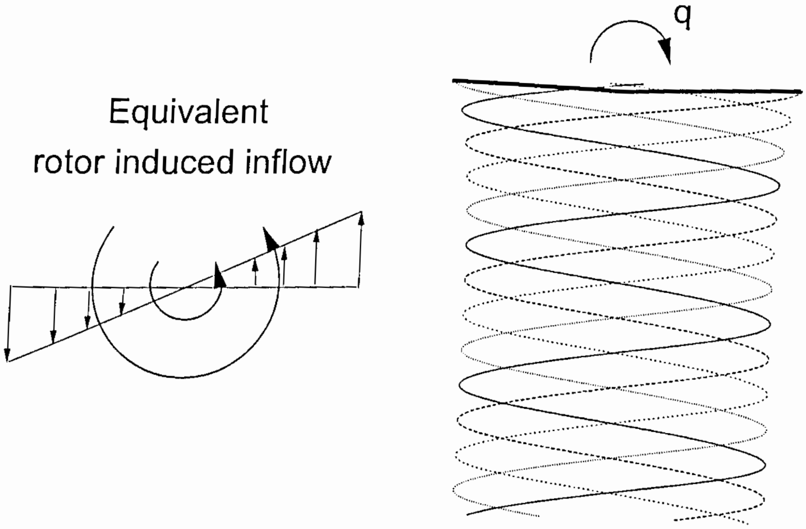

(b) Wake distortions under a maneuver rate

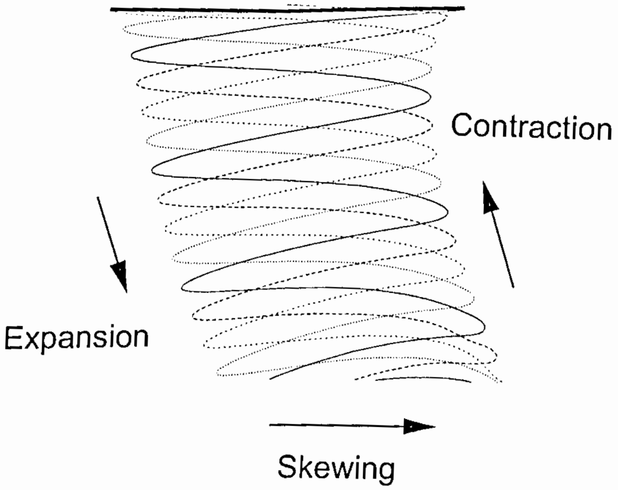

Figure 7.1: Schematic diagram showing the approach to include maneuver induced wake distortions on the wake geometry. (a) Initial wake structure. (b) Wake distortions under a maneuver rate.

term, which is the y-component of the velocity resulting from a roll rate, p, has a similar skewing effect on the rotor wake along the lateral axis. This is often referred to as a "bending" effect because it essentially results in curvature of the wake. The third term $(qx - py)$, produces an axial stretching distortion of the wake. Typically, the wake vortices will be closer to the rotor on one side, and on the other side will lie further away from the rotor. This effect further influences the rotor induced velocities, as will be shown later in this chapter.

Nose-Up Pitch Rate Starting from Hover

In hovering flight, the rotor wake is axisymmetric. However, with the introduction of a pitch or roll rate, the rotor wake undergoes both a lateral and a longitudinal distortion. This is a consequence of the additional maneuver related apparent free-stream velocity components, as described in the previous section. As a result, the wake is no longer axisymmetric.

An example of the rotor wake geometry for a rotor undergoing a nose-up pitching motion is shown in Fig. 7.2. The rotor in this case is identical to the four-bladed 2MRTS rotor examined earlier in Section 5.2. The rotor thrust coefficient is $C_T = 0.012$, and the pitch rate is $q/\Omega = 0.024$. Note that this is a relatively high pitch rate for a helicopter, but is used in this example to exaggerate the maneuver related wake distortion effects for the purpose of explaining this behavior. The rotor wake geometry corresponding to the initial hovering flight is also shown for comparison. The time-accurate solution after 20 rotor revolutions is shown, the rotor wake being almost periodic after that time.

Figure 7.2(a) shows that the the tip vortex filaments are further away from the TPP at the front of the disk as compared to their locations found in hovering flight. At the

(a) Side view

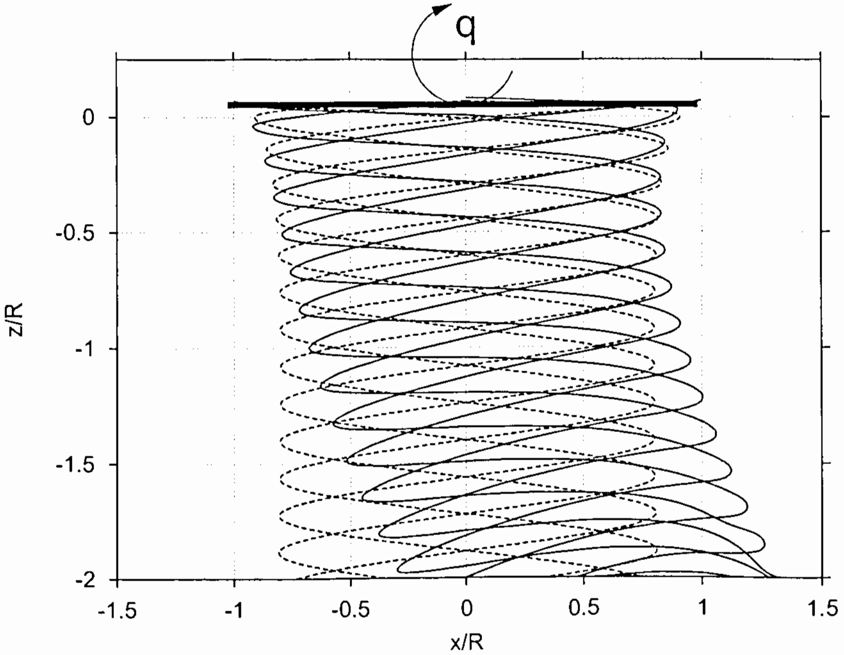

(b) Rear view

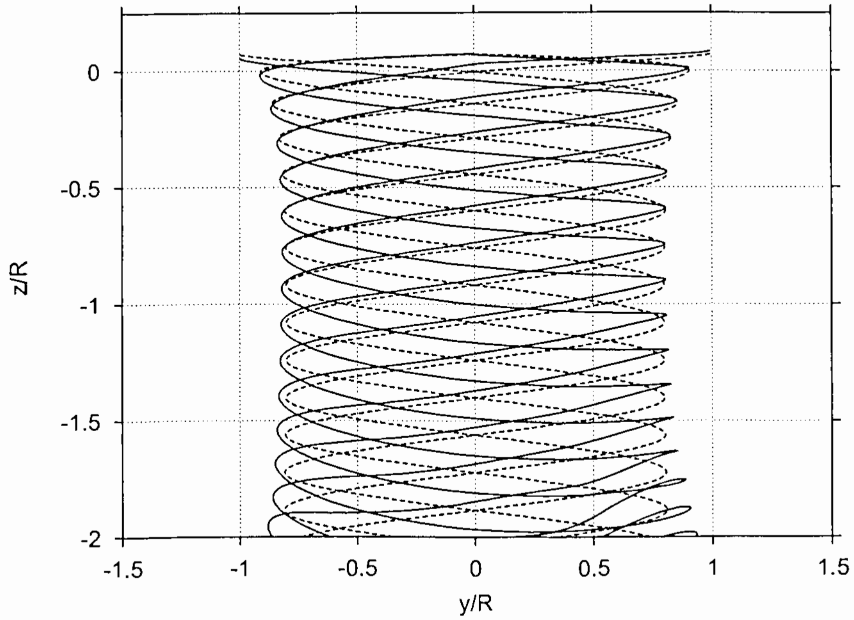

Figure 7.2: Predicted tip vortex geometries for a four-bladed hovering rotor with and without an imposed nose-up pitch rate. $\overline{q} = 0.024$, $C_T = 0.012$. (a) Side view, (b) Rear view. The baseline non-maneuvering wake geometry is shown with dashed lines, while the maneuvering wake is shown as solid lines.

rear of the rotor disk, the tip vortices are closer to the TPP as compared to the baseline hovering case. Note that the axial displacements of the tip vortex filaments near the wake centerline are also different. This combination of expansion and contraction is the so called "wake curvature" effect, a term previously suggested by several researchers (e.g., Refs. 105–107). Figure 7.2(b) shows that the wake undergoes little lateral distortion in response to a pitching motion. This is expected, because the velocity contribution resulting from a pitching motion is only in the axial and longitudinal directions. However, there is some lateral wake distortion in the far wake, and a slight wake expansion is observed because of the self and mutually induced effects of the rotor wake vortices.

Clearly, the rotor wake undergoes significant distortions because of the angular rates imposed on the rotor, and will certainly affect the induced velocity distribution at the rotor disk. As shown in Fig. 7.2, the "contraction" and "expansion" of the rotor wake on the front and rear of the rotor disk, respectively, will influence the longitudinal rotor inflow distribution. Recall from that the rotor induced velocity field can be approximated by a linear inflow model, as mentioned earlier in Section 5.2. That is, the inflow field can be represented by

$$\lambda_i = \lambda_0 + \lambda_{1c} \cos\psi + \lambda_{1s} \sin\psi \tag{7.2}$$

$$= \lambda_0 \left(1 + k_x \frac{x}{R} + k_y \frac{y}{R}\right) \tag{7.3}$$

The Biot-Savart law (Ref. 8, Ch. 2, pp. 93–94) shows that the vortex induced velocities are inversely proportional to the distance from the vortex filament axis. Therefore, at the front of the disk there should be a reduction in rotor inflow because the vortices are located further away from the TPP. Similarly, there should be an increased induced inflow at the rear of the rotor disk. Therefore, the maneuver induced wake distortions would result in a negative longitudinal inflow perturbation, i.e., $\Delta\lambda_{1c} < 0$, for a nose-up pitch rate. Because the inflow gradients (K_x, K_y) are normalized with the mean inflow, a nose-pitching motion will lead to a wake induced inflow gradient with $K_x < 0$.

It is interesting to note that from purely kinematic considerations, the nose-up pitching motion results in a positive perturbation to the longitudinal inflow gradient. The inflow contribution because of the maneuver related velocities can be readily calculated from Eq. 7.1 as $\Delta\lambda_{\text{kin}} = qx = qr\cos\psi$ and, therefore, $\Delta\lambda_{1c} = q$, or

$$\Delta K_x = \frac{q}{\lambda_0} \quad \text{and} \quad \Delta K_y = -\frac{p}{\lambda_0} \tag{7.4}$$

This positive longitudinal inflow perturbation will lead to an increase in lift over the rear of the disk and a reduction in lift on the front of the disk. This means that the rotor blades would exhibit predominantly a lateral flapping, β_{1s}. This argument, however, neglects the effects of wake distortion, which are usually found to be opposite to the kinematic effects (see also Ref. 108). In the next section, the inflow perturbations resulting from steady-state wake distortion effects because of the maneuver are examined in more detail.

7.1.1 Steady-State Results

In this section, the steady-state results following a pitch or roll maneuver are explained — that is, the rotor aerodynamic behavior after sufficiently long time following the start of the maneuver. In all cases, the time-accurate wake model was used and the solution was calculated up to a sufficiently large number of rotor revolutions to ensure that the wake geometry became almost periodic and had reached a "steady-state."

Figure 7.3 shows the induced inflow distribution along the lateral and longitudinal axes of the rotor disk. The rotor thrust coefficient in this case is $C_T = 0.012$ and the non-dimensional pitch rate is $\overline{q} = 0.024$. The induced inflow for hovering flight is also shown as a reference for comparison. Because the blades have a linear twist, the inflow distribution in hover is nominally uniform over most of the blade span. Because of the imposed pitching maneuver, the kinematic inflow gradient gives an increased inflow at the front of the rotor disk. The wake induced inflow resulting from the distortion of the wake, however, has an opposite effect, resulting in a decreased inflow on the front of the rotor disk, as shown in Fig. 7.3(a). The net induced inflow distribution experienced by the rotor blades is in the same sense as that suggested by kinematics alone, but to a much lesser magnitude. Notice that kinematic considerations alone suggest that the lateral inflow distribution remains unaffected in a pitching maneuver. However, because of the off-axis blade flapping response and various maneuver induced wake distortions, the free-vortex wake analysis shows that there is also an off-axis induced inflow perturbation resulting from the pitching motion of the rotor hub. In this case, the rotor experiences an increase in inflow on the advancing side of the rotor disk and a slight decrease in inflow on the retreating side, resulting in a lateral inflow gradient. Therefore, this results in an on-axis (longitudinal) blade flapping response following an imposed pitch rate.

Figure 7.4 shows the longitudinal inflow gradient perturbation as a function of the pitch rate. The kinematic inflow gradient is linear with respect to the pitch rate, i.e., $\Delta K_x = q/\lambda_0$. The negative slope of the kinematic gradient results from the longitudinal inflow coefficient being normalized by the mean inflow, λ_0, which is negative. The wake-induced inflow perturbation is opposite to that based on the kinematic inflow gradients, with an increased inflow at the rear of the rotor disk. Notice that the wake induced inflow is almost linear with respect to the pitch rate. As a result, the net inflow perturbation encountered by the rotor blades is smaller in magnitude than that expected

(a) Longitudinal (on-axis) inflow perturbation

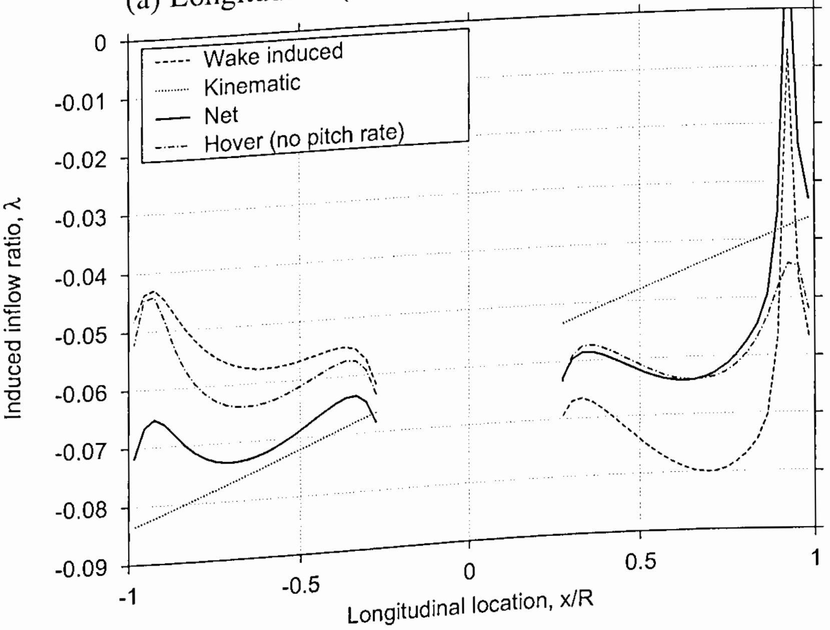

(b) Lateral (off-axis) inflow perturbation

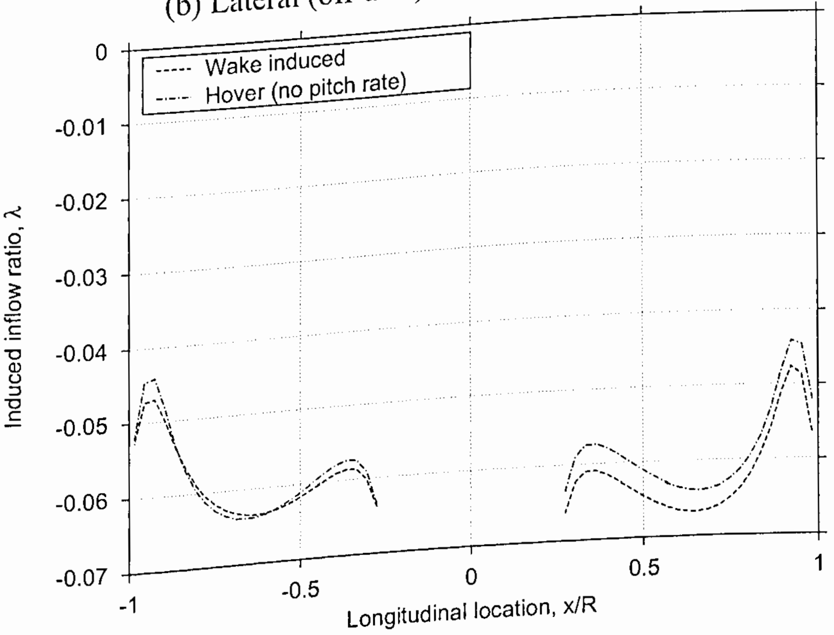

Figure 7.3: Induced inflow perturbations because of a nose-up pitching motion for a four-bladed rotor, $C_T = 0.012$. (a) Longitudinal (on-axis) inflow perturbations, (b) Lateral (off-axis) inflow perturbation.

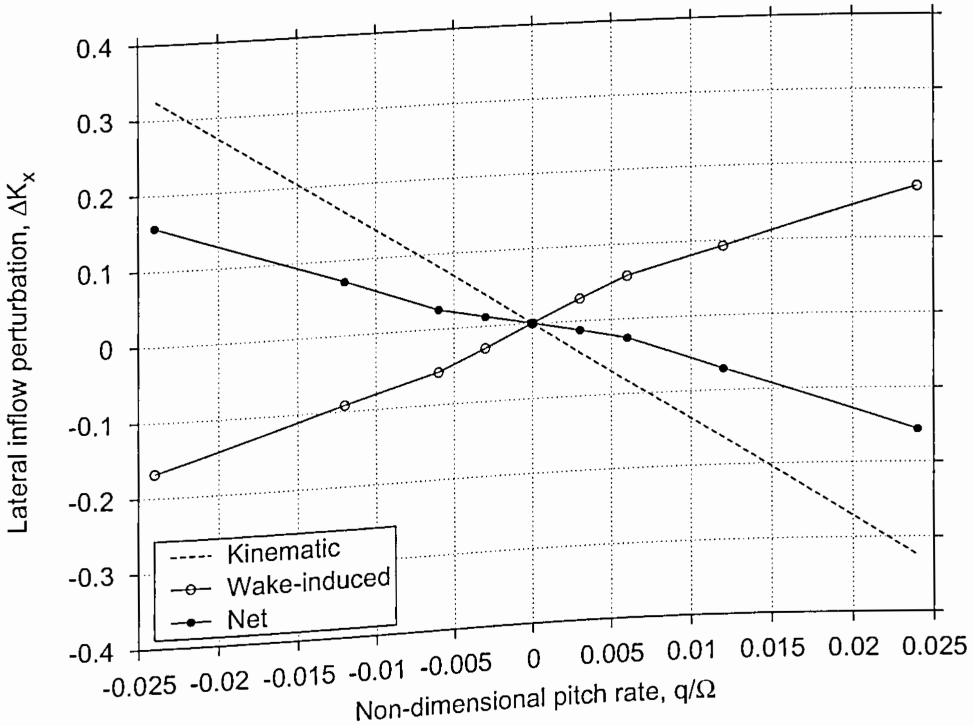

Figure 7.4: Rotor induced inflow perturbation resulting from pitching motion of the rotor. Only the on-axis (longitudinal) inflow perturbation is shown.

based on kinematic considerations alone. The corresponding blade flapping response would also be smaller.

The results shown in the following sections include two levels of modeling of the inflow perturbations resulting from an imposed maneuver rate. These are

Level 1: Only kinematic effects on linear inflow gradient perturbations.

Level 2: Both kinematic and wake distortion effects on linear inflow gradient perturbations are considered. This is done by calculating the rotor induced inflow field using the time-accurate wake model, and then deriving the linear inflow coefficients from these results by a least-square approximation.

The free-vortex wake analysis developed in the present work solves the blade flapping equations by time-integration in a manner fully coupled with the rotor wake solution. However, the blade flapping response can also be estimated based on a linearized inflow model. One simplified approach is to only include linear inflow perturbations on the basis of kinematic considerations alone, as given by Eq. 7.4. A better approximation to the blade flapping response may be obtained by estimating the linear inflow perturbations from the wake-induced inflow as calculated using the present free-vortex wake analysis. This approach inherently includes the effects of maneuver induced wake distortion, along with the kinematic effects on the inflow gradients. The motivation for such simpler modeling approaches is the ability to integrate them into real-time flight simulations, where a complete free-vortex wake solution is not likely to be feasible. Note that production level flight mechanics analyses typically use some such simplified rotor inflow model. In summary, the blade flapping response may be predicted with three levels of modeling, i.e.,

Level 1: Estimated flapping response based on linear inflow perturbations resulting from kinematic effects alone (Level 1 inflow perturbation model).

Level 2: Estimated flapping response based on linear inflow gradient perturbations resulting from both kinematic and wake distortion effects as given by the free-vortex wake solution (Level 2 inflow perturbation model).

Level 3: Calculated by time-integration of the blade flapping equations coupled with the free-vortex wake solution.

In the following sections, these approximations to the blade flapping response are compared with the coupled blade flapping and time-accurate wake solutions to better understand the expected fidelity obtained with such levels of approximations.

Based on a linearized inflow model, the blade flapping response to the induced inflow perturbations can now be calculated in the same manner that as described in Section 4.2.2. Assuming the flapping hinge to be coincident with the rotational axis, the contributions of the inflow perturbations to the aerodynamic flapping moment are given by

$$\Delta\overline{M}_{\beta} = \frac{\gamma}{2}\int_{0}^{1} \left[\mu \Delta\lambda\, r \sin\psi + \Delta\lambda\, r^{2}\right] dr \tag{7.5}$$

where $\Delta\lambda = \Delta\lambda_0 + \Delta\lambda_{1c} r\cos\psi + \Delta\lambda_{1s} r\sin\psi$ based on a simple linear inflow model. Integrating the above expression (Eq. 7.5) gives

$$\left.\begin{aligned} \Delta\overline{M}_{\beta_0} &= -\gamma\left[\frac{\Delta\lambda_0}{6} + \mu\frac{\lambda_{1s}}{12}\right] \\ \Delta\overline{M}_{\beta_{1c}} &= -\gamma\frac{\Delta\lambda 1c}{8} \\ \Delta\overline{M}_{\beta_{1s}} &= -\gamma\left[\frac{\Delta\lambda_{1s}}{8} + \mu\frac{\lambda_0}{4}\right] \end{aligned}\right\} \tag{7.6}$$

Now, following the results from Section 4.2.2, the blade flapping response can be calculated using Eqs. 4.81–4.83 as

$$\Delta\beta_0 = -\frac{\gamma}{6}\left[\Delta\lambda_0 + \mu\frac{\Delta\lambda_{1s}}{2}\right] \tag{7.7}$$

$$\Delta\beta_{1c} = \left(\frac{1}{1-\frac{\mu^2}{2}}\right)\left[\Delta\lambda_{1s} + 2\mu\Delta\lambda_0\right] \tag{7.8}$$

$$\Delta\beta_{1s} = -\left(\frac{1}{1+\frac{\mu^2}{2}}\right)\Delta\lambda_{1c} \tag{7.9}$$

The blade flapping response estimated using the above equations is shown in Fig. 7.5 based on the first level of approximation for the rotor induced inflow perturbation, that is where only the kinematic effects are included. The on-axis (longitudinal) inflow perturbations are shown in Fig. 7.5(a) as a function of pitch rate, and the corresponding off-axis (lateral) blade flapping response is shown in Fig. 7.5(b). The results obtained by time-integrating the flapping equations coupled with the free-vortex wake solution are also shown as a reference. Clearly, the including only the kinematic inflow gradient perturbations results in significant overprediction of the flapping response. As mentioned earlier, the maneuver induced wake distortion effects in hovering flight contribute an opposite inflow gradient perturbation. Therefore, inclusion of wake-induced inflow perturbations is expected to give a better physical representation of the blade flapping in response to the imposed maneuver rates.

Figure 7.6(a) shows the on-axis linear inflow perturbations based on the rotor induced velocity predicted using the present free-vortex wake model. In this case, both the kinematic as well as wake-induced effects are intrinsically included in the inflow calculations. The estimated off-axis blade flapping response based on this linear inflow perturbation is shown in Fig. 7.6(b), along with the results calculated by time-integration of the blade flapping equations. Because the wake geometry reaches a nearly periodic steady-state, the results obtained from the above steady-state analysis are almost the same as the results obtained using time-integration of the flapping equations. It should be noted that off-axis flapping response is substantially reduced because wake-induced inflow perturbations are opposite to the kinematic inflow perturbation. In some cases, the wake induced inflow perturbation could be even greater than the kinematic inflow gradient. In such cases, the rotor blade flapping response would then be in an opposite sense to that predicted using kinematic considerations alone (see Eq. 7.4).

Because of the axisymmetric nature of the aerodynamic problem, the response of a hovering rotor to an imposed roll rate is the same as that to an imposed pitch rate, but phased by 90°. Figure 7.7(a) shows the inflow perturbations from imposed roll and pitch rates. The results obtained for the perturbations ΔK_x and $-\Delta K_y$ are identical as expected, providing a check for the present analysis. Figure 7.7(b) shows the

(a) On-axis inflow perturbations

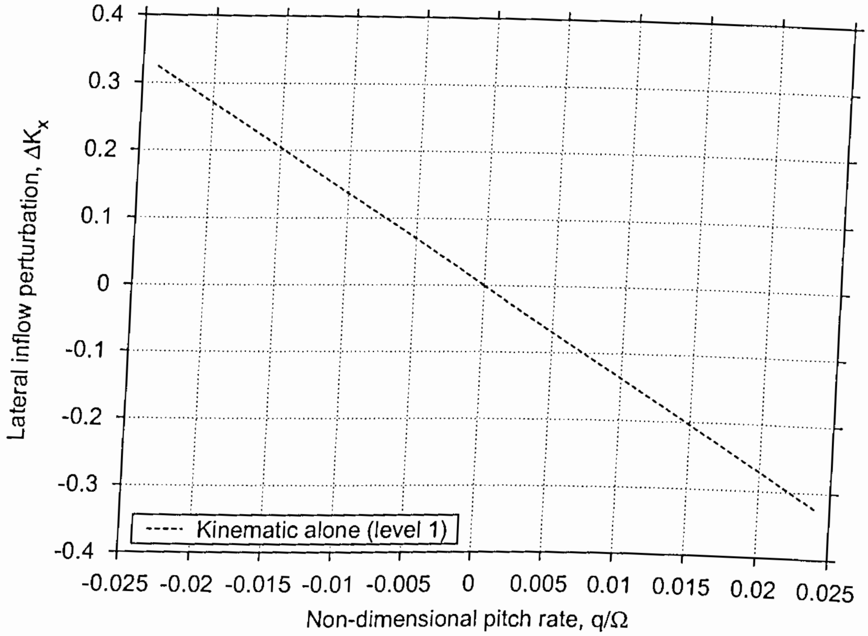

(b) Off-axis blade Flapping response

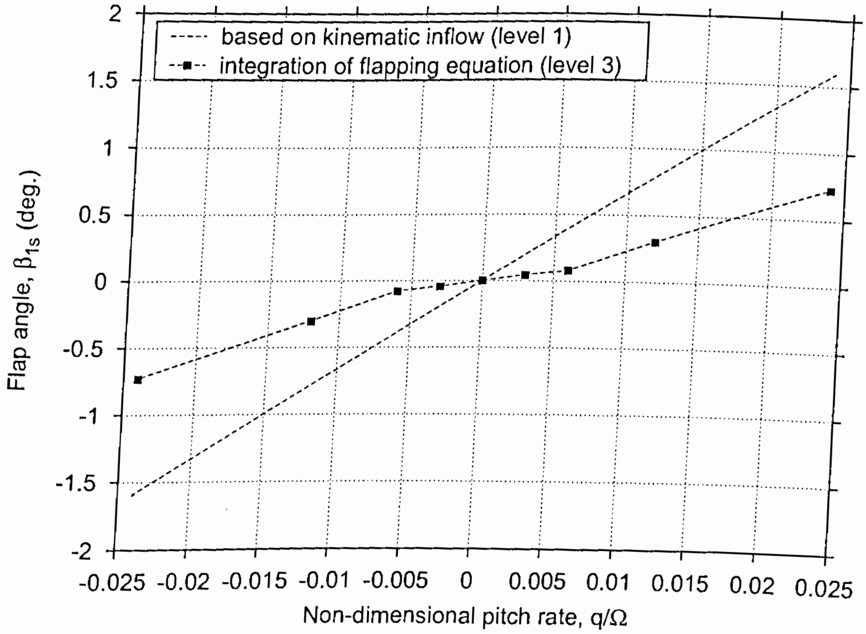

Figure 7.5: Off-axis rotor blade flapping response because of on-axis induced inflow gradient perturbations resulting from imposed pitch rate based on kinematic considerations alone. (a) On-axis inflow gradient perturbations. (b) Off-axis blade flapping response.

(a) On-axis inflow gradient perturbations

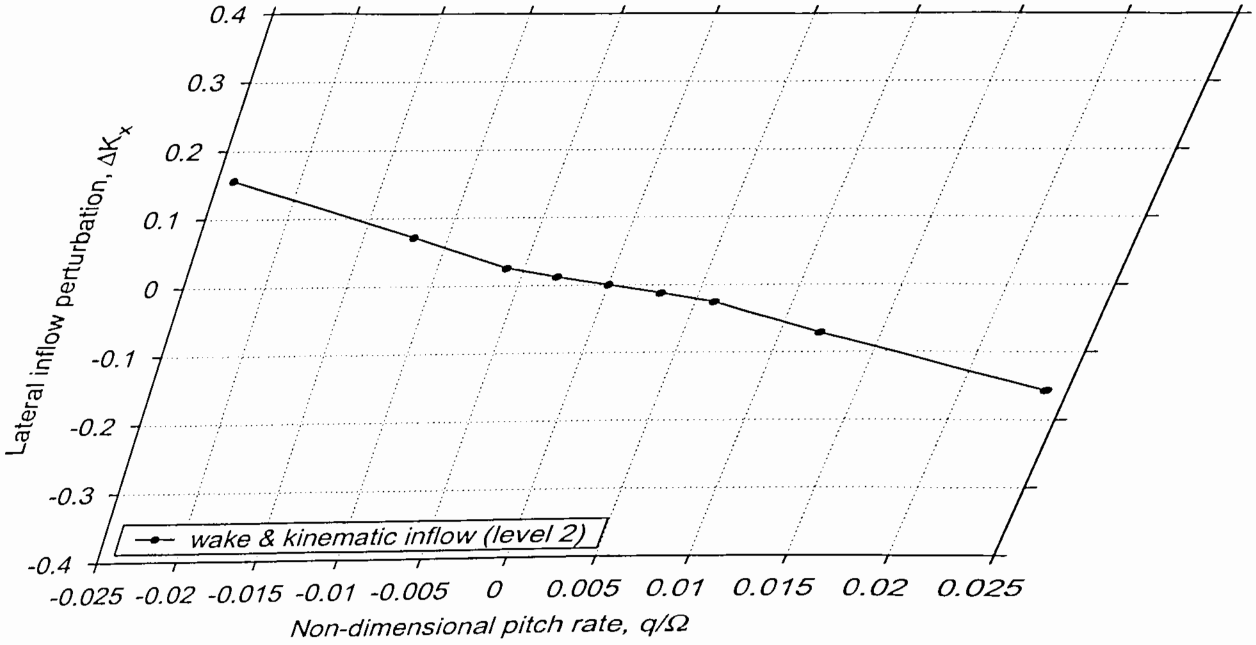

(b) Off-axis blade flapping response

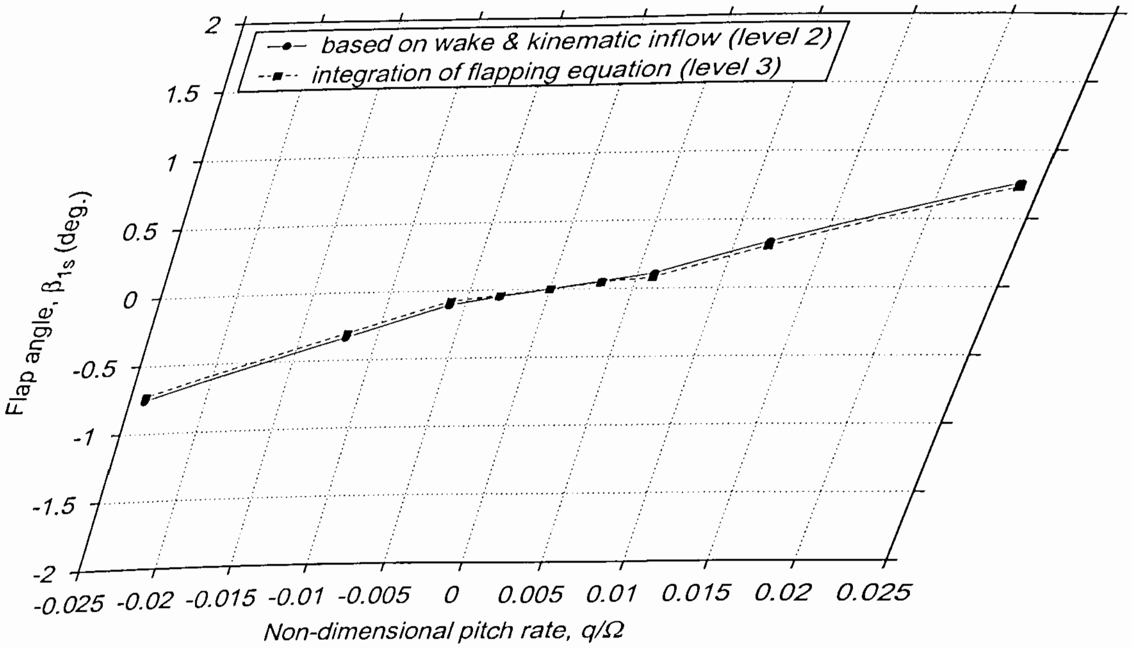

Figure 7.6: Off-axis rotor blade flapping response because of on-axis wake-induc inflow gradient perturbations resulting from imposed pitch rate based on the inflo calculations from the free-vortex wake analysis. (a) On-axis inflow gradient perturbation. (b) Off-axis blade flapping response.

corresponding off-axis blade flapping response. Again, the steady-state blade flapping angles calculated using time-integration agree with those predicted on the basis of the steady-state inflow perturbations predicted by the free-vortex wake analysis. The inflow perturbations based on kinematic considerations alone result in an overprediction of the blade flapping response.

Recall that the above steady-results are time-accurate solutions computed for a large number of rotor revolutions (i.e., at a sufficiently large time) when the rotor wake attains a periodic structure. This is not, in general, the same as the steady-state solution obtained using the relaxation method, where wake periodicity condition is explicitly enforced. For example, the rotor response derived from the relaxation solution is shown in Fig. 7.8. Note that for the two lowest imposed angular rates, the linear inflow perturbations based on the relaxation wake solution (as shown in Fig. 7.8(a)) are the same as those based on the time-accurate wake solution, as shown in Fig. 7.7(a). Consequently, the predicted blade flapping response based on the inflow perturbations is also the same for both the relaxation and the time-accurate wake models, as shown in Fig. 7.7(b) and 7.8(b). This is expected because for very low angular rates the time-lag associated with the maneuver effects on the rotor wake are small, and the overall wake behavior is nearly periodic or reaches a "steady-state." However, for larger maneuver rates (i.e., $\overline{q} \geq 0.012$), the two predictions show significant differences. Also, the periodic blade flapping response calculated in a coupled manner with the relaxation wake solution is substantially smaller than the blade flapping response estimated based on the linear inflow perturbations obtained using the same relaxation wake solution.

To better illustrate the similarity and differences between the time-accurate and relaxation (steady-state) solution methodologies, the results are plotted again in Fig. 7.9. The on-axis inflow gradients and the off-axis flapping response are shown relative to

(a) On-axis inflow gradient perturbations

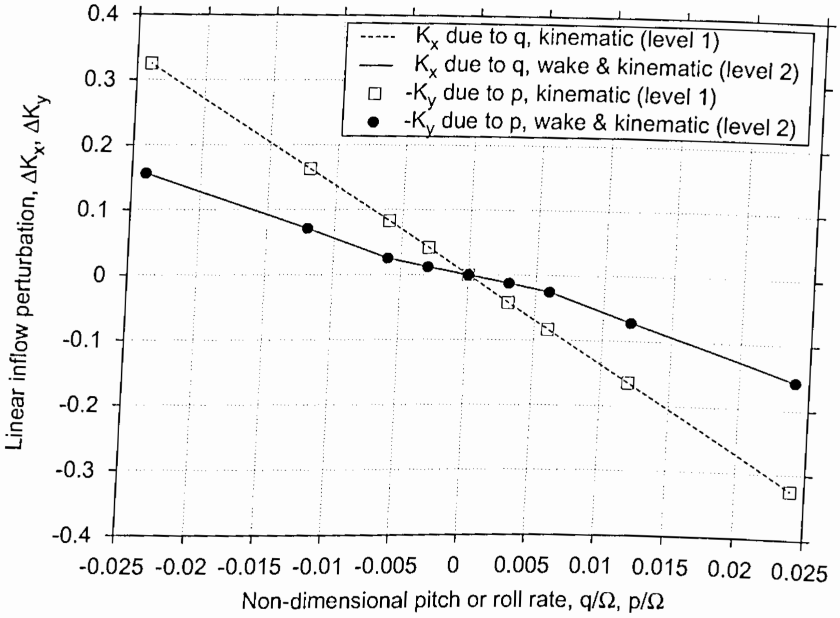

(b) Off-axis blade flapping response

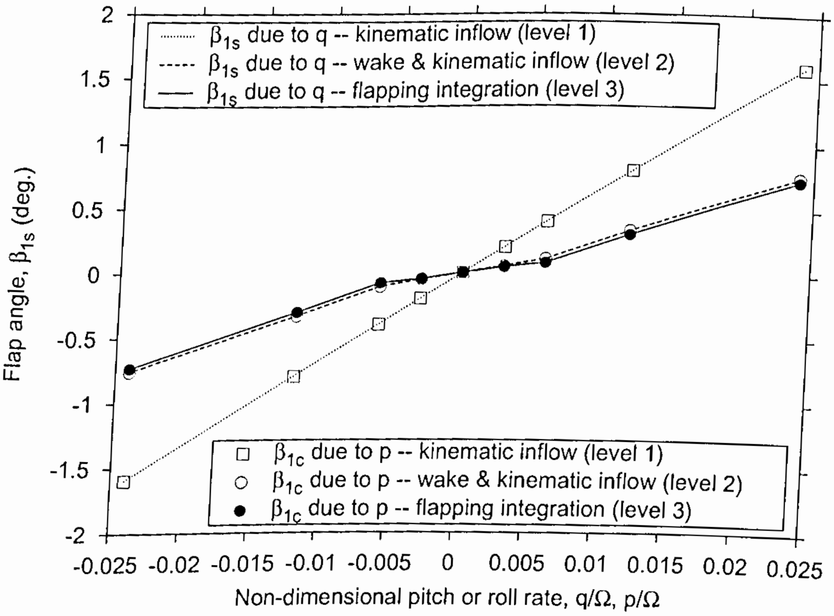

Figure 7.7: Induced inflow perturbations and the corresponding blade flapping response resulting from rotor angular rates. (a) On-axis inflow gradient perturbations, (b) Off-axis blade flapping response.

(a) On-axis inflow gradient perturbations

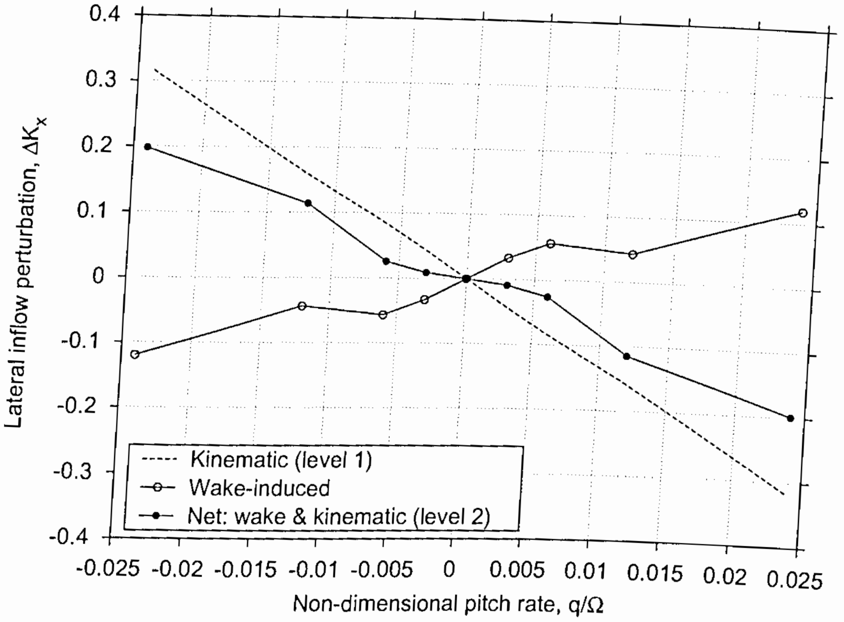

(b) Off-axis blade flapping response

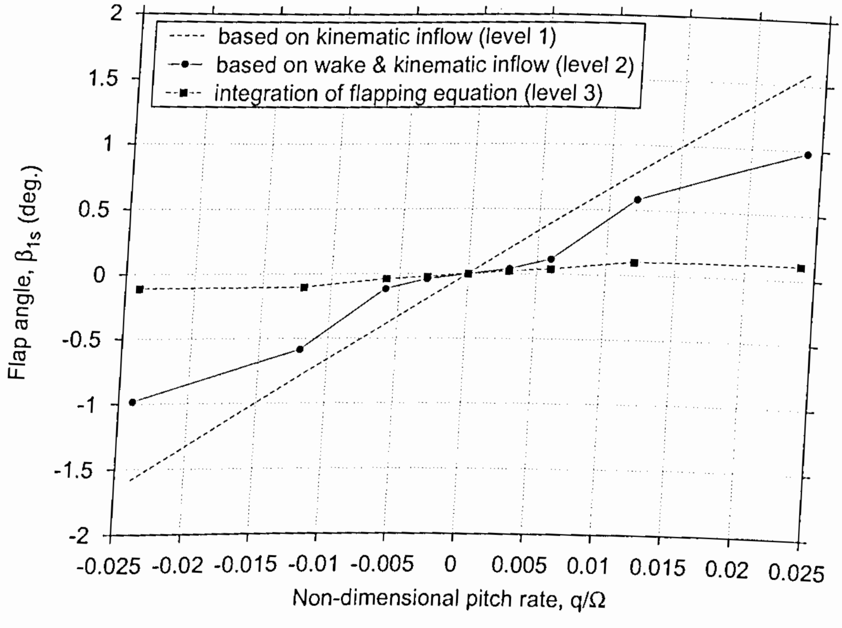

Figure 7.8: Induced inflow perturbations and the corresponding blade flapping response resulting from rotor angular rates as obtained using the steady-state (relaxation) wake. (a) On-axis inflow gradient perturbations, (b) Off-axis blade flapping response.

the values expected based on only kinematic considerations alone. It is clear that for low angular rates, the predicted inflow perturbations using both the steady-state and the time-accurate models are coincident, as shown in Fig. 7.9(a). For higher angular rates, however, the relaxation wake significantly underpredicts the effects of the maneuver induced wake distortion. As a result, the inflow perturbation is actually closer to the value expected based on kinematic considerations alone.

A similar agreement for low angular rates was seen in the predicted off-axis flapping response, as shown in Fig. 7.9(b). Note that the flapping response can be directly calculated by integrating the blade flapping dynamic equation coupled with the free-vortex wake equations. The flapping response may also be estimated based on the linear inflow perturbations calculated using the free-vortex wake model, as mentioned at the beginning of this section. Ideally, both these results should agree if the maneuver induced wake distortions are periodic at the rotor frequency with only first harmonic components. As shown in Fig. 7.9(b) the results obtained using both the wake model and the time-integration of the blade flapping equations coincide only for low angular rates. For higher angular rates, the flapping response based on the periodic (relaxation) wake model were significantly different than those using the time-integrated blade flapping response. This is because the inflow perturbations were not correctly represented using the relaxation wake model, as shown in Fig. 7.9(a). These differences suggests that the rotor wake becomes significantly non-periodic at higher maneuvering angular rates, and a steady-state, periodic model is not suitable. This also suggests that a steady-state wake methodology, like the relaxation wake method, may not be adequate for modeling the maneuver induced wake distortions under transient maneuvers, such as pull-up, tight turns, etc. In the next section, time-histories of the inflow perturbations and blade flapping response will be examined to better understand these effects.

(a) On-axis inflow gradient perturbations

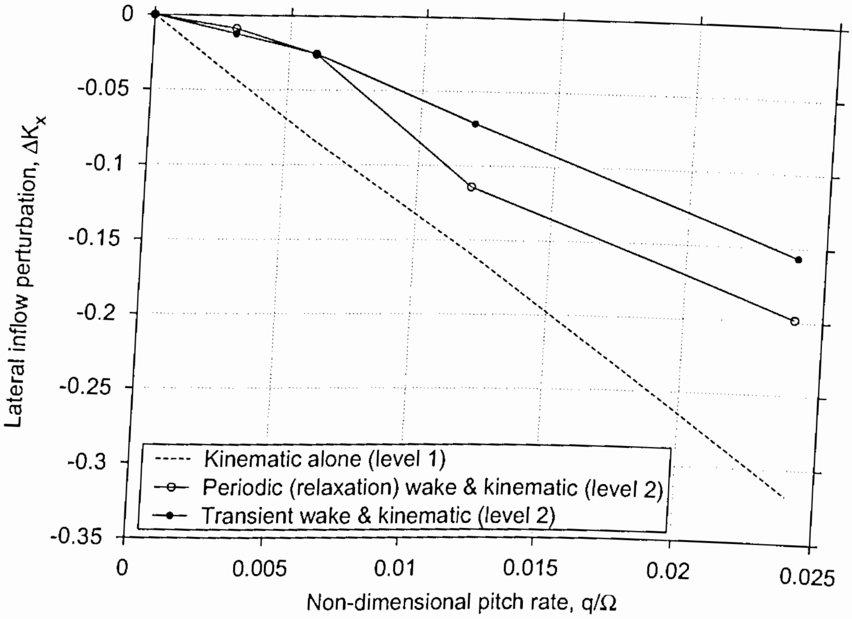

(b) Off-axis blade flapping response

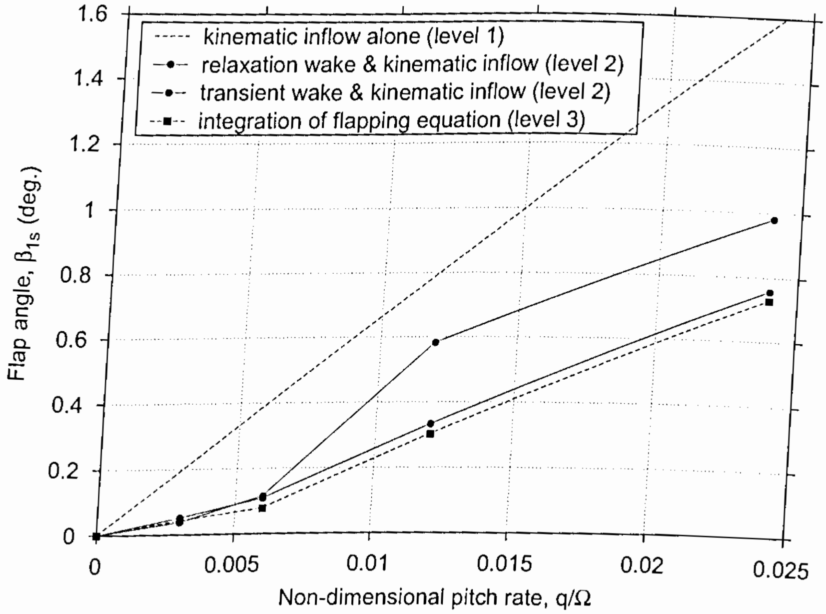

Figure 7.9: Induced inflow perturbations and the corresponding blade flapping response resulting from rotor angular rates as obtained using the periodic (relaxation) and the transient free-vortex wake models. Only positive pitch rates are shown for clarity. (a) On-axis inflow gradient perturbations, (b) Off-axis blade flapping response.

7.1.2 Transient Wake Solutions for Maneuvering Flight

Theodore & Celi (Ref. 109) have incorporated both a dynamic inflow model and a steady-state free wake models into a flight mechanics simulation to study the response of a helicopter to cyclic blade pitch inputs. Although they showed improved predictions of overall trends in the blade flapping response using the free-vortex wake model, the quantitative predictions were not substantially improved. Part of the reason could be that a steady-state (relaxation) wake model is not completely representative of the rotor wake aerodynamics for such maneuvering flight conditions.

An example of the transient (linear) induced inflow perturbation is shown in Fig. 7.10 in the form of Fourier coordinate transforms (FCT) of the calculated inflow. Only the longitudinal and lateral components, i.e., the first harmonics, are shown. Notice that the mean rotor inflow remains almost constant throughout the maneuver. The inflow perturbations without the maneuver induced wake distortion effects, i.e., based on kinematic considerations alone are also shown for comparison. The inflow response is normalized with respect to the kinematic value of $\lambda_{1c_{\mathrm{kin}}} = q/\Omega$.

Immediately after the rotor starts to undergo the pitching motion, the induced inflow showed a longitudinal perturbation equal to $\overline{q}$. After that, as the rotor wake started to undergo distortions resulting from the maneuver velocities, the inflow perturbation changed. Recall that the inflow perturbation resulting from the wake distortion was in an opposite sense to the kinematic perturbation in inflow. Therefore, the total induced inflow perturbation decreases in magnitude. After about five rotor revolutions, the inflow perturbation appeared to reach a steady-state value, and thereafter became invariant from one rotor revolution to another. It is interesting to note that the maneuver induced wake distortions also resulted in an off-axis inflow perturbation, i.e., a lateral inflow perturbation resulting from rotor pitching motion. However, the magni-

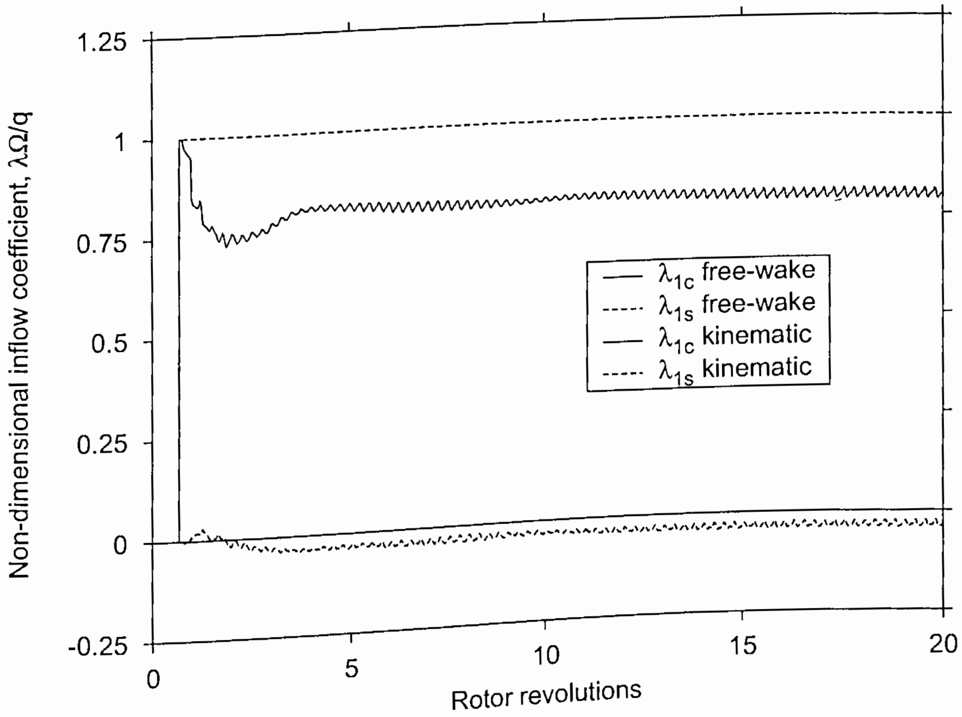

Figure 7.10: Rotor induced inflow perturbation because of nose-up pitching motion of the rotor. Four-bladed rotor, $C_T = 0.012, \bar{q} = 0.024$.

tude of this off-axis inflow perturbation is relatively small. Notice also that the small oscillatory behavior in the inflow response in the steady-state condition indicates the presence of small higher harmonics of the inflow at the rotor disk. This implies that the rotor wake is not completely axisymmetric. However, the linear inflow coefficients in a time-averaged sense (averaged over one rotor revolution) were found to reach a steady-state value, suggesting a relatively periodic wake structure.

The corresponding time-history of the rotor blade flapping response, as calculated by integrating the blade flapping equation along with the free-vortex wake equations, is shown in Fig. 7.11. The results using only the kinematic inflow perturbations, that is ignoring all maneuver induced wake distortion effects, are also shown for comparison. Note that the predominant blade flapping response is off-axis, i.e., a lateral blade flapping response resulting from the longitudinal inflow perturbation. There is a small on-axis flapping response, even based on the kinematic inflow considerations, which is because the hinge offset resulting in a control phase angle of not exactly a 90° lag with respect to the aerodynamic forcing. Notice that the off-axis blade flapping response is substantially decreased because of the wake distortion effects.

Effects of Rotor Thrust on Maneuver Induced Wake Distortion

Because the rotor inflow depends on the rotor operating conditions, the wake distortions produced in response to maneuvers (or rotor angular rates) will, in general, be dependent on the blade loading and/or rotor thrust coefficient. To examine this effect, time-accurate free vortex wake solutions were obtained for three rotor thrust coefficients of $C_T = 0.006$, 0.008, and 0.012 while keeping all other operating parameters constant. An example of the rotor response at these three different thrust levels is shown in Fig. 7.12 in terms of (a) the rotor induced inflow coefficient, and (b) the blade flapping response. As described previously, the inflow coefficients are normalized with respect to the kinematic value (Eq. 7.4) to bring out the relative effects of the maneuver induced wake distortions.

At the highest thrust level of $C_T = 0.012$, the inflow perturbation shows a small transient and reaches a steady-state within five rotor revolutions. At smaller thrusts, the inflow response shows much longer transients with significant unsteadiness. At the lowest thrust coefficient of $C_T = 0.006$, the inflow response shows significant oscillations even after twenty rotor revolutions, as shown in Fig. 7.12(a). In Section 2.5 it was shown that the divergence rates associated with the rotor wake increased with decreasing rotor thrust. This means that the wake becomes more unstable as the rotor

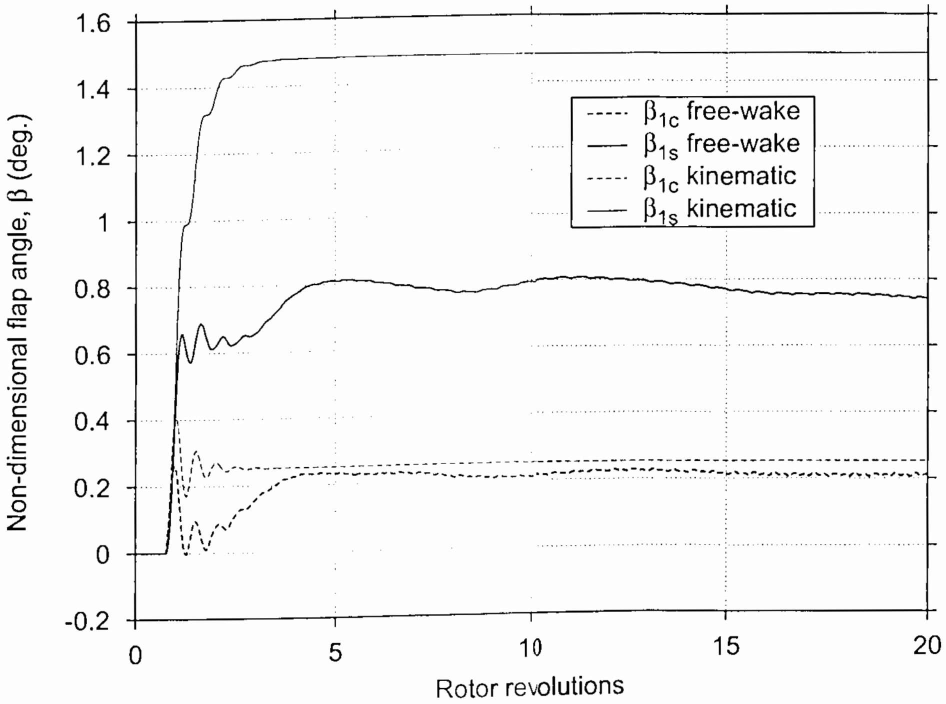

Figure 7.11: Rotor blade flapping response because of nose-up pitching motion of the rotor. Four-bladed rotor, $C_T = 0.012$, $\overline{q} = 0.024$.

thrust decreases. Therefore, for lower values of thrust, the maneuver induced wake distortions take a much longer time to reach to a periodic, steady-state structure.

The corresponding blade flapping angles for this problem are shown in Fig. 7.12(b), along with the blade flapping angles predicted based on kinematic inflow considerations alone. The blade flapping response also shows an increased "unsteadiness," i.e., aperiodicity, at lower thrust levels. At the highest thrust coefficient of $C_T = 0.012$, the blade flapping reaches a periodic form within five rotor revolutions after the beginning of pitching motion.

The oscillatory behavior of the rotor inflow and blade flapping response at low and moderate thrust levels is best understood by looking at the wake geometry during the

(a) Mean rotor induced inflow

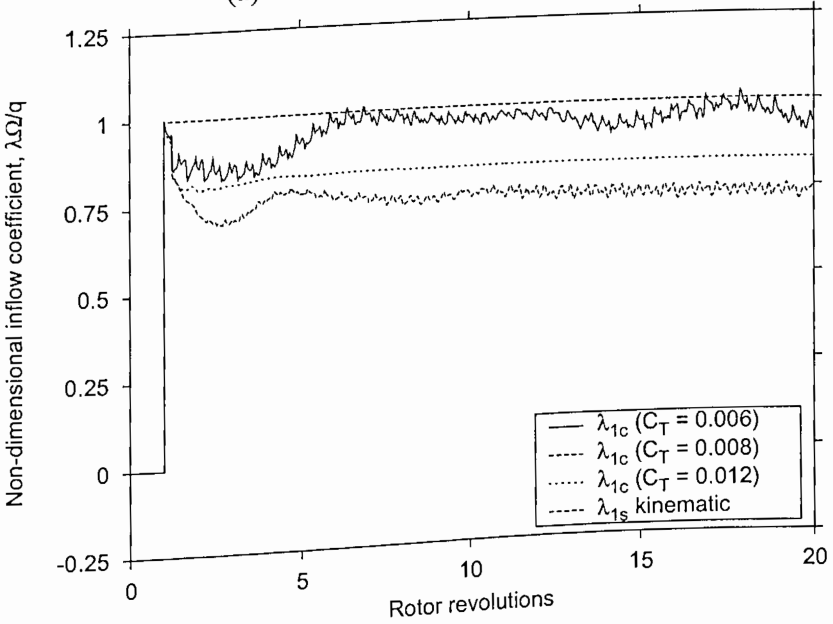

(b) Blade flapping response

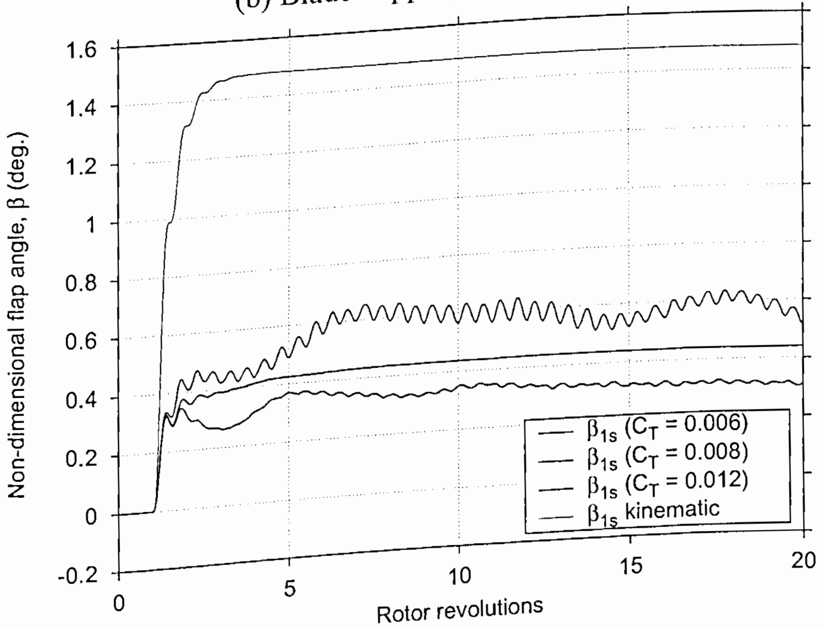

Figure 7.12: Induced inflow perturbations and the corresponding blade flapping response resulting from rotor angular rates for three different rotor thrusts. (a) Mean rotor induced inflow, (b) Blade flapping response.

maneuver. Figure 7.13 shows a sequence of wake geometries corresponding to a moderate thrust of $C_T = 0.008$ with a nose-up pitch rate of $\overline{q} = 0.012$. The geometry of the tip vortex filaments trailed from the four blades is shown at approximately 2, 4, 8, 10, 16 and 17 rotor revolutions after the beginning of the nose-up pitching maneuver. Figure 7.13(a) shows that after only two rotor revolutions, the wake geometry shows the so-called bending distortion. A disturbance in the wake structure is also apparent in the form of localized bundling of the wake vortices. After four rotor revolutions, as shown in Fig. 7.13(b), this disturbance grows as well as convects further downstream below the rotor. After about eight rotor revolutions, this localized disturbance moves significantly downstream and moves out of the computational domain. However, the wake structure develops wave-like disturbances along its length. Figures 7.13(d)–(f) show that these waves of alternating contraction and expansion convect downstream below the rotor in the form of a helical disturbance. This is qualitatively similarly to the behavior of the rotor following a oscillatory cyclic blade pitch excitation – see Fig. 6.29. This similarity is expected because the maneuver rates also result in a cyclic perturbation to the rotor induced velocity field similar to the cyclic blade pitch excitations.

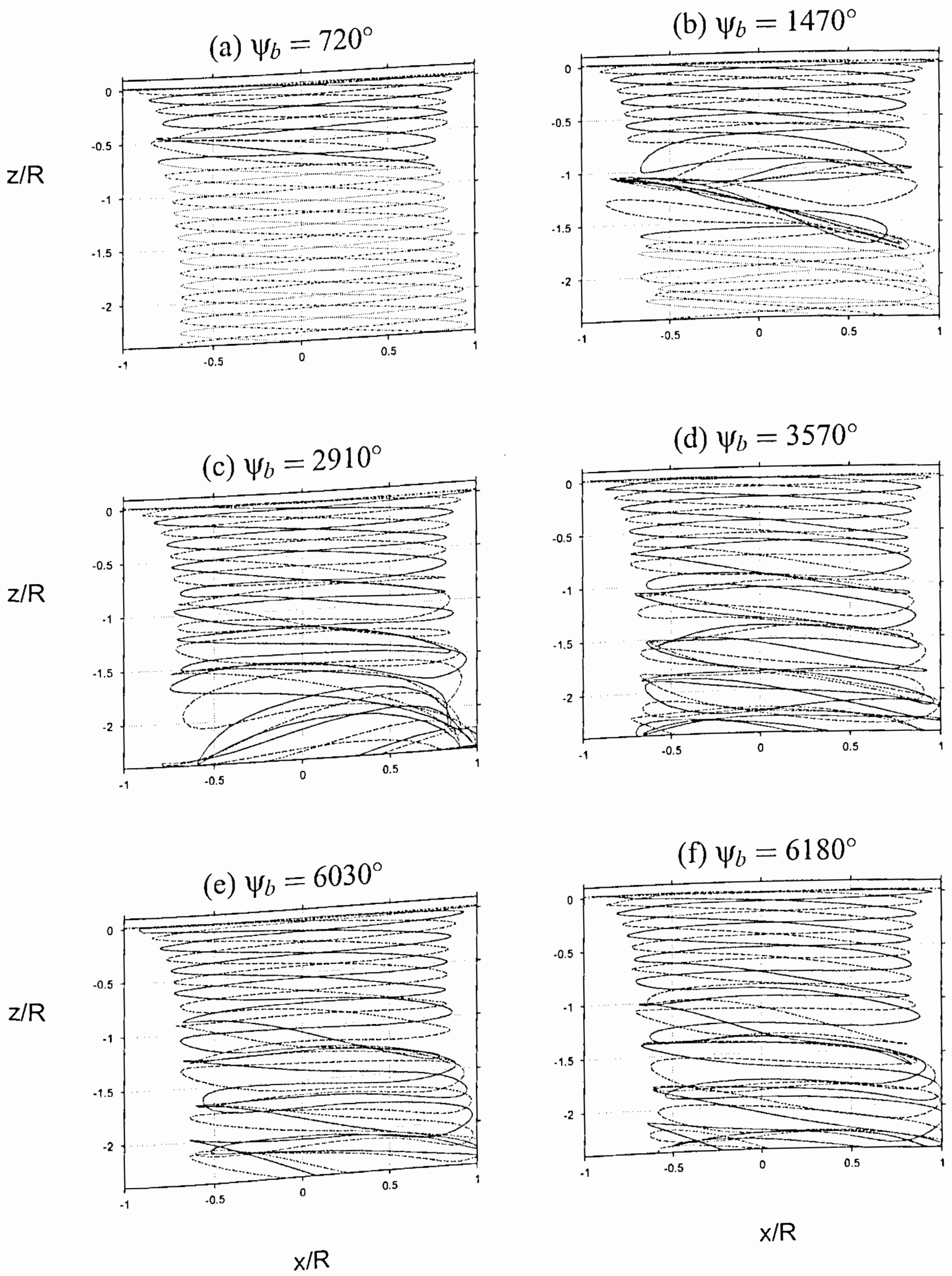

(a) $\psi_b = 720^\circ$

(b) $\psi_b = 1470^\circ$

(c) $\psi_b = 2910^\circ$

(d) $\psi_b = 3570^\circ$

(e) $\psi_b = 6030^\circ$

(f) $\psi_b = 6180^\circ$

Figure 7.13: Dynamic evolution of the tip vortices trailed from a four-bladed rotor following a nose-up pitch rate maneuver of $\overline{q} = 0.012$, $C_T = 0.008$. (a) $\psi_b = 720^\circ$, (b) $\psi_b = 1470^\circ$, (c) $\psi_b = 2910^\circ$, (d) $\psi_b = 2570^\circ$, (e) $\psi_b = 6030^\circ$, and (f) $\psi_b = 6180^\circ$.

Effects of Blade Flapping Frequency on Maneuver Induced Wake Distortion

Another factor that may influence the rotor response under maneuvering flight conditions is the blade flapping hinge offset. For articulated rotors, the hinge offset is typically small, of the order of 5% rotor radius. The baseline rotor configuration being examined here had a flapping hinge located at 6.54% radius. Modern hingeless rotors are much stiffer, have a higher equivalent flapping hinge offset. To examine the qualitative influence of the flapping hinge offset, the calculations were also performed with half and double the hinge offsets, i.e., with $e/R = 0.0327$ and $e/R = 0.1308$.

These results are shown in Fig. 7.14. The induced inflow perturbations for the smallest flapping hinge offset showed some degree "of unsteadiness" over the first ten rotor revolutions, as shown in Fig. 7.14(a). Thereafter, the inflow perturbation reached a constant value suggesting a periodic (steady-state) wake geometry. For higher hinge offsets, the non-dimensional inflow perturbations reached a steady-state value within five rotor revolutions. The steady-state value is found to be nearly independent of the hinge offset. Therefore, the relative wake distortion effects resulting from a maneuver are not strongly influenced by the hinge offset, beyond a certain value. For lower hinge offsets, the flapping frequency is nearly equal to unity. This would result in larger blade flapping angles, and in turn would affect the wake distortions. The blade-flapping angles, as shown in Fig. 7.14(b), suggest that the maneuver induced wake distortion effects are relatively mild for small hinge offsets. In this case, the rotor induced inflow perturbation is almost the same as those predicted based on kinematic considerations alone.

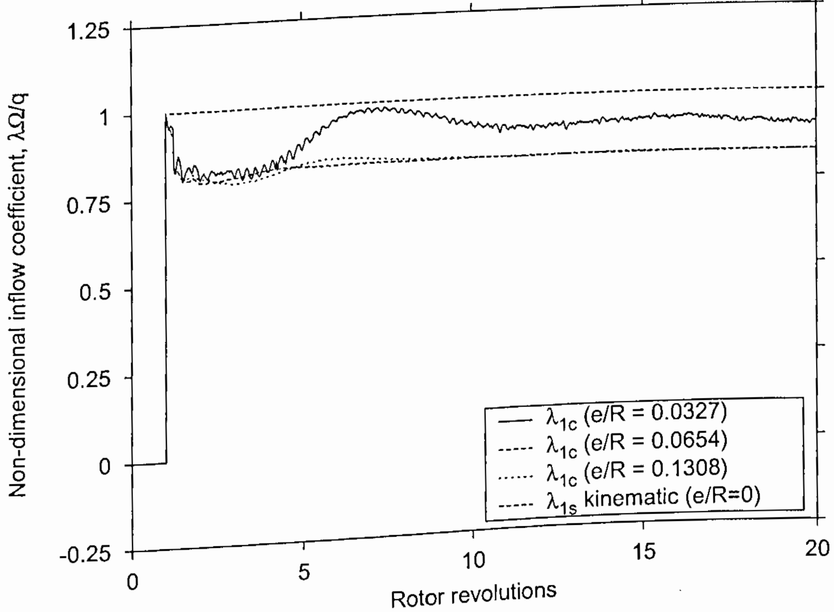
(a) Mean rotor induced inflow

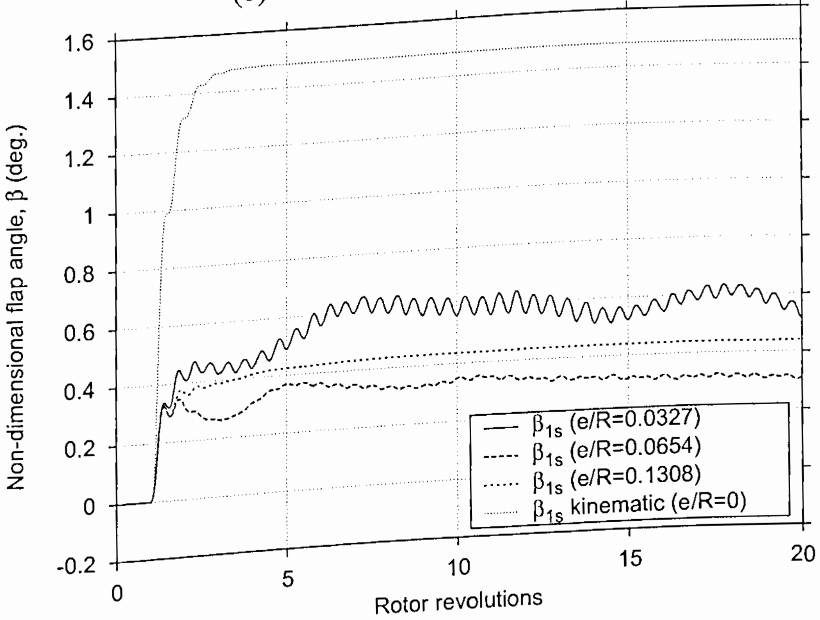
(b) Blade flapping response

Figure 7.14: Induced inflow perturbations and corresponding blade flapping response resulting from rotor angular rates for three different flapping hinge locations. (a) Mean rotor induced inflow, (b) Blade flapping response.

7.1.3 Wake Distortion Factor

The ratio of the wake induced inflow perturbation to the kinematic inflow perturbation is an important quantity for flight mechanics simulations. Keller & Curtiss (Ref. 106) introduced a K_R factor to represent the maneuver induced wake distortion effects on the inflow perturbations. This was termed as the "inflow gradient effect" because of the wake "curvature" and "stretching" distortions so produced. The K_R factor is defined as the ratio of inflow perturbations resulting from maneuver related wake distortions to that resulting from kinematics of the problem alone. To formalize this, the K_R factor can be written as

$$K_R = -\frac{\Delta K_{x_{\text{wake-induced}}}}{\Delta K_{x_{\text{kinematic}}}} = -\frac{\Delta K_{x_{\text{wake-induced}}}}{\overline{q}\lambda_0} \tag{7.10}$$

also,

$$K_R = -\frac{\Delta K_{y_{\text{wake-induced}}}}{-\overline{p}\lambda_0} \tag{7.11}$$

To examine the behavior of the K_R-factor, time-accurate free-vortex wake calculations were performed at three different thrust levels. Figure 7.15 shows the net inflow perturbations (i.e., the total of kinematic and maneuver induced wake distortion effects), as calculated by the free-vortex wake analysis, for increasing pitch rate, $\overline{q}$. The results are shown for three different rotor thrust coefficients of $C_T = 0.006, 0.008$ and 0.012. Figure 7.16 shows the corresponding blade flapping response.

At the lowest thrust value of $C_T = 0.006$, the non-dimensional inflow perturbations are nearly of the same magnitude. This suggests that a constant K_R factor may be used to "model" the maneuver induced wake distortion effects. However, at low thrust conditions, the rotor inflow as well as blade flapping response are highly unsteady and non-periodic. Such unsteady induced inflow and airloads are a result of close

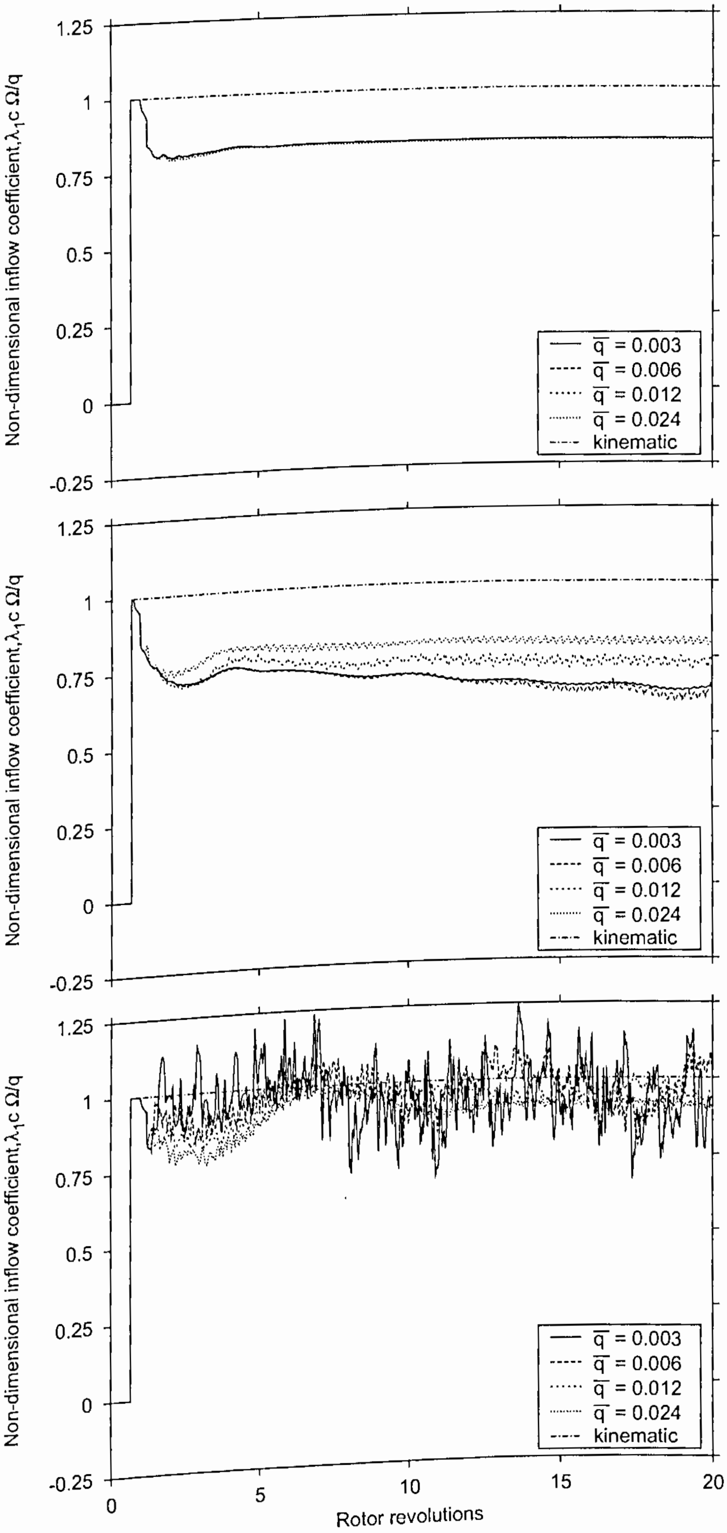

(a)

$C_T = 0.012$

(b)

$C_T = 0.008$

(c)

$C_T = 0.006$

Figure 7.15: Induced inflow perturbations with increasing pitch rate in hover, (a) $C_T = 0.012$, (b) $C_T = 0.008$, (c) $C_T = 0.006$.

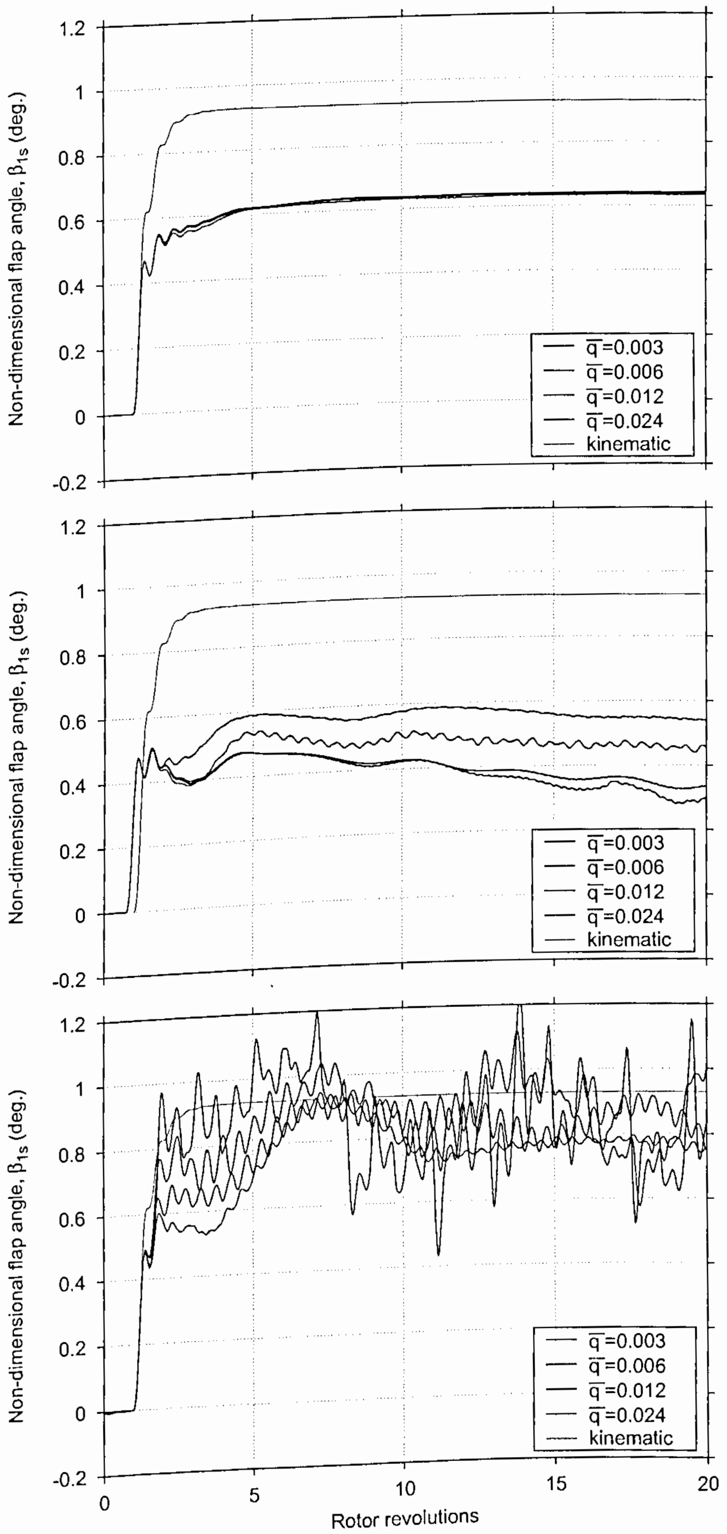

(a)

$C_T = 0.012$

(b)

$C_T = 0.008$

(c)

$C_T = 0.006$

Figure 7.16: Rotor blade flapping response with increasing pitch rate in hover, (a) $C_T = 0.012$, (b) $C_T = 0.008$, (c) $C_T = 0.006$.

interactions of the tip vortices with the following blade(s). Recall that a pitch rate about the hub causes a wake contraction at the rear of the rotor disk (see Fig. 7.2). For low values of rotor thrust, the axial wake displacements are small, and axial contraction would bring the tip vortex filaments very close to the rotor TPP resulting in BVI-like interactions – see Fig. 7.17. Note that even for the lowest pitch rate of $\overline{q} = 0.003$, the wake vortex filaments closely interact with the rotor blades resulting in strong induced velocity perturbations, and in turn, oscillatory blade airloads. At the highest pitch rate of $\overline{q} = 0.024$, the wake shows significantly larger distortions in the form of wake curvature. However, close to the TPP the vortex filaments show similar displacements as in the case of the smaller pitch rate. This is probably the reason why the (non-dimensional) inflow time-history shows oscillations of comparable magnitude.

Because such interactions occur only on the rear of the rotor disk, the rotor blades will experience N_b-per-revolution inflow perturbations. Therefore, a periodic or steady-state wake or inflow model (which includes only the first harmonics) may not be adequate to describe the rotor behavior correctly. To bring out this oscillatory nature of the induced velocity field, a contour plot of the induced velocity through the rotor disk is shown in Fig. 7.18. The overall rotor induced velocity field showed an essentially linear distribution, with a predominantly longitudinal gradient. However, small regions of high induced velocity can be seen at the front of the rotor disk – see the third and fourth quadrants of the rotor disk in Fig. 7.18. This is clearly a result of the close interactions between the rotor blades and tip vortices, and must be the cause of the oscillatory rotor response.

At an intermediate thrust of $C_T = 0.008$, the inflow perturbations are different for the smaller pitch rates. At higher pitch rates, however, the non-dimensional inflow perturbations are the same. At the highest thrust of $C_T = 0.012$, the time-histories for

(a) Pitch rate $\overline{q} = 0.003$

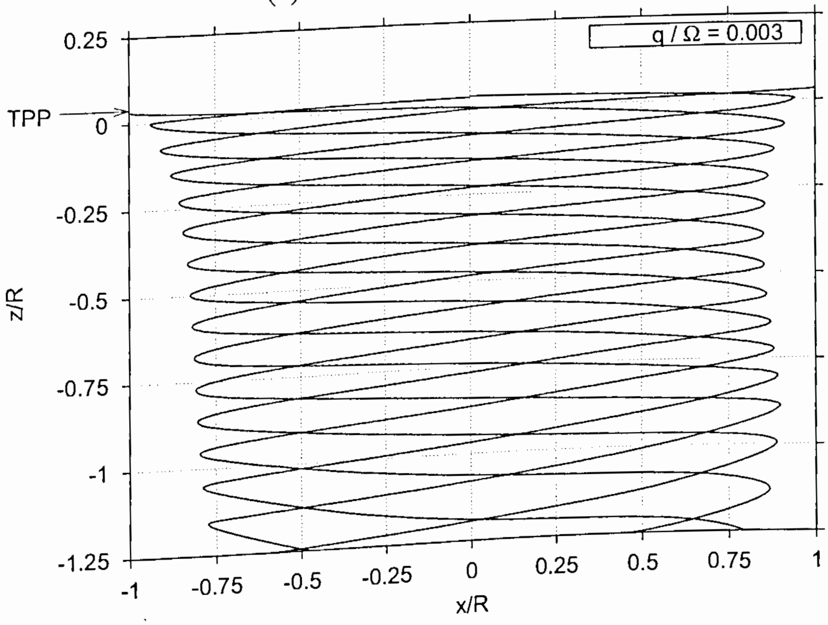

(b) Pitch rate $\overline{q} = 0.024$

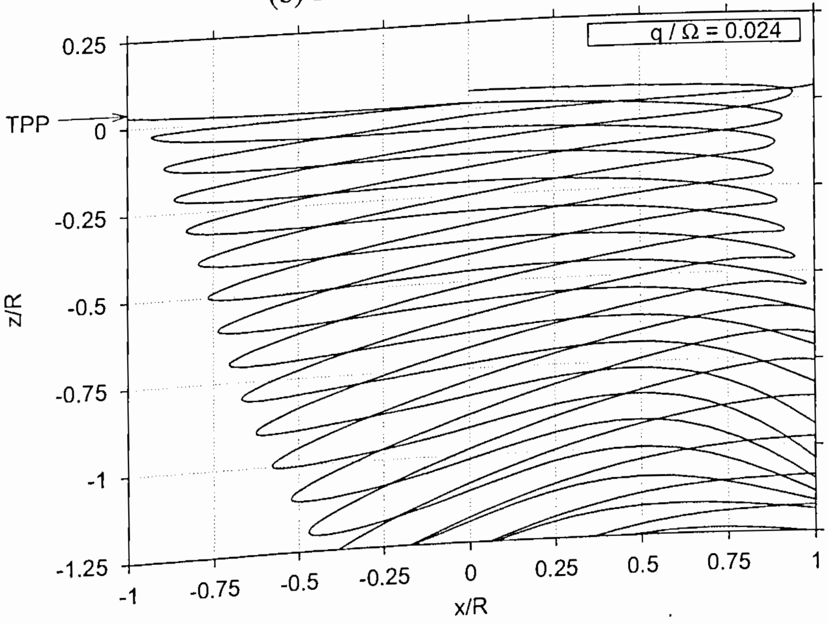

Figure 7.17: The wake distortions because of a nose-up pitch maneuver starting from hovering flight, $N_b = 4$, $C_T = 0.006$. (a) Pitch rate $\overline{q} = 0.003$, (b) Pitch rate $\overline{q} = 0.024$.

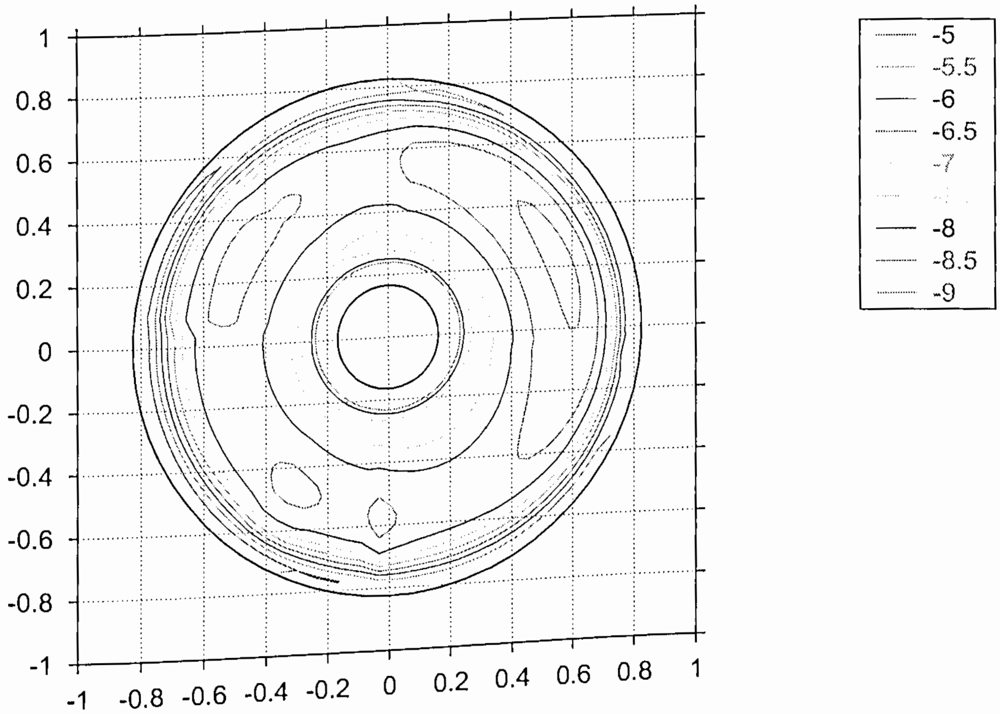

Figure 7.18: The rotor induced velocity field resulting from wake distortions during nose-up pitch maneuver starting from hovering flight, $N_b = 4$, $C_T = 0.006$, $\overline{q} = 0.024$.

different pitch rates coalesce onto a single curve when plotted in a non-dimensional form. The blade flapping response shows essentially the same trends as the inflow perturbations. Therefore, it is apparent that a constant K_R factor to represent wake maneuver induced distortion effects is suitable only for operating conditions at high thrust and/or high angular rates about the hub. For low and intermediate thrusts, such a simple model for wake distortion effects is not accurate, as evident from results shown in Figs. 7.15 and 7.16. It must also be noted that such a simplified model using a constant wake distortion factor is only possible in hovering flight where the rotor response to pitch and roll motions is essentially the same because of axisymmetry considerations. In forward flight, the rotor response may be significantly different in response to pitch and roll rate inputs. Some example calculations for a maneuvering rotor in forward flight will be shown in the next section.

The free-vortex wake results presented earlier are shown again in Fig. 7.19 in the form of this K_R factor. Figure 7.19(a) shows the effect of rotor thrust on K_R for increasing angular rates. Bagai *et al.* (Ref. 108) have shown that the blade twist may influence the K_R factor. Other operating parameters may also influence the maneuver related wake distortion effects. The influence of rotor thrust is apparent from Fig. 7.19(a), where the values for K_R are shown for three thrust coefficients. At a thrust of $C_T = 0.006$, the wake distortion effects were found to be small and increased with angular rate. As the thrust increases, the variations in K_R with angular rate are found to decrease, and at the highest thrust of $C_T = 0.012$, the K_R value is nearly independent of the angular rate.

Other results are shown in Fig. 7.19(b) for three flapping hinge offsets considered previously in Section 7.1.2. For the lowest hinge offset of $e/R = 0.0327$, the maneuver induced wake distortion effect was found to increase approximately linearly with increasing angular rate. However, for higher hinge offsets the wake distortion factor was found to be independent of the angular rates. These results suggest that a constant K_R factor is not a universal model for the wake distortion effects. Rather, a K_R factor depending on various operating conditions should be formulated empirically using free-vortex wake results, such as those presented here.

7.1.4 Imposed Pitch/Roll Rates in Forward Flight

In forward flight, the rotor wake structure is non-axisymmetric, with the tip vortices being closer to the TPP in the second and third quadrants of the rotor disk. The close proximity of the tip vortices to the TPP makes it difficult to idealize the inflow distri-

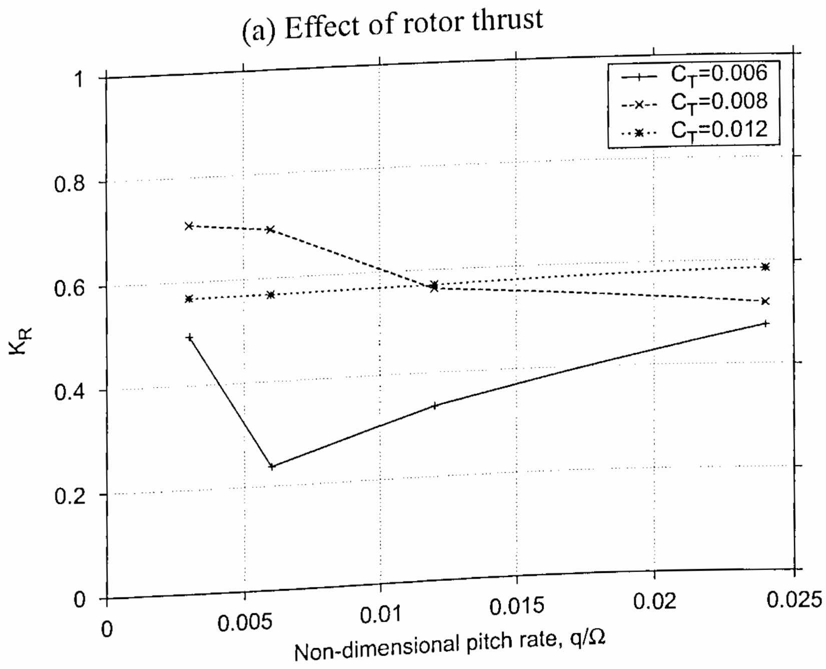

(a) Effect of rotor thrust

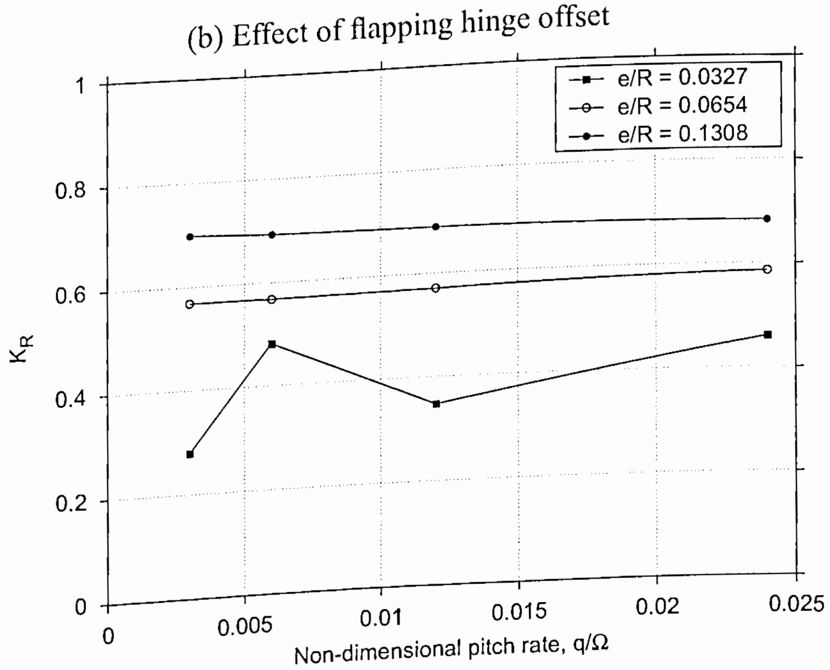

(b) Effect of flapping hinge offset

Figure 7.19: The effect of operating and geometric parameters on the K_R factor extracted from the time-accurate free wake results as a function of increasing pitch rate. (a) Effect of rotor thrust. (b) Effect of flapping hinge offset.

bution as a linear approximation (as shown previously in Section 5.2), and also to estimate the effects on blade flapping response. The effects of pitch and roll rates can be significantly different, unlike hovering flight where these are equivalent because of the axisymmetric nature of the wake. Furthermore, the effects of nose-up and nose-down pitch rates, or left/right roll rates, may not be symmetric because of the asymmetry of the baseline (non-maneuvering) rotor wake structure.

Effects of Maneuver Angular Rates in Forward Flight

Representive examples of the rotor wake geometry for an advance ratio of $\mu = 0.1$ are shown in Fig. 7.20(a) and (b) for nose-up and nose-down pitch rates, respectively. As with hovering flight, the imposed pitch rate causes a "curvature" of the wake geometry such that for a nose-up pitching motion, the tip vortices lie further away from the TPP at the front of the rotor disk. Similarly, at the rear of the rotor disk, the tip vortices lie further away from the TPP for a nose-up pitching motion. The opposite curvature effect was found for a nose-down pitch rate, with the tip vortices closely intersecting the TPP at the front of the rotor disk, as shown by Fig. 7.20(b).

This wake curvature effect is better illustrated in Fig. 7.21, where the vertical displacements of the tip vortices in a plane passing through the longitudinal centerline of the rotor are plotted for increasing vortex age. Note from Fig. 7.21(a) that at the front of the rotor disk with no imposed angular pitch rate, the tip vortices convect only slightly above the TPP. After the first blade passage, which corresponds to $\zeta = 90°$, the vortices convect just below the TPP. During the maneuver with a nose-down pitch rate, the vortices move significantly above the TPP, as mentioned previously. After the first three blade passages, at $\zeta = 90°$, $180°$ and $270°$ respectively, the tip vortices experience vertically downward velocity perturbations when they are finally convected down through the TPP. The effect of a nose-up pitch rate is to move the tip vortices further away from the TPP.

At the rear of the rotor disk, as shown in Fig. 7.21(b), the tip vortices lie much further below the TPP, and the effects of blade passages are not noticeable. In this case, a nose-up pitch rate moves the tip vortices closer to the TPP, while a nose-down pitch rate moves them further away from the TPP. These effects suggest that the primary effects of maneuver induced wake distortion on the rotor induced inflow would be similar to those found in hover, i.e., a pitch-up motion results in a positive longitudinal inflow gradient and a negative value of ΔK_x. Note that this effect is again in the opposite sense to that of the kinematic inflow gradient, as shown in the previous section for rotors operating in hovering flight.

The primary wake distortion produced by a roll rate is in the lateral direction, although some longitudinal wake distortion is also produced. The wake geometry resulting from imposed angular rates at an advance ratio of $\mu = 0.1$ is shown in Fig. 7.22 for both a positive roll rate (roll left) and a negative roll rate (roll right). Note that even in the absence of any imposed roll rate, the wake geometry shows some lateral distortion with the tip vortices being closer to the TPP on the retreating side. However, this baseline lateral distortion is much smaller than the longitudinal distortion as shown earlier in the results of Fig. 7.20. The effect of an imposed roll rate is a curvature of the wake geometry in the lateral direction; for a left roll the tip vortices lie closer to the TPP on the retreating side, and further away from the TPP on the advancing side. The wake curvature effects induced because of a right roll are essentially opposite to those for a left roll.

Figure 7.23 shows the wake curvature effects of imposed roll rate in terms of the tip vortex displacements in a lateral plane as a function of vortex age. Note that for the

(a) Nose-up pitch rate, $\overline{q} = +0.012$

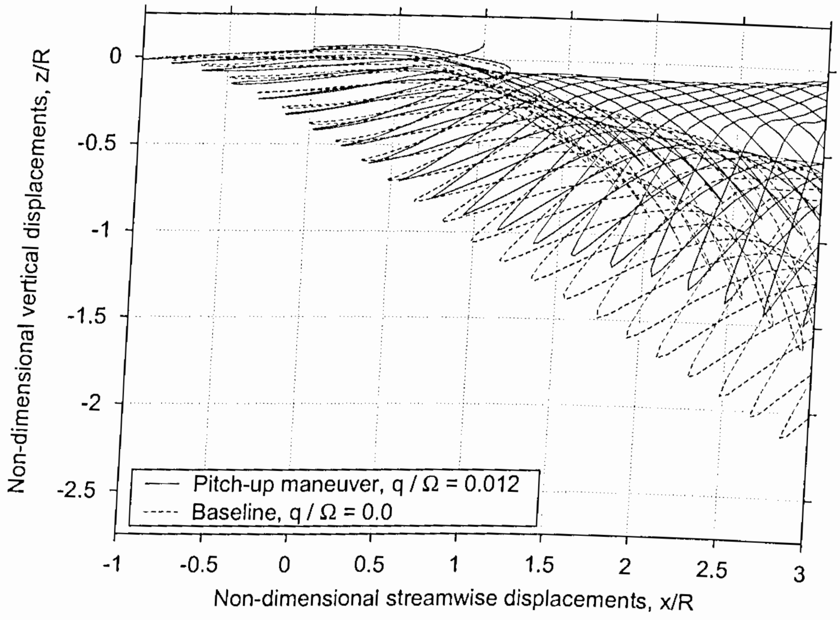

(b) Nose-down pitch rate, $\overline{q} = -0.012$

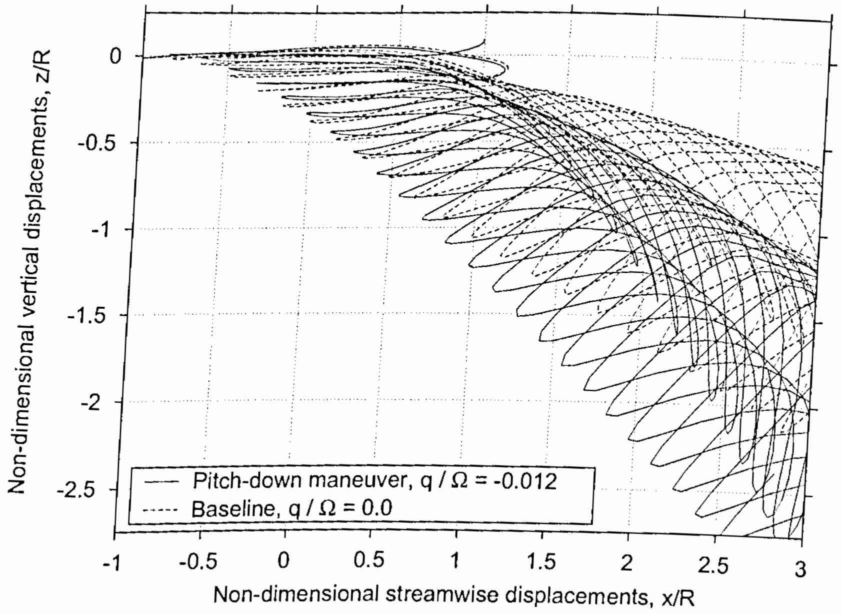

Figure 7.20: Effects of pitch rate on rotor wake geometry for a four-bladed rotor in forward flight at $\mu = 0.1$. (a) Nose-up pitch rate, $\overline{q} = 0.012$. (b) Nose-down pitch rate, $\overline{q} = -0.012$.

(a) Front of the rotor disk

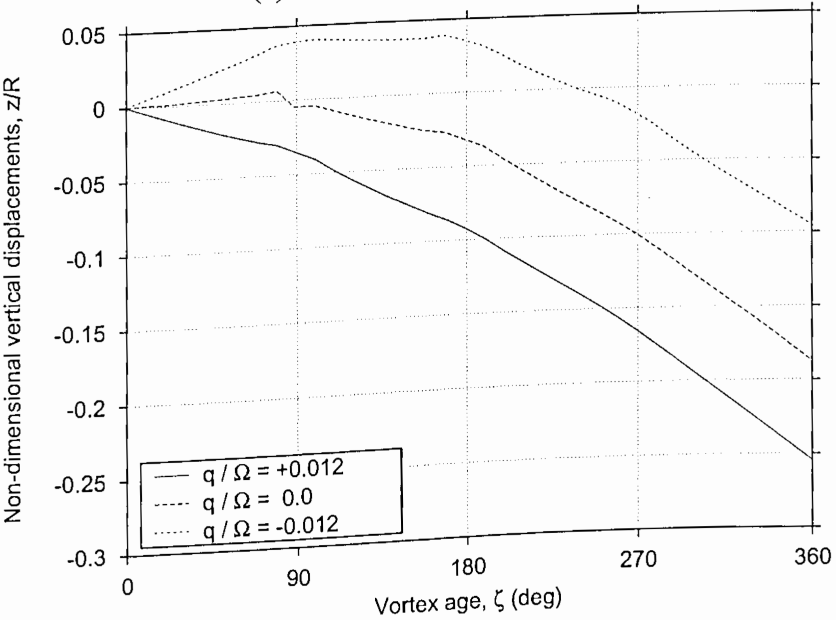

(b) Rear of the rotor disk

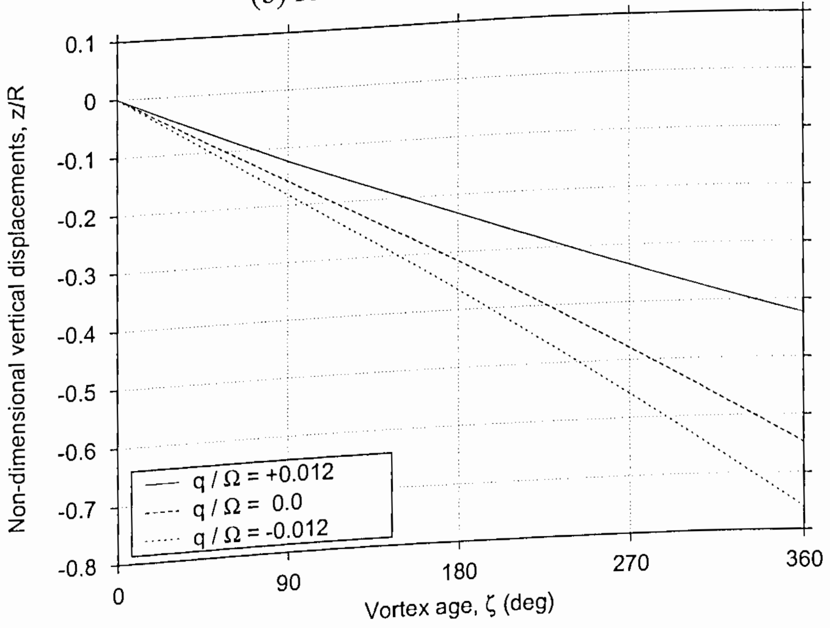

Figure 7.21: Effects of pitch rate on tip vortex vertical displacements for a four-bladed rotor in forward flight at $\mu = 0.1$. (a) Front of the rotor disk. (b) Rear of the rotor disk

baseline case with no imposed roll maneuver rates, the tip vortex displacements show a small lateral distortion with the tip vortices lying closer to TPP on the advancing side. As shown in Fig. 7.23(a), on the advancing side the tip vortices closely intersect the TPP under the effects of an imposed right roll. At each blade passage, the tip vortices experience a downward perturbation, and eventually convect below the TPP. On the retreating side the opposite effect is seen, with the tip vortices being closer to the TPP for an imposed left roll (positive roll rate), as shown in Fig. 7.23(b).

The effects of these maneuver related wake distortions resulting from an imposed pitch rate on the rotor induced inflow and the flapping response is shown in Fig. 7.24. As described previously, the kinematic effect of an imposed pitching motion is a negative longitudinal inflow gradient perturbation, ΔK_x. Recall from the results shown in Fig. 5.13 that for a rotor in forward flight at $\mu = 0.1$, there is a longitudinal inflow gradient, K_x, even in the absence of any imposed maneuver rates. Therefore, to understand the effects of the maneuver alone, the results are presented as a perturbation to the baseline inflow gradient, i.e.,

$$\Delta K_x = K_{x_{\text{maneuver}}} - K_{x_{\text{baseline}}} \tag{7.12}$$

Similarly, the blade flapping angles are presented as perturbations from the baseline flapping angles found with no maneuver rates.

Figure 7.24 shows the inflow gradient perturbations as a function of pitch rate. Note that only kinematic considerations give a negative longitudinal (on-axis) inflow gradient because of a positive pitch rate. The effects of maneuver induced wake distortion are opposite to this kinematic effect, as mentioned previously. Therefore, the combined effect of the wake and kinematics is a slightly lower inflow gradient perturbation, as shown in Fig. 7.24(a). For the present flight condition at an advance ratio of $\mu = 0.1$, the effect of wake distortion on the on-axis inflow gradient appears to be

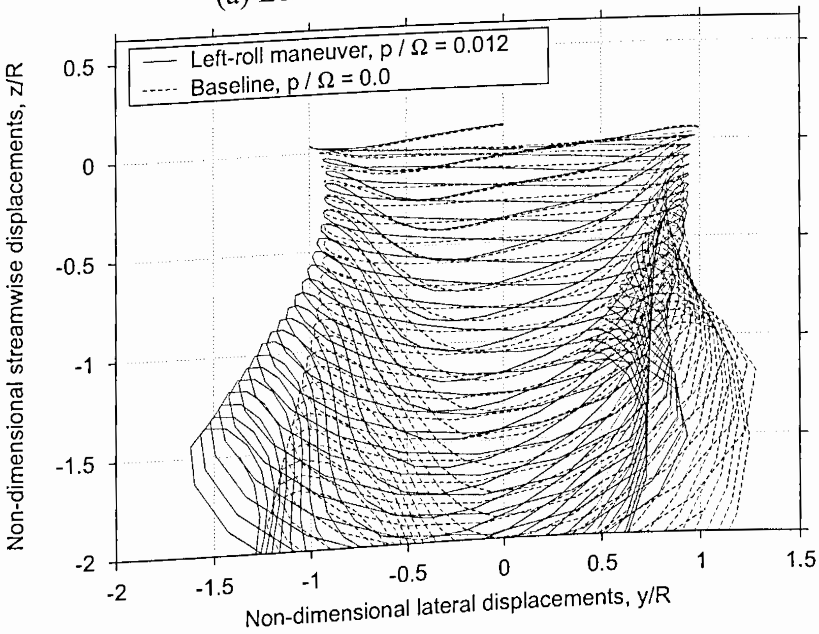
(a) Left roll rate, $\overline{p} = +0.012$

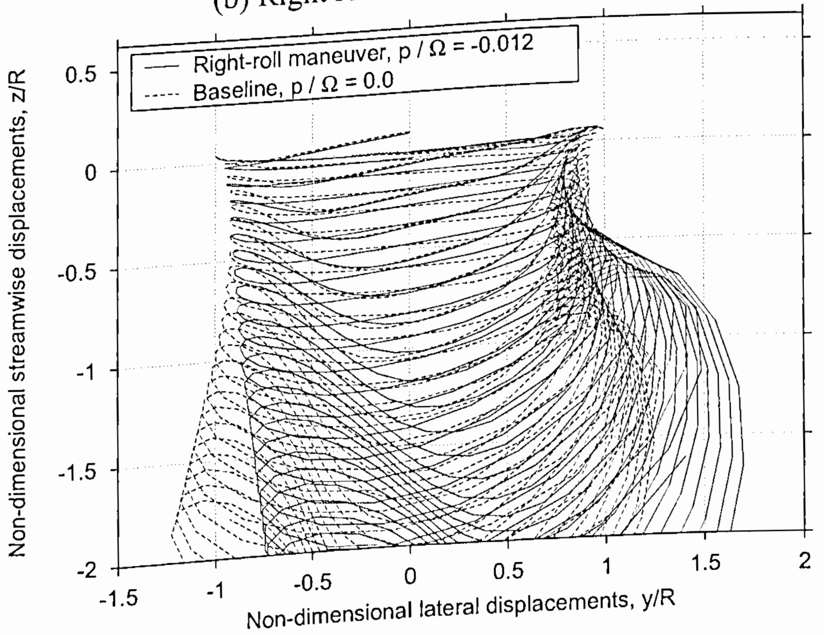
(b) Right roll rate, $\overline{p} = -0.012$

Figure 7.22: Effects of roll rate on rotor wake geometry for a four-bladed rotor in forward flight at $\mu = 0.1$. (a) Left roll rate, $\overline{p} = 0.012$, (b) Right roll rate, $\overline{p} = -0.012$.

(a) Advancing side

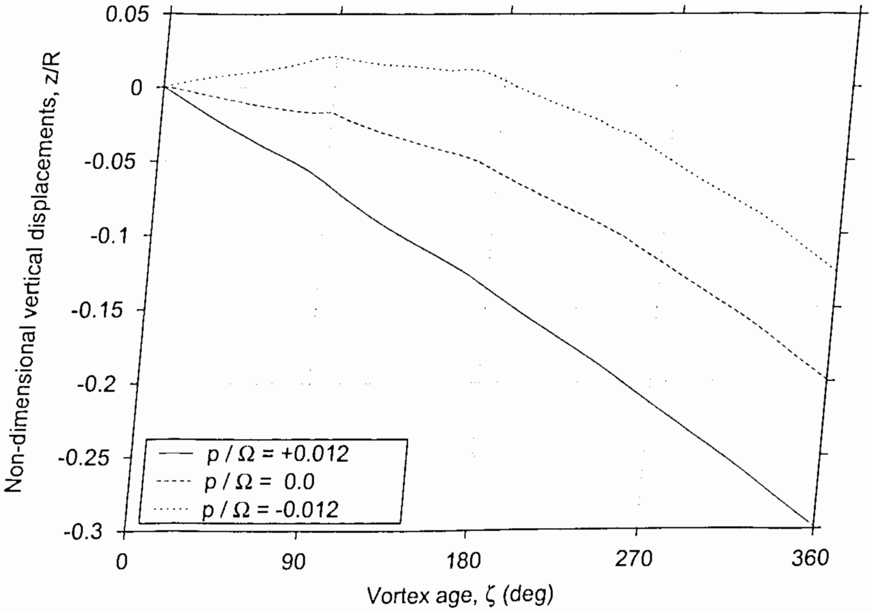

(b) Retreating side

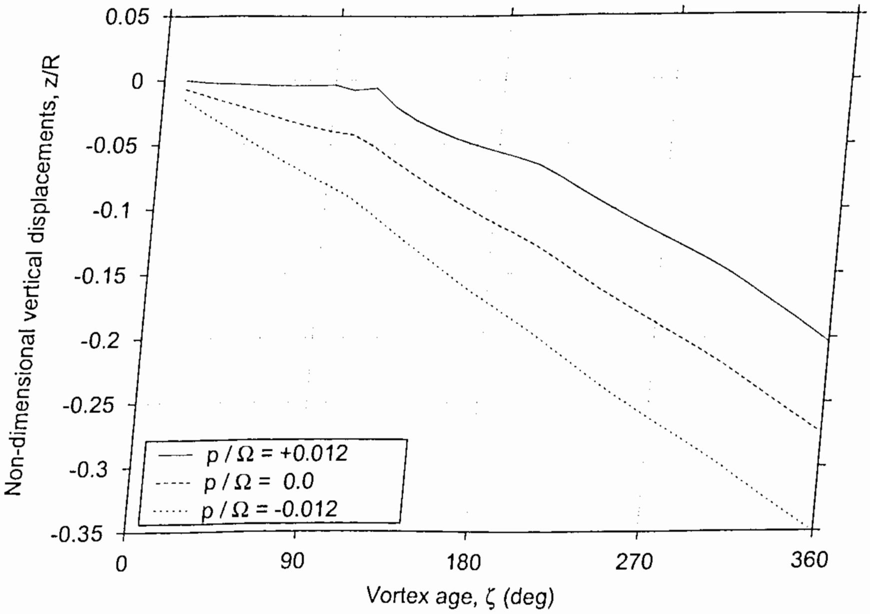

Figure 7.23: Effects of roll rate on tip vortex vertical displacements for a four-bladed rotor in forward flight at $\mu = 0.1$. (a) Advancing side, and (b) Retreating side.

small. However, the wake distortion also produced a lateral (off-axis) inflow gradient perturbation, ΔK_y, which is not expected based on kinematic considerations alone. It is also interesting to note that the wake induced inflow gradients are not symmetric with positive and negative imposed pitch rates. This suggests that in forward flight, the maneuver related wake distortion effects may not be completely modeled using a simple (linear) correction to the kinematic inflow perturbation.

The off-axis blade flapping response calculated by time-integration of the flapping equations is shown in Fig. 7.24(b), along with estimated periodic blade flapping based on inflow gradient perturbations. Because the effect of maneuver induced wake distortion on the on-axis inflow gradient perturbation was found to be small, the estimated off-axis blade flapping response was also found to be small. Note that the estimated flapping response is slightly smaller than the time-integration results. This is because of the approximations involved in the periodic flapping estimates given in Eqs. 7.7–7.9. Nevertheless the estimated flapping response gave good predictions of the trends.

As mentioned earlier, an imposed pitch rate also resulted in lateral inflow gradient perturbations. The off-axis inflow gradient would result in an on-axis (longitudinal) flapping response. This effect is shown in Fig. 7.25, along with the coning angle perturbations. Note that kinematic considerations alone predict no on-axis flapping response. The estimated flapping response based on linear inflow perturbations significantly underpredicts the on-axis blade flapping. This suggests that under such maneuvering flight conditions, a simple linear inflow representation is unsuitable to model the rotor induced velocity field and a non-linear inflow model, like the present free-vortex wake model, would be necessary to completely resolve the maneuver-related effects on the rotor inflow and blade flapping response.

Results for the linear inflow perturbations resulting from an imposed roll rate are

(a) Induced inflow perturbations

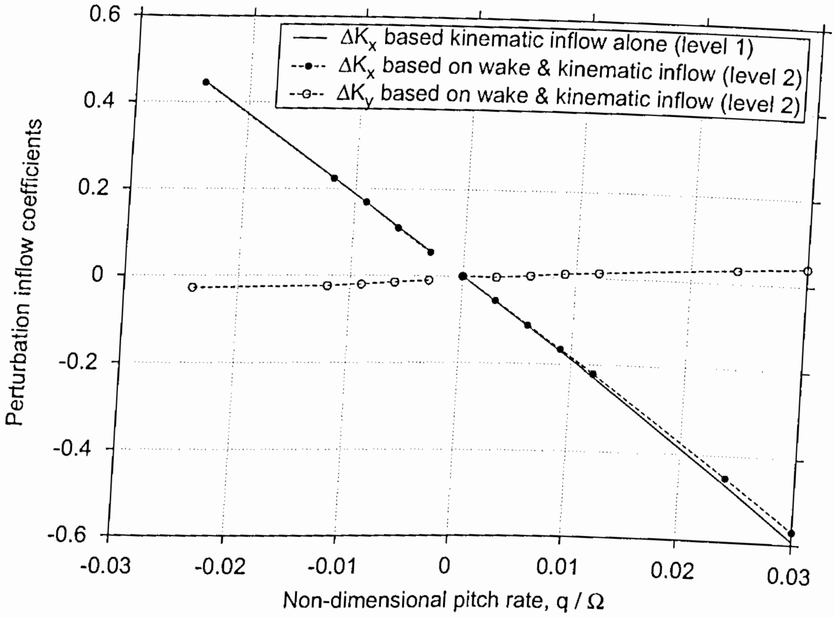

(b) Blade flapping response

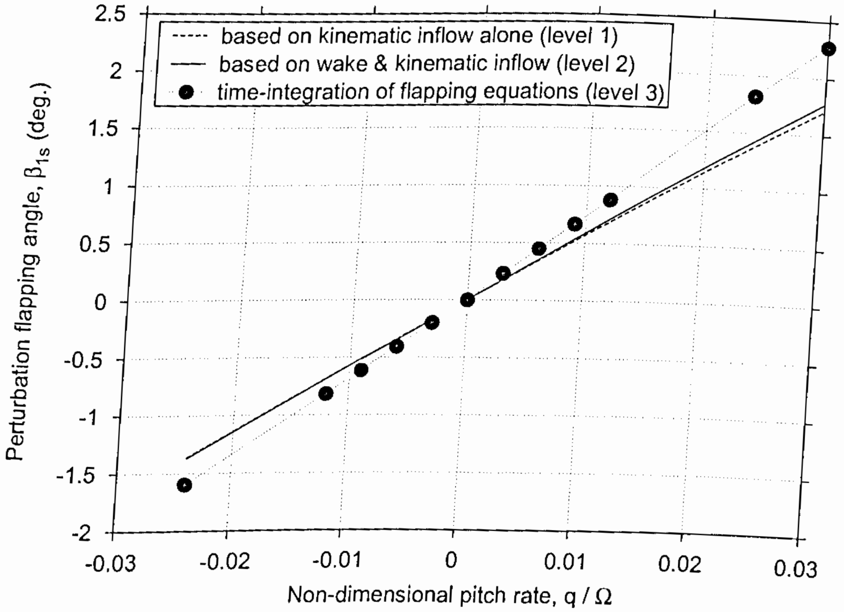

Figure 7.24: Induced inflow perturbations and corresponding blade flapping response resulting from imposed pitch rate on a four bladed rotor in forward flight at $\mu = 0.1$. (a) Induced inflow perturbations. (b) Blade flapping response.

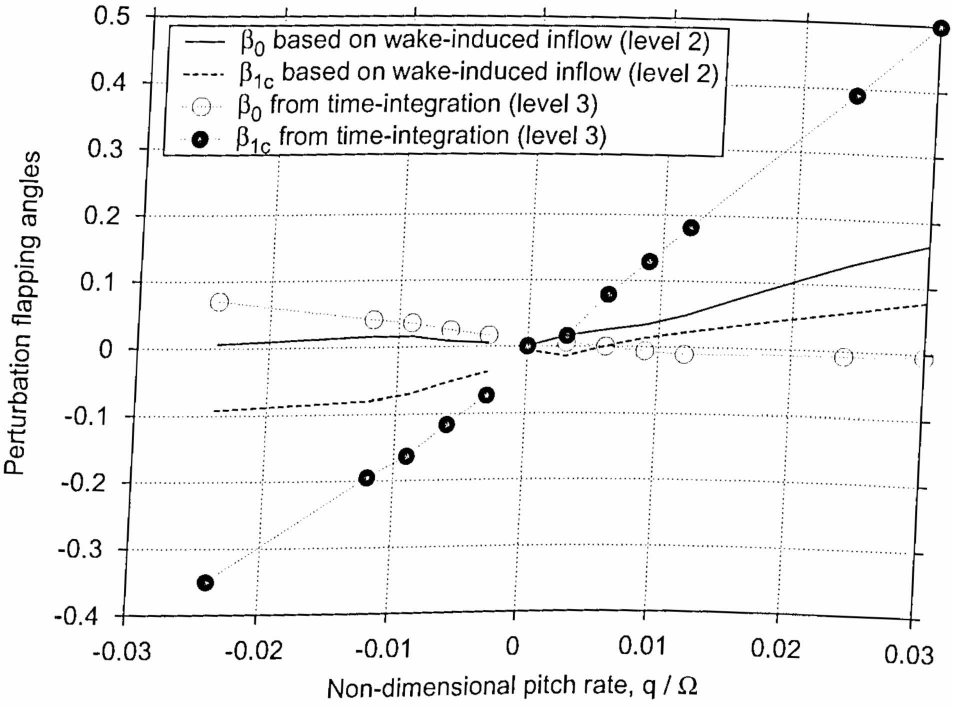

Figure 7.25: The on-axis flapping response resulting from a imposed pitch rate for a four-bladed rotor in forward flight at $\mu = 0.1$.

shown in Fig. 7.26. In this case, kinematic considerations suggest that a positive roll rate leads to a positive lateral inflow perturbation as shown in Fig. 7.26(a). The effects of maneuver induced wake distortion are in an opposite direction (negative lateral inflow perturbation) and, therefore, the total inflow gradient perturbation is smaller than that because of kinematic considerations alone. Because the lateral inflow gradient is small for the baseline non-maneuvering condition (without any imposed roll rate), the maneuver related wake distortion effects vary more of less linearly with the roll rate. The off-axis blade flapping response resulting from the imposed roll rate calculated by time-integration of the blade flapping equations coupled with the wake solution is shown in Fig. 7.26(b). The estimated flapping response based on linear (on-axis) inflow perturbations is also shown for comparison. It can be seen that a linear inflow perturbation based on kinematics alone overpredicts the blade flapping response. Inclusion of the wake-induced effects in the linear inflow gradients gives a better estimate of the blade flapping response.

The behavior described above is essentially similar to that observed in hovering flight, as shown previously in Fig. 7.7. This suggests a simple representation of the maneuver induced wake distortion effects using a wake distortion factor, K_R (see Section 7.1.3, Eqs. 7.10 and 7.11), may be useful to estimate the relative effects of wake distortion on the on-axis inflow gradient perturbation. Note that the wake distortion factor resulting from pitch and roll rates are different in forward flight. Therefore, it is convenient to define two different wake distortion factors K_{R_x} and K_{R_y} corresponding to the effects of pitch and roll angular rates, i.e.,

$$\begin{aligned} K_{R_x} &= -\frac{\Delta K_{x_{\text{wake-induced}}}}{\Delta K_{x_{\text{kinematic}}}} \\ \text{for imposed pitch rate,} \qquad K_{R_x} &= -\frac{\Delta K_{x_{\text{wake-induced}}}}{\bar{q}\lambda_0} \end{aligned} \tag{7.13}$$

$$\begin{aligned} K_{R_y} &= -\frac{\Delta K_{y_{\text{wake-induced}}}}{\Delta K_{y_{\text{kinematic}}}} \\ \text{for imposed roll rate,} \qquad K_{R_y} &= -\frac{\Delta K_{y_{\text{wake-induced}}}}{-\bar{p}\lambda_0} \end{aligned} \tag{7.14}$$

The results for these two wake distortion factors are shown in Fig. 7.27. As mentioned earlier, an imposed pitch rate resulted in very small wake distortion effects on the linear inflow gradients. Therefore, the wake distortion factor K_R has a very small value. The imposed roll rate however showed a significant wake distortion effects on the inflow gradients, as also shown by the larger value of the K_{R_y} factor given in Fig. 7.27.

Similar to the imposed pitch rate, an imposed roll rate also resulted in an off-axis inflow perturbation, i.e., a longitudinal inflow gradient. This also resulted in on-axis

(a) Induced inflow perturbations

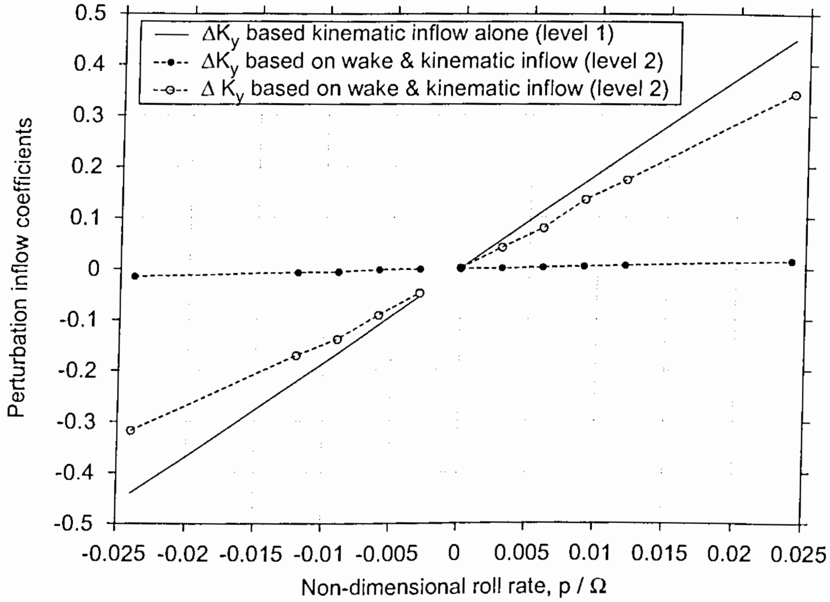

(b) Blade flapping response

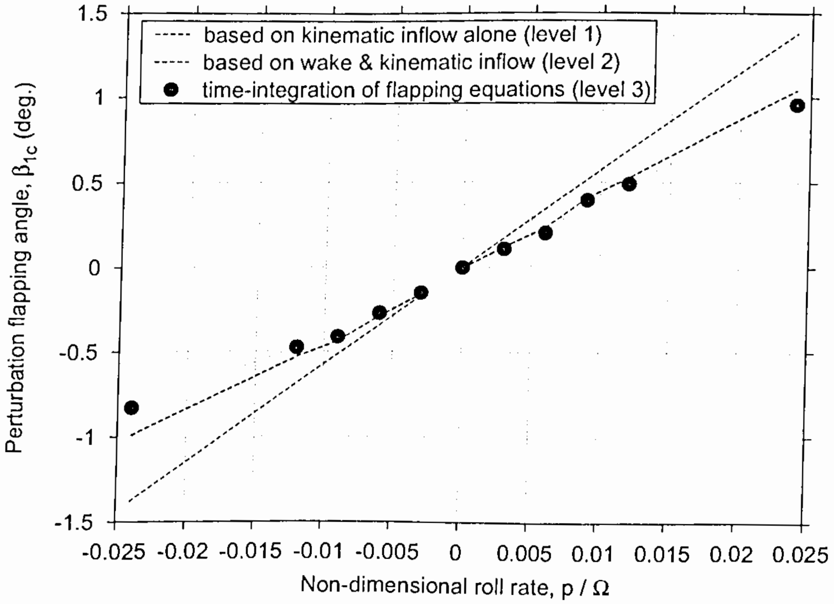

Figure 7.26: Induced inflow perturbations and corresponding blade flapping response resulting from imposed roll rate on a four bladed rotor in forward flight at $\mu = 0.1$. (a) Induced inflow perturbations. (b) Blade flapping response.

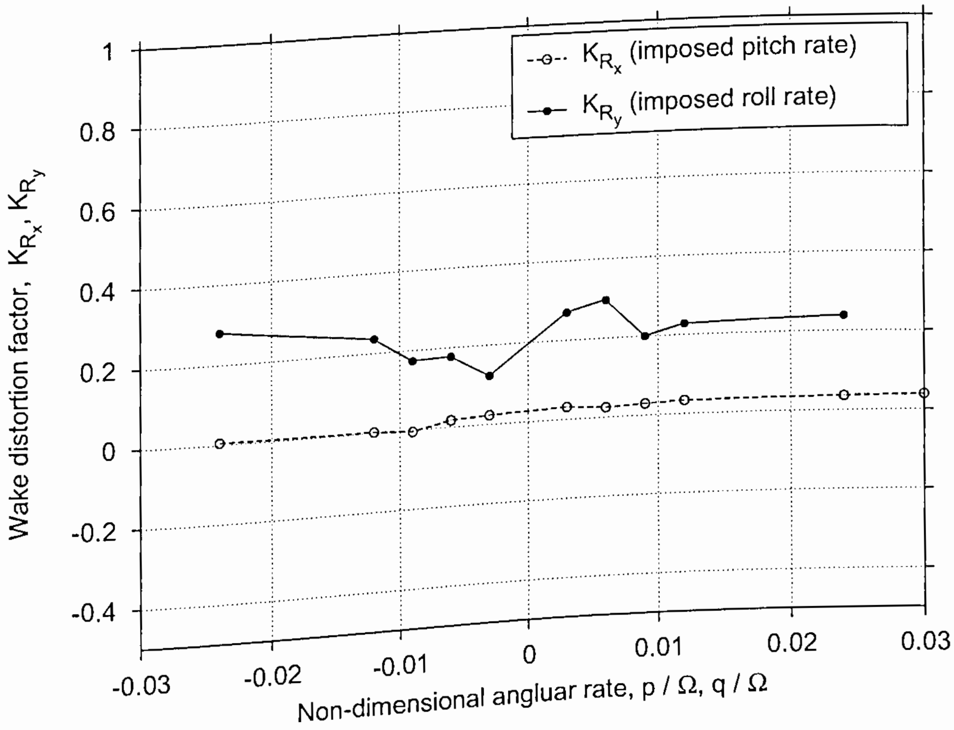

Figure 7.27: The K_{R_x} and K_{R_y} factors extracted from the time-accurate free wake results for a four-bladed rotor in forward flight at $\mu = 0.1$ with imposed pitch and roll rates, respectively.

(lateral) blade flapping response. These results are shown in Fig. 7.28. Note that kinematic considerations suggest no such on-axis flapping response. The inflow gradients derived by including the maneuver induced wake distortion effects in the free-vortex wake calculations, showed an off-axis inflow gradient perturbation. The flapping response based on these gradients, however, is lower than the blade flapping calculated by time-integration. This again suggests that a simple linear inflow model may not be satisfactory to fully represent maneuver related effects on the rotor response, and a complete solution with a free-vortex wake model may be necessary under many flight conditions.

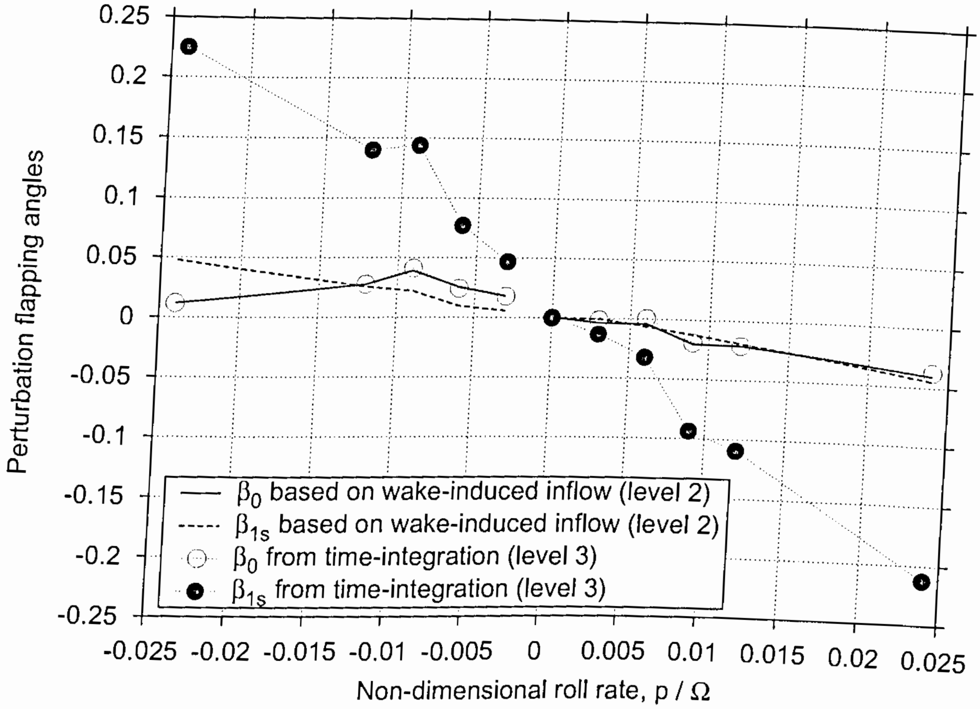

Figure 7.28: On-axis flapping response resulting from a imposed roll rate for a four-bladed rotor in forward flight at $\mu = 0.1$.

Effect of Advance Ratio on Wake Distortions During Pitching Motion

The relative effects of maneuver induced wake distortion on the induced inflow distribution were found to be greater in hovering flight than in forward flight at an advance ratio of 0.1. As mentioned previously, the main reason for these differences lies in the fact that the wake geometry is significantly non-axisymmetric in forward flight. In particular, the displacements of the tip vortices relative to the TPP are different at the front and the rear of the rotor disk. This results in a strong longitudinal inflow gradient with high downwash over the rear of the rotor disk, and a reduced downwash (possibly an upwash) at the front of the rotor disk. This implies that the vortex induced velocities at the rotor blades are not linear. Recall from Fig. 7.24 that the effects of positive and negative imposed pitching motion were not axisymmetric. Therefore, the effects of maneuver rates may not be considered as a superposition of various linearized inflow gradients. It would appear that the relative effects of the maneuver related wake distortions would also be different for different advance ratios.

Figure 7.29(a) shows the on-axis (longitudinal) inflow gradient perturbations resulting from a positive (nose-up) pitching motion as a function of increasing advance ratio. The kinematic inflow gradient shows a negative perturbation for positive pitching rate. The kinematic inflow perturbation slowly increases in magnitude because of the slow decrease in mean rotor induced inflow with increasing advance ratio. At low advance ratios, including hover, the effect of maneuver induced wake distortion on the inflow perturbation is, in a sense, opposite to the kinematic effects. At approximately an advance ratio of $\mu = 0.1$, the trend reverses and the wake distortion results in an inflow gradient perturbation in the same sense as the kinematic inflow perturbation. Therefore, the net inflow gradient perturbation experienced by the rotor is increased at advance ratios of $\mu \geq 0.1$

The corresponding blade flapping response resulting from imposed pitch rate is shown in Fig. 7.29(b). The off-axis flapping response based on kinematic inflow gradients alone is almost constant with advance ratio. The solution obtained by time-integration of the blade flapping equations showed significant differences from this trend. At low advance ratios, including hover, the blade flapping is smaller than that expected based on kinematic considerations. This is because the wake distortion because of the imposed pitch rate produces on-axis inflow gradients, which are opposite to the kinematic inflow gradient perturbations. At higher advance ratios, however, the wake distortion effects produce inflow gradients similar in magnitude to the kinematic gradients, thereby resulting in a higher off-axis blade flapping response. Clearly, the wake induced effects on the linear inflow perturbations must be included to get a better estimate of the blade flapping response.

In hovering flight, the effects of nose-down pitching motion were found to be symmetrically equivalent to the corresponding effects of nose-down pitching motion. In forward flight, where the wake is non-axisymmetric, this may not be the case. Figure 7.30 shows the longitudinal inflow gradients obtained from the free-vortex wake calculations for both positive (nose-up) and negative (nose-down) pitch rates in forward flight. The baseline (non-maneuvering) case is also shown to emphasize the basic longitudinal inflow gradient resulting from non-axisymmetry of the wake in forward flight. A nose-up pitching motion further increases the longitudinal inflow gradient, while a nose-down pitching decreases the gradient. The perturbations relative to the baseline case, however, are not symmetric.

The perturbation inflow gradients as described in Eq. 7.12 are shown in Fig. 7.31 for increasing advance ratio. The inflow perturbations based on kinematic considerations alone are also shown for comparison. Notice that although the kinematic effects result in symmetric inflow perturbation with respect to pitch rate, the maneuver related wake distortion effects are significantly asymmetric. The wake distortion effects are much stronger for a nose-down pitching motion as compared to a nose-up pitching motion. This suggests that the rotor response to imposed angular rates in forward flight is highly non-linear, probably because of the high baseline longitudinal inflow gradients even in the absence of any maneuvering conditions. Recall from Fig. 5.13 in Section 5.2, that the longitudinal inflow gradient reaches an almost constant value at high advance ratios. A pitch-up motion under such high-speed flight does not result in additional inflow perturbations resulting from wake distortions. The inflow gradient perturbations are essentially the same as those because of kinematic considerations. A

(a) Induced inflow perturbations

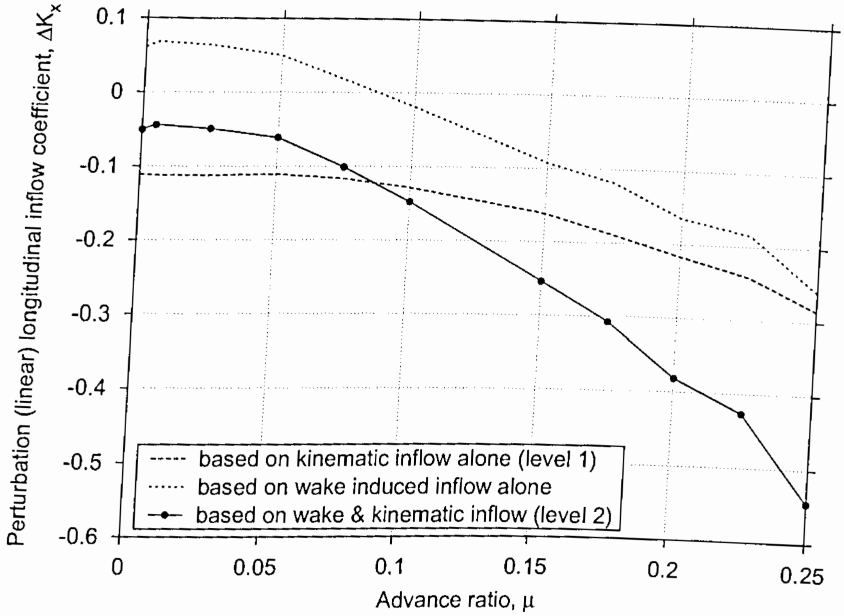

(b) Blade flapping response

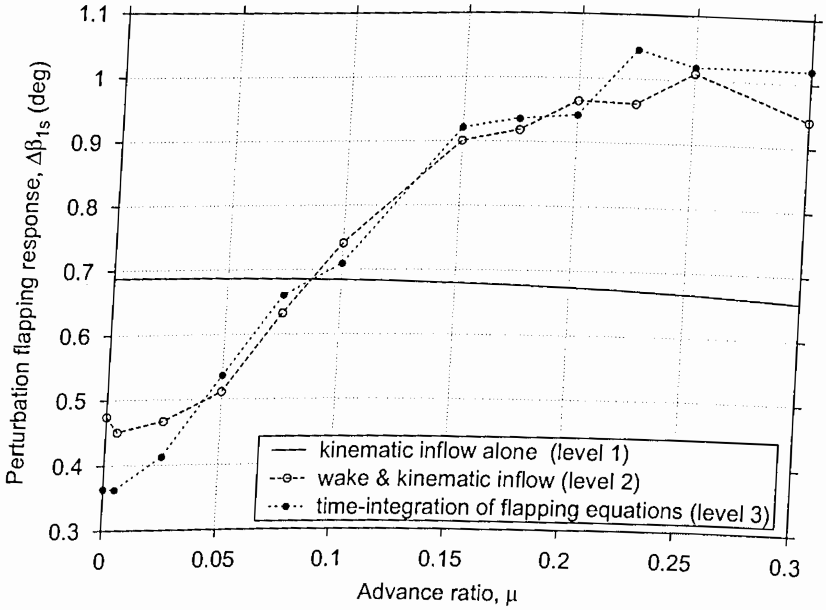

Figure 7.29: Induced inflow perturbations and corresponding blade flapping response resulting from imposed pitch rates on a four bladed rotor as a function of advance ratio. (a) Induced inflow perturbations, (b) Blade flapping response.

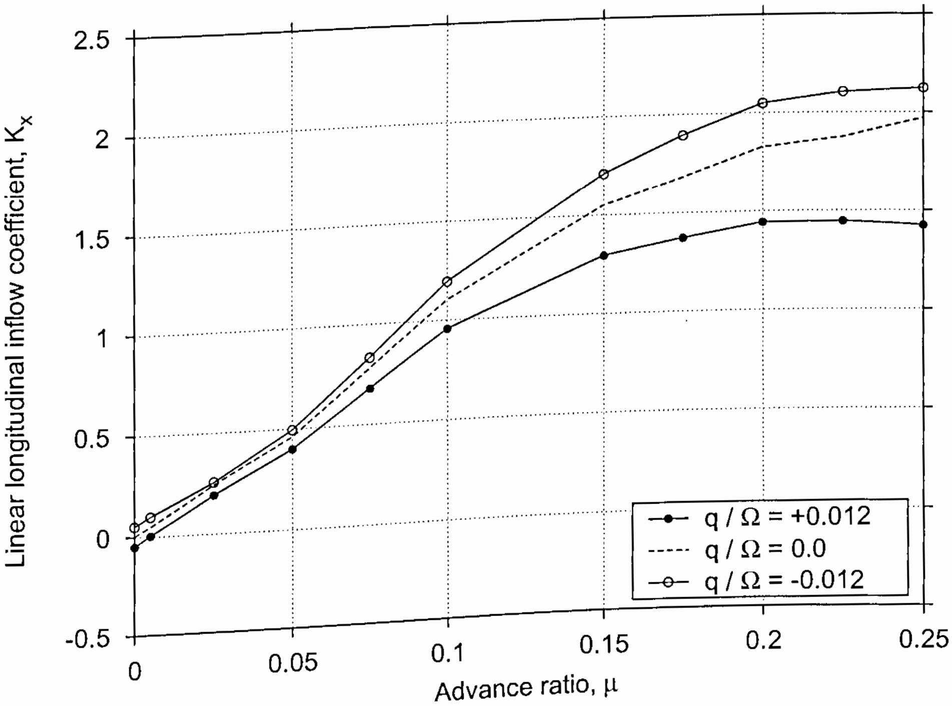

Figure 7.30: Longitudinal linear inflow gradients resulting from a pitching maneuver as a function of advance ratio. Results include both kinematic and wake distortion effects (level 2 model).

nose-down pitching motion, however, results in a further reduction in the longitudinal inflow gradient because of maneuver induced wake distortions as well as the kinematic effects.

This asymmetry in the inflow gradient perturbation can be better understood by examining the maneuver effects on the rotor wake geometry. Figure 7.32 shows the axial displacement of the tip vortices at the front and the rear of the rotor disk at an advance ratio of 0.2. At the front of the disk, a nose-up pitching motion results in the tip vortices being convected further away from the TPP. However, a nose-down pitching motion of the same magnitude has a much smaller effect on the tip vortex

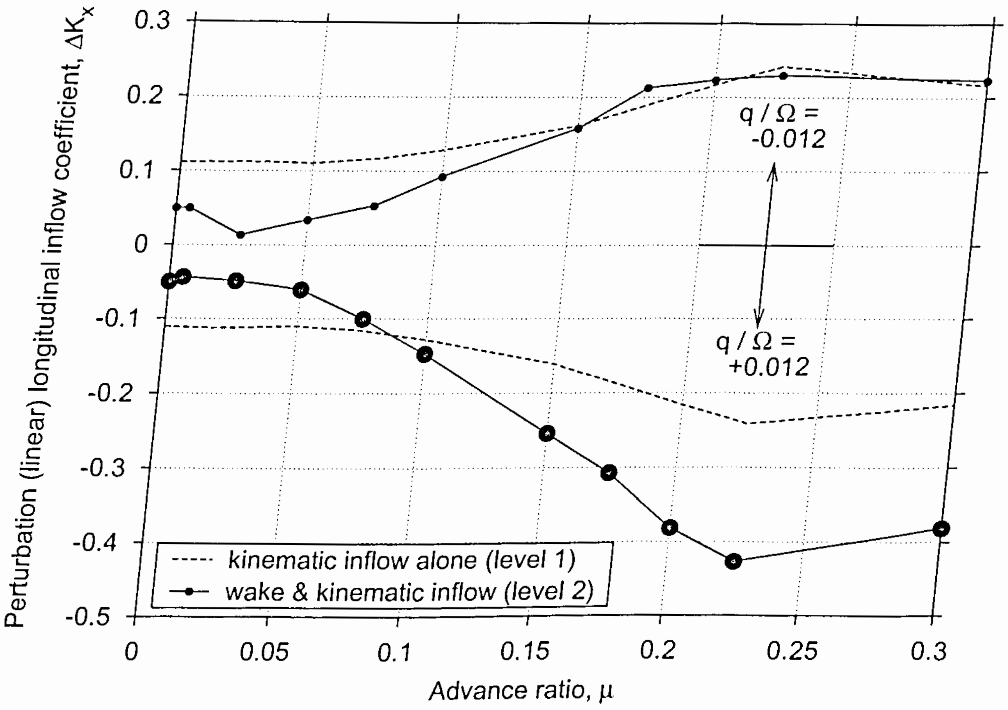

Figure 7.31: Longitudinal (linear) inflow gradient perturbations resulting from a pitching maneuver as a function of advance ratio.

displacements. In this case, the tip vortices initially convect above the TPP, but this upward convection is very small in magnitude — compare with Fig. 7.21 at a smaller advance ratio of $\mu = 0.1$. At the rear of the disk, a nose-up pitching motion results in the vortices convecting further away from the TPP, while a nose-down pitching motion results in the opposite effect. Because of the smaller maneuver induced wake distortion effects with a nose-down pitch rate, the overall wake distortion is not symmetric with positive/negative pitch rates. At higher advance ratios, a nose-down pitch rate results in a very small wake distortion close to the rotor, and the overall inflow perturbations are essentially because of kinematic effects, as shown in Fig. 7.31.

The blade flapping response resulting from a pitching motion is shown in Fig. 7.33

(a) Front of the rotor disk

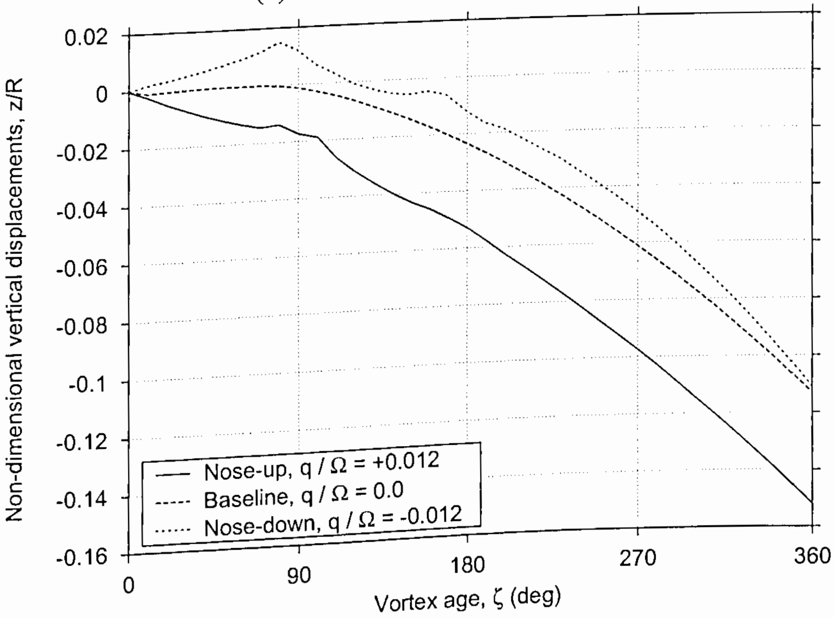

(b) Rear of the rotor disk

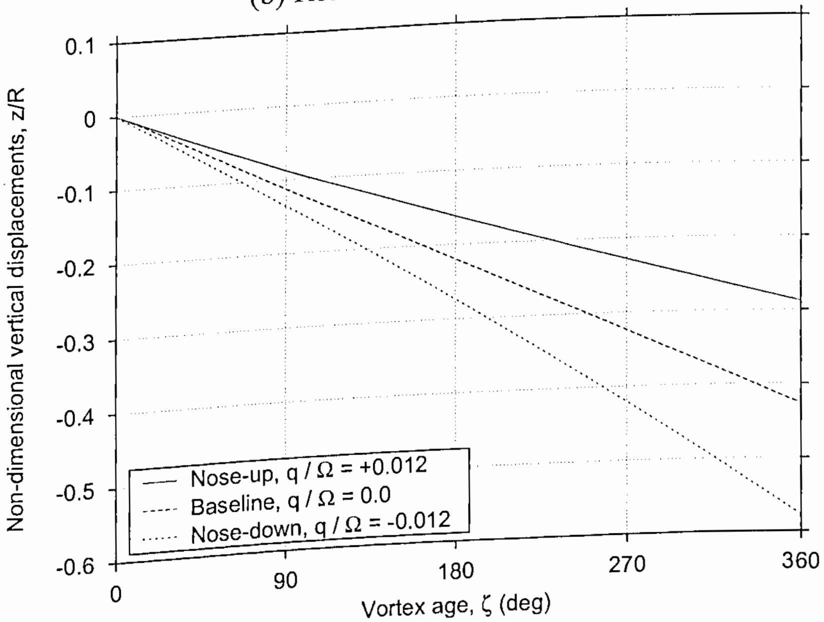

Figure 7.32: Effects of pitch rate on tip vortex vertical displacements for a four-bladed rotor in forward flight at $\mu = 0.2$. (a) Front of the rotor disk. (b) Rear of the rotor disk.

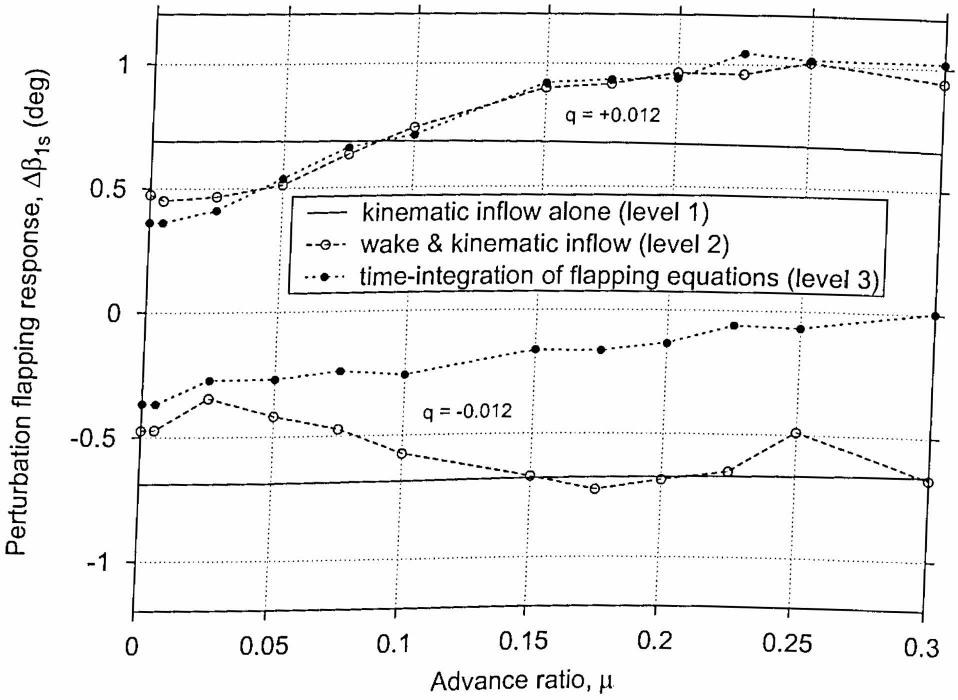

Figure 7.33: Lateral (off-axis) flapping response resulting from a pitching maneuver as a function of advance ratio.

for increasing advance ratio. The flapping response based on linear inflow perturbations obtained from the inflow calculations using the free-vortex wake method is shown, along with that calculated by time-integration of the blade flapping equations. The flapping response based on inflow perturbations using kinematic considerations alone is also shown. Notice that a linear inflow approximation shows a good agreement with the calculated flapping response for a positive (nose-up) pitching motion. However, for a nose-down pitching motion, the response based on linear inflow approximations is significantly different. This is because the maneuver induced wake distortion effects close to the rotor are small, and the corresponding wake-induced inflow gradient perturbations are also correspondingly small. However, because of close proximity between the tip vortices and the rotor blades, the rotor wake response to this type of maneuver (angular) rates is highly non-linear and, in general, a linear inflow approximation is not a completely adequate representation of these effects. A complete coupled solution for both blade flapping motion and the free-vortex wake would be necessary to accurately represent the maneuver induced wake distortion effects on the rotor response.

Finally, a wake distortion factor was derived from the inflow gradient perturbations calculated using the present free-vortex wake analysis. Figure 7.34 shows the wake distortion factor resulting from an imposed pitch rate of $\overline{q} = \pm 0.012$ as a function of increasing advance ratio. Recall from Eq. 7.10 that a positive K_R-factor implies that the inflow perturbations resulting from maneuver induced wake distortions are in a sense opposite to the inflow gradients based on kinematic considerations alone. For low advance ratios the K_R factor is positive, similar to the results found in hovering flight, as shown in Fig. 7.19. The wake distortion factor decreases with increasing advance ratio and changes sign around an advance ratio of $\mu = 0.1$. Recall from Fig. 7.27 the maneuver related wake distortion effects were found to be very small as compared to the kinematic effects at an advance ratio of $\mu = 0.1$. At higher advance ratios, however, the maneuver induced wake distortion effects result in inflow perturbations in the same direction as the kinematic effects, thereby amplifying the maneuver related effects on the blade flapping response.

Effect of Advance Ratio on Wake Distortions During Rolling Motion

The response of the rotor wake to imposed rolling motions in forward flight was found to be only qualitatively similar to that for an imposed pitching motion. This is because the baseline lateral inflow gradients are significantly different from the longitudinal

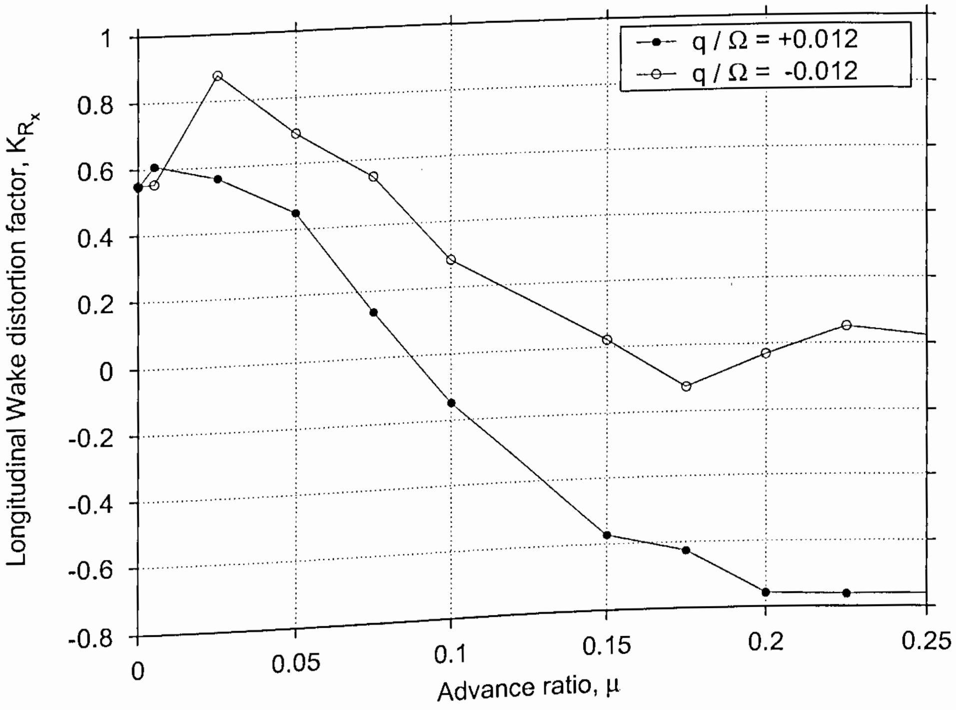

Figure 7.34: The K_R factor extracted from the time-accurate free wake results as a function of increasing advance ratio for a four-bladed rotor with imposed pitch rate.

inflow gradients. For low speed forward flight, the lateral inflow distribution is essentially uniform and, therefore, the response to positive/negative roll rates may be expected to be symmetric. For high speed forward flight, however, this may not be the case.

Figure 7.35 shows the lateral inflow gradients for imposed roll rates for increasing advance ratio. The baseline (non-maneuvering) inflow gradients are also shown for comparison. Note that the maneuver induced wake distortions in forward flight result in a significant lateral inflow gradient at high advance ratio, even in the absence of any imposed angular rates. The inflow gradient perturbations, i.e., changes from to these baseline inflow gradients, are shown in Fig. 7.36.

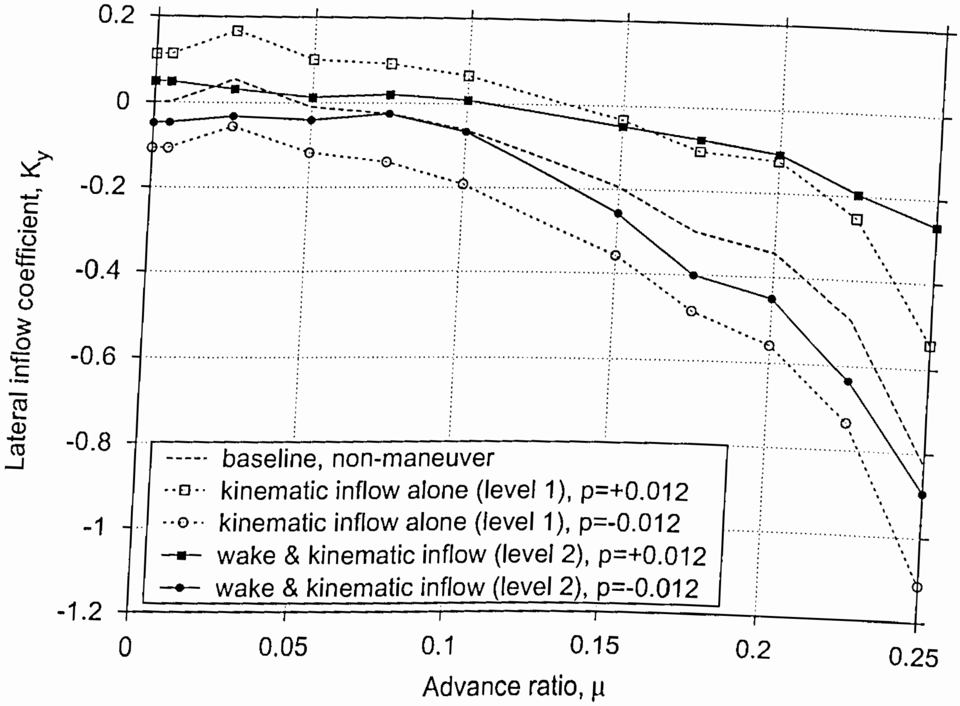

Figure 7.35: Lateral linear inflow gradients resulting from a roll maneuver as a function of advance ratio.

For low speed flight, the roll rate induced wake distortion effects produce a lateral inflow gradient that is in a sense opposite to that resulting from kinematic effects alone. This behavior is essentially similar to that observed in forward flight. However, some asymmetry is seen for positive and negative roll rates even at moderate forward speeds. At higher forward speeds, the wake distortion effects on the inflow gradient are appear to be smaller for a positive roll rate than for a corresponding negative roll rate.

The blade flapping response resulting from a roll rate is shown in Fig. 7.37 for increasing advance ratio. The approximate flapping response estimated using the inflow gradient perturbations is also shown. Similar to the results found for hovering flight, consideration of kinematic inflow gradient perturbations alone did not give good esti-

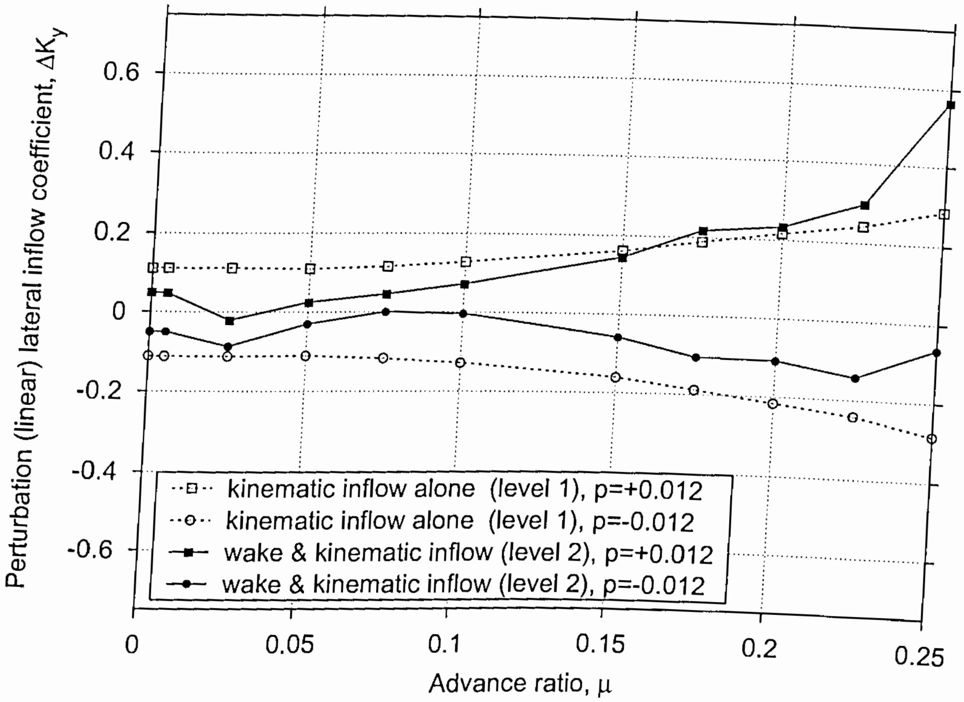

Figure 7.36: Lateral linear inflow gradient perturbations resulting from a roll maneuver as a function of advance ratio.

mate of the blade flapping. Inclusion of the maneuver induced wake distortion effects in the inflow perturbations improved the estimated response, as compared to the blade flapping response calculated by time-integrating the flapping equations. However, at higher advance ratios, such simple linear inflow perturbation model did not give a complete representation of the maneuver effects. It is interesting to note that at low advance ratios ($\mu \leq 0.1$) the response to positive and negative imposed roll rates is almost symmetric. However, for higher advance ratios, the response is significantly asymmetric.

Finally, a wake distortion factor was estimated based on the inflow perturbations calculated from the present free-vortex wake analysis. These results are shown in

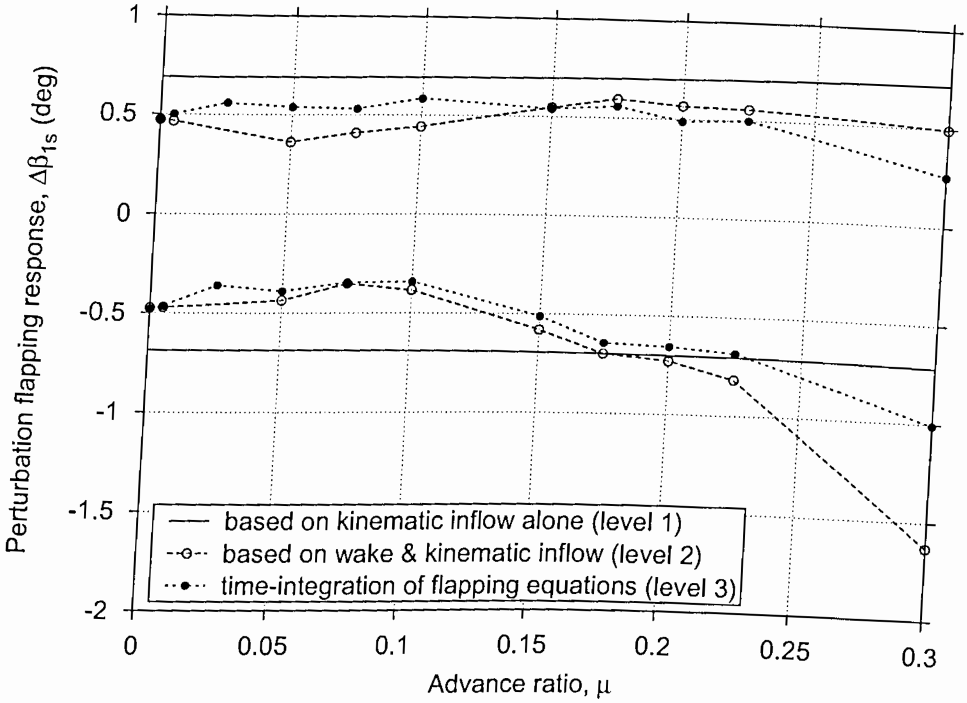

Figure 7.37: Longitudinal (off-axis) flapping response resulting from a roll maneuver as a function of advance ratio.

Fig. 7.38 as a function of advance ratio. For a small advance ratio of $\mu = 0.025$ the K_R-factor has value higher than unity. This suggests that the maneuver induced wake distortion effects are opposite to the kinematic effects and also of a higher magnitude – see Eq. 7.11. Therefore, the blade flapping response may be opposite of that expected based on kinematic considerations alone. Note that the flapping response, as shown in Fig. 7.37 was found to be significantly smaller in magnitude than that estimated based on kinematic effects alone, but of the same sign. This again confirms that the rotor response to angular rates is highly non-linear, and a simple representation based on linearized inflow perturbations may not be completely adequate to describe these effects under many flight conditions.

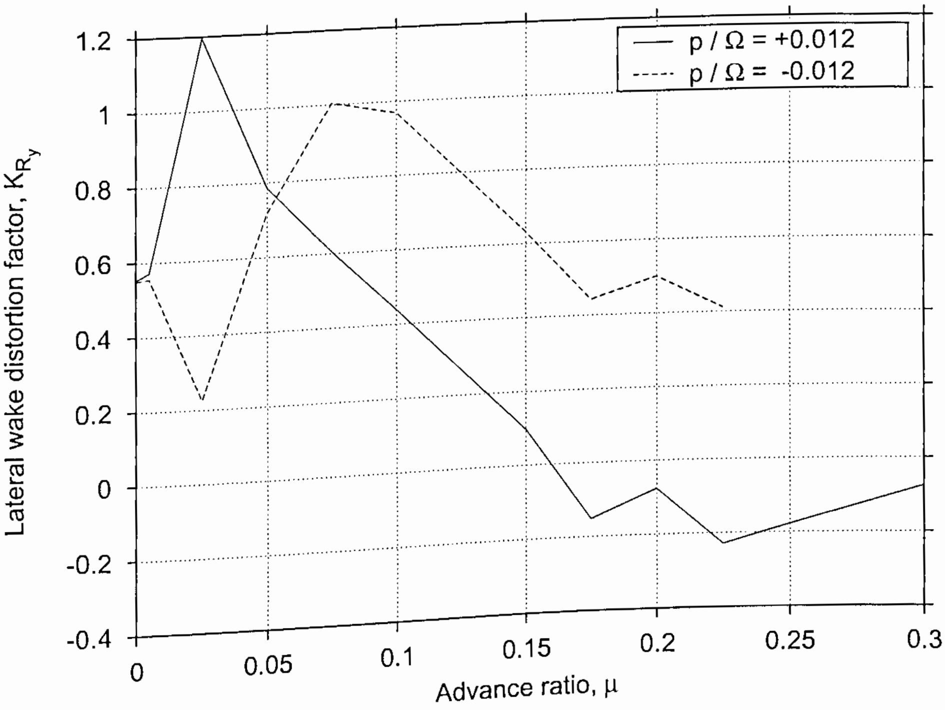

Figure 7.38: The K_R factor extracted from the time-accurate free wake results as a function of increasing advance ratio for a four-bladed rotor with imposed roll rate.

7.2 Descending Flight through the Vortex Ring State

Another good application of the time-accurate rotor wake model is to the prediction of the blade and rotor airloads during descending flight conditions. In low speed descents the rotor response is known to be significantly unsteady (non-periodic), with the maximum fluctuations in the rotor response occurring near the so-called vortex ring state (VRS). Simple momentum theory is strictly invalid in this flight regime because of the ambiguity in defining a flow direction and a well-defined slipstream boundary (e.g., Ref. 2). Also, steady-state (periodic) vortex wake models fail to predict the rotor behavior near the VRS because of the inherent flow unsteadiness. A time-accurate free-vortex wake model, however, provides a powerful first-principle based tool to study the aerodynamics of the rotor wake under such flight conditions.

7.2.1 Rotor in Axial Descent

Simple momentum theory gives a solution for axial climb with the climb velocity $V_c > 0$. For axial descent, however, the solution is valid only for $V_c < -2V_h$, where V_h is the rotor induced velocity in hovering flight. In these flight regimes, the flow through the rotor disk has a unique direction and a slip-stream boundary can be defined for application of the conservation laws. The induced velocity through the rotor can then be solved, and the results are

$$\frac{v_i}{V_h} = -\left(\frac{V_c}{2V_h}\right) + \sqrt{\left(\frac{V_c}{2V_h}\right)^2 + 1} \qquad \frac{V_c}{V_h} > 0 \tag{7.15}$$

$$\frac{v_i}{V_h} = -\left(\frac{V_c}{2V_h}\right) - \sqrt{\left(\frac{V_c}{2V_h}\right)^2 - 1} \qquad \frac{V_c}{V_h} < -2 \tag{7.16}$$

Similarly, the induced power is given by

$$\frac{P_i}{P_h} = \left(\frac{V_c}{2V_h}\right) + \sqrt{\left(\frac{V_c}{2V_h}\right)^2 + 1} \qquad \frac{V_c}{V_h} > 0 \tag{7.17}$$

$$\frac{P_i}{P_h} = \left(\frac{V_c}{2V_h}\right) - \sqrt{\left(\frac{V_c}{2V_h}\right)^2 - 1} \qquad \frac{V_c}{V_h} < -2 \tag{7.18}$$

These solutions based on simple momentum theory are strictly not valid in the descent velocity range $-2 < V_c/V_h < 0$ because a well-defined slip-stream boundary cannot be identified to properly apply the conservation laws. These results are also invalid in the vortex ring state, and empirical results must be used. However, as will be shown later, the physical rotor wake behavior somewhat resembles these non-physical solution branches in the region $-2 < V_c/V_h < 0$.

The basic VRS phenomenon manifests itself as a substantial increase in the required induced power necessary to overcome the additional aerodynamic losses as the rotor descends into its own wake. The VRS condition is often referred to by pilots as "settling with power" but this term reflects a piloting interpretation of the usual behavior of a rotorcraft operating at or near the VRS and is not a descriptor of the aerodynamic flow state at the rotor. More importantly, however, the unsteady flow obtained during transition into and through the VRS may result in highly fluctuating blade airloads leading to considerable blade flapping, high piloting workload, and even a possible loss of rotor control. While operation in the VRS is undesirable, transition through the VRS may be required to reach autorotative conditions. Therefore, the VRS phenomenon is of particular interest to the rotor aerodynamicist.

To this end, despite the many inherent difficulties in conducting experiments of the problem, several researchers have experimentally measured rotor behavior in descending flight – see, e.g., Refs. 110–114. These studies, as well as the work of Refs. 115 and 116, have mostly used an extension of simple momentum theory into the VRS to help understand the problem. Although the momentum theory seems to provide reasonable overall (time-averaged) predictions in some cases, it does not provide a means of predicting either the higher induced power requirements of the rotor associated with operation in its own wake or the inherent unsteadiness of the flow in the VRS. Also, the oscillatory airloads result in unsteady blade flapping response and significant oscillations of the TPP. These may result in highly oscillatory roll/pitch moments on the aircraft and make it difficult to control. This behavior is important from piloting perspective. However, momentum theory or its variations are inadequate to predict such behavior

To illustrate the transient unsteady flow state during operation in the VRS, Fig. 7.39 shows representative predictions of the rotor response during a transition from hovering flight through the VRS into steady descending flight. Rotor thrust and torque coefficients, as well as blade flapping (coning) angle, are shown in Fig. 7.39. As the rotor begins to descend starting from hover, small oscillations in rotor thrust and blade flapping are observed. During the transition into the VRS, the rotor response shows significant unsteadiness, as can be seen from the fluctuating behavior of both rotor thrust and blade flapping. During this transition process, the rotor begins to extract power from the surrounding air. In this flight regime, the flow field surrounding the rotor is aperiodic. As the descent rate increases further, the rotor begins to transition out of VRS and enters into the turbulent wake state and finally into the windmill brake state, as shown by the near zero power consumption in Fig. 7.39(c). At these higher rates of descent the unsteadiness in rotor response (i.e., magnitude of oscillations) is relatively smaller as the flow becomes mostly periodic when the rotor enters into autorotation. With a further increase in descent rate, the rotor begins to operate in the windmill brake state.

Figure 7.40 documents predictions of the rotor wake boundary during the transition from hover through the VRS into descent. At low descent rates, as shown by Fig. 7.40(b), the rotor wake begins to move up up into the plane of the rotor disk. As shown in Fig. 7.40(c), for higher rates of descent the wake contracts and moves up through the rotor disk and this corresponds to the beginning of the oscillations shown in Fig. 7.39. As the descent rate increases further and approaches a descent velocity that is of the same magnitude but of opposite direction to the average induced velocity through the rotor, i.e., $V_c + V_i \approx 0$, the wake rolls up around and through the rotor disk, with most of the discrete blade tip vortices trailed into the wake being bundled into the plane of the rotor – see Fig. 7.40(d). This is the so-called VRS, and is accompanied by the highest oscillations in blade airloads and rotor flapping response. If the descent rate

(a) Rotor thrust

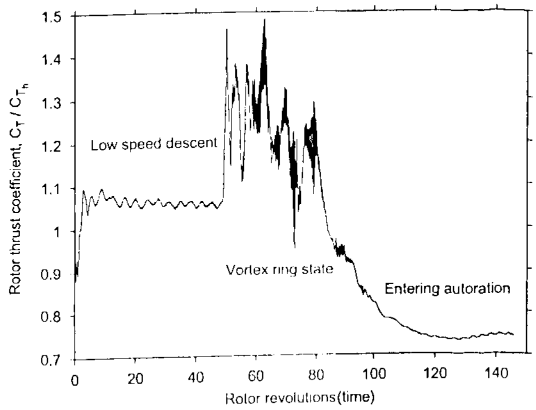

(b) Blade flapping response

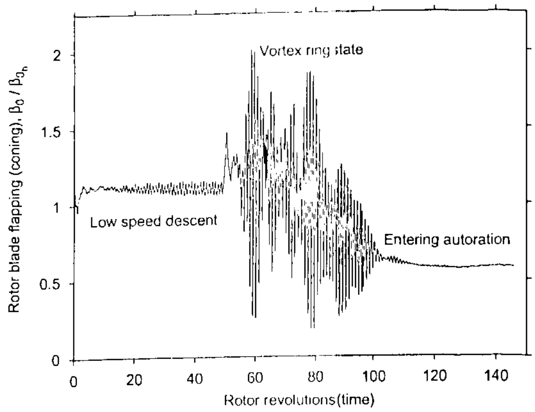

(c) Rotor power (torque)

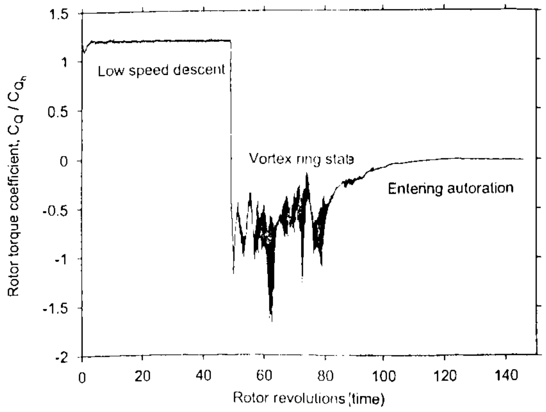

Figure 7.39: Representative time histories for a rotor in transition from hover to a high axial descent rate: (a) Rotor thrust, (b) Blade flapping response, and (c) Rotor power (torque).

continues to increase so that $V_c + V_i < 0$ the rotor enters into the turbulent wake state, with lower fluctuating loads but still a relatively unsteady flow state. At the highest descent rates the rotor begins to enter the windmill brake state and the wake attains a mostly periodic (axisymmetric) wake structure.

Figures 7.41(a) and (b) show the universal power curve for a rotor in axial (vertical) flight. The flight regime of interest is for $-2 \le V_c/V_h \le 0$ where momentum based theories are strictly not valid because of the reasons previously mentioned. Experimental results from Refs. 111, 113 and 114 are shown in Fig. 7.41(a), with the numerical predictions using the time-accurate free-vortex wake model being shown in Fig. 7.41(b). The induced power was estimated from the experimental measurements of total shaft power by assuming that the profile power is a function of the thrust alone, and does not depend on the axial velocity. Therefore, the profile power was estimated from the measurements in hovering flight with the induced power being approximated by the momentum theory result, i.e.,

$$C_{P_0} = \left(C_{P_h} - \frac{C_{T_h}^{3/2}}{2} \right) \tag{7.19}$$

The induced power in axial flight was then calculated by subtracting the profile power from the total measured power as

$$C_{P_i} = C_P - C_{P_0} + \left(\frac{-V_c}{\Omega R} \right) C_T \tag{7.20}$$

Notice from Fig. 7.41 that at low descent rates both the experimental results and the predictions closely follow the non-physical branch of the momentum theory solution. However, in this region, the induced power is somewhat higher than that predicted based by momentum theory. This is because under these conditions the rotor operates inside its own vortical wake so that to produce the same thrust the rotor must consume

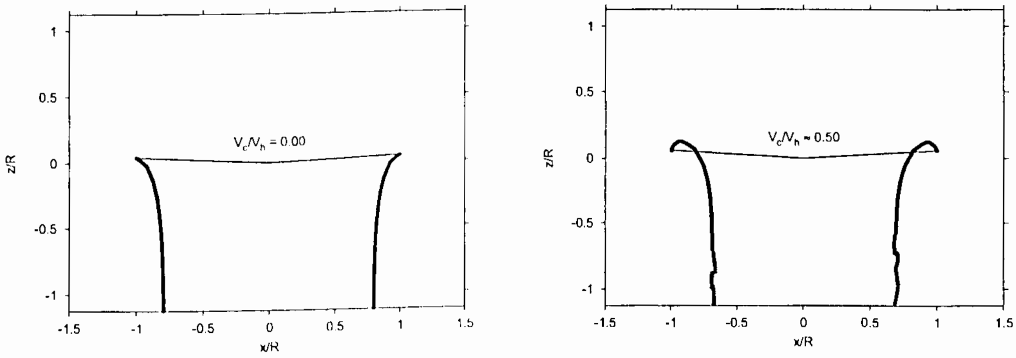

(a) Hovering flight

(b) Low descent rate

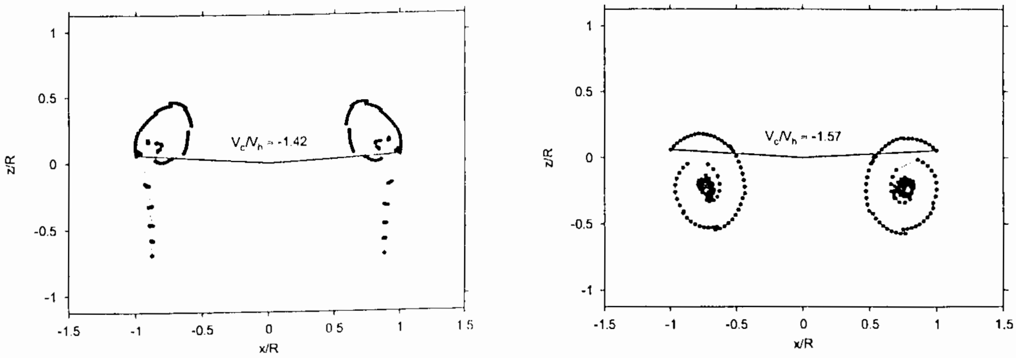

(c) Entering vortex ring state

(d) Vortex ring state

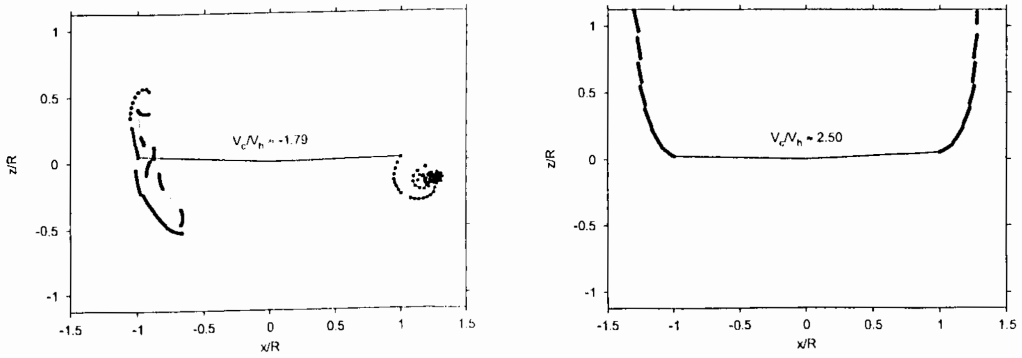

(e) Turbulent wake after vortex ring state

(f) Windmill brake state

Figure 7.40: Rotor wake boundary as viewed in a plane normal to the rotor disk during axial descent. (a) Hovering flight, (b) Low descent rate, (c) Entering vortex ring state, (d) Vortex ring state, (e) Turbulent wake state, (f) Windmill brake state.

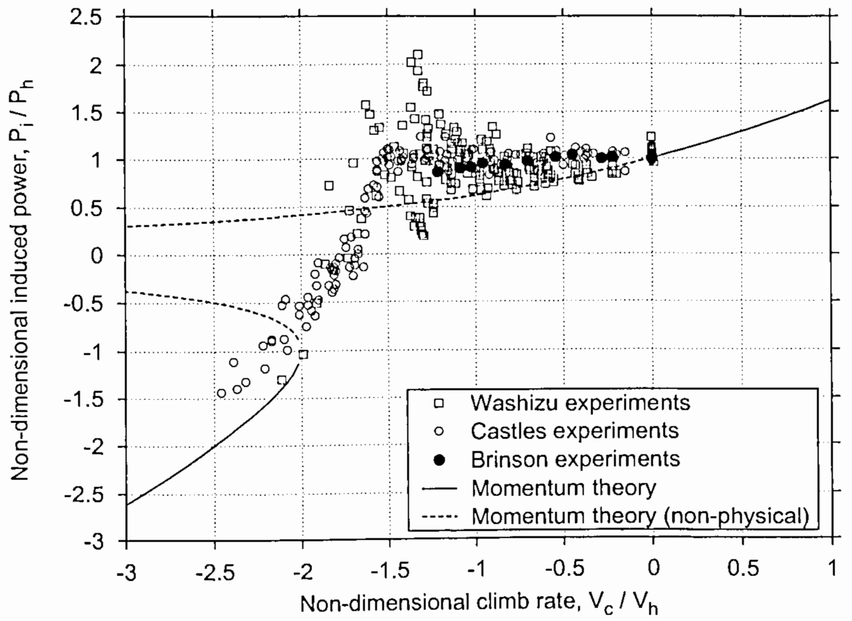
(a) Experimental measurements

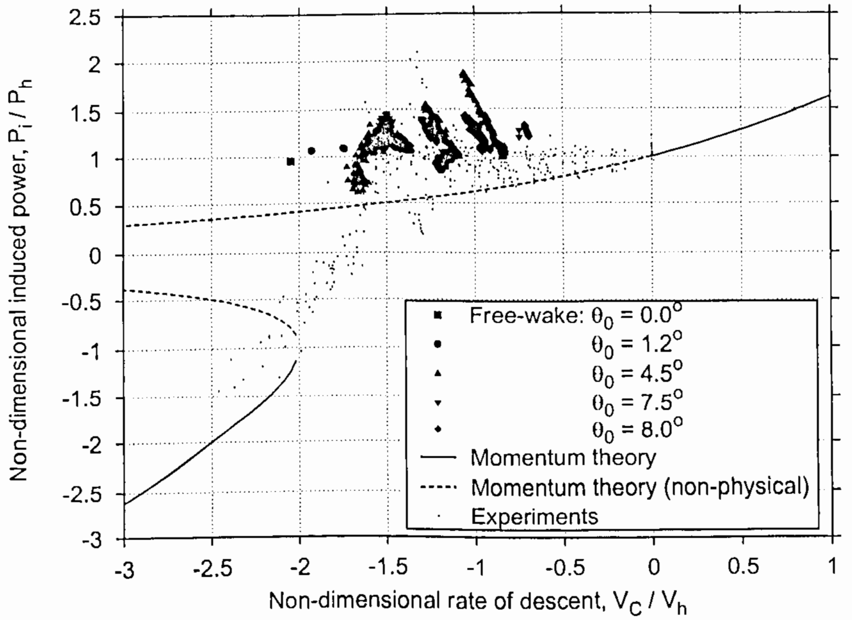
Free-vortex wake predictions

Figure 7.41: Universal power curve for a rotor in axial flight (descent): (a) Experimental measurements (b) Free-vortex wake predictions.

more induced power. The free-vortex results quantitatively predict this increased induced power requirement. Notice that the fluctuations shown in the predictions are because the solution never reaches a steady-state and continuously changes with time because of the highly unsteady flow conditions.

The corresponding complete induced velocity curve in axial flight is shown in Fig. 7.42. The experimental results in Fig. 7.41 show the induced velocity, which was estimated from the induced power measurements by using

$$\frac{V_i}{V_c} = \frac{P_i}{P_h} - \frac{V_c}{V_h} \tag{7.21}$$

where the subscript h refers to the values in hovering flight. Notice that the free-vortex wake predictions show a good correlation with the experimental results. Again, the induced velocity closely is found to follow the non-physical branch of the momentum theory solution at low descent rates. However, notice that both the predicted and experimental values are somewhat larger than the momentum theory results. This suggests that the momentum theory may only be used as a lower bound for predictions of the induced power or induced velocity. For descent rates less than 1.5 ($V_c/V_h < -1.5$), the solution jumps somewhat abruptly to the lower solution branch and follows the physical solution for the windmill brake state at descent rates of 2.0 and higher ($V_c/V_h < -2$).

Washizu *et al.* (Ref. 113) have quantified the increased induced power measured during equilibrium axial descent in terms of a power loss factor, κ_v – see Ref. 113 for details – where κ_v is defined as

$$\kappa_v = \frac{P_i}{T V_{MT}} - 1 \tag{7.22}$$

where P_i is the rotor induced power (Eq. 7.20) and V_{MT} refers to the rotor induced velocity as given by momentum theory in axial flight (Eq. 7.15 & 7.16). This power

(a) Experimental measurements

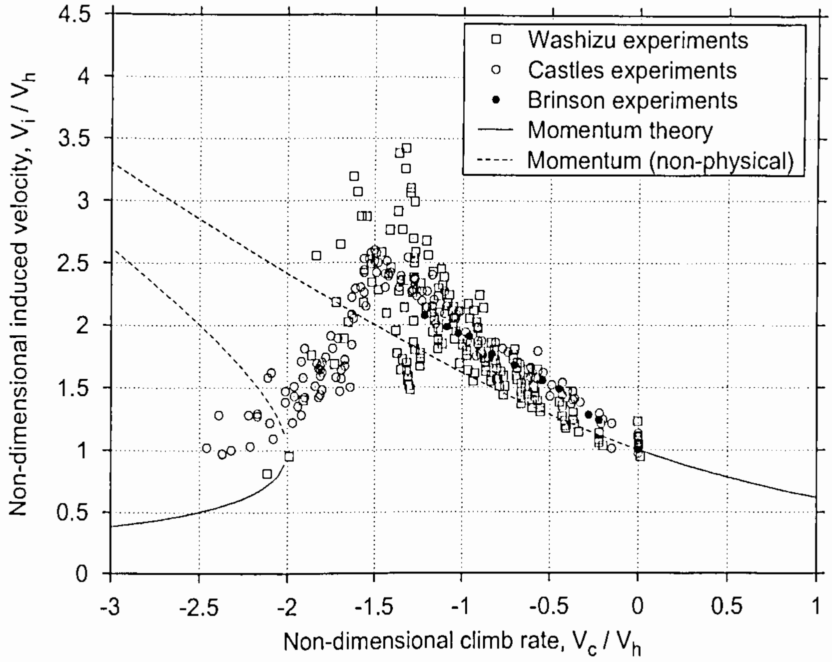

(b) Free-vortex wake predictions

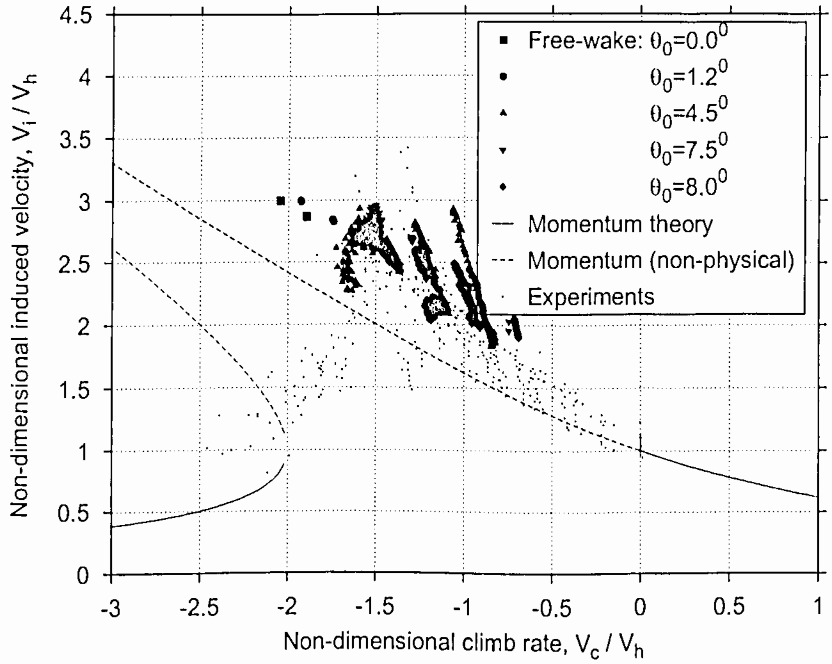

Figure 7.42: Complete induced velocity curve for a rotor in axial flight (descent). (a) Experimental measurements (b) Free-vortex wake predictions.

loss factor is essentially a measure of the extra induced power required by the rotor to produce useful work (i.e., thrust) as it descends into its own vortical wake as compared to the momentum theory solution. Recall that the momentum theory solution is not physically valid for descent rates of $-2 < V_c/V_h < 0$. The power loss factor, κ_v, allows one to empirically correct the non-physical momentum theory solution to give better predictions of rotor performance for this range of descent rates. The measured values in Fig. 7.43(a) show a distribution as a function of descent velocity with a maximum loss occurring around a non-dimensional descent rate of $V_c/V_h \approx$ -1 to -1.2. The free-wake results closely predict this behavior and are in good quantitative agreement with the experimental measurements, as shown in Fig. 7.43(b). Based on these results, it is possible that estimates of such a power loss factor obtained using the free-vortex model may be used to make predictions that allow corrections to the simple momentum theory to enable more routine quantitative predictions of rotor performance in the VRS.

7.2.2 Rotor in Inclined Descent

Note that a correction for power loss, κ_v, may also be applied to inclined descent conditions, i.e., a combination of descent and forward velocity. For an inclined descent at an angle of α, where the velocity components normal and parallel to the rotor disk is $V_c \sin\alpha$ and $V_c \cos\alpha$, respectively, a momentum theory solution may be obtained. Momentum theory is not strictly valid under such flight conditions as explained previously, however, assuming the theory to be valid the induced velocity is given by the solution of

$$\frac{V_c}{V_h} = \frac{V_i}{V_h}\sin^2\alpha \pm \sin\alpha\sqrt{\left(\frac{V_h}{V_i}\right)^2 - \left(\frac{V_i}{V_h}\right)^2\cos^2\alpha} \tag{7.23}$$

The experimental measurements of Ref. 113 showed that the overall rotor performance closely follows the trend based on momentum theory in Eq. 7.23. These results are

(a) Experimental measurements

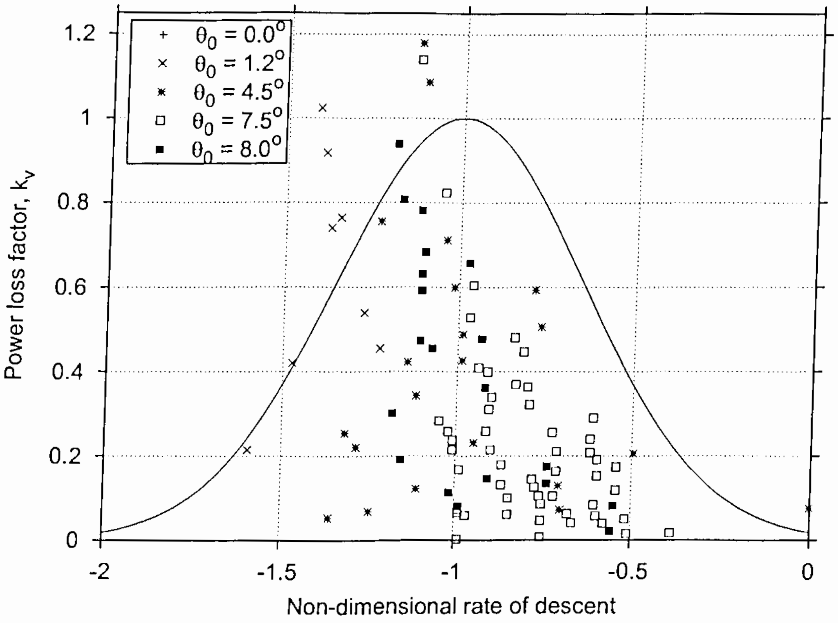

(b) Free-vortex wake predictions

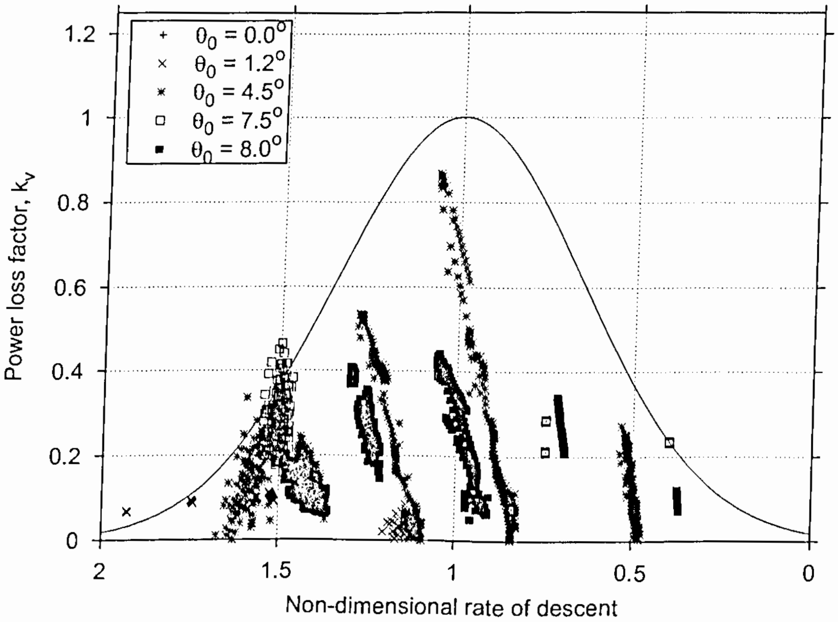

Figure 7.43: Power loss factor in axial descent. (a) Experimental measurements. (b) Free-vortex wake predictions.

shown in Fig. 7.44 for three angles of inclination: (a) $\alpha = 20°$, (b) $\alpha = 50°$, and (c) $\alpha = 70°$. The predictions obtained using the present free-vortex wake analysis are also shown for comparison. Similar to axial descent the present analysis was found to give good agreement with the experimental results. It is also interesting to note that both the experimental measurements and the free-vortex wake results showed essentially the same trend as given by a simple momentum theory in Eq. 7.23.

7.2.3 Estimating Vortex Ring State Boundary

Using the time-accurate results for axial and inclined descending flight, the free-vortex wake analysis can used to predict the various regions of the rotor flight envelope where the rotor may enter into the VRS. This is important for several operation reasons, including the fact that it may be necessary for the helicopter to pass through the VRS, albeit briefly, to enter into equilibrium autorotational flight. The boundary of the VRS can be established, for example, by sequentially mapping out combinations of the rotor operating conditions such as flight path angle, descent velocity and forward speed where the rotor experiences high fluctuations in thrust, shaft torque, blade flapping, or combinations of such. As previously explained, these fluctuations occur because of the highly time-varying and recirculating wake state that is typically found near the rotor under the conditions known to be typical of the VRS. The VRS boundary can only accurately determined empirically by wind-tunnel or flight tests, although because of the difficulties in maintaining equilibrium flight at or near to the VRS conditions and the variability in the results for different types of rotors (e.g., Ref. 111), there is usually considerable uncertainty in this process. The unsteady vortex theory, as in the present analysis, provides a much more rigorous basis for estimating the flight conditions that may encompass the conditions typical of the VRS.

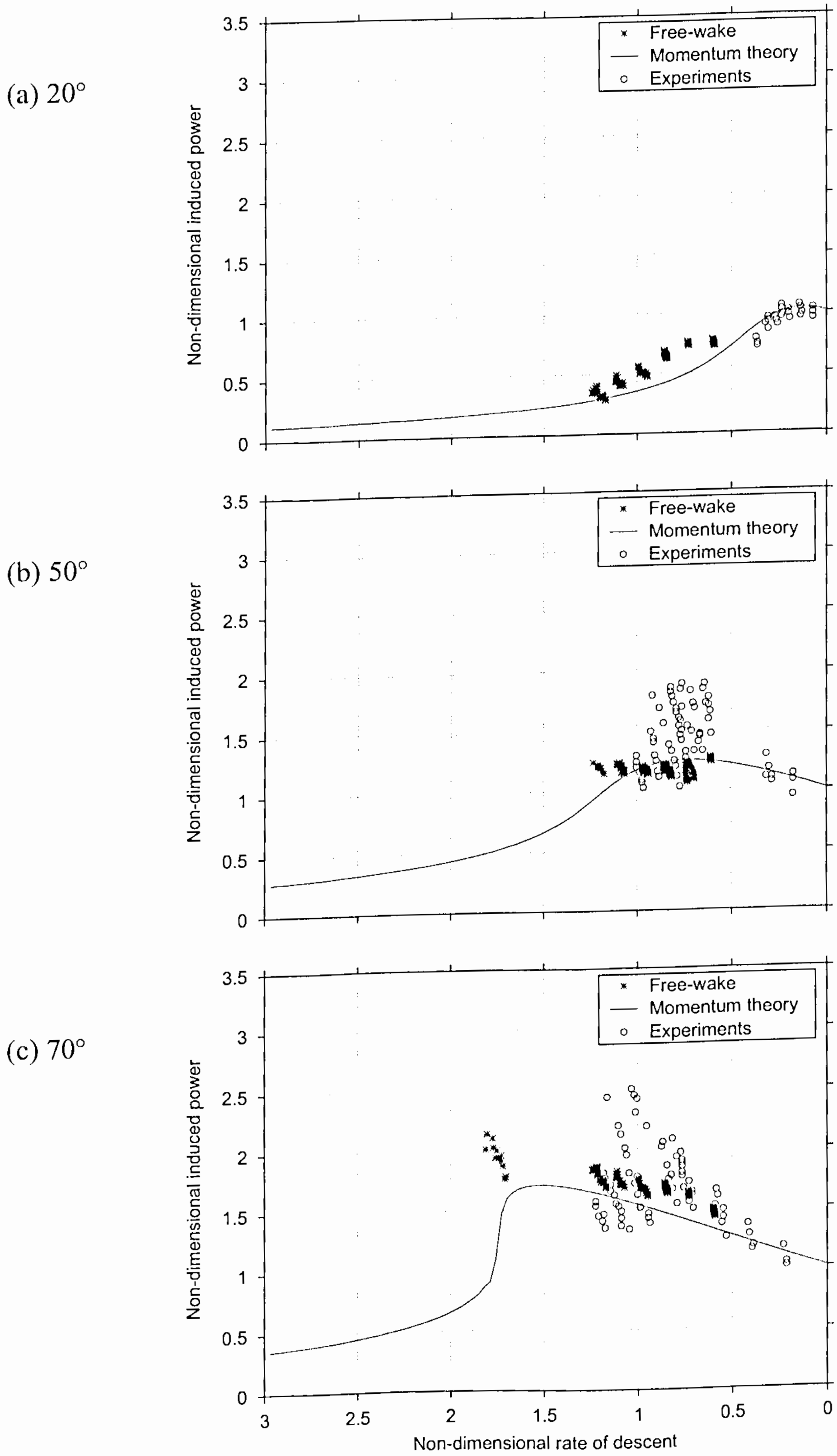

Figure 7.44: Induced velocity for a rotor in inclined descent at an angle of (a) 20°, (b) 50°, and (c) 70°. Experimental measurements from Ref. 113.

Predictions of a representative VRS boundary as a function of rate of descent normal to the rotor disk and forward flight speed are shown in Fig. 7.45(a) in terms of contours of constant rotor thrust fluctuations. The results in this figure were obtained for over 100 different operating conditions and using bilinear interpolation to map the results to a regular grid for contour plotting. The relative magnitude of the rotor thrust oscillations near and in the VRS was found to be significant, with the largest fluctuations ($\approx$ 20% of the mean thrust) occurring in near vertical descent. Smaller fluctuations ($\approx$ 5% of the mean thrust) were obtained at slightly lower or higher rates of descent and also in forward flight, which suggests that the conditions where the VRS may be encountered extend over a relatively wide range of flight conditions. The predictions closely follow the boundary where the net velocity normal to the rotor disk (approximately sum of induced velocity and descent velocity) is approximately zero.

Such large fluctuations in rotor thrust can cause significant flapping of rotor blades. Figure 7.45(b) shows that the corresponding oscillations in blade flapping found under these conditions is also significant. These results are a composite of coning and cyclic flapping. Such oscillations in cyclic flapping lead to highly unsteady changes in the orientation of the tip path plane. This may produce significant roll/pitch moments on the helicopter, leading to piloting difficulties and even a loss of control authority. Figure 7.45(c) shows the same type of VRS boundary predicted on the basis of a fluctuating rotor torque. Notice that this boundary is slightly different to either the boundaries predicted using the fluctuating thrust or blade flapping as a metric, but it is also important because the torque fluctuations may lead to directional (yaw) control issues and a further increase in pilot workload during operations near to or at the VRS. All of these results are in generally good qualitative agreement with the boundaries of the VRS estimated on the basis of experiments (Refs. 110, 113, 115).

(a) Thrust fluctuations

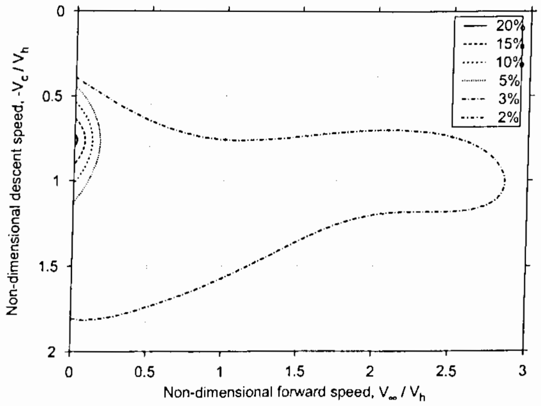

(b) Blade flapping fluctuations

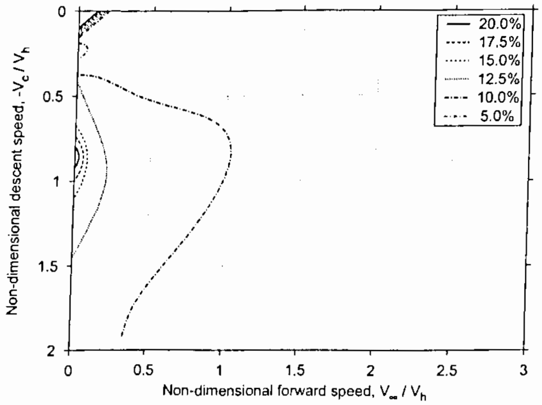

(c) Power (torque) fluctuations

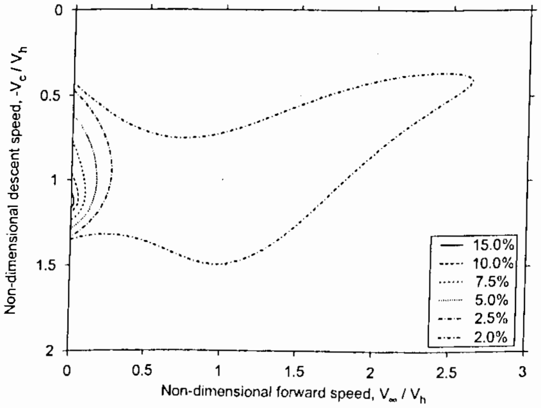

Figure 7.45: Vortex ring state boundary based on fluctuating rotor thrust, torque and blade flapping response as estimated from the free-vortex wake results.

7.3 Summary

In this chapter, the present analysis was applied to idealized pitch/roll maneuvers in hovering and forward flight to study the relative effects of the wake-induced inflow dynamics. The results suggested that during such transient flight conditions, the rotor wake dynamics plays a significant role in the overall rotor response and, therefore, must be correctly modeled for airloads predictions. The relative effects of the maneuver induced wake distortions were quantified as a wake distortion (K_R) factor. It was shown that such approximate representation is not general, and can be sensitive to geometric and operating parameters of the rotor. In general, a simple correction for the maneuver induced wake distortion effects on the inflow perturbations was found to be inadequate and a complete time-accurate wake model was necessary.

Finally, the present free-vortex wake methodology was applied to study the problem of a rotor in axial and/or inclined descent passing through the vortex ring state. The vortex ring state is a highly unsteady (non-periodic) condition and, therefore, warrants the use of high-fidelity time-accurate wake models like the present analysis. The predictions showed good agreement with available experimental measurements for induced velocity and power for several different descent rates. Potential application of the present analysis to predict vortex ring state boundaries was also demonstrated.

Chapter 8

Summary & Conclusions

Improved designs of the modern helicopter require versatile and robust numerical methodologies, with the capability to accurately predict the key aerodynamic features of the rotor wake under different flight conditions. To this end, the present work makes a contribution toward a better understanding and predictive capability for rotating wing aircraft. This chapter presents a summary of the present work and the conclusions drawn from the dissertation.

The main focus of this dissertation has been on development of a time-accurate model for the vortical wake structure generated by a helicopter rotor. With this overall objective, several numerical/physical issues associated with the rotor wake dynamics were rigorously examined. Two main areas of focus were the aerodynamic stability of the rotor wake and the convergence of the numerical algorithms, especially for the time-accurate solutions used to model the evolution and dynamics of the rotor wake. The stability of rotor wakes has been a long-standing issue in rotor wake modeling. In Chapter 2 this issue was formally analyzed using a linearized stability analysis. Chapter 3 presents a formal accuracy and stability analysis of the time-marching algorithms. Chapter 4 describes the rotor equations for the lift and blade flapping angles, and also describes the solution methodologies for these problems. Solution convergence and the grid-independent nature of the solutions was demonstrated, along with a second-order accuracy. The predicted wake geometry solution was validated with experimental results in Chapters 5 and 6. Finally in Chapter 7, the present analysis was applied to study some non-steady flight conditions such as idealized maneuvers and descending flight.

8.1 Summary

A major limitation in the development time-marching free-vortex wake models is that the vortical wake structure is inherently unstable in hovering and axial flight. Although this fact has been known for a long time, a systematic analysis of the aerodynamic stability has not previously been performed. The second chapter in this dissertation was devoted to a linearized stability analysis of rotor wakes and the possible impact of any instabilities on the time-accurate wake solution methods. The stability results have been supported by experimental measurements of the observed rotor wake behavior. The hovering helicopter rotor wake was shown to be intrinsically unstable, with the tip vortices exhibiting several possible unstable deformation modes. The so-called "vortex pairing" phenomenon was identified as a primary (most unstable) deformation mode for a two-bladed rotor. The stability analysis was also applied to study the effects of numerical parameters on the time-marching wake solutions, and to provide some insight into the subsequent development of a stable, convergent "time-accurate" wake model.

The time-accurate wake model was developed based second-order backward difference approximation for the time derivative. Because the wake structure may be unstable under some flight conditions, the stability of the numerical algorithm was important to ensure solution convergence. To ensure that the numerical model is consistent with the governing equations, the accuracy of all discrete approximations was examined. The straight-line vortex segmentation used to discretize the vortex filaments was rigorously examined using the well-known vortex ring problem. This approach was shown to be second-order accurate, and was able to properly resolve the self-induced velocity effects associated with the vortex filament curvature. An extrapolation method was used to demonstrate the possibility of possibly extending the methodology to a higher-order (in this case, a fourth-order) accuracy.

The stability of the time-marching algorithm was examined using a linear stability analysis. Modified equations were also used to further understand the stability characteristics of the algorithms. The proposed second-order backward algorithm was shown to provide higher-order dissipation to make the algorithm numerically stable. The convergence of the numerical wake solutions was also verified by successively increasing the grid resolution. The solution was shown to converge with the expected second-order accuracy, and a grid-independent solution was obtained for small discretizations. Such mathematical aspects of the numerical methodology are especially important to ensure that the methodology is equally suitable for applications in both steady (periodic) as well as transient (non-periodic) flight conditions.

The methodology was then applied to flow conditions of practical interest and the results were validated against experimental results, wherever available. The correlation study included comparisons of tip vortex trajectories obtained using flow visualization techniques, rotor induced velocity field measurements, and also isolated rotor performance measurements. A validation study for transient problems included the rotor response to ramp and oscillatory pitch inputs, and performance of the rotor in descending flight through the vortex ring state. In general, it was found that both the steady-state free-vortex wake model produced good agreement with the experimental measurements with only a few discrepancies. Such discrepancies may be associated with not only the uncertainties in experimental measurements, but also the lack of modeling of some viscous and compressible flow phenomena in the rotor wake. However, in spite of such discrepancies, the present free-vortex wake analysis is able to properly represent all physical trends of the wake structure and the induced velocity field. Overall, the present analysis provided a first-principle based robust and versatile tool for modeling the rotor aerodynamics.

8.2 Conclusions

The salient observations made in the present work and conclusions drawn from these are summarized in this section. The conclusions are divided into four separate subsections which deal with different aspects of the present work. The first part focuses on the results for the aerodynamic stability of rotor wakes, the second on the various numerical issues in the development of the time-marching methodology, and the third on validating the predictions against experimental measurements. Finally, the conclusions drawn from the various numerical experiments performed the course of this work are summarized.

8.2.1 Aerodynamic Stability of Rotor Wakes

Previous analytic work on the stability infinite vortex filaments suggested by analogy that the vortical trailed wake generated by a helicopter rotor is unstable. In the present work, a linearized stability analysis was developed to examine the stability of rotor wakes. The present wake stability analysis gave similar results for interdigitated infinite helical vortex filaments, as found using earlier analyses. Similar to helical vortex filaments, the rotor wake was also found be physically unstable in hovering and axial flight, with several unstable wake deformation modes. The wake stability analysis provided a better understanding of the global behavior of the rotor wakes and, in turn, provided insights for the development of the time-accurate solution methodology. Some observations and inferences from the wake stability results are summarized below.

1. The so-called vortex pairing phenomenon, as observed in both rotor experiments and numerical solutions of the rotor wake, is recognized in this work as a long-wave instability mode of the wake. This instability manifests in experiments because of various inherent physical disturbances. In numerical solutions, these disturbances have their origin in truncation/round-off errors, as shown by its dependence on numerical parameters like discretization level and number of wake turns. Therefore, agreement between experiments and numerical results is not always possible, and many otherwise good correlations may often be fortuitous.

2. The wake divergence rate showed a rapid increase at a vortex age corresponding to the first blade passage. This suggests that the rotor wake is relatively stable while it is undergoing the initial radial contraction, which typically occurs over the first half rotor revolution. The divergence rate for an instability mode also decreases with increasing rotor thrust. Although, the strength of the vortices also increases with thrust, the increased vortex separation distance (or the helical pitch) has a stronger influence on the wake stability characteristics. Therefore, the divergence rates also showed a decreasing trend with climb rate.

3. Any possible mistracking of rotor blades was shown to result in increased susceptibility of the rotor wake to instabilities and an early onset of tip vortex pairing in the wake. Such (small) mistracking did not significantly alter the divergence rates associated with the wake structure. However, the wake asymmetry resulting from unequal tip vortex strengths lead to an early onset of tip vortex pairing. These observations were found to be consistent with experimental results for a deliberately mistracked rotor.

4. The steady-state relaxation (iterative) free-vortex wake algorithms converge to equilibrium periodic wake geometries, while time-accurate algorithms typically exhibit instabilities. By enforcing periodicity, the relaxation algorithms allow only N_b-per-revolution disturbances. Because these disturbance modes are least unstable, the periodic wake algorithms, like relaxation methods, are generally not susceptible to non-physical wake instabilities.

5. In the free-vortex wake scheme, increasing the resolution of the vortex field decreased the numerical truncation errors, and thereby affected the onset of wake instabilities and vortex pairing. With smaller grid discretization vortex pairing occurred at later vortex ages. Increasing number of free-vortex wake turns showed a smaller influence on the vortex pairing phenomenon. For very few number of turns, the errors resulting from wake truncations result in pronounced instability modes. However, for moderate to high number of free-vortex wake turns, the solutions showed no significant differences.

6. The viscous vortex core models used with free-vortex wake methods can play some role in the stability of numerical solutions. The semi-empirical vortex model used in the present work is shown to be consistent with available ex-

perimental measurements of tip vortices. It was shown that using a large (non-physical) viscous core growth rate can significantly decrease the divergence rates associated with the wake structure. This may suppress the growth of numerical instabilities and give improved numerical convergence, albeit for the wrong underlying reasons. Instead, in the present work, solution convergence was ensured using a careful choice of the numerical algorithm.

8.2.2 Numerical Issues: Stability & Convergence

The stability and accuracy of the time-marching wake algorithm was rigorously examined using a linearized analysis, and also using modified equations. Solution convergence was then verified through numerical experimentation. It has been shown that because the governing equations are highly nonlinear, a classic linear stability analysis is insufficient to guarantee a stable algorithm and a convergent solution. Two new time-marching algorithms were developed during the course of the present work to better understand the numerical issues associated with the rotor wake solution. The first algorithm, called the PCC algorithm, was predictor-corrector type algorithm based on central difference approximations. The second algorithm, the PC2B algorithm, was based on a second-order backward difference approximation to the time derivative. A numerical analysis of these two algorithms was performed, and showed the importance of the stability of the time-marching algorithm to the overall wake solution. The PC2B algorithm was chosen for the present type of analysis because it was stable and gave a convergent rotor wake solution. The conclusions drawn from this analysis are summarized as follows:

1. The accuracy of each discrete approximation involved in the time-marching solution algorithms was examined using a Taylor-series analysis. The finite differ-

ence approximations for derivatives on the LHS of the governing equation were shown to be second-order accurate. Similarly, the velocity averaging procedure was also shown to be second-order accurate.

2. The numerical accuracy of straight-line segmentation of a general curvilinear vortex filament was rigorously examined. Using the vortex ring problem as a basis, this approach was shown to be second-order accurate for both an inviscid (potential) vortex and a viscous vortex. The analysis has also shown that with reasonably small segments, the straight-line segmentation approach can be successfully applied to force-free vortex convection without special treatment of the self-induced velocity resulting from vortex curvature. It was found that for most problems a wake filament discretization of 5° or smaller is necessary to properly resolve wake curvature effects and to obtain a grid-independent solution.

   Because the discretization approach gives a clean second-order accuracy, it was found to be amenable to numerical analysis techniques to improve the accuracy. The order of accuracy can, in principle, be arbitrarily improved by employing Richardson's extrapolation using a linear combination of two lower resolution solutions. It was shown that using a combination of two discretization levels, the induced velocity calculations could be performed with fourth-order accuracy.

3. The discretized wake equations were shown to be consistent with the governing equations for both time-marching algorithms. Therefore, by stability of the solution algorithm would ensure solution convergence. Based on linear considerations, both the algorithms were stable and should not lead to unbounded growth of numerical errors. However, the PCC algorithm may be considered unstable in the sense that it results in growth of numerical errors with time, albeit

bounded for a given grid discretization.

Modified equations were examined to better understand the nature of the extra (higher-order) terms in the discretized equations. Discretization of the induced velocity source term and the velocity averaging resulted in nonlinear dispersive and possibly anti-dissipative numerical errors. These anti-dissipative terms in the modified equations make the equations unstable, thereby resulting in growing numerical instabilities in the wake geometry solution. Therefore, it is necessary to ensure that the modified equations are stable with no non-physical anti-dissipative terms.

4. The central difference approximation to the time derivative introduced no numerical dissipation in the solution. The second-order backward difference approximation, however, introduced damping for high frequency disturbance modes. These higher-order terms play a key role in the stability of the algorithm. Therefore, the PCC algorithm was found to be unstable, while the PC2B algorithm was found to be stable and therefore prevented growth of numerical errors.

5. A numerical experiment with grid refinement showed that the PCC algorithm did not exhibit convergence with the expected order of accuracy. Because this algorithm was consistent, the absence of a converging trend confirms that the algorithm is unstable for the nonlinear equations governing the rotor wake.

6. The numerical experiment also showed that the PC2B algorithm exhibited second-order accuracy as well as convergence of numerical solution. For finer discretizations, with a wake filament discretization of 5° or smaller, the wake geometry solution was shown to be grid-independent. This confirmed that the PC2B algorithm was stable, consistent and convergent, and, therefore, suitable for nu-

merical modeling of time-accurate rotor wake dynamics. Therefore, the PC2B algorithm was chosen for the present free-vortex wake analysis.

8.2.3 Comparison With Experiments

The numerical analysis of the free-vortex wake solution algorithms ensured that the discretized solutions converge to the "exact" solution of the governing vorticity transport theorem. The numerical solution was then compared against experimental measurements of rotor wakes to validate the physics modeling of the present analysis. Comparisons were made of wake geometry measurements made using various flow visualization techniques. Comparisons were also made with experimental measurements of rotor induced velocity field and performance characteristics to validate the predictive capability of the present analysis. A summary of these results is now presented.

Comparison with Steady-State Measurements

The steady-state results obtained using the present analysis are important from the point of view of overall rotor performance predictions. The predictions obtained using the present analysis were compared with wake geometry measurements, rotor induced velocity field, as well as rotor performance measurements.

1. The predictions obtained using the present analysis showed a good agreement with laser light sheet measurements of the tip vortex locations for one- and two-bladed isolated rotors. The predictions of time-averaged rotor induced velocity field also correlated well with the corresponding inflow measurements obtained using laser Doppler velocimetry. The bound circulation distribution for these

rotors was estimated using experimental measurements of the velocity field surrounding the rotor blade(s). For the one-bladed rotor, the predicted bound circulation distribution agreed closely with the experimentally deduced results. For the two-bladed rotor, the predicted loading distribution was found to be essentially the same as that for the one-bladed rotor. The corresponding experimental measurements, however, showed some uncertainties because of close proximity of the returning wake to the rotor blades.

2. The predicted tip vortex displacements for a Mach-scaled four-bladed rotor operating at several advance ratios were found to be in good agreement with experimental results obtained using shadowgraphy. At the front of the rotor disk, the tip vortices were found to initially convect above the rotor TPP. The present analysis was able to correctly predict this physical trend.

3. The lateral and inflow linear inflow gradients are important for modeling the rotor aerodynamics in forward flight. The predicted lateral/longitudinal inflow distributions were compared with experimental measurements of the time-averaged velocity field, and found to give a good agreement. The corresponding predictions of the tip vortex geometry also showed a good agreement with experimental observations using laser light sheet flow visualization.

4. The present analysis could also be applied to study rotor performance trends. The predictions showed a good agreement with measured values of rotor thrust and power in both hovering and forward flight. The total power predictions were found to be somewhat sensitive to the modeling of airfoil lift/drag characteristics. A non-linear airfoil model was incorporated into the present analysis, which enabled predictions of rotor performance degradation because of blade stall.

5. The present methodology can be extended to study multiple rotors, such as tandem/coaxial or quad-rotor configurations. The multiple rotor analysis can also be applied to study ground effect by using a mirror-image configuration. Although this was outside the scope of the present work, some representive results have been shown.

Comparison with Time-Dependent Measurements

To validate the present time-accurate free-vortex wake methodology, the predicted results were compared with available time-dependent experimental measurements of rotor flow fields. After validation against experiments, the analysis was used to predict some rotor flow fields of practical interests.

1. Hovering rotor wakes often showed presence of vortex instabilities in the wake. These instabilities manifest in the form of aperiodicity of the wake, i.e., deviations from a periodic, axisymmetric wake structure. The wake stability analysis developed as a part of the present work provides predictions of the growth rate of such instabilities in the rotor wake. The results obtained using the stability analysis for the growth of aperiodicity in the rotor wake showed good agreement with experimental measurements. The exponential growth of aperiodicity for a given experimental set-up was found to remain constant from one test to another, despite of variations in the absolute magnitudes of aperiodicity.

2. Aperiodicity in the vortical rotor wake could also be simulated in the time-accurate free-vortex calculations by imposing a random disturbance velocity field to model turbulence and recirculation effects. The predictions obtained using such a disturbance field showed the same behavior as found in rotor wake

experiments and was characterized by the presence of tip vortex pairing in the far wake.

3. The time-accurate wake model was shown to provide good predictions of the rotor response following a ramp increase in rotor collective pitch. Predictions of rotor thrust, mean induced inflow, as well as blade flapping response were found to agree closely with experimental measurements. The rotor response in this case was found to be dominated by the dynamic evolution of the trailed wake (tip vortex) system and not the unsteady aerodynamic effects associated with the shed wake or apparent mass effects. Dynamic inflow models use an apparent mass term to model the time-lag in inflow build-up following a change in blade pitch inputs. The present calculations verified that this was actually be a non-inertial effect resulting from the dynamics of trailed vorticity.

4. The present analysis was also applied to study the rotor inflow response resulting from oscillatory collective and cyclic pitch inputs. The inflow frequency response showed a good agreement with experimental measurements for both cyclic and collective pitch inputs.

5. The gain of the inflow frequency was found to be highly biased towards the blade tips. The maximum in the inflow gain was found to correspond to the spanwise location of the maximum blade lift, consistent with a combined blade-element/momentum theory. This observation also confirmed that the tip vortices are indeed the most dominant flow features in the rotor wake, and the effects of inboard trailed/shed vorticity sheet are relatively small.

6. The free-vortex wake methodology was successfully applied to axial as well as inclined descending flight through the vortex ring state. The predictions showed

a good agreement with available experimental results for induced power and averaged induced velocity through the rotor.

7. The induced power in low-speed descending flight was found to closely follow the non-physical momentum theory solution in these flight conditions. Both experimental measurements and the present predictions suggested that the induced power showed the momentum theory trend with small deviations. These deviations could be quantified as an additional induced power loss factor. The predictions of this power loss factor for axial descent obtained using the present analysis showed a good agreement with the values deduced from experimental measurements.

8. The methodology was also applied to predictions of the vortex ring state boundary. This is important from piloting perspective to help identify the flight conditions where the rotor may experience significant blade flapping, and the pilot may have control difficulties. The VRS boundary was estimated based on the relative magnitude of oscillations in the rotor thrust, torque or flapping response. Although traditional wisdom suggests that the rotor will enter VRS in axial descent, the present results showed presence of significant oscillations in the rotor response in forward flight. The VRS boundary was also found to extended into regions of descending flight with significant forward flight speeds.

Numerical Experiments Using the Present Analysis

After the validation study, the present analysis was applied to study the rotor response under maneuvering flight conditions with imposed rotor angular rates. A parametric study was performed to better understand the effects of maneuver related wake distortions on the overall rotor response. A summary of these results is now presented.

1. The present methodology was applied to examine the effects of pitch and roll maneuvers in hovering flight. Kinematic considerations alone suggest a linear inflow gradient perturbation to the mean (ideally uniform) inflow distribution in hover. The effects of wake distortions on the inflow distribution, at least in hover, were found to be in a sense opposite to that expected based on kinematic considerations alone.

2. The ratio of wake-induced inflow gradient perturbations to the kinematic inflow perturbations was found to be almost constant for different pitch/roll rates at a given rotor thrust coefficient. This observation supports the idea of using a "wake distortion factor" to model the maneuver related wake distortion effects. However, such a wake distortion factor was found to vary with rotor thrust coefficient, as well as with rotor geometric parameters like the blade flapping frequency (hinge offset). Therefore, the values of wake distortion factors must be determined empirically, either by using experiments or analytical tools like the present free-vortex wake model.

3. In forward flight, the effects of wake distortion on the inflow gradient was found to vary significantly with advance ratio. In this case, a simple model in the form of a wake distortion factor was found to be insufficient to completely represent the maneuver-induced effects on the rotor wake.

4. The rotor blade flapping response was calculated in the present analysis by time-integration of the flapping equation in a manner coupled with the rotor wake equations. In maneuvering flight, an approximate flapping response could be estimated based on the linear inflow perturbations. In hovering flight, this approach was found to give good estimates of the flapping response when the wake

distortion effects were included in the inflow gradient perturbations. In forward flight, however, this approach did not give proper representations of the flapping response even though the wake distortion effects were included in the linear inflow gradients. This suggests that a simple linear inflow model is not completely representive of the rotor flow field in maneuvering forward flight. A complete non-linear inflow model, like the present time-accurate free-vortex wake model, would be necessary to properly model the aerodynamic effects associated with such maneuvers.

8.3 Recommendations for Future Work

1. Numerical experiments performed to examine the effects of maneuvers on the rotor wake showed significant effects on the rotor response, depending on the operating conditions. In the present study, the maneuvering motion was idealized as angular rates about the rotor hub or the center of the rotor disk. Helicopter maneuvers typically involve angular motions about the center of gravity of the helicopter, which is always vertically offset from the rotor hub. A parametric study of angular rates about a proper maneuver axis would be necessary to properly understand the practical implications of wake distortions resulting from such maneuvers.

2. The time-accurate wake model can be integrated with a flight-mechanical model to model the dynamics of a complete helicopter. For example, an increase in collective pitch in hovering flight should produce excess thrust and accelerate the helicopter vertically upwards. A longitudinal pitch input in hover should result in a pitching motion, which would tilt the TPP, thereby generating a propulsive

force and forward motion. This will provide first-principle based methodology to study various non-periodic flight conditions such as a low-speed descent, and may also help in a better understanding of the so-called off-axis response problem.

3. The present analysis is based on a simplified model for the blade lift solution. The airfoil model is essentially that based on thin airfoil theory with linear aerodynamics. Clearly, a simple linear aerodynamic model for airfoil characteristics is not representive of realistic rotor performance because even under moderate flight conditions the rotor blades may experience stall and compressibility effects. Some improvement in airloads prediction may be achieved using a localized CFD solution surrounding the blade(s) along with a Lagrangian free-vortex wake model for the far-wake.

4. The present free-vortex wake model solves for only the convective part of vorticity transport equation. The viscous diffusion effects are superimposed using an semi-empirical vortex core model. The vorticity stretching effects, however, are not included. In hovering flight the effects of vortex stretching appear to be negligible, as suggested by the good agreement between predictions and experimental measurements. However, in general the rotor wake vortices experience significant strain because of wake distortions. The viscous diffusion may also be different depending on the extend of vorticity stretching. A better understanding of these effects is necessary to properly model the rotor wake behavior, especially during non-steady flight conditions like maneuvers and low-speed descents. A combined experimental and analytical modeling study would provide further insights into these vorticity stretching and diffusion effects.

5. The present analysis can accurately predict the rotor induced velocity field. However, the rotor dynamic model is a simple rigid blade model. Integrating the present analysis with a comprehensive rotor/helicopter analysis code will help in understanding the various effects of blade/vortex interactions on rotor performance and vibration levels. Coupling an aeroacoustic analysis with the induced inflow calculations obtained using the present method would help in identifying sources of BVI noise, and provide an improved understanding of various noise control strategies.

6. Multiple rotor configurations can be examined using the present analysis. This applicable to problems involving main-rotor/tail-rotor interactions, or multi-rotor aircraft such as tandem and coaxial configurations. The present methodology may be applied to study the susceptibility of multi-rotor configurations such as a tandem (e.g., the Chinook) or a side-by-side rotor (e.g., the V-22 Osprey) to the vortex ring state phenomenon during descending flight. The rotor performance benefits resulting from ground effect can also be quantified using the present analysis by solving for a mirror-image rotor system.

Appendix A

Tip Vortex Model

The free-vortex wake analysis described in this dissertation is based on inviscid, incompressible flow. Nevertheless, the formation of the wake behind any lifting wing must be considered at some level as a viscous phenomenon. Typically, viscous phenomena are restricted to much smaller length scales compared to potential flow phenomena. However, the epicycloidal nature of the rotating wing wake geometry (the "returning" wake) implies that the detailed, viscous structure of the vortices is important even at large length scales, of the order of the rotor radius. Therefore, every aerodynamics model for the rotor wake must include effects of viscosity, such as wake formation and evolution, which are important even under moderate operating conditions. In the present analysis, the viscous core structure and associated diffusion is incorporated using a semi-empirical vortex model.

A viscous core model for trailing vortices is also important in other applications of vortex methods. Because of the persistence of aircraft tip vortices, there exists a wake-hazard problem that is a major factor limiting the capacity of large airports (Ref. 117). The prediction of induced velocities and strength history of the tip vortices as they trail behind the aircraft has been the subject of much research over the past five decades (e.g., Refs. 118–121). However, the properties of the vortex such as its turbulence structures and the related diffusive and dissipative characteristics are still not fully understood. Also, there had been no general has yet been developed to properly relate the properties of the trailed vortices to the aerodynamic lifting characteristics of the generating wing.

For rotating-wing aircraft such as helicopter, the understanding of the blade tip vortices is essential to predict the performance, vibration, and acoustics of the rotor. Unlike a fixed-wing aircraft where the vortices trail downstream, rotor blade tip vortices will always lie relatively close to the rotor. Under some conditions, these vortices may closely interact with following blades. This is known as blade vortex interaction (BVI), and can manifest as high rotor vibrations and strong impulsive noise, e.g., Refs. 122 and 123. Rotor tip vortices can also interact with the fuselage (Refs. 124, 125) and the tail rotor or empennage (Ref. 126), thereby affecting overall performance of the aircraft. An improved modeling capability of tip vortices directly translates into improved predictions of rotor performance and acoustics (Refs. 13, 127–130).

A complete description of a viscous trailing vortex requires solution of the full Navier-Stokes (N-S) equations. Analytical solution to these non-linear set of equations is not possible. Closed-form solutions can only be obtained by further simplifying the governing equations, e.g., Refs. 70, 131–133. Numerical solutions are limited by computational resources and also developments in turbulence modeling. The complicated boundary conditions and the fact that swirl velocity is more dominant than the other velocities make numerical approaches even more difficult. Therefore, several semi-empirical models have been developed, e.g. Refs. 134–137, and have been applied to modeling the tip vortices with generally good results.

Algebraic models are popular in engineering applications because these are computationally efficient. One of the most commonly used models is the algebraic model suggested by Scully & Sullivan (Ref. 134) and also by Kaufmann (Ref. 135). This model predicts the overall velocity distribution very well, but for both fixed and rotating wings the model tends to underpredict the peak swirl velocity (Refs. 138, 137). A family of algebraic velocity models was proposed by Vatistas (Ref. 136), which showed a good comparison with the observed swirl velocities (Refs. 90, 130, 139). The success of these algebraic models in predicting vortex velocities was one motivation for the development of the present model, which extends the approach to a representation of the axial and radial velocities. These velocity profiles are a solution to a simplified form of the Navier-Stokes (N-S) equations, and are obtained following an approach similar to Newman (Ref. 132). The swirl velocity profile is identical to that given by Vatistas (Ref. 136). The derived models showed a very good comparison with tip vortex measurements for both fixed-wing and rotating-wings.

A.1 Previous Formulations

The swirl velocity field induced by a trailing vortex resembles that of a potential vortex at large distance from the vortex centerline. Near the vortex centerline, however, the velocity field resembles a solid-body rotation with a zero induced velocity at the center. The induced velocity reaches a peak at some distance from the center, which is referred to as a core radius. With this general picture of the induced swirl velocity, a model for the tip vortex can be hypothesized.

The simplest model for a vortex with a finite core is the Rankine vortex (Ref. 140). This model exhibits the key features of a viscous vortex, that is solid body-like rotation near the vortex center, and a free (potential) vortex away from the center, i.e.,

$$V_\theta(\bar{r}) = \begin{cases} \left(\dfrac{\Gamma_v}{2\pi r_c}\right)\bar{r}, & 0 \leq \bar{r} \leq 1, \\ \\ \left(\dfrac{\Gamma_v}{2\pi r_c}\right)\dfrac{1}{\bar{r}}, & \bar{r} > 1. \end{cases} \tag{1.1}$$

where $\bar{r} = r/r_c$ is the non-dimensional radial location. However, the swirl velocity, and so the vorticity and circulation, are discontinuous at the vortex core.

Another vortex model given by Lamb (Ref. 70), and also by Oseen, is a solution to the one-dimensional N-S equations, i.e., a solution for swirl velocity with the assumption that the axial/radial velocities are zero. The Lamb-Oseen vortex model for the swirl velocity gives

$$V_\theta(r) = \frac{\Gamma}{2\pi r}\left[1 - \exp\left(-\frac{r^2}{4\nu t}\right)\right] \tag{1.2}$$

The viscous core radius is the radial location where the swirl velocity is a maximum. This can be solved by differentiating the above equation w.r.t. r, and setting the derivative to zero. In order to eliminate the parameter $(4\nu t)$ from the solution, a change of variables is introduced using

$$x = \frac{r}{\sqrt{4\nu t}} \tag{1.3}$$

Therefore, the Lamb swirl velocity profile becomes

$$V_\theta(x) = \frac{\Gamma}{2\pi x\sqrt{4\nu t}}\left[1 - \exp\left(-x^2\right)\right] \tag{1.4}$$

The extrema in $V_\theta(x)$ are found using

$$\begin{aligned} \frac{dV_\theta}{dx} &= \frac{\Gamma}{2\pi\sqrt{4\nu t}}\left[-\frac{1}{x^2} + \frac{1}{x^2}\exp\left(-x^2\right) + 2\exp\left(-x^2\right)\right] \\ &= \frac{\Gamma}{2\pi x^2\sqrt{4\nu t}}\left[\left(1 + 2x^2\right)\exp\left(-x^2\right) - 1\right] \\ &= 0 \end{aligned} \tag{1.5}$$

Therefore, the extrema in the swirl velocity profile are given by the solutions of the equation

$$f(x) = \left(1+2x^2\right)\exp\left(-x^2\right) - 1 = 0 \tag{1.6}$$

The zero of $f(x)$ in Eq. 1.6 can be easily found graphically or numerically as $x = 1.1209$. An analytical solution is also possible in terms of the Lambert-W function, which is given by the relation

$$W(x) + \exp\left(W(x)\right) = x \tag{1.7}$$

Because the equation $y\exp(y) = x$ has an infinite number of solutions y for each (non-zero) value of x, the Lambert-W function has an infinite number of branches. However, exactly one of these branches is analytic at 0. These branches are numbered from the negative real-axis, and therefore $W(k,x)$, for integer k corresponds to the k^{th} branch of the Lambert-W function.

Therefore, the above function, $f(x)$, has three zeros, given by

$$\begin{aligned} & x = 0, \quad x = \pm\frac{1}{2}\sqrt{-2-4W\left(-1,-\frac{e^{-\frac{1}{2}}}{2}\right)} \\ \text{i.e.,} \quad & x = 0, \quad x = \pm 1.1209064227785340320 \end{aligned} \tag{1.8}$$

The first zero clearly corresponds to the center of the vortex core, where the swirl velocity is a minimum (zero). The second positive root gives the viscous core radius, where the swirl velocity is a maximum, and the third negative root is ignored. Therefore, the swirl velocity is maximum when

$$x = \frac{r}{\sqrt{4\nu t}} = 1.1209064 \tag{1.9}$$

i.e., at the radial location

$$\begin{aligned} r^2 &= (1.1209064)^2 4\nu t \\ &= 4\alpha\nu t \end{aligned} \tag{1.10}$$

where $\alpha = 1.25643$, and the viscous vortex core radius is given by

$$r_c = \sqrt{4\alpha\nu t} \tag{1.11}$$

The Lamb-Oseen vortex model can now be written in the form

$$V_\theta(\bar{r}) = \frac{\Gamma_v}{2\pi r_c}\left(\frac{1 - e^{-\alpha\bar{r}^2}}{\bar{r}}\right) \tag{1.12}$$

It is interesting to note that the well-known "Scully model" (Ref. 23) is, in fact, an approximation to the Lamb vortex. Using a vortex length scale of $\tilde{r}_c = \sqrt{4\nu t}$, the Lamb vortex model (Eq. 1.2) can be written as a function of non-dimensional radial distance $\tilde{r} = r/\tilde{r}_c$

$$V_\theta(\tilde{r}) = \frac{\Gamma}{2\pi\tilde{r}_c\tilde{r}}\left[1 - e^{-\tilde{r}^2}\right] \tag{1.13}$$

using a series expansion for the exponential term and ignoring higher order terms, it can be shown that

$$\begin{aligned} V_\theta(\tilde{r}) &= \frac{\Gamma}{2\pi\tilde{r}_c\tilde{r}}\left[1 - \frac{1}{1 + \tilde{r}^2 + \frac{\tilde{r}^4}{2} + \cdots}\right] \\ &\approx \frac{\Gamma}{2\pi\tilde{r}_c}\left(\frac{\tilde{r}}{1 + \tilde{r}^2}\right) \qquad \text{for small } \tilde{r} \\ &\approx \frac{\Gamma}{2\pi}\left(\frac{r}{r^2 + \tilde{r}_c^2}\right) \end{aligned} \tag{1.14}$$

This is the so-called Scully vortex model (Ref. 23).

The Lamb model has been found to give improved comparison between the observed and predicted tip vortex induced velocities (Ref. 90). Squire (Ref. 118) showed that the solution for a trailing vortex is identical to the Lamb solution with the time, t, replaced by z/V_∞. He further proposed inclusion of an apparent or eddy viscosity parameter δ to account for effects of turbulence on the vortex diffusion. An effective origin offset was proposed to give a finite vortex core at the origin of the trailing vortex at the wing. Therefore, the core radius is given by

$$r_c = \sqrt{4\alpha\delta\nu\left(\frac{z+z_0}{V_\infty}\right)} \tag{1.15}$$

The Burgers (Ref. 131) vortex model includes a swirl velocity similar to the Lamb model, along with a linear distribution of radial velocity. However, this implies a constant axial velocity, which is not consistent with experimental observations. Also, the linearly increasing radial velocity makes the model applicable to only small regions near the vortex center.

Newman (Ref. 132) derived exponential solution for all three components of velocity of a trailing vortex by solving a simplified version of the three-dimensional N-S equations. The swirl velocity in this case is the same as that given by the Lamb-Oseen model. This model was shown to give good correlation with tip vortex measurements (Ref. 119).

One interesting observation made from these models is that the velocity field of a trailing vortex is self-similar. That is, the velocity profile can be represented using a single function by appropriately scaling the distances and velocities. This self-similarity of vortex induced velocity profile is also observed in experimental measurements (see, e.g., Ref. 90). Therefore, the length scale corresponding to the vortex core radius is very important. In the present analysis, a semi-empirical model for the vortex core radius growth model is used. The core growth is represented by a model similar to that given by Eq. 1.15, and the eddy viscosity parameter must be estimated from experimental measurements.

A.2 Effects of Turbulence on Vortex Diffusion

Clearly, the most important parameter in modeling the trailing vortices is the characteristic length scale of the vortex, i.e., the core radius. The effects of turbulence on the growth of the vortex core are not clear. Experimental results may lead to contradictory conclusions. There appears to be some evidence that the core growth is dominated by viscous (laminar) effects, and the turbulent effects are negligibly small. However, there is also some experimental evidence suggesting that turbulent effects increase the diffusion of vortex core. Following an approach similar to Iversen (Ref. 141), Bhagwat & Leishman (Ref. 90) have shown a correlation of the form

$$\overline{V}_{\theta_{max}} \left(\overline{d}+\overline{d}_0\right)^{\frac{1}{2}} = k \tag{1.16}$$

to be valid, where the constants d_0 and k were determined empirically (see Ref. 90). The non-dimensional velocity, $\overline{V}_{\theta_{max}}$, and non-dimensional downstream distance, $\overline{d}$, are given by

$$\overline{V}_{\theta_{max}} = \left(\frac{V_{\theta_{max}}}{V_\infty}\right)\left(\frac{V_\infty c}{\Gamma_v}\right) \tag{1.17}$$

$$\overline{d} = \left(\frac{z}{c}\right)\left(\frac{\Gamma_v}{V_\infty c}\right) \tag{1.18}$$

respectively. Example correlation curves are shown in Figs. A.1 and A.2. In both cases, the measurements show a definitive trend as given by Eq. 1.16. With the transformation $t = z/V_\infty$, the correlation given by Eq. 1.16 shows that

$$V_{\theta_{max}} \propto \sqrt{\frac{\Gamma_v}{t}} \tag{1.19}$$

The maximum swirl velocity as given by the Lamb or Newman model is

$$V_{\theta_{max}} \propto \frac{\Gamma_v}{2\pi r_c} \propto \frac{\Gamma_v}{\sqrt{\delta \nu t}} \tag{1.20}$$

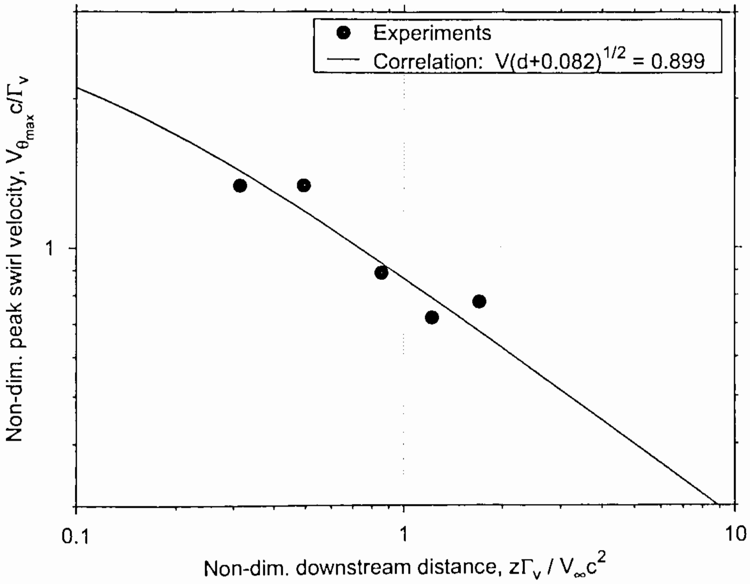

Figure A.1: Correlation of peak swirl velocity with fixed-wing tip vortex measurements from Ref. 119.

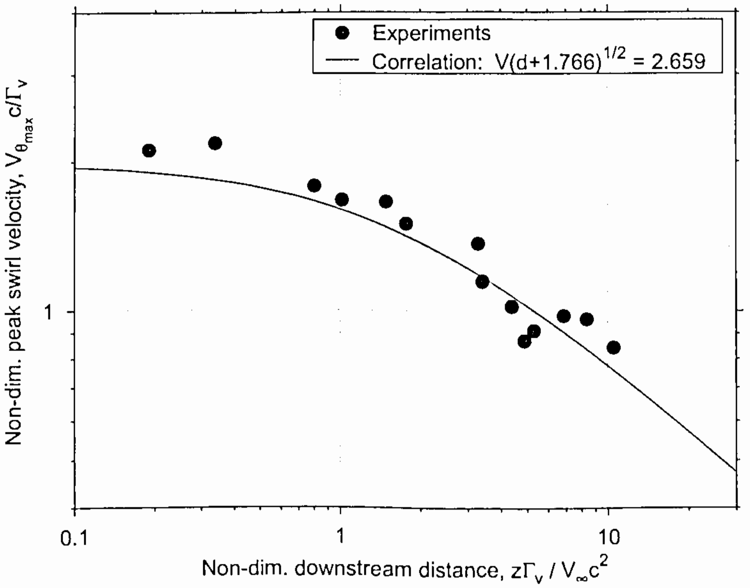

Figure A.2: Correlation of peak swirl velocity with rotor tip vortex measurements from Ref. 90.

Therefore,

$$V_{\theta_{max}} \propto \sqrt{\frac{\Gamma_v}{t}}\sqrt{\frac{1}{\delta}\left(\frac{\Gamma_v}{\nu}\right)} \tag{1.21}$$

Comparing these two latter expressions (Eqs. 1.19 & 1.21), it follows that the apparent or eddy viscosity coefficient, δ, is proportional to the vortex Reynolds number, (Γ_v/ν). Therefore, the correlations reported by Iversen (Ref. 141) and by Bhagwat & Leishman (Ref. 90) support Squire's hypothesis, which relates the eddy viscosity coefficient to the vortex Reynolds number by the equation

$$\delta = 1 + a_1 \frac{\Gamma_v}{\nu} \tag{1.22}$$

Therefore, vortex diffusion is expected to increase with increasing vortex Reynolds number. However, a recent analysis reported by Cotel & Breidenthal (Ref. 142) suggests to the contrary. They conclude based on stratified entrainment of the vortex core that the vortex diffusion is dominated by viscous (laminar) effects, and effects of turbulence are almost negligible. Similar inference is also drawn from rotating wing measurements (see Refs. 143). Results from several trailing vortex measurements are presented in the form of non-dimensional core growth rate, b_1, as

$$b_1 = 2\sqrt{\frac{t}{\Gamma_v}\frac{dr_c}{dt}} \tag{1.23}$$

The growth rate is shown to be inversely proportional the vortex Reynolds number, thus suggesting laminar viscous diffusion. Indeed, using the core growth model as given by Eq. 1.11 or Eq. 1.15 it follows that

$$b_1 \propto \left(\frac{\Gamma_v}{\nu}\right)^{-\frac{1}{2}} \quad \Longrightarrow \quad \delta = \text{constant} \tag{1.24}$$

Note that $\delta = 1$ corresponds to the laminar case, and a small value of δ would suggest that the core growth is essentially laminar. However, the experimental data reported in Ref. 142 was from small-scale tests and was restricted to vortex Reynolds numbers smaller than 10^5. Iversen (Ref. 141) reports that the turbulent effects in the vortex core are apparent only for vortex Reynolds numbers greater than 10^5. This may be part of the reason why turbulence effects are not apparent from the results.

Figure A.3 shows similar results with additional experimental measurements from Refs. 139, 143–154 including full-scale fixed-wing as well as rotary-wing trailing vortices. The predominantly dominant laminar trend, as in Ref. 142, is shown along with the trends using Squire's hypothesis. For smaller Reynolds numbers a the experiments show a somewhat laminar-like trend. Yet, at larger Reynolds numbers the core growth rate appears to remain nominally constant. The trend lines for Squire's hypothesis suggest that this behavior is because of turbulence effects. Note that the trend given by Squire's hypothesis describes the vortex core growth at both low and high vortex Reynolds numbers.

The same results are presented again in Fig. A.4 as the apparent (eddy) viscosity coefficient, δ as a function of vortex Reynolds number. Evidently, the turbulence effects are manifest as increasing apparent viscosity with increasing Reynolds number. Note that values of $\delta < 1$ are not physically realistic because they imply turbulent mixing is even smaller than the laminar case. Various uncertainties in experimental measurements may lead to such anomalous inconsistencies. The overall experimental evidence, however, strongly suggests the validity of Squire's hypothesis that the turbulence effects in the vortex core are directly proportional to the vortex Reynolds number. Two values for the constant a_1 are shown in Fig. A.4. It appears that the rotary-wing results show a slightly higher viscous diffusion corresponding to an average value of $a_1 = 2 \times 10^{-4}$, while the fixed-wing results show a lower diffusion with $a_1 = 5 \times 10^{-5}$. Figure A.5 shows the values of a_1 corresponding to these experiments. Clearly, the average value of a_1 is of the order of 10^{-4} to 10^{-5} in all the cases.

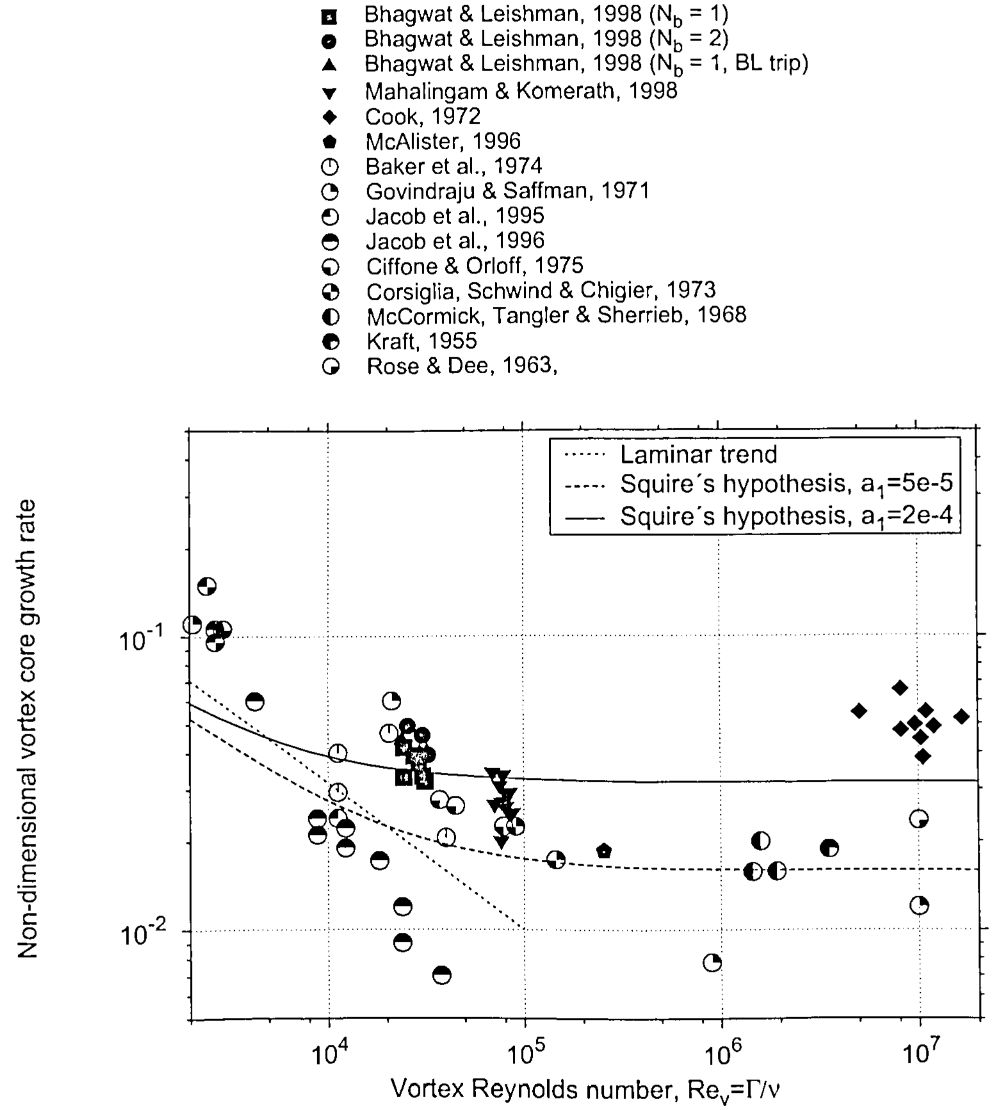

Figure A.3: Non-dimensional vortex core growth rate for several trailing vortex measurements as a function of vortex Reynolds number.

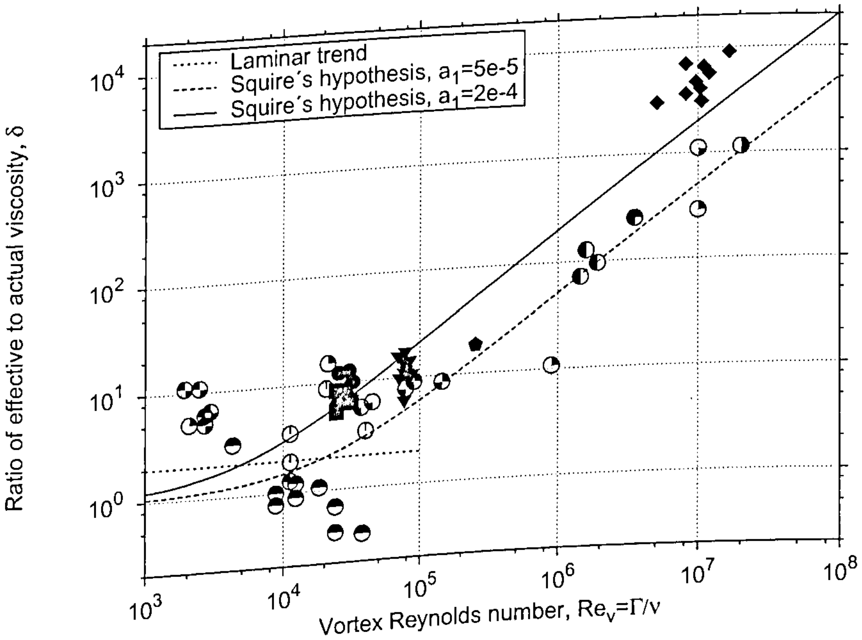

Figure A.4: The apparent viscosity coefficient deduced from several trailing vortex measurements as a function of vortex Reynolds number.

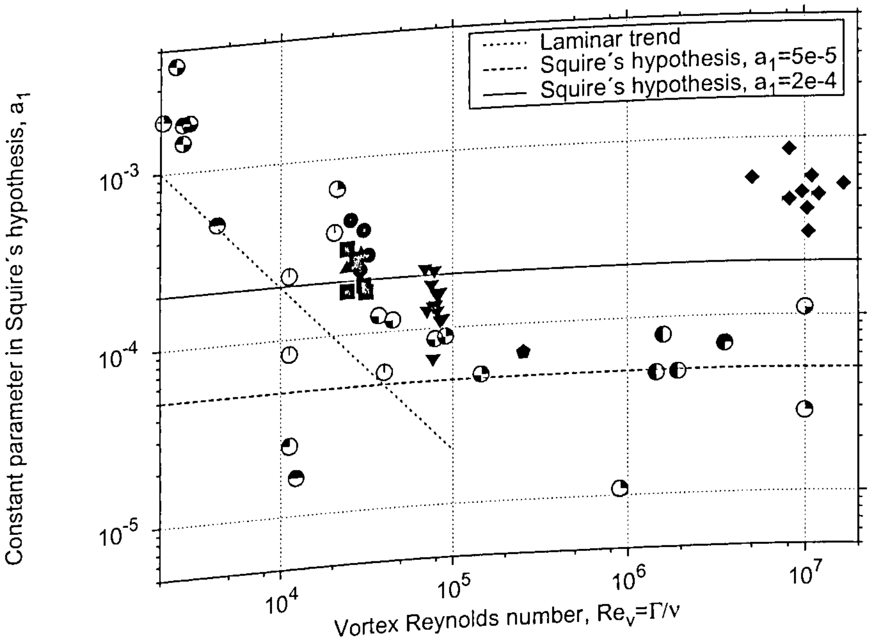

Figure A.5: Apparent or eddy viscosity parameter in the vortex core growth model based on Squire's hypothesis (Ref. 118).

A.3 Self-Similarity of Vortex Velocity Profiles

The tip vortex flow can be examined in a cylindrical coordinate system with the origin at the blade tip. The vortex trajectory, which is along the longitudinal axis of the vortex, z, is fixed relative to the wing tip, i.e., the vortex is examined under steady flow conditions. It should be noted that the axial velocity relative to the wing is the sum of the freestream velocity and the vortex induced velocity, i.e., $V_\infty + V_z$. The induced velocities are assumed to dependent only on r and z, i.e., the vortex is assumed to be axisymmetric. This is a reasonable assumption because, in practice, even though both fixed and rotating wing tip vortices are not completely axisymmetric, the asymmetry is observed only near the vortex origin and is usually small. As the vortex convects downstream, the velocity profiles become axisymmetric.

The governing (N-S) equations in cylindrical coordinates for incompressible flow are:

Continuity

$$\frac{1}{r}\frac{\partial}{\partial r}(rV_r) + \frac{\partial V_z}{\partial z} = 0 \qquad (1.25)$$

$r - momentum$

$$V_r\frac{\partial V_r}{\partial r} + V_\infty\frac{\partial V_r}{\partial z} + V_z\frac{\partial V_r}{\partial z} - \frac{V_\theta^2}{r} = -\frac{1}{\rho}\frac{\partial p}{\partial r} + \nu\left[\nabla^2 V_r - \frac{V_r}{r^2}\right] \qquad (1.26)$$

$\theta - momentum$

$$V_r\frac{\partial V_\theta}{\partial r} + V_\infty\frac{\partial V_\theta}{\partial z} + V_z\frac{\partial V_\theta}{\partial z} + \frac{V_r V_\theta}{r} = \nu\left[\nabla^2 V_\theta - \frac{V_\theta}{r^2}\right] \qquad (1.27)$$

$z - momentum$

$$V_r\frac{\partial V_z}{\partial r} + V_\infty\frac{\partial V_z}{\partial z} + V_z\frac{\partial V_z}{\partial z} = -\frac{1}{\rho}\frac{\partial p}{\partial z} + \nu\left[\nabla^2 V_z\right] \qquad (1.28)$$

where the operator ∇^2 is given by

$$\nabla^2 = \frac{\partial^2}{\partial r^2} + \frac{1}{r}\frac{\partial}{\partial r} + \frac{\partial^2}{\partial z^2} \qquad (1.29)$$

The required boundary conditions can be obtained by assuming that the vortex is generated as a "free" vortex, i.e., a potential vortex of strength Γ_v at $z = 0$, and it diffuses until at large distances the vortex induced velocities become zero — see Ref. 132. These boundary conditions can be formalized as:

1. At $z = 0$, $V_\theta = \Gamma_v/2\pi r$ and $V_z, V_r = 0$. Note that there is a singularity at $r = 0$.

2. For $z > 0$, $V_\theta, V_z, V_r \longrightarrow 0$ for large r.

3. As $z \longrightarrow \infty$, $V_\theta, V_z, V_r \longrightarrow 0$ for all r.

The governing N-S equations are now rewritten in a non-dimensional form so as to allow some simplifications. The velocities are normalized with the freestream velocity, V_∞, i.e.,

$$\overline{V_i} = \frac{V_i}{V_\infty}, \quad i = r, \theta, z \tag{1.30}$$

The distances are normalized by the wing chord, c, i.e.

$$\overline{r} = \frac{r}{c} \quad \overline{z} = \frac{z}{c} \tag{1.31}$$

The pressure is normalized with the dynamic pressure

$$\overline{p} = \frac{p}{\rho V_\infty^2} \tag{1.32}$$

and the flow Reynolds number is given by

$$Re = \frac{V_\infty c}{\nu} \tag{1.33}$$

To simplify the governing equations, an ordering scheme may be employed to establish the relative magnitudes of the non-dimensional terms in the conservation laws. The swirl and axial velocities induced by the tip vortex are smaller as compared to the freestream velocity, typical values being 0.1 to 0.3 (see Refs. 90, 119, 139, 143, 155–

157), i.e. $\overline{V_\theta}$ and $\overline{V_z}$ are $O(\varepsilon)$. Typically the tip vortex core radius is of the order of the airfoil thickness (e.g., Refs. 130, 158), i.e., typically 5 to 15% of the wing or blade chord. The tip vortex can be observed, and induces significant velocities, for several chord lengths downstream of the generating wing. This implies that, if $\bar{z}$ is $O(1)$ then $\bar{r}$ is $O(\varepsilon)$. The continuity equation implies that the radial velocity, $\overline{V_r}$, is $O(\varepsilon^2)$. This is also consistent with the observation that the radial velocities induced by the tip vortices are very small (Ref. 119). The radial momentum equation (Eq. 1.26) indicates that the pressure, $\bar{p}$, is $O(\varepsilon^2)$. Typically, for a transport aircraft or a helicopter rotor, the chord Reynolds number is approximately 10^7. Even in wind tunnel experiments with scaled models, the Reynolds numbers are always greater than 10^4. Therefore, Re can be assumed to be $O(1/\varepsilon^4)$.

The conservation laws are now rewritten in the non-dimensional form with the order of magnitudes of each term being indicated below each term. Note that, all the variables are non-dimensional, but the overbar has been omitted.

Continuity:

$$\underset{\varepsilon}{\frac{1}{r}\frac{\partial}{\partial r}(rV_r)} + \underset{\varepsilon}{\frac{\partial V_z}{\partial z}} = 0 \tag{1.34}$$

$r-$ *momentum* :

$$\underset{\varepsilon^3}{V_r\frac{\partial V_r}{\partial r}} + \underset{\varepsilon^2}{\frac{\partial V_r}{\partial z}} + \underset{\varepsilon^3}{V_z\frac{\partial V_r}{\partial z}} - \underset{\varepsilon}{\frac{V_\theta^2}{r}} = \underset{\varepsilon}{-\frac{\partial p}{\partial r}} + \underset{\varepsilon^4}{\frac{1}{Re}\left[\nabla^2 V_r - \frac{V_r}{r^2}\right]} \tag{1.35}$$

$\theta -$ *momentum* :

$$\underset{\varepsilon^2}{V_r\frac{\partial V_\theta}{\partial r}} + \underset{\varepsilon}{\frac{\partial V_\theta}{\partial z}} + \underset{\varepsilon^2}{V_z\frac{\partial V_\theta}{\partial z}} + \underset{\varepsilon^2}{\frac{V_rV_\theta}{r}} = \underset{\varepsilon^3}{\frac{1}{Re}\left[\nabla^2 V_\theta - \frac{V_\theta}{r^2}\right]} \tag{1.36}$$

$z-momentum:$

$$
\begin{array}{ccccccccc}
V_r\dfrac{\partial V_z}{\partial r} & + & \dfrac{\partial V_z}{\partial z} & + & V_z\dfrac{\partial V_z}{\partial z} & = & -\dfrac{\partial p}{\partial z} & + & \dfrac{1}{Re}\left[\nabla^2 V_z\right] \\
\varepsilon^2 & & \varepsilon & & \varepsilon^2 & & \varepsilon^2 & & \varepsilon^3
\end{array}
\tag{1.37}
$$

An algebraic model for concentrated self-similar vortices, first suggested by Vatistas (Ref. 136), has shown good correlation with the swirl velocities induced by both fixed-wing and rotor tip vortices (Refs. 90, 130, 139). Therefore, the swirl velocity was assumed to be given by the Vatistas expression

$$V_\theta = \frac{\Gamma_v}{2\pi}\left\{\frac{r}{\left(r_c^{2n}+r^{2n}\right)^{1/n}}\right\} \tag{1.38}$$

with the exponent n taking integer values. Note that r_c is the viscous core radius of the tip vortex, that is the swirl velocity exhibits a maximum at $r = r_c$. This algebraic velocity profile is an approximation to the Lamb-Oseen solution (Eq. 1.12), i.e., an approximate solution to the one-dimensional N-S equation

$$V_\infty \frac{\partial V_\theta}{\partial z} = \nu\left[\nabla^2 V_\theta - \frac{V_\theta}{r^2}\right] \tag{1.39}$$

Also, the viscous core radius is given by Eq. 1.15 as described previously. Under these assumptions, the θ-momentum equation reduces to

$$V_r\frac{\partial V_\theta}{\partial r} + V_z\frac{\partial V_\theta}{\partial z} + \frac{V_r V_\theta}{r} = 0 \tag{1.40}$$

which is obtained by using Eq. 1.39 and Eq. 1.27. The other two momentum equations can be simplifies by further assuming that ε is small and, therefore, higher order terms in ε are negligible relative to the lower order terms. Therefore, Eq. 1.26 and 1.28 are reduced to

$$\frac{\partial p}{\partial r} - \frac{V_\theta^2}{r} = 0 \qquad O(\varepsilon^2) \tag{1.41}$$

$$\frac{\partial V_z}{\partial z} = 0 \qquad O(\varepsilon^2) \tag{1.42}$$

The continuity equation remains unchanged as both the terms are of the same order. Therefore, the axial and radial velocity components can be solved for by satisfying the continuity equation (Eq. 1.25) and Eq. 1.40. These components are given by

$$V_z = -\frac{A}{z}\left\{1 - \frac{r^2}{\left(r_c^{2n} + r^{2n}\right)^{1/n}}\right\} \tag{1.43}$$

$$V_r = -\frac{Ar}{2z^2}\left\{1 - \frac{r^2}{\left(r_c^{2n} + r^{2n}\right)^{1/n}}\right\} \tag{1.44}$$

where A is a constant. Following the approach taken by Newman (Ref. 132), the constant A may be determined based on the drag of the generating wing. The static pressure distribution in the vortex can be determined by integrating Eq. 1.41 with respect to r the radial momentum equation, i.e.,

$$p = \int_0^r \frac{V_\theta^2}{r} \tag{1.45}$$

The non-dimensional induced velocity profiles given by this model for different values of the parameter n are shown in Fig. A.6. As the parameter $n \to \infty$, the present model reduces to the Rankine vortex models with a solid body vortex core. The exponential velocity model proposed by Newman (Ref. 132) is also shown for comparison. For $n = 2$, the present closely resembles the Newman velocity model.

The results obtained using this model are now compared with experimentally measured vortex induced velocities. Figure A.7 shows the swirl and axial velocities in the tip vortex of a fixed wing, with experimental results from Dosanjh *et al.* (Ref. 119). Both velocity profiles are non-dimensionalized with the maximum velocity in the core, whereas the distance is normalized with the vortex core radius as defined previously. Both the measured velocity profiles are found to be self-similar and showed a good agreement with the present model for $n = 2$.

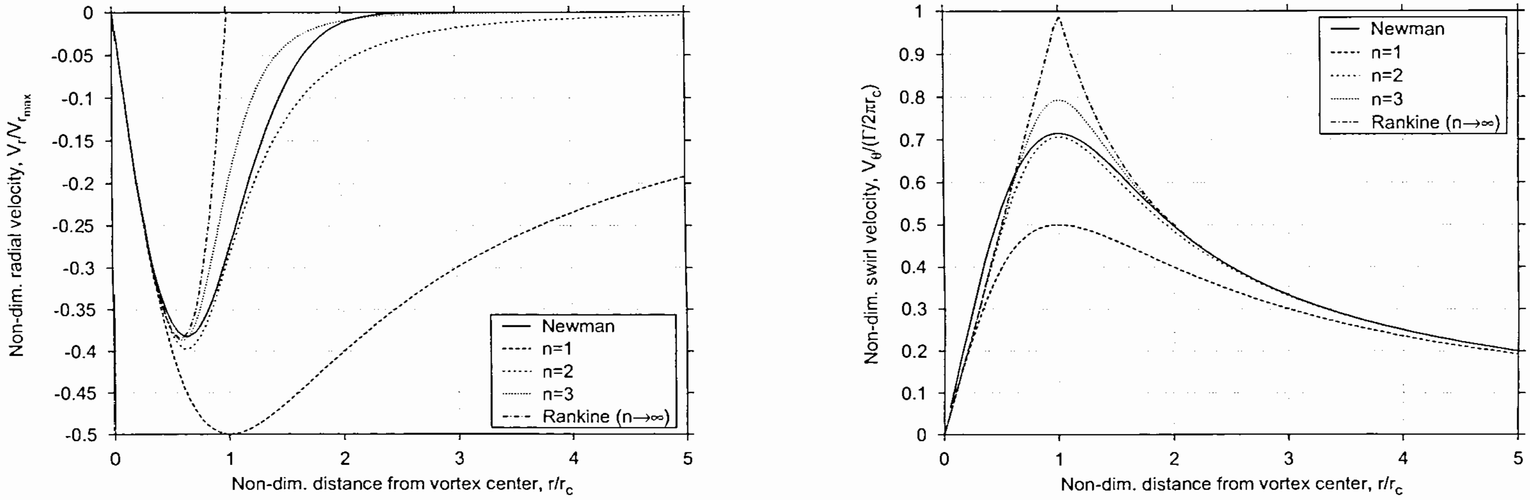
(a) Radial velocity

(b) Swirl (tangential) velocity

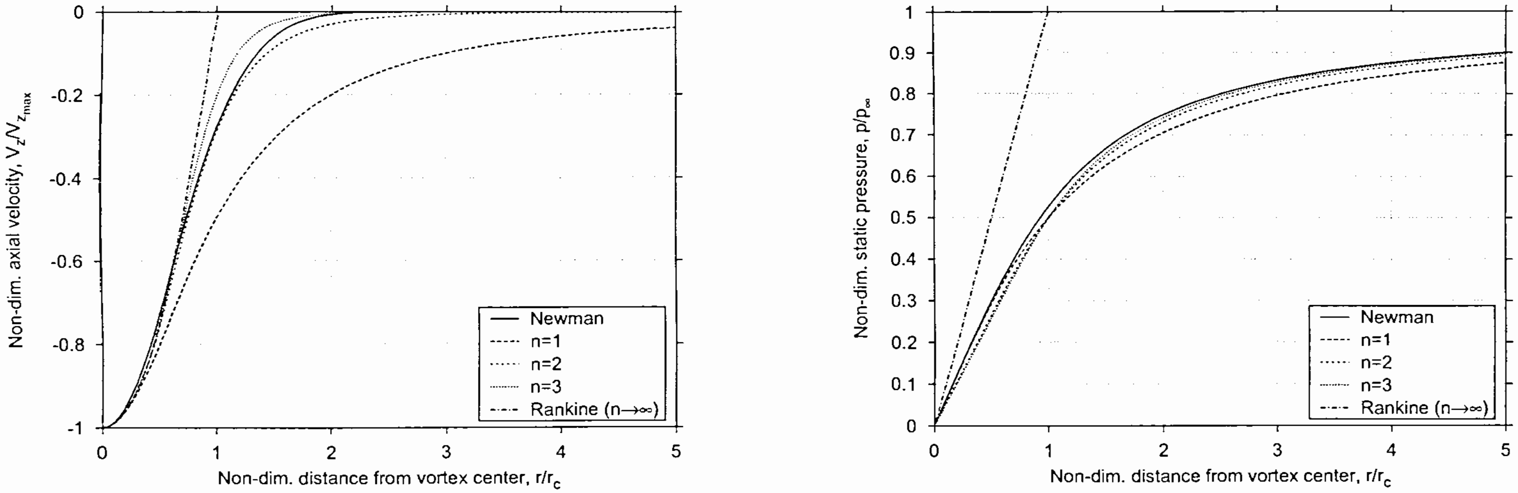
(c) Axial velocity

(d) Static pressure distribution

Figure A.6: Vortex induced velocities given by the present model for various values of the parameter n. Newman's model (Ref. 132) is also shown for comparison. (a) Radial velocity, (b) Swirl (tangential) velocity, (c) Axial velocity. (d) Static pressure distribution

(a) Swirl velocity

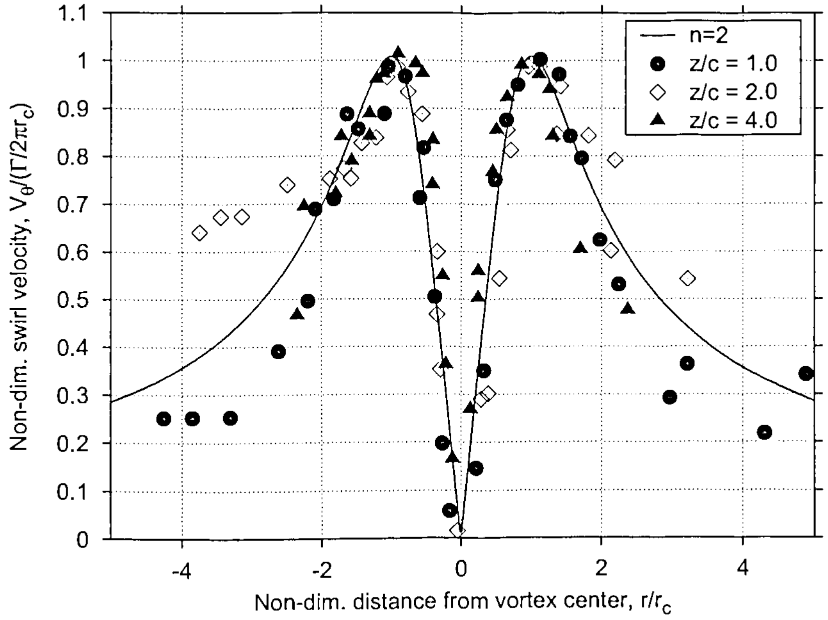

(b) Axial velocity

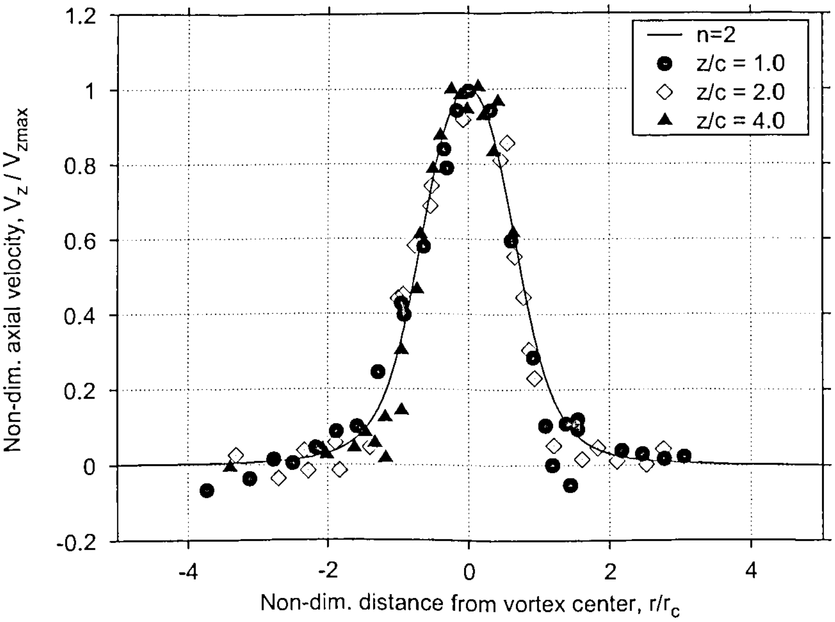

Figure A.7: Vortex induced velocities given by the present model for $n = 2$ compared with fixed-wing experimental measurements (Ref. 119). (a) Swirl velocity, (b) Axial velocity.

Figure A.8 shows similar results for a rotating wing tip vortex, with experimental data from Ref. 90. In this case the measured swirl velocity data showed a strongly self-similar profile consistent with the present model. The axial velocity measurements showed some deviations from the self-similar profile. However, overall agreement with the present model is good.

The radial velocities in the tip vortex are of a much smaller magnitude as described previously. Therefore, the radial velocities are more sensitive to measurement uncertainties, and accurate measurements of radial velocity are, in general, more difficult. The measured velocity distribution from Ref. 119 is shown in Fig. A.9. The measurements showed some fluctuations, but the overall trend agrees with that predicted using the present model for $n = 2$.

(a) Swirl velocity

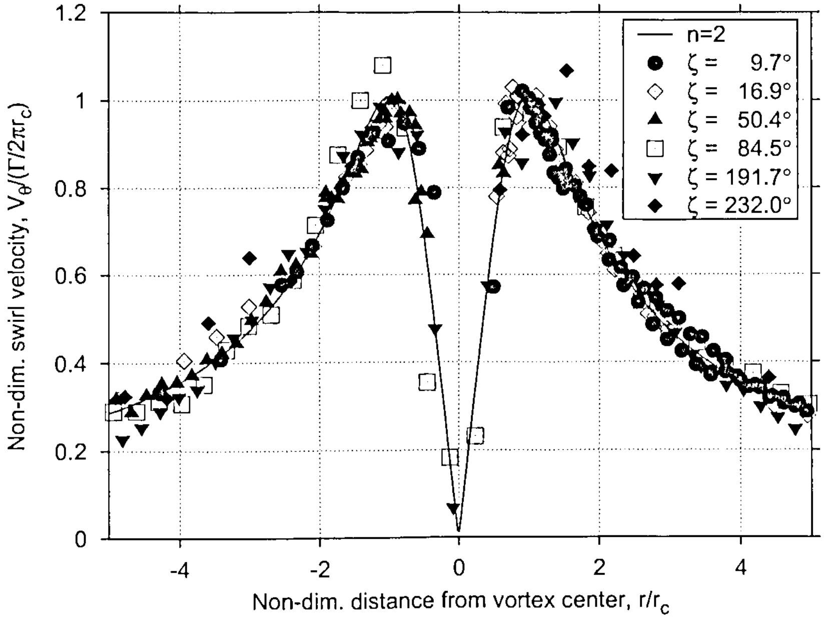

(b) Axial velocity

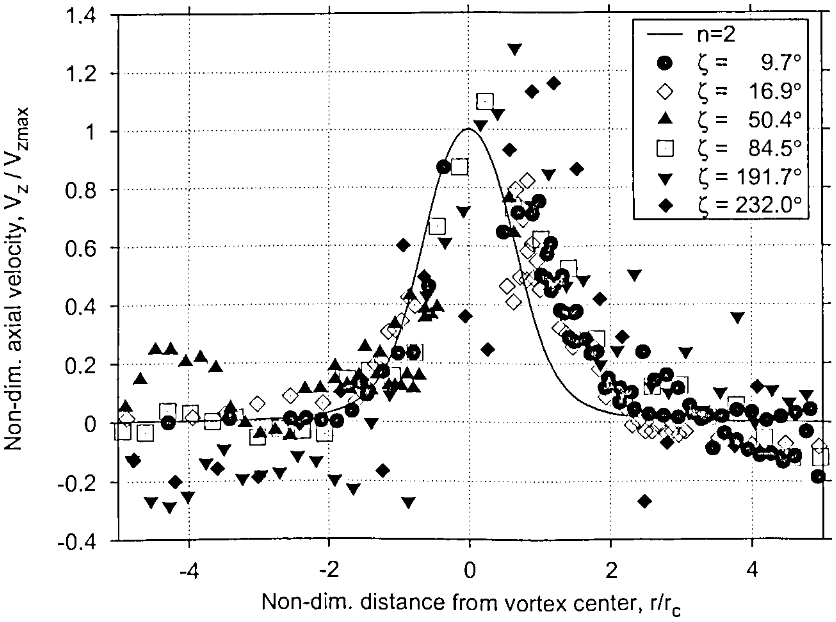

Figure A.8: Vortex induced velocities given by the present model for $n = 2$ compared with rotating wing experimental measurements (Ref. 90). (a) Swirl velocity, (b) Axial velocity.

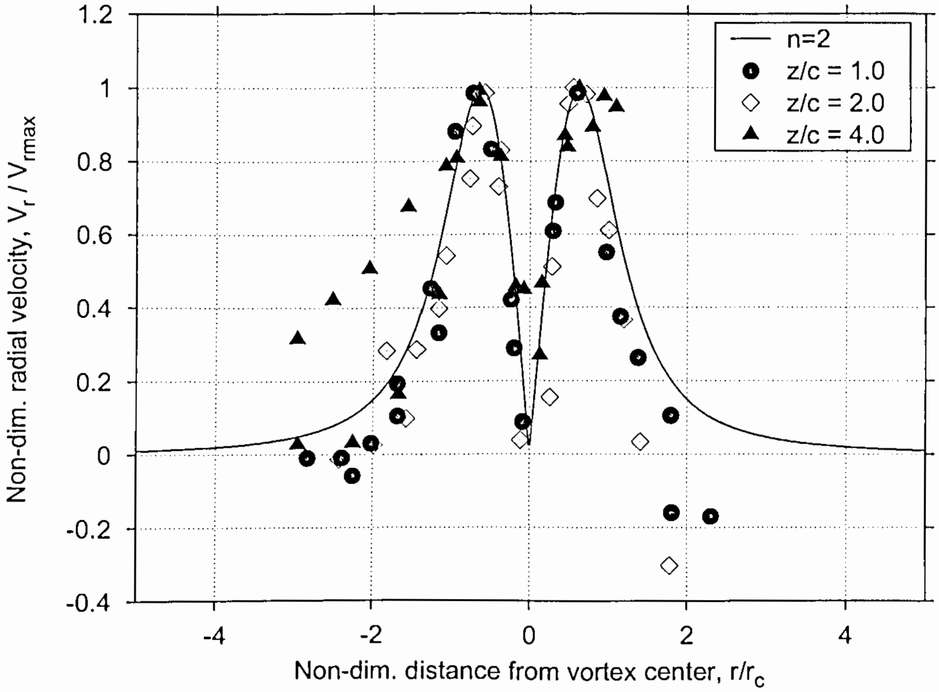

Figure A.9: Radial velocity profiles in the trailing vortex of a fixed wing tip vortex compared with the present model. Experimental measurements from Ref. 119.

Appendix B

Rotor Trim Methodology

The trim solution for a helicopter is fairly complex, involving the calculation of main and tail rotor control settings, helicopter orientation, and blade flapping motion. The trim equations include force and moment equilibria, kinematic relations expressing constraints and several rotor equations for blade flapping solution. There are two different trim methodologies: the propulsive trim methodology simulates flight conditions for a free flying helicopter and the wind-tunnel trim is used especially for experimentally testing isolated rotors. The present analysis includes a wind-tunnel trim methodology developed by Bagai (Ref. 55). This methodology involves only force equilibrium because in the case of wind tunnel experiments the rotor is typically rigidly mounted to a support structure.

Wind-tunnel trim, in practice, is achieved by controlling rotor cyclic inputs to minimize any cyclic blade flapping motion. With no cyclic blade flapping, the TPP is then perpendicular to the rotor shaft. Therefore, the only force component on the rotor is the rotor thrust acting along the shaft. This satisfies the force equilibrium in the lateral and longitudinal directions. The vertical force equation simply specifies a desired thrust value. The three rotor control inputs are the collective and cyclic pitch inputs. The rotor hub orientation is, typically, specified in terms of the shaft tilt. The rotor hub orientation is, typically, specified in terms of the shaft tilt.

Mathematically, the wind-tunnel trim problem has three unknowns which are the the rotor pitch controls, θ_0, θ_{1c} and θ_{1s}. The corresponding three equations are formed by setting two cyclic blade flapping angles, and the difference between actual and desired rotor thrust to zero. This can be written in a matrix form as follows

$$\left\{ \begin{array}{c} C_T - C_{T_{\text{desired}}} \\ \beta_{1c} \\ \beta_{1s} \end{array} \right\} = \left[\quad M \quad \right] \left\{ \begin{array}{c} \theta_0 \\ \theta_{1c} \\ \theta_{1s} \end{array} \right\} = 0 \qquad (2.1)$$

or

$$\{f\} = 0 \qquad (2.2)$$

The rotor aerodynamics, in general, are a highly coupled, non-linear function of the control inputs mainly because of the wake induced inflow. Although collective pitch predominantly controls the rotor thrust, it can also influence the blade flapping through the wake induced inflow. Similarly, the cyclic pitch inputs essentially control the cyclic blade flapping but can also affect the overall rotor thrust. Therefore, the matrix $[M]$ in the above equation is a fully populated matrix. The matrix elements are highly nonlinear terms because of the vortex induced velocities. The matrix is not diagonally dominant because of the cross-coupling effects of rotor cyclic pitch inputs and the cyclic blade flapping response. Therefore, a direct inversion is not generally possible and the control inputs required for rotor trim must be calculated iteratively as a solution of a set of non-linear algebraic equations.

The non-linear equations $\{f\} = 0$ are linearized about some mean operating condition. In general, this mean operating condition is initially estimated based on momentum theory uniform inflow corresponding to the desired rotor thrust. A Jacobian matrix relating the perturbations in the function $\{f\}$ to small perturbations in the input vector $\{\theta\}$ is then calculated numerically. This is equivalent to a Taylor-expansion of the function about the mean input vector $\{\theta\}_0$, i.e.,

$$\begin{aligned} \Delta\{f\} &= \Big\{f(\theta_0+\Delta\theta)\Big\} - \Big\{f(\theta_0)\Big\} \\ &= [J]\{\Delta\theta\} + \cdots \quad \text{higher order terms} \end{aligned} \tag{2.3}$$

The Jacobian matrix is evaluated numerically by applying small control input perturbations to the rotor and recalculating the wake-induced inflow, and the resultant blade loading and flapping response. By applying small perturbations to all three inputs, the entire Jacobian matrix can be constructed as

$$[J] = \frac{\partial f_i}{\partial \theta_j} = \begin{bmatrix} \frac{\partial C_T}{\partial \theta_0} & \frac{\partial C_T}{\partial \theta_{1c}} & \frac{\partial C_T}{\partial \theta_{1s}} \\ \frac{\partial \beta_{1c}}{\partial \theta_0} & \frac{\partial \beta_{1c}}{\partial \theta_{1c}} & \frac{\partial \beta_{1c}}{\partial \theta_{1s}} \\ \frac{\partial \beta_{1s}}{\partial \theta_0} & \frac{\partial \beta_{1s}}{\partial \theta_{1c}} & \frac{\partial \beta_{1s}}{\partial \theta_{1s}} \end{bmatrix} \approx \begin{bmatrix} \frac{\Delta C_T}{\Delta \theta_0} & \frac{\Delta C_T}{\Delta \theta_{1c}} & \frac{\Delta C_T}{\Delta \theta_{1s}} \\ \frac{\Delta \beta_{1c}}{\Delta \theta_0} & \frac{\Delta \beta_{1c}}{\Delta \theta_{1c}} & \frac{\Delta \beta_{1c}}{\Delta \theta_{1s}} \\ \frac{\Delta \beta_{1s}}{\Delta \theta_0} & \frac{\Delta \beta_{1s}}{\Delta \theta_{1c}} & \frac{\Delta \beta_{1s}}{\Delta \theta_{1s}} \end{bmatrix} \tag{2.4}$$

Now, the control inputs can be updated along with the free wake solution by inverting the numerical Jacobian matrix, i.e.,

$$\Delta\theta = [J]^{-1}\{f\} \tag{2.5}$$

The rotor control inputs are updated after each wake iteration, until both the rotor controls and the wake solutions converge together. This process is illustrated schematically in Fig. B.1.

Represenitive variations in the control input angles (collective and cyclic pitch angles) are shown in Fig. B.2 as calculated using the free-vortex wake model and the wind-tunnel trim methodology. The trim settings of a UH-1H helicopter in free flight (Ref. 159) are also shown for comparison. The shaft tilt angle was specified and the control inputs were calculated based on minimum cyclic flapping as described earlier. Note that the wind-tunnel trim solves for only an isolated rotor and does not

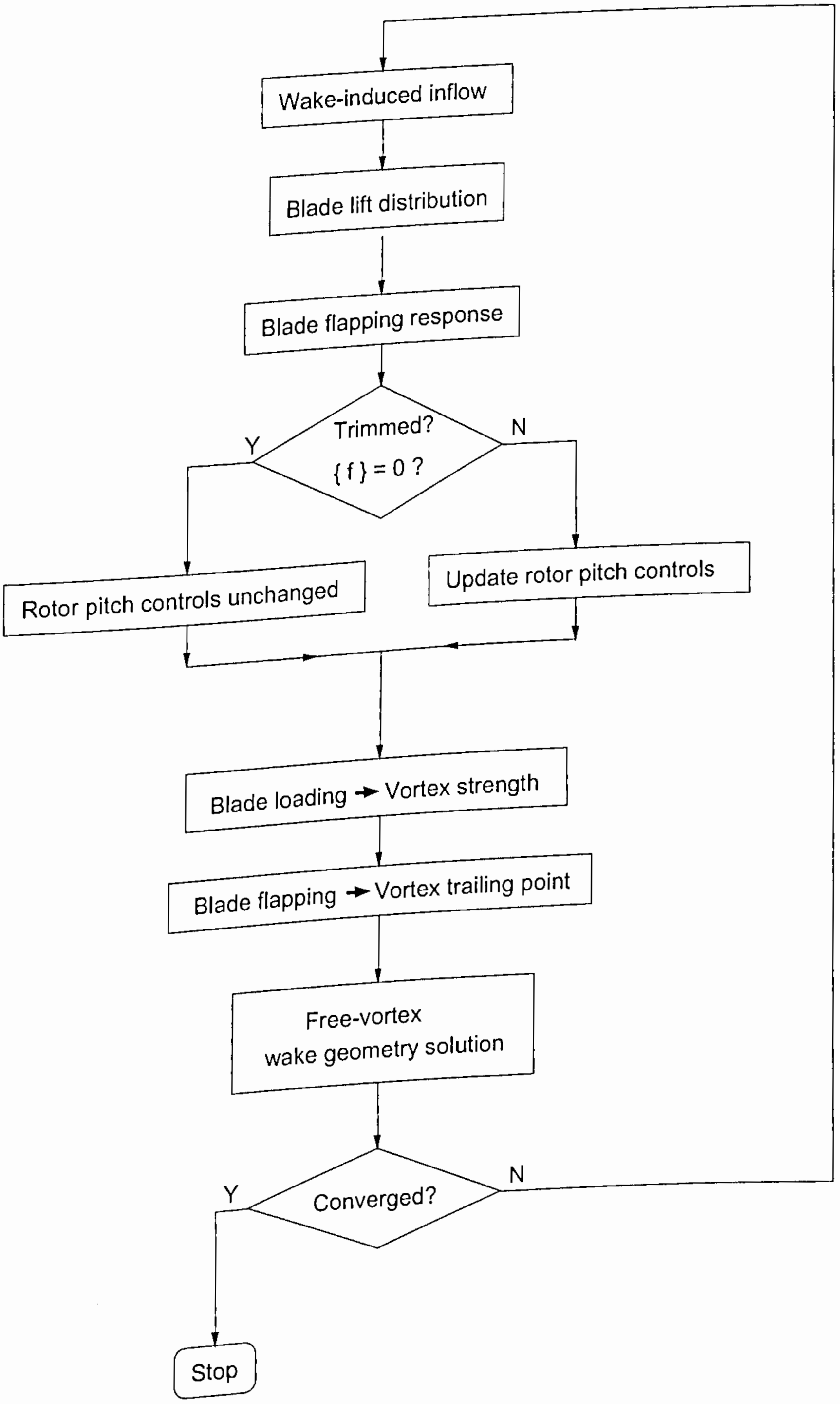

Figure B.1: Flowchart illustrating the coupled rotor trim procedure.

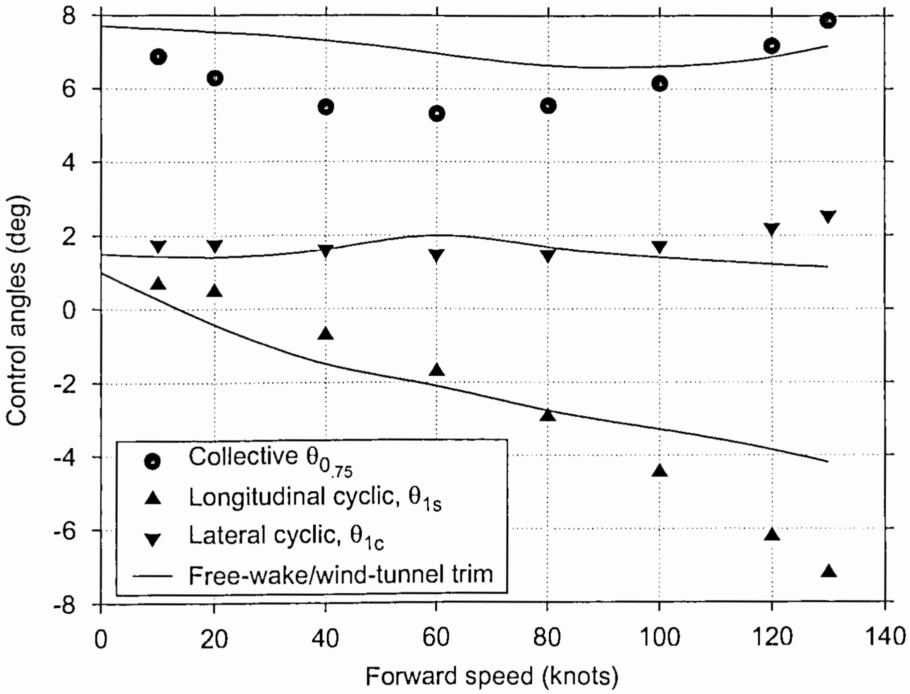

Figure B.2: Representive variations in collective and cyclic pitch inputs required to trim a rotor in forward flight. Experimental results from Ref. 159.

correspond to the free flight conditions of the flight test experiments shown. Therefore, the control angles as a function of forward speed may only be considered representive, but are indicative of typical inputs required for any single rotor helicopter.

Appendix C

Coordinate Transformations for Counter-Rotating Rotors

The present methodology can be readily extended to multiple rotor systems. However, counter-rotating rotor systems like tandem/coaxial require some special considerations in terms of coordinate transformations. Note that while the collocation points on the vortical wake are defined in a fixed axes (wind axes) coordinate system, the velocities encountered by the blades are referenced to a local, blade fixed frame. These two coordinate systems are defined in Fig. C.1, where the fixed frame coordinates are represented by (x,y,z), while the rotating frame coordinates are represented by $(\bar{x},\bar{y},\bar{z})$. The present analysis accounts for the transformation between these two frames through three rotations from the fixed frame to the rotating frame: the rotor shaft tilt, α, the blade azimuthal rotation, ψ, and the blade flapping angle, β. For counter-rotating rotors, the second rotation would change sign because of the opposite sense of rotation of the rotor blades. The global coordinates used in the present analysis have their origin located at the rotor hub with the x-axis pointing in the direction of freestream velocity. Therefore, they are often termed as wind-axes. The z-axis points vertically upward and the coordinate system is right-handed.

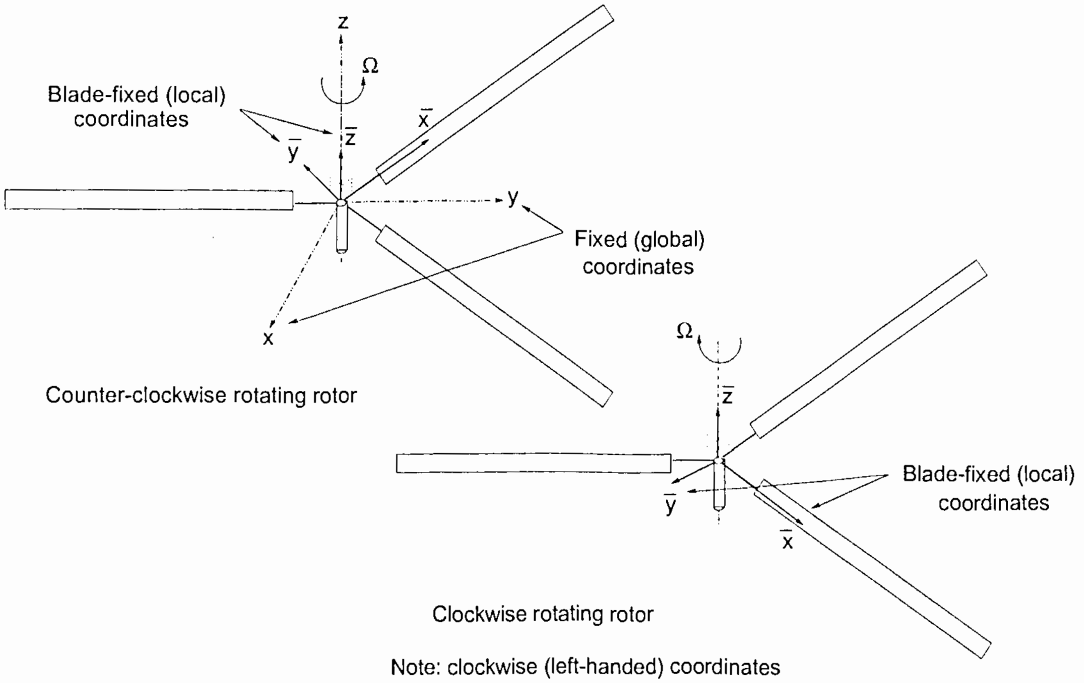

Figure C.1: Coordinate systems for anti-clockwise and clockwise rotors.

Note that the local (blade-fixed coordinate system for the anti-clockwise rotating rotor is right-handed, while that for the clockwise rotating rotor is left-handed. The blade azimuth is referenced to the global x-axis such that the $\psi = 0$ radial lines are aligned with x-axis for all rotors. The blade azimuth angle is then measured from this reference in the same direction as the direction of rotation. Therefore, the transformation from rotating to fixed frame, and vice versa, is slightly different for the counter-rotating rotors. These transformations are now defined as three rotations from the global coordinate system.

C.1 Rotation about the y-axis: Shaft tilt α

Figure C.2 shows the rotation about the global y-axis through angle α. The transformed coordinates can be easily shown to be

$$\begin{aligned} x_1 &= x\cos\alpha - z\sin\alpha \\ y_1 &= y \\ z_1 &= x\sin\alpha + z\cos\alpha \end{aligned} \tag{3.1}$$

The angle α corresponds to the rotor shaft tilt. Although by convention the angle $\alpha > 0$ corresponds to a backward shaft tilt, it is common to refer to shaft tilt as positive forward. Therefore, the tilt angle in the above expression can be replaced by $\alpha = -\alpha_s$. The transformation can be written in matrix form as

$$\begin{Bmatrix} x_1 \\ y_1 \\ z_1 \end{Bmatrix} = \begin{bmatrix} \cos(-\alpha_s) & 0 & -\sin(-\alpha_s) \\ 0 & 1 & 0 \\ \sin(-\alpha_s) & 0 & \cos(-\alpha_s) \end{bmatrix} \begin{Bmatrix} x \\ y \\ z \end{Bmatrix} \tag{3.2}$$

This transformation matrix is denoted by $[T_\alpha]$

C.2 Rotation about the z_1-axis: azimuth ψ

Next consider the rotation about the z_1-axis through the blade azimuth angle ψ. First, consider the right-handed coordinate system where ψ is anti-clockwise, as shown in Fig. C.3(a). The corresponding transformations can be written as

$$\begin{Bmatrix} x_2 \\ y_2 \\ z_2 \end{Bmatrix} = \begin{bmatrix} \cos\psi & \sin\psi & 0 \\ 0 & 0 & 1 \\ -\sin\psi & \cos\psi & 0 \end{bmatrix} \begin{Bmatrix} x_1 \\ y_1 \\ z_1 \end{Bmatrix} \tag{3.3}$$

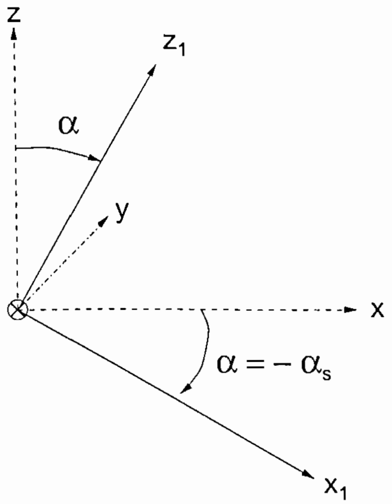

Figure C.2: Rotation about the y-axis through angle α.

This transformation matrix is denoted by $[T_\psi]$. For a clockwise rotating rotor, the direction of positive ψ is reversed as shown in Fig. C.3(b). This will change the sign of the terms in $\sin\psi$ in the above transformation matrix. For simplicity, a notation for sign of rotation is introduced as

$$S_n = \left.\begin{array}{ll} 1, & \text{anti-clockwise rotation} \\ -1, & \text{clockwise rotation} \end{array}\right\} \tag{3.4}$$

Therefore, the second transformation can be rewritten as

$$\begin{Bmatrix} x_2 \\ y_2 \\ z_2 \end{Bmatrix} = \begin{bmatrix} \cos(S_n\psi) & S_n \sin(S_n\psi) & 0 \\ -S_n \sin(S_n\psi) & \cos(S_n\psi) & 0 \\ 0 & 0 & 1 \end{bmatrix} \begin{Bmatrix} x_1 \\ y_1 \\ z_1 \end{Bmatrix} \tag{3.5}$$

C.3 Rotation about the y_2-axis

Finally, consider the rotation about the y_2-axis, which incidently corresponds to the blade-fixed $\bar{y}$-axis, through the blade flapping angle, β. Note that the blade flapping

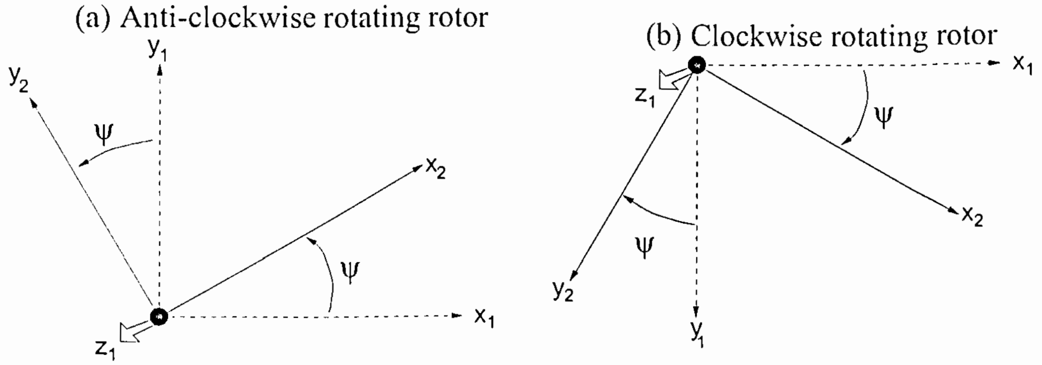
(a) Anti-clockwise rotating rotor

(b) Clockwise rotating rotor

Figure C.3: Rotation about the z_1-axis through angle ψ. (a) Anti-clockwise rotating rotor, (b) Clockwise rotating rotor.

angles are defined as positive for flapping up motion. Therefore, this transformation is identical for both anti-clockwise and clockwise rotating rotors, except for a change in sign of the y-axis. From Fig. C.4, it can be shown that

$$\begin{Bmatrix} \bar{x} \\ \bar{y} \\ \bar{z} \end{Bmatrix} = \begin{bmatrix} \cos\beta & 0 & -\sin\beta \\ 0 & S_n & 0 \\ \sin\beta & 0 & \cos\beta \end{bmatrix} \begin{Bmatrix} x_2 \\ y_2 \\ z_2 \end{Bmatrix} \tag{3.6}$$

This transformation matrix is denoted by $[T_\beta]$

Now, the the complete transformation from the global (fixed) frame to the local

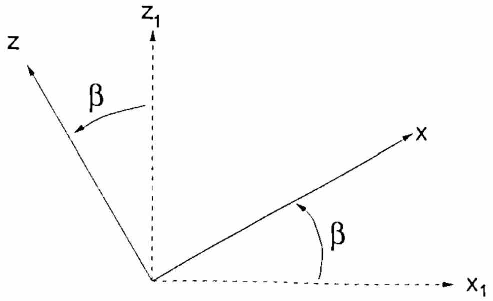

Figure C.4: Rotation about the y_2-axis through angle β.

(rotating) frame can be written as

$$\begin{Bmatrix} \bar{x} \\ \bar{y} \\ \bar{z} \end{Bmatrix} = [T_\alpha]\,[T_\psi]\,[T_\beta] \begin{Bmatrix} x \\ y \\ z \end{Bmatrix} \tag{3.7}$$

or, in a combined matrix as

$$[T] = \begin{bmatrix} \begin{matrix} \cos\beta\cos(S_n\psi)\cos(S_n\psi) \\ +\sin\beta\sin(-\alpha_s) \end{matrix} & S_n^2\cos\beta\sin(S_n\psi) & \begin{matrix} -\cos\beta\cos(S_n\psi)\sin(S_n\psi) \\ +\sin\beta\cos(-\alpha_s) \end{matrix} \\ -S_n\sin(S_n\psi)\cos(-\alpha_s) & S_n\cos(S_n\psi) & S_n\sin(S_n\psi)\sin(-\alpha_s) \\ \begin{matrix} -\sin\beta\cos(S_n\psi)\cos(S_n\psi) \\ +\cos\beta\sin(-\alpha_s) \end{matrix} & S_n^2\sin\beta\sin(S_n\psi) & \begin{matrix} \sin\beta\cos(S_n\psi)\sin(S_n\psi) \\ +\cos\beta\cos(-\alpha_s) \end{matrix} \end{bmatrix} \tag{3.8}$$

Note that the S_n^2 term is always equal to unity. Because a clockwise rotating rotor has a left-handed coordinate system, the sense of vortex circulation is also left-handed. In the implementation of the present analysis, the Biot-Savart induced velocity calculations are performed assuming a right-handed coordinate system. Therefore, all vortex induced velocities are also corrected using the sign of rotation, S_n. The rotor control inputs (cyclic pitch) do not include such a sign correction because they are defined relative to the blade azimuth for the rotor, which already includes a correction for the sign of rotation. Similarly, the cyclic flapping angles also inherently include the sign of rotation.

Appendix D

Matrices for Vortex Stability

The matrices for perturbation velocity calculations in Section 2.2.1 are given by:

$$
\begin{aligned}
P_{1,1} &= h(\cos\theta_1 - \cos\theta_2)\left(-\frac{C_xC_yl_{12_z}}{C^3} + \frac{C_zC_xl_{12_y}}{C^3}\right) \\
&+ he_x\left(\frac{\cos\theta_2 r_{2_x}}{r_2{}^2} - \frac{l_{12_x}}{r_2 l_{12}} - \frac{\cos\theta_1 r_{1_x}}{r_1{}^2} + \frac{l_{12_x}}{r_1 l_{12}}\right) \\
&+ h_f(\cos\theta_1 - \cos(\theta_2))\,e_x\left(\frac{C_yl_{12_z}}{l_{12}C} - \frac{C_zl_{12_y}}{l_{12}C}\right) \\
P_{1,2} &= h(\cos\theta_1 - \cos\theta_2)\left(-\frac{C_zC_xl_{12_x}}{C^3} - \frac{l_{12_z}}{C} + \frac{C_x{}^2l_{12_z}}{C^3}\right) \\
&+ he_x\left(\frac{\cos(\theta_2)r_{2_y}}{r_2{}^2} - \frac{l_{12_y}}{r_2 l_{12}} - \frac{\cos\theta_1 r_{1_y}}{r_1{}^2} + \frac{l_{12_y}}{r_1 l_{12}}\right) \\
&+ h_f(\cos(\theta_1) - \cos\theta_2)\,e_x\left(\frac{C_zl_{12_x}}{l_{12}C} - \frac{C_xl_{12_z}}{l_{12}C}\right) \\
P_{1,3} &= h(\cos\theta_1 - \cos\theta_2)\left(-\frac{C_x{}^2l_{12_y}}{C^3} + \frac{l_{12_y}}{C} + \frac{C_xC_yl_{12_x}}{C^3}\right) \\
&+ he_x\left(-\frac{\cos(\theta_1)r_{1_z}}{r_1{}^2} + \frac{l_{12_z}}{r_1 l_{12}} + \frac{\cos\theta_2 r_{2_z}}{r_2{}^2} - \frac{l_{12_z}}{r_2 l_{12}}\right) \\
&+ h_f(\cos(\theta_1) - \cos\theta_2)\,e_x\left(\frac{C_xl_{12_y}}{l_{12}C} - \frac{C_yl_{12_x}}{l_{12}C}\right) \\
P_{2,1} &= h(\cos\theta_1 - \cos\theta_2)\left(-\frac{C_y{}^2l_{12_z}}{C^3} + \frac{l_{12_z}}{C} + \frac{C_yC_zl_{12_y}}{C^3}\right) \\
&+ he_y\left(\frac{\cos(\theta_2)r_{2_x}}{r_2{}^2} - \frac{l_{12_x}}{r_2 l_{12}} - \frac{\cos\theta_1 r_{1_x}}{r_1{}^2} + \frac{l_{12_x}}{r_1 l_{12}}\right) \\
&+ h_f(\cos(\theta_1) - \cos\theta_2)\,e_y\left(\frac{C_yl_{12_z}}{l_{12}C} - \frac{C_zl_{12_y}}{l_{12}C}\right)
\end{aligned}
$$

$$\begin{aligned}
P_{2,2} &= h\left(\cos\theta_1-\cos\theta_2\right)\left(-\frac{C_yC_zl_{12_x}}{C^3}+\frac{C_xC_yl_{12_z}}{C^3}\right)\\
&+ he_y\left(\frac{\cos\theta_2 r_{2_y}}{r_2{}^2}-\frac{l_{12_y}}{r_2\,l_{12}}-\frac{\cos(\theta_1)r_{1_y}}{r_1{}^2}+\frac{l_{12_y}}{r_1\,l_{12}}\right)\\
&+ h_f\left(\cos\theta_1-\cos(\theta_2)\right)e_y\left(\frac{C_zl_{12_x}}{l_{12}C}-\frac{C_xl_{12_z}}{l_{12}C}\right)\\
P_{2,3} &= h\left(\cos\theta_1-\cos\theta_2\right)\left(-\frac{l_{12_x}}{C}-\frac{C_xC_yl_{12_y}}{C^3}+\frac{C_y{}^2l_{12_x}}{C^3}\right)\\
&+ he_y\left(-\frac{\cos(\theta_1)r_{1_z}}{r_1{}^2}+\frac{l_{12_z}}{r_1\,l_{12}}+\frac{\cos\theta_2 r_{2_z}}{r_2{}^2}-\frac{l_{12_z}}{r_2\,l_{12}}\right)\\
&+ h_f\left(\cos(\theta_1)-\cos\theta_2\right)e_y\left(\frac{C_xl_{12_y}}{l_{12}C}-\frac{C_yl_{12_x}}{l_{12}C}\right)\\
P_{3,1} &= h\left(\cos\theta_1-\cos\theta_2\right)\left(\frac{C_z{}^2l_{12_y}}{C^3}-\frac{l_{12_y}}{C}-\frac{C_yC_zl_{12_z}}{C^3}\right)\\
&+ he_z\left(\frac{\cos(\theta_2)r_{2_x}}{r_2{}^2}-\frac{l_{12_x}}{r_2\,l_{12}}-\frac{\cos\theta_1 r_{1_x}}{r_1{}^2}+\frac{l_{12_x}}{r_1\,l_{12}}\right)\\
&+ h_f\left(\cos(\theta_1)-\cos\theta_2\right)e_z\left(\frac{C_yl_{12_z}}{l_{12}C}-\frac{C_zl_{12_y}}{l_{12}C}\right)\\
P_{3,2} &= h\left(\cos\theta_1-\cos\theta_2\right)\left(-\frac{C_z{}^2l_{12_x}}{C^3}+\frac{l_{12_x}}{C}+\frac{C_zC_xl_{12_z}}{C^3}\right)\\
&+ he_z\left(\frac{\cos(\theta_2)r_{2_y}}{r_2{}^2}-\frac{l_{12_y}}{r_2\,l_{12}}-\frac{\cos\theta_1 r_{1_y}}{r_1{}^2}+\frac{l_{12_y}}{r_1\,l_{12}}\right)\\
&+ h_f\left(\cos(\theta_1)-\cos\theta_2\right)e_z\left(\frac{C_zl_{12_x}}{l_{12}C}-\frac{C_xl_{12_z}}{l_{12}C}\right)\\
P_{3,3} &= h\left(\cos\theta_1-\cos\theta_2\right)\left(\frac{C_yC_zl_{12_x}}{C^3}-\frac{C_zC_xl_{12_y}}{C^3}\right)\\
&+ he_z\left(-\frac{\cos\theta_1 r_{1_z}}{r_1{}^2}+\frac{l_{12_z}}{r_1\,l_{12}}+\frac{\cos(\theta_2)r_{2_z}}{r_2{}^2}-\frac{l_{12_z}}{r_2\,l_{12}}\right)\\
&+ h_f\left(\cos\theta_1-\cos(\theta_2)\right)e_z\left(\frac{C_xl_{12_y}}{l_{12}C}-\frac{C_yl_{12_x}}{l_{12}C}\right)
\end{aligned}$$

$$\begin{aligned}
A_{1,1} &= h\left(\cos\theta_1-\cos\theta_2\right)\left(-\frac{C_xC_yr_{2_z}}{C^3}+\frac{C_xC_zr_{2_y}}{C^3}\right)\\
&+ he_x\left(-\frac{\cos\theta_2 l_{12_x}}{l_{12}{}^2}+\frac{r_{2_x}}{r_2\,l_{12}}-\cos\theta_1\left(-\frac{r_1\,l_{12_x}}{l_{12}{}^2r_1}-\frac{r_{1_x}l_{12}}{r_1{}^2\,l_{12}}\right)+\frac{-r_{1_x}-l_{12_x}}{r_1\,l_{12}}\right)\\
&+ h_f\left(\cos\theta_1-\cos\theta_2\right)e_x\left(\frac{Cl_{12_x}}{l_{12}{}^3}+\frac{C_yr_{2_z}}{l_{12}C}-\frac{C_zr_{2_y}}{l_{12}C}\right)\\
A_{1,2} &= h\left(\cos\theta_1-\cos\theta_2\right)\left(-\frac{C_xC_zr_{2_x}}{C^3}-\frac{r_{1_z}}{C}+\frac{l_{12_z}}{C}+\frac{C_x{}^2r_{2_z}}{C^3}\right)
\end{aligned}$$

$$
\begin{aligned}
&+ \quad he_x\left(-\cos\theta_1\left(-\frac{r_1 l_{12_y}}{l_{12}^2 r_1}-\frac{r_{1_y} l_{12}}{r_1^2 l_{12}}\right)+\frac{-l_{12_y}-r_{1_y}}{r_1 l_{12}}-\frac{\cos\theta_2 l_{12_y}}{l_{12}^2}+\frac{r_{2_y}}{r_2 l_{12}}\right)\\
&+ \quad h_f(\cos\theta_1-\cos\theta_2)\,e_x\left(\frac{Cl_{12_y}}{l_{12}^3}-\frac{C_x r_{2_z}}{l_{12}C}+\frac{C_z r_{2_x}}{l_{12}C}\right)\\
A_{1,3} \quad &= \quad h(\cos\theta_1-\cos\theta_2)\left(\frac{r_{1_y}}{C}+\frac{C_x C_y r_{2_x}}{C^3}-\frac{C_x^2 r_{2_y}}{C^3}-\frac{l_{12_y}}{C}\right)\\
&+ \quad he_x\left(-\frac{\cos\theta_2 l_{12_z}}{l_{12}^2}+\frac{r_{2_z}}{r_2 l_{12}}-\cos\theta_1\left(-\frac{r_1 l_{12_z}}{l_{12}^2 r_1}-\frac{r_{1_z} l_{12}}{r_1^2 l_{12}}\right)+\frac{-r_{1_z}-l_{12_z}}{r_1 l_{12}}\right)\\
&+ \quad h_f(\cos\theta_1-\cos\theta_2)\,e_x\left(\frac{Cl_{12_z}}{l_{12}^3}-\frac{C_y r_{2_x}}{l_{12}C}+\frac{C_x r_{2_y}}{l_{12}C}\right)\\
A_{2,1} \quad &= \quad h(\cos\theta_1-\cos\theta_2)\left(\frac{r_{1_z}}{C}+\frac{C_y C_z r_{2_y}}{C^3}-\frac{l_{12_z}}{C}-\frac{C_y^2 r_{2_z}}{C^3}\right)\\
&+ \quad he_y\left(-\frac{\cos\theta_2 l_{12_x}}{l_{12}^2}+\frac{r_{2_x}}{r_2 l_{12}}-\cos\theta_1\left(-\frac{r_1 l_{12_x}}{l_{12}}-\frac{r_{1_x} l_{12}}{r_1^2 l_{12}}\right)+\frac{-r_{1_x}-l_{12_x}}{r_1 l_{12}}\right)\\
&+ \quad h_f(\cos\theta_1-\cos\theta_2)\,e_y\left(\frac{Cl_{12_x}}{l_{12}^3}+\frac{C_y r_{2_z}}{l_{12}C}-\frac{C_z r_{2_y}}{l_{12}C}\right)\\
A_{2,2} \quad &= \quad h(\cos\theta_1-\cos\theta_2)\left(\frac{C_x C_y r_{2_z}}{C^3}-\frac{C_y C_z r_{2_x}}{C^3}\right)\\
&+ \quad he_y\left(-\cos\theta_1\left(-\frac{r_1 l_{12_y}}{l_{12}^2 r_1}-\frac{r_{1_y} l_{12}}{r_1^2 l_{12}}\right)+\frac{-l_{12_y}-r_{1_y}}{r_1 l_{12}}-\frac{\cos\theta_2 l_{12_y}}{l_{12}^2}+\frac{r_{2_y}}{r_2 l_{12}}\right)\\
&+ \quad h_f(\cos\theta_1-\cos\theta_2)\,e_y\left(\frac{Cl_{12_y}}{l_{12}^3}-\frac{C_x r_{2_z}}{l_{12}C}+\frac{C_z r_{2_x}}{l_{12}C}\right)\\
A_{2,3} \quad &= \quad h(\cos\theta_1-\cos\theta_2)\left(-\frac{C_x C_y r_{2_y}}{C^3}+\frac{l_{12_x}}{C}-\frac{r_{1_x}}{C}+\frac{C_y^2 r_{2_x}}{C^3}\right)\\
&+ \quad he_y\left(-\frac{\cos\theta_2 l_{12_z}}{l_{12}^2}+\frac{r_{2_z}}{r_2 l_{12}}-\cos\theta_1\left(-\frac{r_1 l_{12_z}}{l_{12}^2 r_1}-\frac{r_{1_z} l_{12}}{r_1^2 l_{12}}\right)+\frac{-r_{1_z}-l_{12_z}}{r_1 l_{12}}\right)\\
&+ \quad h_f(\cos\theta_1-\cos\theta_2)\,e_y\left(\frac{Cl_{12_z}}{l_{12}^3}-\frac{C_y r_{2_x}}{l_{12}C}+\frac{C_x r_{2_y}}{l_{12}C}\right)\\
A_{3,1} \quad &= \quad h(\cos\theta_1-\cos\theta_2)\left(\frac{l_{12_y}}{C}-\frac{C_z C_y r_{2_z}}{C^3}+\frac{C_z^2 r_{2_y}}{C^3}-\frac{r_{1_y}}{C}\right)\\
&+ \quad he_z\left(-\frac{\cos\theta_2 l_{12_x}}{l_{12}^2}+\frac{r_{2_x}}{r_2 l_{12}}-\cos\theta_1\left(-\frac{r_1 l_{12_x}}{l_{12}^2 r_1}-\frac{r_{1_x} l_{12}}{r_1^2 l_{12}}\right)+\frac{-r_{1_x}-l_{12_x}}{r_1 l_{12}}\right)\\
&+ \quad h_f(\cos\theta_1-\cos\theta_2)\,e_z\left(\frac{Cl_{12_x}}{l_{12}^3}+\frac{C_y r_{2_z}}{l_{12}C}-\frac{C_z r_{2_y}}{l_{12}C}\right)\\
A_{3,2} \quad &= \quad h(\cos\theta_1-\cos\theta_2)\left(\frac{r_{1_x}}{C}+\frac{C_z C_x r_{2_z}}{C^3}-\frac{l_{12_x}}{C}-\frac{C_z^2 r_{2_x}}{C^3}\right)\\
&+ \quad he_z\left(-\cos\theta_1\left(-\frac{r_1 l_{12_y}}{l_{12}^2 r_1}-\frac{r_{1_y} l_{12}}{r_1^2 l_{12}}\right)+\frac{-l_{12_y}-r_{1_y}}{r_1 l_{12}}-\frac{\cos\theta_2 l_{12_y}}{l_{12}^2}+\frac{r_{2_y}}{r_2 l_{12}}\right)
\end{aligned}
$$

$$
\begin{aligned}
& + \quad h_f(\cos\theta_1 - \cos\theta_2)\, e_z \left(\frac{C l_{12_y}}{{l_{12}}^3} - \frac{C_x r_{2_z}}{l_{12} C} + \frac{C_z r_{2_x}}{l_{12} C} \right) \\
A_{3,3} \quad & = \quad h(\cos\theta_1 - \cos\theta_2) \left(\frac{C_y C_z r_{2_x}}{C^3} - \frac{C_x C_z r_{2_y}}{C^3} \right) \\
& + \quad h e_z \left(-\frac{\cos\theta_2 l_{12_z}}{{l_{12}}^2} + \frac{r_{2_z}}{r_2 l_{12}} - \cos\theta_1 \left(-\frac{r_1 l_{12_z}}{{l_{12}}^2 r_1} - \frac{r_{1_z} l_{12}}{{r_1}^2 l_{12}} \right) + \frac{-r_{1_z} - l_{12_z}}{r_1 l_{12}} \right) \\
& + \quad h_f(\cos\theta_1 - \cos\theta_2)\, e_z \left(\frac{C l_{12_z}}{{l_{12}}^3} - \frac{C_y r_{2_x}}{l_{12} C} + \frac{C_x r_{2_y}}{l_{12} C} \right)
\end{aligned}
$$

$$
\begin{aligned}
B_{1,1} \quad & = \quad h(\cos\theta_1 - \cos\theta_2) \left(-\frac{C_x C_z r_{1_y}}{C^3} + \frac{C_x C_y r_{1_z}}{C^3} \right) \\
& + \quad h e_x \left(-\frac{\cos\theta_1 l_{12_x}}{{l_{12}}^2} + \frac{r_{1_x}}{r_1 l_{12}} + \cos(\theta_2) \left(\frac{r_2 l_{12_x}}{l_{12}} - \frac{r_{2_x} l_{12}}{r_2} \right) {r_2}^{-1} {l_{12}}^{-1} - \frac{-l_{12_x} + r_{2_x}}{r_2 l_{12}} \right) \\
& + \quad h_f(\cos\theta_1 - \cos\theta_2)\, e_x \left(-\frac{C l_{12_x}}{{l_{12}}^3} + \frac{C_z r_{1_y}}{l_{12} C} - \frac{C_y r_{1_z}}{l_{12} C} \right) \\
B_{1,2} \quad & = \quad h(\cos\theta_1 - \cos\theta_2) \left(\frac{r_{1_z}}{C} + \frac{C_x C_z r_{1_x}}{C^3} - \frac{{C_x}^2 r_{1_z}}{C^3} \right) \\
& + \quad h e_x \left(\cos\theta_2 \left(\frac{r_2 l_{12_y}}{l_{12}} - \frac{r_{2_y} l_{12}}{r_2} \right) {r_2}^{-1} {l_{12}}^{-1} - \frac{-l_{12_y} + r_{2_y}}{r_2 l_{12}} - \frac{\cos\theta_1 l_{12_y}}{{l_{12}}^2} + \frac{r_{1_y}}{r_1 l_{12}} \right) \\
& + \quad h_f(\cos\theta_1 - \cos\theta_2)\, e_x \left(-\frac{C l_{12_y}}{{l_{12}}^3} + \frac{C_x r_{1_z}}{l_{12} C} - \frac{C_z r_{1_x}}{l_{12} C} \right) \\
B_{1,3} \quad & = \quad h(\cos\theta_1 - \cos\theta_2) \left(\frac{{C_x}^2 r_{1_y}}{C^3} - \frac{r_{1_y}}{C} - \frac{C_x C_y r_{1_x}}{C^3} \right) \\
& + \quad h e_x \left(-\frac{\cos(\theta_1) l_{12_z}}{{l_{12}}^2} + \frac{r_{1_z}}{r_1 l_{12}} + \cos\theta_2 \left(\frac{r_2 l_{12_z}}{l_{12}} - \frac{r_{2_z} l_{12}}{r_2} \right) {r_2}^{-1} {l_{12}}^{-1} - \frac{-l_{12_z} + r_{2_z}}{r_2 l_{12}} \right) \\
& + \quad h_f(\cos\theta_1 - \cos\theta_2)\, e_x \left(-\frac{C l_{12_z}}{{l_{12}}^3} + \frac{C_y r_{1_x}}{l_{12} C} - \frac{C_x r_{1_y}}{l_{12} C} \right) \\
B_{2,1} \quad & = \quad h(\cos\theta_1 - \cos\theta_2) \left(-\frac{r_{1_z}}{C} - \frac{C_y C_z r_{1_y}}{C^3} + \frac{{C_y}^2 r_{1_z}}{C^3} \right) \\
& + \quad h e_y \left(-\frac{\cos(\theta_1) l_{12_x}}{{l_{12}}^2} + \frac{r_{1_x}}{r_1 l_{12}} + \cos\theta_2 \left(\frac{r_2 l_{12_x}}{l_{12}} - \frac{r_{2_x} l_{12}}{r_2} \right) {r_2}^{-1} {l_{12}}^{-1} - \frac{-l_{12_x} + r_{2_x}}{r_2 l_{12}} \right) \\
& + \quad h_f(\cos\theta_1 - \cos\theta_2)\, e_y \left(-\frac{C l_{12_x}}{{l_{12}}^3} + \frac{C_z r_{1_y}}{l_{12} C} - \frac{C_y r_{1_z}}{l_{12} C} \right) \\
B_{2,2} \quad & = \quad h(\cos\theta_1 - \cos\theta_2) \left(\frac{C_y C_z r_{1_x}}{C^3} - \frac{C_x C_y r_{1_z}}{C^3} \right) \\
& + \quad h e_y \left(\cos\theta_2 \left(\frac{r_2 l_{12_y}}{l_{12}} - \frac{r_{2_y} l_{12}}{r_2} \right) {r_2}^{-1} {l_{12}}^{-1} - \frac{-l_{12_y} + r_{2_y}}{r_2 l_{12}} - \frac{\cos\theta_1 l_{12_y}}{{l_{12}}^2} + \frac{r_{1_y}}{r_1 l_{12}} \right) \\
& + \quad h_f(\cos\theta_1 - \cos\theta_2)\, e_y \left(-\frac{C l_{12_y}}{{l_{12}}^3} + \frac{C_x r_{1_z}}{l_{12} C} - \frac{C_z r_{1_x}}{l_{12} C} \right)
\end{aligned}
$$

$$
\begin{aligned}
B_{2,3} &= h\left(\cos\theta_1-\cos\theta_2\right)\left(\frac{r_{1_x}}{C}+\frac{C_x C_y r_{1_y}}{C^3}-\frac{{C_y}^2 r_{1_x}}{C^3}\right)\\
&+ h e_y\left(-\frac{\cos(\theta_1) l_{12_z}}{{l_{12}}^2}+\frac{r_{1_z}}{r_1 l_{12}}+\cos\theta_2\left(\frac{r_2 l_{12_z}}{l_{12}}-\frac{r_{2_z} l_{12}}{r_2}\right){r_2}^{-1}{l_{12}}^{-1}-\frac{-l_{12_z}+r_{2_z}}{r_2 l_{12}}\right)\\
&+ h_f\left(\cos\theta_1-\cos\theta_2\right)e_y\left(-\frac{C l_{12_z}}{{l_{12}}^3}+\frac{C_y r_{1_x}}{l_{12} C}-\frac{C_x r_{1_y}}{l_{12} C}\right)\\
B_{3,1} &= h\left(\cos\theta_1-\cos\theta_2\right)\left(\frac{C_y C_z r_{1_z}}{C^3}-\frac{{C_z}^2 r_{1_y}}{C^3}+\frac{r_{1_y}}{C}\right)\\
&+ h e_z\left(-\frac{\cos(\theta_1) l_{12_x}}{{l_{12}}^2}+\frac{r_{1_x}}{r_1 l_{12}}+\cos\theta_2\left(\frac{r_2 l_{12_x}}{l_{12}}-\frac{r_{2_x} l_{12}}{r_2}\right){r_2}^{-1}{l_{12}}^{-1}-\frac{-l_{12_x}+r_{2_x}}{r_2 l_{12}}\right)\\
&+ h_f\left(\cos\theta_1-\cos\theta_2\right)e_z\left(-\frac{C l_{12_x}}{{l_{12}}^3}+\frac{C_z r_{1_y}}{l_{12} C}-\frac{C_y r_{1_z}}{l_{12} C}\right)\\
B_{3,2} &= h\left(\cos\theta_1-\cos\theta_2\right)\left(-\frac{C_z C_x r_{1_z}}{C^3}-\frac{r_{1_x}}{C}+\frac{{C_z}^2 r_{1_x}}{C^3}\right)\\
&+ h e_z\left(\cos\theta_2\left(\frac{r_2 l_{12_y}}{l_{12}}-\frac{r_{2_y} l_{12}}{r_2}\right){r_2}^{-1}{l_{12}}^{-1}-\frac{-l_{12_y}+r_{2_y}}{r_2 l_{12}}-\frac{\cos\theta_1 l_{12_y}}{{l_{12}}^2}+\frac{r_{1_y}}{r_1 l_{12}}\right)\\
&+ h_f\left(\cos\theta_1-\cos\theta_2\right)e_z\left(-\frac{C l_{12_y}}{{l_{12}}^3}+\frac{C_x r_{1_z}}{l_{12} C}-\frac{C_z r_{1_x}}{l_{12} C}\right)\\
B_{3,3} &= h\left(\cos\theta_1-\cos\theta_2\right)\left(\frac{C_z C_x r_{1_y}}{C^3}-\frac{C_y C_z r_{1_x}}{C^3}\right)\\
&+ h e_z\left(-\frac{\cos\theta_1 l_{12_z}}{{l_{12}}^2}+\frac{r_{1_z}}{r_1 l_{12}}+\cos(\theta_2)\left(\frac{r_2 l_{12_z}}{l_{12}}-\frac{r_{2_z} l_{12}}{r_2}\right){r_2}^{-1}{l_{12}}^{-1}-\frac{-l_{12_z}+r_{2_z}}{r_2 l_{12}}\right)\\
&+ h_f\left(\cos\theta_1-\cos\theta_2\right)e_z\left(-\frac{C l_{12_z}}{{l_{12}}^3}+\frac{C_y r_{1_x}}{l_{12} C}-\frac{C_x r_{1_y}}{l_{12} C}\right)
\end{aligned}
$$

Appendix E

Far-Wake Boundary Condition: Velocity Extrapolation

It was shown in Chapter 3 that the vorticity transport theorem governing the rotor wake geometry has the same form as a one-dimensional wave equation with a non-linear source term, i.e.,

$$\frac{d\vec{r}(\psi,\zeta)}{d\psi}+\frac{d\vec{r}(\psi,\zeta)}{d\zeta}=\left(\frac{\vec{V}_{\text{freestream}}+\vec{V}_{\text{induced}}}{\Omega}\right) \tag{5.1}$$

where $\vec{V}_{\text{freestream}}$ is the freestream convection velocity, while $\vec{V}_{\text{induced}}$ represents the self and mutually induced velocities from all the vortex segments comprising the rotor wake.

The LHS of Eq. 5.1 is a wave equation with the characteristic speed equal to unity. The integration of this equation requires one initial condition in time (ψ) and one boundary condition in space (ζ), which is given by the condition that the vortex segment must be attached to the blade at its origin at $\zeta = 0$. If the wake is truncated after some finite vortex age, say ζ_{max}, another boundary condition may be required. By the nature of the basic wave equation, the solution propagates along the characteristic lines with $\mathrm{d}\psi/\mathrm{d}\zeta = 1$, and no boundary condition is required at the far-wake truncation – see Fig. E.1. This is because the solution propagation along the characteristic to a new value of ψ needs only the information from older values of ζ than the one being

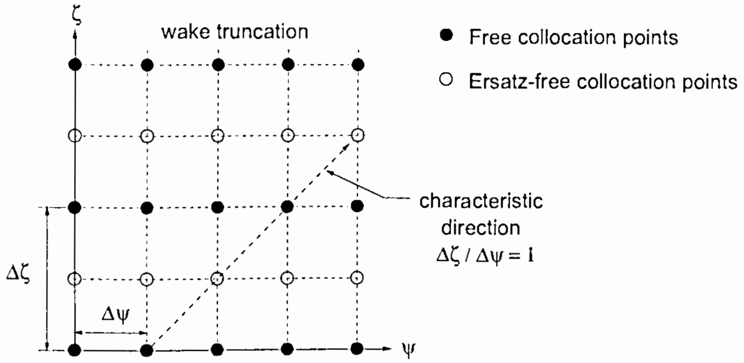

Figure E.1: Computational domain for the wake geometry solution showing the characteristic solution propagation direction and the wake truncation in the far-wake.

calculated. However, the inherent nature of the induced velocity source term on the RHS of Eq. 5.1 requires some boundary condition to be satisfied in the far-wake.

To better understand the reason for such a boundary condition, the induced velocities can be written in a discrete form as

$$\vec{V}_{\text{ind}}(\psi_k, \zeta_l) = \sum_{i=1}^{\infty} \vec{V}_{\text{BS}}(\psi_k, \zeta_l; \zeta_i) \tag{5.2}$$

where $\vec{V}_{\text{BS}}(\psi_k, \zeta_l; \zeta_i)$ represents the velocity induced by the i^{th} vortex element extending from $\vec{r}(\psi_k, \zeta_{i-1})$ to $\vec{r}(\psi_k, \zeta_i)$ at a collocation point at $\vec{r}(\psi_k, \zeta_l)$. The net induced velocity at this collocation point is found by integrating along the length of each vortex filament extending from the blade tip to, ideally, infinity. The induced velocity can be further divided into two parts as

$$\vec{V}_{\text{ind}}(\psi_k, \zeta_l) = \underbrace{\sum_{i=1}^{l} \vec{V}_{\text{BS}}(\psi_k, \zeta_l; \zeta_i)}_{\text{younger vortex elements}} + \underbrace{\sum_{i=l}^{\infty} \vec{V}_{\text{BS}}(\psi_k, \zeta_l; \zeta_i)}_{\text{older vortex elements}} \tag{5.3}$$

The force-free equilibrium position of each vortex segment collocation point located at $\vec{r}(\psi_k, \zeta_k)$ is given by an equilibrium between these two components of the induced velocity. To illustrate this effect, a representative hovering wake geometry is shown in Fig. E.2. When the point $\vec{r}(\psi_k, \zeta_k)$ is in equilibrium (or steady state condition), the net velocity induced at that point is directed along the vortex filament trajectory. All the 'younger' vortex elements, i.e., $\zeta_i < \zeta_l$, induce a velocity at the point $\vec{r}(\psi_k, \zeta_k)$, which is directed radially outward. However, all the 'older' vortex elements, i.e., $\zeta_i > \zeta_l$ induce a radially inward velocity. Therefore, the vortex element at $\vec{r}(\psi_k, \zeta_k)$ remains in equilibrium.

If the wake is truncated at $\zeta_{\max}$, then only one part of the induced velocity is affected. The above equation (Eq. 5.3) can be rewritten to identify the velocity terms that are being neglected because of this wake truncation, this gives

$$\vec{V}_{\text{ind}}(\psi_k, \zeta_l) = \underbrace{\sum_{i=1}^{l} \vec{V}_{\text{BS}}(\psi_k, \zeta_l; \zeta_i)}_{\text{younger}} + \underbrace{\sum_{i=l}^{l_{\max}} \vec{V}_{\text{BS}}(\psi_k, \zeta_l; \zeta_i)}_{\text{older}} + \underbrace{\sum_{i=l_{\max}}^{\infty} \vec{V}_{\text{BS}}(\psi_k, \zeta_l; \zeta_i)}_{\text{wake truncation}} \tag{5.4}$$

Clearly, when the point $\vec{r}(\psi_k, \zeta_l)$ is close to the wake-truncation region, i.e., ζ_l is close to $\zeta_{\max}$, the equilibrium position of the collocation point would be significantly disturbed because of truncation. In Fig. E.2, if the wake was truncated near $\vec{r}(\psi_k, \zeta_l)$, then that part of the wake would exhibit radial expansion, which is not physically correct. Therefore, a far-wake boundary condition will be required to correctly represent the induced velocities.

An example of a non-physical wake expansion because of incorrect representation of induced velocities is shown in Fig. E.3. A solution was obtained using a large number (> 20) of wake turns, and is compared with experimental measurements of the hovering wake boundary from Ref. 72. Notice that for more that 20 free-wake turns, the wake geometry within two rotor radii below the rotor remained independent

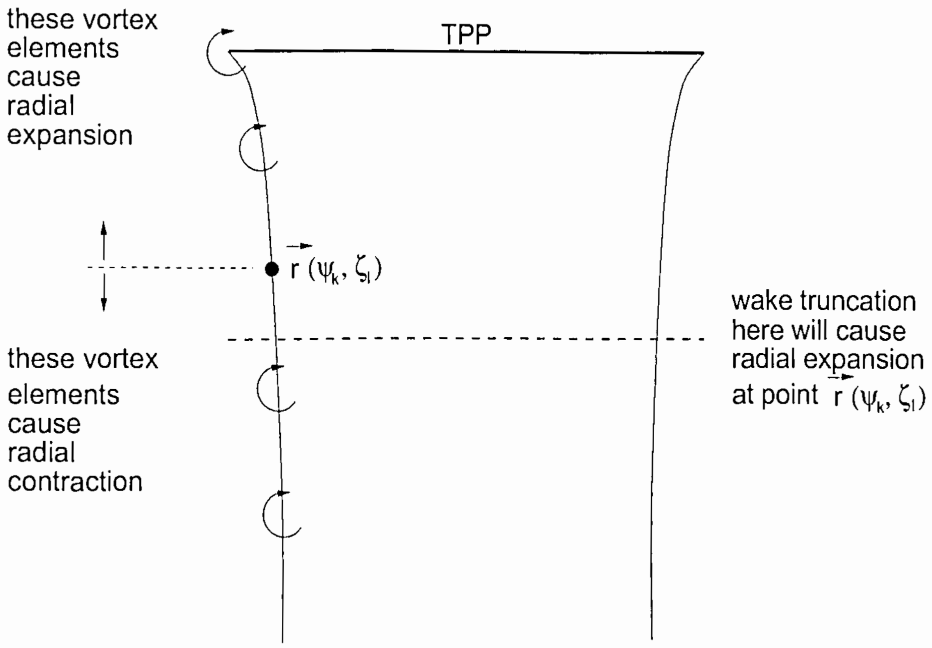

Figure E.2: Schematic of hovering rotor wake geometry explaining the effect of wake truncation on the wake

of the total number of free turns. Therefore, such a large number of wake turns this may be considered representive of a wake extending to infinity below the rotor. In the case of wake truncation after four turns, notice that there is clearly a (non-physical) radial expansion. This radial expansion is purely of numerical origin, resulting from the wake truncation alone. A slight radial expansion of hovering wake is observed in experiments (Ref. 66), which is because of the viscous diffusion of tip vortices and the corresponding reduction in induced velocities. However, such an expansion resulting from viscous diffusion of the vortices is much smaller than the numerical effects associated with wake truncation. Clearly, the wake truncation with four free turns of the wake does not give satisfactory predictions of the wake geometry.

Note that in forward or axial (vertical) flight, with higher freestream effective convection velocities, such a truncation boundary condition may not be required. This is

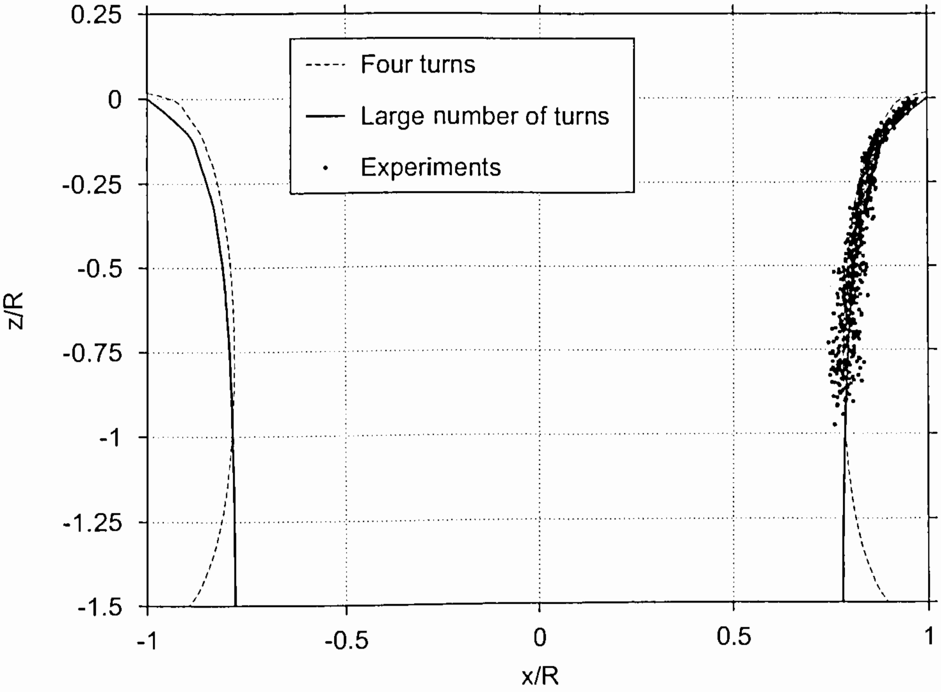

Figure E.3: Numerical solutions to the hovering rotor wake showing non-physical expansion because of wake truncation in the far-wake. Experimental results from Ref. 72

because the *relative* errors introduced by truncation are small, i.e.,

$$\begin{array}{c}\text{relative velocity errors}\\ \text{due to truncation}\end{array} = \frac{\sum_{i=I_{\max}}^{\infty} \vec{V}_{\text{BS}}(\psi_k, \zeta_l; \zeta_i)}{\vec{V}_{\text{freestream}} + \sum_{i=1}^{\infty} \vec{V}_{\text{BS}}(\psi_k, \zeta_l; \zeta_i)} \tag{5.5}$$

Clearly, the relative errors in the velocity calculations decrease with increasing freestream convection velocity. Therefore, a far-wake boundary condition may not be necessary for high-speed forward flight conditions. However, in near hovering flight conditions, the far-wake boundary condition is especially important.

There are several approaches that can be used to prescribe a boundary condition in the far-wake of a hovering rotor. One approach is to prescribe an semi-infinite cylinder of vorticity below the free-vortex wake to model the wake extending to infinity. The induced velocity by such a cylinder can be calculated analytically (Refs. 160 & 161). The strength and radius of the cylinder could be determined from the wake solution – see Refs. 38 & 39. Another variation would be to use a stack of vortex rings to numerically model these extra wake turns (e.g., Refs. 162 & 47). However, these approaches are only applicable to hovering flight and extension to other flight conditions is mathematically formidable. Another approach would be to use prescribed wake geometry for the wake beyond a specified number of free turns (e.g., Ref. 25). With the development of several empirical prescribed wake models, this approach is suitable for many steady state flight conditions. For time-accurate calculations, however, such a prescribed boundary condition may be unsuitable.

Another 'engineering' solution to this boundary condition problem is to use a finite number turns in the numerical solution and neglect the last one or two turns which are most affected because of wake truncation. The approach followed in Ref. 36 was to extrapolate the last two free wake turns to obtain a number of additional turns of the wake to simulate a boundary condition wake. In the present analysis, a far-wake boundary condition was developed along similar lines, which would be applicable to all flight conditions. Also, the same boundary condition could be used for both steady-state and time-accurate solution algorithms. The key feature of the present approach that a velocity field extrapolation technique is used instead of simple geometric wake extrapolation.

Figure E.4 shows a schematic of the rotor wake in hovering and forward flight, which can be used to explain the idea of velocity field extrapolation. The free-vortex solution is solved up to N wake turns. However, more wake turns are specified as a boundary condition. For sufficiently large N, it is reasonable to assume that the induced velocity field experienced by the $N+1^{\text{th}}$ turns is the same as that of the N^{th} turn. In general, experimental observations suggest that the rotor wake geometry shows an asymptotic behavior after four or five turns (revolutions) below the rotor.

To extrapolate the induced velocity field, the free-vortex wake is calculated up to, say, a wake age of ζ_F. For collocation points older than ζ_F, the velocity field is not explicitly calculated, but extrapolated along the characteristic, $\mathrm{d}\psi/\mathrm{d}\zeta = 1$. Therefore, this gives

$$\vec{V}(\psi_k, \zeta_i) - \vec{V}(\psi_k - \Delta\psi, \zeta_i - \Delta\zeta) = \vec{V}(\psi_k, \zeta_i - 2\pi) - \vec{V}(\psi_k - \Delta\psi, \zeta_i - 2\pi - \Delta\zeta) \tag{5.6}$$

where an equal discretization ($\Delta\psi = \Delta\zeta$) has been assumed. Therefore, the velocity field for the boundary condition turns of the rotor wake can be calculated based on the free-vortex wake solution. Recall that the solution methodology calculates the velocity at the grid mid-points to update the position vectors of the wake collocation points. This is done for both the time-marching and the relaxation methods. With the central difference PCC scheme (see Section 3.2.2), the equation may be written in the form

$$\begin{aligned} \frac{\vec{r}(\psi_k, \zeta_i) - \vec{r}(\psi_k - \Delta\psi, \zeta_i - \Delta\zeta)}{\Delta\psi} &= \frac{1}{4}\Big[\vec{V}(\psi_k - \Delta\psi, \zeta_i - \Delta\zeta) + \vec{V}(\psi_k - \Delta\psi, \zeta_i) \\ &\quad + \vec{V}(\psi_k, \zeta_i - \Delta\zeta) + \vec{V}(\psi_k, \zeta_i)\Big] \\ &\approx \vec{V}(\psi_k - \Delta\psi/2, \zeta_i - \Delta\zeta/2) \end{aligned} \tag{5.7}$$

Using the extrapolated boundary condition for the induced velocities, the collocation points on the boundary condition turns become

$$\vec{V}(\psi_k - \Delta\psi/2, \zeta_i - \Delta\zeta/2) = \vec{V}(\psi_k - \Delta\psi/2, \zeta_i - \Delta\zeta/2 - 2\pi) \tag{5.8}$$

therefore,

$$\frac{\vec{r}(\psi_k, \zeta_i) - \vec{r}(\psi_k - \Delta\psi, \zeta_i - \Delta\zeta)}{\Delta\zeta} = \frac{\vec{r}(\psi_k, \zeta_i - 2\pi) - \vec{r}(\psi_k - \Delta\psi, \zeta_i - \Delta\zeta - 2\pi)}{\Delta\zeta} \tag{5.9}$$

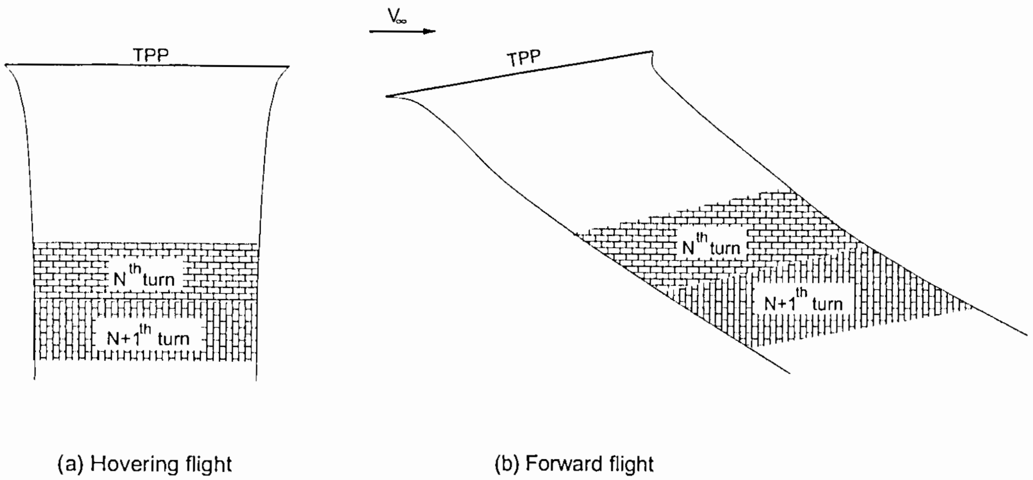

(a) Hovering flight (b) Forward flight

Figure E.4: Schematic explaining the philosophy behind the extrapolation boundary condition for the rotor far wake. The wake geometry in hover and forward flight is shown to bring out the similarities between two consecutive wake turns.

Now, the wake collocation points for the boundary condition turns can be readily calculated from the free wake turns as obtained using a solution step.

An example of the numerical solutions for the rotor wake obtained using this far-field boundary condition is shown in Fig. E.5(a). Here a numerical solution obtained using four turns of free wake with two equivalent turns as a boundary condition is shown along with a solution obtained using a very large number of turns. This shows that the boundary condition mimics the force free behavior of the wake very well. The two solutions showed only small differences in the far-wake. Therefore, it is expected that the blade loads and rotor performance will not be affected by the wake truncation boundary condition. Figure E.5(b) shows the radial distribution of the blade bound circulation, which shows that by using four turns of the free wake and the boundary condition, the results obtained are essentially identical to those obtained using a large number of free turns. This approach is also preferable because the associated computational cost is significantly lower than that for the solution with a large number of free wake turns.

In forward flight, the freestream convection velocity dominates over the vortex induced velocities and the effects of the far-wake boundary are even smaller. This is shown in Fig. E.6(a) in the form of a plan view of the wake geometry obtained using four free wake turns along with that obtained using two free turns and two boundary condition turns. The differences between the two solutions are very small and the corresponding blade bound circulation distributions are almost identical.

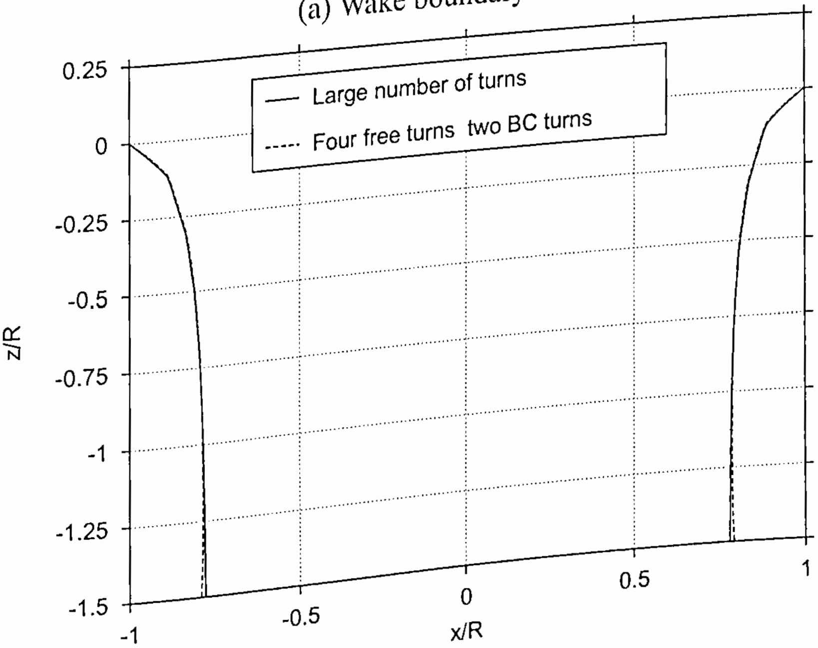
(a) Wake boundary

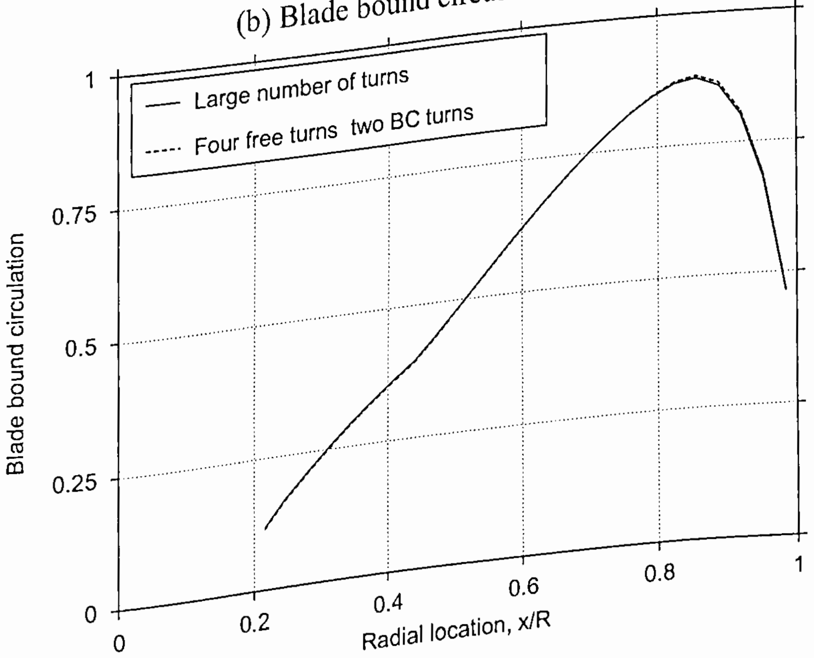
(b) Blade bound circulation

Figure E.5: Example showing the effect of the velocity field extrapolation boundary condition on the wake geometry solution in hover. (a) Wake boundary, (b) Blade bound circulation.

(a) Wake boundary

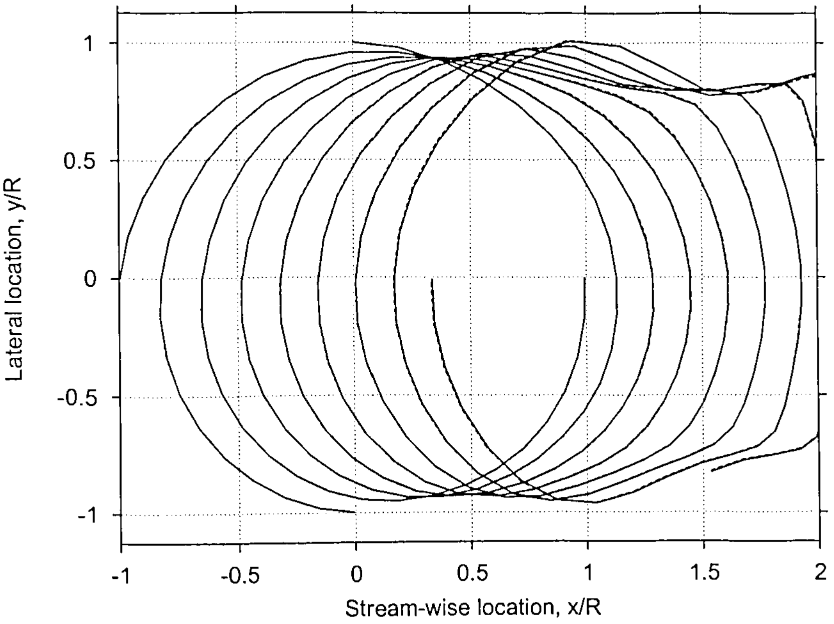

(b) Blade bound circulation

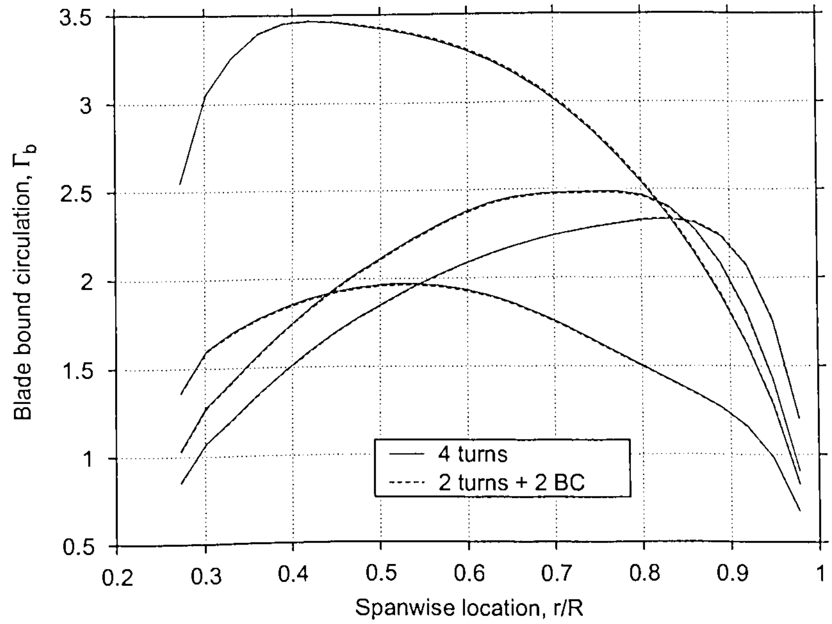

Figure E.6: Example showing the effect of the velocity field extrapolation boundary condition on the wake geometry solution in forward flight. (a) Wake boundary, (b) Blade bound circulation.

Appendix F

Empirical Model for Airfoil Characteristics

The non-linear behavior in airfoil lift/drag characteristics near blade stall is modeled using the Beddoes model (Ref. 163). In this case, a modified form of Kirchoff/Helmholtz solution for the lift on a flat plate with a fixed separation point if used. The lift or normal force component is related to the flow separation point, and is approximated by

$$C_n = 2\pi \left(\frac{1+\sqrt{f}}{2} \right)^2 \alpha \tag{6.1}$$

where 2π is the normal force (lift-curve) slope based on potential flow, and f is the trailing edge separation point as a fraction of the chord – see Thwaites (Ref. 164). Compressibility and viscous corrections can be included by replacing 2π by the appropriate lift-curve slope for a given Mach and Reynolds number. In the present analysis, compressibility effects are modeled using the Prandtl-Glauert correction factor, $\beta = \sqrt{1-M^2}$, as

$$C_n = \frac{2\pi}{\sqrt{1-M^2}} \left(\frac{1+\sqrt{f}}{2} \right)^2 \alpha \tag{6.2}$$

Alternatively the Kaplan rule (Ref. 165), which is an extension of the Prandtl-Glauert correction to include airfoil thickness effects (see also Ref. 166), can be employed as

$$\frac{C_{n_\alpha}}{2\pi} = \frac{1}{\sqrt{1-M^2}} + \frac{(t/c)}{1+(t/c)}\left[\frac{1}{\sqrt{1-M^2}}\left(\frac{1}{\sqrt{1-M^2}}-1\right)+\frac{1}{4}(\gamma+1.0)\left(\frac{1}{1-M^2}-1\right)^2\right] \tag{6.3}$$

where γ is the ratio of specific heats.

In general, the relationship between the separation point f, and the operating angle of attack, α, can be deduced from experimental measurements of static C_n variation with angle of attack. In the present analysis, a generalized empirical model for f is used, as suggested by Beddoes (Ref. 163). This is given by

$$f = \begin{cases} 1-0.3\exp\left(\frac{(\alpha-\alpha_0)-\alpha_1}{S_1}\right) & \text{for } \alpha \le \alpha_1 \\ 0.04+0.66\exp\left(\frac{\alpha_1-(\alpha-\alpha_0)}{S_2}\right) & \text{for } \alpha > \alpha_1 \end{cases} \tag{6.4}$$

where α_0 is the zero-lift angle of attack of the airfoil. The exponents S_1 and S_2 define the static stall characteristics, i.e., whether the stall is progressive of abrupt depending on the flow Mach number. The angle of attack α_1 represents the break point corresponding to $f = 0.7$. Beddoes presents results for these parameters deduced from static measurements on a NACA 0012 airfoil. In the present case, a continuous model is introduced to represent these parameters as a function of Mach number. The empirical model is given by

$$S_1(M) = 1.8\exp\left(-\left(\frac{(M-0.45)}{0.3}\right)^2\right) \tag{6.5}$$

$$S_2(M) = 3.6\exp\left(-\left(\frac{(M-0.525)}{0.25}\right)^2\right) \tag{6.6}$$

$$\alpha_1(M) = 21.5-25M+2.0\exp\left(-\left(\frac{(M-0.65)}{0.125}\right)^2\right) \quad \text{(deg)} \tag{6.7}$$

The results obtained using the above model for the parameters is shown in Figure F.1, along with the empirical results deduced from experimental measurements for the

NACA 0012 airfoil. The advantage of using such a continuous model is that no interpolation is necessary to establish these parameters at arbitrary Mach numbers.

Now, the lift coefficient can be determined from the local angle of attack, α, as

$$C_l(\alpha) = \frac{2\pi}{\sqrt{1-M^2}}\left(\frac{1+\sqrt{f}}{2}\right)^2 \alpha\cos\alpha \tag{6.8}$$

The model for local drag coefficient is based on the same concepts as the lift model. In this case, the additional parameters required are the zero lift drag coefficient, C_{d_0} and the drag divergence angle of attack, α_{DD}. These parameters are given as a function of Mach number as

$$\begin{aligned} C_{d_0}(M) &= 0.01 + 0.002\mathrm{erf}(50(M-0.8)) && (6.9) \\ \alpha_{DD}(M) &= 16.0 - 20M + 0.5\exp\left(-\left(\frac{M-0.6}{0.125}\right)^2\right) \quad (\mathrm{deg}) && (6.10) \end{aligned}$$

The drag coefficient is given by

$$C_d = C_{d_0} + 0.035C_n\sin\alpha + K_D C_n \sin(\alpha - \alpha_{DD}) \tag{6.11}$$

where the factor K_D is given by

$$K_D = \begin{cases} 0 & \alpha \le \alpha_{DD} \\ 2.7\exp(-d_f f) & \alpha > \alpha_{DD} \end{cases} \tag{6.12}$$

and the factor d_f is given by

$$d_f = 6.1 - 7M + 0.5\exp\left(-\left(\frac{M-0.6}{0.125}\right)^2\right) \tag{6.13}$$

These parameters in the drag model are shown in Fig. F.2 along with the values deduced from experimental measurements. The results for the blade lift coefficient obtained using the model described above are shown in Fig. F.3 for four different local Mach numbers. Figure F.4 shows the corresponding results for drag coefficients as a function of angle of attack.

(a) Lift curve slope

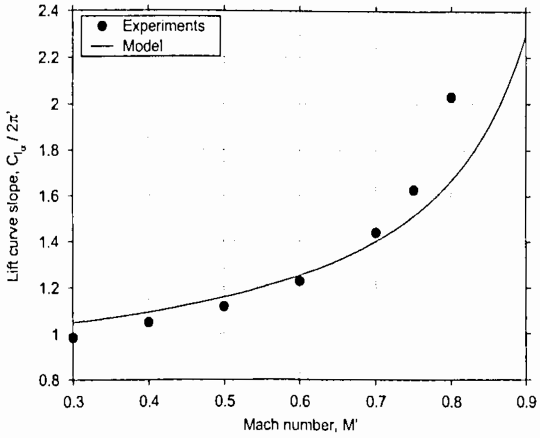

(b) Stall angle of attack, α_1

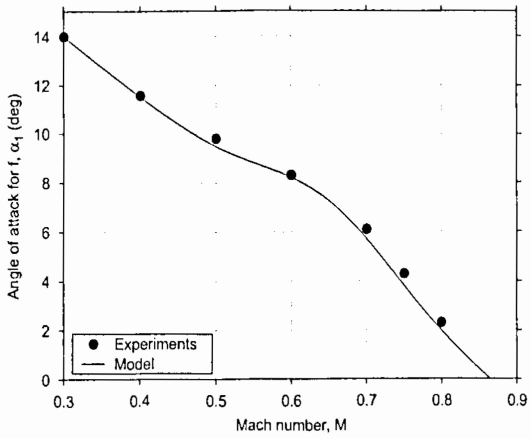

(c) Exponents S_1 and S_2

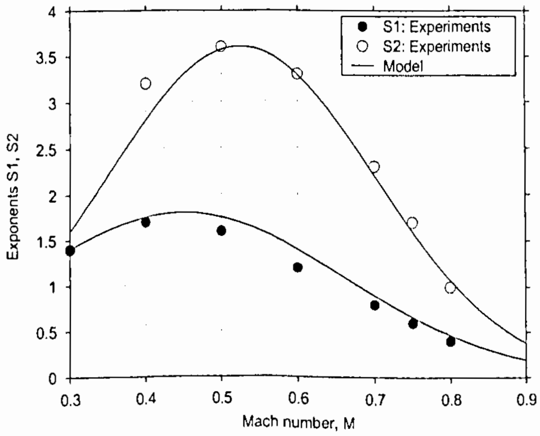

Figure F.1: Parameters for the lift model, (a) Lift curve slope, (b) Stall angle, α_1, (c) Exponents S_1 and S_2.

(a) Zero-lift drag coefficient C_{d_0}

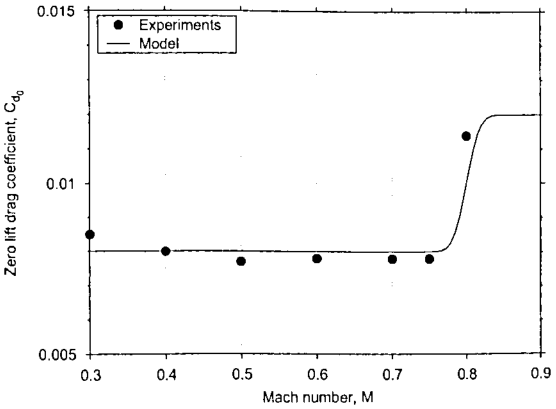

(b) Drag divergence angle of attack, α_{DD}

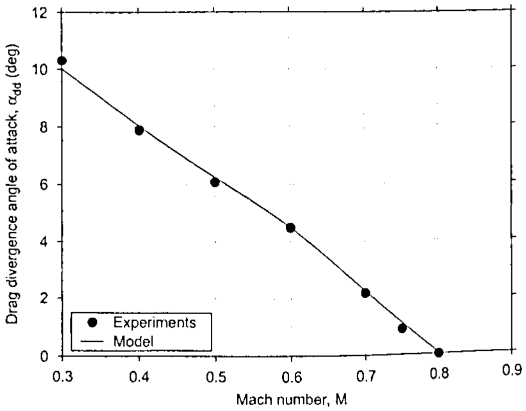

(c) Exponent factor, d_f

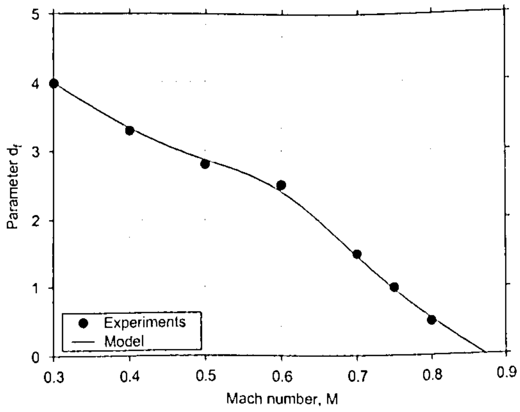

Figure F.2: Parameters defining the airfoil drag model. (a) Zero-lift drag coefficient, C_{d_0} (b) Drag divergence angle of attack, α_{DD}, and (c) Exponent factor, d_f

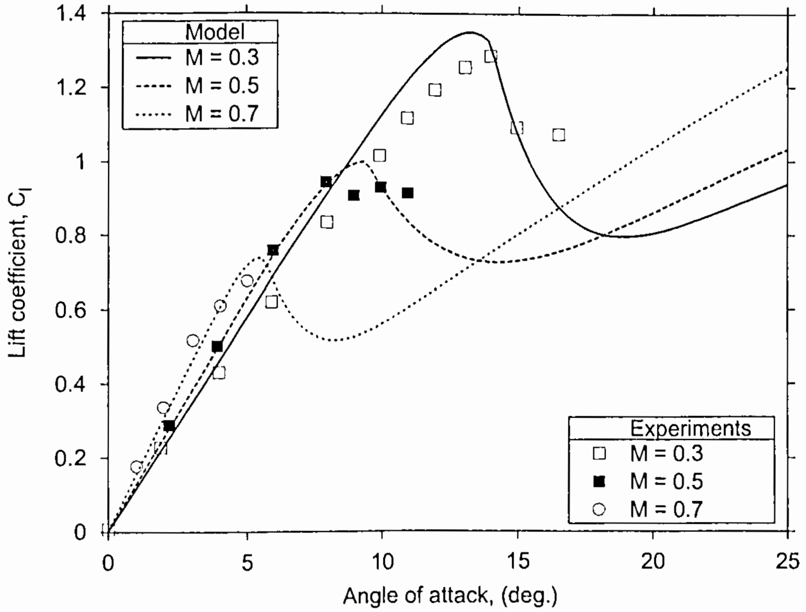

Figure F.3: Lift coefficient based on the empirical non-linear lift model as suggested by Beddoes (Ref. 163).

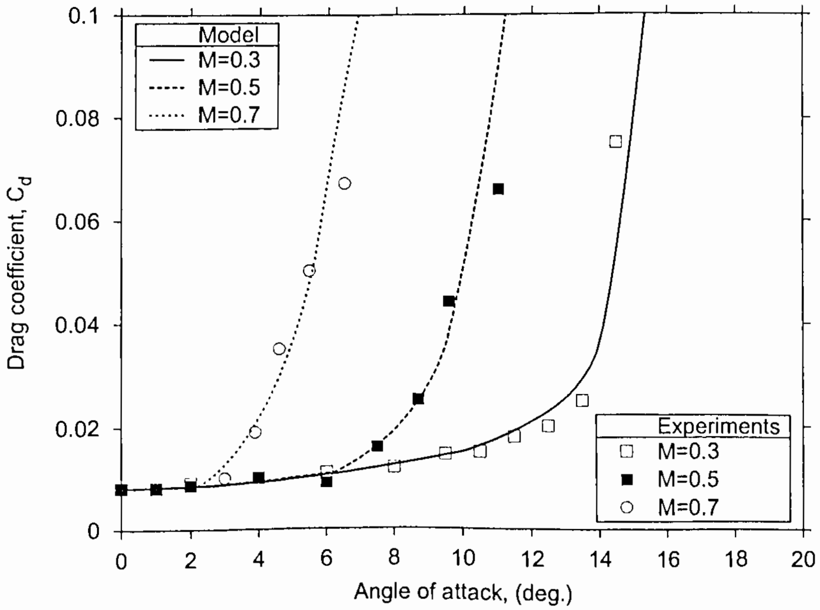

Figure F.4: Drag coefficient based on the empirical non-linear airfoil model as suggested by Beddoes (Ref. 163).

F.1 Effects on Rotor Performance Prediction

A linear aerodynamics model for the airfoil lift characteristics, based on thin airfoil theory provides acceptable predictions of rotor thrust at low to moderate thrust levels. However, at hight thrust values may lead to unrealistic performance trends at high rotor thrusts because of the lack of modeling airfoil stall. If the rotor collective pitch is increased, using linear aerodynamics the rotor thrust would also increase correspondingly. In reality, the rotor thrust reaches a maximum value when the blades begin to stall, typically on the inboard sections near the root. A further increase in collective pitch would then not result in higher thrust, but may, in fact, result in loss of thrust if the stall propagates outward along the entire blade span. The inclusion of Beddoes model into the present free-vortex wake analysis allows a relatively simple prediction of this behavior. An example of this is shown in Fig. F.5 where the rotor thrust is plotted as a function of collective pitch. Corresponding results obtained using a linear aerodynamics model (thin airfoil theory) are also shown for comparison. In this case, the thrust varies almost linearly with the blade collective pitch as expected. The use of Beddoes model, however, shows blade stall effects in the form of diminishing thrust at high collective pitch inputs.

Figure F.6 shows the corresponding rotor shaft power plotted versus the rotor thrust. With the onset of stall, the rotor thrust was found to remain almost constant with increasing collective pitch, as shown in Fig. F.5. However, the onset of blade lift stall also results in rapid increase in sectional drag. This resulted in a significant increase in rotor power because of stall. The rotor power calculated based on linear aerodynamics is also shown to bring out the effects of blade stall modeling.

An example of the sectional lift distribution along the blade span is shown in Fig. F.7. With a linear aerodynamics model, the inboard sections of the blade were

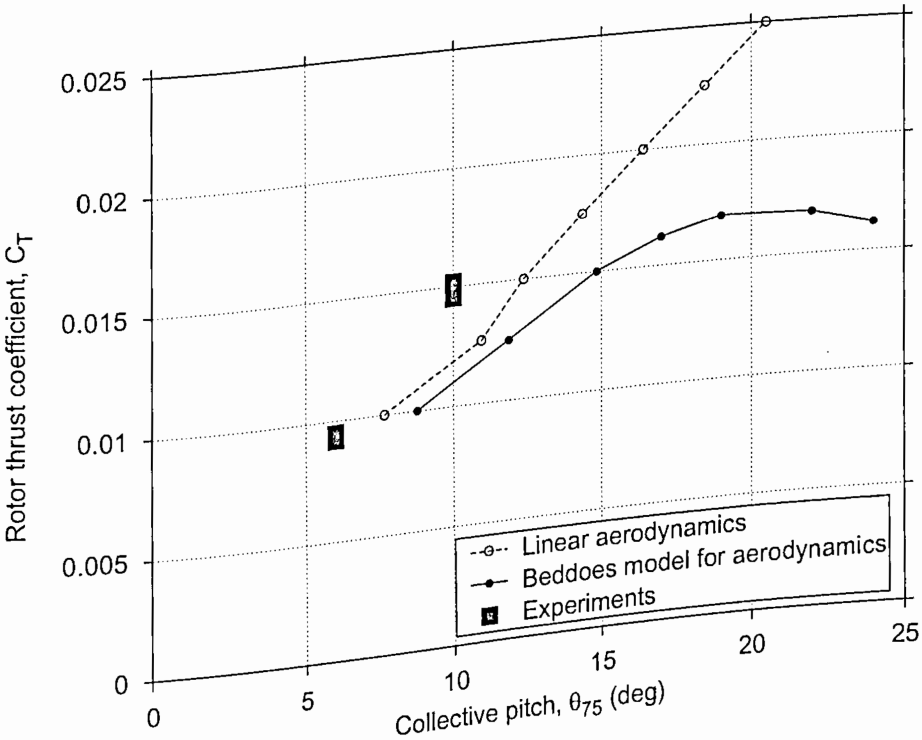

Figure F.5: Predicted values of rotor thrust for increasing collective pitch using Beddoes model with the present free-vortex wake analysis.

found to operate at significantly high values of C_l. This is because, at the inboard sections the effective sectional angle of attack is very high. Inclusion of Beddoes model, improves the predictions of lift distribution by including effects of blade stall on the inboard sections, as shown for the case of $\theta_0 = 58°$. The lift is somewhat more biased towards the blade tips than the lift distribution corresponding to linear aerodynamics. At a higher collective angle of 65°, the blade stall spreads outboard from the root end of the blades towards the tips. The lift in this case is strongly biased towards the blade tip. A further increase in collective pitch would lead to a complete blade stall, and a loss of rotor thrust. This type of non-linear aerodynamic model for airfoil characteristics is especially important for rotor performance prediction in descents and autorotation.

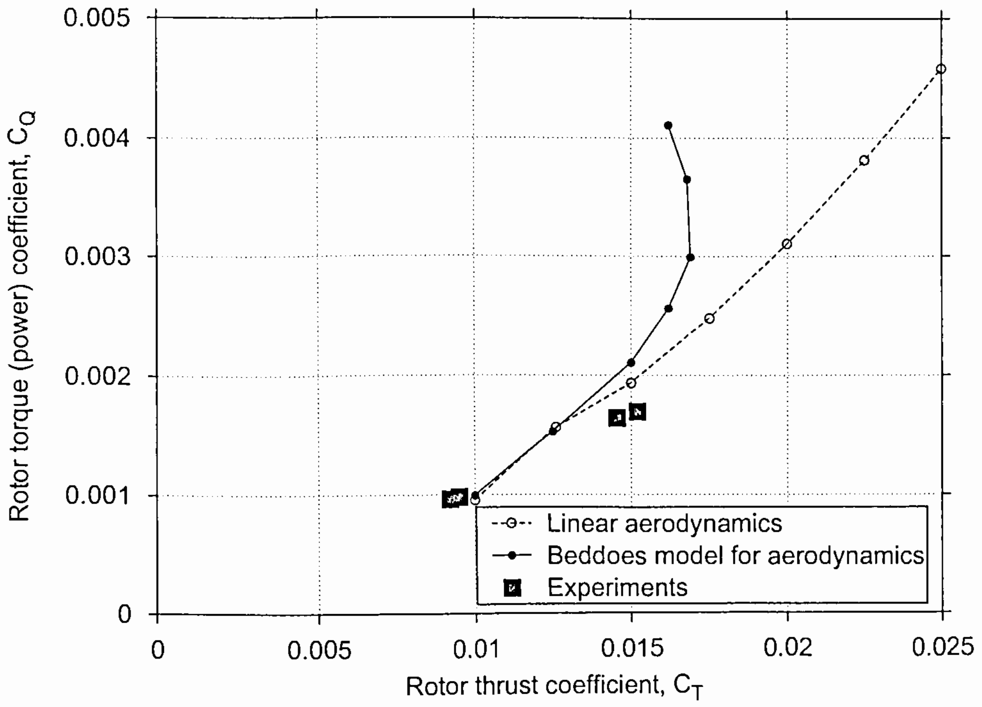

Figure F.6: Predicted values of rotor thrust and power using Beddoes model with the present free-vortex wake analysis.

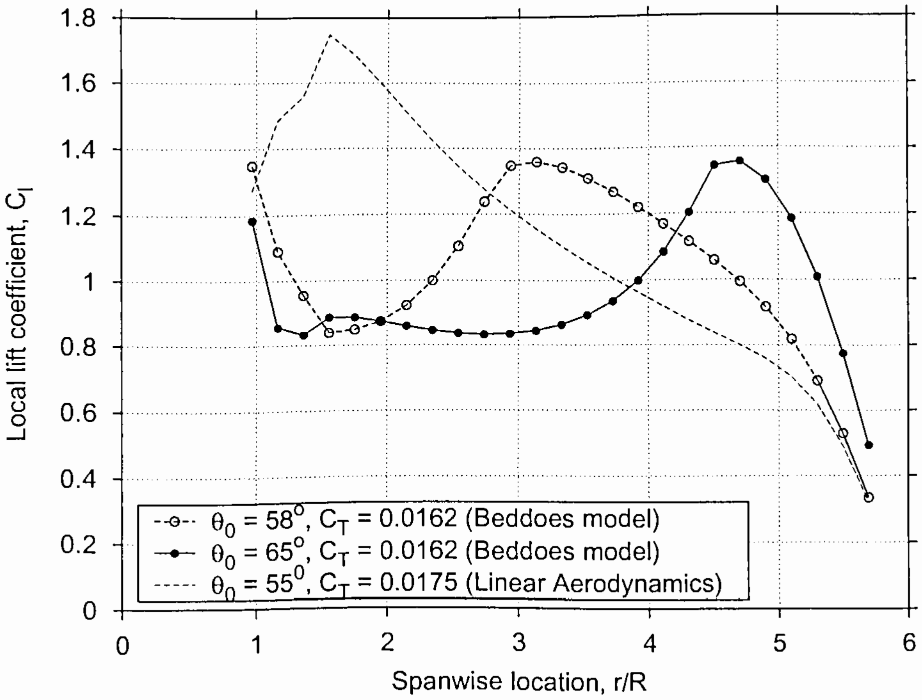

Figure F.7: Spanwise lift distribution with blade stall predicted using Beddoes model with the present free-vortex wake analysis.

References

[1] Sikorsky, I. I., *The Story of the Winged-S: An Autobiography,* Dodd, Mead & Co., New York, NY, 1938.

[2] Leishman, J. G., *Principles of Helicopter Aerodynamics,* Cambridge University Press, New York, 2000.

[3] Durand, W. F., *Aerodynamic Theory*, Vol. IV Julius Springer, Berlin, Germany, 1934.

[4] Goldstein, L., "On the Vortex Theory of Screw Propellers," Proceedings of the Royal Society, 1929, Vol. 123, No. 792 of *A*, p. 440.

[5] Lock, C. N. H., "Application of Goldstein's Theory to the Practical Design of Airscrews," British ARC R & M No. 1377, 1931.

[6] Piziali, R., and DuWaldt, F., "Computation of Rotary Wing Harmonic Airloads and Comparison with Experimental Results," American Helicopter Society 18^{th} Annual National Forum, Washington, DC, 1962.

[7] Truesdell, C., *The Kinematics of Vorticity,* Indiana Univ. Press, Bloomington, IN, 1954, Ch. II, pp. 82–88.

[8] Batchelor, G. K., *An Introduction to Fluid Dynamics,* Cambridge University Press, Cambridge, UK, 1967.

[9] Karamcheti, K., *Principles of Ideal-Fluid Aerodynamics,* John Wiley & Sons, Inc., New York, 1966.

[10] Crimi, P., "Theoretical Prediction of the Flow in the Wake of a Helicopter Rotor," Cornell Aeronautical Laboratory Report BB-1994-5-1, Buffalo NY, September 1965.

[11] Scully, M. P., "A Method of Computing Helicopter Vortex Wake Distortion," Massachusetts Institute of Technology Report No. ASRL TR 138-1, June 1967.

[12] Landgrebe, A. J., "An Analytical Method for Predicting Rotor Wake Geometry," Presented at the AIAA/AHS VTOL Research, Design & Operations Meeting, Atlanta, GA, February 1969.

[13] Landgrebe, A. J., "The Wake Geometry of a Hovering Rotor and its Influence on Rotor Performance," *Journal of the American Helicopter Society*, Vol. 17, No. 4, October 1972, pp. 2–15.

[14] Tangler, J. L., Wohlfeld, R. M., and Miley, S. J., "An Experimental Investigation of Vortex Stability, Tip Shapes, Compressibility, and Noise for Hovering Model Rotors," NASA CR-2305, September 1973.

[15] Anonymous "Evaluation of Blade Tip Planform Effects on Hover Performance," Analytical Methods Inc. Report No. 7908, November 1979.

[16] Kocurek, J. D., and Tangler, J. L., "A Prescribed Wake Lifting Surface Hover Performance Analysis," *Journal of the American Helicopter Society*, Vol. 22, No. 1, January 1977, pp. 24–35.

[17] Kocurek, J. D., and Berkovitz, L. F., "Velocity Coupling: A New Concept for Hover and Axial Flow Wake Analysis and Design," AGARD CP-334, May 1982.

[18] Egolf, T. A., and Landgrebe, A. J., "Helicopter Rotor Wake Geometry and its Influence in Forward Flight, Vol. 1 — Generalized Wake Geometry and Wake Effects in Rotor Airloads and Performance," NASA CR-3726, October 1983.

[19] Beddoes, T. S., "A Wake Model for High Resolution Airloads," Proceedings of the 2^{nd} International Conference on Basic Rotorcraft Research, Triangle Park, NC, 1985.

[20] Mil, M. L., Nekrasov, A. V., Braverman, A. S., and Grodko, L. N. Leykand, M. A., "Helicopters Calculation and Design, Vol. I, Aerodynamics," NASA TT F-492, September 1967.

[21] Baskin, V. E., Vil'dgrube, L. S., Vozhdayev, Y. S., and Maykapar, G. I., "Theory of the Lifting Airscrew," NASA TT F-823, February 1973.

[22] Clark, D. R., and Leiper, A. C., "The Free Wake Analysis – A Method for Prediction of Helicopter Rotor Hovering Performance," *Journal of the American Helicopter Society*, Vol. 15, No. 1, January 1970, pp. 3–11 Also presented at the American Helicopter Society 25th Annual Forum, May 1969.

[23] Scully, M. P., "Computation of Helicopter Rotor Wake Geometry and Its Influence on Rotor Harmonic Airloads," Massachusetts Institute of Technology Report No. ASRL TR 178-1, March 1975.

[24] Jenney, D. S., Olson, J. R., and John, L. A., "A Reassessment of Rotor Hovering Performance Prediction Methods," *Journal of the American Helicopter Society*, Vol. 13, No. 2, April 1968, pp. 1–26.

[25] Sadler, S. G., "A Method for Predicting Helicopter Wake Geometry, Wake-Induced Inflow and Wake Effects on Blade Airloads," American Helicopter Society 27^{th} Annual National Forum, Washington, DC, May 1971.

[26] Sadler, S. G., "Main Rotor Free Wake Geometry Effects on Blade Air Loads and Response for Helicopters in Steady Maneuvers, Vol. 1 – Theoretical Formulation and Analysis of Results," NASA CR-2110, September 1972.

[27] Bliss, D. B., Teske, M. E., and Quackenbush, T. R., "A New Methodology for Free Wake Analysis using Curved Vortex Elements," NASA CR-3958, December 1987.

[28] Bliss, D. B., Dadone, L., and Wachspress, D. A., "Rotor Wake Modeling for High Speed Applications," American Helicopter Society 43^{th} Annual National Forum, St. Louis, MO, May 18–20 1987.

[29] Quackenbush, T. R., Lam, C. M. G., Wachspress, D. A., and Bliss, D. B., "Analysis of High Resolution Unsteady Airloads for Helicopter Rotor Blades," American Helicopter Society 50^{th} Annual National Forum, Washington, DC, May 11–13 1994.

[30] Berry, J. D., "Prediction of Time-Dependent Fuselage Pressures in the Wake of a Helicopter Rotor," Proceedings of the 2^{nd} International Conference on Basic Rotorcraft Research, Univ. of Maryland, College Park, MD, February 1988.

[31] Berry, J., and Bettschart, N., "Rotor-Fuselage Interaction: Analysis and Validation with Experiment," American Helicopter Society 53^{rd} Annual National Forum, Virginia Beach, VA, April 29–May 1 1997.

[32] Egolf, T. A., and Massar, J. P., "Helicopter Free Wake Implementation on Advanced Computer Architecture," Proceedings of the 2nd International Conference on Rotorcraft Basis Research, College Park, MD, February 1988.

[33] Egolf, T. A., "Rotor Wake Modeling for High Speed Applications," American Helicopter Society 44th Annual National Forum, Washington, DC, June 16–18 1988.

[34] Miller, W. O., and Bliss, D. B., "Direct Periodic Solutions of Rotor Free Wake Calculations," *Journal of the American Helicopter Society*, Vol. 38, No. 2, April 1993, pp. 53–60.

[35] Baron, A., and Boffadosi, M., "Unsteady Free Wake Analysis of Closely Interfering Helicopter Rotors," Nineteenth European Rotorcraft Forum, Cernobbio, Italy, September 14–16 1993.

[36] Soliman, M. M., "A "Force-Free" Rotor Wake Model for Advanced Research Applications," Twenty-Second European Rotorcraft Forum, Brighton, UK, September 17–19 1996.

[37] Lee, D. J., and Na, S. U., "Predictions of Airloads and Wake Geometry for Slowly Starting Rotor Blades in Hovering Flight by using Time Marching Free Vortex Blob Method," American Helicopter Society 52nd Annual National Forum, Washington, DC, June 4–6 1996.

[38] Jain, R., Conlisk, A. T., Mahalingam, R., and Komerath, N. M., "Interaction of Tip-Vortices in the Wake of a Two-Bladed Rotor," American Helicopter Society 54th Annual National Forum, Washington, DC, May 20–22 1998.

[39] Jain, R., and Conlisk, A. T., "Interaction of Tip-Vortices in the Wake of a Two-Bladed Rotor in Axial Flight," *Journal of the American Helicopter Society*, Vol. 45, No. 3, 2000, pp. 157–164.

[40] Caradonna, F., Hendley, E., Silva, M., Huang, S., Komerath, N., Reddy, U., Mahalingam, R., Funk, R., Wong, O., Ames, R., Darden, L., Villareal, L., and Gregory, J., "Performance Measurement and Wake Characteristics of a Model Rotor in Axial Flight," *Journal of the American Helicopter Society*, Vol. 44, No. 2, 1999, pp. 101–108 (Errata, Vol. 44, No. 3).

[41] Chung, K. H., Na, S. U., Jeon, W. H., and Lee, D. J., "A Study on Rotor Tip-Vortex Roll-Up Phenomenon by Using Time-Marching Free-Wake Method," American Helicopter Society 56^{th} Annual National Forum, Virginia Beach, VA, May 2–4 2000.

[42] Johnson, W., "A Comprehensive Analytical Model of Rotorcraft Aerodynamics and Dynamics, Part I: Analytical Development," NASA TM 81182, 1980.

[43] Johnson, W., "Wake Model for Helicopter Rotors in High Speed Flight," NASA CR-1177507, USAVSCOM TR-88-A-008, November 1988.

[44] Johnson, W., "A General Free Wake Geometry Calculation For Wings and Rotors," American Helicopter Society 51^{st} Annual National Forum, Fort Worth, TX, May 9–11 1995.

[45] Miller, R. H., "A Simplified Approach to the Free Wake Analysis of a Hovering Rotor," *Vertica*, Vol. 6, 1982, pp. 89–95.

[46] Weissinger, J., "The Lift Distribution of Swept-Back Wings," NACA TM 1120, 1947.

[47] Bliss, D. B., Quackenbush, T. R., and Bilanin, A. J., "A New Methodology for Helicopter Free-Wake Analyses," American Helicopter Society 39^{th} Annual National Forum, St. Louis, MO, May 9–11 1983.

[48] Bliss, D. B., Washspress, D. A., and Quackenbush, T. R., "A New Approach to the Free Wake Problem for Hovering Rotors," American Helicopter Society 41^{st} Annual National Forum, Fort Worth, TX, May 15–17 1985.

[49] Quackenbush, T. R., Bliss, D. B., Wachspress, D. A., and Ong, C. C., "Free Wake Analysis of Hover Performance Using a New Influence Coefficient Method," NASA CR-4309, July 1990.

[50] Miller, W. O., "A Fast Adaptive Resolution Method for Efficient Free Wake Calculations," American Helicopter Society 49^{th} Annual National Forum, St. Louis, MO, May 19–21 1993.

[51] Anderson, D. A., Tannehill, J. C., and Pletcher, R. H., *Computational Fluid Mechanics and Heat Transfer,* McGraw Hill, New York, 1984.

[52] Bliss, D. B., and Miller, W. O., "Efficient Free Wake Calculations Using Analytical/Numerical Matching," *Journal of the American Helicopter Society*, Vol. 38, No. 2, April 1993, pp. 53–60.

[53] Crouse, Jr., G. L., and Leishman, J. G., "A New Method for Improved Rotor Free Wake Convergence," 31^{st} AIAA Aerospace Sciences Meeting and Exhibit, Reno, NV, January 1993.

[54] Crouse, Jr., G. L., *An Analytical Study of Rotor/Airframe Interactions in Hover and Forward Flight,* PhD thesis, University of Maryland, 1992.

[55] Bagai, A., *Contributions to the Mathematical Modeling of Rotor Flow-Fields using a Pseudo-Implicit Free-Wake Analysis,* PhD thesis, University of Maryland, 1995.

[56] Bagai, A., and Leishman, J. G., "Rotor Free-Wake Modeling Using a Relaxation Technique - Including Comparisons with Experimental Data," *Journal of the American Helicopter Society*, Vol. 40, No. 3, July 1995, pp. 29–41.

[57] Bagai, A., and Leishman, J. G., "Rotor Free-Wake Modeling using a Pseudoimplicit Relaxation Algorithm," *Journal of Aircraft*, Vol. 32, No. 6, Nov.-Dec. 1995, pp. 1276–1285.

[58] Bagai, A., and Leishman, J. G., "Free-Wake Analysis of Tandem, Tilt-Rotor and Coaxial Rotor Configurations," *Journal of the American Helicopter Society*, Vol. 41, No. 3, July 1996, pp. 196–207.

[59] Bagai, A., and Leishman, J. G., "Adaptive Grid Sequencing and Interpolation Schemes for Rotor Free-Wake Analyses," *AIAA Journal*, Vol. 36, No. 9, September 1998, pp. 1593–1602.

[60] Bagai, A., and Leishman, J. G., "The Maryland Free-Wake Analysis: Theory, Implementation & User's Manual," NASA Langley Research Center Report under Contract No. 01-5-2685, 1995.

[61] Bagai, A., and Leishman, J. G., "Computationally Efficient Coding for the MFW Analysis: Theory, Implementation & User's Manual," NASA Langley Research Center Report under Contract No. 01-5-26360, 1997.

[62] Leishman, J. G., and Bagai, A., "Challenges in Understanding the Vortex Dynamics of Helicopter Rotor Wakes," *AIAA Journal*, Vol. 36, No. 7, July 1998, pp. 1130–1140.

[63] Levy, H., and Forsdyke, A. G., "The Steady Motion and Stability of a Helical Vortex," *Proceedings of the Royal Society, Series A*, Vol. 120, 1928.

[64] Widnall, S. E., "The Stability of a Helical Vortex Filament," *Journal of Fluid Mechanics*, Vol. 54, No. 4, 1972, pp. 641–663.

[65] Gupta, B. P., and Loewy, R. G., "Theoretical Analysis of the Aerodynamic Stability of Multiple, Interdigitated Helical Vortices," *AIAA Journal*, Vol. 12, No. 10, October 1974, pp. 1381–1387.

[66] Martin, P. B., Bhagwat, M. J., and Leishman, J. G., "Strobed Laser-Sheet Visualization of a Helicopter Rotor Wake," Paper PF118, Proceedings of PSFVIP-2, Honolulu, HI, May 1999. Also, *Journal of Flow Visualization & Image Processing* (in press).

[67] Leishman, J. G., "On the Aperiodicity of Helicopter Rotor Wakes," *Experiments in Fluids*, Vol. 25, 1998, pp. 352–361.

[68] Miller, W. O., and Bliss, D. B., "Direct Periodic Solutions of Rotor Free Wake Calculations," American Helicopter Society 46^{th} Annual National Forum, Washington, DC, May 21–23 1990.

[69] Quackenbush, T. R., Bliss, D. B., and Wachspress, D. A., "Computational Analysis of Hover Performance using a New Free Wake Method," Proceedings of the 2^{nd} International Conference on Rotorcraft Basis Research, College Park, MD, February 1988.

[70] Lamb, H., *Hydrodynamics*, 6th ed., Cambridge University Press, Cambridge, UK, 1932.

[71] Quackenbush, T. R., Bliss, D. B., and Wachspress, D. A., "New Free Wake Analysis of Rotorcraft Hover Performance Using Influence Coefficients," *Journal of Aircraft*, Vol. 26, No. 12, December 1990, pp. 1090–1097.

[72] Bhagwat, M. J., "On the Relationship Between Rotor Blade Lift and Tip Vortex Characteristics,," M. S. Thesis, University of Maryland, 1998.

[73] Milne-Thomson, L. M., *Theoretical Aerodynamics*, 4th ed., Dover, New York, 1973, Ch. IX, pp. 168–170.

[74] Lee, D. J., and Na, S. U., "Numerical Simulations of Wake Structure Generated by Rotating Blades Using a Time Marching Free Vortex Blob Method," *European Journal of Fluid Mechanics -B/Fluids*, Vol. 17, No. 4, 1998, pp. 1–13.

[75] Quackenbush, T. R., Wachspress, D. A., and Boschitsch, A. H., "Computation of Rotor Aerodynamic Loads with a Constant Vorticity Contour Free Wake Model," AIAA Paper 91-3229, 9th AIAA Applied Aerodynamics Conference, Baltimore, MD, September 1991.

[76] Johnson, W., *Helicopter Theory,* Princeton University Press, 1980.

[77] Bernard, P., "A Vortex Method for Wall Bounded Turbulent Flows," In *Vortex Flows and Related Numerical Methods, II,* Y. Gagnon et al., Eds., Vol. 1. ESAIM Proc., 1997, pp. 15–31.

[78] Saffman, P. G., *Vortex Dynamics,* Cambridge University Press, Cambridge, UK, 1992.

[79] Saffman, P. G., "The Velocity of Viscous Vortex Rings," Aircraft Wake Turbulence and its Detection: Symposium on Aircraft Wake Turbulence, Seattle, WA, Sept. 1970, pp. 9–10.

[80] Heath, M. T., *Scientific Computing: An Introductory Survey,* WCB/McGraw-Hill, New York, 1997.

[81] Conte, S. D., and De Boor, C., *Elementary Numerical Analysis : An Algorithmic Approach,* McGraw-Hill, New York, 1980.

[82] Chapra, S. C., and Canale, R. P., *Numerical Methods for Engineers*, 3rd ed., McGraw-Hill, New York, 1998.

[83] Laney, C. B., *Computational Gasdynamics,* Cambridge University Press, New York, NY, 1998.

[84] LeVeque, R. J., *Numerical Methods for Conservation Laws*, 2nd ed., Basel: BirkHäuser Verlag, 1992.

[85] Bagai, A., and Leishman, J. G., "A Study of Rotor Wake Development and Wake/Body Interactions in Hover," *Journal of the American Helicopter Society*, Vol. 37, No. 4, October 1992, pp. 48–57.

[86] Betz, A., "Behaviour of Vortex Systems," NACA TM 713, 1933.

[87] De Young, J., and Harper, C. W., "Theoretical Symmetric Span Loading at Subsonic Speeds for Wings Having Arbitrary Plan Form," NACA Report 9210, 1948.

[88] Johnson, W., "Recent Developments in Rotary-Wing Aerodynamic Theory," *AIAA Journal*, Vol. 24, No. 8, August 1986, pp. 1219–1245.

[89] Bhagwat, M. J., and Leishman, J. G., "Measurements of Bound and Wake Circulation on a Helicopter Rotor," *Journal of Aircraft*, Vol. 37, No. 2, 2000, pp. 227–234.

[90] Bhagwat, M. J., and Leishman, J. G., "Correlation of Helicopter Tip Vortex Measurements," *AIAA Journal*, Vol. 38, No. 2, February 2000, pp. 301–308.

[91] Elliot, J. W., Althoff, S. L., and Sailey, R. H., "Inflow Measurements Made with a Laser Velocimeter on a Helicopter Model in Forward Flight, Volume I: Rectangular Planform at an Advance Ratio of 0.15," NASA TM 100545, April 1988.

[92] Elliot, J. W., Althoff, S. L., and Sailey, R. H., "Inflow Measurements Made with a Laser Velocimeter on a Helicopter Model in Forward Flight, Volume II: Rectangular Planform at an Advance Ratio of 0.23," NASA TM 100545, April 1988.

[93] Elliot, J. W., Althoff, S. L., and Sailey, R. H., "Inflow Measurements Made with a Laser Velocimeter on a Helicopter Model in Forward Flight, Volume III: Rectangular Planform at an Advance Ratio of 0.30," NASA TM 100545, April 1988.

[94] Ghee, T. A., and Elliott, J. W., "The Wake of a Small-Scale Rotor Model in Forward Flight using Flow Visualization," *Journal of the American Helicopter Society*, Vol. 40, No. 3, July 1995, pp. 52–65.

[95] Althoff, S. L., and Noonan, K. W., "Effect of Blade Planform Variation on a Small-Scale Hovering Rotor," NASA TM 4146, 1990.

[96] Dingeldein, R. C., "Wind Tunnel Studies of the Performance of Multirotor Configurations," NACA TN 3236, 1954.

[97] Stepniewski, W. Z., and Keys, C. N., *Rotary-Wing Aerodynamics,* Dover, New York, NY, 1984.

[98] Carpenter, P. J., and Fridovich, B., "Effect of A Rapid Blade-Pitch Increase on the Thrust and Induced-Velocity Response of a Full-Scale Helicopter Rotor," NACA TN 3044, November 1953.

[99] Munk, M. M., "Some Tables of the Factor of Apparent Additional Mass," NACA TN 197, July 1924.

[100] Ormiston, R. A., and Peters, D. A., "Hingeless Rotor Response with Nonuniform Inflow and Elastic Blade Bending," *Journal of Aircraft*, Vol. 9, No. 10, October 1972, pp. 730–736.

[101] Gaonkar, G. H., and Peters, D. A., "Effectiveness of Current Dynamic Inflow Models in Hover and Forward Flight," *Journal of the American Helicopter Society*, Vol. 31, No. 2, April 1986, pp. 47–57.

[102] Ellenrieder, T. J., and Brinson, P. R., "The Dynamic Induced Velocity Field of a Model Rotor in Hover Conditions," *The Aeronautical Journal*, June/July 1998, pp. 331–335.

[103] Liou, S. G., and Komerath, M., "Measurements around a Rotor Blade Excited in Pitch, Part 1: Dynamic Inflow," *Journal of the American Helicopter Society*, Vol. 39, No. 2, April 1994.

[104] Crews, S. T., Hohenemser, K. H., and Ormiston, R. A., "An Insteady Wake Model for a Hingeless Rotor," *Journal of Aircraft*, Vol. 10, No. 12, December 1973, pp. 758–760.

[105] Rosen, A., and Isser, A., "A New Model for Rotor Dynamics During Pitch and Roll of a Hovering Helicopter," *Journal of the American Helicopter Society*, Vol. 40, No. 3, 1995, pp. 17–28.

[106] Keller, J. D., and Curtiss, H. C., "Modeling the Induced Velocity of a Maneuvering Helicopter," American Helicopter Society 52^{nd} Annual National Forum, Washington, DC, June 4–6 1996.

[107] Barocela, E., Peters, D. A., Kothapalli, K. R., and Prasad, J. V. R., "The Effect of Wake Distortion on Rotor Inflow Gradients and Off-Axis Coupling," AIAA Flight Mechanics Conference Proceedings, San Diego, CA, July 29–31 1997.

[108] Bagai, A., Leishman, J. G., and Park, J., "Aerodynamic Analysis of a Helicopter in Steady Maneuvering Flight Using a Free-Vortex Rotor Wake Model," *Journal of the American Helicopter Society*, Vol. 44, No. 2, April 1999, pp. 109–120.

[109] Theodore, C., and Celi, R., "Flight Dynamic Simulation of Hingeless Rotor Helicopters Including a Maneuvering Free Wake Model," American Helicopter Society 54^{th} Annual National Forum, Washington, DC, May 20–22 1998.

[110] Drees, J. M., and Hendal, W. P., "The Field of Flow Through a Helicopter Rotor Obtained from Wind Tunnel Smoke Tests," Versl. Nat. Luchtvlab, Report A.1205, February 1950. Also, Journal of Aircraft Engineering, Vol. 23, No. 266, pp. 107–111.

[111] Castles, Jr., W., and Gray, R. B., "Empirical Relation between Induced Velocity, Thrust, and Rate of Descent of a Helicopter Rotor as Determined by Wind-Tunnel Tests on Four Model Rotors," NASA TN-2474, October 1951.

[112] Yaggy, P. F., and Mort, K. W., "Wind-Tunnel Tests of Two VTOL Propellers in Descent," NASA TN D-1766, March 1963.

[113] Washizu, K., Azuma, A., Kōo, J., and Oka, T., "Experiments on a Model Helicopter Rotor Operating in the Vortex Ring State," *Journal of Aircraft*, Vol. 3, No. 3, May-June 1966, pp. 225–230.

[114] Brinson, P., and Ellenrieder, T., "Experimental Investigation of Vortex Ring Condition," 24^{th} European Rotorcraft Forum, Marseilles, France, Septembet 15–17 1998.

[115] Wolkovitch, J., "Analytical Prediction of Vortex-Ring Boundaries for Helicopters in Steep Descents," *Journal of the American Helicopter Society*, Vol. 17, No. 3, 1972, pp. 13–19.

[116] Heyson, H. H., "A Momentum Analysis of Helicopters and Autogyros in Inclined Descent, with Comments on Operational Restrictions," NASA TN D-7917, October 1975.

[117] Sarpkaya, T., "Decay of Wake Vortices of Large Aircraft," *AIAA Journal*, Vol. 36, No. 9, September 1998, pp. 1671–1679.

[118] Squire, H. B., "The Growth of a Vortex In Turbulent Flow," *Aeronautical Quarterly*, Vol. 16, August 1965, pp. 302–306.

[119] Dosanjh, D. S., Gasparek, E. P., and Eskinazi, S., "Decay of a Viscous Trailing Vortex," *The Aeronautical Quarterly*, Vol. 3, No. 3, 1962, pp. 167–188.

[120] Owen, P. R., "The Decay of a Turbulent Trailing Vortex," *The Aeronautical Quarterly*, February 1969, pp. 69–78.

[121] Kantha, L. H., "Empirical Model of Transport and Decay of Aircraft Wake Vortices," *Journal of Aircraft*, Vol. 35, No. 4, 1998, pp. 649–652.

[122] Schmitz, F. H., "Rotor Noise," In *Aeroacoustics of Flight Vehicles: Theory and Practice*, Vol. 1. NASA Reference Publication, August 1991, Ch. 2, p. 1258.

[123] Ringler, T. D., George, A. R., and Steele, J. B., "The Study of Blade-Vortex Interaction Sound Generation and Directionality," Proceedings of the AHS Technical Specialists Meeting, Philadelphia, PA, October 1991.

[124] Sheridan, P., and Smith, R., "Interactional Aerodynamics - A New Challenge to Helicopter Technology," American Helicopter Society 35th Annual National Forum, Washington, DC, May 21–23 1979.

[125] Crouse, G. L., Leishman, J. G., and Bi, N., "Theoretical and Experimental Study of Unsteady Rotor/Body Aerodynamic Interactions," *Journal of the American Helicopter Society*, Vol. 37, No. 1, January 1992, pp. 55–65.

[126] Torok, M. S., and Ream, D. T., "Investigation of Empennage Airloads Induced by a Helicopter Main Rotor Wake," American Helicopter Society 49th Annual National Forum, St. Louis, MO, May 19–21 1993.

[127] Landgrebe, A. J., and Bellinger, E. D., "An Investigation of the Quantitative Applicability of Model Helicopter Rotor Wake Patterns Obtained from a Water Tunnel," UARL K910917-23, December 1971.

[128] Tangler, J. L., "Schlieren and Noise Studies of Rotors in Forward Flight," American Helicopter Society 33rd Annual National Forum, Washington, DC, May 9–11 1977.

[129] Leishman, J. G., and Bagai, A., "Rotor Wake Visualization in Low Speed Forward Flight," AIAA Paper 91-3232, AIAA 9th Applied Aerodynamics Conference, Baltimore, MD, June 1991.

[130] Bagai, A., and Leishman, J. G., "Flow Visualization of Compressible Vortex Structures Using Density Gradient Techniques," *Experiments in Fluids*, Vol. 15, 1993, pp. 431–442.

[131] Burgers, J. M., "A Mathematical Model Illustrating the Theory of Turbulence," *Advances in Applied Mechanics*, Vol. 1, 1948, pp. 171–199.

[132] Newman, B. G., "Flow in a Viscous Trailing Vortex," *The Aeronautical Quarterly*, May 1959, pp. 167–188.

[133] Ogawa, A., *Vortex Flow, CRC Series on Fine Particle Science and Technology* CRC Press Inc., 1993.

[134] Scully, M. P., and Sullivan, J. P., "Helicopter Rotor Wake Geometry and Airloads and Development of Laser Doppler Velocimeter for Use in Helicopter Rotor Wakes," Massachusetts Institute of Technology Aerophysics Laboratory Technical Report 183, MIT DSR No. 73032, August 1972.

[135] Kaufmann, W., "Uber die Ausbreitung kreiszlindrischer Wirbel in zahen Flussigkeiten," *Ing. Arch.*, Vol. 31, No. 1, 1962, p. 1.

[136] Vatistas, G. H., Kozel, V., and Mih, W. C., "A Simpler Model for Concentrated Vortices," *Experiments in Fluids*, Vol. 11, 1991, pp. 73–76.

[137] Vatistas, G. H., "New Model for Intense Self-Similar Vortices," *Journal of Propulsion and Power*, Vol. 14, No. 4, 1998, pp. 462–469.

[138] Coyne, A. J., Bhagwat, M. J., and Leishman, J. G., "Investigation into the Rollup and Diffusion of Rotor Tip Vortices using Laser Doppler Velocimetry," American Helicopter Society 53rd Annual National Forum, Virginia Beach, VA, April 29–May 1 1997.

[139] Bhagwat, M. J., and Leishman, J. G., "On the Relationship between the Blade Lift and the Tip Vortex Characteristics," American Helicopter Society 54*th* Annual National Forum, Washington, DC, May 20–22 1998.

[140] Rankine, W. J. M., *Manual of Applied Mechanics,* C. Griffen Co., London, 1858.

[141] Iversen, J. D., "Correlation of Turbulent Trailing Vortex Decay Data," *Journal of Aircraft*, Vol. 13, No. 5, May 1996, pp. 338–342.

[142] Cotel, A. J., and Breidenthal, R. E., "Turbulence Inside a Vortex," *Physics of Fluids*, Vol. 11, No. 10, October 1999, pp. 3026–3029.

[143] Mahalingam, R., and Komerath, N. M., "Measurements of the Near Wake of a Rotor in Forward Flight," AIAA Paper 98-0692, 36*th* Aerospace Sciences Meeting & Exhibit, Reno, NV, January 12–15 1998.

[144] Cook, C. V., "The Structure of the Rotor Blade Tip Vortex," Paper 3, Aerodynamics of Rotary Wings, AGARD CP-111, September 13–15 1972.

[145] McAlister, K. W., "Measurements in the Near Wake of a Hovering Rotor," AIAA Paper 96-1958, 27th AIAA Fluid Dynamic Conference, New Orleans, June 18–20 1996.

[146] Baker, G. R., Barker, S. J., Bofah, K. K., and Saffman, P. G., "Laser Anemometer Measurements of Trailing Vortices in Water," *Journal of Fluid Mechanics*, Vol. 65, 1974, pp. 325–336.

[147] Govindraju, S. P., and Saffman, P. G., "Laser Anemometer Measurements of Trailing Vortices in Water," *Physics of Fluids*, Vol. 14, No. 10, October 1971, pp. 2074–2080.

[148] Jacob, J., Savas, O., and Liepmann, D., "Trailing Vortex Wake Growth Characteristics of a High Aspect Ratio Rectangular Airfoil," *AIAA Journal*, Vol. 35, 1995, p. 275.

[149] Jacob, J., Savas, O., and Liepmann, D., "Experimental Investigation of Forced Wake Vortices on a Rectangular Wing," AIAA Paper 96-2497, 14th AIAA Applied Aerodynamics Conference, New Orleans, LA, June 1996.

[150] Ciffone, D. L., and Orloff, K. L., "Far-Field Wake-Vortex Characteristics of Wings," *Journal of Aircraft*, Vol. 12, No. 5, May 1975, pp. 464–470.

[151] Corsiglia, V. R., Schwind, R. G., and Chigier, N. A., "Rapid Scanning, Three Dimensional Hot Wire Anemometer Surveys of Wing-Tip Vortices," NASA CR-2180, 1973.

[152] McCormick, B. W., Tangler, J. L., and Sherrieb, H. E., "Structure of Trailing Vortices," *Journal of Aircraft*, Vol. 5, No. 3, July 1968, pp. 260–267.

[153] Kraft, C. C., "Flight Measurements of The Velocity Distribution and Persistence of the Trailing Vortices of an Airplane," NACA TN 3377, 1955.

[154] Rose, R., and Dee, W. F., "Airfract Vortex Wake and Their Effects on Aircraft," Aeronautical Research Council Report No. CP-795, 1965.

[155] Takahashi, R. K., and McAlister, K. W., "Preliminary Study of a Wing-Tip Vortex Using Laser Velocimetry," NASA TM 88343, January 1987.

[156] McAlister, K. W., Sculer, C. A., Branum, L., and Wu, J. C., "3-D Wake Measurements Near a Hovering Rotor for Determining Profile and Induced Drag," NASA TP 3577, 1995.

[157] Thompson, T. L., Komerath, N. M., and Gray, R. B., "Visualization and Measurement of the Tip Vortex Core of a Rotor Blade in Hover," *Journal of Aircraft*, Vol. 25, No. 12, December 1988, pp. 1113–1121.

[158] Sullivan, J. P., "An Experimental Investigation of Vortex Rings and Helicopter Rotor Wakes Using a Laser Doppler Velocimeter," Massachusetts Institute of Technology Aerophysics Laboratory Technical Report 183, MIT DSR No. 80038, June 1973.

[159] Heffley, R. K., Jewell, W. F., Lehman, J. M., and van Winkle, R. A., "A Compilation and Analysis of Helicopter Handling Qualities Data, Volume One: Data Compilation," NASA CR-3144, August 1979.

[160] Wood, D. H., and Mayer, C., "Two New Methods for Calculating Velocities Induced by a Constant Diameter Far-Wake," *Journal of Aircraft*, Vol. 28, No. 8, August 1991, pp. 526–531.

[161] Radcliff, T. D., Burggraf, O. R., and Conlisk, A. T., "Axial Core Flow Effects on the Interaction of a Rotor-Tip Vortex with an Airframe," AIAA Paper 97-0658, 35^{th} AIAA Aerospace Sciences Meeting and Exhibit, Reno, NV, January 1997.

[162] Clark, D. R., and Leiper, A. C., "The Free Wake Analysis: A Method for the Prediction of Helicopter Hovering Peformance," American Helicopter Society 25^{th} Annual National Forum, Washington, DC, May 14–16 1969.

[163] Beddoes, T. S., "Representation of Airfoil Behavior," *Vertica*, Vol. 7, No. 2, 1983, pp. 183–197.

[164] Thwaites, B., *Incompressible Aerodynamics,* Oxford Univ. Press, Oxford, UK, 1960, Ch. IV, pp. 168–170.

[165] Kaplan, C., "Effect of Compressibility at High Subsonic Velocities on the Lifting Force Acting on an Elliptic Cylinder," NACA TN 1118, 1946.

[166] Abbott, I. H., and Von Doenhoff, A. E., *Theory of Wing Sections,* Dover, New York, 1959, Ch. 9, pp. 256–257.